A lithological, petrographic and geochemical investigation of the M4 borehole core, Morokweng Impact Structure, South Africa

S'lindile S. Wela

Dissertation submitted to the Faculty of Science,

University of the Witwatersrand, Johannesburg,

in fulfillment of the requirements for the degree of:

MASTER OF SCIENCE

Supervisors: Prof. R.L. Gibson
: Dr. M.A.G. Andreoli

September, 2017

Declaration

I, **S'lindile S. Wela** declare that the thesis entitled: A lithological, petrographic and geochemical investigation of the M4 borehole core, Morokweng Impact Structure, South Africa; is my own work based on the results of the research carried out by me and under supervision of my supervisors. Any significant contribution of other authors or researchers is referenced or acknowledged. This thesis is being submitted for the degree of Master of Science at the University of the Witwatersrand, Johannesburg. It has not been submitted before for any degree or examination at any other University.

(*Signature*)

19th day of September 2017

Abstract

This study investigates the mineralogical, petrographic and geochemical characteristics of target rocks and impact-formed breccias (impactites) intersected by the 368 m long M4 drillcore located 18 km NNW from the estimated centre of the 145 ± 2 Ma, Morokweng impact structure (MIS), South Africa. M4 is the only core from the central parts of the Morokweng impact structure not to intersect fractionated granophyric impact melt directly beneath 35-100 m of Cenozoic Kalahari Group sediments. Instead it intersects highly fractured, cataclased and shocked, crystalline target rocks that are cut by mm- to m-scale melt-matrix breccia and suevite dykes. The target rocks comprise granitic, granodioritic, trondhjemitic and dioritic Archaean gneisses, metadolerite and dolerite. The gneisses and metadolerite show signs of quartz veining and metasomatism linked to localised mylonitic to brittle fault deformation that predated the impact. The suevite and melt-matrix breccia dykes make up ~10% of the core. All rocks show signs of low-T hydrothermal effects that occurred after the impact. The target rocks contain a complex network of shear fractures that contain cataclasite and which grade into monomict lithic breccia. The cataclasite contains shocked mineral fragments, which indicates that the shear fracturing postdated the initial shock stage of the impact. The melt-matrix breccia and suevite dykes show signs that they intruded along the fractures, although there is also evidence that shear fracturing continued after quenching of the melt. This suggests that the intrusion of the dykes overlapped the brittle deformation of the target rocks.

Shock features in the M4 core lithologies include planar fractures, feather features, decorated planar deformation features (PDF), mosaic extinction and toasting in quartz; oblique lamellae, reduced birefringence and patchy (mosaic) extinction in plagioclase, and chevron-style spindle-shaped lamellae in microcline, as well as kink bands in biotite and planar fractures in titanite and zircon. Universal Stage measurements of PDF sets in quartz from 8 target rocks and 6 impactite dykes revealed four dominant sets: 0°(0001), 22.95°$\{10\bar{1}3\}$, 17.62°$\{10\bar{1}4\}$, 32.42°$\{10\bar{1}2\}$; with no significant change in shock intensity with depth nor significant differences in PDF orientations or intensity between melt-matrix breccias, suevites and target rocks. Based on these observations the average peak shock pressures are estimated at 10 - 25 GPa.

Apart from one suevite dyke that contains exotic clasts and an unusual bulk composition, all suevite and melt-matrix breccia dykes show major, trace and REE compositions and lithic and mineral clasts that indicate that they were formed from the target rocks found in the M4 core. The individual impactite dykes show good compositional correlation with their wallrocks, which

supports limited transport of the melt and suevite. This is also supported by evidence of small-scale variation of the melt composition in the melt-matrix breccias, which indicates that not enough time was available for complete mixing to happen. The similarity in matrix composition and in lithic and mineral clast types in the melt-matrix breccias to their wallrocks, is consistent with a friction melt origin. These dykes are thus interpreted as pseudotachylite. Macroscopic and microscopic evidence suggests that the melts intruded cataclasite-filled fractures and that interfingering and infolding between the melts and incohesive cataclasite allowed the melt to assimilate cataclasite. The melt clasts in the suevite show the same composition and clast features as the melt-matrix breccias. Based on this evidence it is proposed that the melt clasts in the suevite in the M4 core are fragments of quenched pseudotachylite that became separated and mechanically mixed into the cataclasite matrix when movement continued along the cataclasite-bearing fractures after the melt quenched. This was possible because the cataclasite was still incohesive and because strong vertical and horizontal displacements of the entire M4 sequence happened during the crater modification stage of the impact, possibly for 1-2 minutes after the impact.

The melt-matrix breccias are compositionally distinct from the Morokweng granophyric impact-melt rock intersected in the other central borehole cores. Melt particles are pervasively hydrothermally altered to a secondary mineral assemblage of zeolites and smectites, attributed to impact-induced hydrothermal fluid circulation in the MIS. The upper parts of the core are marked by abundant haematite but in the deeper levels of the core, chlorite-epidote-andradite garnet is found, which may indicate a vertically-zoned hydrothermal system after the impact. The hydrothermal effects also explain the abundance of decorated PDF in shocked quartz grains and the lack of glass in the PDF in quartz.

The 10-25 GPa shock levels in the target rocks support them lying close to the transient crater floor and initially close (<10 km) to the point of impact. The high structural position of the rocks relative to the impact-melt sheet suggests that the M4 sequence represents part of the peak ring of the Morokweng impact structure. The rocks of the peak ring would have experienced strong vertical and centrifugal displacement during the crater excavation and modification stages, which can explain the intense shear fracturing and cataclasis, brecciation and friction melting as well as the strong block movements that could disrupt and disperse the pseudotachylite melt dykes to produce suevite. A peak ring radius of 18 km would suggest that the original Morokweng crater rim diameter would have been >70 km, but between 1 and 2 km of post-impact erosion before the deposition of the Kalahari Group means that this could be a minimum estimate.

Dedication

This thesis is dedicated to my daughters, Nkazimulo Ziyafezeka Wela and Nqobangothando Lizobongwa Wela.

Acknowledgements

First and foremost, I would like to thank my supervisors: Prof. R.L. Gibson and Dr. M.A.G. Andreoli for their constant motivation, input and critique. Their guidance and focus on excellence during this project resulted in my professional research development. The detailed study of the M4 borehole only became a possibility when Dr. Andreoli allowed access to this core after decades of preservation. Special thanks to him, for allowing this enlightening suite of rocks and findings to be shared with the world.

Special appreciation also goes to Kosmas Goriat Chenjerai, CEO at Pan African Mineral Development Company (Pty) Ltd, for making the M4 core available for this study. I greatly appreciate the financial assistance I received from a Wits Postgraduate Merit Award (Wits), Prof. Gibson's RINC-NRF funds and the Impact Cratering Research Group (ICRG). This project became a success because the financial assistance offered covered sample preparation and analytical costs.

I would like to thank all the staff of the School of Geosciences who offered technical support in processing my data. Special thanks go to: Mr Alex Mathebula, Mr. Musa Cebekhulu and Mr. Caiphus Majola, for thin and polished sections; Prof. Allan Wilson, Mr. Marlin Patchappa, and Ms. Janine Robinson for XRF and ICP-MS analysis, and Mr. Joe Aphane for zircon extraction. Mr M. Kitching is thanked for his assistance in laying out the core.

The late Dr. Peter Gräser (Geology Department at the University of Pretoria); Dr. Christian Reinke (SPECTRAU at the University of Johannesburg) and Dr. Gabi Costin (Geology Department at Rhodes University) are thanked for their time and expertise in assisting with Electron Microprobe Analysis of the samples. Keabetswe Hlaole-Lehong and Dr. Gabi Costin (Geology Department at Rhodes University); Prof. Alexander Ziegler (Microscopy and Microanalysis Unit at the University of Witwatersrand) and Eve Kroukamp (SPECTRAU at the University of Johannesburg) are thanked for their assistance with the Scanning Electron Microscopy (SEM) and Energy-dispersive X-ray Spectroscopy (EDS) analysis. Prof. Dave Billing (Chemistry Department at the University of Witwatersrand) is thanked for his assistance with X-ray diffraction analysis (XRD) of samples. Dr. Zubair Jinnah (School of Geosciences at the University of Witwatersrand) and Arthur Moya (Chemistry Department at the University of

Witwatersrand) are thanked for their time and willingness to share their expertise in interpreting the XRD results.

Many people have played an important personal role in assisting me during my MSc journey: I would like to extend my gratitude to Prof. Gill Drennan for academic and personal guidance. I appreciate all her valuable life lessons, advice and patience. Dr. Phindile Khoza is acknowledged for her assistance with housing me during my stay in Grahamstown. Dr. Louise Coney is thanked for her valuable input during the academic discussions we had and for teaching me how to use the Universal Stage to measure PDF orientations. For informal but informative discussions, I would like to extend my gratitude to Prof. J.A. Kinnaird, Dr. T. Owen-Smith, Dr. G.M. Bybee and Prof. R.G. Cawthorn. Dr. Musa Manzi, Khuliso Masindi, Sarah Glynn and fellow graduate research students in the School of Geosciences are thanked for peer support, friendship and encouragement. I would like to give my special thanks to the Petroleum Agency SA management and colleagues for their support and time allowance to write up my thesis.

Finally, I would like to extend my sincere thanks to my parents, extended family and close friends for their support, understanding and encouragement throughout this intellectually challenging phase of my life. To the establisher, the source of my strength; thank you. I'm eternally grateful to my husband, Emmanuel, daughter Nkazimulo and my sisters, Siphesihle and Samkelisiwe, for their moral support and unconditional love. I am sure we all finally saw that diligence surely does bear fruit.

Table of Contents

Declaration.....i

Abstract ii

Dedication.....iv

Acknowledgements.....v

Table of Contents.....vii

List of appendices xiii

Abbreviations.....xv

Chapter 1: Introduction

1.1 Introduction.....1

1.2 Impact cratering mechanics 3

1.2.1 Contact and compression stage 5

1.2.2 Excavation and the transient crater formation.....8

1.2.3 Collapse and modification stage.....10

1.2.3.1 Simple Crater Morphology.....11

1.2.3.2 Complex Crater Morphology.....12

1.2.3.2.1 Multi-ring Basins 15

1.3 Impactites.....16

1.3.1 Impactite types.....17

1.3.2 Pseudotachylite.....19

1.3.3 Impact-melt rocks 20

1.3.4 Ejecta - tektites and micro-tektites.....20

1.4 Diagnostic shock metamorphic features in minerals and rocks 21

1.4.1 Shock-induced macroscopic deformation in rocks.....23

1.4.1.1 Shatter Cones.....23

1.4.2 Shock metamorphism in minerals 24

1.4.2.1 Shock metamorphism in quartz 24
1.4.2.2 Planar microstructures 24
1.4.2.3 High-pressure polymorphs 27
1.4.2.4 Mosaicism in quartz and other minerals 28
1.4.2.5 Diaplectic glasses 28
1.4.2.6 Post-shock thermal features 29
1.4.2.6 Kink banding in micas 29
1.4.3 Selective mineral and whole-rock melting 30
1.5 Regional Geology 31
1.5.1 Geophysical studies and modelling of the Morokweng impact structure 33
1.5.2 Morokweng borehole core stratigraphy 37
1.5.3 Petrography and geochemistry of Morokweng impactites 39

Chapter 2: Lithological and petrographic description

2.1 Introduction 41
2.2 Methodology 43
2.3 Macroscopic and microscopic observations of the M4 drillcore target lithologies 44
2.3.1 Granitic and granodioritic gneisses 44
2.3.1.1 Macroscopic characteristics 44
2.3.1.2 Petrographic characteristics 45
2.3.2 Trondhjemitic gneiss 48
2.3.2.1 Macroscopic characteristics 48
2.3.2.2 Petrographic characteristics 50
2.3.3 Dioritic Gneiss 51
2.3.3.1 Macroscopic characteristics 51
2.3.3.2 Petrographic characteristics 51
2.3.4 Metadolerite and dolerite 53

2.3.4.1 Meta-dolerite macroscopic characteristics....54
2.3.4.2 Dolerite macroscopic characteristics....54
2.3.4.3 Metadolerite petrographic characteristics....56
2.3.4.4 Dolerite petrographic characteristics....57
2.4 Macroscopic and microscopic observations of impactites....59
2.4.1 Monomict breccia and cataclasite....61
2.4.1.1 Macroscopic characteristics....61
2.4.1.2 Microscopic characteristics....66
2.4.2 Melt-matrix breccia (MMBr)....68
2.4.2.1 Macroscopic characteristics....68
2.4.2.2 Microscopic characteristics....73
2.4.3 Suevite....78
2.4.3.1 Macroscopic characteristics....78
2.4.3.2 Microscopic characteristics....82
2.4.4 Composite impactite dykes....87
2.5 Pre-and post-impact alteration....90
2.5.1 Pre-impact alteration....90
2.5.2 Post-impact alteration....91
2.6 Summary....97

Chapter 3: Whole-rock Geochemistry

3.1 Introduction....99
3.2 Major element analysis of target rocks....99
3.2.1 Granitoid gneisses....100
3.2.2 Dolerite and metadolerite....107
3.3 Major element analysis of impactites....108
3.3.1. Comparison of suevite and melt-matrix breccias....109

3.3.2 Comparison of impactites and target rocks 109
3.3.3 Depth-dependence of major elements in target rocks and impactites 113
3.4 Trace element analysis of M4 lithologies 116
3.4.1 Trace element analysis in target rocks 118
3.4.1.1 Granitoid gneisses 118
3.4.1.2 Dolerite and metadolerite 120
3.5 Trace element analysis of impactites 121
3.5.1. Comparison of impactites and target rocks 121
3.5.2 Depth-dependence of trace elements in target rocks and impactites ..... .123
3.6 Rare earth element (REE) analysis of target rocks 125
3.6.1 Granitoid Gneisses 125
3.6.2 Dolerite and metadolerite 128
3.7 Rare earth element (REE) analysis of impactites 128
3.7.1 Comparison of suevites and melt-matrix breccias 129
3.7.2 Comparison of impactites and target rocks 132
3.8 Multi-element Spidergrams 132
3.8 Summary 134

Chapter 4: Mineral chemistry

4.1 Introduction 136
4.2 Previous studies 137
4.3 Methodology 138
4.4 Mineral chemistry results for M4 core target rocks and impactites ..... .138
4.4.1 Feldspars 139
4.4.1.1 Granitoid gneisses 139
4.4.1.2 Metadolerite and dolerite 139
4.4.1.3 Feldspar chemistry of mineral and lithic clasts enclosed in impactites ..... .140

4.4.2 Biotite and chlorite 146
4.4.2.1 Granitoid gneisses 146
4.4.2.2 Metadolerite and dolerite 148
4.4.2.3 Biotite chemistry of mineral clasts enclosed in impactites ..... .148
4.4.3 Clinopyroxene and amphibole 148
4.4.3.1 Clinopyroxene and amphibole in target rocks 148
4.4.3.2 Pyroxene chemistry of mineral and lithic clasts enclosed in impactites ..... .149
4.4.4 Minor constituents and accessory minerals 153
4.4.4.1 Epidote 153
4.4.4.2 Titanite 153
4.4.4.3 Oxides 153
4.4.4.3 Apatite 154
4.5 Mineralogical and geochemical analysis of impactites 154
4.5.1 XRD Analysis of melt particles and breccia matrices 157
4.5.1.1 Alteration of target rocks 158
4.5.1.2 Glass in melt particles and MMBr matrix? 159
4.5.1.3 XRD spectra for melt clasts in suevite and suevite matrices 161
4.5.1.4 XRD analysis of composite impactite dyke 163
4.5.1.5 Variation in XRD mineralogy within impactite types and with depth ..... .164
4.5.2 EPMA analysis MMBr matrix and melt clasts ..... .165
4.5.2.1 Bulk data analysis ..... .166
4.5.2.2 MMBr melt matrix ..... .172
4.5.2.3 Melt particles in MMBr ..... .173
4.5.2.4 Melt clast in suevite ..... .175
4.6 Summary 179

Chapter 5: Shock Petrography

5.1. Introduction....180

5.1.1 Shock pressure determination using PDF crystallographic orientations in quartz....182

5.1.2 Previous work....184

5.2 Methodology....185

5.3 Shock microdeformation features in the M4 core lithologies....186

5.3.1 Petrographic properties of shocked quartz in the M4 core lithologies....187

5.3.2 PDF measurements for the M4 core lithologies....190

5.3.2.1 PDF crystallographic orientations in target rocks....190

5.3.2.2 PDF crystallographic orientations in impactites....197

5.3.2.2.2 PDF crystallographic orientations in melt-matrix breccias....198

5.4 Shock metamorphic evidence in other minerals....204

5.5 Timing of micro-scale deformation....208

5.6 Comparison of shock intensity in M4 core target and impactite samples with previous studies. 209

5.7 Summary....210

Chapter 6: Discussion and Conclusions

6.1 Introduction....213

6.2 Nature of the M4 target rocks....213

6.2.1 Granitoid gneisses....213

6.2.1.1 M4 granitoids in comparison to Morokweng impact structure granitoids....214

6.2.1.2 M4 granitoids in comparison to regional granitoids....214

6.2.2 Metadolerite and dolerite....216

6.2.2.1. Comparison of M4 metadolerites and dolerites with regional dykes....216

6.2.3 Geotectonic setting of the MIS target granitoids....219

6.2.4 M4 granitoids gneiss compositions in comparison to average crust....220

6.3 Nature of the M4 impactites 221
6.3.1 Comparison of the M4 impactites to Morokweng impact melt 221
6.3.2 Origin of the melt-matrix breccia in the M4 core 225
6.3.3 Origin of suevite in the M4 core 228
6.4 Hydrothermal alteration of the M4 drillcore lithologies 232
6.5 Shock distribution within the M4 drillcore and MIS 234
6.6 A peak ring setting for the M4 core? 235
6.6.1 MIS in comparison to other peak-ring impact structures 236
6.7 Conclusions and recommendations 240

References 243

List of appendices

Appendix 1: Methodology

1A: Borehole logging, sample selection and petrographic analysis
1B: Whole Rock X-Ray Fluorescence (XRF) analysis and Inductively Coupled Plasma Mass Spectrometry (ICP-MS)
1C: X-ray diffraction (XRD)
1D: Scanning Electron Microscopy (SEM)
1E: Electron microprobe analyses (EMPA)
1F: Universal stage data

Appendix 2: M4 Core – Logging and sampling

2A: M4 borehole log
2B: Sample list for this study

Appendix 3: Geochemical analysis

3A: Whole Rock X-Ray Fluorescence (XRF) data for target rocks

3B: Whole Rock X-Ray Fluorescence (XRF) data for impactites

3C: Inductively Coupled Plasma Mass Spectrometry (ICP-MS) data for target rocks

3D: Inductively Coupled Plasma Mass Spectrometry (ICP-MS) data for impactites

Appendix 4: Mineral Chemistry

4A: Electron microprobe analyses (EMPA) data for mineral constituents of target rocks

4B: EMPA data for lithic and mineral fragments enclosed in impactites

4C: X-ray diffraction (XRD) profiles

4D: Melt particle traverses

Appendix 5: Universal stage data

5A: Crystallographic measurements of PDF from selected quartz grain from representative M4 target rocks

5B: Crystallographic measurements of PDF from selected quartz grain from representative M4 impactites

5C: Histograms showing frequency distribution of angles between c-axis and poles to PDF in 5° intervals.

Abbreviations

ANIE - Automated Numerical Index Executor

BSE – Back-scattered electron image

BSEM- Back-scatter scanning electron microscopy

EMPA - Electron microprobe analyses

FF - Feather features

MIS – Morokweng impact structure

MMBr - Melt-matrix breccia

PDF – Planar deformation features

SEM - Scanning Electron Microscopy

XRD - X-Ray Powder Diffractometry

XRF - X-Ray Fluorescence

Chapter 1

Introduction

1.1 Introduction

South Africa hosts four (Vredefort, Tswaing, Kalkkop and Morokweng) of the 190 confirmed impact structures on Earth (Earth Impact Database: *http://www.passc.net/EarthImpactDatabase/index.html*; last accessed February, 2017). The Tswaing crater (1.13 km diameter) situated 40 km north of Pretoria can be considered to be relatively well preserved (Koeberl, 1994, Brandt, 1999). The smaller Kalkkop impact structure, located 51 km southwest of Graaff-Reinet (Eastern Cape), is partially eroded and defined only by a 640-m wide remnant of limestone crater fill (Koeberl, 1994; Reimold et al., 1998; Mthembi, 2014; Reimold and Koeberl, 2014). The oldest and largest confirmed impact structure on Earth is centered on Vredefort, ~120 km SW of Johannesburg (Henkel and Reimold, 2002; Gibson and Reimold, 2008). This well-studied structure has been deeply eroded by ~10 km and consequently, a well-defined margin is no longer visible; however, it is believed to have originally been at least 250 km in diameter (Gibson and Reimold, 2008). Although the Vredefort impact structure is partially buried beneath Permian Karoo Supergroup sediments, its northern half exposes a wealth of information (Gibson and Reimold, 2008). The most enigmatic of South Africa's impact structures is located near Morokweng, in the North-West Province, 140 km west of Vryburg at 26º 20´S, 23º 32´E (Figure 1.1). The 145 ± 2 Ma (Hart et al., 1997, Koeberl et al., 1997) Morokweng impact structure (MIS) is almost completely buried beneath an ~ 60-100 m thick veneer of <70 Ma, Cenozoic, Kalahari Group sand and calcrete (Andreoli et al., 1996; Hart et al., 1997, Andreoli et al., 1999; Bootsman et al., 1999). The MIS has thus largely been studied from drillcore samples and geophysical methods, which can provide only limited information. Published results indicate that the Morokweng crater must have undergone significant erosion of at least several hundred metres prior to the deposition of the Kalahari Group. This has significance for estimates of its size. At present on the Earth Impact database the size of the MIS is recorded as 70 km, although this view is not universally accepted, with contrasting estimates ranging from 70-80 km (Reimold et al., 2002; Henkel et al., 2002) to ~250 km (Andreoli et al., 2007; Andreoli et al., 2008a) and 300-340 km (Corner et al., 1997; Hart et al., 1997).

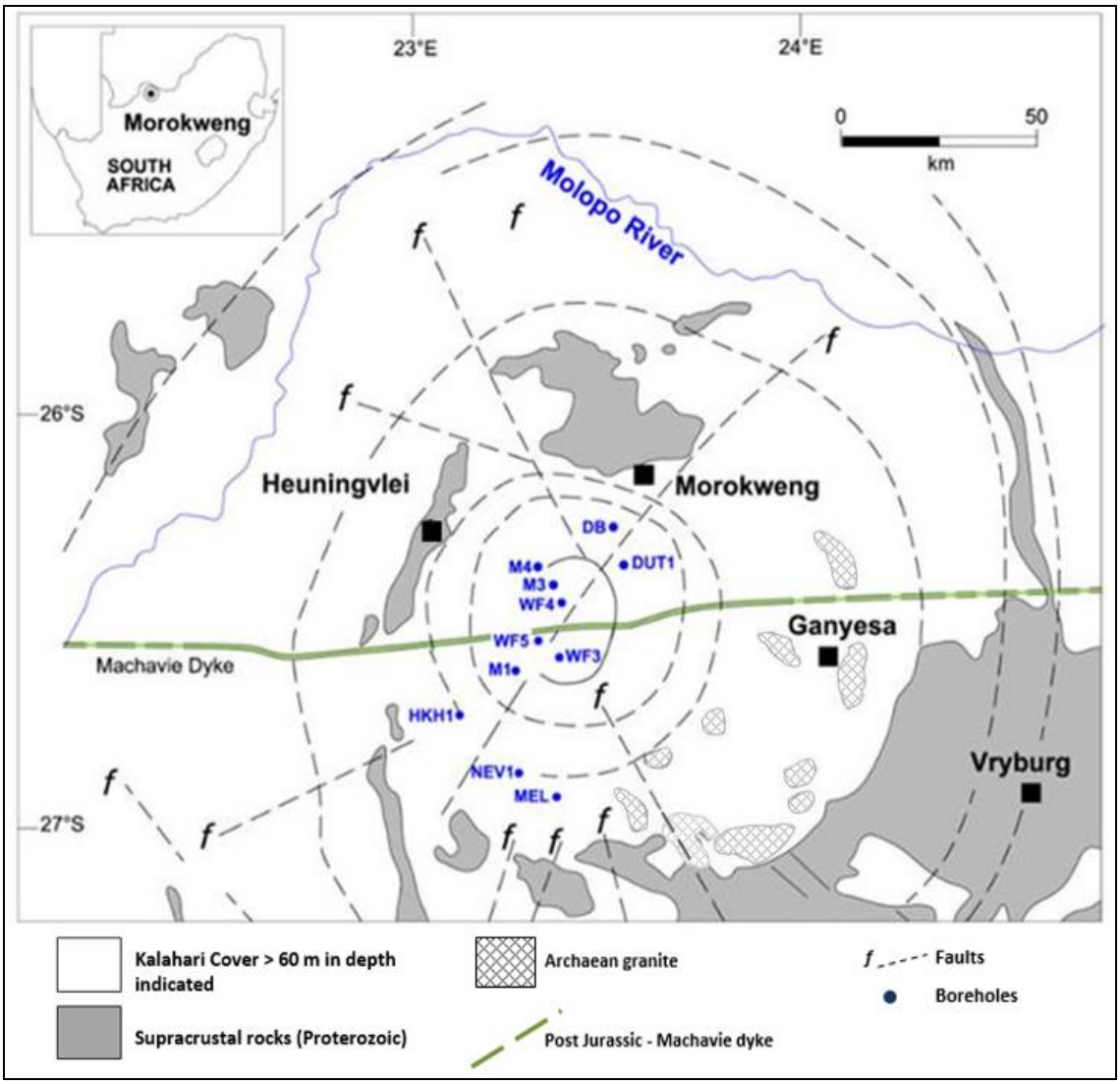

Figure 1.1: Geological outcrop map of the Morokweng impact structure, showing major structural features inferred from geophysics and the locations of boreholes (modified from Andreoli et al., 1995, Andreoli et al., 2008a, M.A.G. Andreoli, unpublished data), including the study borehole M4. Inset shows the location of the Morokweng impact structure on the map of South Africa.

This study examines the lithologic, petrographic and geochemical characteristics and structural features of lithologies intersected in the 368-m deep M4 drillcore located 18 km from the centre of the MIS (Figure 1.1). This borehole was drilled into a small aeromagnetic anomaly as part of an exploration programme for base metals in the MIS by Pan African Mineral Development Company (Pty) Ltd. An examination of this core aims to identify and interpret the pre-impact history of the target rocks, impact-related features, and post-impact features of the core in order to

further constrain the morphology, size and depth of erosion of the MIS. In order to discuss the mineralogic, petrographic and geochemical characteristics of the M4 core lithologies in context it is imperative to first provide a short overview of impact crater formation and criteria for their recognition.

Objectives of this study include:

- Construction of a lithological log of the M4 borehole, identifying the chronology of pre-, syn- and possibly post-impact lithologies.

- Petrographic, structural, metamorphic and geochemical characterization of target rock lithologies and their comparison to the known literature for the western Kaapvaal craton, thus establishing a pre-impact geological history.

- Petrographic and geochemical characterization of M4 core impactites with the aim of understanding their source rock types and genesis.

- Description and systematic study of the structural relationships between target rocks and impact breccias, with the aim of understanding impact-related deformation and the formation and/or emplacement processes of the breccias.

- Estimation of the peak shock levels and the spatial distribution of shock features in both the target rocks and impact breccias.

- Examination of the post-impact modification (hydrothermal alteration) of the impactites.

- Reconstruction of the specific setting of the M4 core within the MIS and its use in constraining the size of the MIS.

1.2 Impact cratering mechanics

All the bodies in our solar system have been subjected to bombardment by bolides (asteroids or comets) but, unlike the impact craters preserved in the relatively dormant extraterrestrial

environments, the ones on Earth have commonly been subjected to post-impact processes such as erosion, sediment deposition and/or tectonic activity, thereby affecting their preservation (Grieve and Pilkington, 1996; French, 1998; Bland, 2005). Estimations of crater size are hampered where craters have been partially eroded and/or covered by younger sedimentary deposits (Grieve and Pilkington, 1996). As the study of impact craters on other planets is restricted to remote sensing and, in rare cases, a few samples returned by manned or robotic missions, the more easily accessible terrestrial impact structures are especially important in assisting geoscientists in understanding impact cratering processes, notwithstanding these modifications (French, 1998; McCall, 2009, Osinski and Pierazzo, 2012).

The term impact crater is used to refer to the usually circular feature that results from the high-velocity (typically > 11 km/s; French, 1998) impact of a bolide with a planetary surface. The term impact structure refers to the remnants of the crater and deformed rock volume observable after geological modification of the crater (Montanari and Koeberl, 2000). However, for simplicity a generic term impact structure is now used even if the original crater form is still preserved (Grieve and Pilkington, 1996). During the impact, as the impactor/bolide hits the ground, its kinetic energy is transferred into the target rocks by a shock wave (Melosh, 1989, French, 1998; Montanari and Koeberl, 2000; McCall, 2009). The transient shock wave is characterized by high pressures up to 100 GPa and velocities of >10 km/s (French, 1998), which cannot be produced by internal geological processes on Earth (Melosh, 1989). Because of the near-instantaneous nature of the impact process, the shock wave propagates through the target rock causing irreversible effects (deforming, brecciating and even melting rock) within seconds (Melosh, 1989; French, 1998).

The impact cratering processes are broadly the same irrespective of the planetary target (Melosh, 1989). Differences in the resulting crater occur depending on the velocity, size and density of the bolide and its angle of penetration, and the nature of the target (Grieve, 1987; French, 1998). Three stages occur during the cratering process: contact and compression stage, excavation stage and modification stage. These are dominated by different forces and mechanisms (Melosh 1989, French, 1998; McCall, 2009). Structural modifications and phase changes in the minerals of the target rocks occur in the compression stage and the morphology of a crater is developed in the excavation and modification stages (Melosh 1989, French, 1998; McCall, 2009; French and Koeberl, 2010). The specific characteristics of these stages are described in the sections below.

No actual observation of these processes has been made since no actual impact has occurred in recorded history and these are too immense to be reproduced in a laboratory (French,1998); the inference about these three stages, mechanics of cratering and crater forms has been based on extraterrestrial crater observations and detailed study of existing terrestrial impact structures (McCall, 2009). Stöffler et al. (2013) have suggested that the traditional 3-stage model should be expanded to include post-cratering stages related to cooling of the crater and its deposits (Figure 1.2).

Impact structures vary in terms of morphology from simple impact craters, which are bowl-shaped, to complex impact craters, which have a central uplift (peak or peak-ring) surrounded by an annular trough and terraced rim structure (French, 1998; Dressler and Reimold, 2001). During the formation of impact structures, a range of rock types and shock metamorphic effects are produced as the shock wave propagates into the target rocks (French, 1998). Geophysical data have proved useful in identifying impact structures through noting circular gravity and/or magnetic anomalies, and reflection and refraction seismic profiles showing dense melt-rocks, less dense fractured crater basement and/or low-angle listric faults (French, 1998). Although impact-induced geophysical anomalies may be present they are not, by themselves, conclusive. Apart from their morphological elements, circular impact structures must also be confirmed from identification of shock process effects in their rocks; both in the form of macroscopic (suevites, impact melt breccias, shatter cones) and microscopic (planar deformation features, diaplectic glass and shock melts, high-pressure mineral polymorphs) shock features (French, 1998, Stöffler and Reimold, 2006; Stöffler and Grieve, 2007; French and Koeberl, 2010). In nature, there are other circular landforms such as volcanic craters, sinkholes and salt diapirs, which can be formed by alternative geological processes, hence it is important to understand the structural and lithological character of impact craters, processes and products of impact cratering (Ferrière and Osinki, 2013). The examination of lithologies and their distribution within an impact structure is vital in reconstructing the size of the crater and the formation and modification processes and the prevailing temperature and pressure conditions prior to, during and after the impact event (Grieve and Pilkington, 1996).

1.2.1 Contact and compression stage

The contact and compression stage begins as the impactor or projectile makes contact with the target (ground surface) (French, 1998; see Figure 1.3). The momentum and the kinetic energy of

the projectile is transferred into the target in the form of heat and a high-pressure shock wave that radiates outwards (hemispherically) from the contact point (French, 1998, Grieve et al., 2007; French and Koeberl, 2010). The impactor starts deforming upon contact because the shock wave is also reflected back into the impactor (Melosh, 1989; French, 1998; Grieve et.al, 2007). Near the point of impact initial shock pressures may exceed 100 GPa (temperatures exceed 10 000 K), which causes immediate melting and/or vaporization of both the impactor and a significant volume of the target rocks (French, 1998; French and Koeberl, 2010). The resulting increase in internal energy accompanying shock compression and subsequent rarefaction (release) waves also causes shock metamorphism (see Chapter 5) and melting (see Chapters 2 and 4). The contact and compression stage is therefore characterized by both structural and phase changes in target rocks and their minerals (Montanari and Koeberl, 2000). Generated melt may be forced downward into the target rocks, resulting in the formation of impact melt dykes and veins which penetrate brecciated basement target rocks (Dressler and Reimold, 2001). Although the impactor is generally believed to be eradicated through vaporization and/or melting (Melosh, 1989), the MIS is unique in that meteorite fragments have been recovered inside impact melt rock in the M3 core (Maier et al., 2006; Figure 1.1).

Away from the impact point, the shock wave loses energy and shock pressures drop to below 1-2 GPa, (see Figure 1.3; French and Koeberl, 2010). This loss of energy is due to two reasons; the shock wave expands into an ever-increasing rock volume, and energy is lost through heating, deformation and acceleration of the target rocks (French, 1998). This stage lasts less than a few seconds and is influenced by the size, composition and original cosmic velocity of the extraterrestrial body (Melosh, 1989). The hemispherical distribution of shock pressure contours around the impact point (Figure 1.3), allows the characterization of unique metamorphic zones in rocks below the crater. Each shock zone is characterized by specific distribution of shock pressures and resultant shock metamorphic features. At low pressures the shock wave degenerates into an elastic or seismic wave; these do not produce any notable impact diagnostic deformation, but may induce fracturing, brecciation, faulting and landslides similar to those produced by endogenic seismic waves (French, 1998). This reduction in shock wave intensity explains why shock diagnostic metamorphic features only occur within a fraction of the crater radius (Figures 1.3). The point at which the projectile is completely unloaded is generally considered as the end of the contact and compression stage (Melosh, 1989).

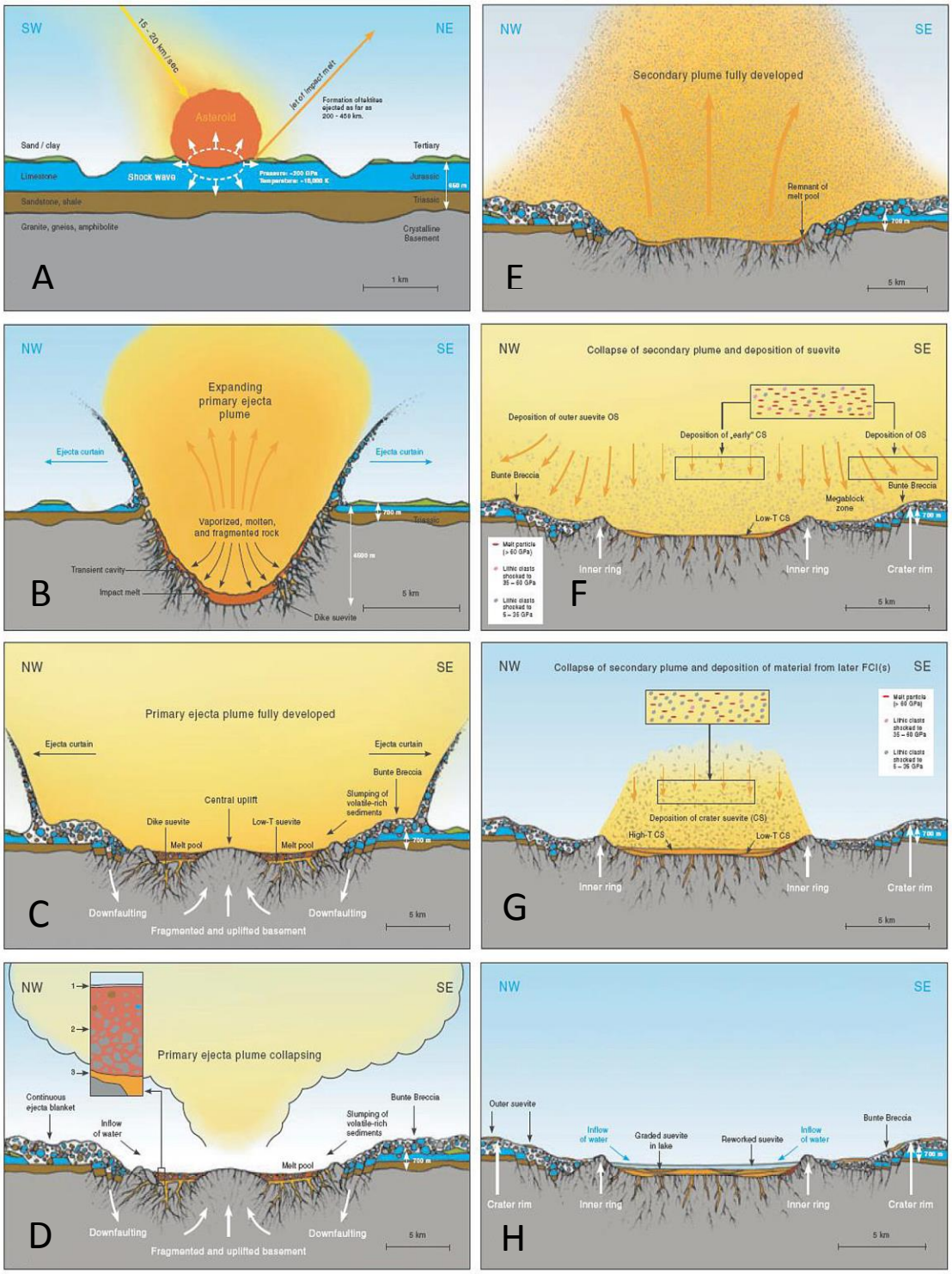

Figure 1.2: Schematic representation of the 5 stages of complex impact crater formation proposed by Stöffler et al. (2013) for the 26 km Ries crater (Germany): **A)** Contact and compression phase showing the projectile impact and wave propagation. **B)** Excavation phase including the formation of the transient crater. **C-D)** Shows the phase of collapse for the transient crater and the formation of the central uplift and the inner ring. **E)** Formation of the secondary plume because of the interaction of water with the hot melt pool. **F-H)** Collapse stages of the secondary plume.

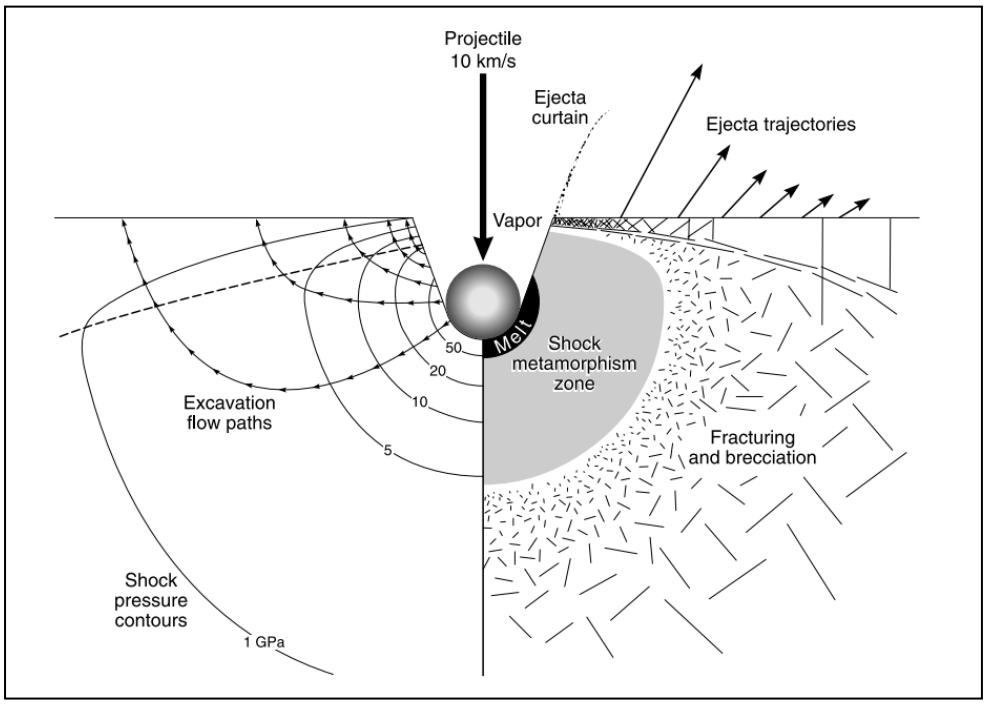

Figure 1.3: Schematic cross-section of an impact structure prior to modification showing shock pressure isobars (pressures in GPa) and excavation flow lines developed around the impact point (from French, 1998). As indicated in the diagram the shock waves that radiate outwards from the projectile-target boundary decrease rapidly in peak pressure and form concentric zones, each with distinctive shock effects. These zones are: melting and formation of a large melt body (> 50 GPa); development of shock deformation features (5-50 GPa) and at 1-5 GPa fracturing and brecciation of the target rock. For future reference for Chapter 5, note the restricted extent of the 20 GPa shock pressure contour.

1.2.2 Excavation and the transient crater formation

The excavation stage is marked by the formation of a transient crater or cavity subsequent to the end of the contact and compression stage (French, 1998; Osinski and Pierazzo, 2012). As a roughly hemispherical shock wave propagates down into the target rocks, it compresses the target (Melosh, 1989), whilst the shock waves that travel upwards intersect the ground surface and then are reflected downward as rarefaction waves (release waves) through the target rocks, fracturing and shattering the rocks (French, 1998; Montanari and Koeberl, 2000; Grieve et al., 2007; French and Koeberl, 2010). Excavation and formation of the transient cavity continues via displacement of material (Pilkington and Grieve, 1992); which is initiated when tensional stress imparted by these waves exceeds the mechanical strength of the target rocks (French, 1998; Kenkmann and Ivanov, 2006). Movement of rock fragments and shock-produced melt form the bowl-shaped

depression (French, 1998: Figure 1.4). The transient crater produced during the excavation stage is usually 20-30 times the diameter of the impactor (French, 1998).

The transient crater is divided into an upper excavated zone (ejection zone) and the lower displaced zone (Melosh, 1989; French, 1998; Figure 1.4). Material in the excavated zone is ejected beyond the transient cavity rim, forming impact ejecta (and vapour plume; see Figure 1.2b). High-velocity jets of highly shocked and commonly melted material (tektites and microtektites, shocked rock and mineral fragments) are ejected over larger distances (Dressler and Reimold, 2001). The material in the displaced zone experiences lower tensional stresses and excavation flow velocities; therefore, remains within the transient cavity, forming crater fill impactites (Figures 1.4-1.7).

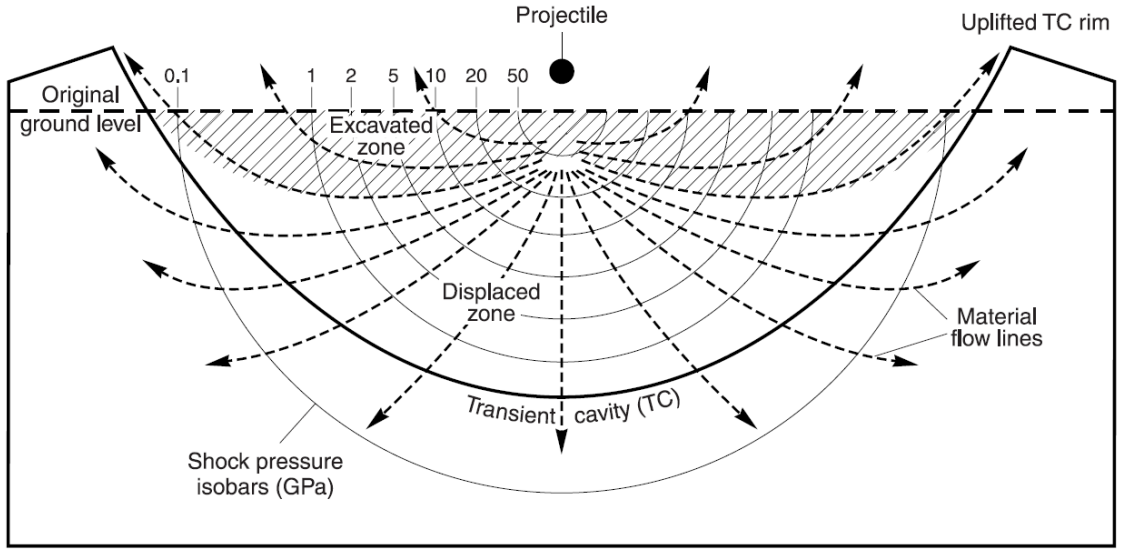

Figure 1.4: Schematic cross section showing the excavation stage and the resulting transient crater. Material in the excavated zone is fractured, excavated and ejected beyond the transient crater rim (i.e., uplifted rim). In the displaced zone the material, though displaced, is not ejected (after French, 1998). In the excavation stage two processes are involved (Figure 1.4): (1) large near-surface fragments are ejected upwards and outwards, and individual fragments are ejected along excavation flow lines, and (2) downward and outward subsurface flow of the target material occurs.

The excavation stage may last for seconds or minutes, depending upon several factors such as: size of impactor, angle of incidence, impact velocity, and presence of a water table or layers of different strength, joints, or original topography in the target (Melosh 1989). Melosh (1989)

estimated that if the excavated flow propagates at 1 km/s, a 200 km wide transient crater is likely excavated in 90 to 120 seconds. The end of the excavation phase occurs when the transient crater reaches its maximum size (maximum depth is approximately one third its diameter); then the modification stage is initiated by collapse and modification of the transient crater to form the final impact crater (French, 1998). The transient crater dimensions can be used in crater formation models to predict or estimate pre-erosion diameter, depth of penetration and size and velocity of the bolide (French 1998).

1.2.3 Collapse and modification stage

The modification stage marks the final stage of the impact cratering process (Figure 1.2C-D). The collapse of the steep unstable rims of the transient crater during the modification stage is largely driven by gravity whilst the magnitude of modifications is dependent on the crater size (Grieve and Pilkington, 1996). In small structures the transient crater is modified by collapse of the upper walls and by displacements along faults; in large structures the modification process involves uplift of the central part of the floor and peripheral collapse around the rim under gravitational forces, forming terraces (Figure 1.2C-D; French, 1998). Additionally, deposition of ejected material into and around the crater takes place. A small, simple, impact crater is characterized by a bowl-shaped depression with a structurally uplifted rim and infill material (fall back ejecta) that includes brecciated and fractured rocks and impact melt rocks (French, 1998; Montanari and Koeberl, 2000; Figure 1.5). The shape (and size) of the final crater is governed by the interaction of the excavation flow and the strength of the target material (i.e., crystalline versus sedimentary rocks), as well as the force of gravity (Melosh, 1989; Melosh and Ivanov, 1999; Osinski and Pierazzo, 2012).

Depending on the extent of modification of the transient crater, three types of crater morphologies/impact structures are recognized on other planets and on Earth: simple craters, complex craters and multi-ring basins (Melosh, 1989; Grieve and Pilkington, 1996; French, 1998). Whether it is a simple crater produced or a complex crater depends on the size of the impact as well as the strength and composition of target rocks and the impact angle and velocity (Grieve et al., 2007).

The diameter at which the transition occurs from simple to complex craters on Earth is approximately 2 km for craters developed in sedimentary targets and approximately 4 km for

those in crystalline lithologies (French, 1998; Osinki and Pierazzo, 2012). The craters are filled by shocked, brecciated and melted rocks (see section 1.3). Whilst the modification stage lasts for less than a minute (in small structures) to a few minutes (in large structures) modification in the form of hydrothermal and chemical alteration, sedimentation and/or erosion may continue for years to millions of years (French, 1998; Grieve and Pilkington, 2002).

1.2.3.1 Simple Crater Morphology

Although not directly appropriate to the study of impact structures as large as the MIS, it is necessary, for completeness, to first consider simple craters. Simple impact craters are bowl shaped and normally have an apparent depth which is about one third of the crater diameter (Grieve, 1987; French, 1998; Montanari and Koeberl, 2000). The interior of these craters has a sloping parabolic profile, with rim diameters of ≤ 2 km in sedimentary target rocks and up to 4 km in crystalline target rocks on Earth (Dence, 1972; Dressler and Reimold, 2001).

Modification of a transient crater to form a simple crater involves small scale or minor collapse of steep transient crater walls and re-deposition of fallback of shocked and un-shocked rock fragments (crater fill breccias) and shock-melted rock (impact melt) which fill approximately half of its original depth (French, 1998; see Figures 1.5 and 1.6). The rim diameter increases during inward collapse of the walls (Melosh, 1989), resulting in the crater diameter being ~15% larger than the transient crater diameter (Gucsik, 2009). In the case of simple craters, modifications are moderate and the structure of the transient crater is largely preserved (French, 1998; Grieve et al., 2007). The simple crater is infilled by disintegrated allochthonous displaced material derived mainly from slumping transient crater walls (Pilkington and Grieve, 1992). Beneath this breccia lens lies the in-situ fractured parautochthonous target rocks (Figure 1.5 and 1.6).

Examples of simple craters on Earth include: the 1.18 km Meteor (Barringer) Crater, Arizona-USA (Shoemaker, 1987; Grieve and Pilkington, 1996); the 1.13 km Tswaing Crater, South Africa (Brandt, 1999; Koeberl, 1994); the 1.83 km Lonar crater, India (Lafond and Dietz, 1964); the 3.8 km Brent crater, Canada (Grieve, 1978) and the 880 m in diameter Wolfe Creek crater, Australia (O'Neill and Heine, 2005).

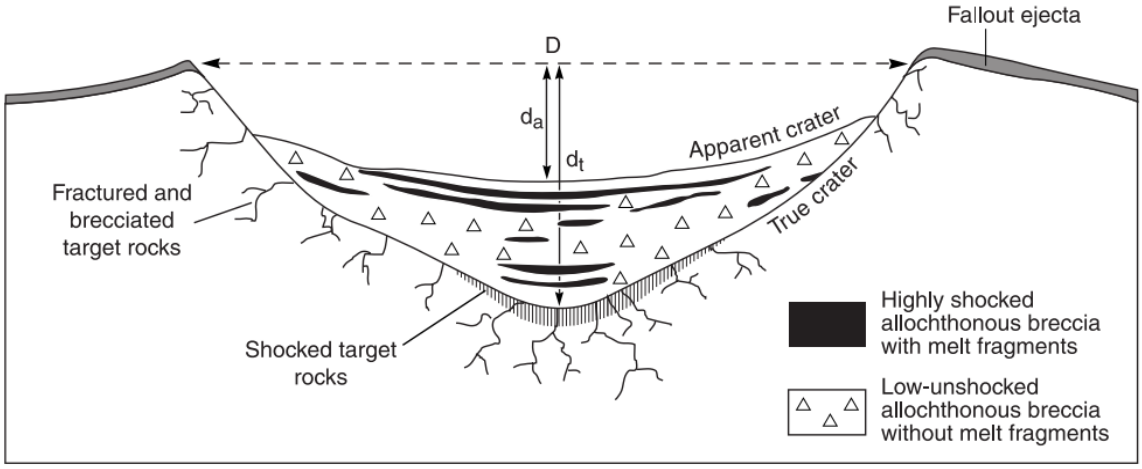

Figure 1.5: Schematic cross section showing the morphology of a simple impact crater, and the location of impactite types in and around the structure. D is the final crater diameter; d_t is the true depth of the crater; d_a is the apparent depth of the crater (French, 1998).

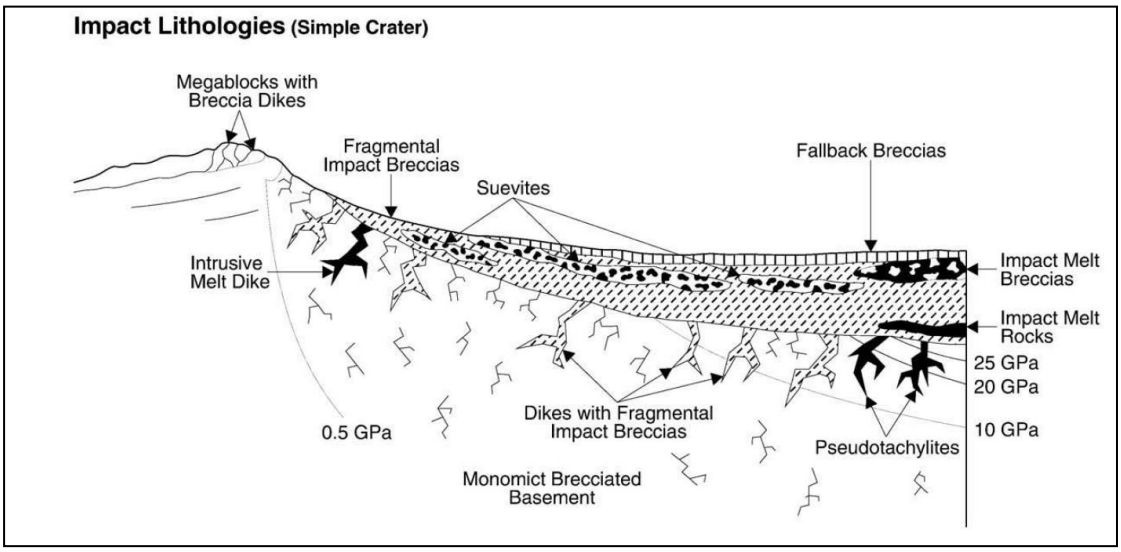

Figure 1.6: Schematic cross-section through a simple impact structure showing details of the impact-produced lithologies and relation of the shock pressure isobars to the final crater diameter (French and Koeberl, 2010).

1.2.3.2 Complex Crater Morphology

The processes involved in the formation of a complex crater are shown in Figure 1.7. The transient crater diameter is ~ 0.5 – 0.65 of the modified final rim diameter (Grieve and Therriault, 2004). Complex impact craters collapse in a significantly different way to simple craters under

the influence of gravity, completely altering the appearance of the bowl-shaped transient crater; thereby producing final craters with a central uplift (central peak or peak ring), downfaulted annular trough, terraced rim and flat floor (Melosh, 1989; Dressler and Reimold, 2001; see Figure 1.8).

The deep-seated rocks beneath the centre of the transient crater rise to form the central uplift as the crater walls collapse inwards (Stöffler and Grieve, 2007). The outer rim slumps inwards and downwards along concentric faults that eventually form terraces (Melosh, 1989). Impact melt pools may be common in the depressions of the terraced blocks (Gucsik, 2009). The central uplift consists of strongly shock metamorphosed uplifted basement rocks from greater depths (French, 1998; see Figure 1.2C). The amount of uplift is ~ 0.1 of the final crater diameter (Ivanov et al. 1982; Melosh, 1989; Grieve and Therriault, 2004). Central uplift formation (Figure 1.7a), is accompanied by decompression of the target rocks which results in breccia formation and melting (Dressler and Reimold, 2001). Three types of basins can be distinguished in terms of increasing diameter: central peak basins (marked by both a central uplift and a peak ring); a peak-ring basin (consisting of only a central peak ring (one ring) and no central uplift) and multi-ring basins (which have two or more interior concentric peak rings) (Wood and Head 1976; Melosh, 1989). The transitions between types is based on morphology marked by the development of a central interior ring(s) or a central peak (Therriault et al., 2002). The exact size constraints have not been confidently finalised (Spudis, 2005). In larger complex craters and multi-ring basins, the central crater floor readjustment may also lead to exhumation of high grade metamorphic and shock metamorphosed rocks (Dressler and Reimold, 2001).

Complex craters with central uplifts have diameters of approximately 4–22 km (French, 1998), an example being the 3.8 km Steinheim impact crater, Germany (Ivanov and Stöffler, 2005); whilst central peak basins have diameters of 22-30 km on Earth, an example being the 28 km Mistastin impact crater (Canada) (French, 1998). Complex impact structures that do not contain either a central uplift or central peak include the 24 km Ries impact structure in Germany and the 23 km Haughton, Canada (Therriault et al., 2002; Grieve and Therriault, 2004). The lack of a central peak in some complex craters is attributed to the nature of the target rocks (Grieve and Therriault, 2004).

Peak-ring basin structures are formed by the interference between the downward and inward radial collapse of the transient cavity in the outer crater and the upward and outward collapse

within the central uplifted region (Morgan et al., 2000; see Figure 1.7B). The resulting structure has an interior consisting of peaks that surround a collapsed central peak thereby forming a basin (depression) which can be infilled by impact melt (French, 1998). Clast-rich and homogeneous impact melt rocks are mostly confined inside the peak ring (Morgan et al., 2000). The peak-ring basin type is characterised by diameters of 30-62 km on Earth (French, 1998), for example the 52 km Siljan crater in Sweden (Henkel and Pesonen, 1992). The cause of the transition from peak-ring complex impact structures to multi-ring basins is not fully understood; currently it is proposed that it could be because of development of a basin-sized crater cavity due to increasing crater diameter or that it is enhanced by conditions of the lithosphere (i.e., presence of a weak asthenosphere at depth within the plate) (Schultz et al., 1981; French, 1998; Baker et al., 2012).

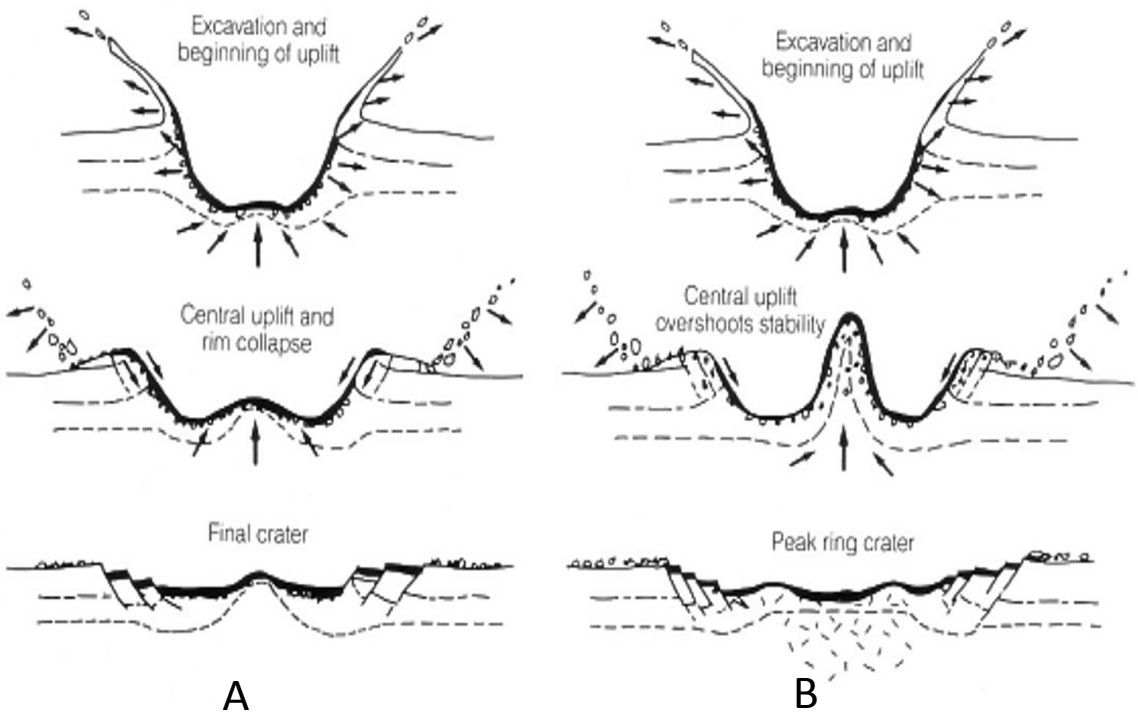

Figure 1.7: Schematic model showing the excavation and modification stages processes that lead to the formation of a complex crater. **(A)** A complex crater with a central uplift and **(B)** A peak-ring impact structure (after Melosh 1989).

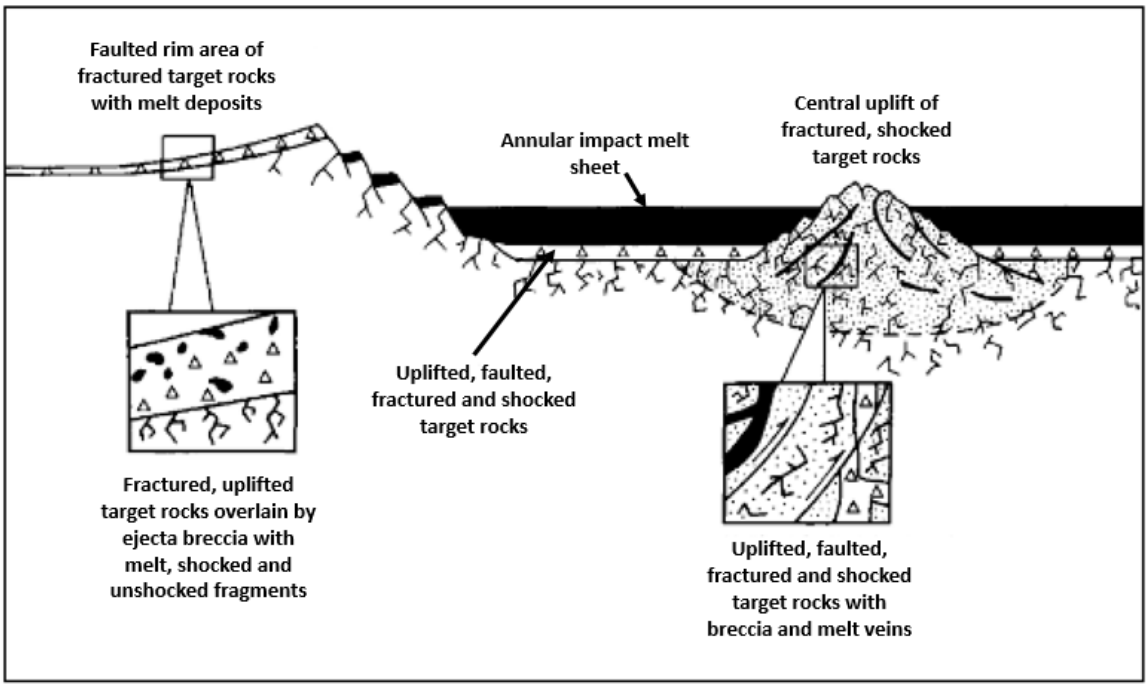

Figure 1.8: Schematic cross section through a complex impact structure showing the nature of the resultant central uplifted region of the impact structure. Note that the annular trough is filled by the impact melt sheet, whilst some of the impact melt is retained in faulted blocks of the terraced rim structure (Spudis, 2005).

1.2.3.2.1 Multi-ring Basins

Multi-ring impact basins are the largest of all impact craters (Spudis, 1994); with diameters of a few hundred kilometers to > 1000 km (French, 1998). Multi-ring basins are said to be produced by projectiles which are tens to hundreds of kilometers in diameter (Melosh, 1989; French, 1998) and are characterized by multiple structural rings around a flat-floored topographic depression (Wood and Head 1976; Dressler and Reimold, 2001). The central uplift is replaced by two or more concentric topographic rings, and ring grabens exist in the outer rim sections (Stöffler and Grieve, 2007). The inner basin rings appear to be produced in response to the catastrophic inward slumping following gravitational collapse of the central uplift (Schultz et al., 1981).

The best-preserved examples of multi-ring basins are on the Moon, Mercury and Mars. The transition to multiring basins on the Moon is 400-600 km (French, 1998). On Earth, multi-ringed basins have diameters greater than 100 km, though it has been difficult to completely identify the multi-ring morphology of these structures on Earth owing to effects of erosion (French, 1998; Grieve and Therriault, 2000; Morgan et al., 2000).

Three large terrestrial structures are considered as likely multi-ring basins, although the first two are significantly eroded and the third is largely buried (Grieve and Therriault, 2000; Poag et al., 2004) are: the 250 – 300 km Vredefort impact structure, South Africa (Grieve and Therriault, 2000; Gibson and Reimold, 2001); the 200 – 250 km Sudbury impact structure, Canada (Grieve and Therriault, 2000) and the 180 km Chicxulub crater, Mexico (Hildebrand et al., 1991; Sharpton et al., 1992; Morgan et al., 1997). Smaller impact structures with only two structural rings are the 90 km Manicouagan, Quebec (Grieve and Dence, 1979; Spray and Thompson, 2008) and the well preserved 100 km Popigai crater, Siberia, Russia (Dence and Grieve, 1979; Grieve et al., 1981; Poag et al., 1999, 2004; Whitehead et al., 2002).

1.3 Impactites

During the cratering process, the target rocks undergo a sequence of events that modify and re-distribute rocks in and around the newly formed structure (Melosh 1989; French, 1998; Osinski et al., 2011; Collins et al., 2012). Modifications of target rocks include (French, 1998; Koeberl et al., 2012): brecciation, shock metamorphism, melting and vaporization. An impactite is formally defined as "a collective term for all rocks affected by one or more hypervelocity impact(s) resulting from collision(s) of planetary bodies" (Stöffler and Grieve, 2007). In this study the classification and nomenclature of impactites will be according to the classification criteria in French (1998) and the International Union of Geological Sciences (IUGS) standards as proposed by Stöffler and Grieve (2007). Several suggestions have been made to modify the impactite nomenclature (Reimold et al. 2008; Stöffler et al., 2013; Grieve and Therriault, 2013) and these will be discussed with the results of the current study in appropriate sections. Stöffler et al.'s (2013) model (Figure 1.2) suggests that impactites may even form significantly after the final crater morphology is established, such as as a result of the interaction of infiltrating water with the hot melt pool.

The lithological classification of impactites is based on texture, lithological components, and the degree of shock metamorphism (Stöffler and Grieve, 2007). Impactites are classified into three groups: **shock metamorphosed target rocks** (both in situ and as fragments in breccias); **breccias** (monomict and polymict) and **impact melt rocks** (holohyaline, hypocrystalline and holocrystalline) (French, 1998; Stöffler and Grieve, 2007; Table 1.1).

Table 1.1: Impactite classification (modified after French, 1998)

CRITERION	CLASSIFICATION		
Location with respect to crater (R_c – crater radius)	**Crater floor and sub-crater**	**Within crater**	**Rim and near surface**
	Parautochthonous rocks: (<5 R_c)	Allochthonous rocks:	Allochthonous rocks: Ejecta –proximal
	Target Rocks (coherent)	Crater fill deposits	–distal (>5 Rc)
	Lithic breccias	Lithic Breccias	
		Melt-bearing breccias	
	Allochthonous rocks (cross-cutting)	-Suevites	
	Breccia dykes	-Impact melt breccias (= melt-matrix breccias)	
	Impact melt dykes	-Impact melt rocks	
	Pseudotachylite		
Source of component materials	**Parautochthonous**		**Allogenic rocks**
	Approximately in place (local)		Derived from single or multiple sources elsewhere
	Original stratigraphy and structure largely preserved		
Breccia characteristics	a. **Fragment character**	**Lithic breccia**	**Suevite (breccia)**
		Rock/mineral fragments only	Melt/glass fragments and rock/mineral fragments
	b. **Fragment lithology**	**Monomict (breccia)**	**Polymict (breccia)**
		Single rock type	Multiple rock types
	c. **Matrix character**	**Clastic-matrix (breccia)**	**Impact melt breccia (= melt-matrix breccia)**
		Discrete fragments	Coherent melt (glassy or crystalline)
Melt rock character	**Holohyaline** (glassy)		
	Hypocrystalline (mixed glassy/crystalline)		
	Holocrystalline (completely crystalline)		

1.3.1 Impactite types

According to Stöffler and Grieve (2007), the sub-classification of impactite types is according to their location (spatial distribution) within the final impact crater and sources of component material (composition), and their style of deformation (Figure 1.6). The impactites in the crater can be autochthonous, parautochthonous or allochthonous (Melosh, 1989, French, 1998, Stöffler and Grieve, 2007; Table 1.1). **Autochthonous** impactites are in situ, non-brecciated, fractured and shocked rocks, which lack evidence of whole-rock melting (Stöffler and Grieve, 2007).

Parautochthonous impactites are those rocks that experienced shock but remained relatively in situ during the impact process (French, 1998). These rocks occur beneath the crater floor, and include the fractured, shock metamorphosed target lithologies and lithic breccias where the original stratigraphy and structure is normally preserved (fractured but non-brecciated) after the impact event (French, 1998). **Allochthonous** refers to rocks or rock components that were produced elsewhere, and then moved into their current location by cratering processes (Grieve et al., 2007). The source of the component material (clasts and fragments) is derived from single (monomict breccias) or multiple (polymict breccias) sources (French, 1998; Stöffler and Grieve, 2007). Allochthonous impactites are subdivided based on their final location within the crater into crater floor deposits, proximal ejecta, or distal ejecta (French, 1998: Table 1.1).

Impact breccias are classified based on whether they contain a clastic or melt matrix (French, 1998). Three groups of clastic-matrix breccias are recognized: monomict (lithic) breccias, polymict lithic breccias and suevites (containing melt fragments); these are further subdivided based on the degree of mixing of various target lithologies, matrix character and whether or not they contain melt particles (Stöffler and Grieve, 2007). Generic and descriptive terms are used to describe these impactites. **Monomict breccias** are produced from a single lithology and are interpreted to form during shock compression and dilation of the crater basement (expansion of the transient crater cavity) (Stöffler and Grieve, 2007). The monomict breccias are postulated to form only during the late modification stage of the impact process (Dressler et al., 1996). Cataclastic rocks are also referred to as monomict breccias and generally have uniform peak shock pressure (Stöffler, 1982). **Polymict lithic breccias** and **suevites** are both breccias that have a clastic matrix enclosing a clast population derived from various target lithologies; the difference between them is the presence of melt fragments in suevite (Stöffler and Grieve 2007). As a result, suevite is defined as a "polymict impact breccia with a particulate matrix containing lithic and mineral clasts in all stages of shock metamorphism including cogenetic melt particles which are in a glassy or crystallized state" (Stöffler and Grieve 2007). Polymict breccias and anastomosing breccia dykes normally form during the central uplift and excavation stages of crater formation (Dressler et al., 1996). **Melt-matrix breccias** (impact melt breccias), on the other hand, are defined as breccias composed of rock and mineral fragments in a matrix of glassy or crystalline melt (French, 1998; Stöffler and Grieve, 2007). In melt-matrix breccias, the melt occurs not as individual fragments but as a matrix (25–75 volume% of the rock; French, 1998).

The location of the impactites relative to the crater (proximal versus distal settings), in conjunction with mode of genesis, melt proportion and shock characteristics of the clasts, can be used to group the impactites into subcrater, crater interior, crater rim and distal regions from crater (Figure 1.8): (a) **Subcrater** – parautochthonous rocks, cross-cutting impact melt/breccia, and pseudotachylitic breccia; (b) **Crater interior** – allochthonous crater-fill deposits (e.g., lithic breccia, suevite, impact melt rock); (c) **Crater rim region** – proximal ejecta deposits (e.g., fallout breccia) and breccia injections into the crater rim strata; and (e) **Distant from crater** – distal ejecta (e.g., tektites).

1.3.2 Pseudotachylite

Pseudotachylite formed in impact structures is defined as "a dyke-like breccia formed by frictional melting in the basement of impact craters, resulting in irregular vein-like networks" (Stöffler and Grieve, 2007). However, as noted by Dressler and Reimold (2004) and others, several other origins have been proposed for" pseudotachylite-like" rocks in impact settings, including shock melting and decompression melting, or a combination thereof (Reimold and Gibson, 2006). Given that rapid movements along fractures can occur at all stages of the impact event, frictional melt breccias could form through all stages of impact cratering (compression, excavation and modification), although Melosh (2005) argues that discreet shear movements may not be feasible during shock loading. The uncertainty about the exact origin led to the term ''pseudotachylitic breccia'' being proposed by Reimold (1995, 1998) for clast-bearing veins and dykes comprising rock and mineral clasts in a fine-grained, aphanitic melt matrix for which the exact origin is unknown.

According to Dressler et al. (1996), the pseudotachylite (dykes and anastomosing veinlets) easily develops along fractures and zones of contact as a result of frictional movement during the compression stage of the impact process (although see Melosh's counter argument). Chemically the formed pseudotachylite (friction melt) is similar to the host rock (Dressler et al., 1996), and clasts can can be generally related to the immediate wallrock, confirming local derivation. In the Sudbury and Vredefort impact structures, however, dykes up to tens of metres to kilometres wide can contain exotic clasts (Dressler, 1984; Reimold and Gibson, 2006). In most cases, however, pseudotachylite dykes are relatively small (m- to mm-wide).

1.3.3 Impact-melt rocks

Whole-rock melting produces impact-melt rocks that are classified according to their content of clasts (clast rich or clast poor) and sub-classified according to the degree of crystallinity of their matrix (Table 1.1). The three types are holohyaline (glassy), hypocrystalline (glassy and crystalline) and holocrystalline (crystalline variety) (Stöffler and Grieve, 2007). Impact melt lithologies can occur as "(1) allochthonous coherent melt sheets, impact melt and/or impact melt breccias; (2) inclusions in polymict impact breccias (suevite); (3) dykes and veins in the autochthonous crater basement, in displaced shocked rock fragments and in displaced (un-shocked) megablocks; (4) individual melt particles on top of the ejecta blanket, glassy or crystallised spheres in global air fall beds; and (5) glassy tektites" (Stöffler and Grieve, 2007). Geochemically, impact glasses have similar compositions to those of individual target rocks or, in the large craters, mixtures of target rocks (Koeberl and Martinez-Ruiz, 2003).

Impact-derived glasses have chemical and isotopic compositions that are similar to those of crater target rocks (Gucsik, 2009). Compared to volcanic glasses and natural glasses, impact glasses have low water contents (0.001-0.05 w.t. %) (Koeberl, 1992). In larger structures, large volumes of melt are formed and generally accumulate on the crater floor, and overlap collapsed terraces at the crater rim. The melts may also form layers and dyke-like intrusions in the fall-back breccias and crater basement (Dressler and Reimold, 2001). Melt formation is substantial in crystalline targets but appears to be lower in volatile-rich sedimentary targets (Dressler and Reimold, 2001).

1.3.4 Ejecta - tektites and micro-tektites

Ejected material during the impact process can be any dislodged material such as breccias, melt and shocked clasts that is expelled beyond the crater rim (French, 1998). Tektites are a form of ejecta that characteristically comprise centimetre-sized, homogeneous glasses formed as a result of melting and quenching of target rocks during the impact event (Montanari and Koeberl, 2000). Tektites are divided into three groups: 1) splash form tektites, 2) aerodynamically-shaped tektites, and 3) the Muong Nong type tektites (i.e., layered tektites). Micro-tektites (Montanari and Koeberl, 2000) may extend over thousands of square kilometres (Table 1.2). Proximal ejecta beyond the crater rim involve a predictable pattern of ballistic ejecta that can contain shock-modified and melt components (Osinski et al. 2011). Tektites have chemical and isotopic compositions that are similar to those of crater target rocks, with high silica contents (> 65 w.t. %) and low water contents (≤ 0.02 w.t. %) (Gucsik, 2009).

1.4 Diagnostic shock metamorphic features in minerals and rocks

Confirmation of the existence of impact structures requires identification of definite shock effects (mineral or rock response to shock compression) in addition to the recognition of the crater morphology (French, 1998; Montanari and Koeberl 2000, French and Koeberl, 2010). Obtaining meteorite fragments or geochemical confirmation for traces of the meteoritic projectile in impact melt rocks to validate the structure is distinctive (Montanari and Koeberl 2000, French and Koeberl, 2010). The term shock metamorphism refers to irreversible chemical, mineralogical and physical solid-state changes (i.e., shock-induced deformation features) in rocks and constituent minerals resulting from the passage of a shock wave through the target rock during the impact event (Melosh, 1989; French, 1998; Langenhorst, 2002; Stöffler and Grieve, 2007; French and Koeberl, 2010). Unlike progressive metamorphism experienced under normal geological processes, shock metamorphism is rapid, resulting in rocks achieving peak shock pressure states instantaneously without passing through the lower pressure stages (French, 1998). A particular shock pressure will also produce a specific post-shock temperature, which depends chiefly on the nature of the target material (French, 1998; French and Koeberl 2010). The distribution of shock pressures within target rocks varies on a variety of scales. Most shock metamorphism in the crater basement is limited to the central portions of the original crater and shock decreases radially with depth and outward towards the rim of the crater (Figure 1.3, 1.6; Grieve and Pilkington, 1996).

During the impact event peak pressures range from < 2 GPa at the transient crater rim to >100 GPa at the point of impact (French, 1998). Under these conditions the target rocks are subjected to shock pressures above their Hugoniot Elastic Limit (HEL), which ranges from 5-10 GPa for most minerals and whole rocks (Sharpton and Grieve, 1990), and 5-8 GPa for quartz (Stöffler and Langenhorst, 1994). The Hugoniot Elastic Limit (HEL) describes the maximum stress in an elastic wave that a material can be subjected to without permanent deformation (Melosh, 1989). Only hypervelocity impacts can generate such high shock pressures that exceed the HEL of geological materials and, as a result, shock metamorphic features evolve (Gucsik, 2009). These shock metamorphic effects occur over a range of shock pressures as summarized in Figure 1.9. Post-shock temperatures increase with increasing shock pressures. In most silicate minerals, the minimum shock pressure required to produce irrevisible mineral changes ranges from 5-10 GPa (Grieve and Pilkington, 1996).

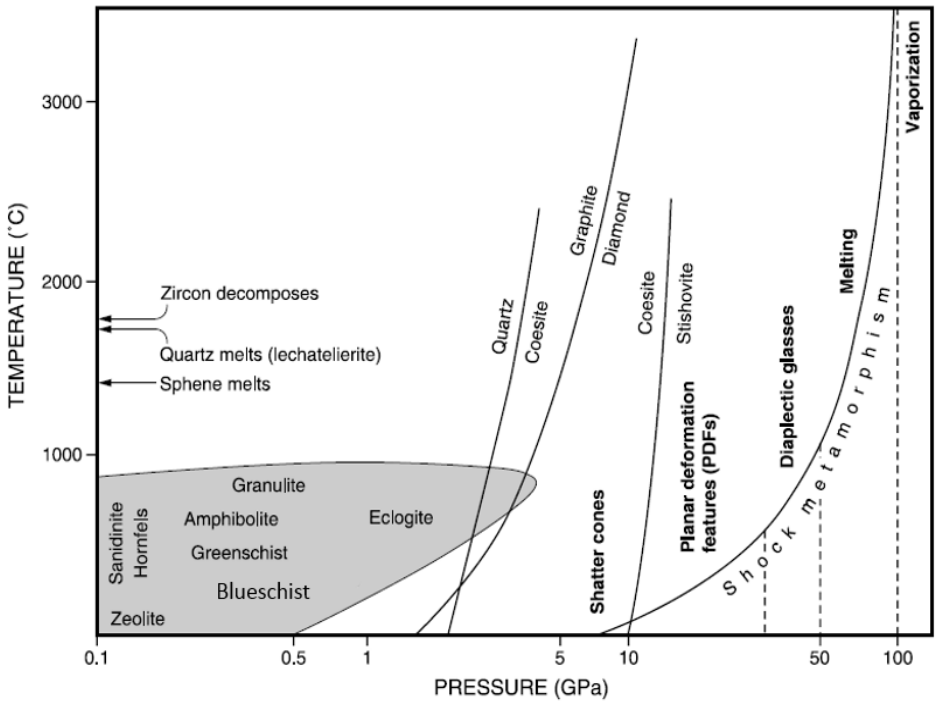

Figure 1.9: Graph showing pressure and temperature conditions of crustal metamorphism (grey zone); shock-related metamorphism and the stability curves for coesite, diamond and stishovite. The diagnostic shock features that develop at certain shock pressures and temperatures are also indicated (from French, 1998).

During the crater formation process shock wave energy is heterogeneously distributed even at the microscopic scale; as a result the developed distinctive shock effects can be highly variable at both the microscopic scale and mesoscopic scale (French and Koeberl, 2010). The development and preservation of diagnostic impact-produced effects is as a result of rock properties such as mineralogy, grain size, porosity, foliation and fracturing (Grieve at al., 1996). The deformation produced by shock is distinct from that seen in endogenic processes. Endogenic metamorphism of crustal rocks does not typically exceed pressures of 2 GPa and temperatures of 1200 ℃. Most features produced at ≥10 GPa are considered to be diagnostic of meteorite impact, since the ones produced at ≤10 GPa (faulting and brecciation) may not be unique to impacts but can also be formed during endogenic processes (French and Koeberl, 2010). Shock metamorphosed rocks are redistributed during crater formation in several ways: allochthonous fragments may occur in breccias within the crater fill and in material ejected from the crater, and the initially spherical

shock isobar pattern in the central crater basement is distorted by complex coherent and incoherent movements during crater modification (French and Koeberl, 2010).

1.4.1 Shock-induced macroscopic deformation in rocks

1.4.1.1 Shatter Cones

Shatter cones are relatively low-pressure (2-10 GPa to ~30 GPa) (Milton, 1977, French and Koeberl, 2010), macroscopic, striated radiating (horse-tail) conical fractures that develop in target rocks as a result of shock wave progression (Grieve et al., 1996, French and Koeberl, 2010; Osinski and Ferrière, 2016). Shatter cones generally show various geometries in terms of "orientation, apical angles, striation angles, sizes" (Baratoux and Reimold. 2016). They are best observed at outcrop scale (macroscopic scale) (French, 1998; French and Koeberl, 2010). They are normally found in situ, in rocks below the crater floor, or usually in the central uplifts of complex structures (Gucsik, 2009; Ferrière and Osinski, 2013); though some shatter cones were noted to form in the rims of complex impact craters (Wieland et al., 2006). Since shatter cones are restricted to these regions, suggestions have been made that the shatter cones form as direct products of shock-wave passage, before the brecciation and excavation of the rocks of the transient cavity (French and Koeberl, 2010). Shatter cones form in all kinds of rocks (carbonates, shales, clastic sediments, granites, gabbros, and other crystalline rocks) and range in size from ≤ 1 cm to several metres (French and Koeberl, 2010). They have been found in individual rock fragments in breccia units or in sub-crater breccia dykes (French, 1998; French and Koeberl, 2010). Shatter cones can be distinguished from fault slickensides and wind-abrasion surfaces by careful examination of the striations as the ones in shatter cones are divergent and penetrative, and may be curved whilst the striations in slickensides tend to be non-pervasive, parallel and linear (French and Koeberl, 2010). Shatter cones have been recovered in a few drillcore samples such as recently (and for the first time) at the Chicxulub impact structure (Morgan et al., 2016). Though cone-shaped features are found in other geological settings, shatter cones are regarded as convincing indicators of meteorite impact cratering even when not associated with other shock effects (French and Koeberl, 2010) and have been widely used to identify terrestrial impact structures (Gucsik, 2009). Since shatter cones require relatively large samples; they will not be discussed further in the context of this borehole study.

1.4.2 Shock metamorphism in minerals

The crystal structure and chemical composition of a mineral exerts an important control on the shock-induced deformation features developed (Sharpton and Grieve, 1990; Langenhorst, 2002). These include structural dislocations, high pressure mineral polymorphs (e.g. coesite and stishovite after quartz; reidite after zircon), ballen quartz, diaplectic mineral glasses, and melt particles; as well as a range of less distinctive features such as mosaicism, reduced birefringence, intragranular fractures and kink bands (French, 1998). Distinctive shock effects are known to occur in many minerals such as quartz, feldspar, zircon, and olivine (French, 1998; Langenhorst, 2002; Wittmann et al. 2006).

1.4.2.1 Shock metamorphism in quartz

Features in quartz have become standard unambiguous indicators of an impact (French and Koeberl, 2010). Between ~ 5 GPa and > 50 GPa, several microscopic shock-induced features are developed in quartz; these include: reduced refractive index, mosaicism, planar microstructures (planar fractures, planar deformation features and feather features), diaplectic glass, high pressure polymorphs (stishovite and coesite) and melting and quenching to lechatelierite (Grieve et al., 1996). In the case of crystalline rocks, quartz starts to melt at > 50 GPa and at shock pressure > 100 GPa quartz is completely vaporized (Grieve et al., 1996); however in porous rocks the pressure needed for melting is lower than these values. Shock features in quartz are known from, and have been calibrated through, shock-recovery experimental work (French and Short, 1968; Melosh, 1989; Stöffler and Langenhorst, 1994), although some uncertainties exist with regards to the predicted/developed shock pressure conditions, as shock waves may last several orders of magnitude longer in nature than in experiments and the impactor speed is much greater than ballistic gun experiments.

1.4.2.2 Planar microstructures

The term planar microstructures is a collective term referring to planar fractures (PF) and planar deformation features (PDF) developed under shock compression (Stöffler and Langenhorst, 1994). Experimental calibrations suggest PDF in quartz form at pressures of between ~ 5 and 35 GPa (Stöffler and Langenhorst, 1994; Stöffler and Grieve, 2007). Planar microstructures in quartz are oriented parallel to specific rational crystallographic planes in the host quartz and these

crystallographic orientations of PDF have been linked to pressure ranges (Langenhorst, 1994; French, 1998). Planar fractures are typically oriented along (0001) and a few other crystallographic planes (Grieve et al., 1996).

1.4.2.2.1 Planar fractures and feather structures

Planar fractures are parallel sets of multiple planar cleavages, open fracture or cracks that are generally 5 to 10 μm wide and 15 to 20 μm apart in quartz and other mineral grains (Robertson et al., 1968; Langenhorst, 2002). They develop at < 10 GPa and usually occur as up to 2-3 sets per grain (Stöffler and Langenhorst, 1994). Closely-spaced open fractures in quartz have been reported in non-impact environments; despite this, PF are used as shock-diagnostic features especially when occurring as multiple sets and accompanied by feather features (French and Koeberl, 2010).

Feather features (FF) are short, narrow-spaced (2-10 μm), parallel to subparallel lamellae that branch off from only one side of a PF (Poelchau and Kenkmann, 2011). FF may be related to a low-level shock pressure regime from ~7 to 10 GPa (Poelchau and Kenkmann, 2011). The formation of FF is related to shearing along the linked PF during shock deformation (Poelchau and Kenkmann, 2011). The acute angle formed between the PF and FF is on average 50-60° and is opened against the direction of shear displacement. FF are crystallographically controlled and are commonly oriented parallel to rational low-index crystallographic planes such as c (0001) (0°), r/z $\{10\bar{1}1\}$ (52°) and ξ $\{11\bar{2}2\}$ (48°); however, ω $\{10\bar{1}3\}$ (23°) and π $\{10\bar{1}2\}$ (32°) orientations have not been identified (Poelchau and Kenkmann, 2011). Close to the base of a PF, FF are straight, but they may become curved with increasing length, thus, the crystallographic control of FF is strongest near the PF (Poelchau and Kenkmann, 2011). Poelchau and Kenkmann (2011) suggest that FF should be considered exclusively diagnostic of shock as, to date, FF have been recognized in 26 impact structures and they have not been reported in endogenically deformed crustal rocks. Data have been produced on these features in studies by Poelchau and Kenkmann (2011) of samples from Nördlinger Ries and the Matt Wilson impact structure. FF have also been described from the Rock Elm Structure (French et al., 2004).

Microscopic planar microstructures are produced in other minerals such as feldspars (plagioclase and K-feldspar), micas (biotite and muscovite), amphiboles, pyroxenes and accessory minerals such as sillimanite, apatite, cordierite, garnet and zircon. At ~8 up to 25 GPa, minerals can

display shock metamorphic planar fractures and planar deformation features (French, 1998). Limited data exists where the other minerals (excluding quartz and feldspar) have been used as unequivocal evidence of impact-produced deformation (Grieve et al., 1996; Langenhorst, 2002).

1.4.2.2.2 Planar deformation features

Planar deformation features occur as single or multiple sets of closely spaced (2-10 μm), narrow (<2-3 μm), straight (parallel) well-defined lamellae (Grieve et al., 1996; Stöffler and Langenhorst, 1994). PDF are formed in minerals such as quartz and feldspar, though they are most commonly described in quartz (French and Koeberl, 2010). PDF in quartz develop over a pressure range of ~ 5-10 GPa to ~ 35 GPa (Stöffler and Langenhorst, 1994). The reliance on PDF in quartz as a shock barometer is because quartz is geologically durable and easy to measure crystallographically (Engelhard and Bertsch, 1969; Stöffler and Langenhorst, 1994; Grieve et al., 1996; Ferrière et al., 2009; French and Koeberl, 2010). There are four different forms of PDF: (1) bands of dislocations, (2) lamellae with different proportions of amorphous silica, (3) Brazil twin lamellae (parallel to *c* - 0001) and (4) ladder structure (Stöffler and Langenhorst, 1994; French, 1998). A common feature of those lamellae is the low birefringence in comparison with the host crystal. PDF occur as solid lamellae (non-decorated) filled with glass or as annealed arrays of small fluid inclusions (decorated PDF) (Grieve et al., 1996). The decorated PDF are formed by annealing of original amorphous PDF (Grieve et al., 1996; French and Koeberl, 2010), particularly in geologically older craters. The decorated PDF still preserve the orientation of the original PDF.

PDF have specific crystallographic orientations that show pressure-dependence (Stöffler and Langenhorst, 1994; Grieve et al., 1996; Langenhorst, 2002), and therefore the measured PDF orientations are useful in estimating the shock pressures experienced by rocks during an impact event (Table 1.2). Recorded shock pressures in quartz can be used to constrain aspects of the cratering process and in estimating the initial crater dimensions (especially in eroded structures) (Grieve et al., 1996). There are 4 PDF orientations recognized in quartz (Stöffler and Langenhorst, 1994; Feldman, 1994; Grieve and Robertson, 1976; French,1998): 1) Type A (Pressure > 7.5 GPa): basal PDF only- **c** (0001); 2) Type B (Pressure > 10 GPa), appearance of **ω** $\{10\bar{1}3\}$ planes, with basal planes, 3) Type C (Pressure > 15 GPa), appearance of **a** $\{22\bar{4}1\}$; **r** $\{10\bar{1}1\}$; **z** $\{01\bar{1}1\}$; ξ$\{11\bar{2}2\}$ planes and 4) Type D (Pressure > 16 GPa), appearance of **π**$\{10\bar{1}2\}$ planes. The most abundant Miller-Bravais Indices are $\{10\bar{1}1\}$ and $\{10\bar{1}3\}$ (French, 1998). Up to 10 sets of PDF can be observed in one quartz grain (Stöffler and Langenhorst, 1994).

Planar microstructures, PF, PDF and kink banding have been observed in micas, pyroxenes, amphiboles, garnet and accessory (apatite, sillimanite, cordierite, garnet, scapolite and zircon) minerals (Stöffler, 1972; French, 1998; Poag et al., 2004), however, the shock effects in these minerals are rarely described as they are often overlooked and not properly investigated in impact settings (Stöffler, 1972; French, 1998; Poag et al., 2004).

Table 1.2: Table showing progressive stages of shock metamorphism in non-porous quartz-bearing rocks (after Stöffler and Langenhorst, 1994). Data for additional rare PDF orientations is from Robertson et al., 1968 and Engelhardt et al., 1968.

Shock Stage	**Critical sets of PF and PDF**	**Additional sets of PF and PDF**	**Optical properties of quartz**
(1) Very weakly shocked	PF: (0001)	PF: $\{10\bar{1}1\}$ rare PDF: none	normal
(2) Weakly shocked	PDF: $\{10\bar{1}3\}$	PF: $\{10\bar{1}1\}$, (0001) PDF: rare	normal
(3) Moderately shocked	PDF: $\{10\bar{1}3\}$	PF: $\{10\bar{1}1\}$, (0001) rare PDF: (0001), $\{10\bar{1}0\}$, $\{11\bar{2}1\}$, $\{11\bar{2}2\}$ $\{10\bar{1}1\}$, $\{21\bar{3}1\}$, $\{51\bar{6}1\}$ *$\{22\bar{4}1\}$, $\{40\bar{4}1\}$, $\{51\bar{6}0\}$, $\{31\bar{4}1\}$	normal or slightly reduced refractive indices
(4) Strongly shocked	PDF: $\{10\bar{1}2\}$, $\{10\bar{1}3\}$	PF: rare or absent PDF: (0001), $\{10\bar{1}0\}$, $\{11\bar{2}1\}$, $\{11\bar{2}2\}$ $\{10\bar{1}1\}$, $\{21\bar{3}1\}$, $\{51\bar{6}1\}$ *$\{22\bar{4}1\}$, $\{40\bar{4}1\}$, $\{51\bar{6}0\}$, $\{31\bar{4}1\}$	reduced refractive indices: 1.546-1.48
(5) Very strongly shocked	PDF: $\{10\bar{1}2\}$, $\{10\bar{1}3\}$	none	reduced refractive indices: < 1.48

** Additional rare PDF orientations*

1.4.2.3 High-pressure polymorphs

Mineral constituents of target rocks change to higher pressure polymorphs when threshold shock pressures are exceeded (French, 1998). The high-pressure polymorphs of quartz - coesite and stishovite - are used extensively as indicators of shock metamorphism (Melosh, 1989). Quartz can be transformed to stishovite at shock pressures of >12-15 GPa and to coesite at >30 GPa (Deer et

al., 1992; Stöffler and Langenhorst, 1994; Ferrière and Osinski, 2013). In sedimentary rocks, coesite is known to form at pressures as low as ~ 5.5 GPa and is common at pressures above 10 GPa (Kieffer et al., 1976). Coesite has been noted in rare ultra-high pressure metamorphic rocks and kimberlites, but stishovite has only been reported from impact structures (Gucsik, 2009) and meteorites (Gillet et al., 2007).

At 30 GPa, other high pressure polymorph minerals that form include: diamonds (from graphite); ringwoodite (from olivine) and reidite (from zircon) (Stöffler and Langenhosrt, 1994; French, 1998; Montanari and Koeberl, 2000). Diamonds may be formed by the shock compression of carbon yielding metastable diamond on quenching (Erskine and Nellis, 1991). The impact-derived nanodiamonds found in the Popigai impact structure in Siberia (Russia) are an intriguing example of how graphite in the pre-impact target rock was transformed to polycrystalline diamonds (Koeberl et al., 1997). Notably jadeite (from plagioclase), majorite (from pyroxene), wadsleyite and ringwoodite (from olivine) have not been documented in terrestrial impact structures but do occur in meteorites (Ohtani et al., 2004; Fritz and Greshake, 2009). The shock indicator phases and associated conditions of formation are summarized in Figure 1.9.

1.4.2.4 Mosaicism in quartz and other minerals

Shock-induced mosaicism (or mosaic structure) in quartz appears as a mottled optical extinction appearance (i.e., patchy extinction pattern) (Grieve et al., 1996, Stöffler and Langenhorst, 1994; Langenhorst, 2002) where a uniform single crystal is composed of a large number of smaller domains displaying crystallographic mismatch (French and Koeberl, 2010). Mosaicism is commonly developed in quartz grains that also exhibit PF and PDF (Stöffler and Langenhorst, 1994). If the mineral was recrystallized during subsequent thermal metamorphism or post-shock annealing, no correlation between pressure and degree of mosaicism can be validated (Osinki and Pierazzo, 2013). Mosaicism, though distinct from tectonically developed undulatory extinction in quartz, cannot be exclusively used as a unique shock diagnostic feature (French and Koeberl, 2010).

1.4.2.5 Diaplectic glasses

At high shock pressures (>30 GPa to 50 GPa) quartz and feldspar form diaplectic quartz glass and diaplectic feldspar glass (maskelynite), respectively; mineral grains are converted (entirely or

partially) to an amorphous or glassy phase via solid-state transformation (Stöffler 1984; Grieve et al., 1996; French and Koeberl, 2010). Unlike other thermally-produced melts, diaplectic glasses do not show flow textures and the original texture and fabric of the mineral grains are preserved (Stöffler, 1984; Stöffler and Langenhorst, 1994; Grieve et al., 1996; French, 1998, Chen and El Goresy, 2000). Diaplectic glasses have low refractive indexes that decrease with increasing pressure (Grieve et al., 1996).

1.4.2.6 Post-shock thermal features

Ballen silica is a <10 to ~200 µm textural feature that appears as a rounded to oval, grape-shaped, bodies (Schmieder and Buchner, 2007; Ferrière et al., 2010). Five types of ballen silica (ballen cristobalite) have been identified (Ferrière et al., 2009): ballen with homogeneous extinction in α-cristobalite ballen (1) and in α-quartz ballen (2), or optically individual ballen (3) with different crystallographic orientations (and extinction), or with intraballen recrystallization (4) and microcrystalline, chert-like ballen (5). The formation mechanism of ballen quartz has generally been accepted to be as a result of cristobalitization of silica at high temperatures of ~1200 ℃ and also at shock pressures in excess of ~ 30–35 GPa (Short, 1970). Ballen quartz and cristobalite occur in diaplectic quartz glass (Bischoff and Stöffler, 1984). Bischoff and Stöffler (1984) proposed that ballen quartz actually represents diaplectic quartz glass that has transitioned to cristobalite and thereafter to α-quartz. The toasted appearance of α-quartz ballen has been noted in several impact structures and is much like the toasting observed in quartz grains in impactites; Ferrière et al. (2009, 2010) attributed this feature to vesicle formation after pressure release at high post-shock temperatures. Ballen quartz can be found in impact craters and occurs predominantly in impact-melt rock and suevite and target rocks that have been mainly affected by post-shock heating (Schmieder and Buchner, 2007; Ferrière et al., 2010). Ballen quartz has also been noted in volcanic rocks, fulgurites, and heated industrial quartz ceramics (Schmieder and Buchner, 2007).

1.4.2.6 Kink banding in micas

Kink bands are possible low shock deformation features that occur as single or multiple sets that lie oblique to the basal cleavage of the mica grain (French and Koeberl, 2010). Kink bands can be developed in both muscovite and biotite (French, 1998). In biotite and muscovite these develop as a result of crystal gliding along the basal plane with external rotation of the crystal lattice

(Stöffler, 1972). Kink bands in mica are not oriented parallel to rational crystallographic planes (Gucsik, 2009) and cannot be exclusively used as a unique shock-diagnostic feature as they can also be produced by tectonic deformation and are commonly reported in ordinary metamorphic rocks (French and Koeberl, 2010).

1.4.3 Selective mineral and whole-rock melting

Near the point of impact the target rock is subjected to progressively higher shock pressures (≥ 60 GPa) and higher post-shock temperatures (≥ 2000 °C) that rapidly melt a large volume of target rock, producing a chemically homogeneous, flow-textured, impact melt body (French, 1998). In non-porous crystalline rocks whole-rock (bulk) melts are generated at ~60 GPa, whilst in porous sedimentary rocks the whole rock melts are generated at much lower pressures (~30–35 GPa; Kieffer et al., 1976). The impact melts are derived from the rocks within the vicinity of the point of impact (French, 1998); see Chapter 1, Figure 1.2. The melt body may incorporate variably assimilated inclusions of the target rock and even traces of vaporized or melted projectile (French, 1998). Impact processes can distribute/move and emplace the impact melt within and outside the crater, as fragmented inclusions in suevitic breccias, or as part of the ejected material (French, 1998).

Under slightly lower shock pressures (> 45 GPa, Stöffler, 1972) and temperatures, melting points for typical rock-forming minerals are exceeded, hence localized shock melting of selective minerals occurs (French, 1998, French and Koeberl, 2010). Research shows that the melting of constituent minerals during the impact process is an instantaneous process where an individual mineral grain melts completely (Keil et al., 1997) forming monomineralic melts (Stöffler, 1984) or normal eutectic melting can occur at grain boundaries of adjacent minerals over a longer time scale, producing melts of mixed compositions (French, 1998). The composition of melt particles can be highly variable depending on whether the case is for incomplete mixing of constituent minerals, complete quenching to glassy state or re-crystallized state (Keil et al., 1997, French, 1998). Selective mineral melting produces unusual textures as some minerals show melting features (contorted flow structures) while adjacent ones remain un-melted or even undeformed (French, 1998). The presence of high-temperature lechatelierite (monomineralic quartz melt), which forms from pure quartz at temperatures >1750ºC (pressures of 50 GPa); baddeleyite which forms from zircon at temperatures of ~1850 ºC and melting of titanite (sphene) at 1450 ºC further substantiate an impact origin (French and Koeberl, 2010). If the amount of flow and mixing is

low, these chemically diverse melts may preserve the original shapes of the precursor grains (French, 1998).

1.5 Regional Geology

The Kaapvaal Craton (KC) of South Africa was amalgamated in response to tectono-magmatic events between 3.6 and 2.7 Ga (Poujol et al., 1996, 2003; Figure 1.10). The western domain of the KC (formed 3.0–2.7 Ga ago) includes the Kraaipan, Amalia, and Madibe greenstone belts (Poujol et al., 1996) and the 2.78-Ga Gaborone Granite Complex (Grobler and Walraven, 1993) in south-eastern Botswana (Figure 1.10). In contrast to the well exposed and well studied occurrences in the eastern and northern sectors of the craton, the Archaean greenstones and associated granite gneisses of the western sector of the KC are relatively poorly exposed owing to its extensive sedimentary and volcanic cover. The latter comprises the 2.7 Ga Ventersdorp Supergroup, the 2.6 – 2.1 Ga Griqualand West (Transvaal) Supergroup and the Late Cretaceous to Cenozoic Kalahari Group (Anhaeusser and Walraven, 1999; Corner et al., 1997; Andreoli et al., 1999). The Kraaipan greenstones were deformed and metamorphosed in conjunction with 4 stages of granitic intrusions: 1) at 3250 Ma, leuco-trondhjemitic gneisses and granodiorites; 2) at 3135-2940 Ma, K_2O - rich granodiorites, adamellites and granitoids; 3) at 2880-2810 Ma, K_2O rich adamellites and granites; and 4) at 2735 Ma, K_2O - rich adamellites and granites (Anhaeusser and Walraven, 1999; Poujol and Anhaeusser, 2001).

In view of the fact that the MIS is almost entirely covered by the continental formations of the Kalahari Group, the study of the pre-Kalahari basement in the area is largely restricted to the examination of the diamond drill borehole cores (see locations in Figure 1.1), percussion-drilled rock fragments from water boreholes, and geophysical data (Hart et al., 1997). The MIS impact melt encountered in boreholes M3, WF3, WF4 and WF5 (Figures 1.1; 1.13) is largely unaltered and contains a large number of lithic clasts of felsic (granitic) to ultramafic composition, as well as fragments of the original meteoritic impactor (Andreoli et al., 1999; Koeberl and Reimold, 2003; Maier et al., 2006). Geochronological results obtained from independent studies by Hart et al. (1997) and Koeberl et al. (1997) constrain the age of the Morokweng impact event to 145 ± 2 Ma. Working on the melt sheet intersected by the WF5 borehole core, Hart et al. (1997) obtained a 206Pb/238U age of 145.2 ± 0.8 Ma from zircons in a dolerite clast, and a 40Ar/39Ar age of 143.5 ± 3.6 Ma from primary biotites in the host quartz norite.

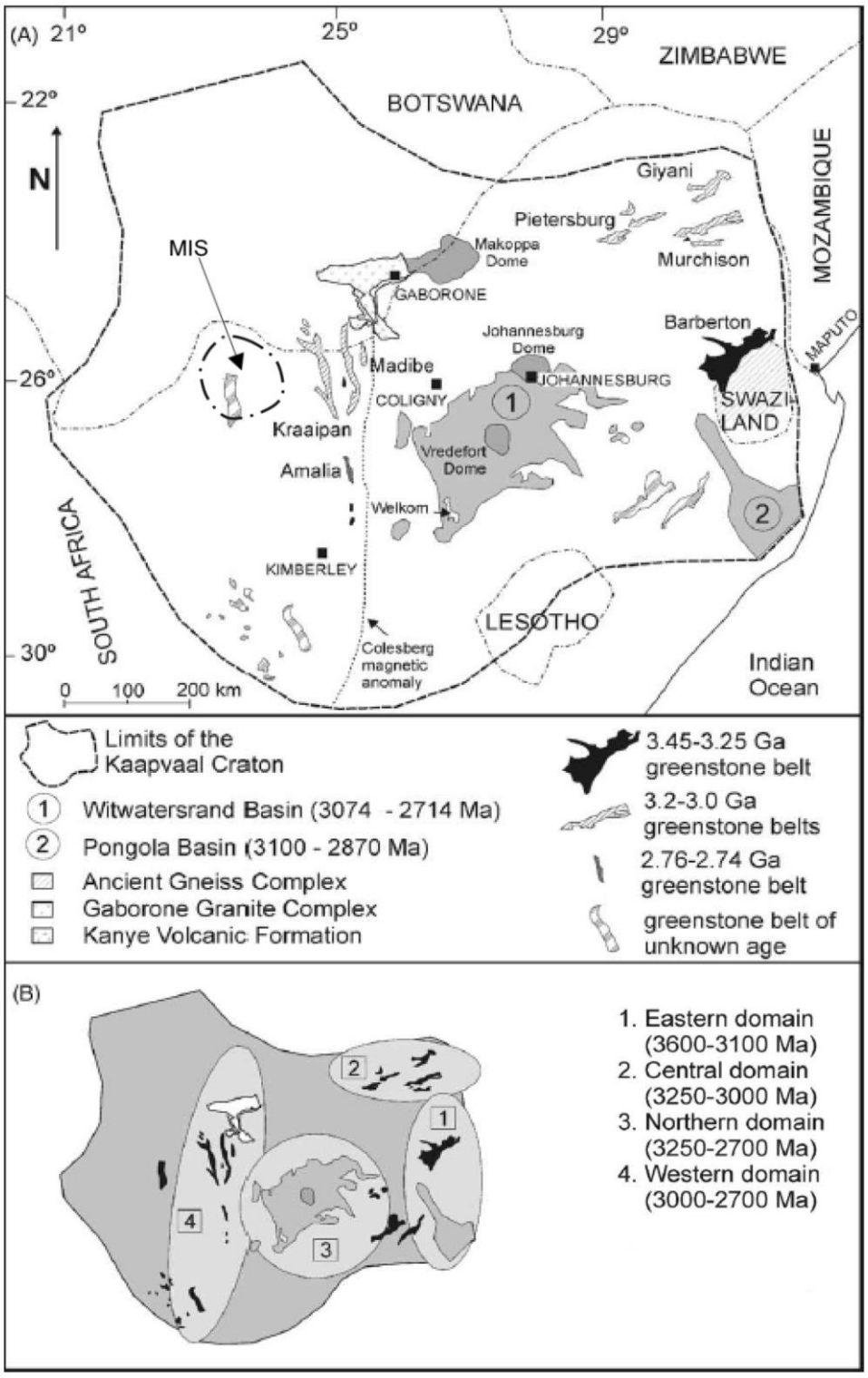

Figure 1.10: Diagram showing the outline of the Kaapvaal Craton and the locations of the eastern, central, northern and western domains (Poujol et al., 2003). MIS – Morokweng impact structure.

Koeberl et al. (1997) dated recrystallized zircons from the impact melt sampled from the WF4 core using the SHRIMP ion microprobe and obtained a 206Pb/238U age of 146.2 ± 1.5 Ma and a 208Pb/232Th age of 147 ± 1.9 Ma. Accordingly, all authors (Hart et al., 1997; Koeberl et al., 1997) concluded that the zircon and mica ages date the end-Jurassic crystallization of the melt sheet and, consequently, the impact.

The regional geology in the Morokweng area consists of an Archaean crystalline basement exposed at the core of a broad structure, until recently known as the Ganyesa dome (after the main town in the area (Andreoli et al., 1999 and references therein). The geological map of the area by Smit (1977) shows only scattered outcrops of Archaean granitoids, with some occurrences of Kraaipan Group (3.0-2.9 Ga) rocks (banded iron formation (BIF) units, metavolcanics and minor ultramafics; Hart et al., 1997). The rocks flanking the dome are largely represented by the Proterozoic (meta) sediments (carbonates and banded iron formations) of the Griqualand West Supergroup (Koeberl and Reimold, 2003). Mafic intrusive and extrusive lithologies occurring regionally also include the ~2.7 Ventersdorp Supergroup lavas (2.7 Ga; Armstrong et al., 1991) and the 2.22 Ga Ongeluk Formation lava (Walraven and Martini, 1995; Gutzmer et al., 2003). The regional geology and major structural features of the Morokweng area are shown in Figure 1.1. A detailed regional aeromagnetic survey (Figure 1.11) has revealed the presence of a number of cross-cutting younger dykes, the major one named Machavie (Figure 1.1), hidden under the Kalahari cover (M.A.G. Andreoli, unpublished data; Andreoli et al., 1999). The Machavie dyke and a second dyke, named Paddakoor, appear to have been emplaced along fractures/faults striking radially (~090° and ~150°, respectively) to the MIS (Andreoli et al., 1999, 2007; Misra and Andreoli, 2012).

1.5.1 Geophysical studies and modelling of the Morokweng impact structure

The Morokweng geological structure (Figure 1.11) was first recognized in the aeromagnetic data of the KC by B. Corner in 1986 and E. Stettler in 1987, who noted a strong ~30 km diameter,

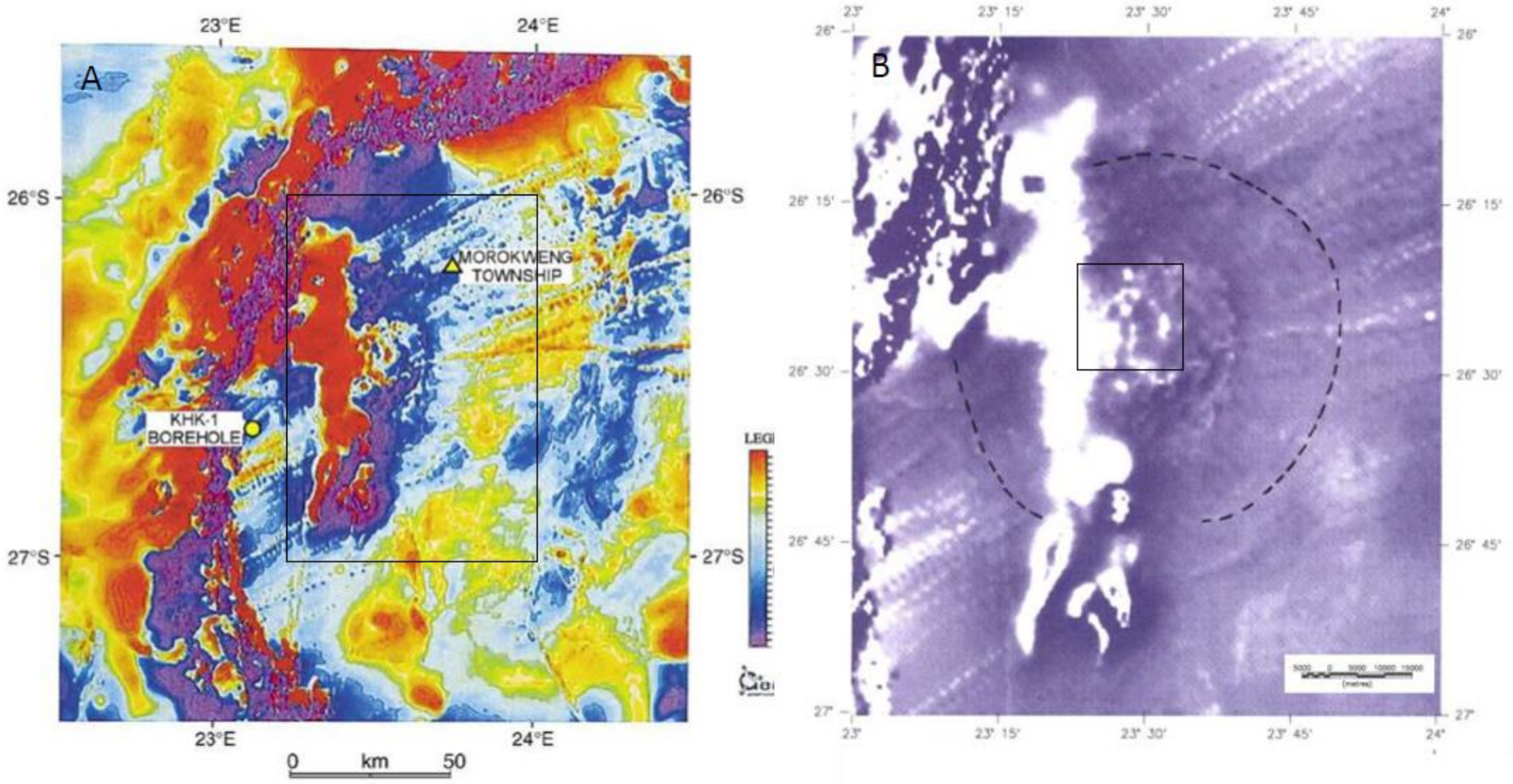

Figure 1.11: **A)** Regional aeromagnetic image of the Morokweng area showing the 30 km circular anomaly of the Morokweng impact crater, ~50 km SW of the Morokweng township, and the NE-SW-trending regional dyke swarm (Henkel et al., 2002; see text for discussion of borehole KHK-1). **B)** Enlarged aeromagnetic image of the Morokweng impact structure (rectangle in Figure A) showing, the same positive anomaly (~ 30 km) surrounded by an ~70 km wide zone (outlined by dotted line) that marks the disruption and/or weakening of the NE-SW-trending, regional dyke swarm (from Corner et al., 1997). Inset: see Figure 1.12 B.

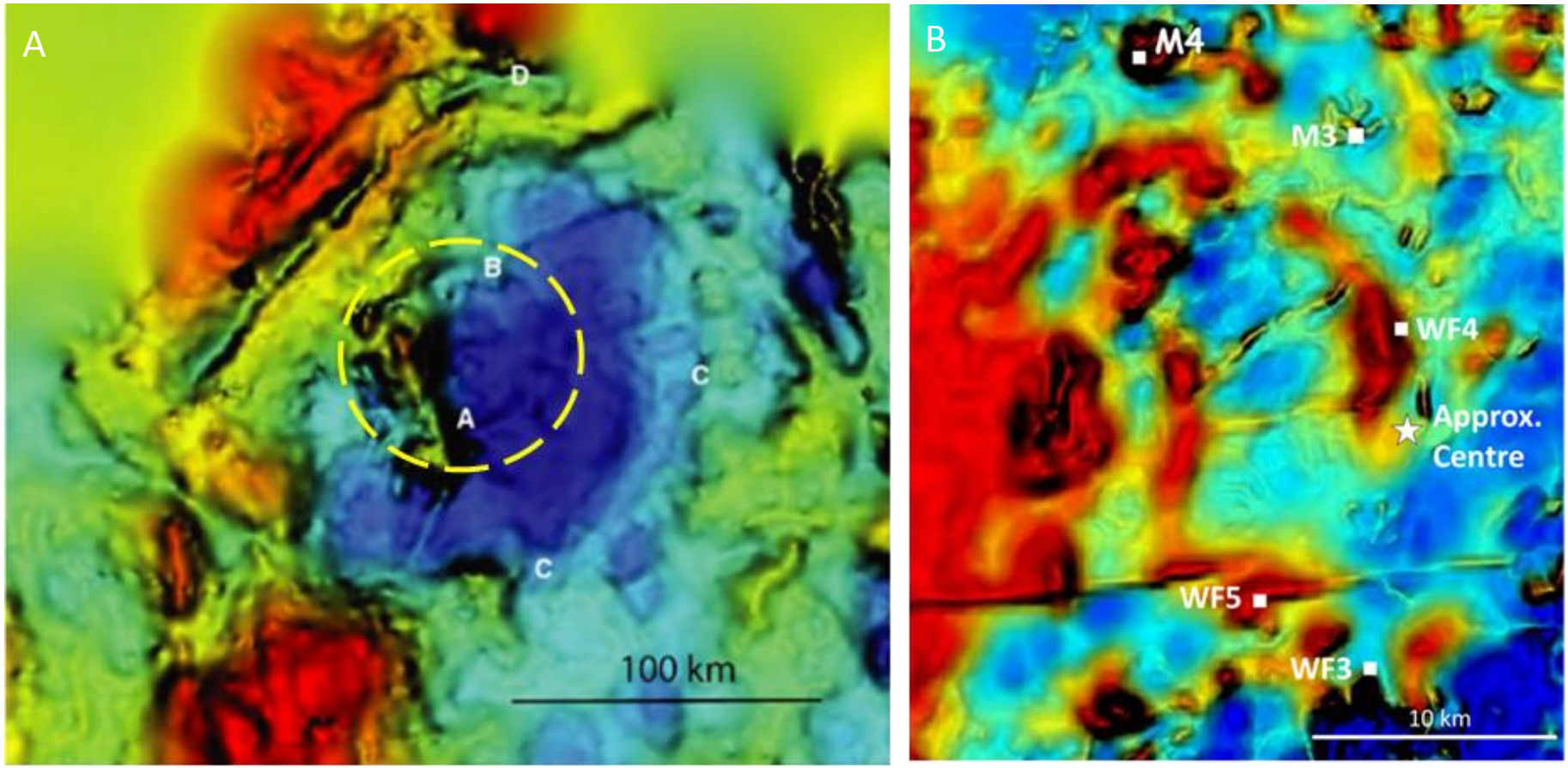

Figure 1.12: A) Bouguer gravity image (edge-enhanced) of the Morokweng area (Andreoli et al., 2008a). A corresponds roughly to the central 30-km-wide magnetic anomaly. Dashed line has a 70 km diameter (see Figure 1.11B). The gravity low of the Morokweng/Ganyesa dome extends to C. **B)** Magnified high-resolution aeromagnetic image of the NW sector of the central anomaly indicated by square in Figure 1.11 B, showing the locations of the 5 central diamond drill exploration boreholes discussed in the text (M.A.G. Andreoli, unpublished).

positive (up to 350 nT) magnetic anomaly surrounded by a ~40 km wide magnetically "subdued" halo (Corner et al., 1997). These authors originally interpreted the feature as representing an igneous intrusion of magnetic syenite or granite composition. Subsequent re-examination of thin sections from borehole WF5 led to the recognition of the impact origin for the same near-circular geophysical anomaly (Andreoli et al., 1995), later reconfirmed and dated at ~145 Ma by a number of studies (Hart et al., 1997; Corner et al., 1997; Koeberl et al., 1997).

Since its discovery, the Morokweng impact structure has generated considerable debate about its original size. The variation in the estimates of the original crater diameter is due to the various interpretations of the geophysical data and their relationship to regional geology and diamond drill borehole lithostratigraphy. Two schools of thought developed. One school has based great importance on the observation that geological maps, satellite imagery, and computer-enhanced geophysical images of the Morokweng (formerly Ganyesa) dome region show a series of arcuate features (i.e., aeromagnetic and gravity anomalies) that are concentric to the well-characterized central impact melt sheet region (Figures 1.1, 1.11B, 1.12A). This approach led Andreoli et al. (1995, 1999, 2007) and Corner et al. (1997) to propose a diameter ranging between 340 km (Corner et al., 1997) and, more recently, 240 km (Andreoli et al., 2007; cf. Figure 1.1). The second school of thought considers instead other sets of data, mainly scaling of impact craters, modelling of geophysical data and borehole core information to propose an original crater diameter of ~70-80 km (cf. www.passc.net/EarthImpactDatabase/; Henkel et al., 2002; Reimold et al., 2002).

According to these latter authors, the centre of the Morokweng crater lies to the west of the centre of the Morokweng/Ganyesa dome, and the association of crater and dome is coincidental. More recently, however, the geometric, concentric nature of the Morokweng impact crater and the Morokweng/Ganyesa dome has been recognized by Reimold and Koeberl (2014). The evidence that the Morokweng impact structure appears to be a multi-ring basin is based on observations by Andreoli et al. (2008a) who proposed a diameter of 260 km based on the re-evaluation of gravity and magnetic data and borehole log observations that suggested, first, that the extent of shock deformation features extends to ~40 km radius. From this, they concluded that the central uplift diameter was 80 km. They also considered the polymict suevitic breccia dyke in the KHK-1 borehole (Reimold et al., 2002); see Figure 1.1 (denoted as HKH-1) and Figure 1.11 as supporting evidence of an 80 km wide central uplift, arguing that such breccia dykes are typical of the lithologies found at the edge (margins) of central uplifts. Second, they identified an outer ring-shaped aeromagnetic anomaly with a radius of 130 km (Andreoli et al., 2008a). The concentric rings are quite distinct on the Bouguer gravity image (Figure 1.12A) and correspond well with the geological interpretation in Figure 1.1.

To date, no seismic data has been obtained across the MIS. Based on the combination of all the geophysical and borehole log data the MIS was divided into five rings (Andreoli et al., 2007; Figure 1.1). These rings are described as follows: Ring I (Ring A, Figure 1.12A), with a radius of ~14 km, marks the limit of impact melt rocks; Ring II (Ring B, Figure 1.12A), with a radius of ~33 km, outlines the limit of allochthonous breccia and melt; Ring III (radius ~40 km) defines the limit of (para)autochthonous breccia, shock metamorphism and structural disruption of the regional dykes; Ring IV (Ring C, Figure 1.12A), with a radius of ~70 km, marks the contact between Archaean granite and its supracrustal cover and Ring V (radius ~ 130 km) represents magnetic banded iron formation (BIFs) of the Late Archaean Kraaipan Group. In Figure 1.12, a feature labelled D relates to significicant rings that other researchers attribute to indicating that the MIS is an impact structure larger than 70 km (Corner et al., 1997).

1.5.2 Morokweng borehole core stratigraphy

The detailed subsurface geology of the Morokweng structure can only be evaluated from the study of the sparse boreholes that have been drilled in the area (see Figures 1.1 and 1.12B for the main diamond drill hole locations); however, their limited number and the lack of outcrops raises more questions, including that of the amount of the pre-Kalahari Group Cretaceous erosion. Levels of post-impact erosion are important in estimation of the original crater diameter. The published, simplified stratigraphic logs of four of the five boreholes shown in Figure 1.12B are provided in Figure 1.13; the fifth core (M4) is the subject of this study. The only drillcore outside the central zone is the KHK-1 borehole located approximately 40 km southwest of the centre of the geophysical anomaly (indicated HKH-1 in Figure 1.1). The KHK-1 core (up to a depth of 3420 m), intersects gabbroic intrusion at 889.1 m and is marked by the occurrence of a 10 cm wide polymict suevite that contains angular fragments of granitoid rock and metasedimentary rocks, PDF and minor angular to rounded glass fragments (Reimold et al., 2002).

The WF3 (130.3 m), WF4 (189.3 m), WF5 (271.3 m) and M3 (1076.13 m) boreholes were all drilled into magnetic anomalies in the central region of the MIS (Figures 1.12B) beneath 50-100 m of Kalahari Group sediments, which comprises well laminated sand, sandstone and crumbly (owing to weathering) calcrete (Hart et al., 1997; Reimold et al., 1999). An ~50 cm thick conglomerate bed containing clasts of altered quartz norite (impact melt rock) and granitoid gneiss was intersected at the base of the Kalahari Group in boreholes WF3 and WF5 (Hart et al., 1997; Reimold et al., 1999; see Figure 1.13). Petrographic analysis of the granite pebbles from this bed showed evidence of shock metamorphism in the form of PDF in quartz, and the melt rock clasts show evidence of hydrothermal alteration (Hart et al., 1997). All cores intersected crystalline melt rocks directly beneath the Late

Cretaceous unconformity, and subsidiary highly shocked granitoid target rocks towards the base in WF5 and M3 (Hart et al., 1997; Koeberl et al., 1997; Andreoli et al., 1999; Reimold et al., 1999; Koeberl and Reimold, 2003). Initially the lower contact of the impact melt rock was thought to have been reached at 225 m depth in the WF5 core (Andreoli et al., 1995; Hart et al., 1997; Koeberl and Reimold, 2003) and the melt sheet itself was considered ~125 m thick and undifferentiated (Koeberl et al., 1997; Reimold et al., 1999). However, analysis of the M3 core revealed that the melt sheet was significantly thicker (~800 m) and differentiated (Figure 1.13; Andreoli et al., 1999; Hart et al., 2002 Maier et al., 2006).

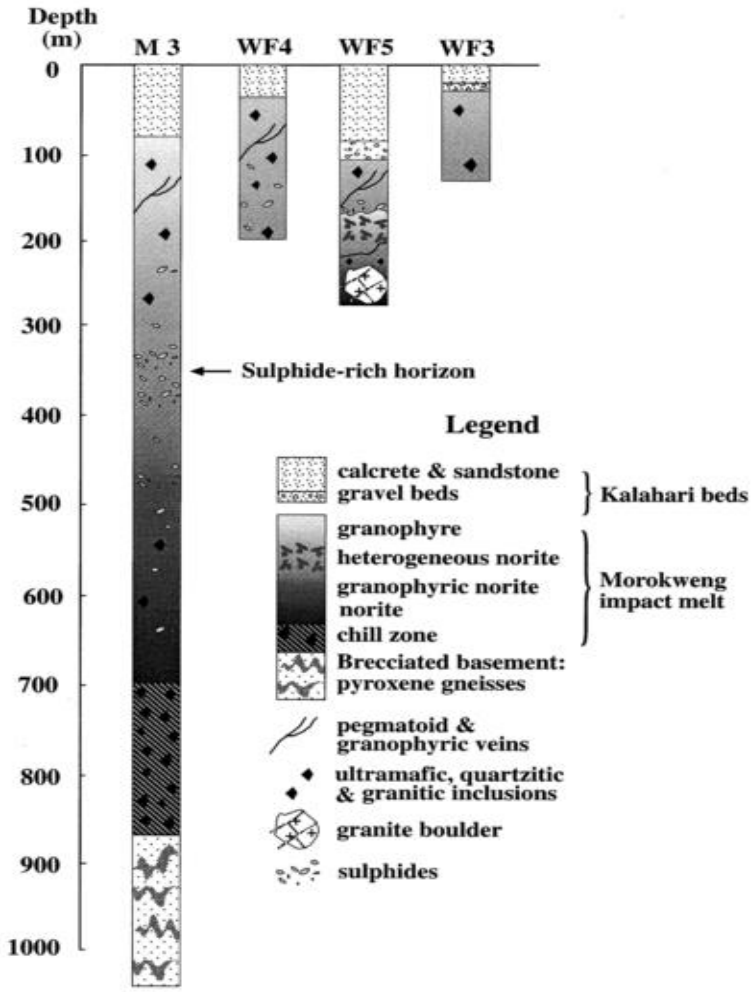

Figure 1.13: Lithological profiles of the M3, WF4, WF5, and WF3 boreholes from the Morokweng impact structure (from Hart et al., 2002).

The upper parts of the impact melt rock are altered and the presence of secondary minerals such as carbonate and epidote in sub-horizontal and shallowly-dipping veinlets (up to 40 cm thick) indicate that this rock was exposed to hydrothermal alteration (Reimold et al., 1999; Koeberl and Reimold,

2003). Alteration ceases about 15 m into the melt rock, below which there is dark brown melt rock (Reimold et al., 1999). The impact melt rocks contain lithic inclusions, the most notable being those of the chondritic impactor found towards the base of the M3 core (Maier et al., 2006). Other lithic clasts are mainly doleritic, gabbroic, granitic and quartzitic (Hart et al., 1997, 2002; Koeberl et al., 1997; Koeberl and Reimold, 2003) in addition, a large boulder of amphibolite was intersected in close proximity to the boulder-size chondritic clast (M. Andreoli, personal communication, 2016). The largest lithic fragment, with a vertical dimension of 47 m, is that found towards the bottom of WF5 (Figure 1.13). It was originally considered the basement beneath the melt sheet (Hart et al., 1997; Andreoli et al., 1999; Koeberl et al., 1997); however, a comparison with the stratigraphy of the melt sheet/basement contact in the deep M3 borehole led Hart et al. (2002) to reinterpret the same granite as a large inclusion within the melt sheet. This conclusion was also reached by Koeberl and Reimold (2003) as they noted no decrease in shock metamophism or annealing with depth. In the same fragment the original minerals are completely recrystallized, the quartz domains preserving brown cores (toasted quartz) which Raman spectroscopy revealed to consist of recrystallized glass and air-filled bubbles (Andreoli et al., 1999). Mineral clasts include large corroded pyroxenes. A second characteristic of the melt sheet is its chemical differentiation, first noted in borehole WF5 (Andreoli et al., 1999) and later also in M3 (Hart et al., 2002). In the former, the impact melt rocks are cut by granophyric and pegmatitic veins (Hart et al., 1997). In the latter, the melt rock progressively grades from more siliceous in the upper sections to more mafic below 500 m depth, followed by a distinct, >100 m, chilled margin at the contact with the mafic pyroxene gneisses of the basement (Figure 1.13; Hart et al., 2002). Chilled re-intrusions of heterogeneous impact melt in coarser, granophyric, quartz norite (WF5) and scattered nodules and veins of Ni, PGM-rich sulphides and oxides (WF4, WF5, M3; Hart et al., 1997; Andreoli et al., 1999; McDonald et al., 2001) also point to differentiation. In particular, a sulphide-rich horizon was intersected in the M3 core at a depth of 350-365 m, consisting of disseminated minerals such as millerite, trevorite and chalcopyrite with minor bornite, which are associated with inclusions of altered and serpentinised ultramafic rock (McDonald et al., 2001; Hart et al., 2002).

1.5.3 Petrography and geochemistry of Morokweng impactites

Documentation of the petrographic, chemical and isotopic data of the impact melt sheet by Hart et al. (1997), Koeberl et al. (1997), Andreoli (1999) and Koeberl and Reimold (2003) allowed further verification of the impact origin of the Morokweng structure. Results obtained include the identification of a dark brown impact melt rock and the description of shock deformation features such as PDF in toasted quartz grains from granite pebbles at the base of the Kalahari unconformity in WF5 (Andreoli et al, 1999; Hart et al., 1997). Corner et al. (1997) identified PDF in quartz and other

shock-diagnostic features from a quartzite boulder in a river bed to the south of the centre of the MIS and in quartz from a brecciated banded ironstone of the Griqualand West Supergroup at a locality west of the centre. Petrographic and chemical analysis of the impact-melt rock has revealed exceptionally high levels of siderophile and other trace elements: 20 ppb Ir, 480 ppm Ni, 360 ppm Cr (Andreoli et al., 1999) and of 32 ppb Ir, 780 ppm Ni, 440 ppm Cr, and 50 ppm Co (Koeberl et al., 1997). The geochemical studies of the impact melt rocks from the WF3, WF4 and WF5 boreholes by Koeberl et al. (1997) similarly revealed high siderophile element concentrations of 440 ppm Cr, 50 ppm Co, 780 ppm Ni, and 32 ppb Ir. The homogeneous medium-grained crystalline rock with igneous texture was described as a quartz norite by Hart et al. (1997) and impact-melt rock by Koeberl et al. (1997) but, based on textural similarities to the Vredefort Granophyre (impact-melt rock). Reimold et al. (1999) termed the Morokweng impact melt rock the Morokweng Granophyre. In this study it will be referred to as impact-melt rock. Additional petrographic data, mineralogical data and geochemical data for target rocks, impact-melt rock and PGE abundances for melt rock samples were provided by Koeberl and Reimold (2003) who analyzed melt rock samples from borehole WF5 for siderophile elements (Ni, Co, Cr and Ir) and PGE (Ru, Rh, Pd, Os, Ir, and Pt) contents. The results obtained indicated that the melt sheet comprises up to 5% meteoritic component from a projectile of L or LL chondritic (stony meteorite) composition. McDonald et al. (2001) used PGE concentrations in the melt sheet to differentiate between the between the different main types of chondrites (i.e., Enstatite, Ordinary, and Carbonaceous) and also concluded that the impacting projectile was an ordinary LL chondrite meteorite, an interpretation confirmed by the discovery in borehole M3 of an intact, 30 cm wide, LL chondrite clast at ~766 m depth (Maier et al., 2006). Detailed petrographic studies showed that this clast is composed of sub-angular chondrite fragments and chondrules (porphyritic orthopyroxene, radial orthopyroxene and barren olivine; Maier et al., 2006). Mineralogical and geochemical analyses showed that the clast lacks troilite (FeS) and metals but contains iron-rich silicates, iron- and nickel-rich sulphides (pyrrhotite and pentlandite) and displays chondritic chromium isotope ratios and PGE element ratios similar to those of the impact melt (Maier et al., 2006). Several smaller fragments, intersected between 345 m and 400 m depth, are similar in composition to the large fragment (Maier et al., 2006). Apart from the chondritic component, mixing calculations also revealed that the impact melt rock composition was reproducible from target rocks found in the Morokweng area (McDonald et al., 2001). In summary, the differentiated Morokweng impact melt, like the Sudbury impact melt, differs from most other comparable melt sheets which tend to be very homogeneous and, at most, with only trace concentrations of the original impactor (Andreoli et al., 1999; Hart et al., 2002; McDonald et al., 2001) The size of the Morokweng melt sheet is also remarkable, as it was estimated by McDonald et al. (2001) and Hart et al. (2002) to be ~30 km wide and ~ 800 m thick (see Figure 1.13). Finally, the study of the M3 borehole, located 12 km from the presumed centre of the Morokweng structure (see Figure 1.1) allows the in-depth study of a voluminous body of granophyric, fractionated, impact melt (Maier et al., 2006).

Chapter 2

Lithological and petrographic description

2.1 Introduction

The M4 core was drilled in 1998-1999 into a magnetic anomaly 18 km NNW from the inferred centre of the MIS located at co-ordinates 26º21'14.36 33"S, 23º27'51.5385"E (M.A.G. Andreoli, unpublished report). The core was initially logged informally as MOROK 5 by M. Andreoli as part of the ongoing search for PGEs in the MIS by Pan African Mineral Development Company (Pty) Ltd. In the re-logging of the M4 core for this study, several inconsistencies were noted as the initial depth labels do not always match the current measurements. Where major discrepancies (> 5 m difference in depth) were found, changes have been made based on compatibility between the core boxes (see Appendix 2A).

The 368.58 m long M4 core originally comprised 94 m of Kalahari Group sand and calcrete (not retained, and not discussed further) underlain by a variety of granitoid gneisses with subsidiary mafic intrusive rocks and impact generated breccias. From 94 m to 103 m, the core comprises highly weathered granite recovered by percussion drilling that was too deteriorated to analyse. The presented parts of the M4 core are thus between 103.00 m and 368.58 m below surface and consist of a mixed association of fractured pre-impact lithologies including granitic-granodioritic- trondhjemitic and dioritic gneisses, metadolerite and dolerite. These lithologies show varying degrees of fracturing and are locally brecciated to cataclasite; they are interspersed with veins of suevite and melt-matrix breccia (MMBr) that are randomly oriented and range from <1 mm to 3 m in vertical "width". The lithostratigraphy of the M4 core is presented in Figure 2.1 and is also shown in a complete corebox catalogue in Appendix 2A. The main aim of this chapter is to present the macro- and micro-scale lithological and petrographic characteristics, contact relationships, structural history and alteration features of the target rocks and impactites present in the M4 core, thus allowing the pre-, syn- and post-impact evolution of the rocks to be inferred. For these reasons, the pre-impact and impact-derived lithologies are discussed separately. Structural relations are of particular significance in determining the sources and origin of the impactites. Based on the interpretation of the core, the impactites are divided into monomict lithic breccia (strictly a cataclasite, see Section 2.4.1), and -

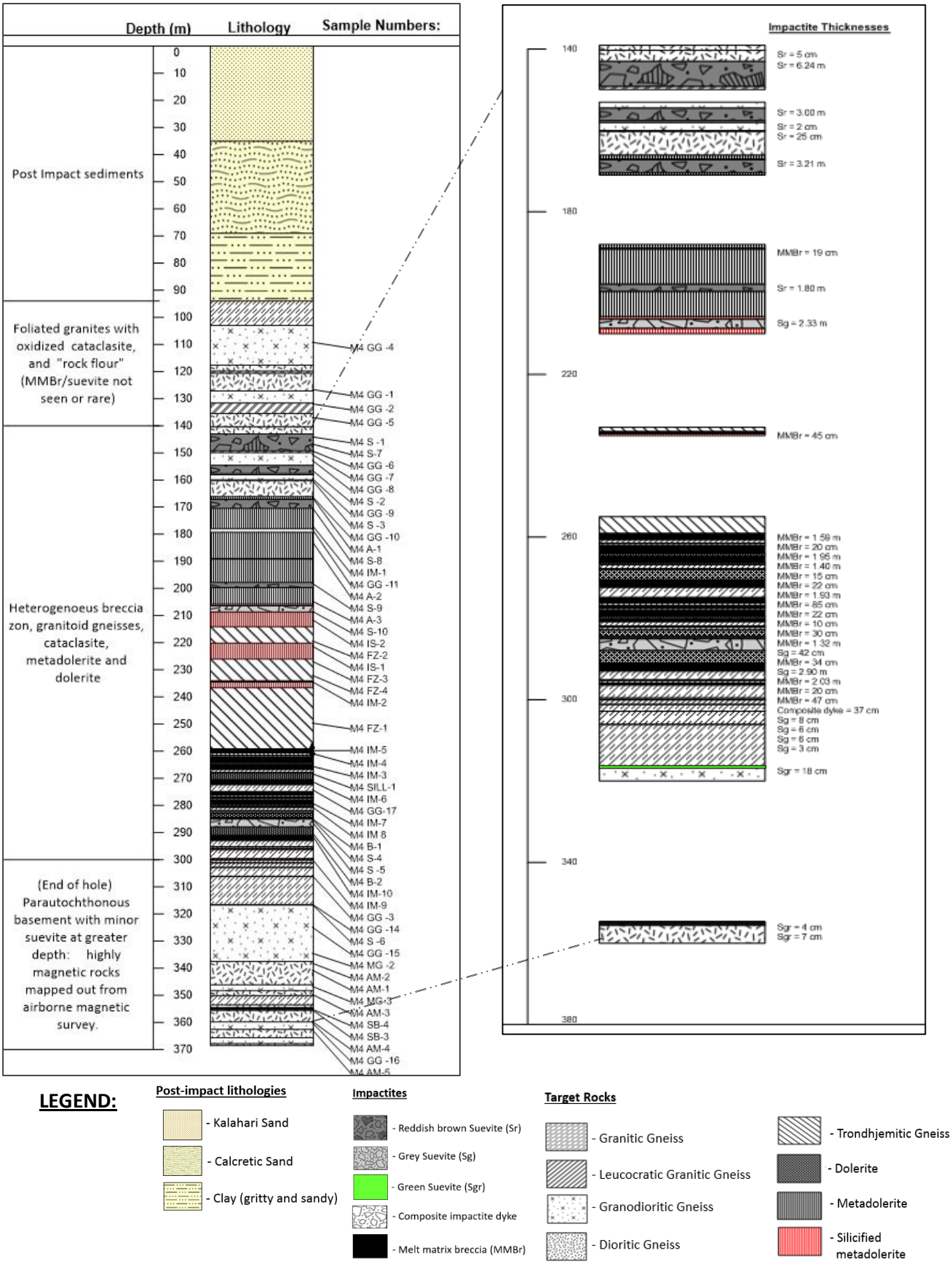

Figure 2.1: Lithostratigraphic log of the M4 borehole core, showing sample depths. The upper 94 m of post-impact sediments comes from descriptions of M.A.G. Andreoli. Samples used for analysis in this study, enlarged impactite intervals and their respective thicknesses are indicated on the right.

polymict breccias (suevite and MMBr, see Section 2.4.2 and 2.4.3). The alteration mineralogy of the various impactites is covered in more detail in Chapter 4; however, for the purposes of analysis, it is necessary to mention that the core shows signs of significant alteration, with many of the impactite dykes showing vugs and loss of core width; core loss is also noted. The upper parts of the core in particular are characterised by haematite staining that is most apparent along, but not confined to, fractures. All lithologies are cut by mm- to cm-wide calcite, zeolite or quartz veins that are more common in the upper parts of the core, and which are mostly horizontal, although some steep veins are noted. The trondhjemitic gneiss and meta-dolerite at 173.30 - 179.95 and 195.13 - 259.11 m depth contain intense quartz veining that is clearly a pre-impact feature, as quartz contains PDF (see Chapter 5) and occurs as clasts in the impactites. Where the core has broken along fractures in both the target rocks and impactites, these almost always display slickenlines. Numerous fractures also contain thin seams or lenses of magnetite that has undergone further oxidation to haematite. These are interpreted as part of the impact generated alteration assemblage that also contains pyrite. It is beyond the scope of the present study to present a detailed analysis of the impact-induced hydrothermal alteration, but aspects of this are covered in at the end of this Chapter and in Chapter 4.

2.2 Methodology

This chapter presents macro- and microscopic lithological observations of the 5cm diameter M4 drillcore from 103.00 m to the base of the hole at 368.58 m. A complete set of photographs of all 31 core boxes is presented in Appendix 2A, with more detailed photographs of selected samples of interest in Appendix 2B. A total of 98 thin sections was cut from 70 selected samples (37 target rocks, 33 impactites) for detailed petrographic analysis, including transmitted light microscopy (modal mineralogy, micro-textural analysis) for target rocks and impactites and back-scatter electron microscopy (BSEM; textural analysis) for impactites. Fifty-three samples were geochemically analysed using XRF and ICP-MS methods (Chapter 3). Samples used for analysis in this study are shown alongside the M4 core lithostratigraphy (Figure 2.1). Mineral chemical data from electron microprobe analysis (EMPA) are presented in Chapter 4. The subdivision of target rocks was initially made based on the macroscopic features (mineralogy, texture) and then refined through petrographic and whole-rock chemical analysis (Chapter 3). For the impactites, classification was based on macroscopic features (clast and matrix characteristics, presence of melt), with further microscopic and chemical analysis of clasts and matrix involving transmitted light microscopy, BSEM, EMPA and limited X-ray diffraction (XRD) analysis (Chapter 4). The limitations of describing gneissic target rocks and impactites in a 5 cm diameter core versus a larger scale was a factor in several cases where the lack of sufficient sample volume created uncertainty in nomenclature.

2.3 Macroscopic and microscopic observations of the M4 drillcore target lithologies

This section deals with macroscopic and petrographic descriptions of representative target lithologies intersected in the M4 drillcore. Transmitted light microscopy (mineralogy, mineral textures) and whole-rock chemical analysis (Chapter 3) form the basis of the subdivisions of the target lithologies into 5 main types: granitic-granodioritic gneisses, which are grouped together based on whole-rock chemistry; trondhjemitic gneiss, dioritic gneiss, dolerite and metadolerite. Sections of metadolerite are notably ferruginised and silicified (herein referred to as siliceous metadolerite) but high levels of alteration have prevented confirmation of its exact origin.

2.3.1 Granitic and granodioritic gneisses

2.3.1.1 Macroscopic characteristics

The granitic-granodioritic gneisses grade in colour from light pink to grey-white, and from medium- to coarse-grained (Figures 2.2 - 2.3). Contact relationships between the granite and granodiorite are indistinct and also appear to be gradational with the dioritic gneiss (Section 2.3.3 and Appendix 2A, box 3 and 4), suggesting a coeval relationship. Single-zircon U/Pb dating of the granitoid lithologies (R.L. Gibson, unpublished data, 2015) confirms that the granite, granodiorite and diorite in the upper part of the core show an identical age of 2906 ± 5 Ma; however, the granite at 302.00 – 316.52 m depth shows a slightly older age of 2922 ± 6 Ma. Whole-rock geochemical data (Chapter 3) do not distinguish between the lower granite and upper granite-granodiorite; however, they do separate the diorite from the granites and granodiorite. All granitoid gneisses contain a foliation defined by aligned biotite ± magnetite/ilmenite and quartzo-feldspathic lenses (Figure 2.2C, D). Locally, cm-scale leucogranitic banding occurs parallel to the gneissosity (Figure 2.3C; Appendix 2A, box 1); these are interpreted as likely late-stage veins that have been deformed together with the wallrock. Apart from grain size, the rocks show a highly variable mafic mineral content (biotite, titanite, ilmenite, magnetite; Figure 2.4). The granitic and granodioritic gneisses are predominantly found in the upper parts of the core (103 - 179.35 m; Figure 2.1) where granodiorite (70 %) dominates over granite (30%). The leucocratic granite variety occurs as cm- to m-wide veins within the granodiorite (Figure 2.3C). The widest granite intersection (3.80 m) occurs at 131.65 m (Box 4, Appendix 2A). The granite veins are more weakly foliated and coarser grained than the granodiorite, and locally contain pink alkali feldspar grains up to 3 cm in size. Notably, these veins are erratic in occurrence and vary in width. Steeply dipping, iron-stained fractures and sub-horizontal calcite veins cut across the granitic-granodioritic gneisses, particularly in the upper sections of the core (Figure 2.4B, Appendix 2A, boxes

1, 2 and 4). In this zone, these rocks are also characterised by a red colouration owing to oxidation of magnetite, ilmenite and ferromagnesian silicates, particularly in and adjacent to fractures. At 292.98-316.52 m depth the thickest and oldest granitic gneiss is intersected (Figure 2.2E; boxes 24, 25, 26, and top of 27 Appendix 2A). This granite is notably different macroscopically in terms of its distinctly pink colour (but not chemically distinct) from the younger granites and leucogranites (restricted to veins) in the upper 150 m (see Figure 2.2E).

There are observable colour variations of granodioritic gneiss with depth, although textural similarities are evident (Figure 2.2C, D). The medium- to coarse-grained magnetite-bearing granodioritic gneiss (sample M4 MG-2, Figure 2.2F) is greyish black owing to its high mafic content compared to the felsic variety sample M4 GG-15 (Figure 2.2 D) (Boxes 28 and 29, Appendix 2A). Highly magnetic portions are observed at 331 m depth. Towards the base of the core, the magnetic granodioritic gneiss forms steep gradational contacts with magnetic dioritic gneiss (Figure 2.3B). M. Andreoli (pers. comm., 2016) has suggested that these magnetic target rocks may be the source of the magnetic anomaly that defined the M4 site selection (see Figure 1.12B).

2.3.1.2 Petrographic characteristics

Microscopically, the granitic and granodioritic gneisses consist of K-feldspar, plagioclase, quartz and minor biotite with accessory titanite, epidote, zircon, ilmenite and/or magnetite (Figure 2.4) and display an average grain size of 1-2 mm. In general, the granitic and granodioritic gneisses can be distinguished from dioritic gneisses by having <10% biotite, and by K-feldspar (microcline) dominating over plagioclase and quartz. K-feldspar modal abundance ranges between 30-45%, whereas quartz ranges between 25-30% and plagioclase between 20-40%. Significant difference in modal mineralogy was noted between the older and the younger granitic gneisses; though geochemically these were relatively similar (see Chapter 3). The oldest granite (2922 Ma old, identified by single-zircon U/Pb dating by R.L. Gibson, pers. comm., 2015) contains 35 % K-feldspar, 30% plagioclase, 30% quartz and 5% biotite (sample M4 GG-3). In the upper parts of the core, alteration involves oxidation of biotite and haematisation of ilmenite/magnetite (which may be linked to the occurrence of calcite veins). Biotite is commonly kinked (see Chapter 5). Plagioclase cores locally contain randomly oriented fine-grained biotite, and plagioclase grains commonly display relatively unaltered rims that are locally continuous with lobate myrmekite where they are in contact with microcline (sample M4 GG-2). Microcline is perthitic in places and is generally interstitial to the plagioclase, which may be subhedral.

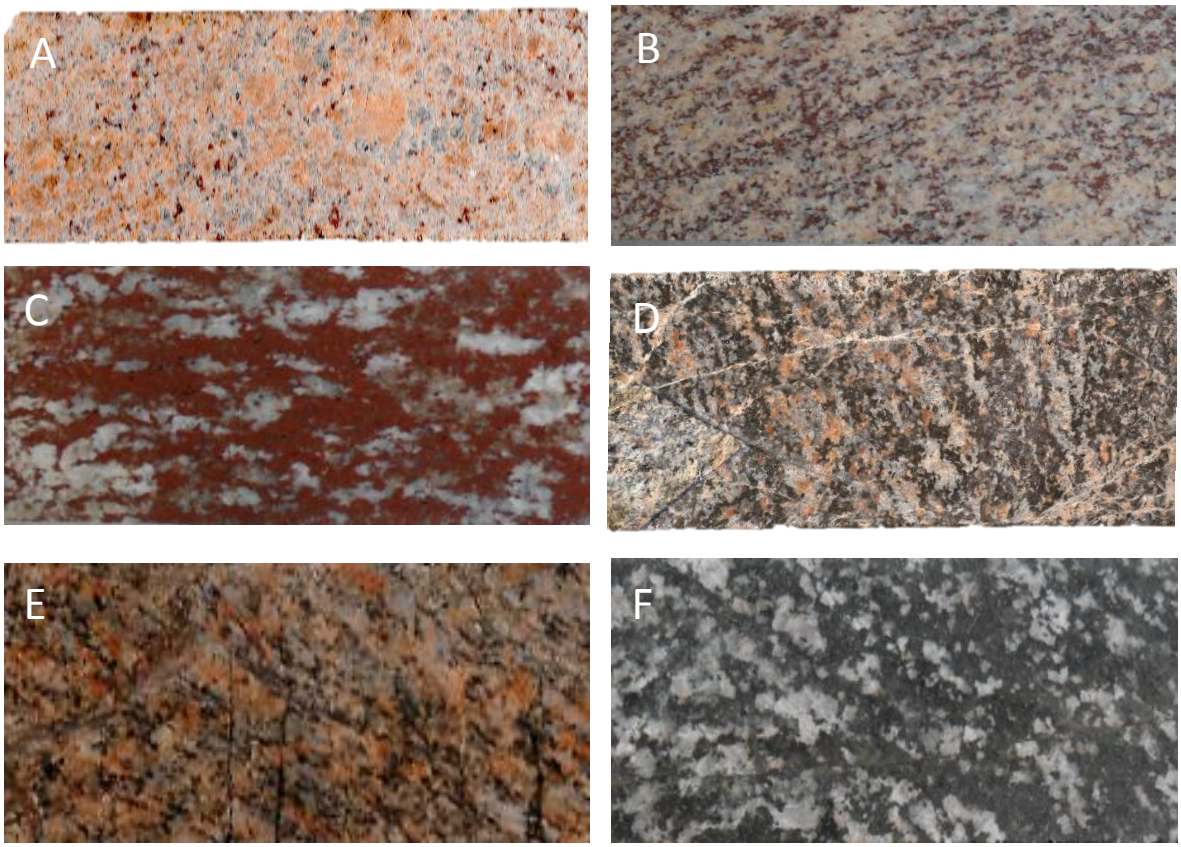

Figure 2.2: Textural variation within the granitic and granodioritic gneisses. **A)** Leucocratic granitic gneiss sample M4 GG-2 from 131.90 m depth. Note the lack of foliation. **B)** Medium-grained granodioritic gneiss sample M4 GG-7 from 150.58 m depth with strong foliation. **C)** Strongly oxidised coarse-grained granodioritic gneiss sample M4 GG-9 from 159.36 m depth, close to a significant fracture zone. **D)** Strongly foliated, slightly banded, granodioritic gneiss sample M4 GG-17 from 274.15 m depth, with irregular crosscutting cataclasite filled fractures. **E)** Oldest granitic gneiss sample M4 GG-3 from 305.82 m depth. Note the strong foliation and the fractured nature of this granitoid. **F)** Coarse-grained magnetic granodioritic gneiss sample M4 MG-2 from 334.52 m depth. Vertical dimension is sample core width (5 cm).

Fine grained, "dusty" alteration occurs in both feldspars, but in plagioclase it may be linked to the so-called "toasting" effect indicative of more intense shock deformation and/or post-shock alteration Figure 5.12C, D). Shock petrography is dealt with in Chapter 5, and includes decorated PDF in quartz as well as oblique lamellae and reduced birefringence in the feldspars. Undulose and/or patchy extinction is common in quartz and feldspar and many samples show cross-cutting cataclasite-filled fractures.

Figure 2.3: Core box photographs showing gradational contact relationships of granitic-granodioritic and dioritic gneisses. **A)** Core box 4 (from 111.40 - 135.65 m depth). Note the gradational contact (arrow) between leucocratic granite gneiss (left) and dioritic gneiss (right). **B)** Core box 30 from 340.56 – 346.55 m depth. Note the oblique gradational contact (arrow) of granodioritic gneiss (right) with dioritic gneiss (left). **C)** Core from 107 - 110.80 m depth, showing granodioritic gneiss with leucocratic banding and weak foliation (core box 1). **D)** Magnetic granite from 331.30 – 335.10 m depth (core box 29). Note the magnetite-rich portion (arrow).

Leuco-granite has a modal composition of 40% K-feldpsar, 15-20% plagioclase, 30% quartz, and 5-10% biotite. Microcline is the most abundant mineral, and occurs as inter-cumulus grains of up to more than 2 mm partially enclosing other phases (Figure 2.4A). Plagioclase myrmekitic intergrowths with quartz are locally present. Post-impact calcite veins displaying syntaxial to granoblastic texture cut across mineral grains (Figure 2.4B). The mesocratic and melanocratic granitic gneisses and the leucocratic granite veins which cross-cut the dioritic gneisses show similar microscopic characteristics and mineralogy, although modes differ (see Figure 2.4).

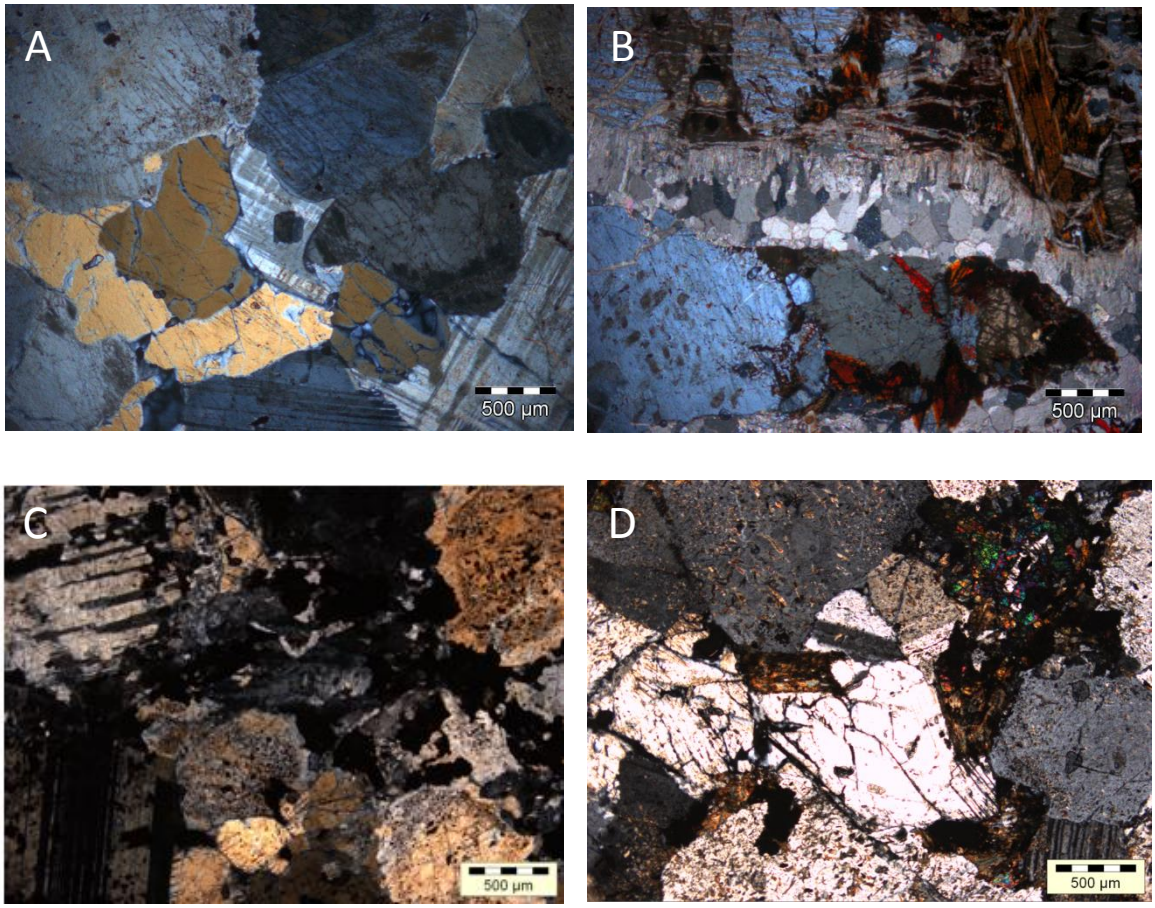

Figure 2.4: Photomicrographs of granitic-granodioritic gneisses. **A)** Sample M4 GG-2 from 131.90 m depth, showing subhedral plagioclase with thin inclusion-free rims, and irregular interstitial microcline and quartz. XPL. **B)** Calcite-filled fracture in sample M4 GG-1 from 126.60 m depth, showing syntaxial marginal and granoblastic core texture. XPL. **C)** Granitic gneiss sample M4 GG-9 from 159.36 m depth. The plagioclase grains are subhedral, and zoned with clear rims (upper right) and cores containing biotite laths (dark spots). XPL. **D**) Magnetic granitic gneiss sample M4 MG-2 from 334.52 m depth, showing subhedral, inclusion-rich plagioclase and large titanite grain (upper right) and biotite. XPL. PPL = plane polarised light; XPL = cross polarised light.

2.3.2 Trondhjemitic gneiss

2.3.2.1 Macroscopic characteristics

Trondhjemitic gneiss occurs together with metadolerite within a broader zone of intense fracturing and quartz veining between 201.5 m and 260 m depth (Figure 2.1; Core boxes 13-20, Appendix 2A). It is characterized by a strong foliation defined by quartzofeldspathic lenses and mafic minerals (Figure 2.5A, B). In places the trondhjemitic gneiss is brecciated and heavily oxidized (Figure 2.5D), and displays cross-cutting quartz veins (Figure 2.5C). Based on whole-rock geochemical analysis

(Section 3.4.1), the trondhjemitic gneiss is interpreted as metasomatised granitic-granodioritic gneiss. This is confirmed by petrographic analysis (section 2.3.2.2). The upper parts of the trondhjemitic gneiss intersection appear to be less brecciated (Figure 2.5 B) but, with depth, the network of fractures and quartz veins become so intense that it becomes difficult to determine a consistent pattern (Appendix 2A, boxes 17 and 19). Like most of the major lithological contacts, the contact of the trondhjemitic gneisses with metadolerite is marked by the occurrence of highly oxidised, silicified metadolerite (Figure 2.1, Appendix 2A - box 13-16) and in places an occurrence of a highly altered, silica-rich melt-matrix impactite (Sample M4 IM-2, Appendix 2B), and the fact that the metadolerite also displays evidence of quartz veining substantiates the fact that the quartz veining event post-dates the intrusion of the metadolerite. The first major contact of trondhjemitic gneiss with silicified metadolerite is marked by a significant occurrence of 2.33 m of grey suevite (Appendix 2A, boxes 13). Fractures in trondhjemitic gneiss display significant haematite staining (Figure 2.5D), which is attributed to post-impact hydrothermal oxidation effects. The presence of angular quartz vein networks in the vicinity of the trondhjemitic gneiss – metadolerite interval may support the contact being a pre-impact fault; however, the interval also contains abundant evidence of impact-induced displacements along shear fractures, which could support impact-related fault movement as well.

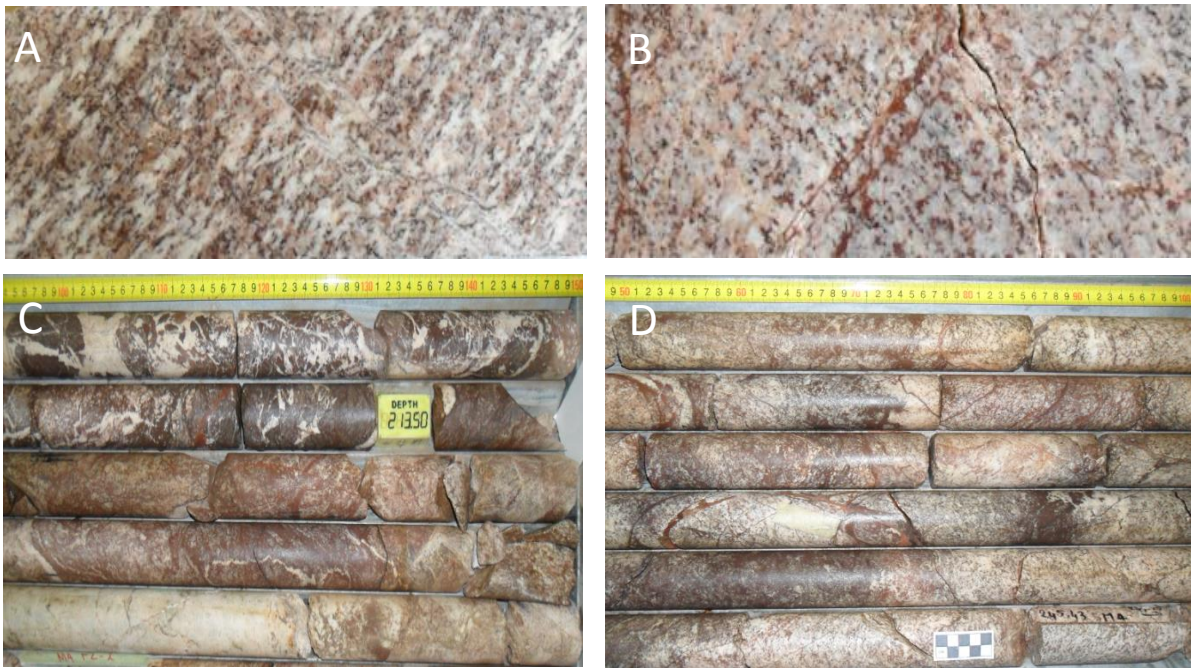

Figure 2.5: Macroscopic characteristics of the trondhjemitic gneiss. **A)** Strongly foliated sample M4 FZ-4 from 233.48 m depth. The oblique anastomosing shear fracture cleavage is linked to the impact. **B)** M4 FZ-3 from 226.80 m depth. The dark oblique fractures and slight crenulation of the gneissosity are interpreted as impact-related. Sample core width = 5 cm. **C)** Core box 14, from 212.03 - 218.33 m depth, shows the structurally complex, quartz-veined, contact of the trondhjemitic gneiss with brecciated metadolerite (top). **D)** Core box 17, from 237.00 - 244.70 m depth, showing intense fracturing and iron oxidation along fractures.

2.3.2.2 Petrographic characteristics

Petrographically the trondhjemitic gneiss is characterised by a similar mineralogy and texture to the granitic-granodioritic gneisses, however it contains less than 10% alkali feldspar. Plagioclase (40-50%) occurs with ≥20-30% quartz, 15% biotite and minor K-feldspar (<10%) (Figure 2.6). Accessory minerals are titanite, epidote, magnetite and zircon. Biotite is almost completely oxidised to orange-red brown pleochroic remnants and haematite and occurs as interstitial anhedral to subhedral grains (Figure 2.6A, B). Titanite, though anhedral, may be brecciated (Figure 2.6C, D). The plagioclase grains contain fine-grained biotite (Figure 2.6 B, D). Significant strain has been experienced by this rock as evidence of bent plagioclase twins and fractured plagioclase grains is observed. (Figure 2.6A, C).

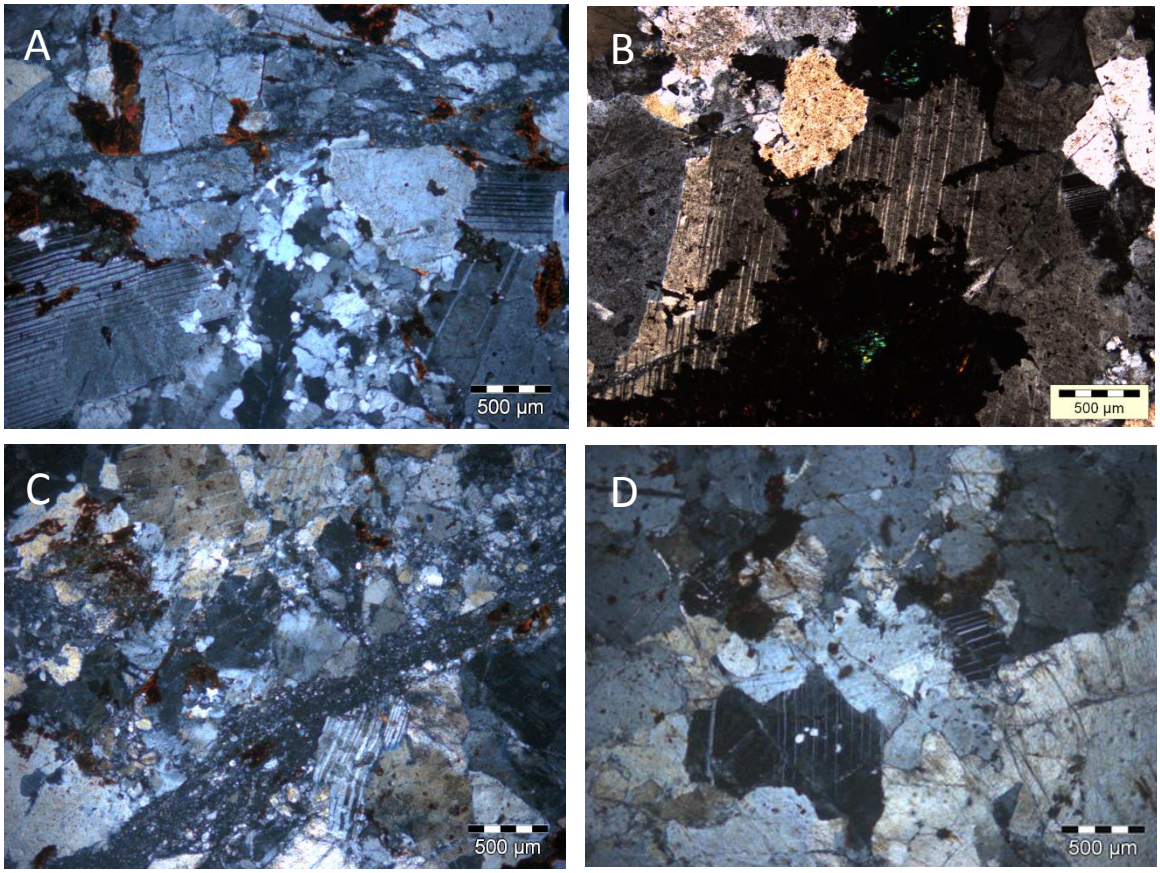

Figure 2.6: Petrographic characteristics of trondhjemitic gneiss. **A)** Sample M4 FZ 1 from 249.62 m depth, showing large anhedral plagioclase and interstitial recrystallized quartz (centre) and altered reddish brown biotite (top left). XPL. **B)** Large plagioclase grains and large altered titanite grains (Sample M4 FZ 4 from 233.48 m depth). XPL. **C)** Sample M4 FZ 4 from 233.48 m depth, showing fine-grained impact-related cataclasite (compare grain size and texture with quartz in A) and bent twins in plagioclase. XPL. **D)** Interstitial plagioclase, with notable biotite inclusions (Sample from 229.79 m depth). XPL. PPL = plane polarised light; XPL = cross polarised light.

In brecciated zones, quartz accounts for 35 %, with 50-55% plagioclase, <10 % K-feldspar, with epidote, titanite and biotite accounting for < 3%. Apatite and zircon are also noted. Epidote appears needle-like in shape and varies in size (Figure 2.6B). No foliated fabric is noted microscopically and the plagioclase and quartz grain boundaries are more irregular, suggesting extensive recrystallization of quartz (Figure 2.6A) and quartz impregnation of the trondhjemitic gneiss and plagioclase, including quartz infill in intragranular microfractures (Figure 2.6B, C). Quartz contains abundant PDF and patchy and undulose extinction, deformation bands and local cataclastic grain size reduction. Shock-related deformation seen in trondhjemitic gneiss is discussed in detail in Chapter 5.

2.3.3 Dioritic Gneiss

2.3.3.1 Macroscopic characteristics

Dioritic gneiss is dark grey (Figure 2.7; Appendix 2A, boxes 29-30), but has experienced intense oxidation in the uppermost parts of the M4 core (Appendix 2A, boxes 3-5), which gives it a reddish brown colour (Figure 2.7 C). In the upper parts of the core the dioritic gneiss is cut by mm-scale post impact calcite and zeolite veins (Figure 2.7A). At depth, this rock is slightly magnetic and displays a more homogeneous, medium- to coarse-grained grain size relative to the granitic-granodiorite gneisses (Figure 2.7). Dioritic gneiss is intercalated with leucogranite in the top parts of the core and with magnetic granite at depth (Figure 2.1). It displays steeply-inclined, gradational contacts with both the granitic and magnetic granitic gneisses and locally displays felsic banding parallel to foliation (Figure 2.7D).

2.3.3.2 Petrographic characteristics

Petrographically the dioritic gneiss consists of 30-50% plagioclase, 20-35% K-feldspar, 10-20% quartz and 10-15% biotite, with epidote and titanite comprising up to 3-5 % in some samples. Magnetite/ilmenite (up to 1%), zircon and apatite are common accessory phases. Plagioclase and K-feldspar (microcline) show identical textural features to the granitic-granodioritic gneisses, with subhedral plagioclase with albite rims, and interstitial microcline, with biotite-apatite-titanite-epidote and opaques (ilmenite and haematite/magnetite) occurring as interstitial aggregates. Plagioclase is slightly more coarse-grained and contains abundant needle- to plate-like biotite grains, as well as

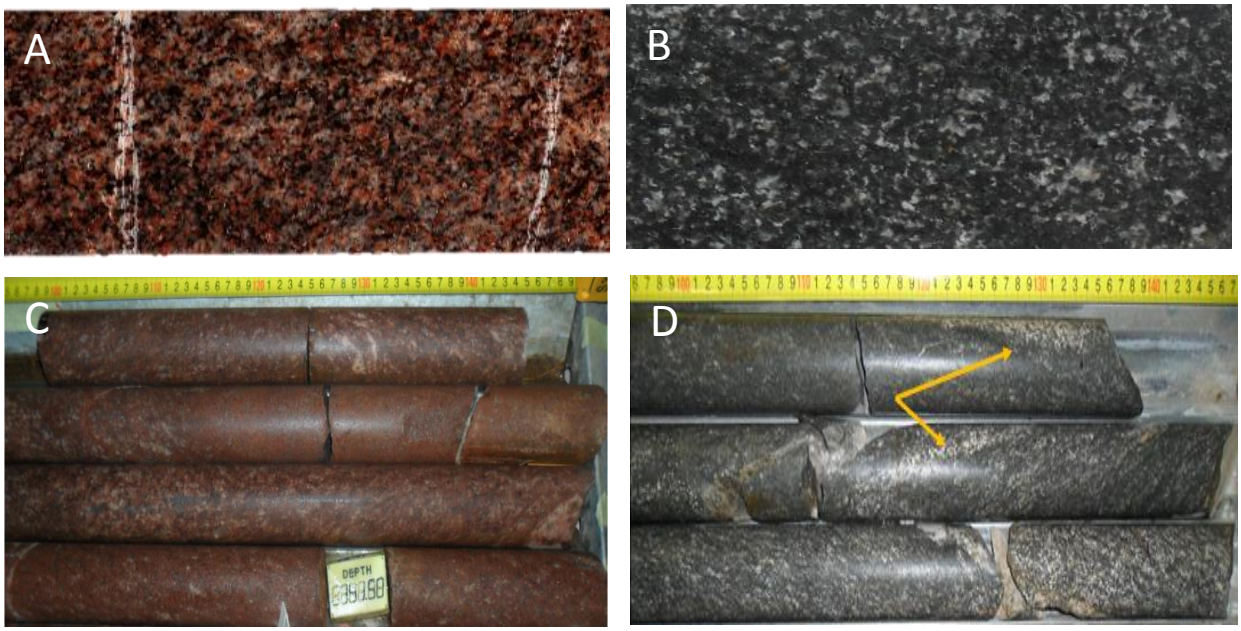

Figure 2.7: Macroscopic character of dioritic gneiss in the M4 drillcore. **A)** Medium-grained dioritic gneiss sample M4GG-1 from 126.50 m depth, cut by calcite-filled fractures. **B)** Sample M4 AM-2 from 338.15 m depth. **C)** Core box photograph showing reddish brown weakly foliated dioritic gneiss from 136.20 m depth. **D)** Foliated dioritic gneiss with locally developed leucocratic bands parallel to well-developed foliation (arrows), from box 32, at 355.92 - 359.12 m depth (Appendix 2A). Sample core width = 5 cm.

epidote in its cores (Figure 2.8A, B). The plagioclase cores can comprise up to 30% biotite and epidote inclusions, but rims are inclusion-poor. Interstitial biotite grains reach up to 1 mm in length and display yellow to red-brown pleochroism in the upper parts of the core, but green pleochroism and alteration to chlorite and prehnite in the lower dioritic gneiss intersection. This may be linked to higher levels of overall post-impact oxidation in the upper parts of the core (see Chapter 4). The quartz and feldspar show signs of shock metamorphism (Chapter 5) and undulose and mosaic extinction, whereas biotite displays bent or kinked cleavage, particularly in the lower dioritic gneiss. Feldspar alteration is very similar to that seen in the granitic-granodioritic gneisses.

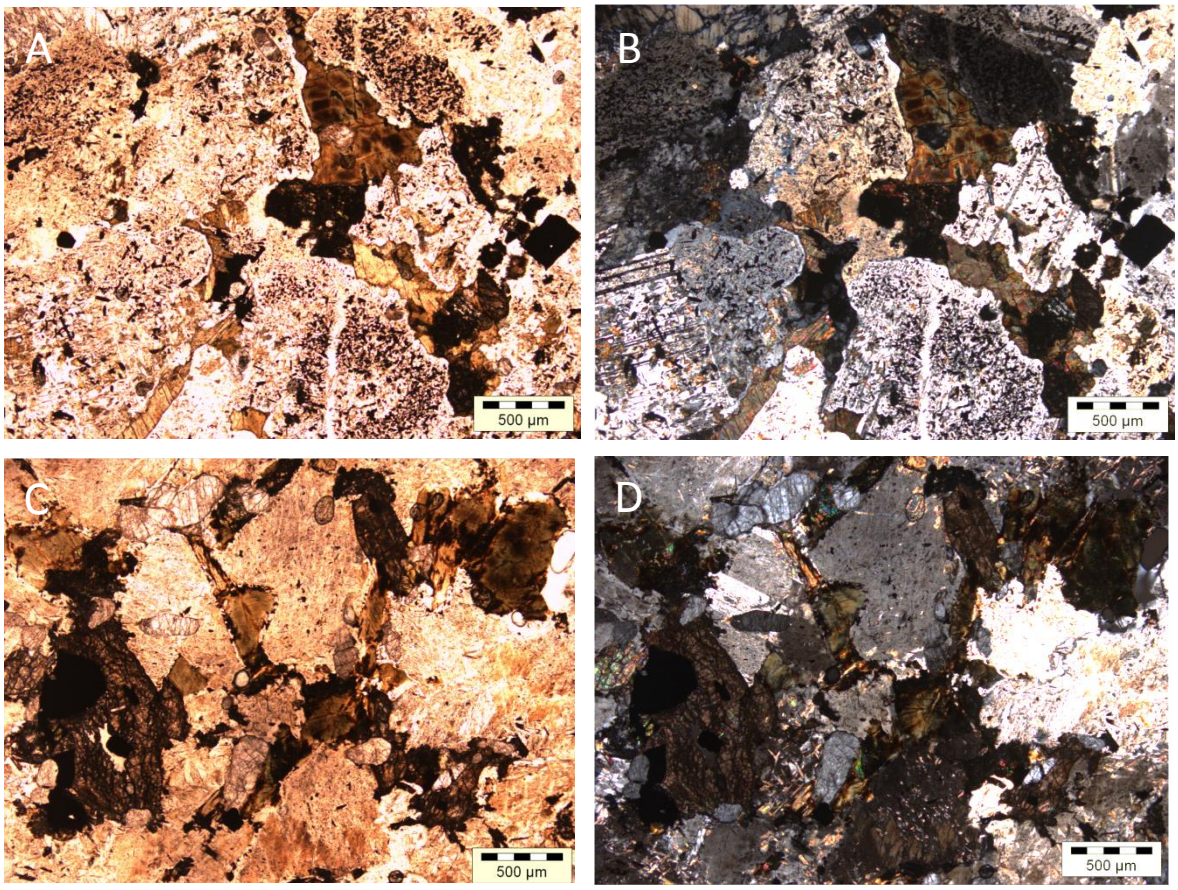

Figure 2.8: Petrographic characteristics of dioritic gneiss. **A)** Sample M4 AM-1 from 340.70 m depth showing interlocking, inclusion-rich plagioclase with clear, inclusion-poor rims, and interstitial chloritised biotite. A euhedral magnetite grain is shown to the right. PPL. **B)** XPL of A, showing a quartz-filled microfracture cutting lower plagioclase. **C)** PPL and **D)** XPL of biotite-rich sample M4 AM-5 from 362.63 m depth, showing subhedral plagioclase, with "toasting" (see Chapter 5) and large fractured titanite grain overgrowing ilmenite (left). PPL = plane polarised light; XPL = cross polarised light.

2.3.4 Metadolerite and dolerite

Two fine-to medium grained rocks of mafic composition are intersected by the M4 core between 166 and 264 m (Figure 2.1); these can be distinguished microscopically based on the level of metamorphic recrystallisation and also whole-rock geochemistry (Chapter 3) into metadolerite and dolerite. Given the distinct geochemical characteristics, they are, thus, described separately. No information is available about the orientation of the intrusions that would indicate whether they are associated with one of the dyke sets observed in the aeromagnetic imagery (Figure 1.12), and core analysis suggests that most contacts are characterised by shear fractures or impactite breccias. The likelihood that these

intrusions may represent differing dyke swarms representing Karoo (≤180 Ma) or Ventersdorp age (~ 2.7 Ga) dykes is explored further in Chapter 6. Regardless of their ages, it remains clear that these dykes are pre-impact dykes as they are incorporated as clasts in the adjacent impactites (see Section 2.4.3).

2.3.4.1 Metadolerite macroscopic characteristics

Metadolerite has a generally uniform, fine-grained, brownish red, macroscopic appearance. The largest portion of metadolerite occurs at 170.41 - 205 m (Figure 2.1; Appendix 2A, box 8-13). Metadolerite is cut by numerous thin, and two >1 m, suevite dykes but more commonly by quartz veins and associated fractures that locally produce an angular "breccia-like" overall appearance in the metadolerite (Appendix 2A, boxes, 12-14 and 16). Locally the rock contains mm-scale white speckles of plagioclase and quartz that are interpreted as part of a metamorphically-altered subophitic texture (Figure 2.9A). Enigmatic, highly siliceous and haematite-rich zones are noted along the metadolerite and trondhjemitic gneiss contact at 208.73 – 213.60 m depth; 219.40 – 226 m depth and 234.53 – 236.60 m depth (see Figure 2.1 and Appendix 2A, box 13, 14, 15, and 16). In the first zone, ~ 2.33 m of grey suevite is intersected (see sample M4 S-10 and S-15, Appendix 2B) and interestingly these suevites enclose the metadolerite, silicified metadolerite and quartz veins as lithic clasts. The combination of high silica, iron, calcium and variable aluminium, seen in bulk rock analysis (Chapter 3) suggests a metamorphosed and metasomatised metadolerite. Further work needs to be done but a name "silicified metadolerite" is used to refer to this lithology. The silicified metadolerite zone is macroscopically distinct from the metadolerite as it is marked by a high proportion of pre-impact vein quartz (Appendix 2A, box 13-14).

2.3.4.2 Dolerite macroscopic characteristics

Dolerite is considerably less abundant than the meta-dolerite and major intersections are: a 2.47 m wide dolerite block incorporated within melt-matrix breccia at 268.00-270.47 m depth (Appendix 2A, boxes 23-24) and in a megabreccia zone as a 1.6 m and 3 m blocks; at 282.85 and at 287.93 m depth respectively. The dolerite is dark brown, fine-grained and has an igneous texture in hand specimen (Figure 2.9B). Several other minor intersections of dolerite <1 m in vertical extent are encountered between 264.15 and 285 m depth; these intersections are interpreted as clasts in the mega-breccia interval which terminates at 290.95 m depth marked by a complex steep contact between dolerite and melt matrix breccia (MMBr) (Box 24, Appendix 2A). Between 282.84 m (Box 23, Appendix 2A) and 288.53 m (Box 24, Appendix 2A), the dolerite displays slightly elliptical, 1 cm-diameter, shiny black

spots that are slightly magnetic (Figure 2.5 C). Similar features are found in the adjacent suevite/MMBr and, whilst originally it was thought that these might be pre-impact features that were incorporated into the impactites, evidence of one spot straddling the dolerite-suevite/MMBr contact suggests that they are a post-impact hydrothermal alteration feature.

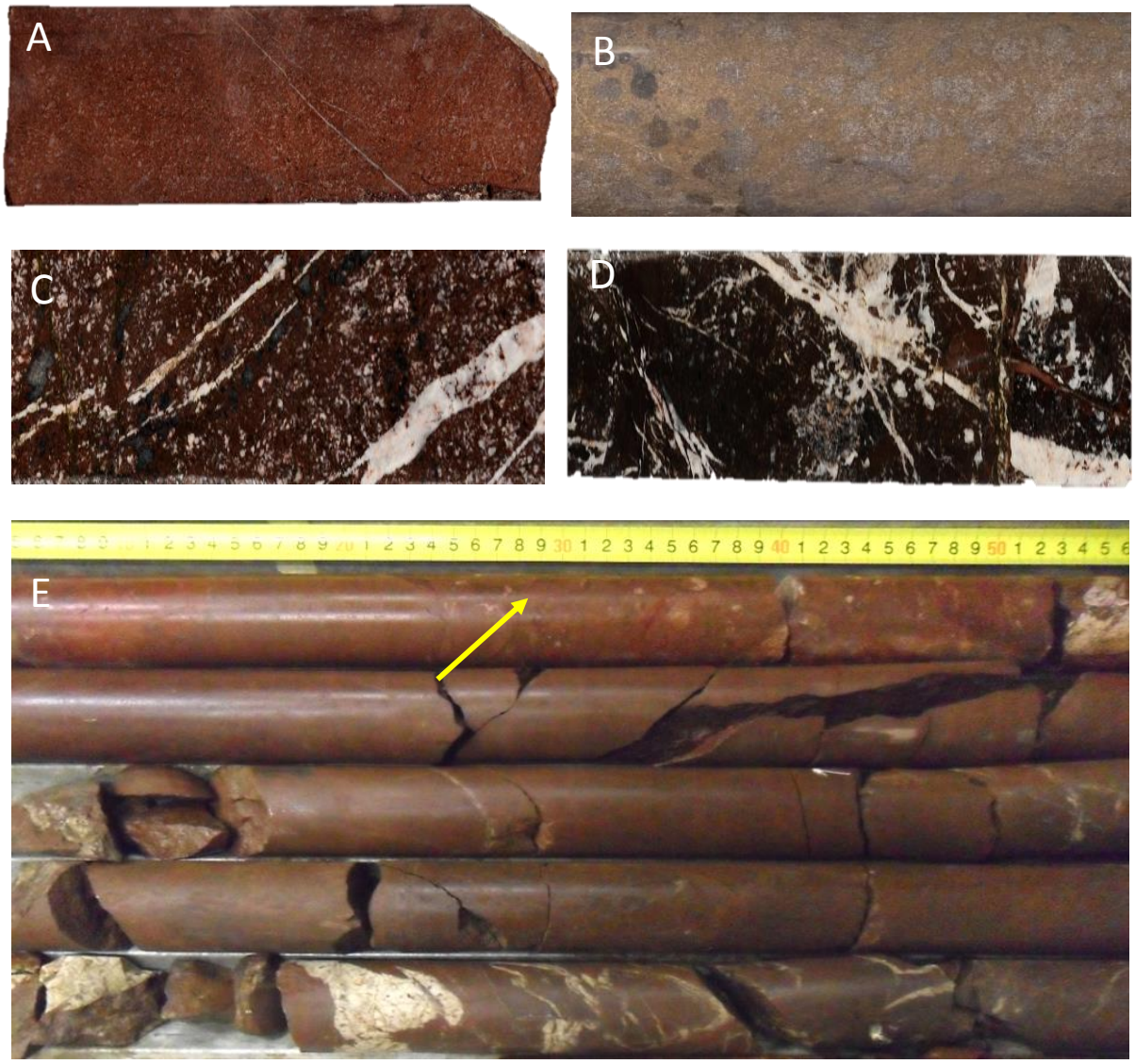

Figure 2.9: Macroscopic characteristics of mafic lithologies in the M4 core. **A)** Speckled metadolerite sample M4 A-1 from 166.33 m depth; note the thin crosscutting quartz vein. **B)** Handspecimen photograph of dolerite sample M4 B-2, from 289.97 m depth. Note the shiny slightly magnetic spherical/elliptical black spots that are related to post-impact alteration. **C)** Silicified metadolerite sample M4 IS -1 (221.20 m depth), showing mm - cm wide oblique quartz veins and small sub-rounded quartz specks set in fine-grained oxidised matrix. **D)** Silicified metadolerite (211.41 m depth) shows increased intensity in angular quartz vein network with depth Note the cross-cutting impact-related shear fractures that displace quartz veins. Sample core width = 5 cm. **E)** Section from 170 m (Appendix 2A, Box 9), showing the variation within the metadolerite. The top interval is marked by the occurrence of a 30 cm thick suevite (yellow arrow) and the lower part is cross cut by a network of quartz veins (white arrow).

2.3.4.3 Metadolerite petrographic characteristics

The metadolerite displays a broadly subophitic texture that has been almost completely recrystallized during metamorphism to an assemblage containing ~40% amphibole (actinolite-actinohornblende, see Chapter 4), ± chlorite, 30% plagioclase, 10% quartz and 10% titanite + epidote, + ilmenite, with the remainder comprising relict clinopyroxene. Whilst poor preservation of the pyroxene has hampered obtaining stoichiometric compositions (Chapter 4), the preservation of herringbone texture in the amphibole aggregates (Figure 2.10B) suggests that they pseudomorphed an augitic clinopyroxene with exsolution lamellae. The actinolite occurs as pseudomorphous aggregates of subidioblastic to idioblastic grains intergrown with fine-grained chlorite, spatially restricted to the relict clinopyroxene sites, although individual acicular crystals up to 3 mm have been noted. Plagioclase and quartz occur in complex fine-grained (<0.1 mm) xenoblastic aggregates. Fine-grained titanite + epidote separates the quartz and feldspar from fine-grained ilmenite cores, consistent with metamorphic reaction of magmatic ilmenite with surrounding plagioclase. Overall, the mineralogy and textures are consistent with upper greenschist facies metamorphism of a dolerite, close to the amphibolite facies transition (Winter, 2010). The uralitised clinopyroxene is further proof of the extent of metamorphism experienced by the dolerites (see Chapter 4). The clinopyroxene-actinolite-chlorite aggregates are extensively oxidised and fractured and the assemblage is cut by cataclasite-bearing fractures. Oxidation is preferentially concentrated along the fractures and is interpreted as a post-impact feature. The amphibole shows an unusual orange to yellow pleochroism that resembles the orange to yellow oxidised biotite in the granitoid gneisses in the upper section of the core. An apparent increase in the levels of metamorphic reaction replacing clinopyroxene adjacent to quartz veins may suggest that the metamorphism occurred together with the quartz veining. Although no geochronological data is available, it is suggested that the greenschist facies metamorphism postdated the metamorphic peak in the granitoid gneisses that was associated with formation of the gneissic foliation.

The siliceous metadolerite consists of 40% quartz, 2% plagioclase, 50% highly oxidised amphibole-pyroxene and 1% rutile, 1% magnetite, 2% titanite and 2% epidote. Quartz is highly re-crystallised and is intergrown with plagioclase. The highly haematised amphibole occurs in clusters and individual crystals are elongate with diamond shaped elongate crystals that range in size from 0.1-0.50 mm (Figure 2.12C). These surround high relief minerals that have non-stoichiometric clinopyroxene-like compositions. Rutile, epidote and sodic plagioclase occur in the vicinity of the shear fractures; which may have been formed by pre-impact or impact-related hydrothermal alteration. Unusually if it is a metadolerite, in places it has macroscopically-visible mm-scale banding, and a speckled texture made from elliptical mm-scale quartz aggregates in a matrix of highly oxidised amphibole pyroxene and titanite. Quartz veins of <1 mm up to 3 cm are noted (Figure 2.12).

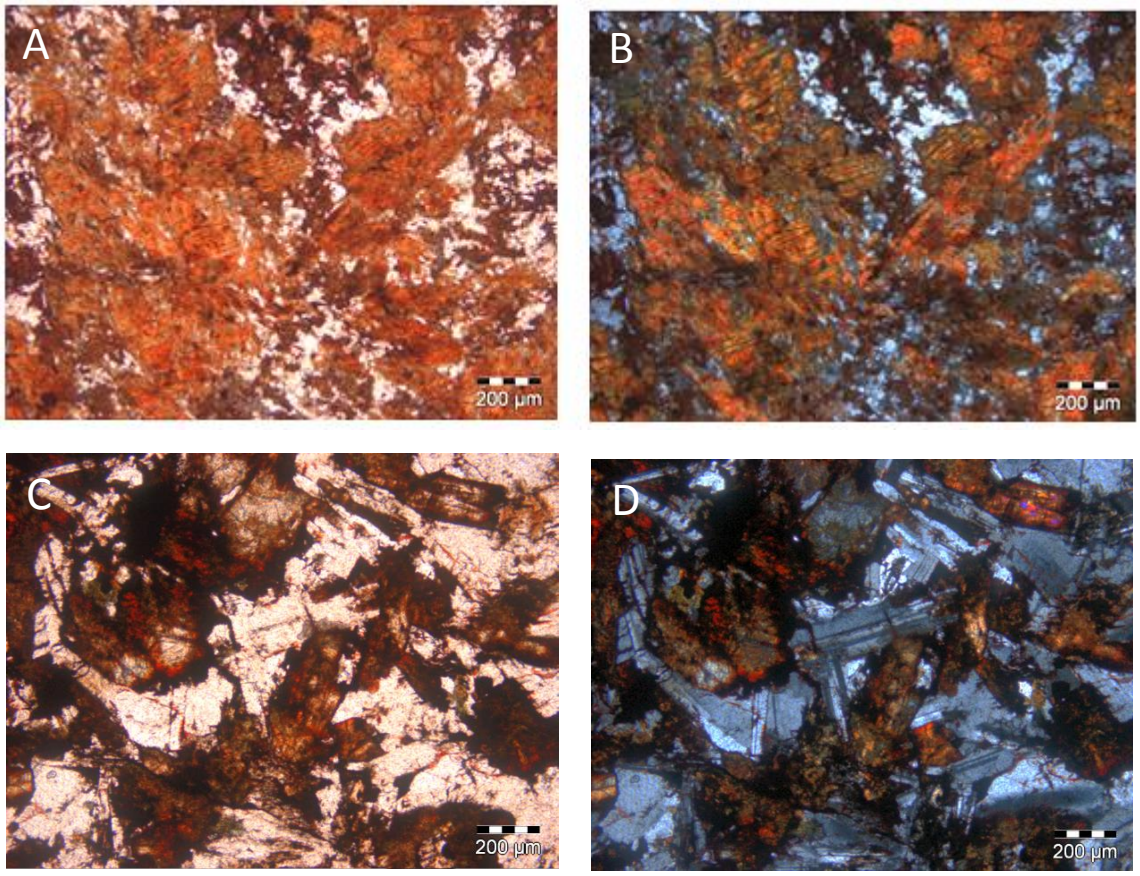

Figure 2.10: Petrographic characteristics of metadolerite and dolerite. **A)** PPL and **B)** XPL of metadolerite sample from 166.33 m depth. The red areas are partially oxidised actinolitic amphibole aggregates that have replaced clinopyroxene. Note the zoned nature of the texture, with plagioclase + quartz between the amphibole aggregates and the dark grey fine-grained titanite-ilmenite aggregates. **C)** PPL and **D)** XPL of dolerite sample M4 SILL -1, from 268.30 m depth, showing the well-preserved subophitic igneous texture, despite partial oxidation of the clinopyroxene. Plagioclase laths are intergrown with altered (uralitised) anhedral clinopyroxenes. PPL = plane polarised light; XPL = cross polarised light.

2.3.4.4 Dolerite petrographic characteristics

The medium-grained dolerite consists of subhedral to euhedral zoned plagioclase laths (60%) up to 1 mm in length intergrown with 0.5-1 mm, uralitised/oxidised subhedral to euhedral clinopyroxene (35%), with accessory quartz, red-brown biotite, titanite and ilmenite. In the less altered domains, most minerals are preserved. Plagioclase laths are randomly oriented and appear un-altered (Figure 2.10D). Very rare interstitial granophyric overgrowths of plagioclase + quartz (see Chapter 5, Figure 5.1C and D) contain the only evidence of shock in dolerite. Clinopyroxene is altered to an orange-brown colour and appears more altered than plagioclase although a few grains still have 90º cleavage and pyroxene exsolution lamellae preserved (Figure 2.10D). The cm-scale elliptical black spots

(Figure 2.9 B) seen in the core samples appear to represent areas that are richer in iron oxide. A few are slightly magnetic, suggesting magnetite, but they are highly oxidized and difficult to investigate petrographically (Figure 2.11).

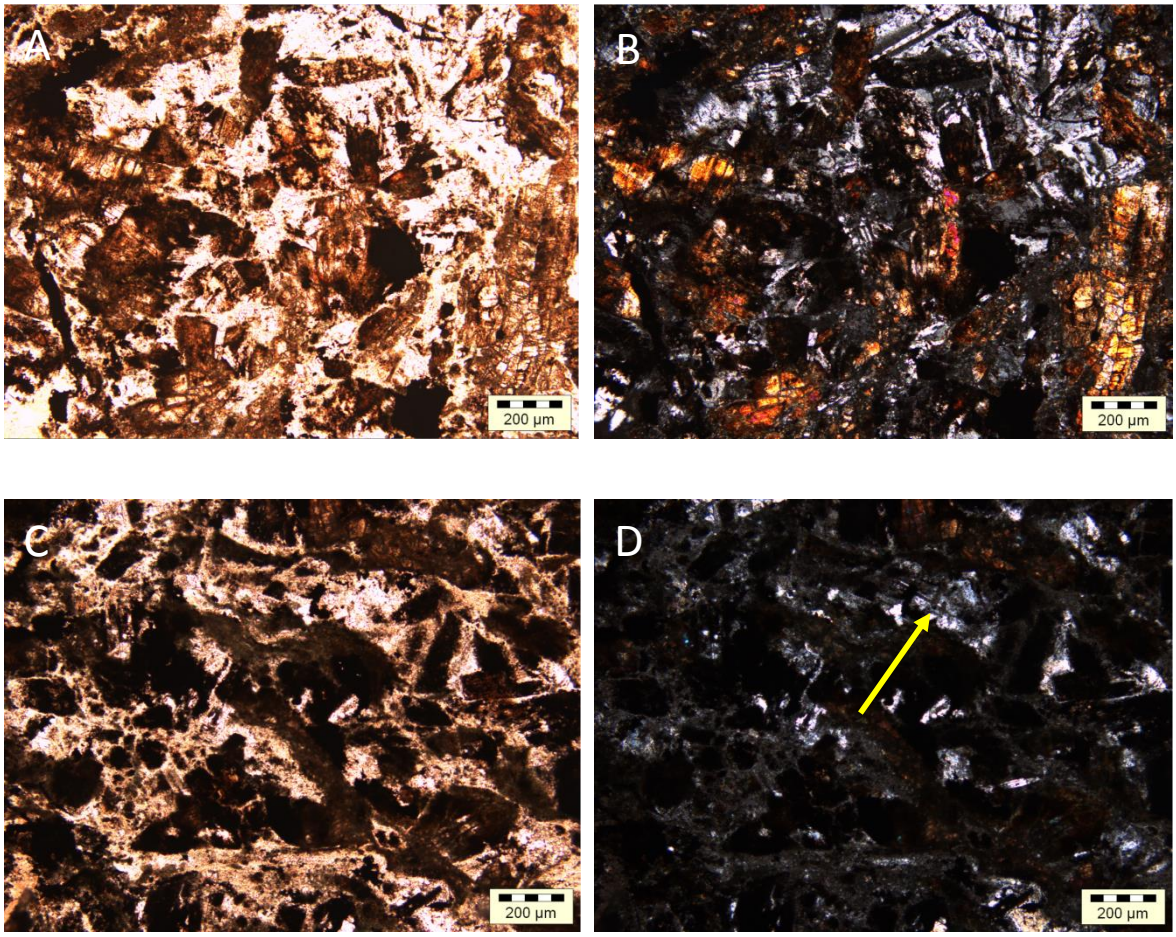

Figure 2.11: Photomicrographs of oxidized magnetite spots in dolerite sample M4 B-2, from 289.97 m depth. **A)** PPL and **B)** XPL photomicrographs showing anhedral grains of clinopyroxene and plagioclase in the less altered part of the rock. **C)** PPL and **D)** XPL photomicrographs of highly oxidized spot. Note the similarity to (A) and (B), with similar grain size and relics of plagioclase laths (yellow arrow) still visible. PPL = plane polarised light; XPL = cross polarised light.

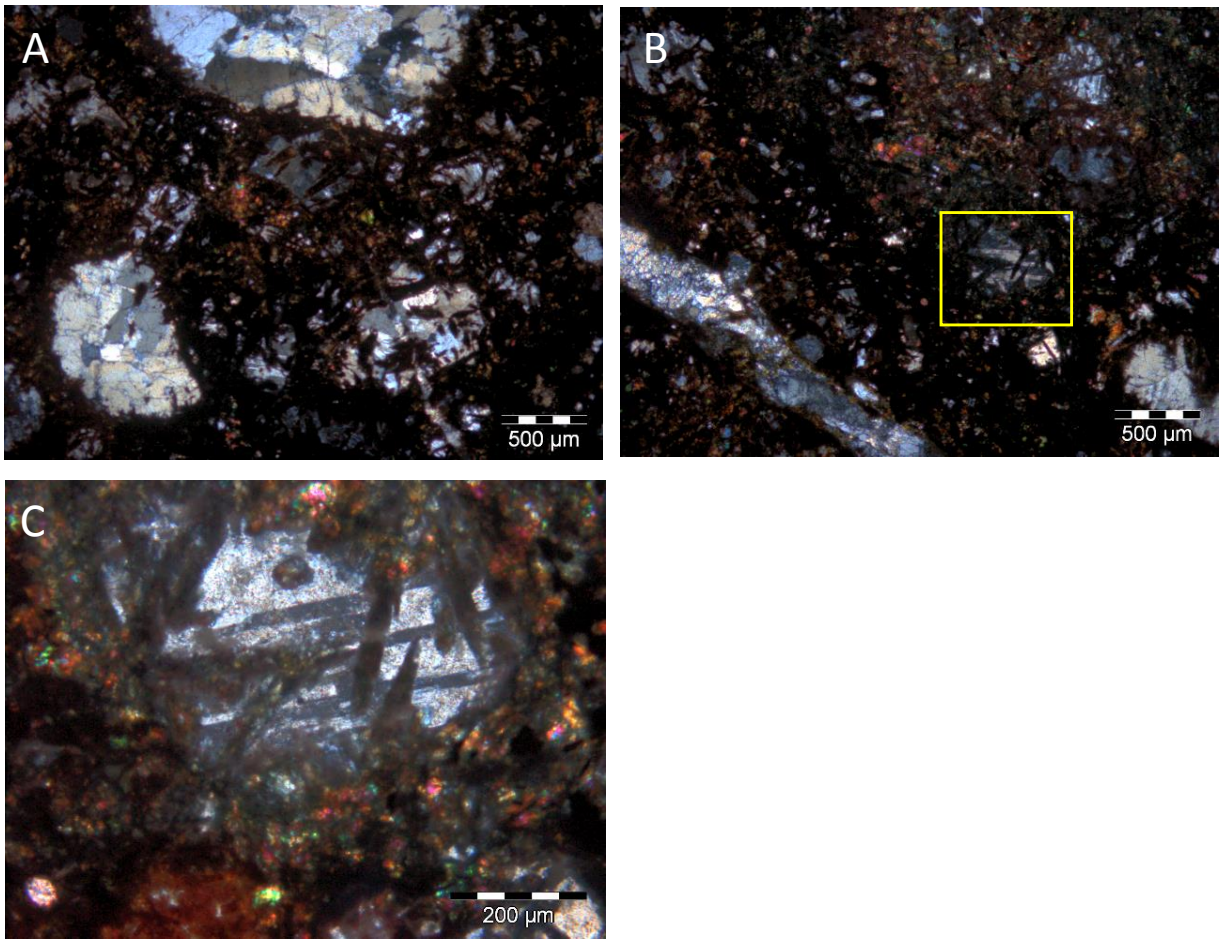

Figure 2.12: Microscopic features of silicified metadolerite from sample M4 IS 1 from 221.20 m depth**. A)** Photomicrograph showing quartz aggregates surrounded by highly altered needle-like crystals of amphibole, titanite and epidote. XPL. **B)** Note the high interference colours which are characteristic of epidote. XPL. **C)** Enlargement of C, showing oxidised amphibole needles and preserved plagioclase grain in sample M4 IS-1. PPL = plane polarised light; XPL = cross polarised light.

2.4 Macroscopic and microscopic observations of impactites

The term *impactite* refers to any impact-formed rock affected or produced as the impact shock wave propagates through the target rocks (French, 1998). This broad definition includes shocked target rocks as well, which means that all target rocks in the M4 core should be classified as impactites based on the petrographic evidence for shock metamorphism (see Chapter 5); however, in order to allow full description of the pre-impact features of the target rocks, this study has chosen to restrict the term to the new rock types (breccias) formed during the impact process. As will be shown below, however, the target rocks contain general macroscopic and microscopic evidence of variable, but generally intense, fracturing, brecciation and cataclasis that is linked to the impact. For this reason, the brittle deformation features in the target rocks must also be described in more detail in this section.

Based on the overall structural assessment of the core, the argument is presented in this section and Chapter 3 that the M4 core intersects a megabreccia that experienced simultaneous brittle shear fracturing, cataclasis and melting during the impact.

The model proposed is that (a) the melt-matrix breccias are friction melt (pseudotachylite) formed along shear fractures and faults towards the end of the excavation stage and/or during the modification stage of cratering (see Section 1.2) and that (b) the suevite represents a local, hybrid, impactite lithology created by mechanical mixing of quenched to partially quenched pseudotachylite melt with cataclasite; this mixing was caused by ongoing complex and rapidly-changing block movements during crater modification. Whilst the classification and nomenclature for impact breccias proposed by Stöffler and Grieve (1994 and 2007) based on texture, lithological components and the degree of shock metamorphism is adopted as it is in line with the International Union of Geological Sciences (IUGS) standards, the evidence presented in this section suggests that the generally accepted definition of suevite would need to be broadened. In the case of M4 core impactites, classification is further complicated by their strong hydrothermal alteration overprint (see Section 2.6 and Chapter 4) that has destroyed all traces of glass and substantially modified the fine-grained matrix of the monomict lithic breccia, cataclasite and suevitic breccias.

In this section, breccias are described on macroscopic and microscopic (optical microscopy and BSEM) scales. The stratigraphic positions of the breccias and their thicknesses are shown in Figure 2.1 (see also Appendix 2A). Based on microscopic differences in the nature of the matrix, melt particle population and the characteristics of the mineral and lithic clast populations, breccias identified in the M4 core are subdivided into 3 categories: monomict cataclasites/breccias, polymict clastic matrix breccias containing altered melt clasts (suevite) and melt-matrix breccia (originally glassy matrix, with limited lithic and/or mineral components). With the exception of sample M4 S6 (316.52 m depth; see Section 2.4.3 and Chapter 3), all lithic clasts in the breccias show petrographic and geochemical evidence that supports them having been derived from the target rocks intersected in the M4 core. Minerals enclosed as clasts in the suevites and MMBr are dominated by quartz, plagioclase and microcline, but also include biotite, epidote, titanite, magnetite, ilmenite, apatite, and clinopyroxene/amphibole, which supports the lithic clast and whole-rock geochemical evidence that the impactites were derived locally. The mineral and melt chemistry is presented in Chapter 4.

2.4.1 Monomict breccia and cataclasite

2.4.1.1 Macroscopic characteristics

According to studies of fault-related rocks, breccia is a term used to describe a fault rock with >30% clasts by volume, whereas fault rock with <30% clasts is classified as cataclasite (Passchier and Trouw, 2005). The M4 core can be classified macroscopically as a breccia based on two features:

1. The target rocks show abundant evidence of fracturing from the microscopic to dm-scale (Figure 2.13), with varying amounts of disorientation of wallrock blocks (Figure 2.14); and

2. Most major lithological contacts are marked by intense fracturing, melt-matrix breccia or suevite, or by core loss (as the cataclasites and breccias, in particular, are strongly hydrothermally altered, this loss owing to poor rock preservation supports the lithological contacts being structural). This suggests that the core could represent a megabreccia or is cut and displaced along large faults with the observed shear fractures being secondary features in m- to dm-scale blocks.

On a smaller scale, however, the fractures themselves contain microbreccia and/or cataclasite fill, and cataclasite masses are found in the suevite and MMBr dykes. These microbreccia zones individually may be no more than a few hundred microns wide but they do merge locally into mm- to cm-wide zones cutting and enclosing brecciated wallrock (Figure 2.14). From a structural geology perspective, cataclasite is typically seen as breccia fault-rock that has undergone shearing-induced comminution. The presence of slickenlines along cataclasite-bearing fractures (Figure 2.15), and of displacements of both the target rocks and impactites throughout the M4 core, support a primary slip/shear displacement origin for the fracture network. Slip displacements along shear fractures in the core typically are no more than a few mm but displacements up to 2 cm have been noted.

Macroscopic analysis of the M4 core shows that the fractures are typically marked by white clay-zeolite seams (Figure 2.13A) in the granitoids but also by haematite/magnetite in all rocks (Figure 2.5A, B). Chlorite, epidote and pyrite become more abundant deeper in the core (Section 2.6). On a cm- to dm-scale, the fractures may show consistent orientation and sense of slip/shear (Figure 2.13C). In places, conjugate patterns may be found; however, on the larger scale fractures anastomose or branch, and commonly display cross-cutting patterns with no obvious consistency in either geometry or age (Figure 2.13A). Where the fractures are particularly closely spaced (≤1 cm), the target rock may display a macroscopic oblique sigmoidal fabric between the fractures that show consistent shear sense over widths of at least several centimetres (Figure 2.13C). This fabric is similar to the S-C structure described in proto-mylonites and mylonites, however, microscopic analysis shows that flow

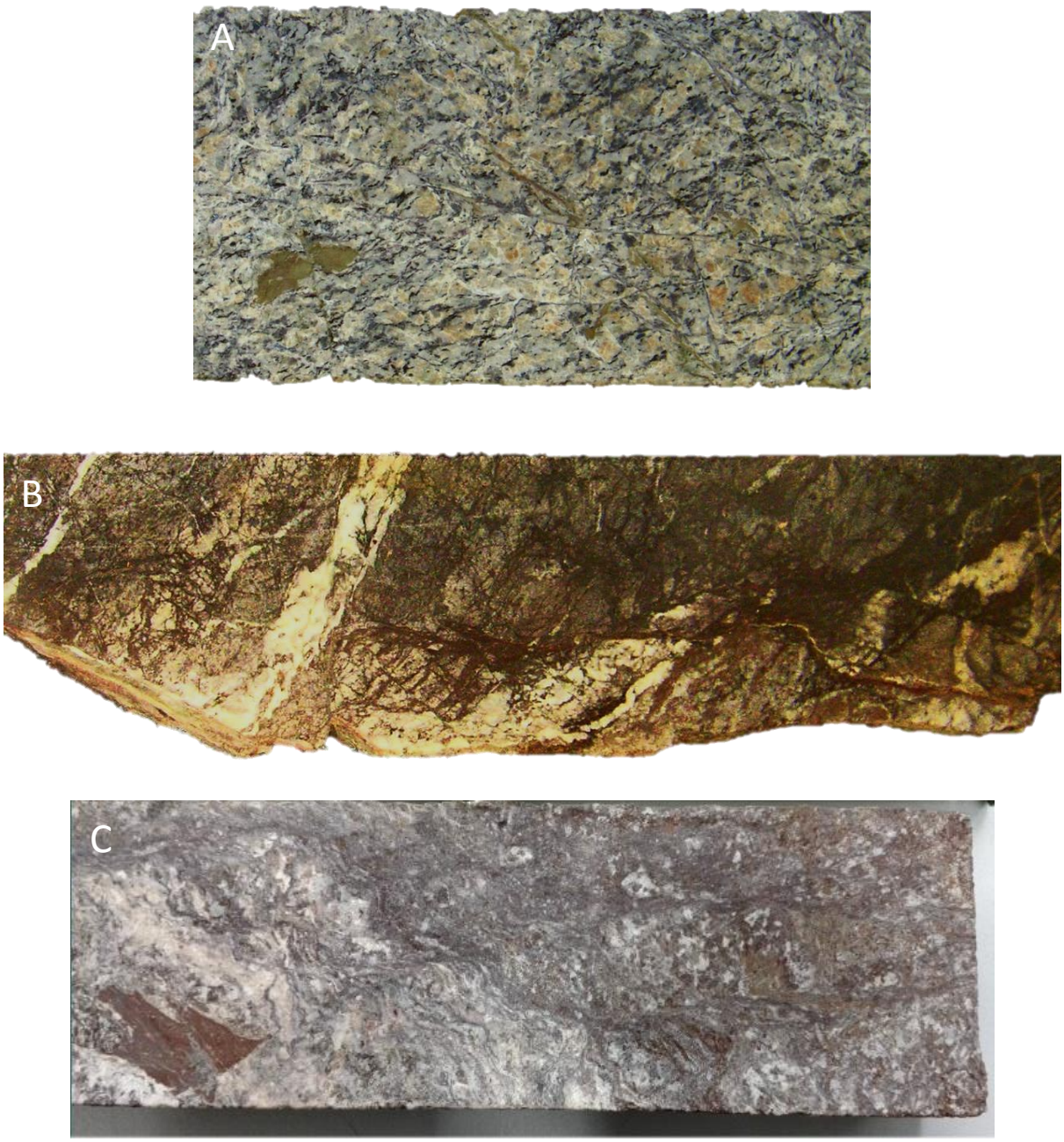

Figure 2.13: Evidence of fracturing in the M4 core**. A)** Shear fracture network in granitoid gneiss sample from 271 m depth. Fractures show mm displacements and contain thin cataclasite with a clay + zeolite matrix. **B)** Shear fractures in dolerite (depth: 213 m) with pre-impact quartz veins. Note the cm-scale displacement on quartz veins (right). Shear fractures are anastomosed and marked by haematite. **C)** Granitoid clast (?) in MMBr zone (263.08 m depth) showing crenulation associated with shear fractures that also appear to truncate a melt particle (left). The crenulated foliation lies parallel to compositional banding (more mafic to the right). Sample core width = 5 cm.

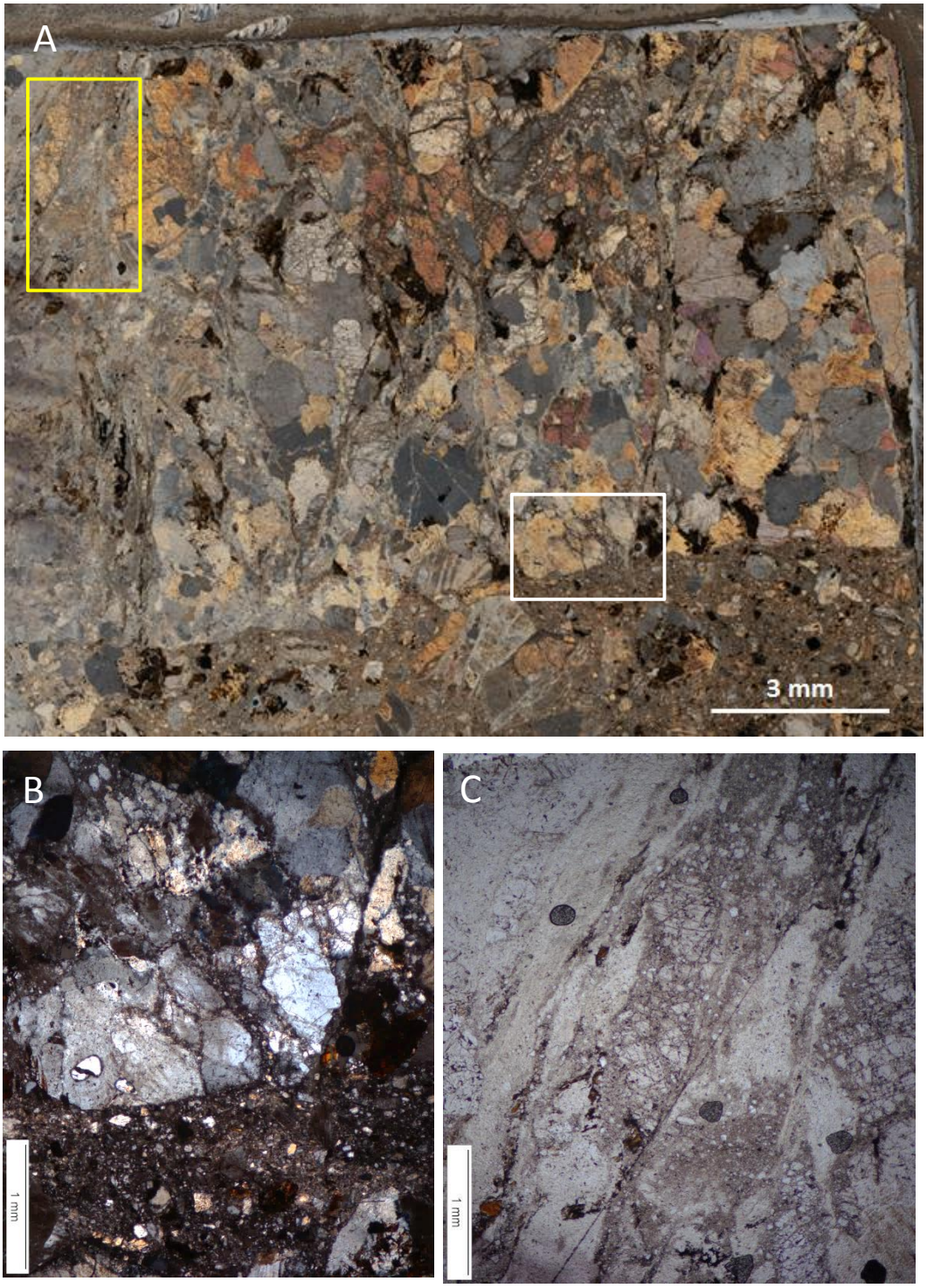

Figure 2.14: A) Circularly polarised light photomicrograph showing shear fractures in granitoid gneiss (sample IM-9 from 299.76 m depth; see location in Figure 2.16). **B)** Enlargement of A (white box) showing the microbrecciation and the cataclasite. XPL. **C)** Enlargement of A (yellow box) showing cataclasite in shear fracture. Cataclased fragments are mostly quartz, with darker patches being biotite and ilmenite. Low relief yellowish- white matrix is mostly Na-Ca zeolite after plagioclase. PPL. PPL = plane polarised light; XPL = cross polarised light.

Figure 2.15: Clay rich shear fracture surface in dioritic gneiss from 362.09 m depth.

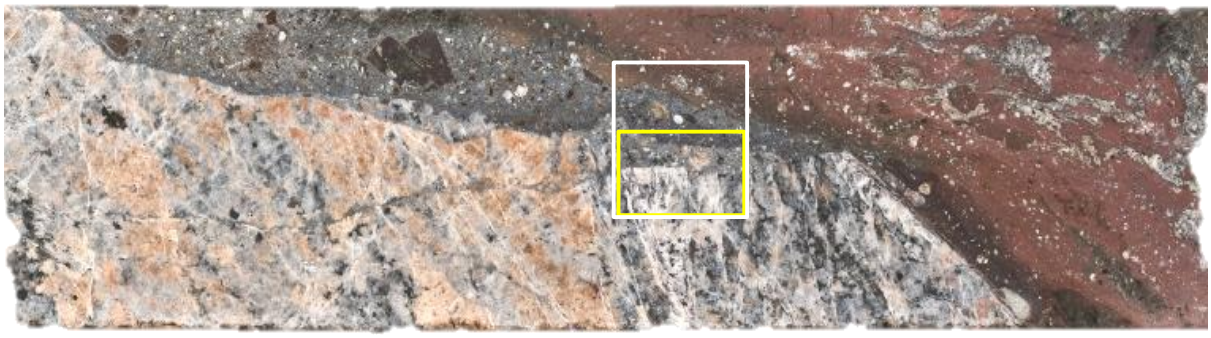

Figure 2.16: Composite impactite dyke (sample IM-9; from 299.76 m depth) showing Relationship between shear fractures, cataclasite, suevite and MMBr. The dyke exploits shear fractures. The yellow box refers to Figure 2.14 and the white box refers to Figure 2.29. Sample core width = 5 cm.

was achieved through cataclasis + comminution rather than crystalplastic processes, and in granitoid gneiss samples containing compositional banding the "S"-foliation is parallel to the gneissose banding, suggesting it is the original pre-impact foliation and that the fabric formed by crenulation/shearing of this gneissose foliation. This feature is more finely spaced and more common in the metadolerite and dolerite than the granitoid gneisses.

Shear fractures generally terminate against suevite and MMBr dykes (Figures 2.14, 2.16), but may widen considerably in the direction of the dyke. Lithic clasts in the dykes contain the same shear fracture patterns as seen in the wallrocks (see Figure 2.21B). This indicates that fracturing predated emplacement of the dykes, but that the shear fracture fill was not cohesive at the time of dyke emplacement. However, shear fractures cutting suevite and MMBr dykes occur in several places in the core, and these may even brecciate melt clasts in suevite (Figure 2.17). These fractures differ from mostly (but not always) horizontal, mm- to cm-wide, planar to slightly anastomosing, extension

fractures (dilation fractures) that contain zeolite, calcite, gypsum or quartz veins and which are most common in the upper parts of the core. These dilational fractures cut shear fractures in the target rocks as well as the impactite dykes, but are purely dilational (Figure 2.18). From these relationships, it is suggested that shear fracture development started slightly before, but continued during and even after the emplacement of the suevite and MMBr dykes and quenching of the melt, and that the dilational fractures formed after the impact during post-impact hydrothermal alteration.

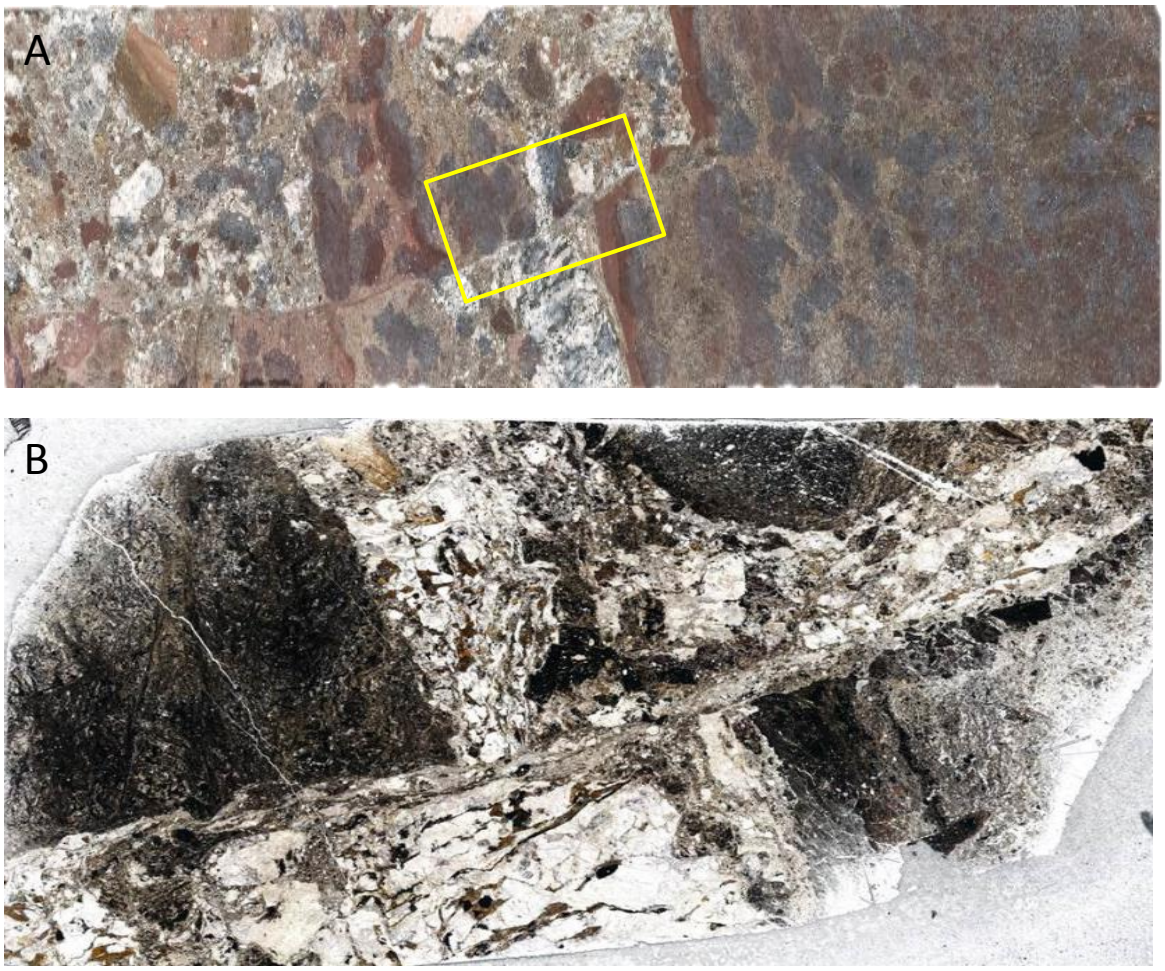

Figure 2.17: **A)** Displacement of suevite dyke by shear fracture (sample M4 S-13, from 279.67 m depth).The black ellipses are magnetite-haematite patches from post-impact alteration (see Section 2.3.4.4). Sample core width = 5 cm. **B)** Thin section of area in (A) showing brecciation of the melt clast (right).

2.4.1.2 Microscopic characteristics

Microscopic analysis of the fractures cutting the target rocks indicates that they are marked by zones of brecciated to cataclased mineral grains from a few tens of microns to >1 mm wide. Breccia grades laterally into cataclasite.

The cataclasite is made up of angular to subrounded and variably comminuted mineral clasts in a micro- to locally crypto-crystalline matrix displaying cataclastic flow (Figure 2.14C), whereas the breccia consists of more angular clasts in a microcrystalline matrix that can usually be correlated with wallrock mineral grains (Figure 2.14B). The breccia mineral clasts are angular and commonly display, sharp, acute-angled corners, and can be pieced back together like a jigsaw puzzle. The cataclasite can display sharp planar or irregular, poorly-defined, brecciated margins with its wallrocks. It shows an overall increase in strain (decrease of clast size, increase in clast rotation and comminution) towards its centre. Quartz in the wallrocks displays increasing intracrystalline deformation towards the shear fractures: farthest from the fracture it displays undulose extinction; closer to the fracture it contains deformation bands with limited fractures, followed by patchy, chessboard-like, extinction and orthogonal fracturing and, finally, brecciation with or without rotation of fragments. Feldspar grains alongside the fractures display undulose and patchy extinction and tend to fracture into elongate fragments in situ, but become more equidimensional within the brecciated fracture fill. In the cataclasite, feldspar is virtually absent as a clast phase. BSEM, EMP and XRD analysis confirm that the fracture fill is cemented by low-T hydrothermal minerals (zeolite, clay, chlorite and chalcedony). The zeolite minerals display an interlocking texture and grain size up to several hundred microns. These minerals suggest that the cataclasite was highly permeable to post-impact hydrothermal fluids, which is supported by the flow-like textures where it is in contact with MMBr or suevite (see Section 2.5.2).

In addition to quartz and feldspar in the granitoid gneisses, the cataclasite can contain clasts of biotite, titanite, epidote, ilmenite and/or magnetite. All minerals show evidence of comminution (lensoid-shaped clasts, locally with “tails” of comminuted fragments) and indicate fracture-parallel shear movement within the cataclasite that may increase towards the centre of the cataclasite (increased rotation of clasts towards the breccia centre), although textures commonly suggest highly variable strain within the mm-wide zones. However, some cataclasite margins display in situ brecciation of quartz grains, with no differential rotation of the angular fragments that are now cemented by zeolite or chalcedony. It is not unusual for the cataclasite to grade locally into a microbreccia, or for cataclasite and microbreccia-filled fractures to intersect with no sign of relative age differences. The microbreccias are most common where coarse-grained quartz occurs in the host rock. The quartz fragments are typically angular and show varying amounts of differential rotation. These fragments

Figure 2.18: Anastomosing zeolite-filled dilational fracture cutting shear fracture (depth: 120.92 m). The zeolite forms part of a post-impact hydrothermal assemblage that also includes clays, calcite, quartz, gypsum, pyrite and magnetite-haematite. Sample core width = 5 cm.

may display decorated PDF (Figure 5.14 A, C) and "continuity" of PDF between fragments confirms that the impact shock predated brecciation related to the shear fractures.

The metadolerite- and dolerite-hosted shear fractures typically display a mm-scale or finer spacing and are individually narrower than the fractures in the granitoid rocks. Although a higher proportion of the fractures in the mafic rocks are subparallel and relatively planar or only slightly curved, conjugate and irregular branching/anastomosing fractures are still common. The rock between the fractures shows the same oblique sigmoidal fabric that is seen in the granitoid rocks, and the sense of asymmetry of this fabric is consistent on at least a thin section scale. Microscale brecciation is very limited. This may be because of the almost complete absence of quartz, the finer grain size of the mafic protoliths and the high proportion of mafic minerals with strong internal cleavage. Disruption of the more regular subparallel fractures by irregular fractures may be associated with highly oxidised, mm-scale, cryptocrystalline, largely amorphous masses that locally show textures suggesting flow folding and cusp-like intrusive offshoots. These are most likely small melt bodies; unfortunately, the post-impact hydrothermal alteration and oxidation prevents confirmation of this and their possible link to the shear fractures.

Fracture relationships in the silicified metadolerite are similar to those described in the mafic rocks, although the high proportion of pre-impact vein quartz contributes to a more widely spaced, irregular, fracture morphology and geometry (example Figure 2.13B).

Although a quantitative analysis of fracture density was not attempted in this study, qualitative analysis of the M4 core suggests that the shear fractures increase in intensity towards the major lithological contacts, which have been interpreted as faults (see Section 2.4.1.1), and that fracturing is most intense adjacent to the suevite and MMBr dykes and in their lithic clasts. Unfortunately, the M4

core does not provide an opportunity to estimate the size of the slip displacements along either the faulted contacts or many of the fractures; however, macroscopic and microscopic analysis confirms at least mm-scale displacements along the fractures. In Chapter 5 evidence of shock features is presented that indicates peak shock pressures of >22 GPa. According to Stöffler and Langenhorst (1994), this would be consistent with shock heating of 200-250 °C (Table 5.1). Assuming an average continental geotherm and that the rocks in the M4 core were originally buried at depths of at least 5 km immediately prior to the impact (see Chapter 6), this would suggest that fracturing occurred under temperatures of low- to mid-greenschist facies (300-350°C). This might have influenced mineral strain behaviour, although at high strain rates it is unlikely that ductile strain could have occurred.

In summary, monomict breccia and cataclasite is associated with intense shear fracturing of the target rocks. The close spacing of shear fractures in certain parts of the core, particularly in the mafic rocks, gives the appearance of a shear foliation, however, microscopic analysis shows no sign of ductile strain processes. The breccias are classified as autochthonous as no exotic mineral or lithic clast occurs. The shear fractures largely predate the emplacement of the suevite and MMBr dykes (dykes contain fractured clasts, shear fractures truncated by dyke or clast margins); however, some shear fractures with mm – cm spacing do cut the dykes (Figure 2.17). It is not clear if these late shear fractures are part of the same generation as the main set of shear fractures. Dilational fractures filled with hydrothermal vein minerals clearly postdate the shear fractures, suevite and MMBr.

2.4.2 Melt-matrix breccia (MMBr)

2.4.2.1 Macroscopic characteristics

Melt-matrix breccia is the name given to planar to highly irregular clast-bearing dykes with vesicles, laminar to chaotic flow banding and an overall aphanitic appearance that range from mm- to dm-width (Figure 2.19). They occur as discrete core intersections of up to ~ 2 m length that are >50% by volume melt. MMBr dykes larger than 1m occur between 259.11-260.70 m (1.59 m thick); 262.20-264.15 m (1.95 m thick); 264.80-266.21 m (1.41 m thick); 270.47-272.40 m (1.93 m thick); 278.00-279.32 m (1.32 m thick) and 290.95-292.98 m (2.03 m thick) in the M4 core (Appendix 2A, boxes 20-25). There are 5-10 cm intersections of MMBr that are notably bright reddish brown and these are limited to the metadolerite intervals from 176.60-190.11 m (Appendix 2A, boxes 10 and 11). MMBr intersections may represent individual dykes; but unfortunately, the limited core diameter makes it impossible to tell if these intersections represent a single melt volume with large clasts, or a network of multiple thinner dykes in a largely intact wallrock (e.g. the 1.59 m thick MMBr dyke in Box 20; Appendix 2A). Microscopic (Section 2.4.2.2) and BSEM and EMP analysis (Chapter 4) indicate that the MMBr matrix is strongly altered and oxidised, so no glass or unequivocal igneous textures have

been found to prove that the dykes were once melt; however, it will be shown below (section 2.4.3) that the MMBr matrix differs strongly from the particulate cataclasite and suevite matrices and is best explained as having once been molten.

The most voluminous MMBr are dark red to red-brown (Figure 2.19A, B), but pink, orange (Figure 2.19C), grey (Figure 2.19D) and black varieties are locally present. These colours can be broadly correlated with the wallrocks – red and brown MMBr is most abundant in the metadolerite and dolerite, whereas the pink and orange MMBr is found in the granitoid rocks and grey MMBr is found in the silicified metadolerite. Millimetre- to dm-wide red and black-brown MMBr dykes are, however, found in the granitoid rocks. One explanation for this would be if the original red and red-brown melts had a low viscosity, enabling them to be injected away from their source. Given that the core does not allow the true geometry of the dykes to be observed, transport distances may not need to have been more than a few meters but cannot be estimated with any confidence in a core. Macroscopically, the MMBr may appear homogeneous and with only a limited number (<5 volume %) of mm-scale clasts visible, but the larger dyke intersections are typically highly heterogeneous (e.g. Figure 2.21; Appendix 2A, boxes 20-25). This heterogeneity is caused either by incomplete mixing of different melts, which show patches or streaks that may be a few mm to several cm wide. The different melts may be distinguished based on differences in colour, clast content and the presence or absence of banding (Figure 2.20). Chaotic flow folding suggests turbulent mixing, although planar to lensoid colour banding in places indicates more laminar flow, particularly along dyke margins (Figure 2.21).

In Chapter 3, evidence is shown that the MMBr dykes are similar geochemically to their wallrocks (Figure 3.8). However, it is also clear that the MMBr has been injected into the wallrocks for significant distances of at least tens of cm (Figure 2.22A). The MMBr contains angular to rounded metadolerite and granitoid gneiss lithic clasts up to dm size (Figure 2.22C). Straight clast edges are typically parallel to internal shear fractures within the clast, showing that the melt may have isolated large clasts by intruding along shear fractures (Figure 2.22B). It is sometimes possible to still see that the planar clast edges line up with fractures in the wallrock, indicating that melt emplacement was controlled by the shear fracture network (Figure 2.22A, B). These shear fractures contain cataclasite (Figure 2.22A) is confirmed by thin injections of melt along fractures in coherent wallrock, some of which still contain cataclasite fill. Also, the margins of some lithic clasts in the MMBr are cataclasitic, again suggesting that the melt intruded along cataclasite-filled fractures (Figure 2.22B). In some cases, the dyke margins show regular steps that can be correlated with intersecting fractures in the wallrock, suggesting that melt was emplaced into en-echelon dilational sites that exploited the fractures (Figure 2.22B). Figure 2.22B shows that melt emplacement did not significantly disrupt the clasts or cataclasite fracture fill. This might indicate limited melt transport and also low melt viscosity and a fairly passive intrusion of the melt.

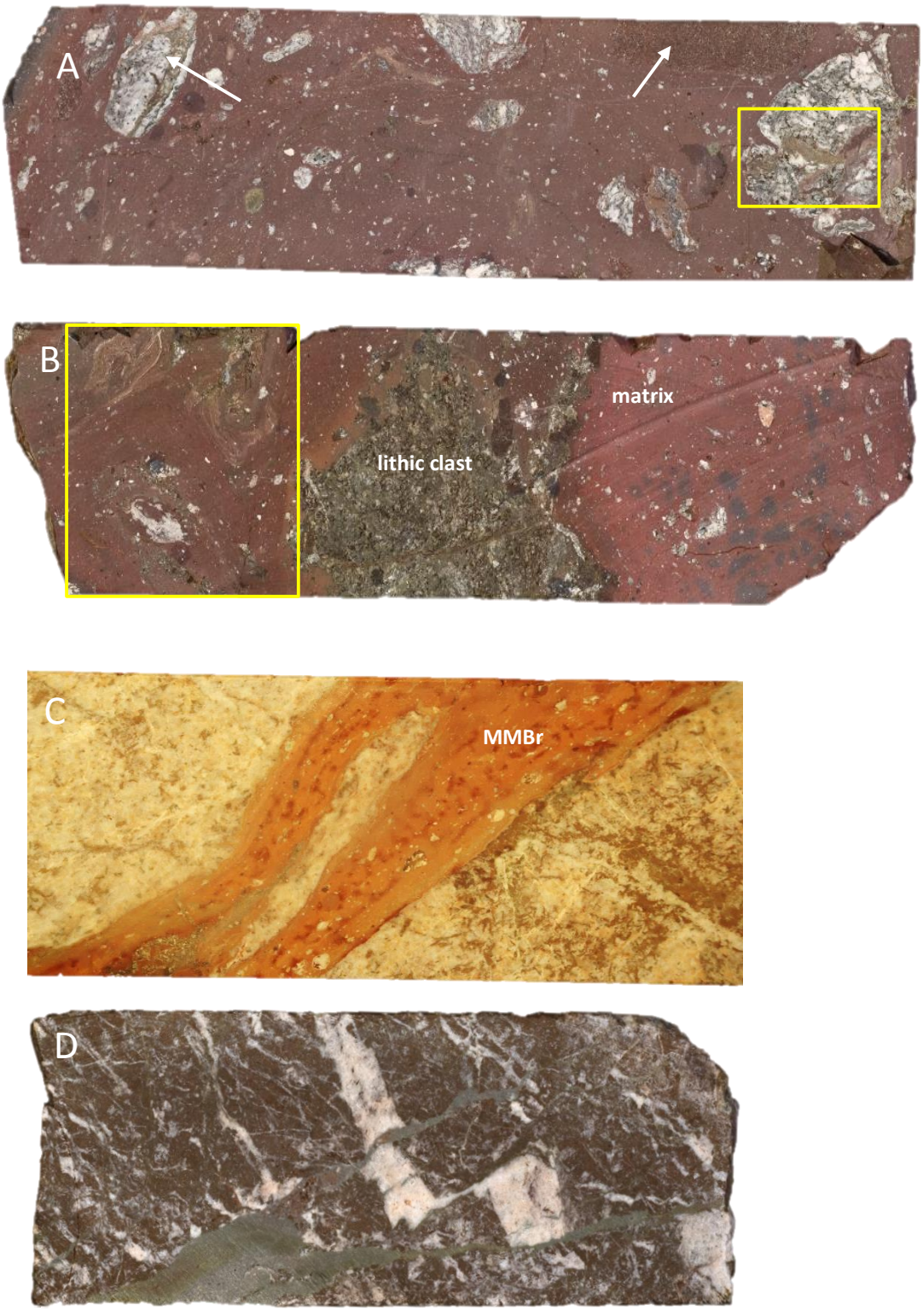

Figure 2.19: Colour variation in MMBr. **A)** Lithic granitoid clasts and dolerite clasts enclosed in MMBr matrix; sample M4 IM-4 (depth: 259.11 m). Yellow box represents the light green melt shown microscopically in Figure 2.24K, L. **B)** MMBr sample M4 IM-6 (depth: 271.17 m). Note the dolerite lithic clast that is not assimilated into the MMBr matrix. Yellow box represents Figure 2.21A. **C)** Pink/orange MMBr injection in trondhjemitic gneiss sample from 230.13 m depth. **D)** MMBr injection dyke into quartz-veined silicified metadolerite sample from 206.28 m depth. Note the displacements along the MMBr injections, suggesting that the veins exploit shear fractures. Sample core width = 5 cm.

Figure 2.20: MMBr sample from 265 m depth, showing clast-poor MMBr dyke with strong flow banding indicated by red and reddish brown colour banding. Note flow folds along dyke margin (arrow) with cataclasite (right). Cataclasite along right and left contacts. Dolerite wall rock is highly fractured (top right). Note cm-scale elliptical dark brown haematite-magnetite nodules in cataclasite and irregular MMBr on left. Sample core width = 5 cm.

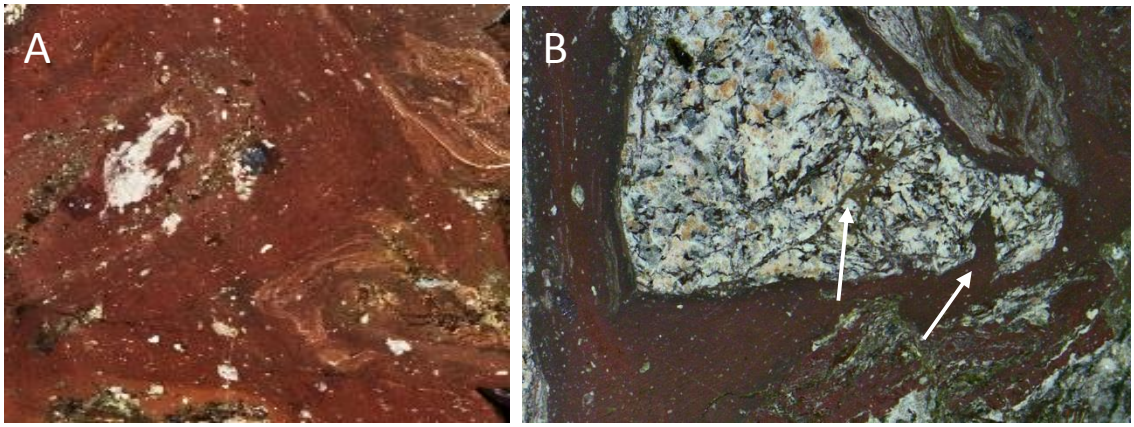

Figure 2.21: Flow banding in MMBr. **A)** Enlargement of Figure 2.19B, showing chaotic (flow folded) incomplete mixing of felsic and mafic "melt" (sample IM-6 from 271.17 m depth). **B)** Millimetre-scale flow banding and laminar flow (especially around the margins of the fractured granitic gneiss clast). Note the injections of MMBr matrix into the pre-existing fractures of the clast (arrowed). Sample from 271 m depth.

Apart from lithic and mineral clasts the MMBr contains lenses, bands, and stringers (1mm to 10 cm wide) of grey clastic material with a typical grain size of <1 mm. Microscopic analysis (see Section 2.4.2.2) indicates that this material is quartzofeldspathic cataclasite from the granitoid gneisses. The elongate and deformed (folded, boudinaged) nature of the cataclasite lenses and stringers in the MMBr, together with evidence along the margins of MMBr of infolding of cataclasite and/or suevite (see Section 2.4.3) suggests that melt was intruded into fracture-fill cataclasite and that this cataclasite was not cohesive at the time. This is further supported by the observations (see Section 2.4.2.2) that the mineral clasts in the MMBr are mostly granitoid derived, even where the MMBr shows strong correlation with metadolerite/dolerite composition (Figure 3.8). The mechanisim of incorporation of the cataclased mineral fragments into the melt can be seen in Figure 2.22B, where the angular and

fractured granitoid lithic clasts are bordered by cataclasite. Stringers of cataclasite extend from the clast edges into the MMBr matrix where they are increasingly disrupted and break apart into fine wispy trails. More commonly the lithic clasts contain rounded lobes of cataclasite along their margins (Figure 2.22A), suggesting shaping of the cataclasite by flow. In places, the ratio of melt matrix to cataclasite approaches 1:1, suggesting that a complete gradation exists between MMBr and cataclasite. This observation is important in understanding the origin of the suevite (see Section 2.4.3).

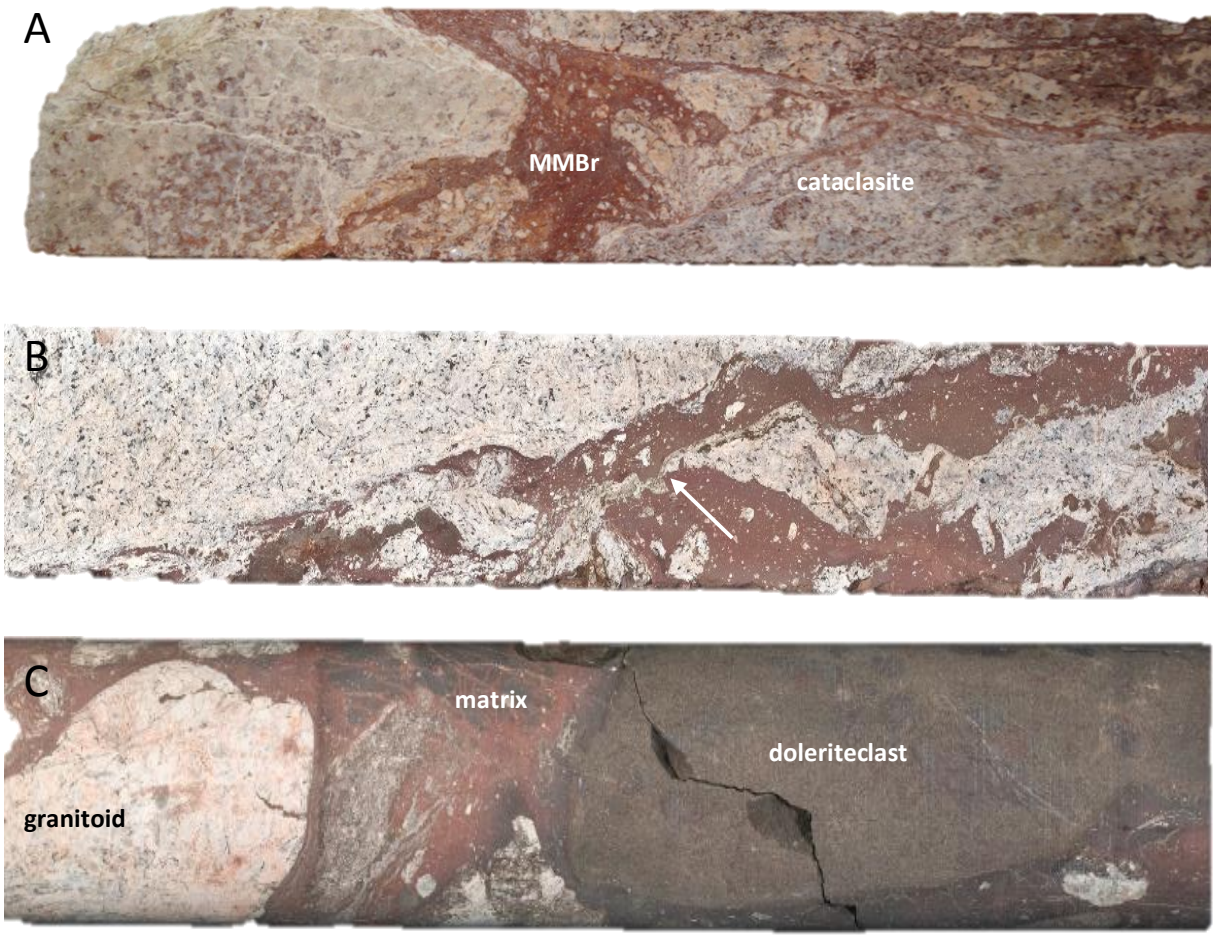

Figure 2.22: Evidence of thin injections of low-viscosity melt. **A)** Granodioritic gneiss sample (158.06 m depth) shows injection of red MMBr along shear fractures, and wedging off of cataclased lithic fragments. **B)** MMBr in granitic gneiss from 295.88 – 296.19 m depth, showing planar, stepped, margin consistent with fracture-controlled emplacement of the dyke. The large clast right-of-centre is still largely coherent (but note injection from below), but the clastic material to the right has flowed with the melt matrix (arrow). **C)** MMBr sample from 260.39 m depth, showing rounded lithic clasts of granitoid gneiss and dolerite entrained in MMBr matrix. Sample core width = 5 cm.

On average the percentage lithic lasts within a MMBr interval varies. The ~ 20 m zone between 259.11 m and 279.32 m depth containing up to 50% MMBr is highly heterogeneous lithologically with multiple dolerite and granitoid intersections (Figure 2.1). The MMBr matrix encloses smaller granitoid and dolerite clasts that constitute 15-30% of the MMBr. There is no consistent variation observed in clast size; therefore, it is not clear whether the wider (>20 cm) granitoid gneiss and dolerite intersections represent clasts entrained within a megabreccia or whether the granitoids are a continuous suite with the overlying trondhjemitic gneisses and the dolerite is a cross-cutting intrusion. Also, it is not clear whether the MMBr is generated along the granitoid-metadolerite contacts either because of a rock competency contrast or because of a pre-existing fault because of the limits of core-based studies. The overall proportions of enclosed granitoid versus metadolerite/dolerite clasts is about 80:20. This reflects the overall proportions of M4 core target lithologies where granitoid gneisses are the dominant lithology type (Figure 2.1).

2.4.2.2 Microscopic characteristics

Transmitted light microscopy of the red to red-brown MMBr shows that the matrix is largely opaque and varies from black to brown to red-brown in colour. It is isotropic under crossed polars but analysis of the edges of thin sections shows that it is cryptocrystalline, rather than glass. This is confirmed by BSEM images, which show a typically 5-10 μm grain size. The distribution of phases appears to be relatively uniform within individual compositional bands and this is interpreted as a sign that the phases crystallised or recrystallised from an extremely homogeneous (on the microscale) precursor, which would suggest either a melt or a glass. A further piece of evidence in support of a molten precursor is that BSEM analysis of the 3 different breccia types shows that the grain size of the MMBr matrix (and melt clasts in the suevite) is much finer-grained than the clastic matrix of the other two breccia types; the MMBr matrix also contains very few fine-grained angular clastic mineral fragments (<20%). Finally, the grain size of the hydrothermal alteration assemblage in the MMBr is up to 1-2 orders of magnitude smaller than in the clastic-matrix breccias. This is taken as a sign that the glassy or ultra-fine-grained MMBr matrix lacked significant porosity for large hydrothermal mineral grains to grow. The strong sub-mm banding and finer grain size along dyke margins might suggest chill margins

Microscopic evidence of flow includes asymmetric to locally sheath-type folds defined by mm-or sub-mm-scale banding, and flow-aligned clasts. A common feature of the MMBr is the presence of mm-scale and smaller viscously deformed melt inclusions within the melt matrix of the MMBr (e.g. Figures 2.21A, 2.24F). These inclusions suggest disruption of a melt of one composition by the main MMBr melt, and insufficient heat to allow full mixing. The highly irregular shapes of these inclusions suggests that incorporation happened whilst both melts were still fluid. The sharp contact between the

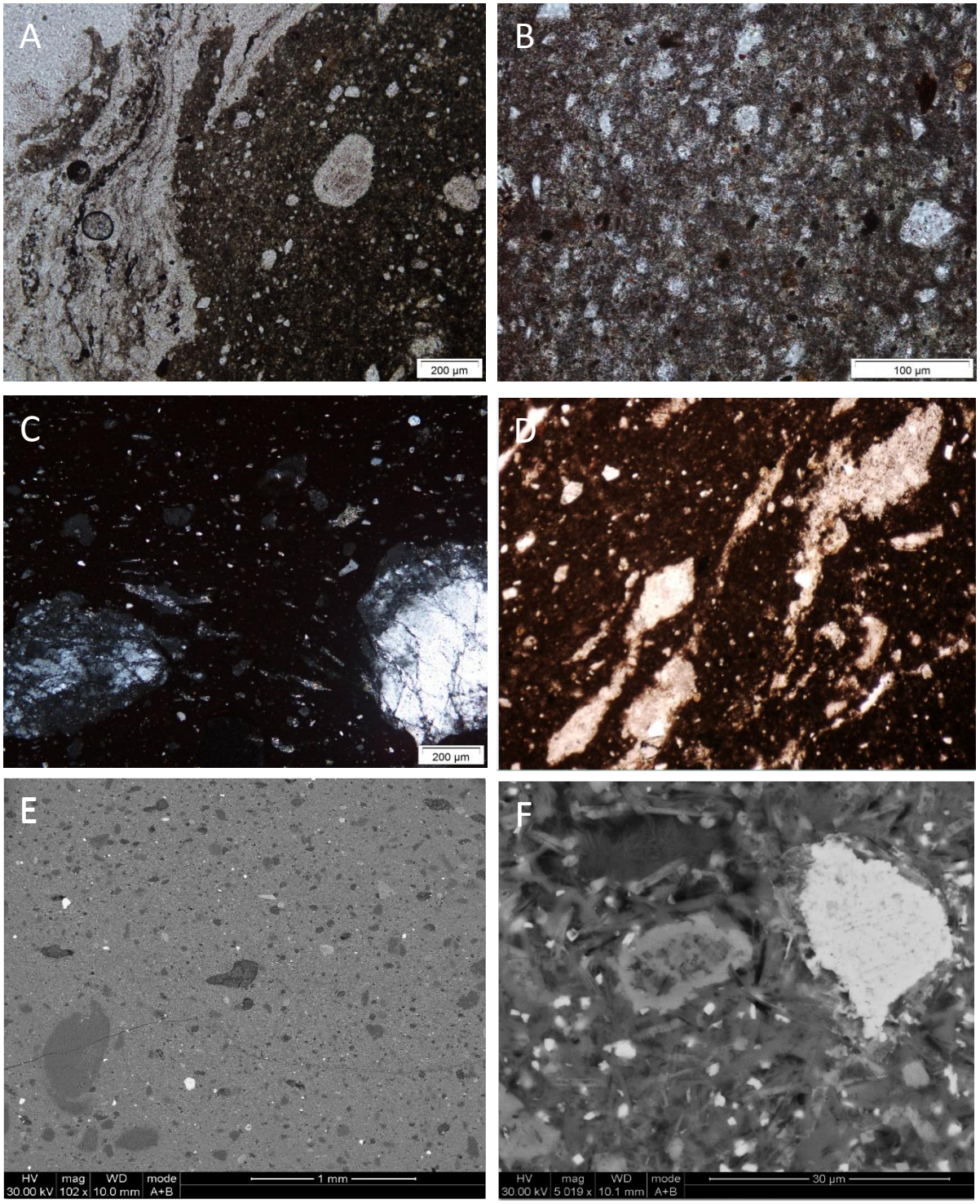

Figure 2.23: MMBr matrix character. **A)** Contact of matrix MMBr (right) infolded with clastic-matrix suevite (sample M4 IM-6; 271.17 m depth). PPL. **B)** Enlargement of A. Note the enclosed mineral clasts of quartz (up to 50 µm) and an opaque phase. The matrix is cryptocrystallineat a <10 µm scale. PPL. **C)** MMBr matrix of sample M4 IM 9 showing fractured, highly cataclastic quartz and feldspar mineral clasts. Note the flow-aligned elongate clasts made up of cryptocrystalline quartz, and the isotropic appearance of the matrix. XPL. **D)** Streaked out plagioclase mineral fragments (An_{22-34} $Ab_{58-62}Or_{2-18}$) entrained but not completely melted?. PPL = plane polarised light; XPL = cross polarised light. **E)** BSEM image of MMBr matrix from sample M4 IM-4 (depth: 259.11 m) shows angular to subrounded quartz, K-feldspar and rare ilmenite clasts in a homogeneous cryptocrystalline matrix. **F)** BSEM image of MMBr matrix from (E) showing devitrified matrix. Note the radiating phyllosilicates that infill the hole (top left) and the subidioblastic fine-grained magnetite (white) found disseminated in the matrix and overgrowing the titanomagnetite clast.

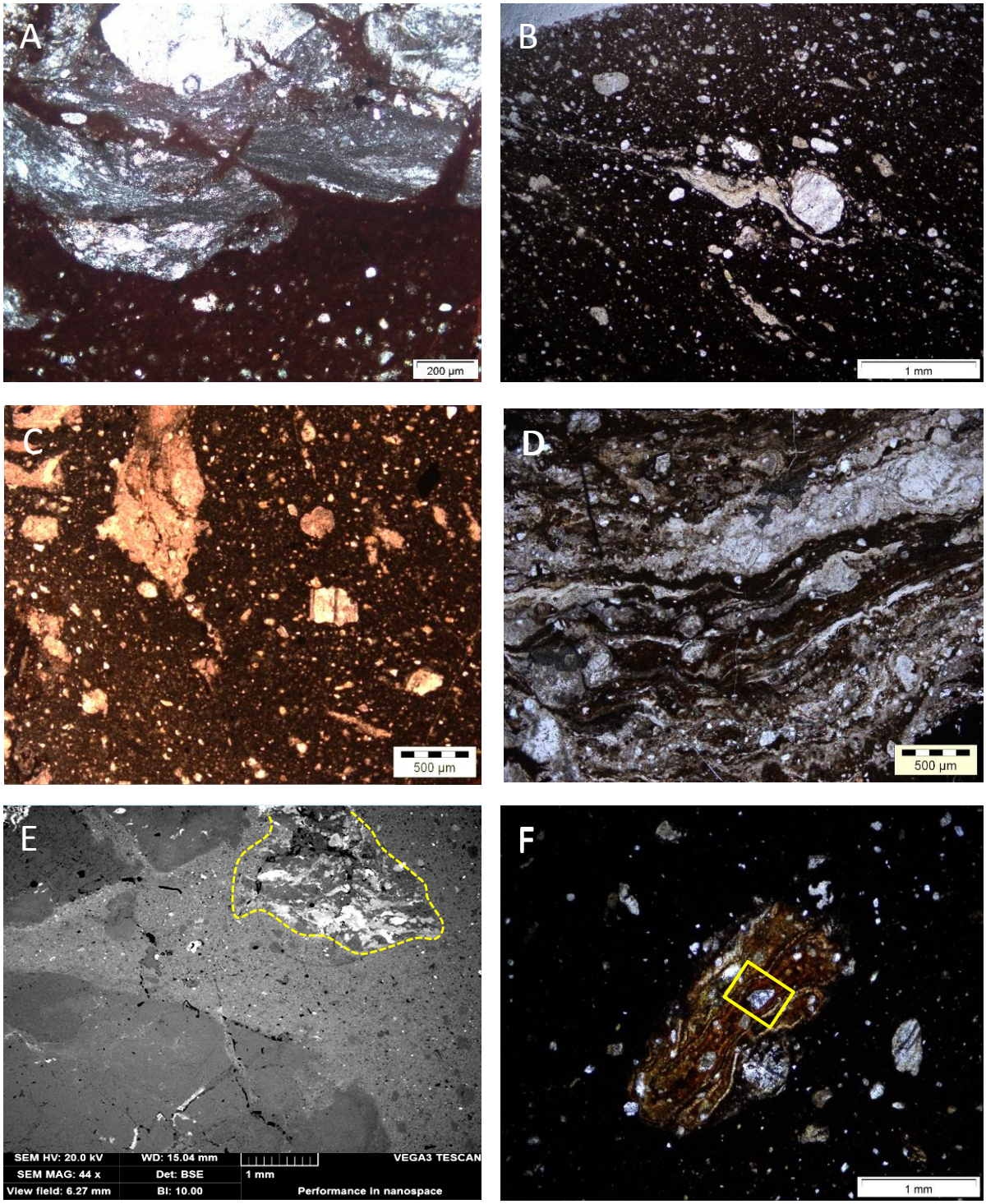

Figure 2.24: Evidence of cataclastic flow in clasts in MMBr. **A)** Cataclased quartz clast showing sections of melt injecting into the fractures (MMBr sample M4 IM-4 from 259.11m depth). **B)** MMBr matrix of sample M4 IM 6 showing ribbon-like cataclasite clasts and mineral clasts, both defining a flow fabric. PPL. Note the matrix is isotropic and very fine grained. **C)** Sample M4 IM-4 from 259.11 m depth. Most clasts are cataclasite. Note the angular plagioclase mineral clast. PPL. **D)** MMBr sample M4 IM-2 from 234 m depth with a schlieric-banded texture. Dark bands are the melt, light bands are cataclased quartz and feldspar that are boudinaged. PPL. **E)** BSEM image of MMBr sample M4 IM-4 from 259.11 m depth showing the injection of MMBr which encloses a partially digested metadolerite lithic fragment (outlined) into the lithic clast (Figure 2.19A, box). **F)** Orange, variegated melt particle in MMBr sample M4 IM-6. XPL. The box is for Figure 2.37A. PPL = plane polarised light; XPL = cross polarised light.

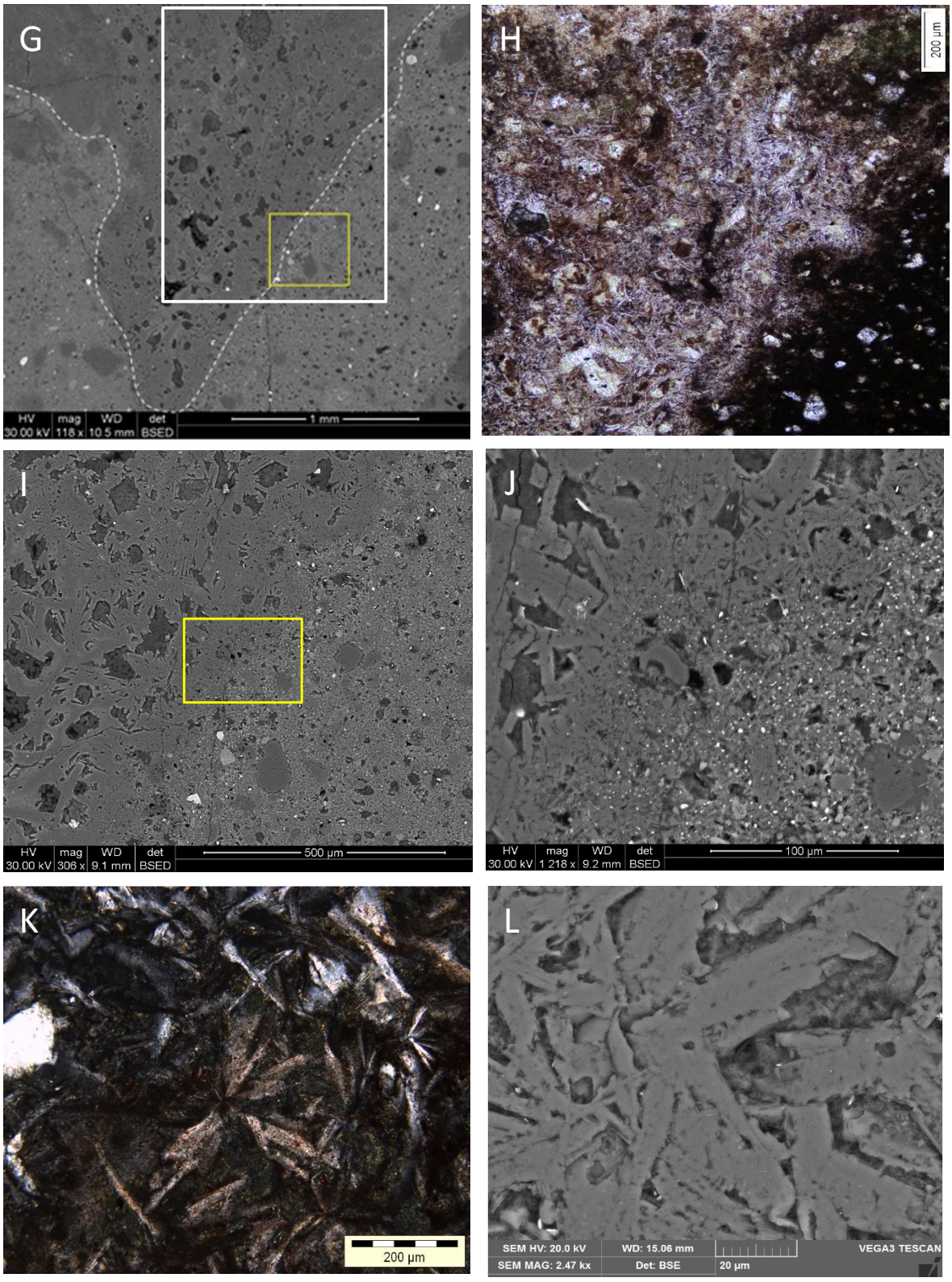

Figure 2.24: *Continued*…: **G)** BSEM image of light green melt particle within the MMBr matrix of sample M4 IM-4, showing randomly oriented phyllosilicates with high porosity. **H)** Transmitted light micrograph of enlargement of G (white box) showing radiating phyllosilicates Note the irregular, fluid-like margin with the MMBr matrix. PPL. **I)** BSEM image enlargement of G (yellow box) showing random to radiating acicular 50–100 µm grains in clast, and finer-grained, clast-laden MMBr matrix. **J)** Enlargement of I, illustrating the finer grain size of the MMBr matrix and the higher proportion of very fine-grained opaques. **K)** Re-crystallized/devitrified light green melt from sample M4 IM-4 (depth: 259.11 m). XPL. **L)** BSEM image of K, showing globular-skeletal textured minerals with cryptocrystalline interstices of zeolites/smectites.

two melts suggest that little mixing occurred. The melt particles may also show differences in mineral clast content relative to the adjacent MMBr matrix or show more internal compositional banding (Figure 2.20). Compositional profiles across some of these clasts (Appendix 4D) did not reveal consistent noticeable differences; further work is needed in this regard. Melt particles are generally isotropic but can be variegated (Figure 2.24F). The lighter orange bands in these particles generally have a more siliceous, feldspathic composition and the darker bands have a more ferromagnesian composition.

Mineral clasts are dominated by rounded to shard-like quartz and microcline, with plagioclase slightly less common. These clasts can be up to several mm in size and polymineralic, although most are monomineralic. All of them show clear evidence of the same range of internal strain features seen associated with the shear fractures and monomict breccia/cataclasite. This includes "tails" of comminuted fragments that are streaked out into the flow-banded matrix alongside larger clasts (Figures 2.23C, 2.24A). More rarely, monomineralic clasts of biotite, magnetite/titanomagnetite, epidote, titanite, zircon and apatite are found. Apart from rare pyroxene, no metadolerite or dolerite minerals have been found although magnetite and titanite could be derived from either a granitoid or a doleritic source, and it is imposible to obtain plagioclase compositions without systematic EMPA. The mineral clast population thus appears strongly biased towards the granitoid target rocks, despite the similarity of bulk chemistry of the red-brown MMBr with the doleritic target rocks (Chapter 3, Figure 3.8). This contradiction can be explained by the clasts being mechanically mixed into the MMBr after melting. This fits with the macroscopic evidence that shows infolding of monomict breccia/cataclasite and/or suevite into the MMBr (Figure 2.23A) and streaky layers and lenses of monomict breccia/cataclasite enclosed within the MMBr matrix (Figures 2.23D, 2.24B, D). Some large clasts show microscopic evidence of intrusion of matrix melt, including wedge-shaped apophyses with internal flow folds indicating flow from the MMBr matrix. Like the margins of some melt breccias, the apophyses look like they are finer-grained and well-banded than the MMBr dyke interiors, although alteration prevents definitive confirmation that these are chill zones.

Although a complete spectrum of lithic clast sizes exists from dm-to-cm-scale down to <<0.1 mm, small clasts are relatively rare, which could indicate that they have been preferentially assimilated by the MMBr. Sample M4 IM-2 (Figure 2.34C), is interpreted as a variegated, complexly banded, MMBr that lies close to the base of the upper granitoid gneiss interval (Appendix 2A, box 16). The sample contains colour bands that range from pink to orange and white and is vuggy. Microscopic analysis shows that the sample is comprehensively altered with a relatively coarse-grained hydrothermal assemblage. Mineral banding may be hydrothermal rather than flow-related.

2.4.3 Suevite

2.4.3.1 Macroscopic characteristics

As defined in Section 1.3, suevite is a clastic-matrix impactite that contains melt fragments. One of the main problems in the M4 drillcore lithologies is the level of alteration of the impactites which may make it difficult to confirm whether a flow banded, plastically deformed, clast was originally melt. In the M4 core, suevite has a cumulative thickness of ~20 m (up to 5 vol. % of the M4 core) (Figure 2.1). Suevite is found throughout the M4 core but mainly between 143.00-149.24 m depth (6.24 m thick), 154.55-157.55 m depth (3.00 m thick), 167.20-170.41 m depth (3.21 m thick) depth, 206.40-208.73 m depth (2.33 m thick) depth and between 285.03-287.93 m depth (2.90 m thick) which are the thickest intervals. Though individual dykes range from a few mm in width up to 6 m, questions remain about whether some target rock intersections bounded above and below by dykes are large clasts in a single dyke or intact wallrock separating two different dykes (e.g. Appendix 2A, boxes 6 and 7). Suevite colour varies from red above ~200 m depth, to grey between 207 m and 310 m, and green below ~307 m (Appendix 2A, B). This is interpreted mostly as the result of the post-impact hydrothermal alteration effects, where the upper zone is more highly oxidised and dominated by haematite, and the lower zone contains abundant chlorite and pyrite (see section 2.5.2).

Suevite in the M4 core is polymict and is generally matrix-supported (Figure 2.25A, B) although some dykes contain portions that are lithic-clast-supported (Figure 2.26A, B). Although some of the lithic-clast-supported areas are polymict, others are monomict and could be brecciated larger lithic clasts. Lithic clast size varies from <1 cm to ~15 cm (e.g. Appendix 2A, Box 6, 147.50 m depth); however, estimating the actual largest clast size is limited by the 5 cm core diameter. Lithic clast content varies from 30% to 60%. Clasts are generally angular and locally shard-like (Figure 2.25A) although, like with the MMBr, they may be partly composed of cataclasite which can lead to more rounded edges with the matrix (e.g. Figure 2.26A). Clasts commonly show internal fractures and cataclasis, and also signs of breaking apart. Lithic clasts are dominantly derived from granitoid gneisses, although metadolerite and dolerite clasts may form up to 20% of the clast population locally (Figure 2.26A, B), except for suevite that is restricted in the metadolerite section where the clast population is dominantly metadoleritic with quartz veins (Figure 2.25D). The lithic clast composition is mostly the same as the immediate wallrock; where there is a lot of quartz veining, monomineralic quartz clasts are noted (e.g. M4 S-9, Appendix 2B), and where the wallrock is metadolerite, metadolerite clasts dominate the formed suevite (e.g M4 S-11, Appendix 2B). Some lithic clasts are flow aligned, as can be seen in sample M4 GG-3 (Appendix 2B).

With one exception in the 6 m wide dyke at 143.00-149.24 m depth, which shows a broad increase in clast size downwards, from mm-size at the top to 1-2 cm at the base (Appendix 2A, box 6) lithic clast size does not appear to vary in a systematic way within or between dykes vertically in the core. However, thinner dykes tend to contain smaller lithic clasts. In some places the smaller clasts show flow alignment parallel to dyke margins (Figure 2.27B) but in general the larger clasts are angular and randomly orientated (Figure 2.25, 2.26). Other evidence of flow in dykes is found in the elongate lenses and layers of cataclasite that may show boudinage (Figure 2.26A, C). Dyke margins are irregular (Figure 2.27A) and close analysis shows that the margins may be defined by cataclasite (e.g. Figure 2.27C and 2.29). This indicates that suevite emplacement is similar to the MMBr dykes, i.e., it occurred along the cataclasite-filled fractures, this is not always the case.

Thin (<1 mm up to 1.5 cm) veins of calcite, chalcedony and zeolite cut the suevite (e.g. suevite sample from 143 m depth, Appendix 2B). These post-impact fractures and veins must have formed after solidification of the suevite.

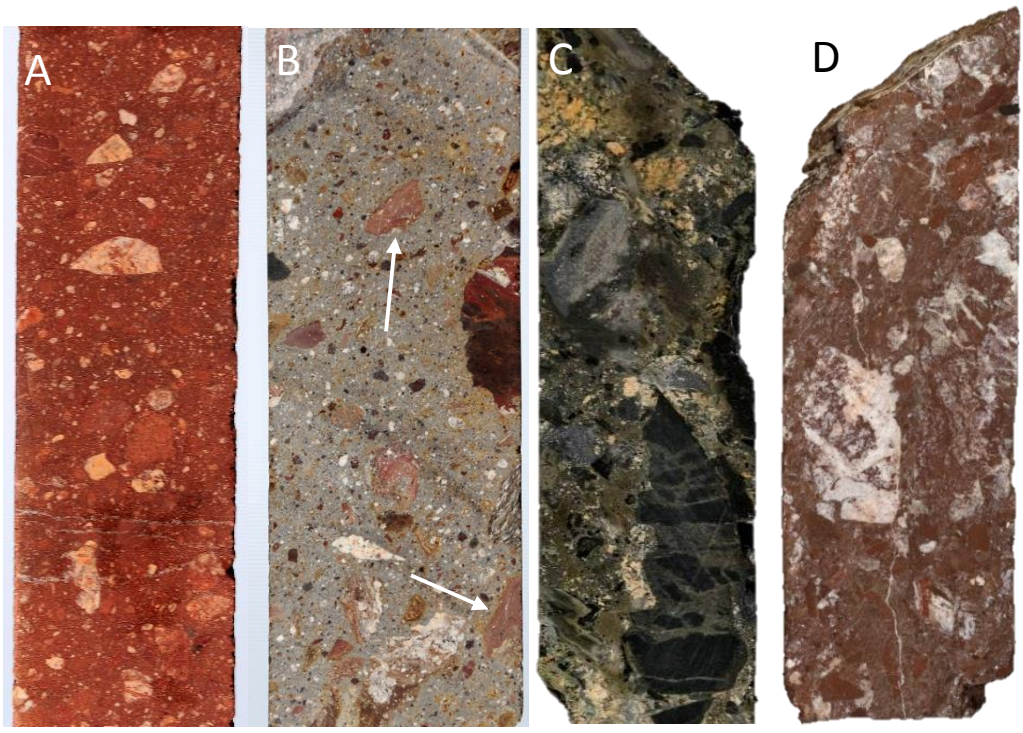

Figure 2.25: Macroscopic characteristics of M4 core suevite. **A)** Suevite sample M4 S-1 from 144.09 m depth, containing mainly angular to subrounded granitoid lithic clasts. The melt clasts are barely visible at macroscale. Note several crosscutting hairline calcite or zeolite veins. **B)** Grey matrix-supported suevite sample (M4 S-5 from 285.97 m depth) showing angular to irregular lithic clasts and a variety of red, pink, reddish brown and grey melt clasts (arrows). **C)** Green suevite from 316.52 m depth (sample M4 S-6). Note the large fragmented altered ultramafic lithic clast (bottom right). **D)** Monomictic suevite sample M4 S-9 from 198.03 m depth, showing metadolerite and quartz vein derived clasts. Sample core width = 5 cm.

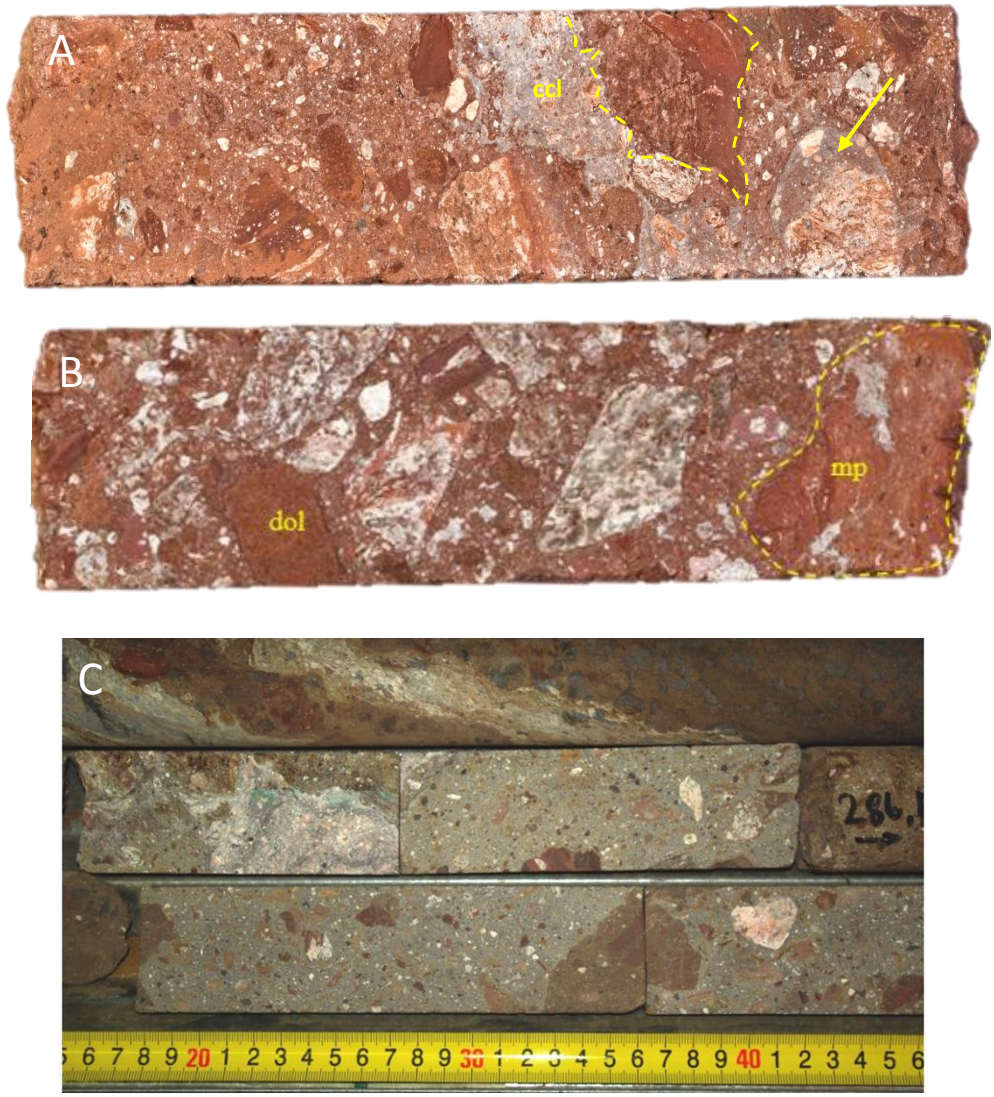

Figure 2.26: Macroscopic characteristics of M4 core suevite. **A)** Clast-rich suevite sample M4 S-14 from 144.35 m depth. The clast size and content increases to the right. Note the irregular (boudinaged) grey cataclasite layer (ccl). The top of the granitoid gneiss clast on the right has a cataclasite rim that is rounded against the suevite matrix (arrow). The largest clast right of the cataclasite layer is a composite lithic-melt clast (outlined). **B)** Reddish brown suevite sample from 146.68 m depth (sample M4 S-7). The lithic clasts enclosed are predominantly of granitic gneiss and dolerite (dol), with a large melt particle (mp) on the right. **C)** Grey suevite sample interval from 285.81 m (Appendix 2A, core box 23) showing fluidised bands (top) and irregular mass (middle) of grey cataclasite, and angular lithic clasts. See Figure 2.25B for detail. Sample core width = 5 cm.

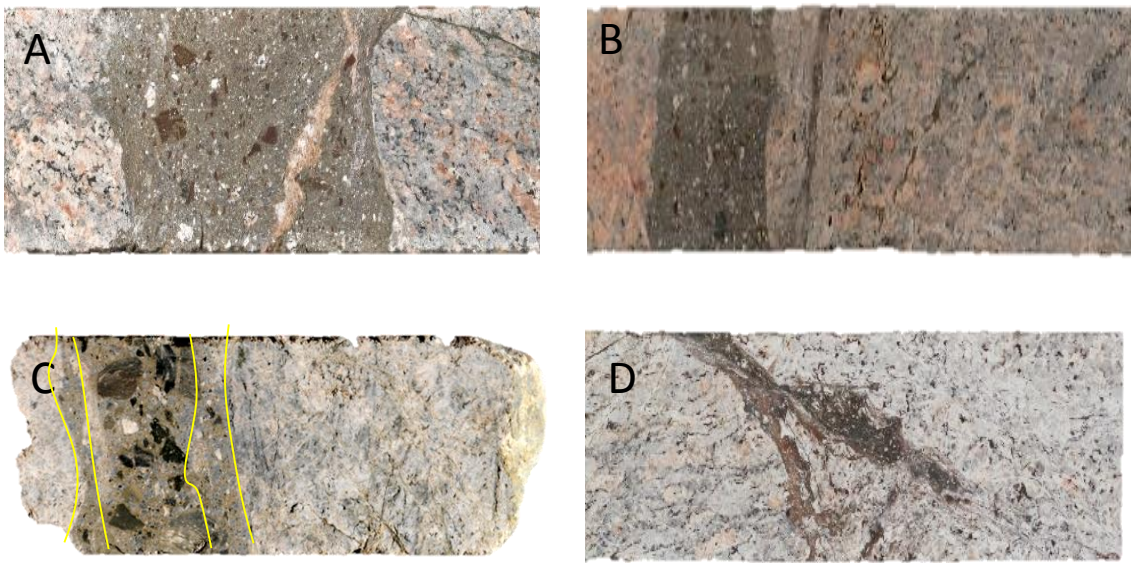

Figure 2.27: Macroscopic characteristics of suevite breccia in the M4 core. **A)** Matrix-supported suevite from 302.74 m depth, showing dark, angular, lithic metadolerite clasts and strung out cataclastic clast. The irregular contact on the left is caused by an embayment into a cataclasite-rich fracture. **B)** Suevite dyke (sample M4 GG-3 from 305.82-306.21 m depth) in contact with granitic gneiss encloses elongate lithic and melt clasts that show a strong flow alignment parallel to the dyke margins. **C)** Composite dyke of green suevite breccia with a high proportion of dark clasts, flanked by monomict cataclastic breccia, suggesting injection of the dyke into a cataclasite-filled fracture. Sample M4 SB-2 from 354.84 m depth. **D)** Highly irregular grey suevite dyke in granitic gneiss from 261.00 m depth. The gneiss is highly fractured and the cuspate intrusions of suevite exploit shear fractures. Sample core width = 5 cm.

Melt clasts in the M4 suevites vary in shape from angular, shard-like, to amoeboid and schlieric varieties (Figures 2.25B, 2.26A, B). Black to reddish brown melt clasts commonly show folded internal layering defined by black and greyish-white bands and lenses. In most cases, at least one boundary of the melt clast is convoluted or infolded with the suevite matrix (Figure 2.30C). Such irregular, cuspate-lobate, margins with the matrix suggest low melt viscosity at least initially during incorporation of the melt clasts into the suevite. Boundaries at a high angle to flow banding in the clasts are usually sharp and truncate the layering (Figure 2.30A), indicating that the melt initially underwent flow but that this was followed by brittle fracturing. Pink, orange and grey melt clasts quite commonly have a shape like a teardrop, with a smoothly curving wider end with what seems like internal flow layering parallel to the clast edge, and the narrow end with a sharp, angular edge. This shape is consistent with a bulbous viscous flow fold, with the neck of the fold snapping off after solidification (see section 2.7). In general, the macroscopic melt clasts vary in size from 1-2 mm up to 5 cm (Figure 2.26B; Appendix 2B). Melts are commonly found in composite clasts attached to the granitoid and metadolerite lithic fragments (e.g. Figure 2.26A). No systematic variation in melt clast

size in or between individual dykes was found. The proportion of melt clasts ranges from 5–30 % although sometimes it is difficult to estimate the melt volume associated with highly altered dolerite/metadolerite clasts, and higher estimates may be skewed by the small core diameter. Melt clasts contain mineral fragments up to a few mm in size.

2.4.3.2 Microscopic characteristics

Microscopic analysis confirms that the lithic clasts in the suevite are derived from the target rocks in the M4 core (except for sample M4 S-6) and that their levels of shock (see Chapter 5), fracturing and cataclasis are similar to what is seen in the target rocks. It also confirms that some lithic clasts must have been loose aggregates at the time of inclusion in the matrix, as a result of intense fracturing and cataclasis. Some show evidence of in situ fragmentation (Figure 2.17A). This supports limited transport of at least some suevite. In terms of mineral clasts, quartz dominates, although feldspar (especially microcline), ilmenite/magnetite/titanomagnetite and rare biotite, epidote and titanite are also noted (Figure 2.28). Grains are angular to shard-like, although some show micron-sized overgrowths related to the alteration assemblage (Figure 2.28F). Fine-grained opaque phases within the matrix are minor (< 2%) and usually <5 μm, which makes identification difficult. Mineral clasts range from a few mm down to a few tens of microns (equivalent to matrix fragment size) and predominate over lithic clasts. All the minerals found in the granitoid gneisses (quartz, microcline, Na-plagioclase, biotite, titanite, epidote, ilmenite, apatite; see Chapter 4) are common, but those from the mafic rocks (Ca-Na-plagioclase, hornblende/actinolite, clinopyroxene) are rare or absent. All mineral clasts show evidence of internal strain, brecciation, cataclasis and/or comminution, consistent with those seen in the monomict breccia and cataclasite in the fractures. Microscopically, the mineral clasts display shock-related features including undulose extinction, kink banding, fractures, quartz with PDF (Figure 2.28C), and chevron pattern in microcline (see Chapter 5). Biotite is kinked, shows frayed edges and is replaced by prehnite and/or chlorite (Figure 2.28D). Titanomagnetite may occur as well-preserved euhedral clasts similar in size to the grains in the target rocks, but opaque minerals are more commonly brecciated into angular fragments.

In the suevite matrix the clastic fragments are set in a matrix cemented in a groundmass (<10 μm) infilled by hydrothermal phyllosilicates (clays) and zeolites and also the matrix is porous, with interstitial cavities ranging from a few microns to several hundred microns (Figure 2.28E, F). This is consistent with macroscopic evidence that shows that the suevites contain visible porosity and vugs up to several mm across.

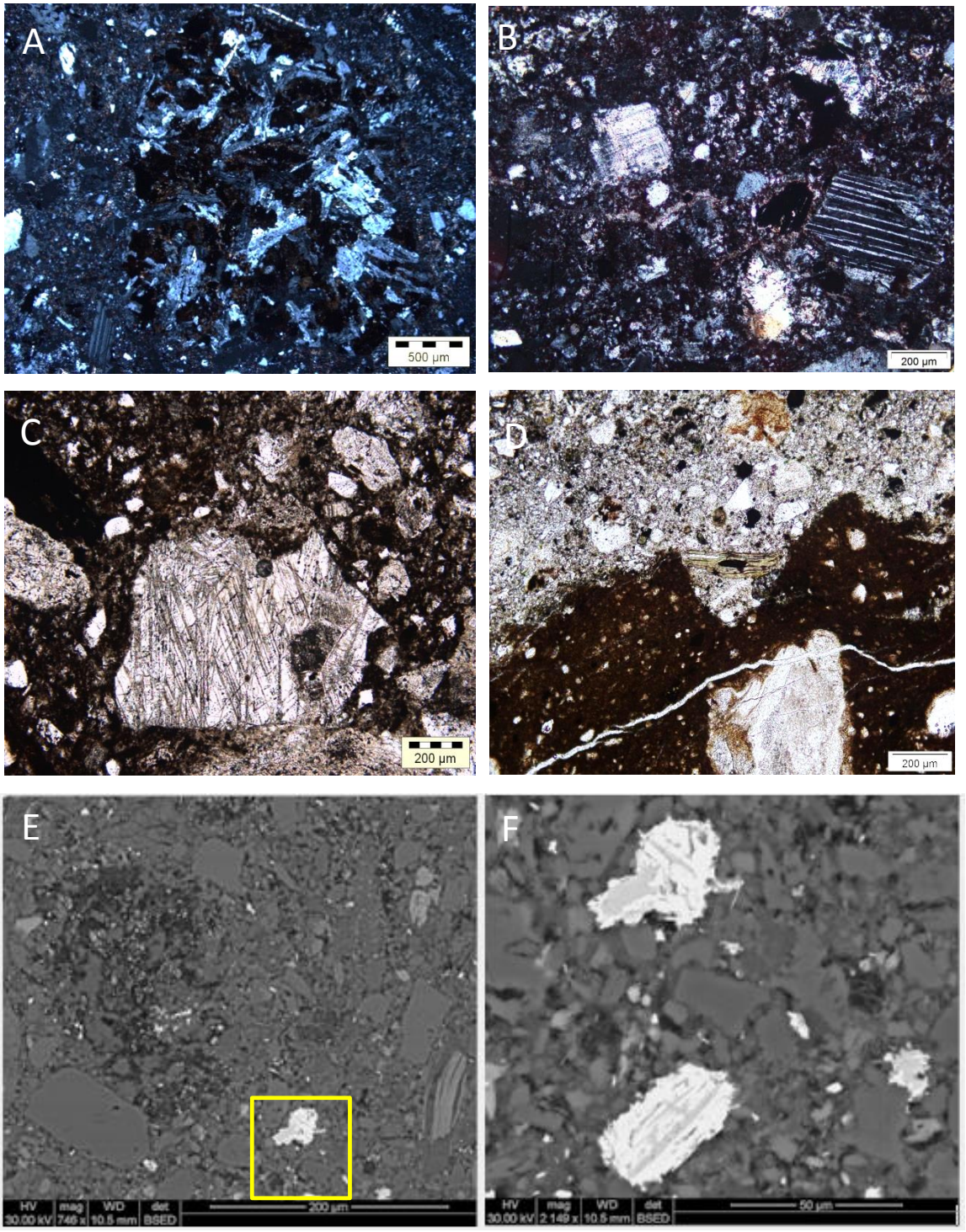

Figure 2.28: Microscopic character of lithic and mineral clasts enclosed in suevite. **A)** Dolerite clast in suevite sample M4 S-7 from 146.68 m depth. The pyroxene components are uralitised. Note the highly irregular clast margins. XPL. **B)** Suevite sample M4 S-1 from 144.09 m depth, showing mineral clasts enclosed in a clastic matrix. Feldspar and opaques show alteration effects. XPL. **C)** Suevite sample M4 S-2 (156.35 m depth) showing angular mineral clasts, including shocked quartz grain with PDF, in a clastic matrix. PPL. **D)** Irregular contact between suevite and MMBr in sample M4 IM-9 showing the larger and more angular character of the mineral clasts in suevite relative to the MMBr. The biotite clast shows prehnite replacement and is deformed as a result of flow along the contact. A zeolite-infilled vein cuts the MMBr. **E)** BSEM image of suevite sample M4 S-5 (depth: 285.97 m). The suevite matrix encloses angular quartz (dark grey), titanomagnetite (white), and biotite (light grey, bottom right). **F)** Enlargement of part of E, showing titanomagnetite (magnetite with ilmenite exsolution lamellae) with a fine-grained magnetite overgrowth. Note the irregular, angular quartz clast shapes and the porosity. PPL = plane polarised light; XPL = cross polarised light.

Millimetre-scale clasts can be both polymineralic (Figure 2.28A) and/or polycrystalline (Figure 2.28B). The polymineralic clasts are fragments of target rocks found in the M4 core, and may occur as broken pieces near larger lithic clasts, or in cataclasite-rich bands. The polycrystalline clasts are mostly quartz and show all the features of cataclasite, with larger angular to rounded mineral fragments surrounded or cut by microcrystalline-cryptocrystalline aggregates that show evidence of comminution and cataclastic flow. Unlike the MMBr, however, it is more difficult to identify streaks of cataclased fragments related to these clasts within the larger suevite matrix as the matrix is also clastic. The very irregular clast boundaries suggest that they were only weakly coherent when they were incorporated into the suevite. The boundary between larger cataclasite and suevite bands may be somewhat irregular, which is further support for mechanical mixing (Figures 2.16, 2.24, 2.29).

Like in the MMBr matrix, no melt crystallization textures or glass have survived the alteration of the M4 impactites; however, quenched melt is inferred to have been present originally from the different character of the melt clasts to the clastic suevite matrix. This includes flow banding, the smaller proportion and greater rounding of small mineral clasts in the melt clasts, and the cryptocrystalline grain size of the alteration assemblage in the clasts. In suevites the melt clasts vary in colour from black to red-brown, pink and orange. Millimetre-sized orange and green clasts are abundant microscopically although the red-brown and black varieties are individually much larger and make up most (>90%) of the melt clast volume (Figures 2.30, 2.31). The red-brown melt clasts show all the same features as the MMBr matrix. They can be homogeneous or flow-banded. The flow-banding occurs on a scale of tens of microns and is mostly planar to slightly curved but locally shows flow folds, and is supported by aligned elongate mineral clasts (Figures 2.20A, D, 2.31A). In places, wider colour banding up to several hundred microns to millimetres (Figure 2.30D) could suggest variable melt chemistry, although defocussed-beam EMPA (see Chapter 4) did not show noticeably different compositions. BSEM suggests it could be caused by slightly different opaque mineral contents. The clasts are usually elongate parallel to the banding, and edges parallel to the banding may be irregular against the suevite matrix (Figures 2.30C, 2.31B). The short edges are sharp, lie at a high angle to the banding, and are planar to smoothly curved (Figures 2.30A, 2.31A). These features suggest the melt clast was still able to flow or deform plastically when it was included in the suevite, but then it was fractured after solidifying and before the suevite was finally emplaced. However, some melt clasts are schlieric, with tapering edges interfingering with the suevite matrix (Figure 2.31C). These must have been initially highly fluid but were undisturbed since solidifying.

All melt clasts contain smaller (usually <500 μm) mineral clasts that also show signs of cataclasis and that vary from angular to rounded. Some of the banding in the melt clasts is seen to be the result of cataclastic quartz-feldspar microbands. Composite melt + lithic fragment clasts are very common

microscopically (Figure 2.31B). Because of the strong alteration of the doleritic rocks and the cataclasite flow features that they show, it is sometimes difficult to tell if a clast is composite or what parts are lithic or were melt. Melt may drape around lithic clasts, but in some cases the melt may form the bulk of the clast. These melts are typically of the red-brown or black variety. They are usually banded but show sharp edges against the lithic component.

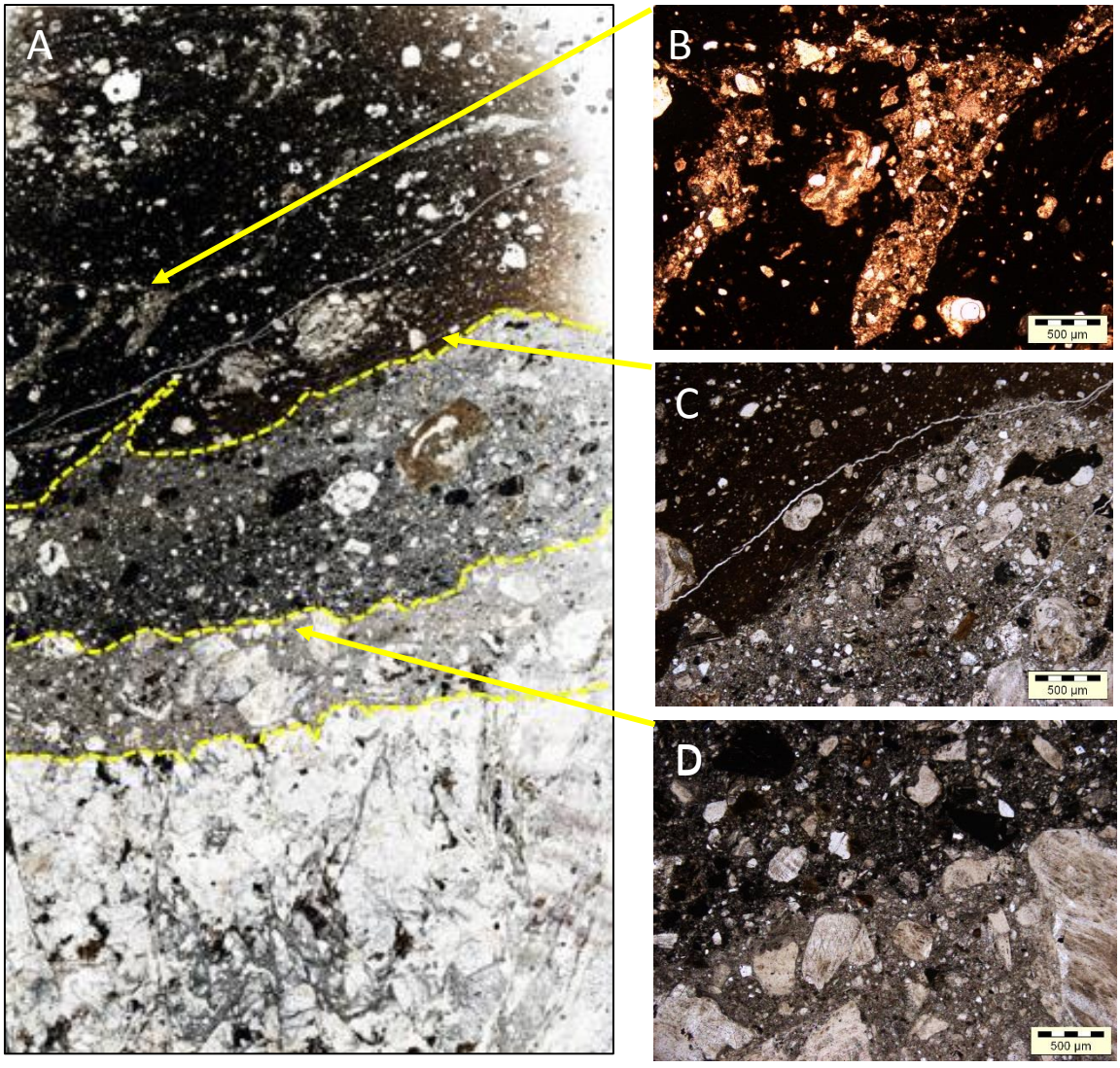

Figure 2.29: Transmitted light micrographs of the composite dyke sample M4 IM-9 from 299.76 m depth, showing the micro-scale impactite relationships. See Figure 2.16 for location. **A)** Whole thin section view (27 × 46 mm) showing the shear-fractured (monomict breccia) granitoid portion (bottom) is flanked by a thin layer of cataclasite. Between the light grey cataclasite and the MMBr (top) lies dark grey suevite that contains a brown melt clast. **B)** Enlargement of MMBr showing cataclasite enclosed within the MMBr matrix section, probably by flow-induced infolding. **C)** Enlargement of MMBr-suevite contact showing its irregular nature. See also infold of contact in A that shows how feature in B may have been produced. **D)** Enlargement of suevite-monomict lithic breccia/cataclasite contact, showing its irregular nature and the similarity in clast type, but decreased clast size and more mafic character of the suevite. PPL = plane polarised light.

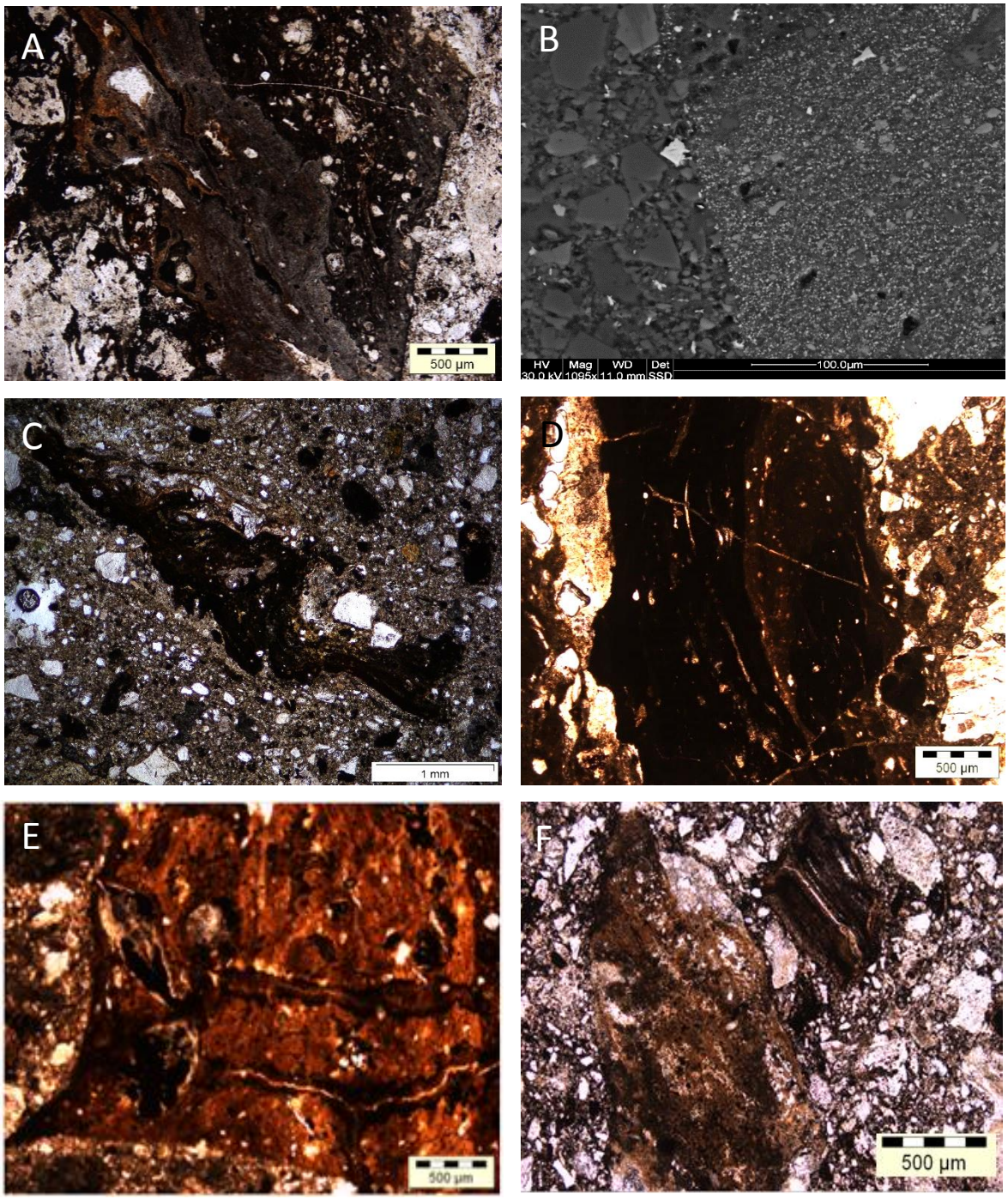

Figure 2.30: Melt clast characteristics in suevite. **A)** Multi-coloured, flow textured clast from reddish brown suevite sample M4 S-7 (146.68 m depth). Note the sharp edge on the right that cuts off the flow banding. PPL. **B)** BSEM image from suevite sample M4 S-5 from 285.97 m depth showing the difference between the devitrified melt particle (right) and clastic suevite matrix. Note the abundance of disseminated opaques inside the melt particle versus in the suevite matrix (left). **C)** Schieric, flow textured, variegated melt clast from grey suevite sample M4 S-5 from 285.97 m depth. PPL. **D)** Black-brown melt clast in green suevite sample M4 S-6 from 316.52 m depth showing an elongate flow fold and irregular margins with suevite matrix. **E)** Photomicrograph of sample M4 S-4, from 285.03 m showing an altered orange melt clast contains fine grained minerals including opaque minerals. Note the cuspate edge of the clast (left). PPL. **F)** Microphotograph showing two angular, altered melt clasts suevite sample M4 S-2 from 156.35 m depth. PPL. PPL = plane polarised light.

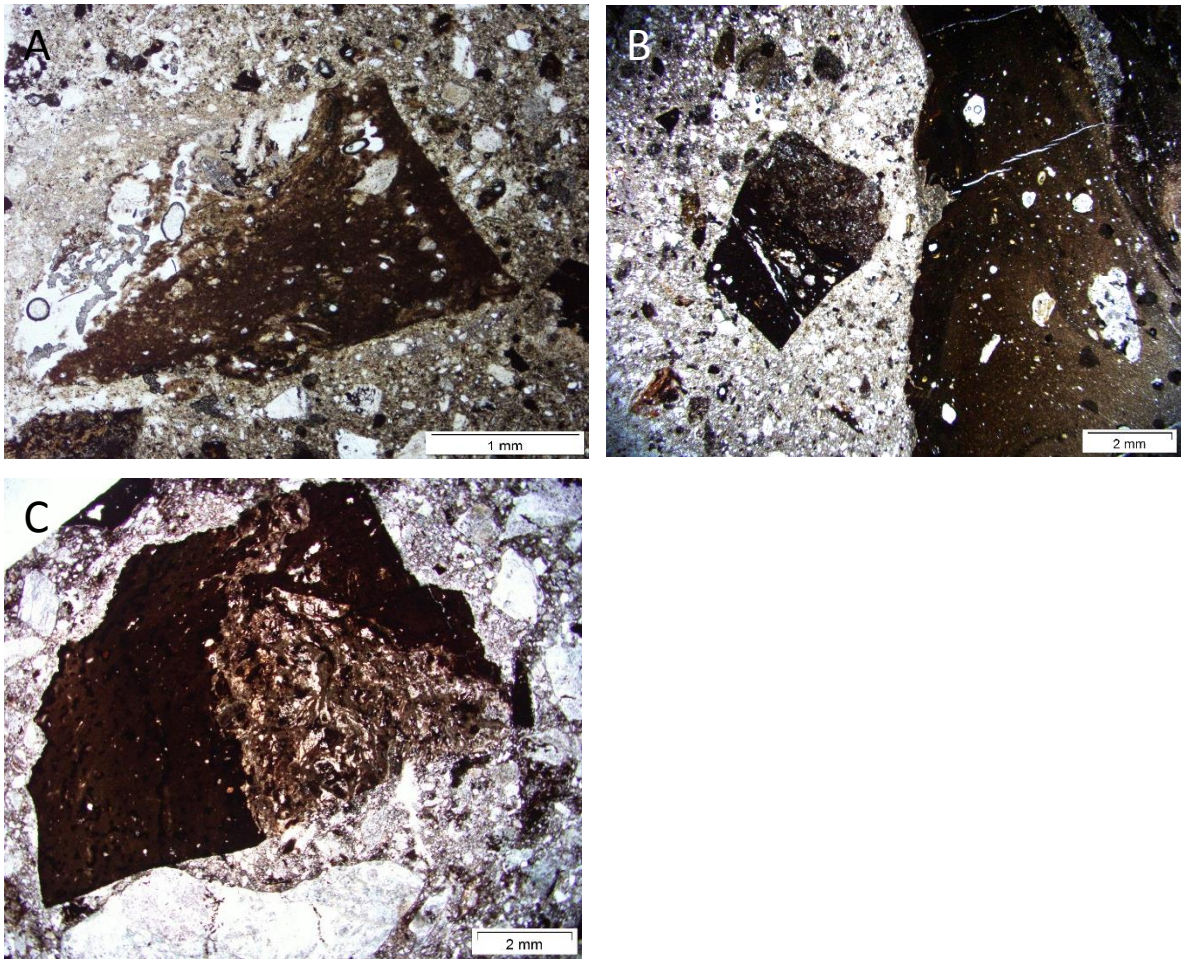

Figure 2.31: Composite clasts in suevite. **A)** Angular brown melt clast with sharp edges from grey suevite sample M4 S-5 (285.87 m depth). The slightly plucked upper edge is a dolerite fragment. PPL **B)** Black melt clast welded to a dolerite fragment (upper part of clast) to the left of a larger flow-folded brown melt clast in suevite sample M4 S-4 from 284.03 m depth. Note the difference in the edges of the melt clasts against the suevite matrix, and the slightly curved zeolite-filled tension fractures that cut across the brown melt clast. C) Brown melt clast enclosing a metadolerite lithic clasts in suevite sample M4 S-2 (depth: 156.35 m) PPL. PPL = plane polarised light.

2.4.4 Composite impactite dykes

In several places in the M4 core (e.g. Appendix 2A, boxes 22 and 24; Appendix 2B, samples M4 IM-7, 8, 10) and M4 S-11 (Figure 2.32); it is impossible to be certain whether the impactite dykes are suevite or MMBr, and many of the dykes should correctly be described as composite on the cm-scale and larger. In several cases, samples were initially misidentified based on their macroscopic character as either melt-rich suevite or clast-rich MMBr. In addition, almost all suevite and MMBr dykes contain cataclasite masses that may occur either between the dyke and the wallrock (Figure 2.27C), or within the dyke (Figure 2.26A, C). In the previous sections, it has already been shown that both the

MMBr and suevite dykes seem to have exploited cataclasite-filled fractures (Figures 2,22A, B, 2.27C), and that many clasts in both dyke types still contain remnants of cataclasite around their edges (Figures 2.22B, 2.26A), suggesting that the clasts are remnants of the shear fracturing seen in the target rocks and that MMBr and suevite dyke intrusion into a brecciated rock then allowed these clasts to be incorporated. On the microscale, most of the mineral and small lithic clasts in the MMBr and suevite, and in the melt clasts in the suevite, show signs of coming from predominantly granitic cataclased target rock.

Sample M4 IM-9 (Figures 2.14, 2.16, 2.29 and 2.33) is a composite impactite dyke that is dominated by MMBr. The MMBr is flanked by suevite, with a <1 cm wide cataclasite found between the suevite and the wallrock in the central part of the core section (Figure 2.14 and 2.16). The cataclasite can be seen to lie along core-parallel shear fractures which extend into the wallrock granitoid gneiss (Figure 2.16). On the right side of the core in Figure 2.16, MMBr is in direct contact with gneiss along a planar contact that is parallel to internal fractures within the gneiss. Flow banding and small asymmetric folds in the MMBr-suevite contact (Figure 2.29) suggest that the melt flowed from bottom right to top left in Figure 2.16. This is supported by the vergence of cataclasite streaks in the MMBr (top right, Figure 2.16). It is proposed that the strong turbulent flow allowed assimilation of cataclasite along the contact on the right side of the photo, and that this was pushed towards the left where a slight change in the orientation of the contact allowed a mixture of cataclasite and broken melt particles to survive as suevite. This also protected some of the cataclasite in a large horizontal shear fracture in situ.

Figure 2.32: Composite dyke sample M4 S-11 from 167.50 m depth showing the suevite (left) and MMBr (right) with strong flow banding along the contact. Such a sample may be interpreted as a suevite dyke with >5 cm melt clasts, or a MMBr with a lens of suevite formed from mixing of cataclasite or disrupted melt. Sample core width = 5 cm.

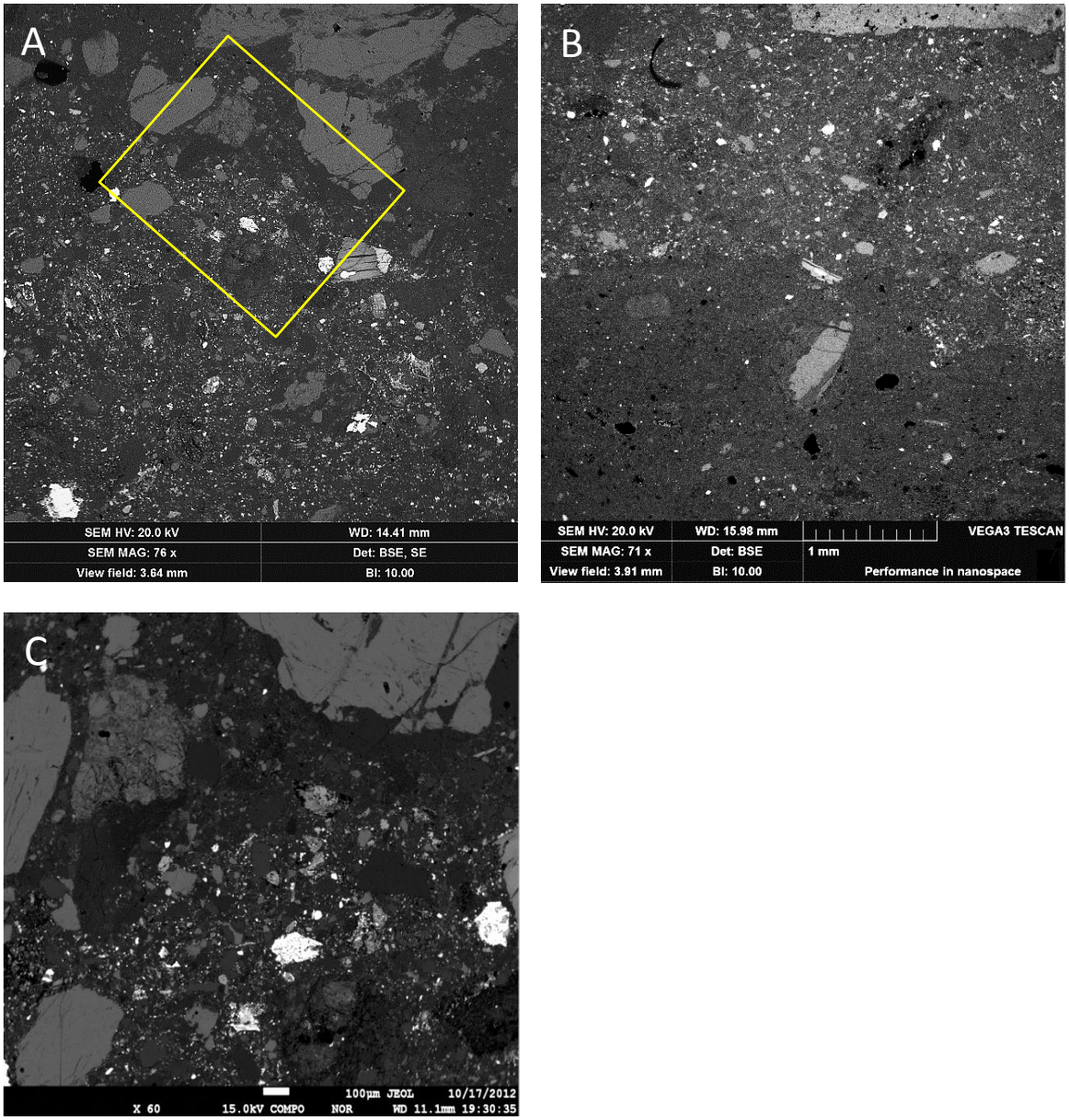

Figure 2.33: BSEM images showing the matrix characteristics of the composite dyke sample M4 IM-9 (299.76 m depth). **A)** BSE image showing the contact between suevite and cataclasite (top right) consisting of intensely shocked, brecciated quartz grains. **B)** BSE image of contact between suevite (top) and MMBr (bottom), showing the significant reduction in matrix grain size and clast volume and shape in the MMBr. The dark colour of the suevite seen in Figure 2.29 can be seen to be caused by a higher abundance ofopaques (ilmenite/magnetite) clasts relative to the MMBr. The relatively uniform grain size and distribution of the opaques in the MMBr supports (re)crystallization from a homogeneous matrix, such as a glass. For reference, the elongate light grey phase along the contact is the biotite clast shown in Figure 2.28D. **C)** Enlargement of A.

2.5 Pre-and post-impact alteration

2.5.1 Pre-impact alteration

The target rocks in the M4 core show evidence for pre-impact alteration, including intense quartz veining in metadolerite and trondhjemitic gneiss (e.g. interval at 211.30 m depth (Figure 2.1 and Appendix 2A, box 14). Petrographic (Section 2.3.2) and geochemical (Section 3.2.1) analysis of the trondhjemitic gneiss suggests that it could represent metasomatically-altered granitic/granodioritic gneiss in which extra silica and Na have been added by fluids. The metadolerite below it also contains abundant mm- to cm-thick quartz veins. This vein quartz is granoblastic and contains multiple decorated PDF (Chapter 5), confirming its pre-impact timing. It is not clear if the veining is related to the foliation in the metadolerite (Figure 2.9A, C). The metadolerite foliation is defined by a mid- to upper greenschist-facies assemblage (actinolite-epidote-albite-chlorite-titanite), which is lower than the metamorphic grade that would have occurred when the gneissosity formed in the granitoid rocks. It could be that the metadolerite foliation formed after the peak of metamorphism, in which case it could be from a localised retrograde shear zone. In trondhjemitic gneiss the largest ~30 cm quartz vein is intersected at 217.90 m (Appendix 2A, box 4). This shear zone could then possibly also have been a channel for retrograde, metasomatic, silica-rich fluids that formed the vein quartz as the rocks cooled. In places the quartz veins appear to be folded as well as cut by fractures (Appendix 2A, box 16), which would favour a brittle-ductile fault/shear zone, but mostly the veins form an angular stock-work with sharp, straight edges. Unfortunately, overprinting impact-related deformation and alteration makes it difficult to understand the exact timing relationships and structures.

Based on the Archaean ages obtained for the granitoid gneisses (R.L. Gibson, pers. comm., 2016; Section 2.3.1.1), the greenschist metamorphism and alteration could also be Archaean. It is also possible that the unusual textures and major element compositions of samples M4 IS-1, 2 and M4 A-1 in this zone could be the result of more complex metasomatism related to these fluids (Figure 2.10 A, B and 2.12). It is unclear if any of the dolerite alteration occurred before the impact. The dolerite occurs as blocks in MMBr and lithic clasts in the MMBr show strong uralitisation of pyroxene (Figure 2.28A), so it is possible that the alteration is a post-impact feature.

Alteration of biotite to chlorite and/or prehnite (Figure 2.35B) suggests similar, or even lower, metamorphic grade affected the target rocks in the lower parts of the core. This may also be linked to the pre-impact event as both textures are preserved in biotite mineral clasts in the impactites (e.g. Figure 2.28D). However, in the target rocks below 300 m, chlorite is a common alteration product of biotite and it occurs in impact-formed shear fractures, so it could also be a sign of post-impact alteration (Figure 2.8).

2.5.2 Post-impact alteration

Core loss in the uppermost parts of the M4 core beneath the Kalahari Group sediments, between 94 m and 103 m is high, and fragments are clay rich and disintegrate easily. This zone is interpreted as the highly weathered palaeosol horizon beneath the Kalahari Group. Below this zone, macroscopic evidence for post-impact hydrothermal alteration is common throughout the core, mostly as zeolite-, calcite-, gypsum-, and quartz-filled fractures that are usually ≤ 1 mm wide but which can reach up to 1.5 cm (e.g., Figures 2.18, 2.34A; Appendix 2A, boxes 12-16). The veins occur mostly above 154 m depth (Appendix 2A), but microscopic veins are found in deeper samples. These veins anastomose or form slightly curved, thin, tension gashes, although angular bridges between overlapping veins are found (Figure 2.35D). The veins are different from the cataclasite-filled shear fractures because they do not show any shearing or cataclasis, and their minerals show no signs of shock deformation (although in rare cases the veins may contain angular mm-scale shocked mineral clasts). The post-impact timing of the veins is confirmed by the fact that they cross-cut the impactites, including melt clasts in suevite (Figure 2.31B), and MMBr (e.g. Figure 2.29C).

The impactites also locally contain vugs up to a few mm in size (Figure 2.34B), and are extremely hygroscopic, indicating high clay and/or zeolite content, which has been confirmed by XRD and EMPA (Chapter 4). Highly silicified and altered samples are seen in several places mostly around important lithological contacts (Figure 2.1; Appendix 2A, 234.33 m (box 16), 205.85 m (box 13) and 290.05 m (box 24)). These are interpreted as highly altered fault zones that could have acted as fluid channels after the impact, but it is not certain if they were hydrothermal fluid channels or channels only for pre- and post-Kalahari Group meteoric water. Most likely they were both. The impactites around these zones are typically extremely friable and red-orange, suggesting strong oxidation alteration. The adjacent target rocks are less altered but are full of hydrothermally altered, haematite-rich, fractures which are usually <1 mm wide (Appendix 2A, boxes 16 and 17). The fracture fill is too altered to see if it is altered melt or altered Fe-oxides precipitated from solution. The haematite that is found along shear fractures in all target rocks, particularly above 200 m depth in the core (e.g. Figures 2.5, 2.13A, B; Appendix 2A, boxes 17 and 19) is also interpreted as a hydrothermally-deposited mineral from fluids infiltrating impact-related shear fractures. Although these fractures are most noticeable above 200 m depth, reflected light microscopy shows that haematite is also present in smaller amounts in fractures with magnetite and pyrite in the lower parts of the core. This suggests that the level of oxidation of the post-impact hydrothermal fluids decreased downwards. Microscopic textural analysis suggests that the haematite formed by oxidation of magnetite and pyrite deposited in the fractures, at least in the deeper levels of the core. This would suggest that fluid compositions became more oxidising with time at these depths.

Several suevite and MMBr samples have vugs that indicate hydrothermal fluid movement (Figure 2.34B), and all samples show zeolite and clay replacement of melt clasts and their matrices, but they still show clear evidence of how they formed (flow textures in the melts, clastic fragments in the suevite matrix). However, in two impactite samples that lie close to highly fractured zones and major lithological contacts, the level of alteration is so high that it is not possible to tell if the matrix was once clastic or if it was melt. Sample M4 IM-2 (from 234.33 m depth) lies near the contact between trondhjemitic gneiss and brecciated metadolerite (Appendix 2A, box 16) and has a much higher SiO_2 content than the other MMBr (see Section 3.31), but it is found in the most siliceous target rock (the trondhjemitic gneiss). Sample M4 IM-10 (not geochemically examined), comes from the contact between metadolerite and MMBr (Appendix 2A, box 24), which could have been a path for high fluid flow. Both samples have been labelled as MMBr macroscopically based on the fine-grained matrix and their banding, which would be agree with a melt matrix, but they are lighter-coloured and more variable in colour than the other dykes. BSEM analysis of other suevite samples shows that the mineral clasts have partially reacted or been partially replaced around their edges (see Figure 2.37C), so it is also possible that samples M4 IM-2 and M4 IM-10 could be original suevite dykes where extreme hydrothermal fluid flow along fractures led to almost all the fine-grained clasts being destroyed by reaction. The larger granitoid clasts in sample M4 IM-2 are surrounded by rims that show columnar mineral textures that would support reaction between a fluid-rich matrix and the clasts (Figure 2.34C).

Apart from the veins and haematite staining, the other macroscopic feature related to post-impact alteration is spherical to slightly elliptical, cm-scale, weakly magnetic, grey-black nodules in both the doleritic and impactite lithologies between 265.55 – 266.55 and 282.88 – 290.71 m depth (Figures 2.9B, 2.17A). Microscopic analysis (Figure 2.11) suggests that these nodules formed by overgrowth of the pre-existing mineral assemblage by amorphous magnetite with or without haematite. Haematisation of the nodules may have occurred in the later stages of hydrothermal alteration, at the same time as the haematite grew in the fractures.

Below 300 m, and especially below 330 m depth (Appendix 2A, boxes 29-33) the granitoid gneisses are darker than in the upper parts of the core. Shear fractures are also darker, and suevite is green rather than red (Section 2.4.3). Microscopic analysis shows that the darkening of the fractures is related to chlorite. Biotite in the dioritic gneiss is strongly chloritized (Figure 2.8A). This could explain the darker, blackish-grey colour. In contrast, biotite in the granitoid gneisses in the upper parts of the core is highly oxidised to haematite (see Figure 5.13A).

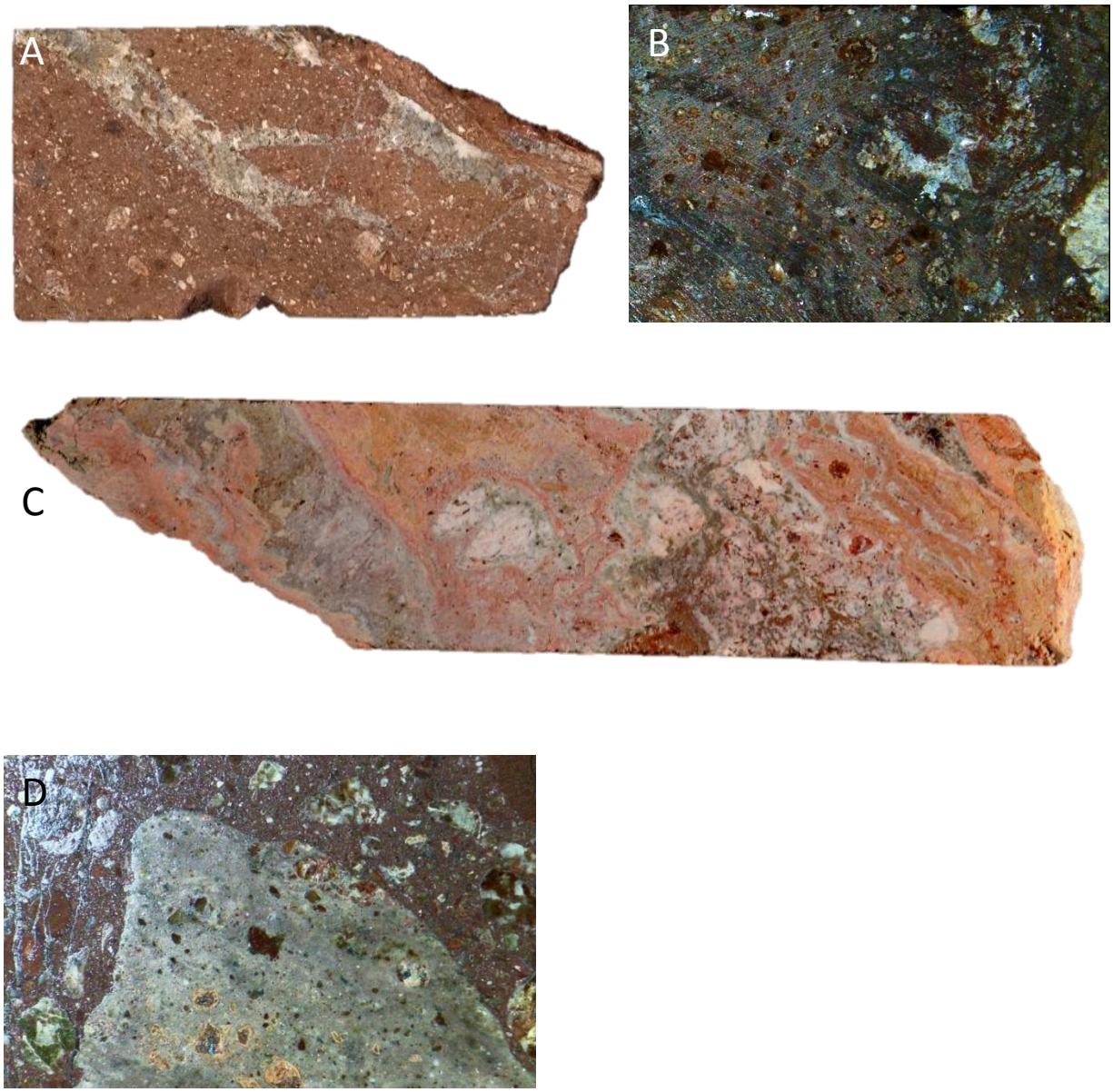

Figure 2.34: Macroscopic evidence of post-impact alteration in the M4 core. **A)** Angular calcite veining in suevite from 143.00 m depth. Sample core width = 5 cm. **B)** Vugs in suevite sample. **C)** Possible strongly hydrothermal altered MMBr or suevite (sample M4 IM-2, from 234.33 m depth). The large granitoid clasts show reaction "shells" around them. The sample matrix contains very few small mineral clasts, but is coarser-grained than the typical MMBr. Sample core width = 5 cm. **D)** Small melt clasts with thin pale green rims in suevite sample from 146.59 m depth.

Another macroscopic sign of alteration is that the small green melt clasts in suevite usually have thin light green rims (Figure 2.34D). These rims can only have formed after the melt fragment was included in the suevite, because they are found all the way around the clasts (see also Figure 2.35A). Microscopically, in the deeper levels of the core, chlorite-filled shear fractures also contain quartz, pyrite and epidote. Epidote is also found as needle-like inclusions in andradite garnet in a zeolite-filled vug in sample M4 S-6 (Figure 2.35A, B). In all other samples, however, BSEM analysis only

found needle- or plate-like zeolite or phyllosilicate minerals and some opaque mineral (see Chapter 4). The grain size of the alteration assemblage is usually cryptocrystalline (<10 μm), except in a few samples, where grain sizes are up to 100-200 μm. No glass was found in any MMBr or melt particles in the suevite by BSEM or XRD. Also, quartz grains show only decorated PDF (Chapter 5), which supports hydrothermal alteration of all glasses. In some samples quartz fragments with PDF are cemented by pyrite (Figure 2.35C) or zeolite.

An attempt to understand the secondary hydrothermal mineralogy in the impactites by XRD and EMPA is presented in Chapter 4, but success has been limited mainly due to the extremely fine grain size. BSEM analysis shows the melt clasts and the MMBr and suevite matrix are recrystallized to cryptocrystalline platy to needle-like mineral assemblages with an average grain size that is usually <10 μm. Most minerals appear to be zeolites or clays, although it was difficult to get proper stoichiometric analyses. BSEM analysis has confirmed that the altered red-brown to black melt particles in the suevite have a much finer grain size, and more homogeneous mineralogy, than the suevite matrix (Figure 2.30B), and that the grain size and homogeneous texture, as well as the relatively higher proportion of <5 μm opaque minerals, are the same as for the MMBr matrix (e.g. Figures 2.24J, 2.37A, F).

The re-crystallized/devitrified light green melt is less abundant; and commonly occurs in limited melt matrix breccia samples (M4 IM-4 and M4 IM-3). This melt type is generally enclosed in MMBr matrix (Figure 2.24G) or is found trapped in granitic, cataclased clasts (Figure 2.19A). Figure 2.24G-J shows the light green melt particle in red MMBr matrix from sample M4 IM-4. Unlike most of the melt particles in the MMBr, which are also red, brown or black and which show a similar cryptocrystalline, opaque-richer mineralogy and texture, this particle is significantly more coarse-grained than the MMBr matrix, with tabular zeolite alteration minerals up to 50-100 μm. The particle has a coarser porosity than the MMBr matrix and contains very few opaque grains and is almost monomineralic. The boundary between the particle and the matrix is slightly gradational (Figure 2.24J).

Small (usually mm- to cm-scale) pink, green and orange melt clasts in the suevite also usually show almost monomineralic alteration (Figure 2.37C, D), but they do contain smaller mineral clasts that come from different minerals (Figure 2.37C), so they cannot have been a melt of only a single mineral. The pale rims seen macroscopically (Figure 2.34D) are also seen microscopically as thin rims up to 100-200 μm wide that are relatively free of inclusions relative to the clast core (Figure 2.36A, B). It is not clear if this is because alteration reactions have consumed the inclusions (mostly quartz); however, XPL shows that the cores and rims of the melt clasts are both replaced by a

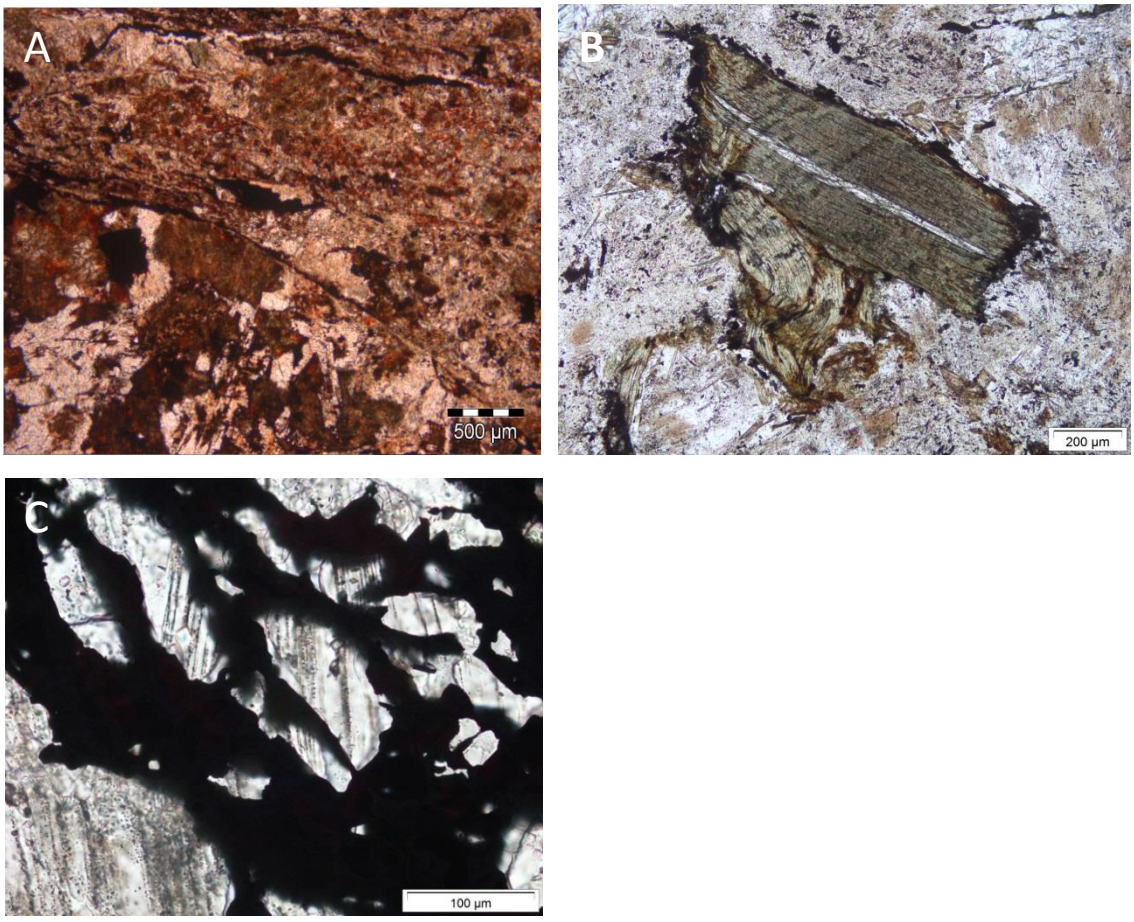

Figure 2.35: Microscopic evidence of post-impact alteration on target rock lithologies. **A)** Photomicrographs of sample M4 SILL -1, from 268.30 m depth showing the fresh versus altered section of the dolerite. **B)** Prehnite in biotite from dioritic gneiss sample M4 AM-5 from 362.63 m depth, and **C)** Pyrite infill along fractured quartz. Note the decorated PDF in quartz (from sample M4 AM-5 from 362.63 m depth).

monomineralic aggregate of a coarse (up to several hundred microns), xenoblastic, interlocking mineral, which appears to be zeolite (see Chapter 4). This texture is similar to what is seen in the cement of the cataclasite-filled fractures. Despite the hydrothermal reaction, the clasts still show sharp, angular to slightly conchoidal edges (Figure 2.37C).

Variegated melt clasts show the most complex replacement textures, with different bands showing different mineral assemblages, grain sizes and textures. Figure 2.37A-B are BSEM enlargements of the melt particle in MMBr sample M4 IM-6 shown in Figure 2.24F). They show that the banding in the melt clast is very complex as a result of hydrothermal reaction. The clast-rich bands show a more homogeneous texture, despite gradational internal changes towards the clast-poor bands, which are more mafic. The mafic bands show continuity with the MMBr matrix (Figure 2.37A) that is hydrothermal (as the clast shape is clearly seen in Figure 2.24F). EMPA profiles across this and other melt particles and clasts (Appendix 4D) produced low totals involving minerals with slight variations

in SiO_2, Al_2O_3, FeO, MgO and alkalis that suggest a range of zeolite and smectite minerals. This variation might support the macro- and microscopic textural evidence presented in Section 2.4.2 that suggests that the banding in the MMBr matrix (and variegated melt particles as well), is caused by interlayered mafic melt and predominantly cataclasite, but possibly also melt, from the felsic granitoid target rocks.

BSEM images of the suevite matrix show a more porous texture than the MMBr and melt particles (Figure 2.37D), including sub-mm vugs, but also that the angular mineral clasts show evidence of corrosion, which suggests that they acted as reactants to produce the hydrothermal mineral assemblage. They also provided nucleation surfaces for the growth of the new hydrothermal crystallites (Figure 2.28F).

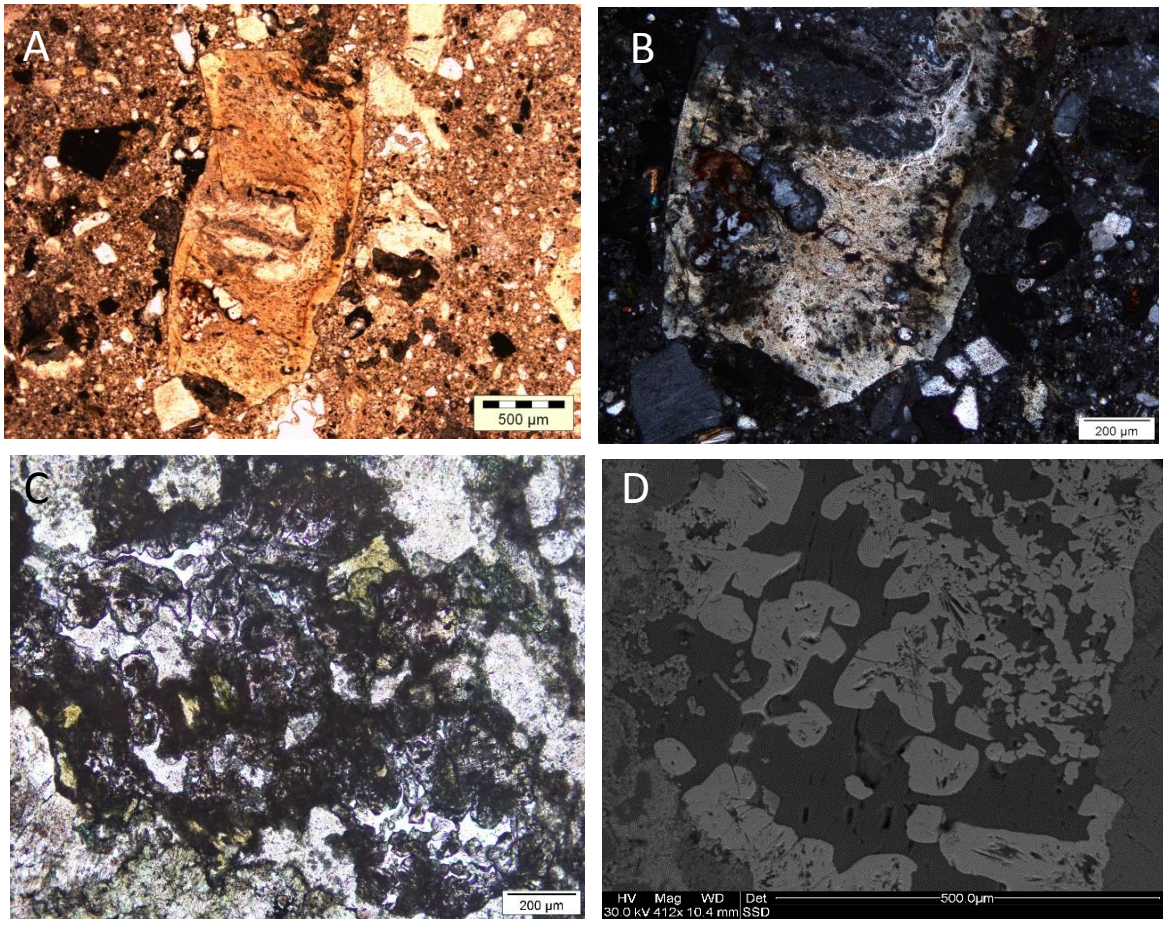

Figure 2.36: Microscopic evidence of alteration in the M4 drillcore lithologies. **A)** Suevite sample M4 S 5(2) from 285.97 m depth, showing a zoned, altered clasts. **B)** An enlargement of A, showing inward replacement of the melt clast. XPL. **C)** Aggregates of garnet associated with epidote in suevite sample M4 S-6 from 316.52 m depth. PPL **D)** BSE image showing garnet aggregates separated by matrix of phyllosicates (high in silica, aluminium and calcium). PPL = plane polarised light; XPL = cross polarised light.

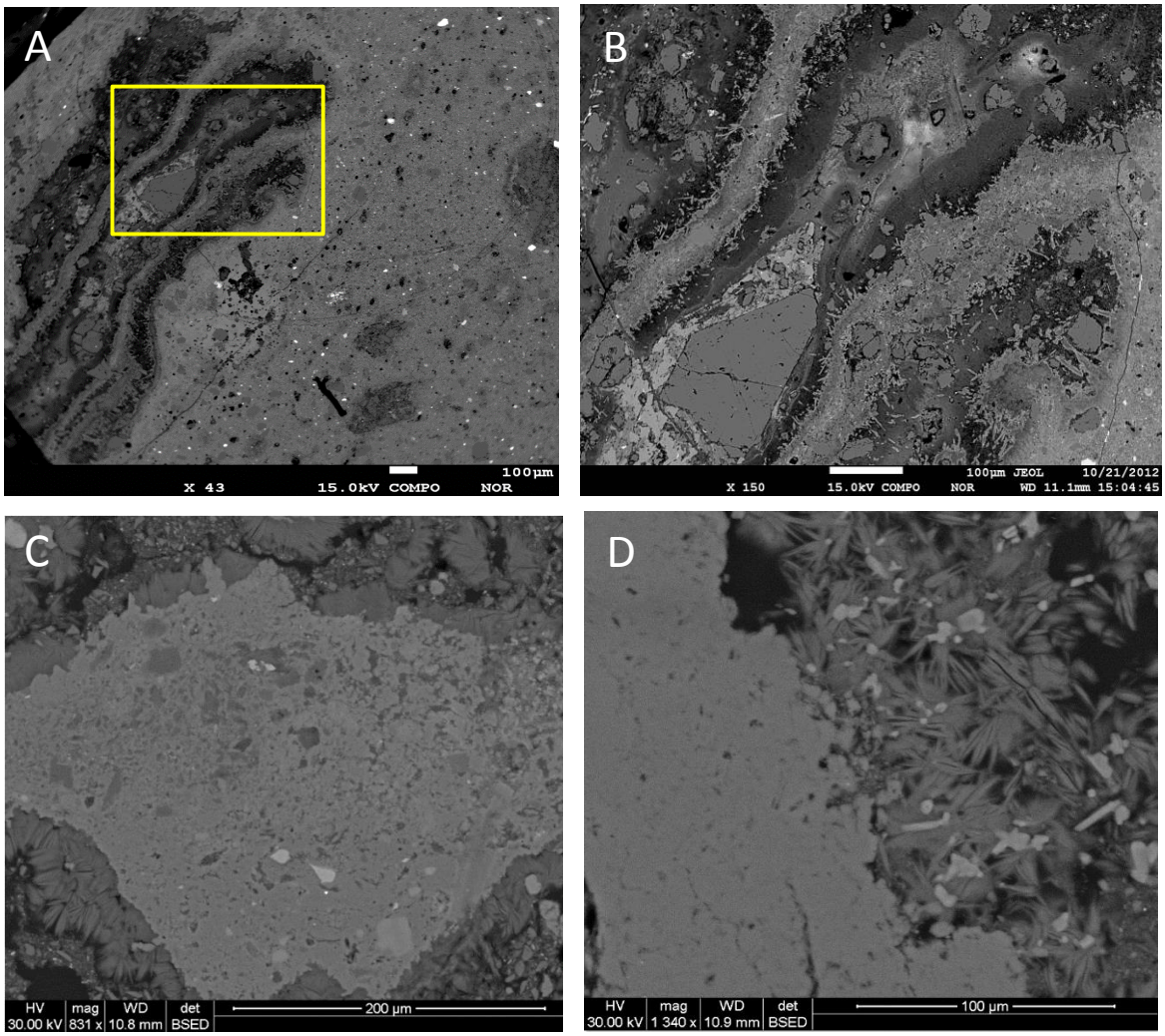

Figure 2.37: BSE images of melt particles and clasts showing alteration effects. **A)** BSE image of altered melt particle (as seen in Figure 2.24F) from sample M4 IM-6 (271.17 m depth). Note the fine-grained nature of the devitrified MMBr matrix even at < 100 µm. **B)** Enlargement of A showing the alteration texture zoning and the angular quartz clasts. **C)** Melt clast in suevite sample M4 S-6 from 316.52 m depth. The clast contains angular quartz, K-feldspar and magnetite clasts and shows an irregular margin with the suevite matrix. **D)** Enlargement of C shows essentially monomineralic alteration of melt clast (left) and <30 µm radiating phyllosilicate with high porosity and a <10-20 µm, idioblastic bright phase replacing suevite matrix.

2.6 Summary

The focus of this chapter was to describe and characterise the target and impactite lithologies intersected by the M4 drill core macroscopically and microscopically. Granitic to dioritic gneisses that occur within the M4 dillcore represent a suite of mutually intrusive Late Archaean rocks that were probably deformed during or shortly after intrusion. These were then intruded by a dolerite that was itself metamorphosed under upper greenschist to epidote-amphibolite facies conditions. Although no evidence of this event can be found in the granitoid gneisses, they must also have experienced this

metamorphism. The youngest pre-impact rock type is a younger, unmetamorphosed, dolerite. The major lithological contacts may all be tectonic, but it is not clear if the displacements were caused by pre-impact or impact faults, or both. Unusual textures and compositions (see Chapter 3) that are recorded in an area of intense quartz veining and fracturing may be related to metasomatism. It is not clear if the fine-grained, highly siliceous, locally finely-banded, but strongly haematised rock found between 208.73 and 236.60 m depth is a separate lithology or a metasomatically altered metadolerite.

Macroscopic analysis of lithic clasts, and microscopic analysis of mineral clasts in the impactites confirms that almost all clasts are derived from the target rocks in the core. Only the sample M4 S-6 from 316.52 m depth contains clasts of a different, possibly ultramafic, lithology. Three separate brittle deformation events can be recognised in the M4 core. Pre-impact fractures brecciated the trondhjemitic gneiss and silicified metadolerite, with white vein quartz filling the spaces between the fragments. The pre-impact timing is confirmed by decorated PDF in the quartz, and by vein quartz clasts and metadolerite-quartz lithic clasts in the suevite. Mineral assemblages of epidote and titanite, which are abundant within these rock types, further prove a greenschist facies level of alteration.

The high level of impact-related brittle deformation in the target rocks seems to extend throughout the core and can be separated from the pre-impact fractures because they fracture shocked mineral grains. With the shock pressure estimates (Chapter 5), this suggests that these rocks were originally located close to the point of impact and close to the transient impact crater floor. The complex relationships that they now show could be because of later processes immediately following the shock event that emplaced them into a jumbled-up sequence, which is common for impact crater floors (e.g. Stöffler et al., 2013).

Macroscopic and microscopic analysis of the brittle deformation in the target rocks and the suevite and MMBr dykes suggests that they are linked. With only the exception of suevite sample M4 S-6, all lithic and mineral clasts in the suevite and MMBr look like they were derived from fractured and cataclased target rocks found in the core. Also, macroscopic analysis of dyke geometries and several composite dykes suggest that (a) the MMBr dykes exploited shear fractures in order to be emplaced and (b) suevite appears to be a mixture of MMBr and cataclasite from the shear fractures. In the next chapter, the origin of the MMBr and suevite are investigated using geochemistry.

Unfortunately, microscopic and BSEM analysis could not find any pristine/fresh glasses and melts in the MMBr and suevite. Both rock types are extensively replaced by a mostly cryptocrystalline low-temperature hydrothermal mineralogy of phyllosilicates (clays) and zeolites, with some slightly higher grade minerals (chlorite, epidote, andradite) in the lower parts of the core. The nature of these minerals (and those with melt crystallization textures) is investigated in Chapter 4.

Chapter 3

Whole-rock Geochemistry

3.1 Introduction

In this chapter the main focus is to characterise the geochemistry of the target rocks and impactites from the M4 drillcore using whole-rock X-ray fluorescence (XRF) and Inductively Coupled Plasma-Mass Spectrometry (ICP-MS) compositional analysis. All analyses were collected in the Earth Lab in the School of Geosciences, University of the Witwatersrand. Sample preparation and analytical methodologies are explained in Appendix 1B. As described in Chapter 2, the M4 borehole consists of approximately 88% target rocks and 12% melt-matrix and suevitic impactites (although intersections of closely-spaced impactites could represent one or more larger breccias). Whole-rock geochemical characteristics (major, trace and rare earth elements) of 53 representative samples, of which 35 represent target rocks (pre-impact lithologies) and 18 represent impactites (suevites and melt-matrix breccias - MMBr), are presented. Individual sample data are presented in Appendix 3 and plotted on all figures in this chapter, however, average values are listed in Tables 3.1 (target rocks), 3.2 (impactites) and 3.3 (average ICP-MS data for both target rocks and impactites).

The data obtained from the whole-rock analyses are used as the basis for classification, nomenclature, and petrogenesis, and are compared with the hand sample descriptions and petrographic observations presented in Chapter 2 (see also Appendix 2). Petrographic features were used in the selection of samples for chemical analysis in order to avoid altered samples wherever possible, however, the impactites show petrographic evidence of comprehensive alteration and the granitoid gneisses and metadolerite show variable alteration particularly where fractured or brecciated. A more comprehensive description of the alteration features is presented in Chapter 2. Wherever possible, impactites carrying large melt and lithic clasts were avoided in order to obtain the most representative compositions for the impactites; however, it must be recognised that these are clast-rich breccias and that their compositions are thus influenced by the clast components.

3.2 Major element analysis of target rocks

Based on macro- and microscopic observations, the pre-impact stratigraphy consists of granitic-granodioritic, dioritic and trondhjemitic gneisses, dolerite and metadolerite (Chapter 2, Figure 2.1). In this section a number of diagrams are plotted to examine and classify the target rocks based on their

chemical compositions. Although the target rocks are classified using several geochemical classification diagrams, the final rock names were assigned on the basis of consistency between the chemical classification, the modal criteria and the IUGS classification for plutonic rocks by Streckeisen (1976).

The complete whole-rock geochemistry dataset for M4 core target rocks is presented in Appendix 3A, and Table 3.1 shows the mean values and standard deviations of their major element oxides. Multivariate normative/modal and bivariate (including Harker) diagrams derived from the major oxides Al_2O_3, Fe_2O_3, FeO, MgO, CaO, Na_2O, K_2O, and SiO_2 for all target rocks are shown in Figures 3.1 to 3.4 and are used to analyse major element trends. The inter-element plots are shown in Fig. 3.5. The chemical data are henceforth presented and assessed by dividing the target rocks into the two main groups of igneous rocks: those that are gneissic and (meta) plutonic, and those that are hypabyssal (dolerite/metadolerite).

Based on clustering of data in the Harker plots (Figure 3.4), three main groups of target rocks are identified: granitoid gneisses (granitic gneiss, granodioritic gneiss, trondhjemitic gneiss and dioritic gneisses), dolerite and metadolerite (Figure 3.4).

3.2.1 Granitoid gneisses

As in Chapter 2, "granitoid gneisses" is used here to include the granitic, granodioritic, dioritic and trondhjemitic gneisses, which show similar petrographic features but which differ in modal mineralogy. On the Q-A-P ternary diagram using normative data from the geochemical analyses (Figure 3.1), 14 granitoid gneiss samples plot in the granodiorite to monzo-granite fields, 8 samples in the monzodiorite to quartz-monzodiorite fields, and 4 in the tonalite field. In comparison, on the TAS diagram that measures alkalis against silica (Figure 3.2), the granite-granodiorite and trondhjemite samples show some overlap in the granite field, whereas the diorite samples form a distinctly separate group in the monzonite to quartz monzonite fields. This discrimination based on SiO_2 content is explored further in the Harker plots (Figure 3.4). On the normative feldspar plot commonly used for Archaean granitoid lithologies (Figure 3.3), most of the data fall on a broad linear trend between the granite and trondhjemite fields, from more alkali feldspar-rich granite-granodiorite to trondhjemite, the samples of which are strongly depleted in potassium. The exception is the dioritic gneiss samples, which are more calcic and straddle the tonalite-trondhjemite boundary. Based on the evidence from Figures 3.1-3.3, in the remainder of this chapter the granitoid gneiss samples have been sub-divided into 3 groups (granitic-granodioritic gneiss; trondhjemitic gneiss; and dioritic gneiss).

Table 3.1: Means and standard deviations for major element oxide abundances for the M4 core target rock samples (all data in wt. %).

	Granitic-granodioritic gneiss				Trondhjemitic Gneiss			
	n = 14		Range		n = 4		Range	
	Mean	S.D.*	Min.**	Max. ^	Mean	S.D. *	Min**	Max. ^
SiO_2	73.77	1.14	71.51	75.30	77.13	2.24	75.79	80.47
TiO_2	0.17	0.07	0.04	0.31	0.20	0.01	0.19	0.21
Al_2O_3	14.56	0.37	14.09	15.38	12.94	1.42	10.82	13.87
Fe_2O_3	0.16	0.04	0.08	0.25	0.12	0.01	0.11	0.13
FeO	1.30	0.35	0.63	2.04	0.98	0.06	0.92	1.07
MnO	0.02	0.01	0.01	0.03	0.01	n.d.	0.01	0.01
MgO	0.44	0.20	0.07	0.77	0.74	0.13	0.66	0.94
CaO	1.47	0.28	1.14	2.13	1.89	0.18	1.73	2.13
Na_2O	5.03	0.66	3.70	6.49	5.73	0.70	4.79	6.48
K_2O	3.11	1.22	1.33	5.34	0.27	0.09	0.19	0.35
P_2O_5	0.06	0.03	0.01	0.11	0.07	0.01	0.06	0.08
Cr_2O_3	n.d.	n.d.	n.d.	0.01	n.d.	n.d.	n.d.	n.d.
NiO	n.d.	n.d.	n.d.	n.d.	n.d.	n.d.	n.d.	n.d.
TOTAL	**100.09**	**0.19**	**99.82**	**100.48**	**100.07**	**0.11**	**99.98**	**100.22**

*n = number of samples; * S.D.: Standard Deviation; Min. **: Minimum; Max. ^: Maximum, n.d.: not detected*

Table 3.1 *Continued...*

	Dioritic Gneiss				Metadolerite			
	n = 8		Range		n = 5		Range	
	Mean	S.D.*	Min.**	Max. ^	Mean	S.D.*	Min.**	Max. ^
SiO_2	61.01	2.08	58.21	63.53	58.85	6.46	55.43	70.37
TiO_2	0.84	0.11	0.70	0.99	0.84	0.19	0.51	0.95
Al_2O_3	18.07	0.53	17.32	18.88	13.39	2.37	11.54	17.53
Fe_2O_3	0.64	0.07	0.55	0.72	0.93	0.26	0.53	1.14
FeO	5.14	0.56	4.46	5.82	7.56	2.13	4.31	9.26
MnO	0.08	0.02	0.04	0.10	0.11	0.06	0.03	0.18
MgO	1.95	0.24	1.69	2.45	5.37	4.10	0.44	8.70
CaO	3.55	0.53	2.89	4.33	11.14	2.18	9.26	14.47
Na_2O	6.34	0.50	5.36	6.92	1.46	0.58	0.69	2.12
K_2O	2.10	0.63	1.47	3.48	0.15	0.10	0.06	0.29
P_2O_5	0.47	0.07	0.40	0.57	0.21	0.17	0.13	0.52
Cr_2O_3	0.01	0.01	n.d.	0.02	0.05	0.03	0.01	0.09
NiO	n.d.	n.d.	n.d.	n.d.	0.02	0.02	n.d.	0.04
TOTAL	**100.19**	**0.20**	**99.83**	**100.49**	**100.09**	**0.29**	**99.65**	**100.47**

*n = number of samples, * S.D.: Standard Deviation; Min. **: Minimum; Max. ^: Maximum, n.d.: not detected*

Table 3.1 *Continued...*

	Dolerite			
	n = 8			
	Mean	**S.D.***	**Min****	**Max^**
SiO_2	53.72	0.48	53.17	54.04
TiO_2	1.33	0.02	1.32	1.36
Al_2O_3	13.80	0.30	13.53	14.13
Fe_2O_3	1.43	0.06	1.37	1.48
FeO	11.56	0.45	11.09	11.98
MnO	0.19	0.01	0.18	0.19
MgO	5.60	0.08	5.53	5.68
CaO	7.85	0.79	7.10	8.68
Na_2O	3.42	0.51	2.92	3.94
K_2O	1.07	0.12	0.94	1.16
P_2O_5	0.14	0.01	0.13	0.14
Cr_2O_3	0.02	n.d.	0.02	0.02
NiO	0.01	n.d.	0.01	0.01
TOTAL	**100.14**	**0.51**	**99.74**	**100.71**

*n = number of samples, S.D. *: Standard Deviation; Min. **: Minimum; Max. ^: Maximum, n.d.: not detected*

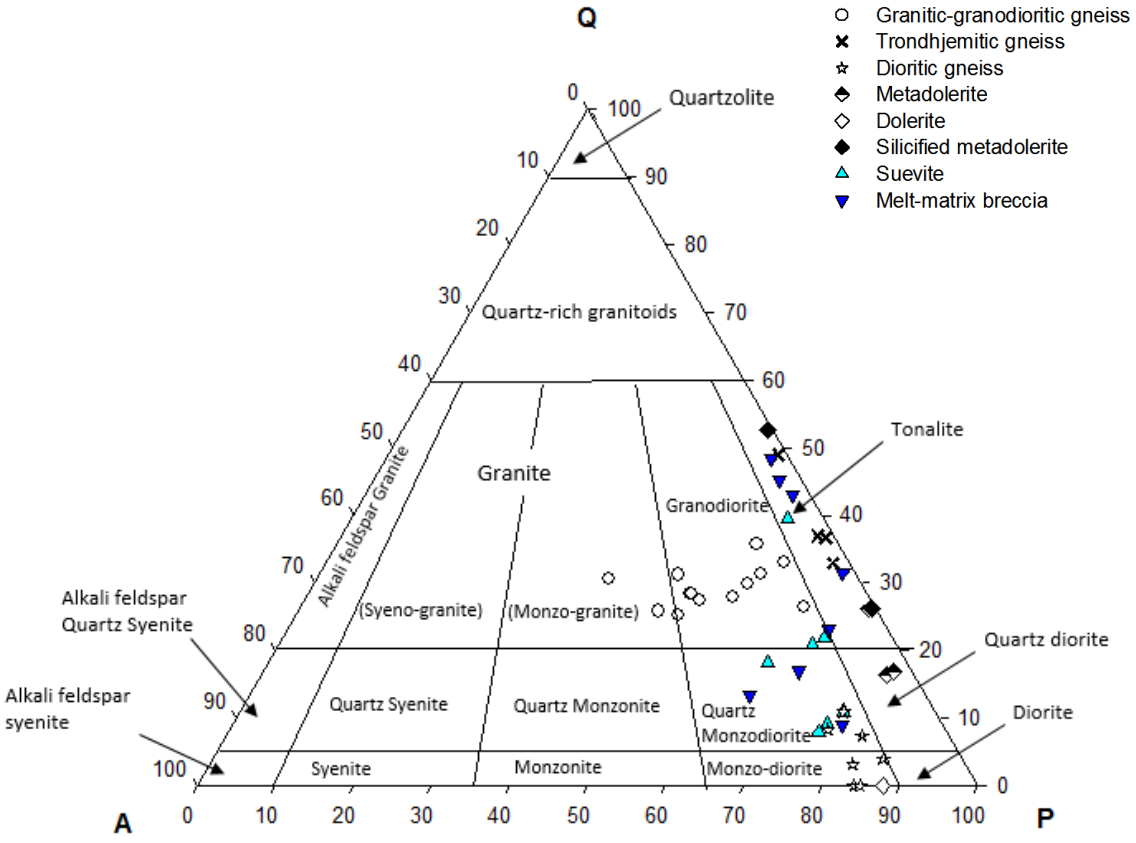

Figure 3.1: Classification of M4 core target rocks using the ternary granitoid classification diagram (after Streckeisen, 1974) using modal and normative proportions of quartz, orthoclase and plagioclase (Q = quartz; A = alkali feldspar; P = plagioclase). Impactites are plotted for comparative purposes.

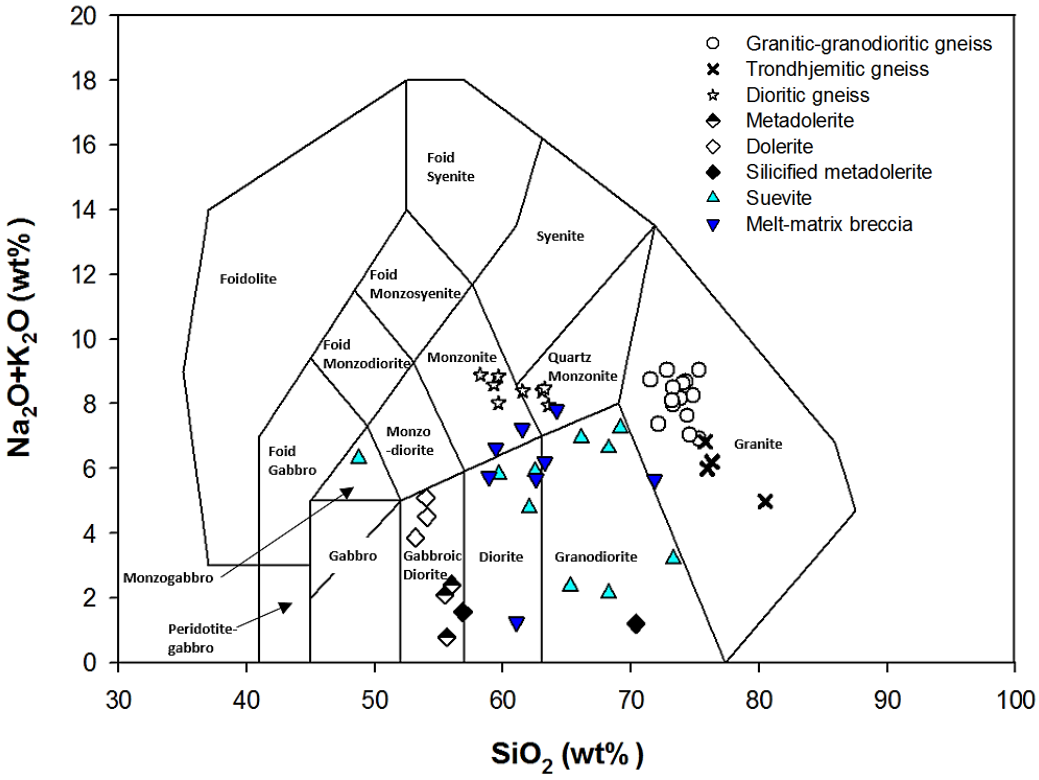

Figure 3.2: Classification of M4 target rocks using the plutonic total alkali versus silica (TAS) diagram (Middlemost, 1994). Impactites are plotted for comparative purposes.

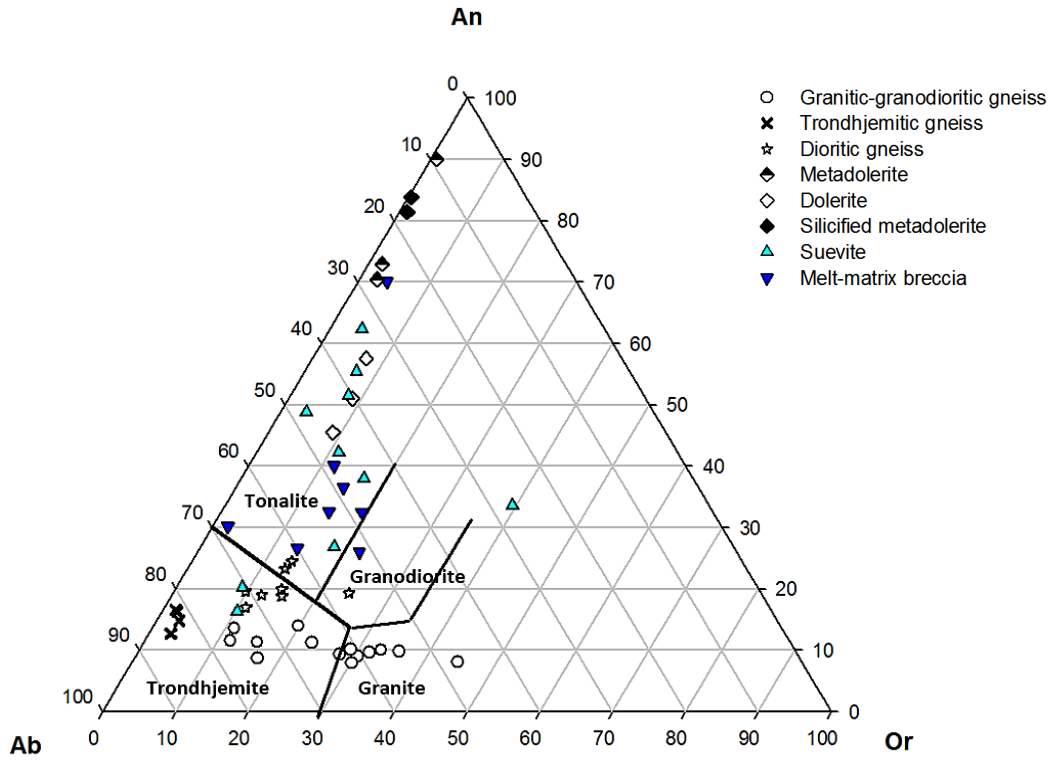

Figure 3.3: Classification of M4 core target rocks using the normative feldspar plot (An - anorthite, Ab - albite, and Or – orthoclase) with field boundaries after Barker (1979) for classifying felsic plutonic rocks. Impactites are plotted for comparative purposes.

Figure 3.4 shows Harker plots of the major elements against SiO_2 for the target rocks in the M4 core. Based on Figure 3.4, the dioritic gneiss and granitic-granodioritic gneisses together display broadly linear fractionation trends with respect to SiO_2 for TiO_2, Al_2O_3, FeO, MgO, CaO and P_2O_5, with particularly strong trends for the ferromagnesian elements, particularly in the dioritic gneiss samples (Figure 3.4 A-D). CaO shows a similar negative trend, but with more scatter in the dioritic and granitic-granodioritic gneisses (Figure 3.4 E). A greater scatter (no observable trend) is found in the alkali elements (Figure 3.4 F, G), and is most extreme for K_2O. In the trace elements Harker plots, great scatter of data points is evident especially for the Sr plots which is mobile. Less immobile elements are thus plotted in subsequent rare earth element plots and spidergrams in order to observe the trace element chemical signature of the M4 core lithologies. Based on petrographic evidence of both pre- and post-impact alteration, including significant alteration of feldspars (Chapters 2 and 4), this variability may reflect the mobility of K^+ and Na^+ in hydrothermal environments (Rollinson, 1993; White, 1998); however, it must also be remembered that drillcore samples of coarse-grained lithologies may display high variability given the limited sample size rocks. Impactites are plotted for comparative purposes.

The granitic-granodioritic gneisses range from 71.51-75.30 wt. % SiO_2 (average 73.77 ± 1.1 wt. %; Table 3.1). Figure 3.4 shows the clear distinction between the granitic-granodioritic gneisses and trondhjemitic gneisses (77 ± 2 wt. %) and the relatively SiO_2-poor dioritic gneisses (61 ± 2 wt. %; Table 3.1). Based on the petrographic evidence (Section 2.3.2) that shows that the trondhjemitic gneiss samples are spatially linked to a zone of intense fracturing and quartz vein development between 213.5 and 259.1 m (Figure 2.1), the higher and more variable values of SiO_2 in the trondhjemites could be interpreted as the product of metasomatic silica addition to, and/or potassium loss from, granitic-granodioritic gneiss. This suggestion may be supported by the lack of variation in all the other major elements except Al_2O_3 and Na_2O (Figure 3.4 B, F). As the most significant oxide after SiO_2, the decrease in Al_2O_3 with the increase in SiO_2 in trondhjemitic gneiss sample M4 FZ-2 (depth: 219.30 m) could be interpreted as being the result of mass balance. The drillcore photograph in Appendix 2B shows sample M4 FZ-2 contains a cm-wide quartz vein. Whilst every care was taken to avoid sampling the vein, it is possible that the abnormal content of SiO_2 (Figure 3.4B), in this sample represents contamination, as smaller veins could have been present. If sample M4 FZ-2 is discounted, then the remaining trondhjemitic gneiss samples are only slightly (1-2 wt. %) more siliceous than the most siliceous granite-granodiorite samples, however, the trondhjemitic gneisses are slightly enriched in TiO_2, MgO, CaO, Na_2O and P_2O_5, and significantly depleted in K_2O, relative to the granitic-granodioritic gneisses. Diagrams of TiO_2, Al_2O_3, FeO, MgO, P_2O_5 and CaO show a negative correlation with SiO_2 content for the granitoid and diorite clusters. In Figures 3.4F and G the three clusters for the gneiss suite are visible but the data points are scattered.

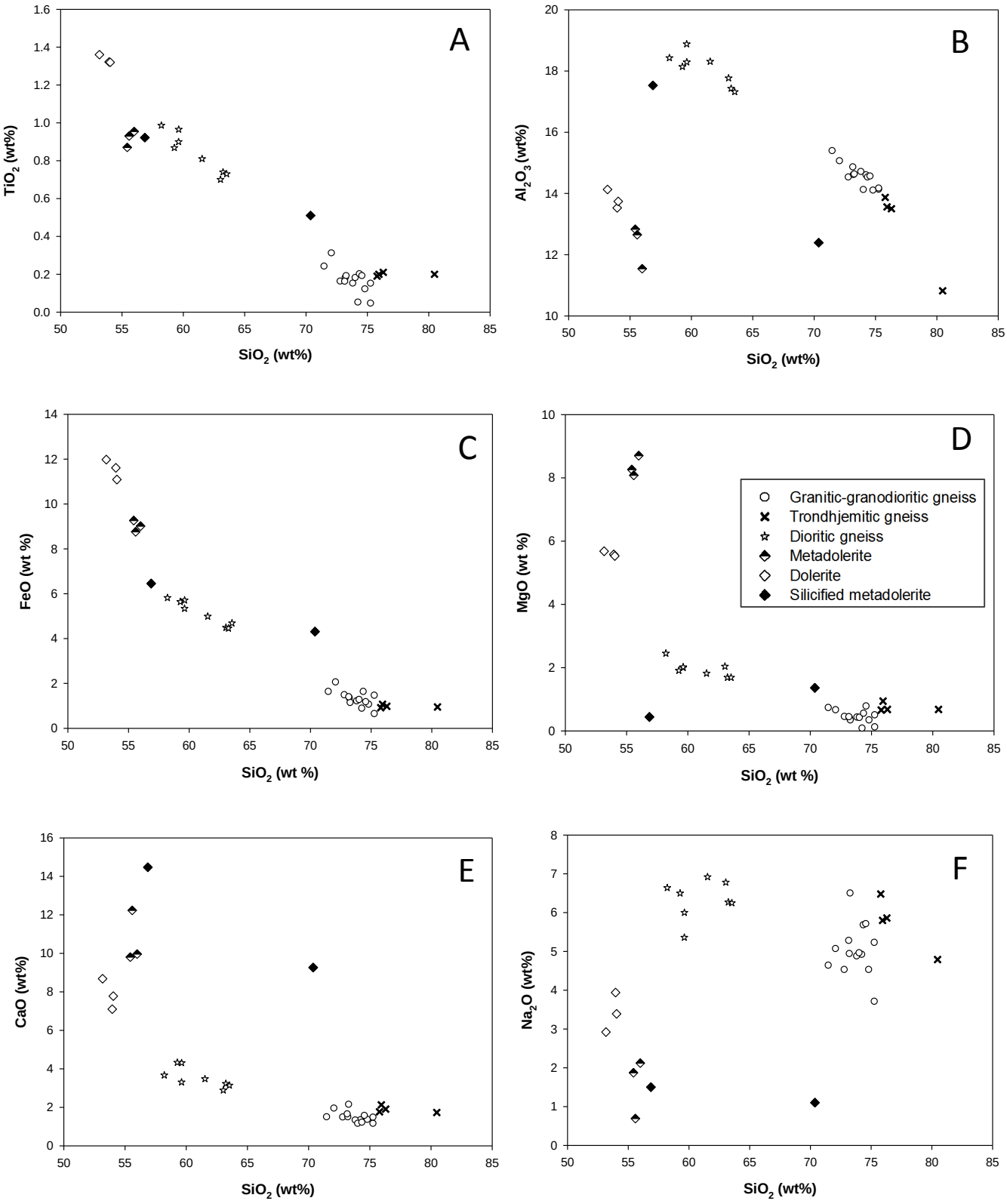

Figure 3.4: Harker plots for M4 core target rocks. Major oxides of TiO_2, Al_2O_3, FeO, MgO, CaO, Na_2O, K_2O and P_2O_5 are plotted versus SiO_2. Three distinct clusters are visible: granitoid cluster (including trondhjemitic gneiss), diorite cluster and the dolerite and metadolerite cluster.

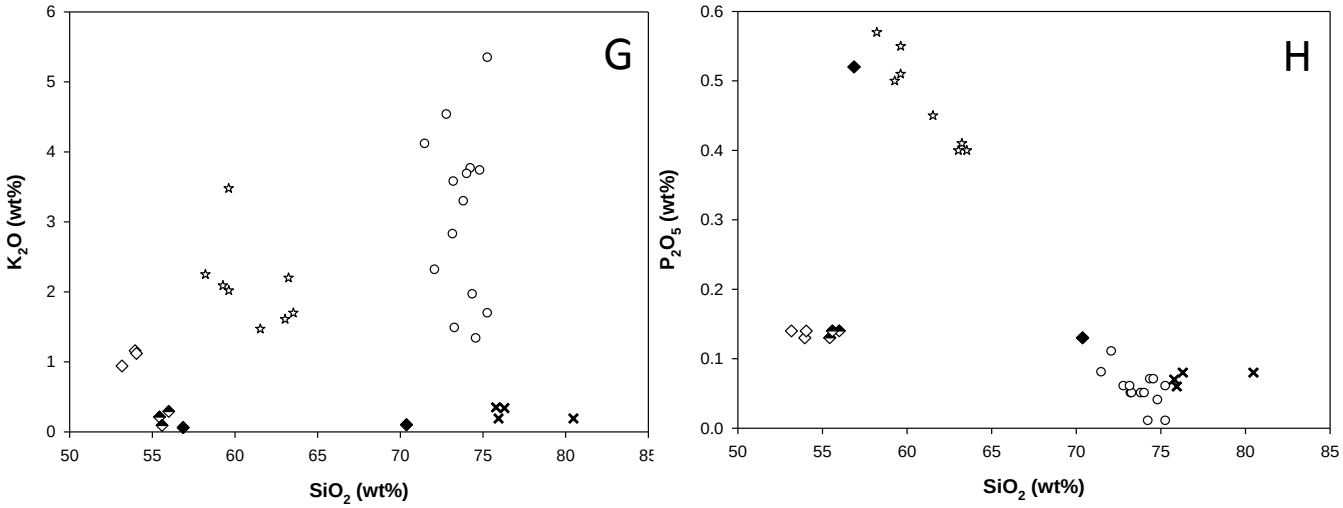

Figure 3.4: *Continued……*Harker plots for M4 core target rocks.

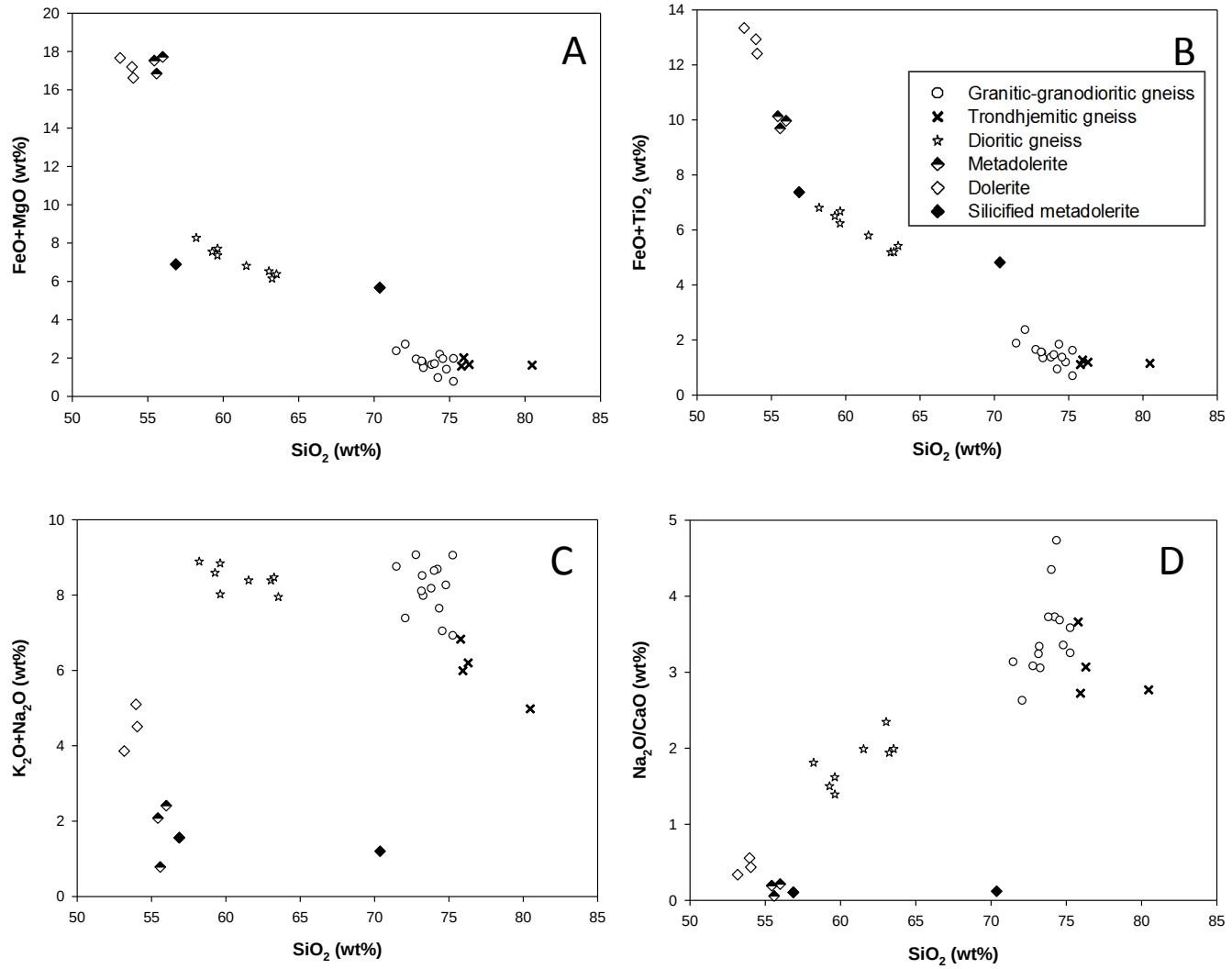

Figure 3.5: Bivariate plots for M4 core target rocks. With one or two outliers (see text), three distinct clusters are visible: granitic-granodioritic-trondhjemitic gneiss cluster, dioritic gneiss cluster and dolerite – metadolerite cluster.

3.2.2 Dolerite and metadolerite

The metadolerite and dolerite occur in two separate intervals within the M4 drillcore: 166.10–236.60 m and 264.00-290.71 m, respectively (Figure 2.1; Appendix 2A, B). The dolerite is interpreted to occur within a broad MMBr-dominated breccia zone as three fragments ranging from 1 m to 2.5 m in size. Each of these fragments was sampled for whole-rock geochemistry. Although the metadolerite intersection is considerably larger, no evidence exits to confirm the actual orientation of the intrusive body, and the presence of a fault zone indicated by the silicified trondhjemitic gneiss and quartz veining that dominate in the intervals 173.30–179.75 m -and 196.63-236.60 m is inferred. This observation, together with the aeromagnetic evidence (Figure 1.10) that indicates abundant (sub) vertical dykes in the region, makes it impossible to confirm if this represents a true thickness. Five metadolerite samples were selected from a range of depths (Figure 2.1, Appendix 2A). Two of the samples, M4 IS-1 and M4 IS-2 from 221.20 and 211.41 respectively, are intensely brecciated, silicified, ferruginised and show abundant quartz veining (Figure 2.9C-D; Appendix 2A, boxes 13-16). Despite efforts to remove the vein quartz, it is apparent from Figure 3.4 that sample M4 IS-2 shows an anomalous SiO_2 content relative to the other metadolerite samples (71 wt. % relative to 58 wt. %; Appendix 3A). It has thus been excluded in average calculations in Table 3.1. However, for the sake of completeness, it is shown on all the diagrams.

On the TAS diagram (Figure 3.2) the metadolerite and dolerite samples (excluding M4 IS-2) plot in the gabbroic diorite field. Although the Streckeisen and normative feldspar diagrams are less useful for mafic rock classification, the whole-rock compositions are plotted to assist with analysis of potential source rocks for the impactites. Figure 3.4 confirms that the dolerite is less siliceous (average silica content of 53.7 ± 0.5 wt. %), than the metadolerite (57.7 ± 6.46 wt. %) (Table 3.1). This may not be surprising, given the extent of micro-fracturing related to quartz veining in the metadolerite, but other elements also allow a distinction. The dolerite samples are also more enriched in TiO_2, Al_2O_3, FeO, Na_2O and K_2O, but depleted in MgO and CaO, relative to the metadolerite (Figure 3.4). The dolerite also shows less scatter than the metadolerite in most oxides, consistent with the lower degrees of metamorphic alteration noted in the petrographic analysis (Section 2.3.4). The metadolerite shows very little variation in the ferromagnesian elements (TiO_2, FeO and MgO), and K_2O values approach zero. Metadolerite sample M4 IS-1 contains an unusual retrograde assemblage rich in epidote, titanite and apatite (Section 2.3.4.3). Although it is only slightly enriched in SiO_2 relative to the remaining 3 metadolerite samples, which suggests that the quartz veins visible in Appendix 2B (Figure 2.2) were avoided, the mineralogy is reflected in the exceptional CaO and P_2O_5 enrichment, and depletion in FeO and MgO, relative to the other samples (Figure 3.4).

3.3 Major element analysis of impactites

As discussed in Chapter 2, the term "impactite" is used here to describe only suevite and MMBr. Geochemical analysis of these breccias needs to consider both the sampling difficulties posed by small sample volume, and the petrographic evidence (Chapters 2, 4) that they have experienced significant hydrothermal alteration. However, such analysis is important in understanding the relationship between the target rocks and the impact-derived lithologies in the M4 core. Major and trace element data for the impactites are presented in Appendix 3B and 3D and the mean values and standard deviations of the major element oxides are presented in Table 3.2. Impactite sample compositions were plotted on similar diagrams to those used for the target rocks (cf. Figures 3.1-3.3). Wherever possible, large clasts were avoided in the sample preparation in order to prevent bias.

Table 3.2: Means and standard deviations analysis of major element oxide abundances for suevite and melt-matrix breccias from the M4 core (data in wt. %).

	Suevite					**Melt-matrix breccia**			
	n=9		**Range**		**M4 S-6**	**n=8**		**Range**	
	Mean	**S.D.***	**Min****	**Max^**		**Mean**	**S.D.***	**Min****	**Max^**
SiO_2	66.03	4.23	59.62	73.32	48.73	62.82	4.05	58.87	71.80
TiO_2	0.64	0.21	0.33	0.97	0.63	0.22	0.06	0.11	0.28
Al_2O_3	13.55	1.64	11.21	15.39	15.00	14.95	0.51	14.06	15.71
Fe_2O_3	0.64	0.17	0.40	0.86	0.98	0.75	0.25	0.22	1.02
FeO	5.17	1.39	3.22	7.00	7.93	6.09	2.05	1.82	8.24
MnO	0.07	0.03	0.04	0.12	0.16	0.09	0.03	0.02	0.13
MgO	3.68	2.13	1.87	8.09	15.60	3.99	2.14	1.01	8.46
CaO	5.26	2.29	2.40	10.31	4.39	4.92	0.67	4.29	6.28
Na_2O	3.81	1.49	1.77	5.96	1.95	4.14	1.40	1.01	5.40
K_2O	1.19	0.72	0.33	2.34	4.34	1.64	0.98	0.23	3.09
P_2O_5	0.19	0.06	0.12	0.27	0.53	0.78	0.24	0.25	0.99
Cr_2O_3	0.02	0.02	0.01	0.06	0.02	0.02	0.02	0.01	0.07
NiO	0.01	0.01	n.d.	0.03	0.04	0.01	0.01	n.d.	0.02
TOTAL	**100.27**	**0.24**	**99.97**	**100.74**	**100.3**	**100.41**	**0.39**	**100.01**	**101.24**

*n = number of samples; * S.D.*: Standard Deviation; Min. **: Minimum; Max. ^: Maximum, n.d: not detected*

3.3.1. Comparison of suevite and melt-matrix breccias

Figure 3.6 shows standard Harker plots for major oxides against SiO_2, for 10 suevite and 8 MMBr samples. On the Harker plots the M4 suevites and the MMBr overlap and the noted differences are relatively subtle, despite the obvious differences in the matrix textures. With the exception of 1 outlier (sample M4 IM-2 from 234.33 m depth), the MMBr samples show a more restricted, and slightly lower, SiO_2 range (58-65 wt. %) (Table 3.2) relative to suevite (60-70 wt. %, with 2 outliers). Sample M4 IM-2 shows exceptionally high SiO_2 content (72 wt. %) and is very distinct from the remaining MMBr. It is located within trondhjemitic gneiss, which also shows an exceptionally high SiO_2 content related to quartz veining (see section 3.2.1; Figure 3.4), so its anomalous composition might be caused by a quartz clast. The one exceptionally SiO_2-poor suevite sample (M4 S-6; SiO_2 = 49 wt.%) is characterized by a green colour and displays an anomalous mineralogy that is interpreted as reflecting an exotic, possibly ultramafic, component (Section 2.11).

Suevite sample M4 S-10 (depth: 208.34 m) is also exceptionally siliceous (SiO_2 = 73.32 wt. %); it is also located within the highly quartz-veined region of the core (Section 3.3.2; Figure 2.1). Based on Figure 3.6 it is apparent that, despite their textural differences, suevite and MMBr in the M4 core display similar compositions. Both the suevite and the MMBr display intermediate SiO_2 contents between the doleritic and granitoid rocks with MMBr being more mafic than suevite. As for the target rocks, only TiO_2, FeO, and perhaps P_2O_5, show reasonably consistent trends relative to SiO_2, although the scatter is greater than in the target rocks.

3.3.2 Comparison of impactites and target rocks

In this section, the compositional variation of the impactite lithologies is compared with the whole-rock chemistry of target rock types. Figure 3.7 is a combination of Figures 3.4 and 3.6. With the exception of one outlier (sample M4 S-6), TiO_2 is strongly negatively correlated with SiO_2 for both the impactites and target rocks (Figure 3.7A), with a reasonably good negative correlation also visible with FeO versus SiO_2 (Figure 3.7 C); however, the correlation is weak for all other major oxides.

The bulk of the MMBr samples display SiO_2 contents that overlap the dioritic gneisses. With one exception (M4 IM-2), they are only slightly more siliceous than the metadolerite and dolerite. They show the closest correlation with the dioritic gneiss samples with regards to TiO_2, CaO and K_2O, but are depleted in Al_2O_3, Na_2O and P_2O_5 and slightly enriched in FeO and MgO. In contrast, the suevites have a slightly more enriched SiO_2 content and lie on a good mixing line between the dioritic and granitic-granodioritic clusters for TiO_2 versus SiO_2 (Figure 3.7 A). The scatter in other oxide plots suggests the additional involvement of dolerite and metadolerite, something that is shown in the clast

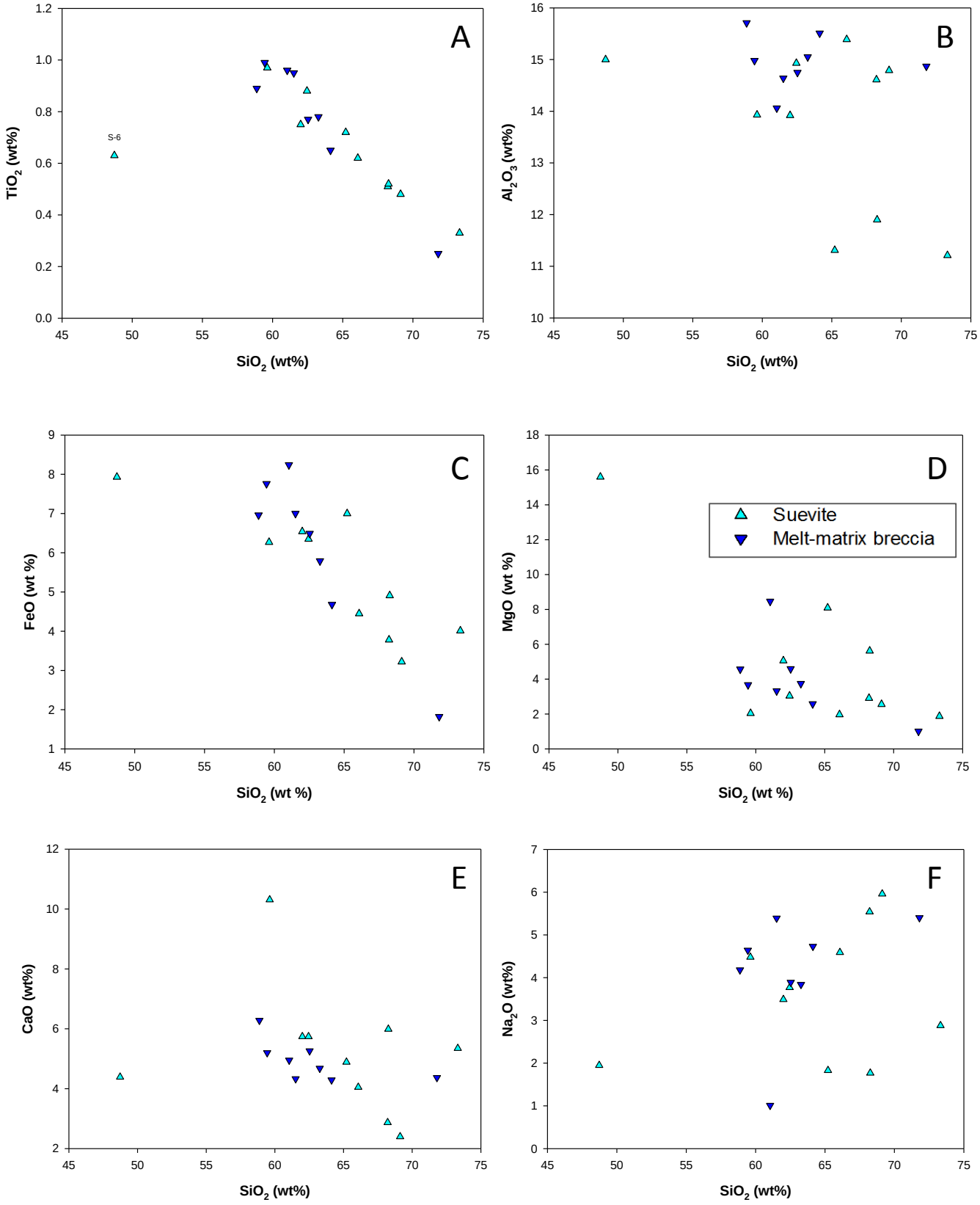

Figure 3.6: Harker plots for impactites in the M4 core. The extremely siliceous samples are M4 S-10 (depth: 208.49 m) with up to 73.32 wt. % SiO_2 and M4 IM-2 (depth: 234.33 m) with 71.80 wt. % SiO_2, whilst sample M4 S-6 (depth: 316.52 m) has an SiO_2 value below 50%.

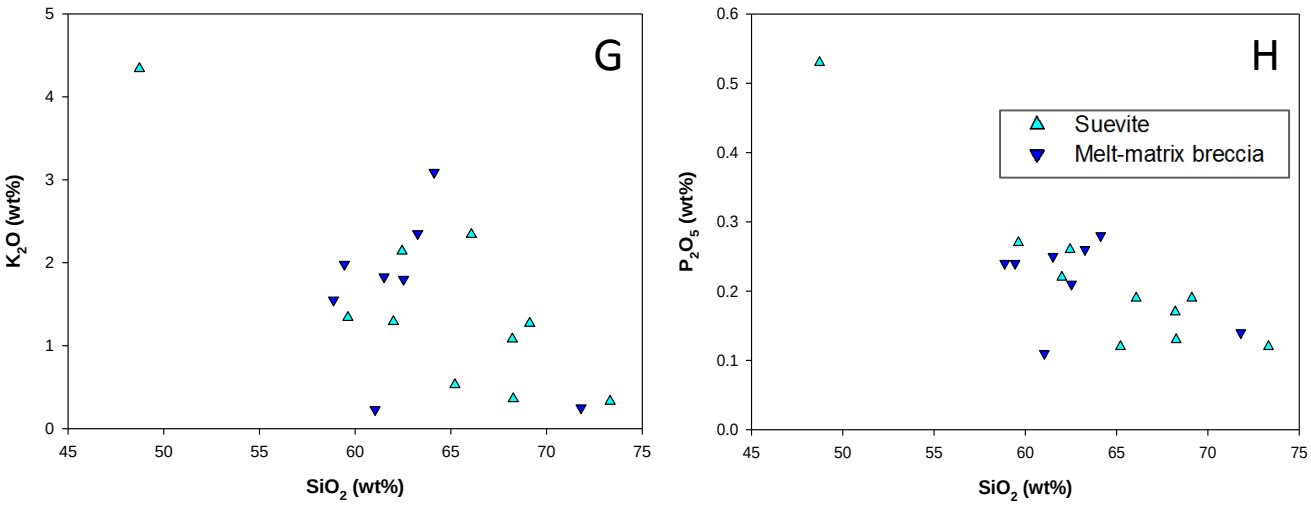

Figure 3.6: *Continued …* Harker plots for impactites in the M4 core.

analysis (Section 2.4.3.1). Whilst it is not possible to tell if TiO_2 or FeO show any influence of the metadolerite or dolerite, both suevite and MMBr Al_2O_3, MgO, CaO, Na_2O and K_2O values are more variable (as for the target rocks) and show a scatter intermediate between the 3-main target rock end-members (granitic-granodioritic gneiss, dioritic gneiss and dolerite ± metadolerite) (Figure 3.7 B, C, D). As a first approximation, this suggests that both the suevites and the MMBr can be successfully explained as having been derived from target lithologies represented in the remainder of the M4 drillcore.

The exceptions to this are samples M4 S-6, which has a SiO_2 content more consistent with an ultramafic source, and suevite samples M4 S-8, M4 S-9 and M4 S-10 from 170.7, 198.03, and 208.34 m depth respectively, which are anomalous in terms of having slightly low Al_2O_3 and Na_2O (Figure 3.7 B, F) and high FeO, MgO and CaO (Figure 3.7 C, D, E). All these samples are located within the metadolerite interval in the core (Appendix 2A), and their compositions might be explained by enrichment in predominantly metadolerite-derived clasts contaminated by a high proportion of vein quartz clasts that have shifted the bulk composition to higher values of SiO_2.

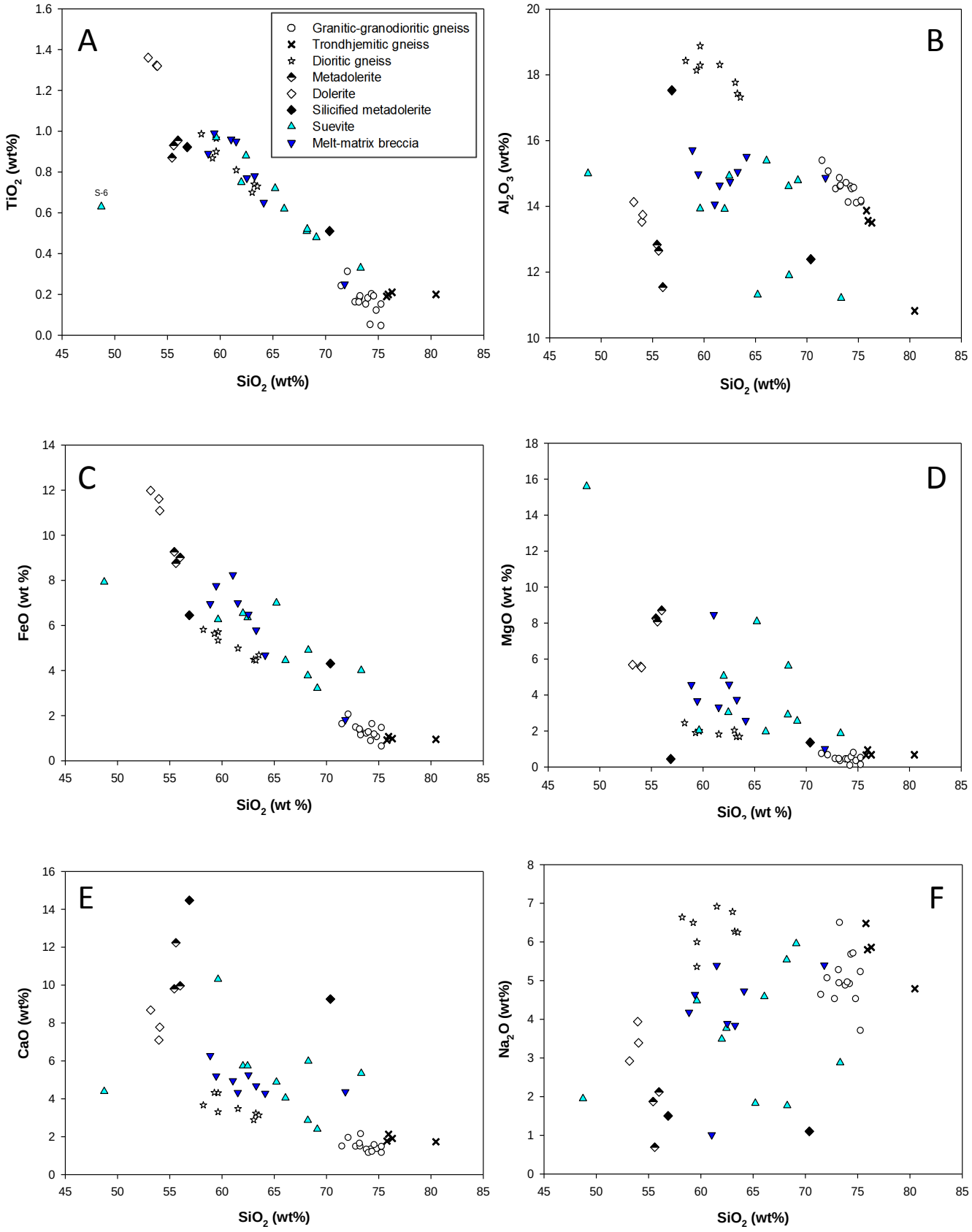

Figure 3.7: Harker plots comparing M4 core target rocks and impactites.

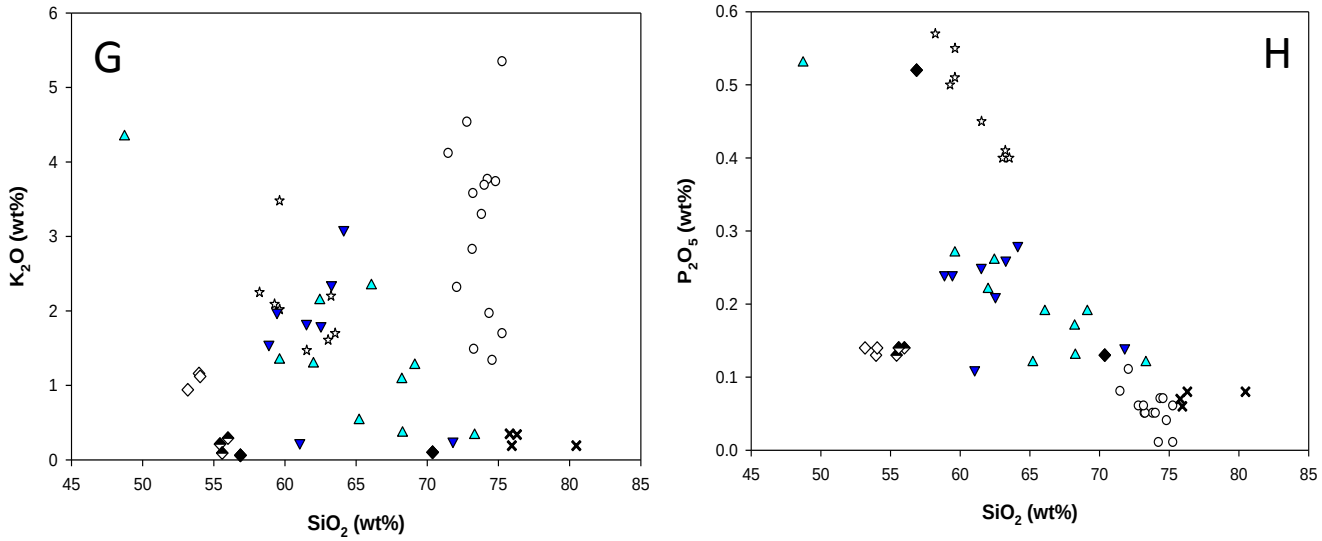

Figure 3.7 *Continued…* : Harker plots for target rocks and impactites

3.3.3 Depth-dependence of major elements in target rocks and impactites

It has been suggested in Section 3.3.2 that the major element compositional variation in the impactites can be adequately explained for many samples by mixing of target rocks intersected in the M4 core. In order to check this and evaluate whether more local compositional controls exist on the impactites, target rock and impactite major element compositions are plotted against borehole depth in Figure 3.8.

Figure 3.8 confirms that (except for M4 S-6 at 316.52 m depth), all major element abundances of impactites lie between the extreme values represented by the granitic–granodioritic-trondhjemitic gneiss cluster and the dolerite and metadolerite cluster. Dioritic gneiss has a more intermediate composition, but overlaps the dolerite and metadolerite groups with regards to some oxides. The individual target rock types remain relatively constant in their major element abundances throughout the core (Figure 3.8), however, impactites show greater variability. Although the impactites are not uniformly distributed within the core, they appear to show a compositional cyclicity (Figure 3.8): between 140-160 m and 185-235 m depth SiO_2 increases; whereas from 160-185 m and 235-280 depth, SiO_2 decreases (Figure 3.8A). A similar cyclicity occurs with respect to Na_2O (Figure 3.8F). This correlation between the impactites and target rocks is considerably better than suggested by Figure 3.7F). In contrast, K_2O in the impactites shows a broad decrease from the upper granitoid interval above 160 m into the metadolerite interval, with a reverse increase below 235 m (Figure 3.8G), closely mimicking the target rock values.

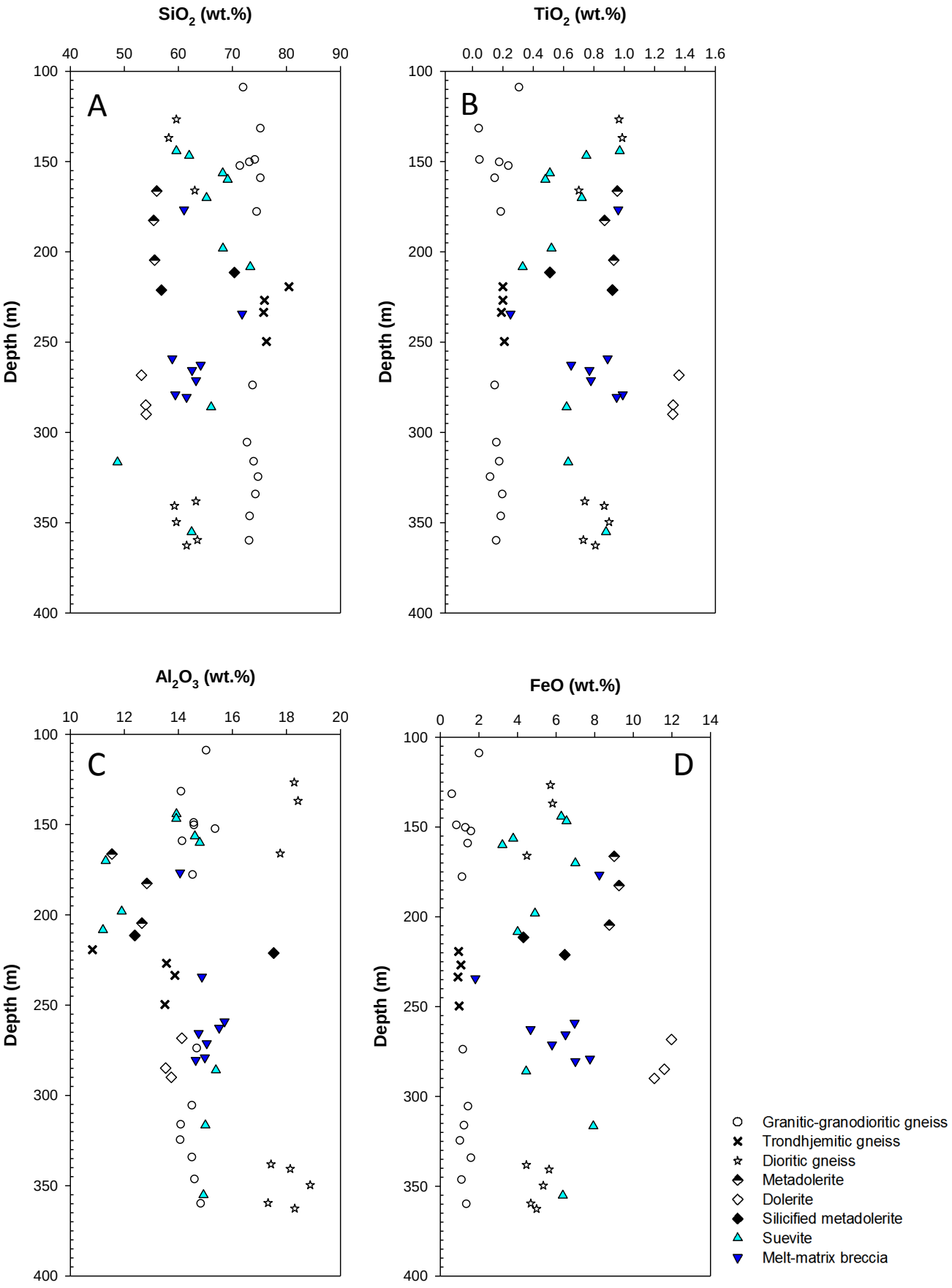

Figure 3.8: Variation in whole-rock major element oxides with depth in the M4 core.

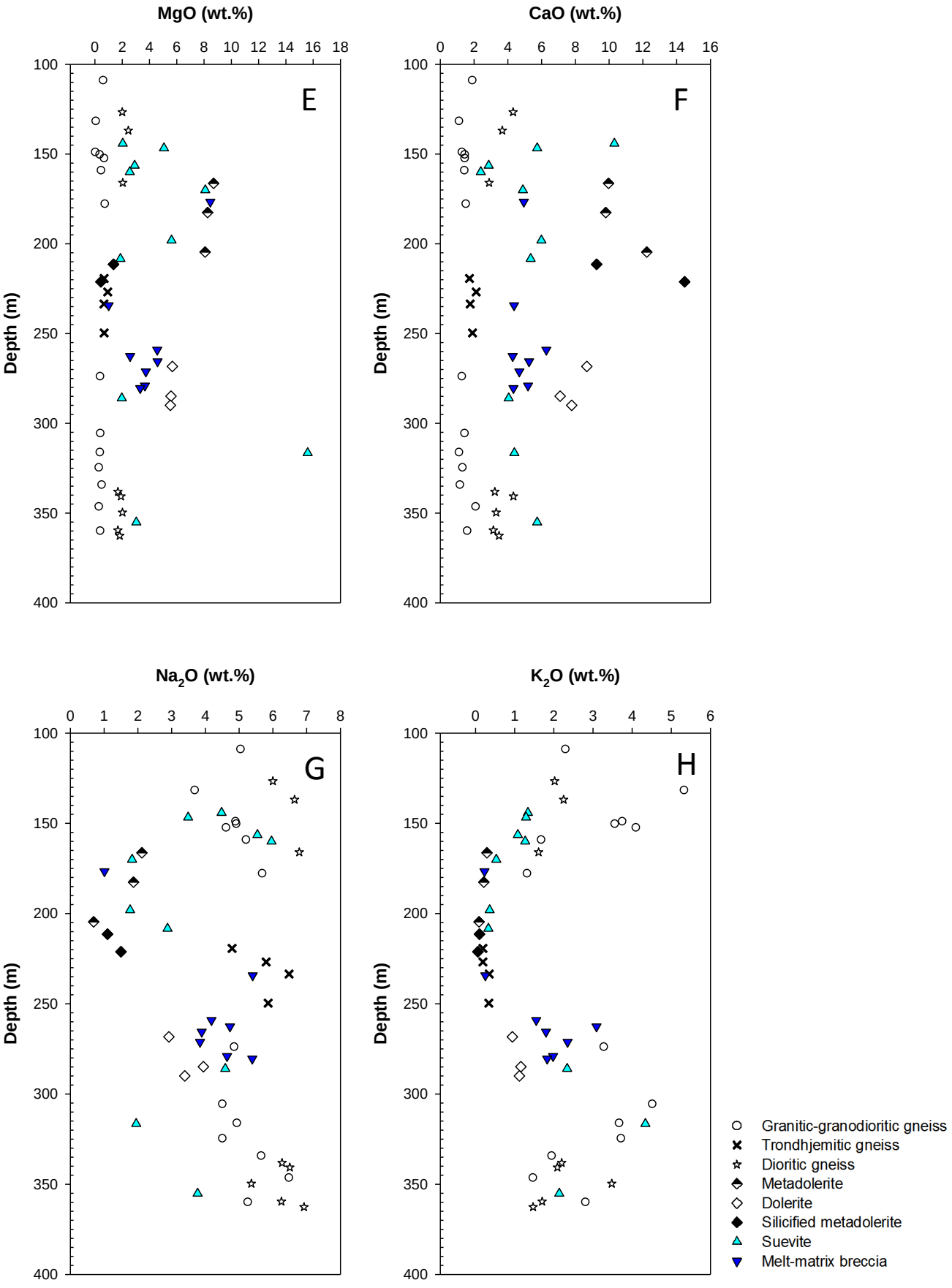

Figure 3.8 *Continued…*: Variation in whole-rock major element oxides with depth in the M4 core.

The inverse relationship to SiO_2 is noted in TiO_2, FeO and MgO. Al_2O_3 in the impactites is relatively constant (at granitic-granodioritic gneiss levels), with the exception of the 185-235 m interval that is dominated by metadolerite (Figure 3.8C). CaO in the impactites is relatively constant, and similar to dioritic gneiss values, below 160 m depth, although suevites from 140-160 m show a strong decrease from values consistent with the metadolerite, to granitoid values (Figure 3.8F). The Na_2O concentration of impactites and target rocks increases with increasing depth (Figure 3.8 G).

3.4 Trace element analysis of M4 lithologies

Evidence that the M4 target rocks and impactites have undergone shock metamorphism and pre-and post-impact alteration has been presented in Chapter 2. Trace element behaviour is crucial when assessing the geochemistry of rocks as different elements behave differently when subjected to weathering and leaching processes, thereby revealing more about the history of the rocks (Rollinson, 1993, 2014; White, 1998). Despite their scarcity, many of the trace elements, mainly Zr, Hf, and the REE are very important because their minerals may resist weathering, hydrothermal alteration, metamorphism up to anatexis, and even magmatic processes (Rollinson, 1993; White, 1998). Other elements, such as U and Mn are sensitive to reduction-oxidation changes. Whole-rock trace element concentrations are controlled by partition coefficients of elements between minerals (White, 1998), and the concentration on the elements is dependent of specific minerals, for example the Sr concentration is influenced by plagioclase; the P by apatite, Zr by zircon and the Ti, Nb and Ta by ilmenite or titanite (Rollinson, 2014). In this section the behaviour of trace elements is examined broadly by plotting selected trace element Harker plots, REE plots and multi-element spidergrams. Multi-element plots reveal more information compared to the REE as they allow comparison between the LILE and the HFSE (Rollinson, 2014). The average whole-rock ICP-MS obtained trace element data for all target rocks and impactites are presented in Table 3.3 and Appendix 3C and D, respectively.

In terms of their behaviour and without going into too much detail, the trace elements relevant to this study may be subdivided into the following major groups (V.M. Goldschmidt and others, in Rollinson, 1993; White, 1998):

1) **Lithophile elements**, characterized by their affinity to oxygen and commonly also silicon. Among the lithophile elements there is a distinction between: a) the Large Ion Lithophile Elements (LILE; e.g., K, Rb, Sr, Ba) that are compatible in the main silicate minerals that make up the continental crust (e.g. feldspars, phyllosilicates); b) the High Field Strength Elements (HFSE) are Zr, Hf, Y, Nb, and the Rare Earth Elements (REE) from La to Lu; Ta, Th and U, that have high ionic charges and are thus unable to fit into the crystal structure of common silicate minerals, and c) the Transition Metals (Sc, Ti, V, Cr).

Table 3.3: Mean and standard deviation data for trace and rare earth elements of target rocks and impactites from the M4 core.

	Granitic Gneiss		Trondhjemitic Gneiss		Metadolerite		Dolerite		Dioritic Gneiss		Suevite		Melt Matrix Breccia	
	n=14		n=4		n=3		n=3		n=8		n=10		n=8	
Trace Element (ppm)	Mean	S.D.*	Mean	S.D.*	Mean	S.D.*	Mean	S.D.*	Mean	S.D.*	Mean	S.D.*	Mean	S.D.*
Li	16.14	7.53	28.87	9.45	34.02	29.74	67.64	0.00	48.68	16.14	71.60	47.60	53.52	28.37
P	228.25	111.67	290.96	32.07	536.50	53.85	620.46	145.36	1990.71	294.27	980.40	634.70	976.05	329.33
Sc	1.21	0.60	2.05	0.40	37.69	7.09	23.93	2.98	6.93	3.20	7.80	6.40	10.14	12.28
Ti	978.61	446.98	1111.86	66.11	4370.78	1385.64	6680.48	2381.99	4432.12	634.25	3306.20	1022.80	4352.74	1419.86
V	16.94	7.76	10.70	1.34	216.73	4.38	282.98	27.73	75.01	6.05	115.50	50.80	135.29	47.18
Cr	8.01	6.39	5.40	0.37	474.67	48.27	60.01	13.95	33.92	40.50	141.70	103.70	123.45	92.42
Co	3.06	0.96	3.55	0.42	41.72	17.07	46.23	15.29	12.30	3.77	21.40	10.70	22.86	9.54
Ni	9.19	9.67	14.03	3.88	168.57	46.07	74.46	31.23	17.58	10.33	132.10	84.10	82.92	24.83
Cu	20.64	46.09	4.16	1.01	40.18	9.02	113.56	43.73	35.61	42.97	91.30	60.00	54.22	30.35
Zn	24.85	23.21	14.44	3.98	47.06	14.30	128.25	76.10	56.41	33.36	58.10	16.40	62.32	25.45
Ga	14.29	1.98	12.35	2.86	13.96	4.53	16.16	4.28	21.22	5.48	22.40	16.90	17.73	2.45
As	0.09	0.05	0.06	0.00	0.62	0.14	0.78	0.38	0.48	0.26	0.40	0.10	0.46	0.18
Rb	69.66	34.55	5.64	1.15	6.47	2.42	56.40	22.06	42.15	23.95	58.40	81.20	53.57	31.61
Sr	297.19	148.08	413.53	124.76	610.96	261.36	343.47	118.68	652.49	149.10	455.10	357.00	514.29	121.40
Y	2.87	1.65	3.25	1.20	20.21	3.69	20.40	0.26	25.39	11.52	13.10	3.60	16.94	4.69
Zr	82.22	37.74	87.04	10.92	71.53	12.96	88.34	28.98	170.31	64.09	123.10	32.20	128.22	18.50
Nb	4.06	2.45	4.48	0.40	3.70	1.13	5.07	1.14	17.55	7.47	14.70	25.00	8.93	2.47
Ba	654.03	270.46	52.53	25.62	39.89	24.07	226.93	123.75	390.46	198.55	388.40	415.00	441.40	251.81
Sn	0.91	0.30	0.77	0.06	1.01	0.00	1.63	0.00	3.40	0.97	1.40	1.20	1.11	0.30
Cs	2.40	1.01	1.15	0.49	0.77	0.19	5.01	1.99	6.36	6.76	5.80	9.70	2.35	0.66
La	10.49	5.56	13.92	2.70	16.72	4.38	13.10	0.74	64.29	8.40	44.50	61.50	25.77	3.65
Ce	18.33	9.47	25.75	3.51	26.91	5.25	25.15	4.44	117.01	27.51	76.80	93.50	50.12	12.76
Pr	2.20	1.22	2.87	0.65	4.30	0.90	3.71	0.19	13.91	2.11	8.70	9.20	6.24	1.12
Nd	7.46	4.12	9.59	2.21	17.25	3.34	15.41	0.71	47.98	7.58	30.30	28.00	23.31	4.57
Sm	1.50	0.57	1.47	0.41	3.53	0.67	3.58	0.14	7.95	2.11	4.70	2.60	4.55	1.03
Eu	0.66	0.14	0.39	0.10	0.99	0.16	1.07	0.11	1.63	0.25	1.30	0.50	1.29	0.30
Gd	0.99	0.51	1.31	0.28	3.54	0.65	3.73	0.30	7.39	1.93	4.50	2.60	4.40	0.96
Tb	0.10	0.06	0.13	0.05	0.57	0.10	0.61	0.03	0.93	0.36	0.50	0.20	0.60	0.14
Dy	0.52	0.31	0.64	0.23	3.50	0.62	3.74	0.16	4.79	2.21	2.70	0.80	3.26	0.85
Ho	0.08	0.05	0.10	0.04	0.70	0.12	0.75	0.03	0.84	0.42	0.50	0.10	0.62	0.17
Er	0.24	0.14	0.27	0.10	1.82	0.32	1.94	0.14	2.25	1.08	1.40	0.40	1.65	0.46
Tm	0.03	0.02	0.03	0.02	0.27	0.05	0.29	0.02	0.32	0.17	0.20	0.10	0.24	0.07
Yb	0.22	0.13	0.22	0.08	1.63	0.26	1.78	0.17	1.92	0.89	1.20	0.30	1.49	0.43
Lu	0.03	0.02	0.03	0.01	0.24	0.03	0.27	0.03	0.26	0.10	0.20	0.00	0.22	0.06
Hf	2.38	1.03	2.41	0.34	1.77	0.30	2.35	0.83	3.86	1.53	3.10	0.80	3.30	0.48
Ta	0.28	0.26	0.16	0.03	0.21	0.06	0.32	0.08	2.05	0.95	0.70	0.40	0.69	0.30
W	0.12	0.06	0.15	0.04	0.50	0.17	0.37	0.10	0.21	0.12	0.60	0.10	0.50	0.19
Pb	11.03	9.05	5.23	1.07	1.67	0.55	7.60	3.45	9.07	6.07	6.70	1.80	9.14	4.34
Th	2.09	1.13	2.66	0.66	1.22	0.26	2.07	0.12	7.32	2.78	3.70	3.50	3.51	0.49
U	1.67	1.69	1.14	0.82	0.25	0.01	0.49	0.16	2.76	1.43	3.10	2.40	1.77	0.16

All analyses by ICP-MS; all data in ppm, n = number of samples; S.D. = Standard Deviation; shaded block: Rare Earth Elements (REE), n.d. = not detected.*

2) **Chalcophile elements,** so named for their affinity to bind with sulphur (Ag, As, Bi, Cd, Cu, Ga, Ge, Hg, In, Pb, Po, S, Sb, Se, Sn, Te, Tl and Zn);

3) **Siderophile elements**, so named for their affinity to iron. They are commonly found in a native state (Au, Co, Fe, Ir, Mo, Ni, Os, Pd, Pt, Rh, Ru, Ge, Ag, W, Mn). These are generally enriched in mantle-derived rocks (basalts/dolerite) and meteorites.

3.4.1 Trace element analysis in target rocks

In Figure 3.9, selected trace elements for target rocks are plotted in order to investigate their concentration and identify variations and distribution within the target rocks. The average whole-rock ICP-MS obtained trace element data for all target rocks are presented in Table 3.3 and individual sample data in Appendix 3C. In Table 3.3, the silicified metadolerites are not included in the mean calculations as they are quite distinct from the other metadolerites. Their trace element concentrations can be viewed in Appendix 3C.

3.4.1.1 Granitoid Gneisses

Rubidium (Figure 3.9A), displays no clear pattern with Sr, among the suite of the trondhjemitic-granitic gneisses. It is almost completely absent in the trondhjemitic gneiss, which is K-feldspar-poor. Dioritic gneiss and, to a lesser extent, the metadolerite are more enriched in Rb relative to Sr when compared to the trondhjemitic gneisses, but are depleted relative to the granitic-granodioritic gneisses. Sr is relatively mobile and is easily leached during weathering (Rollinson, 1993; 2014). Its low concentration is thus probably not surprising for the uppermost samples but it is significantly enriched in the silicifed metadolerite samples (Figure 3.9A). Ba (Figure 3.9E) and Sr (Figure 3.9A), which substitute for Ca, and which are therefore a proxy for plagioclase, show high concentrations in granitic-granodioritic gneisses and dioritic gneisses but, whilst the trondhjemitic gneiss shows overlap with the granitoid gneisses for Sr, it has very distinctly low Ba. Rb (Figure 3.9A), which substitutes for K, shows a good correlation for the granitic-granodioritic gneisses, which confirms a primarily K-feldspar control, its virtual absence in the trondhjemitic gneisses is consistent with the scarcity of K-feldspar.

The Th/U ratio shows considerable variation in all target rocks (Figure 3.9B) with no distinct pattern visible. Most the samples from the M4 core display a Th/U ratio that is less that the average for common crustal rocks (2.8 ppm) (Yanagi, 2011). The dioritic gneisses display a higher but variable Th/U (Figure 3.9B). In Figure 3.9C, Nb versus Y shows diorites with a high concentration in Nb.

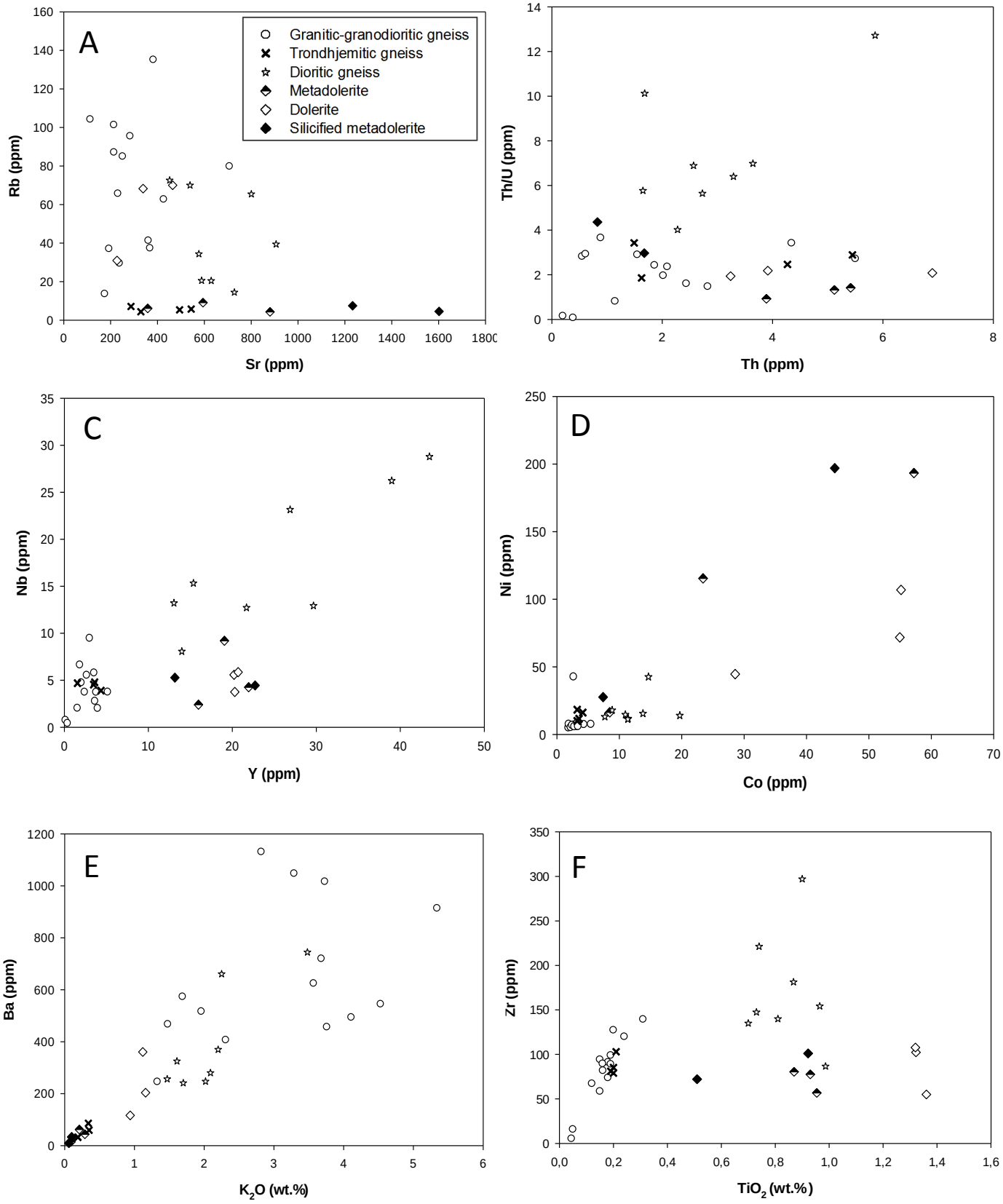

Figure 3.9 (A-F) Binary and inter-element plots for selected M4 core target rocks. All trace element data in ppm.

The Nb concentration is controlled by the presence of titanite or rutile and ilmenite (Rollinson, 2014). The diorites contain relatively abundant ilmenite and titanite. For Ni versus Co (Figure 3.9D), no distinct trend is observable. Barium (Figure 3.9E) is a LILE element and tends therefore to increase with the fractionation of melts, being most compatible with the lattice of K-feldspar, but also to a lesser extent, with that of biotite and plagioclase (White, 1998); for this reason, its high concentration in the K-rich granitoids relative to the trondhjemitic gneisses is not unexpected. Significantly, some dioritic gneiss samples are also enriched in Ba, likely reflecting their higher biotite content relative to the granitoid gneisses. The dioritic gneiss displays similar TiO_2 values to the metadolerite, but very little Cr, suggesting that biotite is the main Ti-reservoir. In Figure 3.9F, there is an observable good clustering of granitic-granodioritic gneisses with trondhjemitic gneisses, but the dioritic gneisses form their own cluster that is significantly enriched in both Zr and Ti (TiO_2), consistent with higher zircon, biotite, titanite and ilmenite contents (Section 2.3.3.2 and Chapter 4). Unusual Zr depletion in granitic rocks mirrors the low zircon contents found in mineral separates (R. Gibson, pers. comm., 2016).

3.4.1.2 Dolerite and metadolerite

The dolerite and the metadolerite samples show distinctive differences in their trace element geochemistry (Figure 3.9 A, D, E, F). Silicified metadolerites have the highest concentrations of Sr although these are the most highly metasomatised target rocks (Figure 3.9 A). The dolerite and metadolerite display Th/U ratios less than the crustal average. The dolerites and metadolerites have high Cr, Ni and Co, which is typical of mafic rocks (Table 3.3). The metadolerite records the highest concentrations/abundances of the siderophile elements (Cr, Co, Ni; Figure 3.9D, Appendix 3C). Cr is compatible in orthopyroxene and clinopyroxene and hence found more in mafic rocks compared to granitoid rocks (White, 1998).

The metadolerite shows higher concentrations in Ni than the dolerite. In Figure 3.9F, there is a good distinction between metadolerites and dolerites. The granitic-granodioritic and trondhjemitic gneisses have Zr concentrations that do not differ significantly from that of the (more Ti-enriched) dolerites (Figure 3.9F). The metadolerite samples show a higher Ni:Co ratio than the dolerite, and Figure 3.9D seems to support the two highly altered samples originally being metadolerite, rather than dolerite or some other rock type.

The metadolerite and dolerite trace element character is further explored in Figure 3.10. The plot of P/Ti versus Zr/P (Bowen et al., 1986) is a discriminatory plot commonly used for volcanics of the Witwatersrand region of the Kaapvaal craton. The metadolerite and dolerite analyses are scattered between the Klipriviersberg Group and Dominion Group basic lavas (Figure 3.10). Note one outlier (M4 IS-1) which erroneously falls in the Rietgat Goedgenoeg group. The Dominion Group basic lavas

are 3.1 Ga and the granitoids are 2.9 Ga which makes the Dominion correlation unlikely; however, these correlations are explored further in Chapter 6.

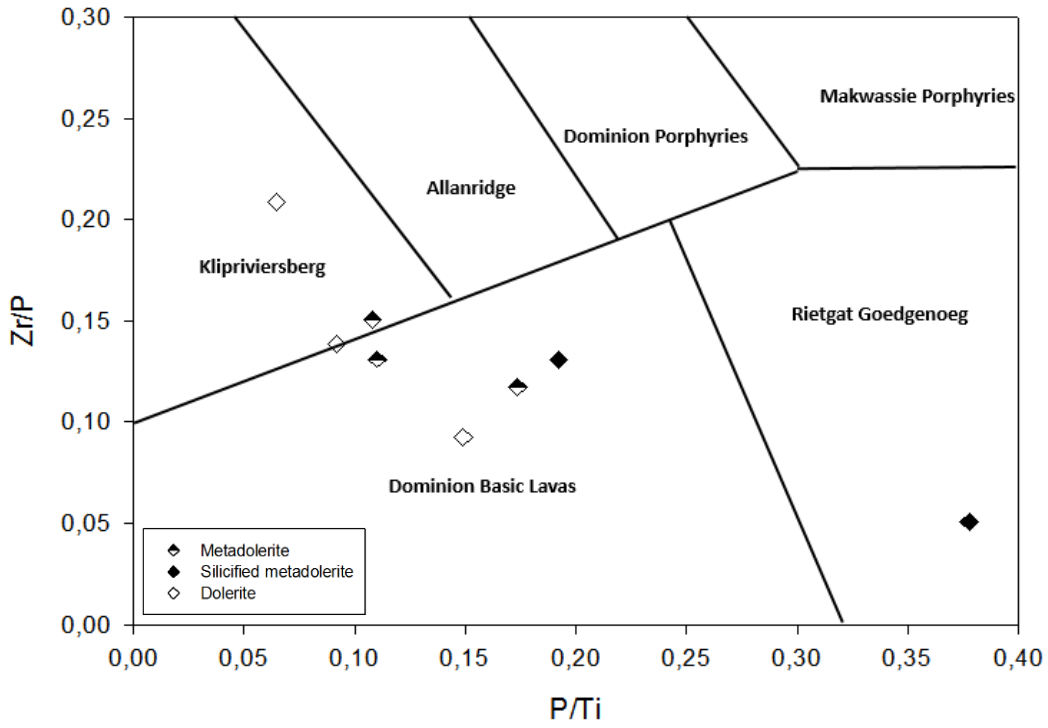

Figure 3.10: Discrimination diagram of volcanic sequences of the Witwatersrand (Bowen et al., 1986).

3.5 Trace element analysis of impactites

The average whole-rock ICP-MS obtained trace element data for all impactites are presented in Table 3.3. The impactites are plotted together with target rocks in Figure 3.11. No discernable trace element trends or patterns are observed in Figure 3.11, other than that there is considerable compositional overlap between the suevites and MMBr and a positive correlation between Nb vs. Y (Figure 3.11C) and Ba vs. K_2O (Figure 3.11E). However, the MMBr are slightly enriched in Rb, and in Th relative to U, although the Th/U ratio falls well below the crustal average for all samples. Suevite M4 S-6 shows anomalous enrichment in Ba, Rb, Sr, Zr and Cr, and a Th/U ratio closest to the crustal average (Figure 3.11B).

3.5.1 Comparison of impactites and target rocks

In all trace element Harker plots, the impactite rock compositions generally lie within the compositional field defined by the target rocks (Figure 3.11). These trends are similar to those noted in Harker plots

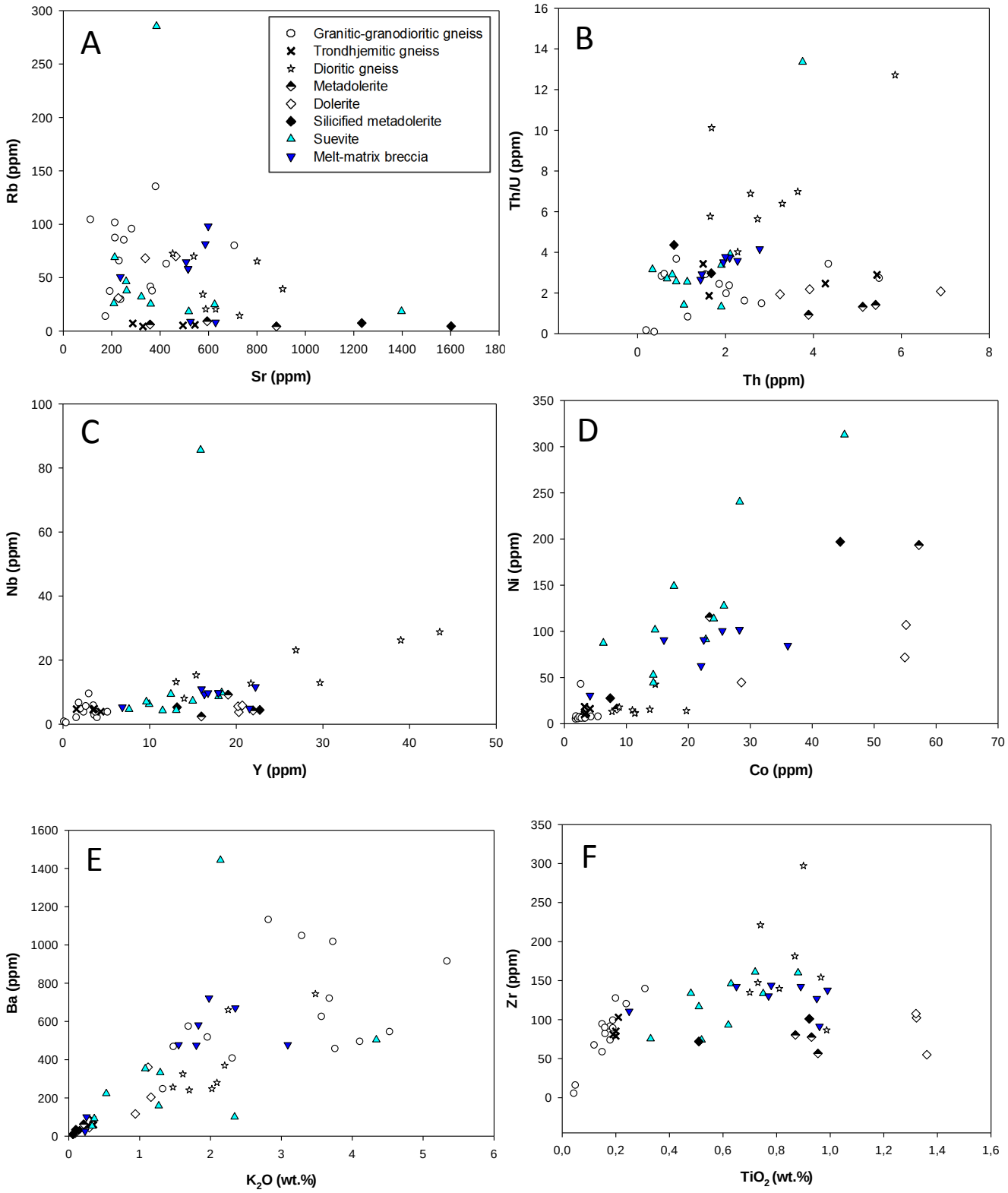

Figure 3:11 Plots of whole-rock trace elements for target rocks and impactites. All data is in ppm unless indicated.

for major elements in Figure 3.6. In Figure 3.11A, suevite sample M4 S-6 shows anomalously high Rb value relative to the other impactites, which generally fall within the field defined by the target rocks. Somewhat surprisingly, given the extensive evidence for hydrothermal alteration (Section 2.5), there appears to be little significant elemental enrichment or depletion of the impactites relative to the less altered target rocks (Figure 3.11A). In Figure 3.11 C, the Nb shows a positive correlation with Y, with distinct clusters of granitic-granodioritic gneisses and trondhjemitic gneisses visible. M4S-6 has a high Nb content and again forms a distinct outlier (see also Figure 3.11B, C). The impactites are to a certain extent more enriched in Ni and Co compared to granitoids (Figure 3.11D) and in Figure 3.11F, the impactites mostly overlap with metadolerites and dioritic gneisses. In both cases, it may be that the impactites contain mineral clasts of zircon and titanite, but this requires further investigation.

3.5.2 Depth-dependence of trace elements in target rocks and impactites

Selected trace elements for both target rocks and impactites are plotted against depth in Figure 3.12 in order to examine their vertical variations in concentration and distribution. The impactites show close correlation with their wallrock host target rocks (Figure 3.12).

Rb (Figure 3.12A) and, to a lesser extent, Ba (Figure 3.12D) are depleted in the intermediate levels (180 m to 250 m depth), dominated by trondhjemitic gneisses and metadolerite. This host rock-impactite correlation is not observed above 180 m nor below 250 m depth where data is more scattered in Figures 3.12A, C and D, although some correlation in these upper and lower zones is observed. The exception is the extremely elevated Rb content of suevite sample M4 S-6 (Figure 3.12A). Zr content is relatively uniform, except for the dioritic gneiss which shows some elevated values (Figure 3.12C). The pattern of Ba with depth (Figure 3.12D) resembles that of K_2O with depth (Figure 3.8H); which is quite expected as the trondhjemites and metadolerites are potassium poor. In contrast, the absence of a distinct pattern for Sr with depth could be because it is mobile during alteration and weathering (Rollinson, 2014) (Figure 3.12B).

Bulk XRD analysis, petrographic and EMP analysis of the suevites and MMBr indicates that the impactites are characterized by complex low-temperature hydrothermal parageneses involving mainly clays and zeolites. This may explain the somewhat greater divergence in Sr and Ba in the more porous impactites relative to the target rocks (Figure 3.12B, D), however, differences are rather small, which might mean that fluid transport of ions over significant distances may have been limited.

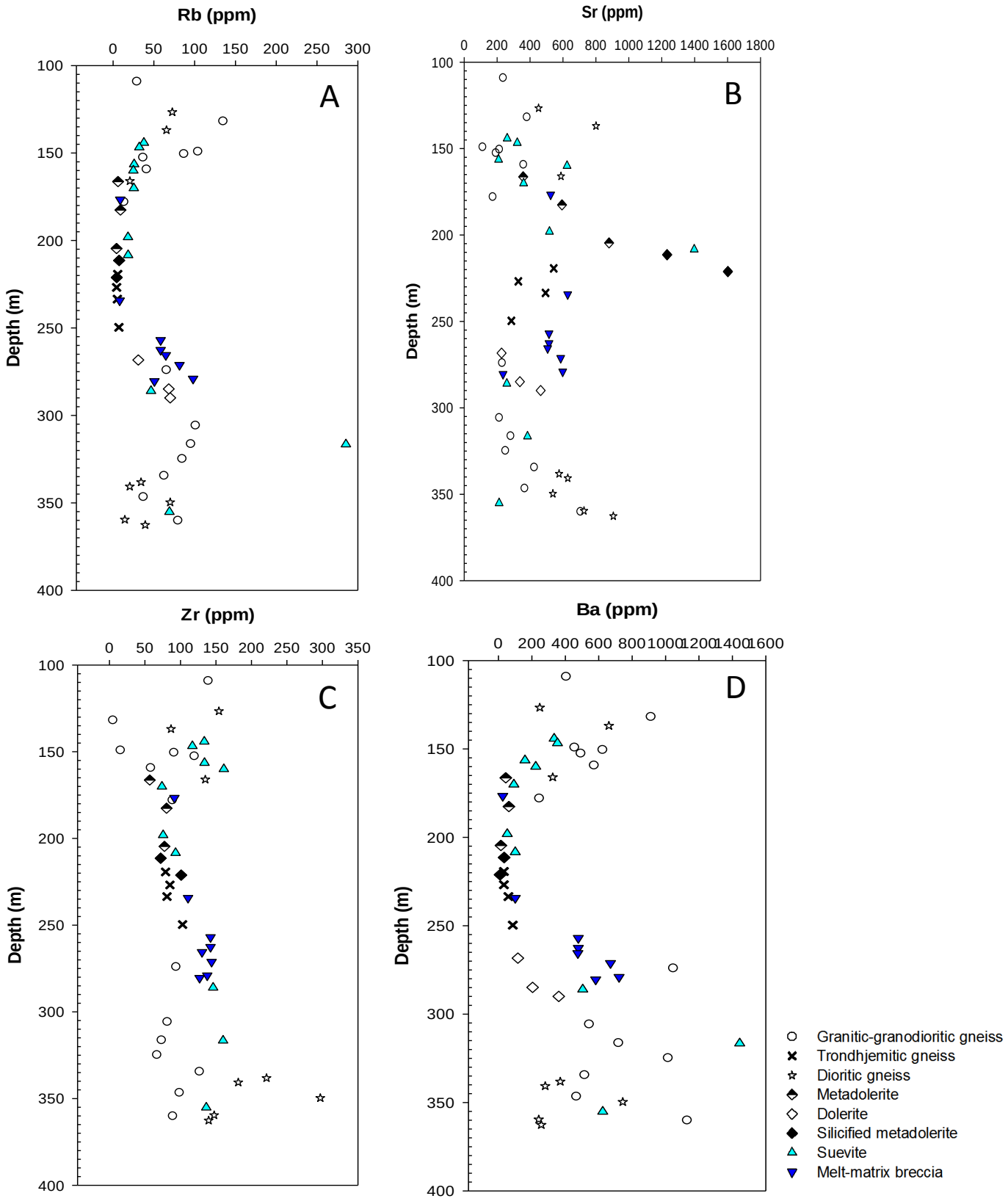

Figure 3.12: Stratigraphic variation in whole-rock content of **A)** Rb, **B)** Sr, **C)** Zr and **D)** Ba versus depth in the M4 core.

3.6 Rare earth element (REE) analysis of target rocks

Mean rare earth element (REE) data obtained by ICP-MS analysis are presented in Table 3.3 with the full dataset being provided in Appendix 3C. The data (normalised to C1-chondrite; Taylor and McLennan, 1985) are plotted in Figures 3.13 and 3.14 according to the main lithological groups identified in Section 3.3. All REE profiles show an enrichment of light rare earth elements (LREE) relative to heavy rare earth elements (HREE), which is typical of upper crustal rocks (Rollinson, 2014). This aspect is explored further in Chapter 6.

3.6.1 Granitoid Gneisses

Comparison of the individual REE profiles of the granitic-granodioritic gneisses (Figure 3.13A), trondhjemitic gneiss (Figure 3.13B) and dioritic gneiss (Figure 3.13C) is made in Figures 3.14A and B. The granitic-granodioritic gneisses have the lowest REE contents relative to other target rocks. All profiles show relative enrichment in LREE relative to HREE, but overall REE abundance is highest in the dioritic gneisses. These gneisses are characterized by a positive Eu anomaly (Figure 3.13A) that reflects the relatively high plagioclase content consistent with petrographic observations (Section 2.3.1.2). The leucocratic granite veins (M4 GG-2 and M4 GG-6) have the most extreme positive Eu and Sm anomalies of all samples, but the lowest overall REE abundance (close to detection limits; confirmed by duplicate runs). This may reflect the extremely leucocratic nature of these veins, with an almost complete absence of mafic or REE-bearing minerals such as monazite and zircon. R. Gibson (pers. comm., 2015) reported that the leucogranite contained almost no zircons for U/Pb dating purposes (see also the low Zr content, Appendix 3A, C). The results of these two samples are kept separate from the other granitoids in the subsequent discussion. A weak negative Ce anomaly is noted in most samples.

The trondhjemitic gneiss samples show REE patterns similar to those of the granitic-granodioritic gneisses (Figures 3.13B; 14A and B). Three samples show slightly negative Eu anomalies, whilst the fourth is slightly positive (sample M4 FZ-3 from 226.80 m depth). The latter also displays a slight positive Ce anomaly, whilst another shows a more marked negative Ce anomaly (Figure 3.11B) that could suggest variable oxidation-reduction reactions during either the pre- or post-impact hydrothermal infiltration events (Rollinson, 1993).

The **dioritic gneiss** samples are enriched in REE relative to the other M4 core granitoid lithologies (Figure 3.13C; 14A and B), and show greater enrichment in LREE relative to HREE. The enrichment in LREE can be related to the enrichment in zircon, apatite, titanite and biotite that was observed in the dioritic gneisses (Section 2.3.3.2). All samples display a negative Eu anomaly and two samples have a negative Ce anomaly whereas another two have a positive anomaly (Figure 3.13C).

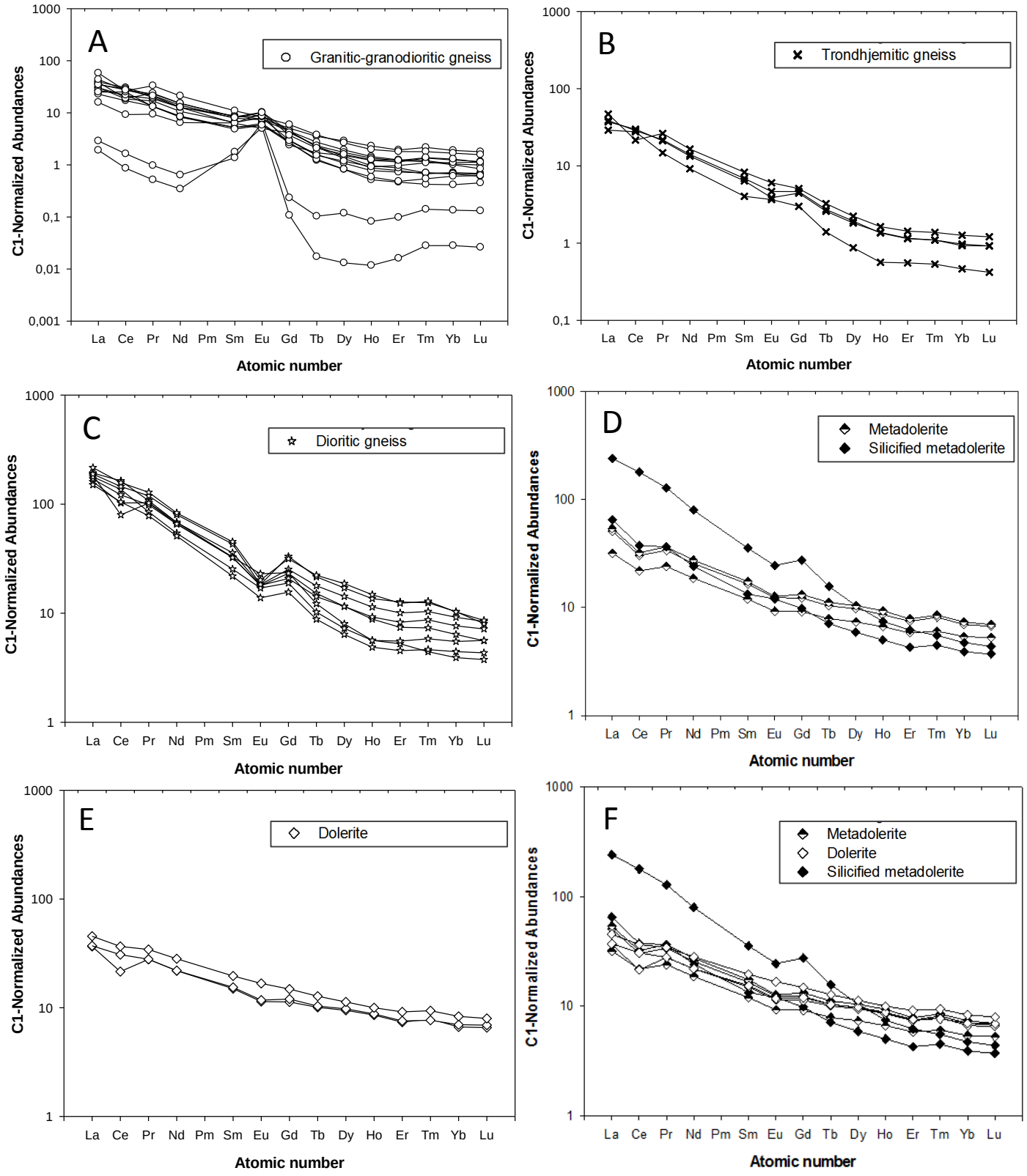

Figure 3.13: Chondrite-normalized rare earth element (REE) abundance diagrams for the M4 core target rocks. Normalization factors from Taylor and Mc Lennan (1985). **A)** REE pattern for **14** granitic-granodioritic gneiss samples. **B)** REE pattern for **4** trondhjemitic gneiss samples. **C)** REE pattern for dioritic gneiss samples. **D)** REE pattern for **3** metadolerite samples and **2** silicified metadolerite samples. **E)** REE pattern for **3** dolerite samples. **F)** REE pattern comparing the REE abundance of dolerite and metadolerite samples.

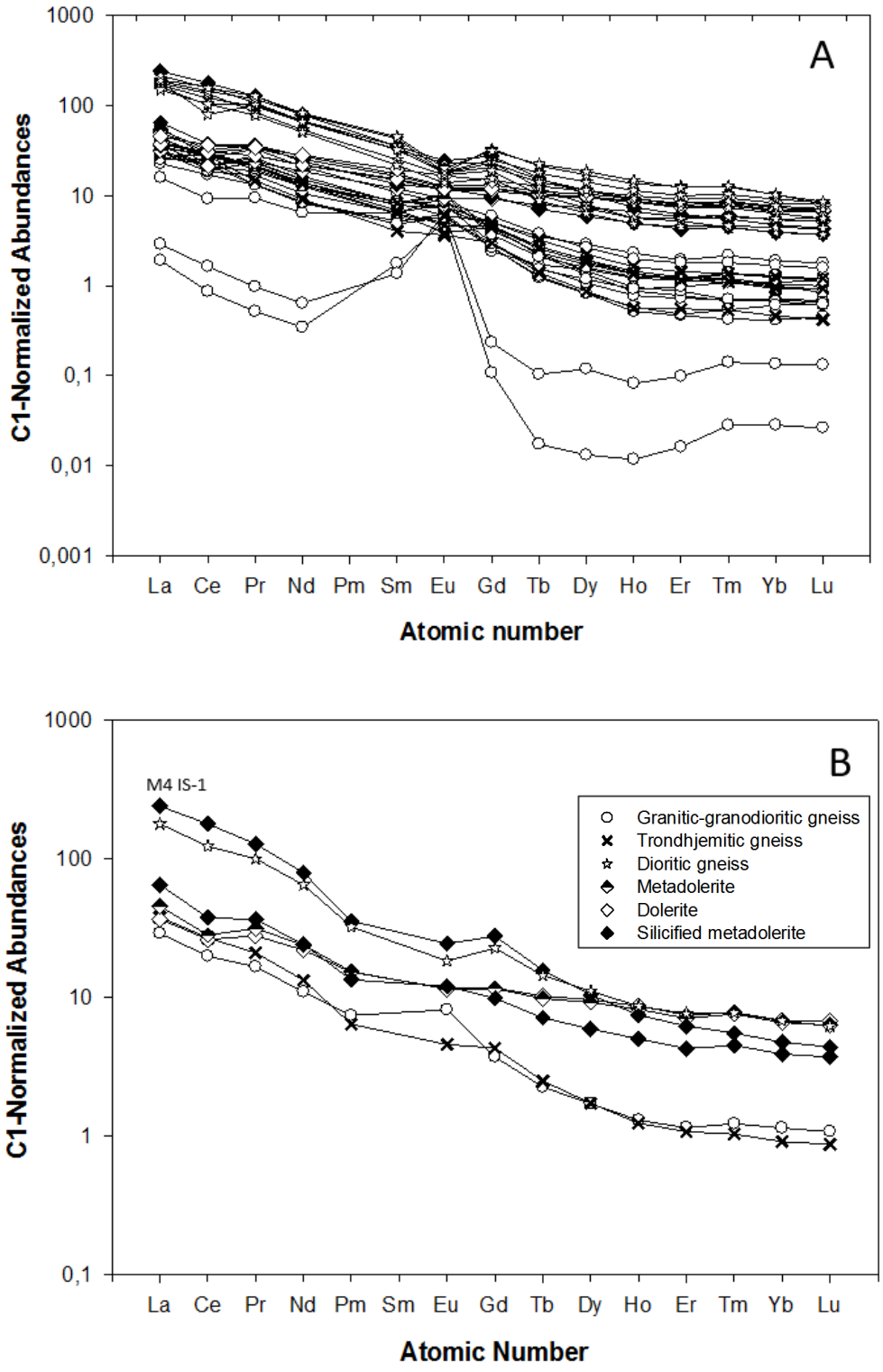

Figure 3.14: **A)** Compilation of REE patterns for all M4 core target rock samples. **B)** Compilation of REE pattern for averages of data for each rock type in A. Normalization factors from Taylor and McLennan (1985).

3.6.2 Dolerite and metadolerite

In Figure 3.13D-F, metadolerite and dolerite samples show REE patterns that indicate a slight enrichment in LREE relative to HREE. Overall, they show less relative enrichment in LREE over HREE compared to the granitoid rocks. In contrast to the major and trace elements, the two suites show very similar REE profiles (Figure 3.13F); however, the samples of metadolerite are more enriched in LREE and depleted in HREE relative to the dolerite samples. All samples have a negative Ce anomaly, possibly indicative ofoxidation alteration influence (Rollinson, 1993), except for one highly LREE-enriched sample (Figure 3.13D). This sample (M4 IS-1 from 221.20 m depth) shows LREE values slightly higher than even the dioritic gneiss. It displays very high degrees of alteration (Section 2.3.4.3; Figure 2.11), having been sampled from a fracture/quartz vein zone with good evidence of metasomatism marked by an assemblage enriched in epidote-titanite and quartz. It also displays a slight negative Eu anomaly, similar to all but one of the other metadolerite samples.

Two dolerite samples show a slight negative Eu anomaly, and one (sample M4 SILL-1 from 268.30 m depth) shows a significant negative Ce anomaly. Figure 3.14 shows all (A) and combined averaged (B) data for the M4 core target rocks, with the two leucogranite and one silicified metadolerite samples excluded.

The granitic-granodioritic gneisses consistently show the most depleted profiles, and the trondhjemitic gneiss shows similar values. The dioritic gneiss and LREE-enriched metadolerite sample are most enriched and show very similar profiles, but they are overlapped by the dolerite suite for HREE. However, the dolerite suite is less LREE-enriched relative to its HREE content than the other lithologies; consequently, its flatter profile lies discordantly with respect to the other target rocks in Figure 3.14, with LREE values approaching those of the granitic-granodioritic gneisses.

3.7 Rare earth element (REE) analysis of impactites

Chondrite-normalized REE profiles for all impactites analysed from the M4 core are shown in Figure 3.15. Except for suevite sample M4 S-6 and MMBr sample M4 IM-1, the impactites show very similar REE patterns (Figure 3.16).

3.7.1 Comparison of suevites and melt-matrix breccias

The suevite samples generally show similar REE profiles defined by a moderate LREE enrichment and a relatively flat HREE profile (Figure 3.15A). It is also worth mentioning that the suevite samples M4 S-8 and M4 S-9 (depth: 170.07 and 198.03 m, respectively) are in the metadolerite interval; this can explain their lower LREE concentrations compared to the other, granitoid-hosted, suevites and provides further support for localised derivation of the M4 core suevite (see Figure 3.12). The most anomalous suevite sample is M4 S-6. It displays significant enrichment in the LREE and MREE and a pronounced positive Gd anomaly compared to the other suevites (Figure 3.15 A). All suevite samples show slight negative Ce anomalies. Suevite sample M4 S-10 (depth: 208.34 m), displays the lowest HREE content of all suevite samples, and a slightly steeper LREE pattern (Figure 3.16).

Melt-matrix breccias show an almost identical pattern to the suevites, with LREE enrichment relative to HREE and relatively flat HREE profiles (Figures 3.15B; 3.16A). However, most samples show a negative Eu anomaly and broadly concordant profiles. The anomalous MMBr samples are M4 IM-1 (depth: 176.60 m) which shows a strong negative Ce anomaly and sample M4 IM-2 (depth: 234.33 m), which is more enriched in LREE relative to HREE (Figure 3.16A). This latter sample shows a significantly lower overall REE abundance than the other MMBr samples, which might be a result of its felsic nature and high hydrothermal alteration state (Section 2.5.2). Samples M4 S-10 and M4 IM-2 both come from more or less the same interval in a zone of silicified metadolerite (Appendix 2A, box 13 and 16).

Except for M4 S-6, most of the REE profiles for suevites and MMBr overlap, including the most REE-depleted suevite and MMBr samples (Figure 3.16A, B). This suggests that the suevites and MMBr are derived from the same source material and that there is no significant difference between the material forming the melt in the MMBr and the clastic matrix in the suevites. This confirms the major and trace element analyses (Section 3.3.3) that suggest the impactites were almost exclusively derived from the target rocks found in the M4 core (Section 2.4), but also the contact relationship observations that show intimate interfingering of clastic-matrix and melt-matrix breccias down to the microscopic level (Chapter 2).

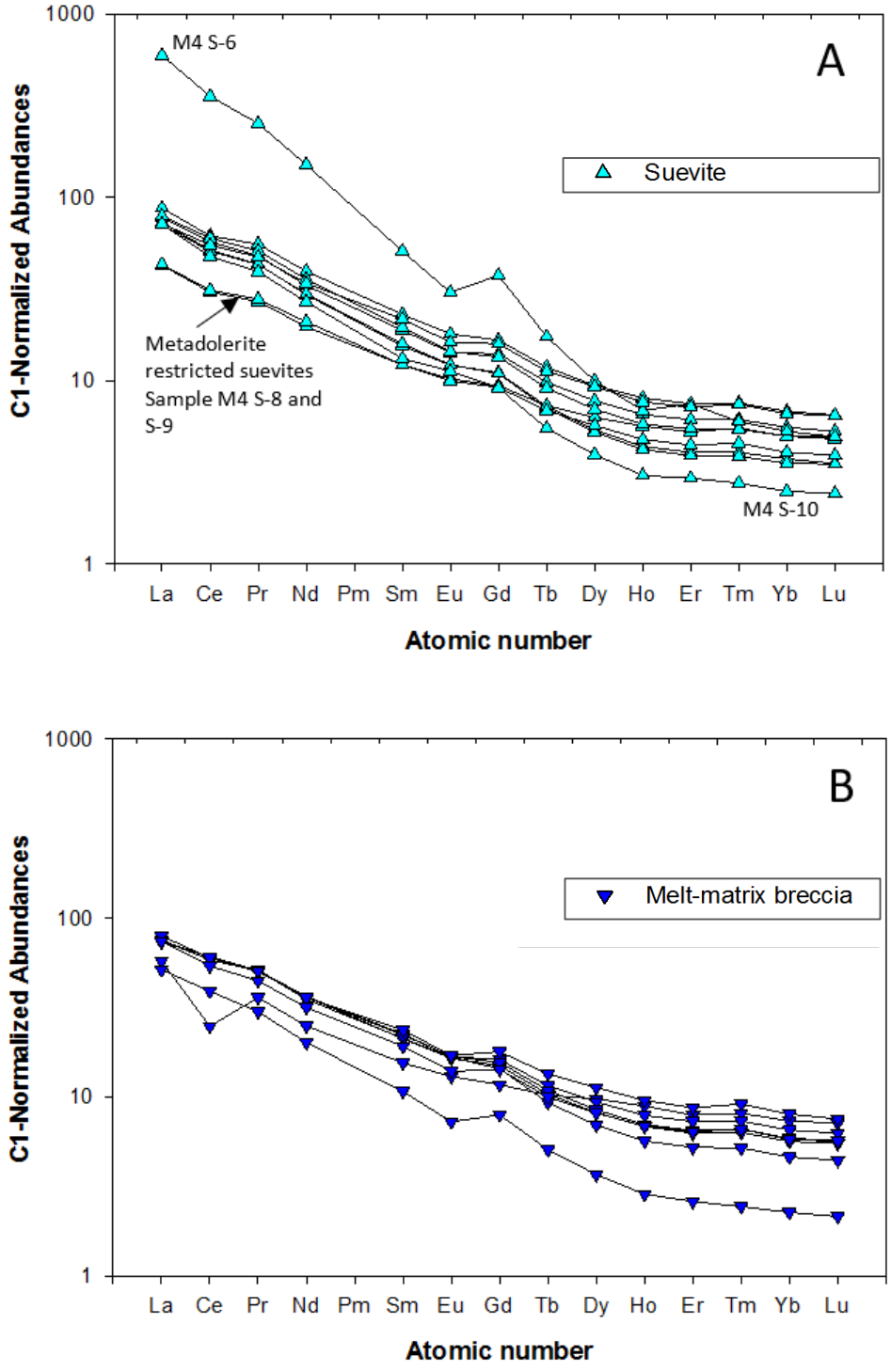

Figure 3.15: Chondrite-normalized rare earth element (REE) abundance diagrams for the M4 core impactites. Normalization factors from Taylor and McLennan (1985). **A)** Suevite REE profiles. **B)** MMBr REE profiles.

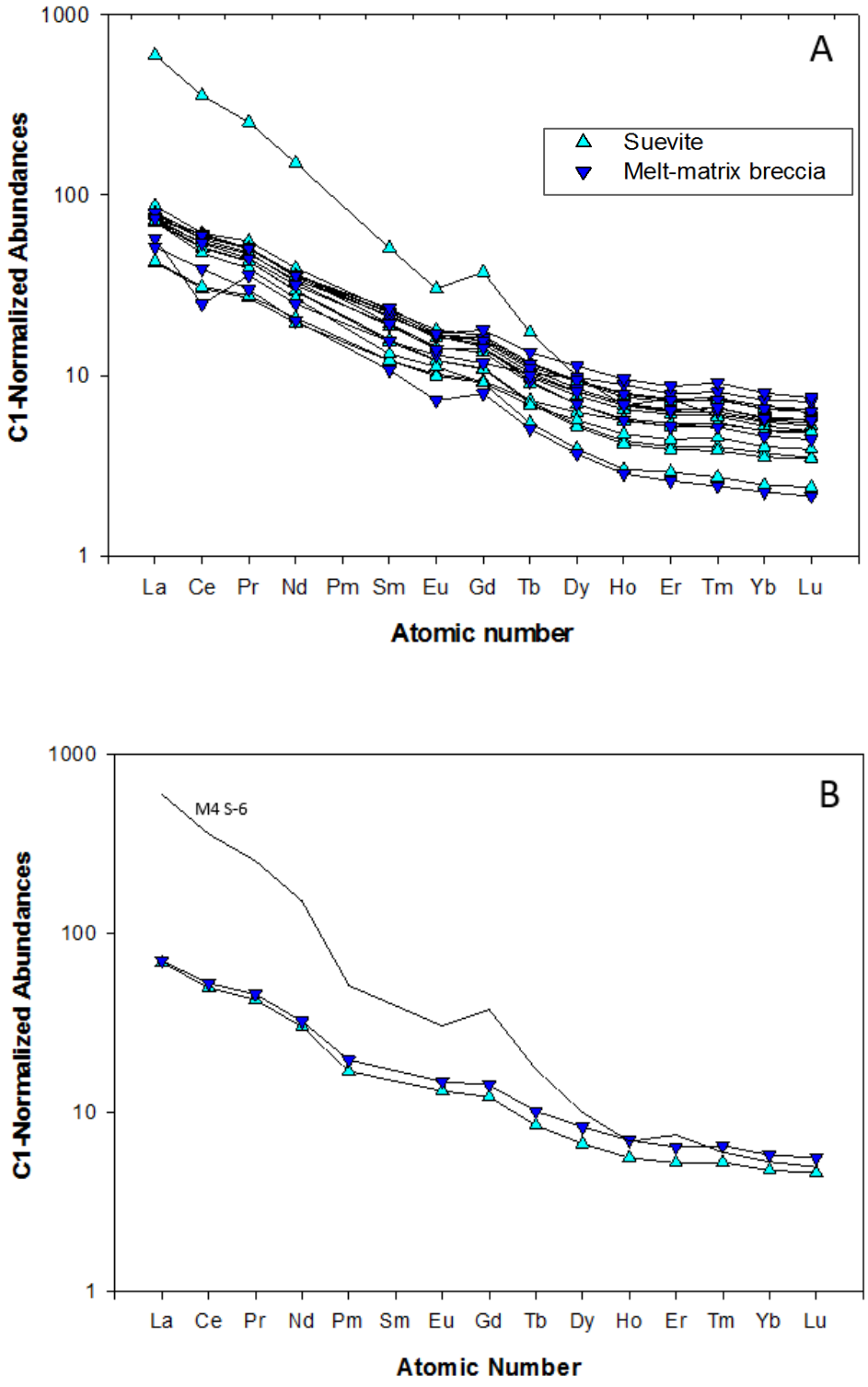

Figure 3.16: **A)** Comparison of chondrite-normalized REE patterns for M4 core suevites and MMBr. **B)** Compilation of REE pattern for averages of data for each rock type in A. The unmarked solid line represents suevite sample M4 S-6. Normalization factors from Taylor and McLennan (1985).

3.7.2 Comparison of impactites and target rocks

In normalized REE diagrams, the suevites and the MMBr have similar REE patterns to the target rocks in the M4 core, with only sample M4 S-6 showing LREE enrichment above the field for the target rocks (Figure 3.17). More specifically, however, the suevites and MMBr most closely mimic the slightly flatter profile (lower LREE enrichment) of the dolerite and metadolerite suites.

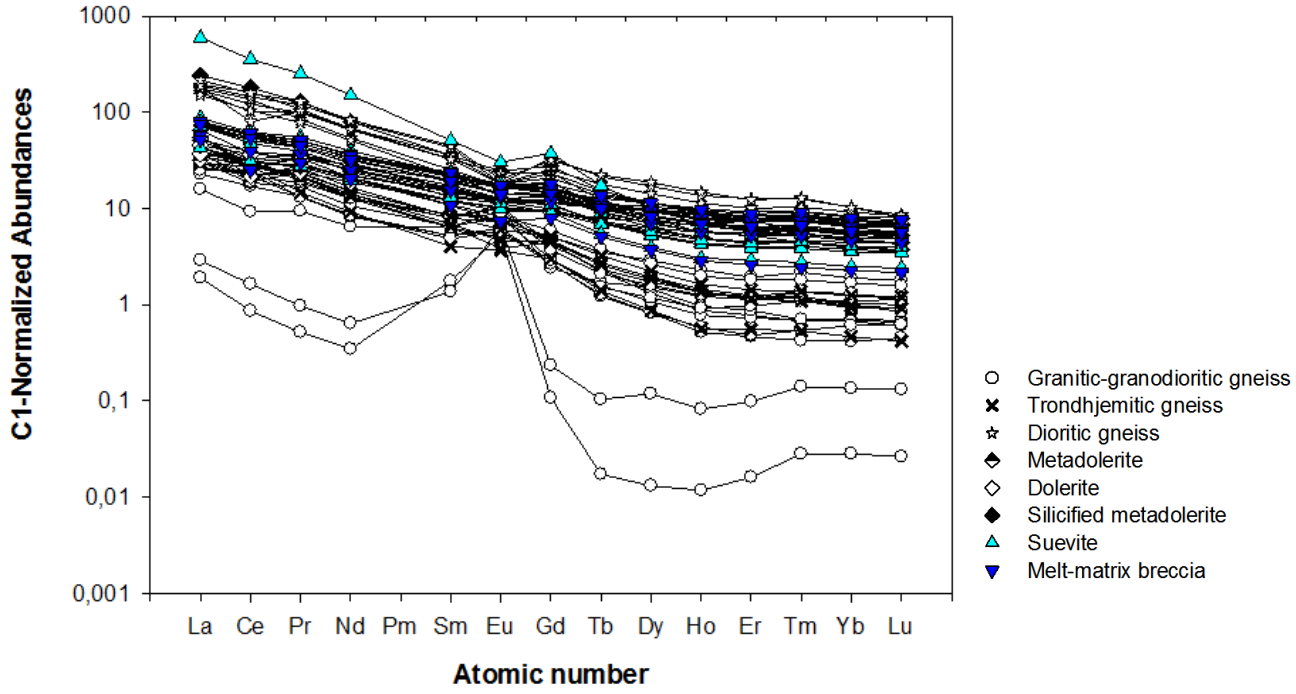

Figure 3.17: Comparison of chondrite-normalized REE patterns for M4 core target rocks and impactites. Normalization factors from Taylor and McLennan (1985).

3.8 Multi-element Spiderdiagrams

The plot of average multi-element compositions, normalised with average continental values from Rudnick and Gao (2003) (Figure 3.18), confirms the overall correspondence between the impactites and major target rock groups. The lower-SiO_2 dioritic gneisses stand out among the target rocks for their enrichment in the HFSE, including the REE, Ta and P. As such they are the most fractionated and differentiated of the granitoid gneisses. The oldest rock identified by U-Pb zircon geochronology (sample M4 GG-3) is 2.92 Ga (R.L. Gibson, personal communication, 2015) and has the highest K, Rb and the lowest Ta, Sr, Ti, Y and HREE of all the granitic-granodioritic gneisses.

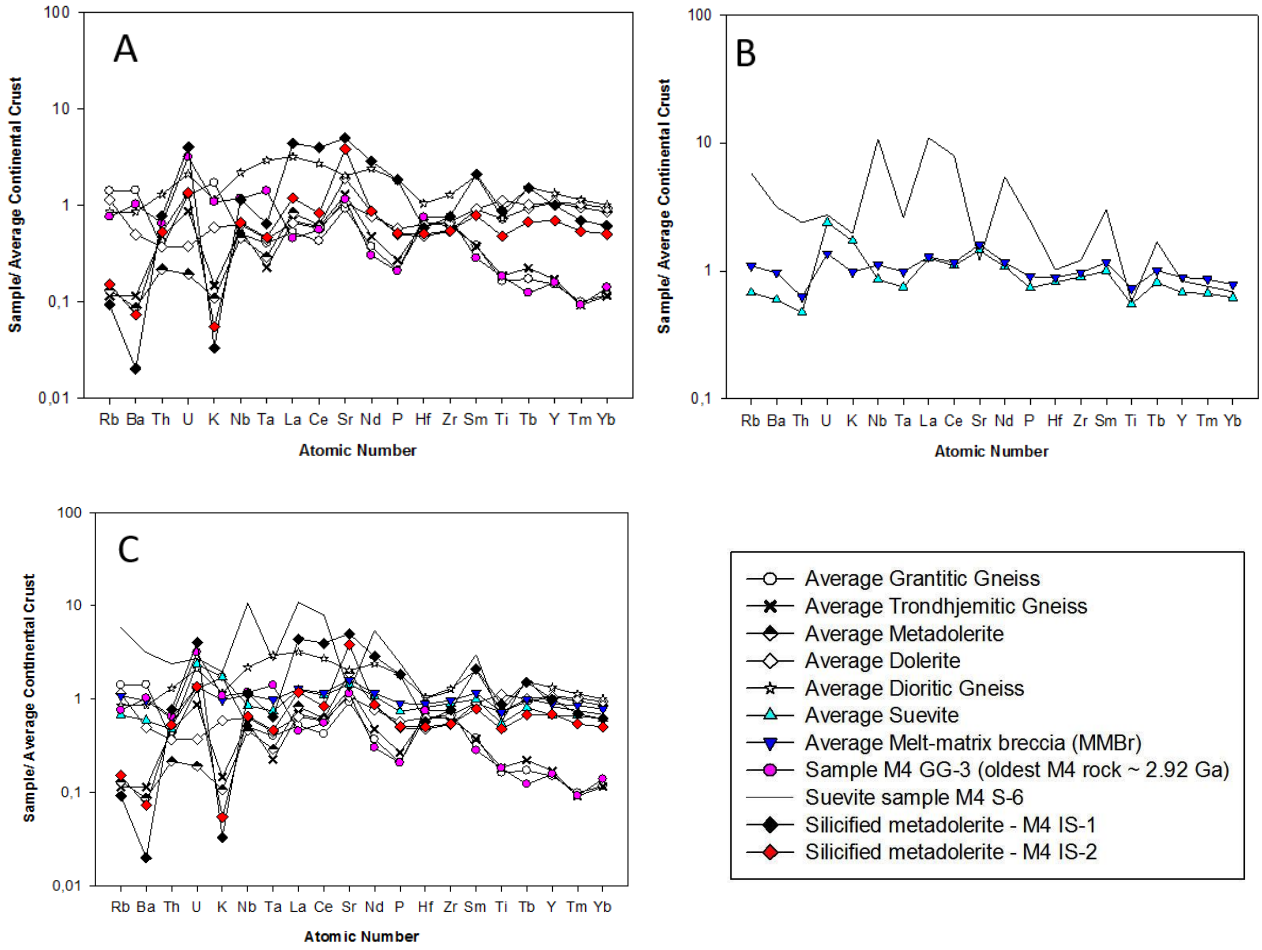

Figure 3.18: Average continental crust normalized multi-element spidergrams for M4 core lithologies. **A)** Target rock lithologies. **B)** Impactite lithologies. **C)** Target rocks and impactites. Normalizing values are from Rudnick and Gao (2003).

The divergence between the two groups towards the right of Figure 3.18A is notable; with the granitic-granodiorite and trondhjemitic gneisses forming one group marked by troughs in Ba, K, P, Ta, Tm, and Ce. The second group consists of dioritic gneiss, dolerite, metadolerite and silicified metadolerite. Dioritic gneiss is quite distinct from the other gneisses. Samples from both groups are enriched in U, and show a negative Ce anomaly except for the dioritic gneiss samples (Figure 3.18A). The granitic-granodioritic-trondhjemitic gneisses are less enriched in Rb, Cs, Ba (heavy LILE), and Sm, Ti, Tb, Y, Tm, Yb compared to other target rocks. Negative Nb is typical for continental crust (Rollinson, 2014), but these M4 lithologies show a positive Nb. Silicified metadolerite is highly enriched in Th and U and has a similar concentration in LILE (Cs, Rb, K, Ba and Sr) to the granitic-granodioritic and trondhjemitic gneisses and metadolerite, whilst they compare to the second group in terms of HFS elements (Y, Hf, Zr, Ti, Nb, and Ta).

The average compositions of most suevite and MMBr samples are very similar, apart from a slight U enrichment, and Rb and K depletion of the former group. The suevite sample M4 S-6 is significantly anomalous compared to the other suevites and MMBr. It is marked by a trough in K, Ta, Sr, Hf, Zr and Ti. Unlike the other suevites and MMBr which are depleted in and Ce, The M4 S-6 has a positive Ce peak and a Sr trough (Figure 3.18B). The depletion in Hf and Zr supports a mantle affinity or derivation of the precursor rocks making up sample M4 S-6 (Rollinson, 2014). Chapter 6 contains more discussion regarding the M4 core lithologies and average continental crust.

3.9 Summary

In all major, trace element and REE discrimination and classification diagrams, three distinct target rock groups are visible: Group 1 (granitic-granodioritic and trondhjemitic gneisses); Group 2 (dioritic gneiss) and Group 3 (metadolerite, silicified metadolerite and dolerite). In the Harker plots of major elements, the Group 1 granitoid gneisses lie on a mixing line which suggests that they are part of the same genetic source, notwithstanding the ca. 20 Myr. difference in age between sample M4 GG-3 and the other samples analysed via single zircon geochronology (R.L. Gibson, personal communication, 2015). Likewise, the trace element data, including the displayed profiles and plots, suggest that the M4 core granitoid target rocks are part of a coherent fractionating system. In South Africa Archaean rocks like these are found in the Vredefort and Johannesburg domes and numerous granite-greenstone terranes such as the well-studied Barberton terrane, where they are generally referred to as the TTG (trondhjemite-tonalite-granodiorite) suite (Lana et al, 2003; Clemens et al, 2006). The Group 2 dioritic gneiss represents a distinct compositional type, as samples display alkaline affinities both in terms of major and trace element geochemistry. The dioritic gneiss is clearly LILE-HFSE-enriched, and in the ternary diagrams of the normative minerals they plot in the monzonite/quartz-monzonite field. Figure 3.3 emphasized the sodic, rather than potassic, character of these intermediate, alkaline rocks. This rock type is not represented in the Kraaipan, Barberton and Vredefort Dome terranes (Lana et al, 2004; Poujol and Anhaeusser, 2001). At present, the chronological/petrogenetic relation between the monzonitic suite and the abovementioned TTG suite gneisses can only be speculated.

The hypabyssal character of the Group 3 mafic intrusive rocks suggests that they are younger cross-cutting sills or dykes (their morphology or geometry cannot be confidently deduced from the drillcore). The rock type classification made based on the chemistry is consistent with that based on petrographic characteristics and modal percentages in Chapter 2. The mafic rocks show a narrow SiO_2 range but significant variability in other major oxides. The notable differences in TiO_2, FeO, MgO, Na_2O and K_2O contents of the dolerite and metadolerite, combined with the differing levels of metamorphism, further confirm them as representing different intrusive events that were, nonetheless, both pre-impact.

The trace element depth plots perfectly reveal the metasomatised nature of trondhjemitic gneiss and the likelihood that the trondhjemitic gneiss and silicified metadadolerite are probably located along a pre-impact fault zone which was likely the pathway for fluids during pre- and post-impact hydrothermal events.

The suevite and MMBr samples overlap compositionally in major and REE plots, but the MMBr shows a narrower and more mafic compositional range compared to the suevite. Most M4 core impactites display intermediate compositions between granitoids and mafic target lithologies found in the core. These observations are supported by macro- and microscopic evidence that shows that the M4 core impactites are largely composed of granitoid gneiss clasts and to a lesser extent mafic clasts. Additionally, the depth dependence assessment verifies the stratigraphic control on the impactites showing that they were derived from the target rocks (except M4 S-6). These lines of evidence, including the noted correlation between the REE profiles of impactite samples and the mafic rocks, support the conclusion that most of the M4 core impactites are locally derived with no exotic component/source (with the exception to this rule being the M4 S-6 suevite sample). The composition of sample M4 S-6 fits that of a calc-alkaline lamprophyre as follows: the calc-alkaline lamprophyres composition ranges from 46-57 wt. % SiO_2 (Rock, 1984); K_2O is 3.85-8.06 wt. %; Rb ranges from 69-262 ppm; Ba ranges from 1090-3270 ppm and troughs are observed in Na-Ta-Ti elements (Aghazadeh et al., 2015). Sample M4 S-6 matches these aspects as it consists of 49 wt % SiO_2, 4.34 wt. % K_2O and troughs are observable in Ta and Ti in Figure 3.18B. The chemistry and trace element geochemistry point to a K_2O-rich, magnesian mafic target rock fitting a calc-alkaline lamprophyre. While this kind of rock has not intersected by the M4 core, it has been described in the Archaean basement of the Johannesburg dome (Prevec et al., 2004). Thus, the possibility that some of the M4 S-6 clasts are fragments of a lamprophyre is suggested.

Chapter 4

Mineral chemistry

4.1 Introduction

The M4 core intersects pre-impact rocks and impact breccias that have been characterised petrographically and chemically in the preceding chapters. Based on macroscopic and whole-rock geochemistry classification, 6 target rock lithologies have been identified, namely: granitic-granodioritic gneiss, trondhjemitic gneiss, dioritic gneiss, metadolerite and dolerite. All these rocks are brecciated and cataclased. They are intruded by mm- to m-scale suevite and MMBr dykes and cut by sub-mm to cm wide quartz (chalcedony), calcite, gypsum and zeolite veins that also contain haematite, magnetite and/or pyrite as significant components in places.

Petrographic analysis of the target rock types in Chapter 2 has revealed that they are dominated by quartz, plagioclase, K-feldspar (microcline), biotite (locally altered to chlorite ± ilmenite/magnetite), titanite, epidote, clinopyroxene, amphibole, ilmenite/magnetite and pyrite. Accessory minerals such as apatite, zircon and rutile were also encountered. There are observed differences in mineral abundances, assemblages and grain sizes of minerals within the different target rock types (see Chapter 2). As will be shown in this chapter, the groundmass of the M4 core impactites (cataclasite, suevite and MMBr) is highly altered, but it also contains abundant mineral clasts from the target lithologies (mainly quartz, plagioclase, microcline, biotite, Fe-Ti oxides, titanite, epidote, apatite and rare clinopyroxene and amphibole) in addition to lithic clasts (mainly granitoid gneisses, metadolerite and dolerite and rare exotic clasts of highly altered alkaline/ultramafic affinity; see Chapter 2). Detailed petrographic description of mineral textures, lithic clasts and melt particles and clasts is presented in Chapter 2. Shock micro-deformation features are discussed in Chapter 5.

In this chapter, the mineral chemistry of representative target rock samples and lithic and mineral clasts derived from electron microprobe analysis (EMPA) is first discussed. This is followed by discussion of the results of a range of analytical techniques that were applied to the impactites to investigate the mineral chemistry of the suevite matrix and chemistry and provenance of melt clasts in the suevite and the matrix and melt inclusions in the MMBr. These techniques include EMPA, whole-sample XRD analysis and SEM-EDX. This part of the study achieved only limited results owing to the complex micro- to cryptocrystalline post-impact hydrothermal mineralogy encountered in the impactites, and it is recommended that follow-up work will be needed that is beyond the scope of this study.

4.2 Previous studies

Previous studies in the Morokweng impact structure have focused on the petrographic and chemical analysis of mineral constituents of the impact melt samples from the central boreholes (WF3, -4 and -5). The impact melt modally consists of 60% plagioclase, 5% K-feldspar, 15-20% orthopyroxene, 5-10% clinopyroxene, 5% quartz and 5% opaque minerals (including magnetite-trevorite, (Ni-) ilmenite, millerite) and rarer amphibole (Hart et al., 1997; Koeberl et al., 1997; Andreoli et al., 1999; Koeberl and Reimold, 2003). Andreoli et al. (1999) described plagioclase in the impact-melt rock as zoned laths (~0.6-1 mm) with an andesine (An_{48}) core and an oligoclase (An_{17}) rim. Associated with the plagioclase are euhedral orthopyroxene ($Wo_{3.3}En_{55-60}$) and interstitial clinopyroxene ($Wo_{40-46}En_{38-12}$), Fs component not reported. The accessory assemblage consists of red-brown biotite, hornblende, apatite and zircon and the Mg# (= 100*Mg/(Mg+Fe)) of clinopyroxene was noted to decrease with increasing depth (Andreoli et al., 1999). Reimold et al. (1999) reported the matrix of the impact melt to consist of alkali feldspar (Ab_{20-77}). The feldspar compositions varied between samples that contained only alkali feldspar and others that contain plagioclase as well as K-feldspar. Electron microprobe analyses of pyroxene indicated the presence of both orthopyroxene ($Wo_4En_{58}Fs_{38}$) and clinopyroxene ($Wo_{40}En_{43}Fs_{17}$) (Reimold et al., 1999). SEM-EDX analyses showed that ortho- and clinopyroxene grains have been partially converted to amphibole (Reimold et al., 1999). Evidence of secondary alteration was noted in a weathered section of the melt rock, with the presence of up to 40 cm wide carbonate veins, secondary biotite and saussuritized plagioclase (Reimold et al., 1999). Biotite and accessory minerals such as epidote, apatite, magnetite, ilmenite, rutile and trevorite, though noted and described, were not chemically analysed by these authors.

The impact melt contains fragments of target rocks such as granite, quartzite, meta-ultramafics, metadolerite, and even a boulder-size clast of almost pristine chondrite (Hart et al., 1997; Maier et al., 2006). Lithic clasts of gabbro were also noted enclosed in the impact melt (Koeberl et al., 1997). Metadolerite is highly recrystallized to fine-grained aggregates of plagioclase and pyroxene with accessory post-impact zircons (Hart et al., 1997). Petrographic and whole-rock geochemical analysis of 77 samples from impact breccias and target rocks from 3 boreholes (WF3, -4 and -5) were reported by Koeberl and Reimold (2003), but no mineral chemical data were presented. The granites are dominated by quartz, plagioclase and K-feldspar and accessory minerals include magnetite, titanomagnetite, ilmenite, rutile and, to a lesser extent, zircon, monazite, and chalcocite. Evidence of shock metamorphism can be seen in the clasts enclosed within the impact melt rock and in the megabreccia granitoids (Andreoli et al., 1999; Hart et al., 1997).

4.3 Methodology

Minerals in 19 samples identified via petrographic analysis (Chapter 2) were subjected to EMPA at the University of Pretoria and, later, Rhodes University following the closure of the Pretoria facility. Table 4.1 lists the samples analysed at each facility, and the sample preparation, operating conditions and mineral standards are outlined in Appendix 1E. To calculate element ratios, the following equations were used: An = 100*Ca/(Ca + Na); Or = 100*K/(K + Na); Ps = 100*Fe^{3+}/(Fe^{3+} + Al) and X_{Mg} = Mg/(Mg + Fe^{2+}). Total iron is presented as FeO, as EMP analysis does not discriminate between Fe^{2+} and Fe^{3+} (Lamb et al., 2012). Representative mineral chemistry data from the target rocks and mineral and lithic clasts from impactites are presented in Appendix 4A and 4B respectively. The melt particle microprobe data from the University of Pretoria and Rhodes University is not stoichiometric and too extensive, and so is not presented in the Appendix. The melt and matrix traverses are presented in Appendix 4D. The data is summarised in major oxide ternary plots in Section 4.5. Tables 4.2 – 4.7 present the average mineral chemical analyses of selected minerals within the analysed rock samples. The granitic-granodioritic gneiss, trondhjemitic gneiss and dioritic gneiss mineral components and features are grouped and discussed first, followed by a discussion of the data of the metadolerite and dolerite samples. Quartz, K-feldspar, plagioclase, ilmenite, magnetite-titanomagnetite and biotite were noted enclosed as mineral clasts or as part of lithic clasts in the matrix of impactites. These are discussed together with rock-forming mineral constituents of target rocks so as to investigate whether the clast population shows similarities to a particular target rock(s) and whether these rocks are source of the impactites and also to investigate any differences that would indicate an exotic component not intersected elsewhere in the core. Large microcline mineral clasts, as well as smaller biotite, plagioclase and epidote were analysed by EMPA. The procedures followed during the use of an SEM, XRD and the EMPA are outlined in the respective sections and the methodology explained in Appendix 1C, D and E. The obtained XRD spectra are presented in Appendix 4C.

4.4 Mineral chemistry results for M4 core target rocks and impactites

In this section the mineral chemical analyses for component minerals of the M4 core target lithologies are presented as per major mineral phase. A total of 716 mineral analyses were obtained from the target rocks and 1015 from the impactites (melt particles, matrices, mineral and lithic clasts), but the impactite melt analyses are not consistent stoichiometrically. A selection of these is presented for each mineral in Appendix 4A, with representative or mean compositional data presented in Tables in this Chapter.

4.4.1 Feldspars

4.4.1.1 Granitoid gneisses

Plagioclase occurs in all samples (target rocks and impactites) and the obtained EMPA of plagioclase from selected samples are shown in Table 4.2. Petrographically, plagioclase in granitoid samples was noted to be texturally zoned, with thin rims around inclusion-rich cores (see Chapter 2). During the EMPA, grains were checked for compositional zoning by analysing traverses from core to rim. The feldspar compositional data for all the target rock types are shown graphically in the Ca-K-Na ternary diagram (Figure 4.1).

Granitoid gneisses in the core contain both plagioclase and, to a lesser extent, alkali feldspar. The anorthite content of plagioclase in granitic-granodioritic gneiss samples ranges from albite (An_{2-9}) to oligoclase (An_{13-20}), with the more sodic compositions towards the rims (Figure 4.1; Table 4.2). The alkali feldspar is locally perthitic and displays a wide orthoclase range (Or_{77-98}; Table 4.2, Figure 4.1A), but no consistent compositional zoning was noted. Microcline and perthite are relatively abundant in sample M4 GG-2 and M4 GG-7 (Table 4.3). Chemical analysis of the perthite from sample M4 GG-7 shows a compositional range of $Or_{87-92}Ab_{7-13}$ (Table 4.3 and Appendix 4A). Plagioclase in trondhjemitic gneiss is albitic (An_{3-9}) (Appendix 4A); however, some oligoclase (An_{18}) was also noted (Figure 4.1A). The compositional range of analysed plagioclase grains in dioritic gneiss is between albite and oligoclase ($An_{0.5-20}$; Table 4.2 and Figure 4.1B). The dominant ranges are An_{18-19} and $An_{0.5-9}$, consistent with the peristerite gap. Several inclusions of apatite, and alteration products including biotite and epidote, are concentrated in the plagioclase cores.

4.4.1.2 Metadolerite and dolerite

Electron microprobe analysis of plagioclase from the analysed dolerite sample M4 SILL-1 ranges from An_{40} to An_{64}, with an average of An_{56} (Table 4.2 and Appendix 4A; Figure 4.2). These compositions represent labradorite, which is the typical calcic plagioclase in mafic igneous rocks such as dolerites and gabbros (Anthony et al., 2011). A single analysis of plagioclase in the metadolerite was obtained and is albitic in composition ($An_3Ab_{93}Or_4$) which might be consistent with the mid- to upper greenschist-grade metamorphic actinolite-epidote-chlorite-biotite-titanite paragenesis that has largely replaced the original igneous mineralogy (Section 2.3.4, Figure 2.10). This analysis however is not included in diagrams and tables as it was obtained in close proximity to a fracture and may be related to hydrothermal effects.

Table 4.1: List of M4 drillcore target rock samples for electron microprobe analysis at the University of Pretoria and Rhodes University.

Sample	Depth (m)	Lithology
M4 GG -1	126.6	Dioritic gneiss
M4 GG -2	131.95	Granitic gneiss
M4 AM -1	340.10	Dioritic gneiss
M4 FZ -1	249.78	Trondhjemitic gneiss
M4 GG-6	156.48	Granitic gneiss
M4 GG-7	156.55	Granodioritic gneiss
M4 GG-10	165.98	Dioritic gneiss
M4 SILL-1	268.30	Dolerite
M4 A-1	166.36	Metadolerite
M4 IS -1*	221.20	Silicified metadolerite

** Sample M4 IS-1 analysed at the University of Rhodes as well.*

4.4.1.3 Feldspar chemistry of mineral and lithic clasts enclosed in impactites

Plagioclase (average $An_3Ab_{94}Or_3$) compositions in mineral clasts within the suevite samples are similar to the lithic clasts and to the target granitoids (Figure 4.2). K-feldspar (microcline; average $Or_{92}Ab_7An_1$) is the most analysed mineral clast as it is second only to quartz (Appendix 4A). The MMBr clasts show a much wider range of feldspar compositions than the suevite clasts (Figure 4.1B) and also show more calcic compositions. Although the anorthite content is not quite as high as the dolerite, it is more calcic than the metadolerite and the granitoid gneisses, suggesting a strong dolerite contribution to the formed MMBr. Figures 2.25D and 2.27 show the textural context of enclosed mineral and lithic clasts in impactites; for detailed description see Chapter 2. Basically, the feldspars analysed from suevites show granitoid/dioritic feldspar compositions, whereas the analyses from MMBr samples show a mixture derived from a sodic and alkaline feldspar source like from granitoids and also from a mafic source such as the doleritic rocks. The analyses from the impactites scatter in the ternary plots. This is interpreted as an effect of higher levels of alteration in impactite feldspars (Figure 3.7F).

Table 4.2: Average EMPA composition and unit formulae of plagioclase, M4 target rocks.

Sample:	**M4 GG-1**		**M4 GG-2**				**M4 GG-6**				**M4 GG-7**			
Depth (m):	**126.5**		**131.9**				**149.24**				**150.58**			
Rock Type:	**Dioritic gneiss**		**Granitic gneiss**				**Granitic gneiss**				**Granodioritic gneiss**			
Mineral:	**Plagioclase**		**Plagioclase**				**Plagioclase**				**Plagioclase**			
	n = 17		n = 14	(rim)	n = 13	(core)	n = 12	(rim)	n = 5	(core)	n = 18	(rim)	n = 9	(core)
(wt.%)	**Mean**	σ	**Mean**	σ	**Mean**	σ	**Mean**	σ	**Mean**	σ	**Mean**	σ	**Mean**	σ
SiO_2	62.54	0.39	67.55	1.28	64.08	0.69	67.47	1.77	65.42	0.77	68.27	0.81	64.31	0.83
TiO_2	0.02	0.02	0.01	0.01	0.01	0.01	0.01	0.01	0.01	0.01	0.01	0.01	0.01	0.02
Al_2O_3	22.28	0.22	19.81	0.91	21.72	0.52	19.19	0.58	21.17	0.32	19.32	0.42	21.88	0.44
FeO*	0.11	0.04	0.03	0.02	0.03	0.02	0.03	0.01	0.02	0.02	0.03	0.02	0.04	0.03
MnO	0.00	0.01	0.01	0.01	0.00	0.00	0.00	0.01	0.01	0.01	0.01	0.01	0.00	0.01
MgO	0.01	0.01	0.02	0.01	0.01	0.01	0.02	0.03	0.01	0.01	0.00	0.00	0.02	0.04
CaO	4.23	0.18	1.10	1.00	3.47	0.57	0.58	0.61	2.88	0.63	0.61	0.47	3.65	0.42
Na_2O	8.67	0.12	10.50	0.75	8.96	0.38	10.10	2.81	9.81	0.26	10.94	0.29	9.18	0.32
K_2O	0.73	0.09	0.51	0.33	0.79	0.34	1.40	4.19	0.29	0.14	0.37	0.17	0.46	0.14
P_2O_5	0.01	0.02	0.02	0.02	0.01	0.02	0.02	0.02	0.02	0.02	0.01	0.02	0.01	0.01
Cr_2O_3	0.01	0.01	0.01	0.01	0.00	0.01	0.01	0.01	0.01	0.02	0.01	0.01	0.01	0.02
BaO	0.02	0.04	0.03	0.02	0.01	0.02	0.03	0.08	0.01	0.02	0.01	0.01	0.01	0.03
ZnO	0.00	0.01	0.01	0.02	0.01	0.02	0.00	0.01	0.00	0.00	0.01	0.01	0.02	0.02
Total	**98.63**	**0.54**	99.60	0.65	99.11	0.56	98.86	0.87	99.66	0.46	**99.61**	**0.82**	**99.62**	**0.55**
Oxygen	8.00		8.00		8.00		8.00		8.00		8.00		8.00	
(Cations)														
Si	2.81	0.01	2.98	0.05	2.87	0.03	3.01	0.04	2.90	0.03	3.01	0.02	2.86	0.03
Ti	0.00	0.00	0.00	0.00	0.00	0.00	0.00	0.00	0.00	0.00	0.00	0.00	0.00	0.00
Al	1.18	0.01	1.03	0.05	1.14	0.03	1.01	0.03	1.11	0.02	1.00	0.02	1.15	0.02
Cr	0.00	0.00	0.00	0.00	0.00	0.00	0.00	0.00	0.00	0.00	0.00	0.00	0.00	0.00
Fe^{+3}	0.00	0.00	0.00	0.00	0.00	0.00	0.00	0.00	0.00	0.00	0.00	0.00	0.00	0.00
Fe^{+2}	0.00	0.00	0.00	0.00	0.00	0.00	0.00	0.00	0.00	0.00	0.00	0.00	0.00	0.00
Mn	0.00	0.00	0.00	0.00	0.00	0.00	0.00	0.00	0.00	0.00	0.00	0.00	0.00	0.00
Mg	0.00	0.00	0.00	0.00	0.00	0.00	0.00	0.00	0.00	0.00	0.00	0.00	0.00	0.00
Ca	0.20	0.01	0.05	0.05	0.17	0.03	0.03	0.03	0.14	0.03	0.03	0.02	0.17	0.02
Ba	0.00	0.00	0.00	0.00	0.00	0.00	0.00	0.00	0.00	0.00	0.00	0.00	0.00	0.00
Na	0.76	0.01	0.90	0.06	0.78	0.03	0.87	0.24	0.84	0.02	0.94	0.02	0.79	0.03
K	0.04	0.01	0.03	0.02	0.05	0.02	0.08	0.25	0.02	0.01	0.02	0.01	0.03	0.01
Total cation	**5.00**		**5.00**		**5.00**		**5.00**		**5.00**		5.00	0.00	5.00	0.00
An	20.34	0.85	5.38	5.05	16.80	2.73	2.81	2.93	13.68	2.72	2.93	2.27	17.56	2.06
Ab	75.50	1.09	91.68	5.16	78.60	3.29	88.80	24.61	84.67	3.37	94.98	2.51	79.83	2.57
Or	4.17	0.53	2.93	1.92	4.59	2.00	8.39	25.17	1.65	0.75	2.09	0.95	2.61	0.77

* *All Fe as FeO;* σ – Standard deviation

Table 4.2: (*Continued*)…

Sample:	**M4 GG-10**		**M4 IS 1**		**M4 FZ 1**		**M4 SILL-1**		**M4 AM-1**			
Depth (m):	**165.98**		**221.2**		**249.62**		**268.3**		**340.7**			
Rock Type:	**Dioritic gneiss**		**Metadolerite**		**Trondhjemitic gneiss**		**Dolerite**		**Dioritic gneiss**			
Mineral:	**Plagioclase**		**Plagioclase**		**Plagioclase**		**Plagioclase**		**Plagioclase**			
	n = 17		n = 8		n = 13		n = 18	(labradorite)	n = 23	(albite)	n = 6	(oligoclase)
(wt.%)	**Mean**	σ	**Mean**	σ	**Mean**	σ	**Mean**	σ	**Mean**	σ	**Mean**	σ
SiO_2	66.84	1.13	67.17	1.49	65.94	1.59	53.41	0.64	66.89	1.01	63.07	0.31
TiO_2	0.01	0.01	0.01	0.01	0.01	0.02	0.05	0.02	0.01	0.01	0.01	0.01
Al_2O_3	19.31	0.56	19.76	1.00	20.66	0.98	27.71	0.49	19.73	0.51	22.46	0.12
FeO*	0.10	0.10	0.13	0.07	0.05	0.02	0.76	0.06	0.09	0.05	0.09	0.03
MnO	0.00	0.01	0.01	0.01	0.01	0.01	0.01	0.01	0.01	0.01	0.01	0.01
MgO	0.04	0.10	0.01	0.01	0.01	0.01	0.10	0.06	0.01	0.02	0.00	0.01
CaO	0.96	0.54	1.40	0.74	1.93	1.10	12.12	0.48	0.88	0.57	4.21	0.07
Na_2O	10.40	0.51	10.34	0.44	10.54	0.94	4.48	0.25	10.48	1.08	8.94	0.04
K_2O	0.63	0.46	0.16	0.06	0.28	0.03	0.25	0.04	0.80	1.54	0.39	0.06
P_2O_5	0.01	0.02	0.01	0.02	0.01	0.01	0.02	0.02	0.01	0.02	0.01	0.02
Cr_2O_3	0.01	0.01	0.01	0.01	0.01	0.01	0.01	0.01	0.01	0.01	0.01	0.01
BaO	0.03	0.05	0.02	0.03	0.02	0.04	0.02	0.02	0.01	0.02	0.04	0.05
ZnO	0.00	0.01	0.00	0.01	0.00	0.01	0.01	0.02	0.01	0.01	0.01	0.02
Total	**98.35**	**1.13**	**99.02**	**0.96**	**99.47**	**1.15**	**98.93**	**0.49**	**98.94**	**0.60**	**99.23**	**0.30**
Oxygen	8.00		8.00		8.00		8.00		8.00		8.00	
(Cations)												
Si	2.99	0.03	2.99	0.06	2.91	0.05	2.45	0.03	2.97	0.03	2.82	0.01
Ti	0.00	0.00	0.00	0.00	0.00	0.00	0.00	0.00	0.00	0.00	0.00	0.00
Al	1.02	0.03	1.04	0.05	1.08	0.05	1.50	0.03	1.03	0.03	1.18	0.01
Cr	0.00	0.00	0.00	0.00	0.00	0.00	0.00	0.00	0.00	0.00	0.00	0.00
Fe^{+3}	0.00	0.00	0.00	0.00	0.00	0.00	0.00	0.00	0.00	0.00	0.00	0.00
Fe^{+2}	0.00	0.00	0.00	0.00	0.00	0.00	0.03	0.00	0.00	0.00	0.00	0.00
Mn	0.00	0.00	0.00	0.00	0.00	0.00	0.00	0.00	0.00	0.00	0.00	0.00
Mg	0.00	0.01	0.00	0.00	0.00	0.00	0.01	0.01	0.00	0.00	0.00	0.00
Ca	0.05	0.03	0.07	0.04	0.09	0.05	0.60	0.02	0.04	0.03	0.20	0.00
Ba	0.00	0.00	0.00	0.00	0.00	0.00	0.00	0.00	0.00	0.00	0.00	0.00
Na	0.90	0.04	0.89	0.04	0.90	0.08	0.40	0.02	0.90	0.09	0.77	0.00
K	0.04	0.03	0.01	0.00	0.02	0.00	0.01	0.00	0.05	0.09	0.02	0.00
Total cations	5.00	0.00	**5.00**	**0.00**	**5.00**		**5.00**		**5.00**		**5.00**	
An	4.66	2.63	6.92	3.66	9.15	5.34	59.01	2.33	4.12	2.74	20.19	0.26
Ab	91.68	4.05	92.14	3.53	89.27	5.42	39.54	2.23	91.28	9.26	77.60	0.56
Or	3.66	2.71	0.94	0.36	1.58	0.18	1.45	0.25	4.60	8.86	2.21	0.36

** All Fe as FeO; σ – Standard deviation*

Table 4.3: Average EMPA composition and unit formulae of alkali feldspar and biotite from M4 target rocks and a clast in M4 IM-9.

Sample:	**M4 GG-2**		**M4 GG-6**		**M4 GG-7**		**M4 GG-1**		**M4 GG-2**		**M4 GG-7**		**M4 GG-10**		**M4 IM-9**	
Depth (m):	**131.90**		**149.24**		**150.58**		**126.50**		**131.90**		**150.58**		**165.98**		**299.76**	
Rock Type:	**Granitic gneiss**		**Granitic Gneiss**		**Granodioritic gneiss**		**Dioritic gneiss**		**Granitic gneiss**		**Granodioritic gneiss**		**Dioritic gneiss**		**MMBr**	
Mineral	**Alkali feldspar (perthite)**		**Alkali feldspar**		**Alkali feldspar**		**Biotite**		**Biotite**		**Biotite**		**Biotite**		**Biotite**	
	n = 11		n = 5		n = 35		n = 49		n = 8		n = 20		n = 35		n = 2	
(wt.%)	**Mean**	σ	**Mean**	σ	**Mean**	σ	**Mean**	**σ**	**Mean**	σ	**Mean**	σ	**Mean**	σ	**Mean**	σ
SiO_2	64.44	0.63	64.14	0.39	64.23	1.13	36.95	1.29	38.38	0.83	38.78	0.82	39.11	1.59	36.82	0.38
TiO_2	0.01	0.01	0.01	0.01	0.02	0.02	2.00	0.44	1.29	0.42	1.62	0.26	1.57	0.48	2.16	0.02
Al_2O_3	17.96	0.21	18.08	0.09	17.80	0.40	15.32	0.81	15.16	0.45	15.10	0.56	15.31	0.73	16.90	0.16
FeO*	0.05	0.05	0.03	0.01	0.05	0.06	14.80	3.38	11.22	1.99	10.83	2.96	10.44	2.42	14.76	0.03
MnO	0.02	0.03	0.01	0.01	0.01	0.01	0.37	0.14	0.12	0.06	0.09	0.07	0.04	0.02	0.29	0.05
MgO	0.01	0.01	0.01	0.01	0.01	0.01	15.57	2.62	18.95	1.59	18.53	2.22	18.38	2.20	14.92	0.27
CaO	0.01	0.02	0.13	0.09	0.03	0.03	0.19	0.22	0.04	0.05	0.10	0.08	0.12	0.23	0.11	0.04
Na_2O	1.14	0.17	1.43	0.34	1.06	0.34	0.32	0.37	0.08	0.01	0.24	0.19	0.21	0.32	0.00	0.00
K_2O	14.66	0.25	14.24	0.61	14.81	0.50	8.07	1.27	9.31	0.80	9.32	0.52	9.65	0.52	10.34	1.01
P_2O_5	0.02	0.02	0.02	0.02	0.01	0.02	0.02	0.03	0.04	0.04	0.01	0.01	0.01	0.01	0.05	0.06
Cr_2O_3	0.00	0.00	0.00	0.00	0.01	0.01	0.01	0.01	0.01	0.01	0.01	0.01	0.01	0.01	0.00	0.00
BaO	0.41	0.10	0.44	0.11	0.33	0.06	0.12	0.05	0.08	0.05	0.07	0.05	0.22	0.12	0.07	0.02
ZnO	0.00	0.01	0.00	0.00	0.01	0.01	0.04	0.04	0.05	0.05	0.01	0.01	0.01	0.01	0.00	0.00
Total	**98.74**	**0.77**	**98.54**	**0.55**	**98.36**	**1.54**	**93.79**	**2.34**	**94.71**	**1.15**	**94.70**	**1.51**	**95.06**	**1.11**	**96.41**	**0.77**
Oxygens	8.00		8.00		8.00		11.00		11.00		11.00		11.00		11.00	
(cations)																
Si	3.02	0.01	3.00	0.01	3.02	0.01	2.79	0.09	2.83	0.03	2.85	0.04	2.86	0.07	2.73	0.02
Ti	0.00	0.00	0.00	0.00	0.00	0.00	0.11	0.03	0.07	0.02	0.09	0.01	0.09	0.03	0.12	0.00
Al	0.99	0.01	1.00	0.00	0.99	0.01	1.36	0.05	1.32	0.05	1.31	0.05	1.32	0.06	1.48	0.02
Cr	0.00	0.00	0.00	0.00	0.00	0.00										
Fe^{+3}	0.00	0.00	0.00	0.00	0.00	0.00	0.00	0.00	0.00	0.00	0.00	0.00	0.00	0.00	0.00	0.00
Fe^{+2}	0.00	0.00	0.00	0.00	0.00	0.00	0.94	0.24	0.69	0.13	0.67	0.19	0.64	0.16	0.92	0.01
Mn	0.00	0.00	0.00	0.00	0.00	0.00	0.02	0.01	0.01	0.00	0.01	0.00	0.00	0.00	0.02	0.00
Mg	0.00	0.00	0.00	0.00	0.00	0.00	1.75	0.28	2.08	0.15	2.03	0.23	2.01	0.24	1.65	0.04
Ca	0.00	0.00	0.01	0.00	0.00	0.00	0.02	0.02	0.00	0.00	0.01	0.01	0.01	0.02	0.01	0.00
Ba	0.01	0.00	0.01	0.00	0.01	0.00										
Na	0.10	0.02	0.13	0.03	0.10	0.03	0.05	0.06	0.01	0.00	0.03	0.03	0.03	0.04	0.00	0.00
K	0.88	0.00	0.85	0.03	0.89	0.04	0.78	0.11	0.87	0.07	0.87	0.05	0.90	0.05	0.98	0.09
Total cations	**5.00**		**5.00**		**5.00**		**7.82**	**0.08**	**7.88**	**0.04**	**7.86**	**0.04**	**7.86**	**0.09**	**7.90**	**0.04**
An	0.06	0.10	0.66	0.45	0.16	0.15										
Ab	10.60	1.49	13.14	3.18	9.78	3.11										
Or	89.35	1.47	86.20	3.62	90.06	3.15										
X_{Mg}							0.65	0.10	0.75	0.05	0.75	0.07	0.76	0.06	0.64	0.00

** All Fe as FeO; σ – Standard deviation*

Table 4.4: Average EMPA composition and unit formulae of pyroxene, amphibole, chlorite and epidote, M4 target rocks.

Sample	**M4 SILL-1**		**M4 SILL-1**		**M4 A-1**		**M4 A-1**		**M4 AM-1**		**M4 A-1**		**M4 FZ. 1**		**M4 AM-1**	
Depth (m)	**268.3**		**268.3**		**166.33-**		**166.36**		**340.7**		**166.36**		**249.62**		**340.7**	
Rock Type:	**Dolerite**		**Dolerite**		**Metadolerite**		**Metadolerite**		**Dioritic gneiss**		**Metadolerite**		**Trondhjemitic gneiss**		**Dioritic gneiss**	
Mineral:	**Clinopyroxene**		**Amphibole**		**Amphibole**		**Chlorite**		**"Chlorite"**		**Epidote**		**Epidote**		**Epidote**	
	n = 23		n = 21		n = 47		n = 16		n=23		n=6		n=9		n=9	
	Mean	**σ**	**Mean**	**σ**	**Mean**	**σ.**	**Mean**	**σ**	**Mean**	**σ**	**Mean**	**σ**	**Mean**	**σ**	**Mean**	**σ**
SiO_2	50.66	1.11	50.27	1.35	52.35	2.04	37.46	4.39	36.22	3.46	43.78	2.38	38.32	2.57	37.79	1.61
TiO_2	0.43	0.12	0.55	0.34	0.22	0.75	0.29	0.11	1.15	0.64	2.06	2.99	0.16	0.12	0.05	0.03
Al_2O_3	2.53	0.62	2.77	0.59	3.34	0.88	16.78	2.14	17.67	4.55	23.71	3.01	22.58	4.11	21.14	1.13
FeO*	12.65	2.55	17.45	2.04	11.91	1.00	22.21	5.43	14.20	3.60	7.91	2.03	13.22	6.49	13.98	0.70
MnO	0.31	0.08	0.35	0.10	0.27	0.03	0.31	0.04	0.16	0.06	0.15	0.04	0.14	0.13	0.15	0.07
MgO	13.89	2.14	12.93	1.60	16.45	0.89	15.80	1.36	14.81	4.52	1.58	1.20	1.42	3.89	0.01	0.01
CaO	18.66	1.72	13.42	1.79	12.86	0.57	0.67	0.08	1.02	0.74	17.32	2.03	19.31	7.14	21.62	1.80
Na_2O	0.32	0.08	0.37	0.09	0.57	0.14	0.46	0.05	0.11	0.07	1.07	0.44	0.86	1.87	0.42	0.60
K_2O	0.07	0.09	0.28	0.16	0.16	0.07	1.08	0.22	6.28	2.29	0.07	0.04	0.05	0.09	0.03	0.04
P_2O_5	0.04	0.06	0.03	0.03	0.02	0.03	0.05	0.04	0.01	0.01	0.03	0.03	0.12	0.13	0.02	0.02
Cr_2O_3	0.04	0.03	0.01	0.02	0.32	0.22	0.03	0.02	0.01	0.01	0.04	0.04	0.01	0.01	0.02	0.02
BaO	0.01	0.02	0.02	0.02	0.02	0.02	0.01	0.02	0.12	0.12	0.07	0.03	0.01	0.01	0.02	0.03
ZnO	**0.02**	0.02	0.01	0.01	0.01	0.02	0.12	0.04	0.03	0.03	0.02	0.03	0.01	0.02	0.01	0.01
Total	99.63	0.91	**98.47**	**1.02**	**98.51**	**1.46**	**95.28**	**2.00**	**91.79**	**1.65**	**97.79**	**1.28**	**96.22**	**0.97**	**95.27**	**2.00**
Wo	38.37	3.34														
En	39.67	5.51														
Fs	20.76	4.62														
Ac	1.20	0.33														
Mg#	0.66	0.08	0.57	0.06	0.71	0.02	55.67	28.99	65.04	68.35						
Ps											19.34	5.82	29.14	13.14	31.96	1.60
Oxygens	6.00		23.00		23.00		14.00		14.00		12.50		12.50		12.50	
Cations per formula unit																
Si	1.92	0.02	7.44	0.14	7.51	0.17	3.51	0.30	3.50	0.22	3.32	0.16	3.05	0.17	3.06	0.12
Ti	0.01	0.00	0.06	0.04	0.02	0.08	0.02	0.01	0.08	0.05	0.12	0.17	0.01	0.01	0.00	0.00
Al	0.11	0.03	0.48	0.10	0.57	0.15	1.85	0.21	2.00	0.43	2.12	0.28	2.12	0.38	2.02	0.09
Cr	0.00	0.00	0.00	0.00	0.00	0.00	0.00	0.00	0.00	0.00						
Fe^{+3}							0.00	0.00	0.00	0.00	0.50	0.13	0.88	0.45	0.95	0.05
Fe^{+2}	0.40	0.09	2.16	0.27	1.44	0.13	1.76	0.49	1.16	0.31	0.00	0.00	0.00	0.00		
Mn	0.01	0.00	0.04	0.01	0.03	0.00	0.02	0.00	0.01	0.00	0.01	0.00	0.00	0.01	0.00	0.01
Mg	0.78	0.11	2.85	0.33	3.53	0.18	2.21	0.20	2.16	0.67	0.18	0.14	0.17	**0.47**	0.00	0.00
Ca	0.76	0.07	2.13	0.28	1.98	0.10	0.07	0.01	0.11	0.08	1.41	0.18	1.64	0.61	1.88	0.14
Na	0.02	0.01	0.11	0.03	0.16	0.04	0.08	0.01	0.02	0.01	0.16	0.06	0.13	0.28	0.07	0.09
K	0.00	0.00	0.05	0.03	0.03	0.01	0.13	0.02	0.77	0.26	0.01	0.00	0.01	0.01	0.00	0.00
Tot. cations	**4.03**	**0.01**	**15.33**	**0.12**	**15.27**	**0.13**	**9.65**	**0.28**	**9.81**	**0.30**	**7.83**	**0.07**	**8.01**	**0.06**	**7.99**	**0.04**

** All Fe as FeO; σ – Standard deviation*

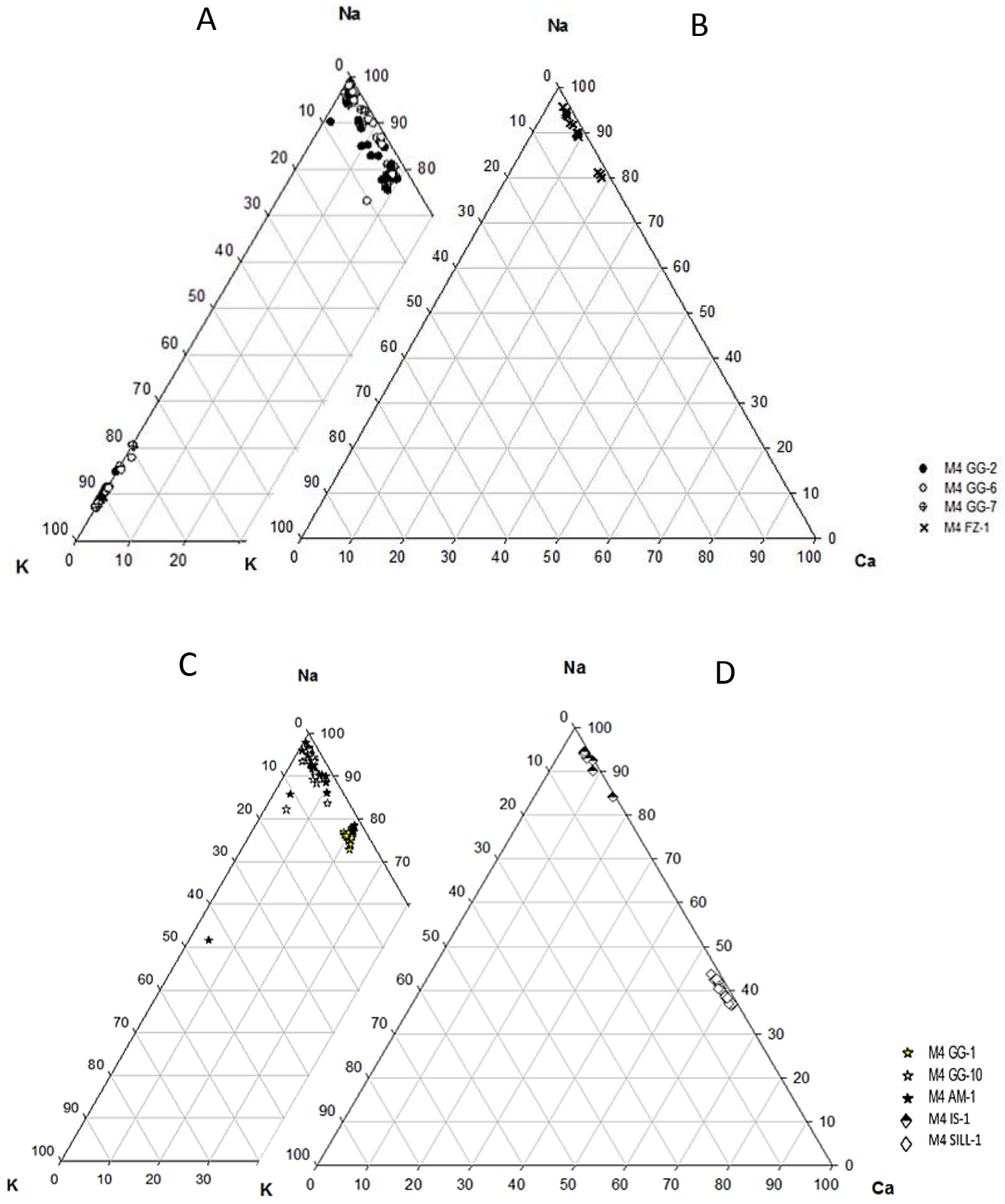

Figure 4.1: Ca-K-Na ternary plots for feldspar analyses in granitoid gneisses in the M4 core. **A)** Granitic-granodioritic gneiss. **B)** Trondhjemitic gneiss. **C)** Dioritic gneiss. **D)** Silicified metadolerite (M4 IS-1) and dolerite (M4 SILL-1) samples from the M4 core.

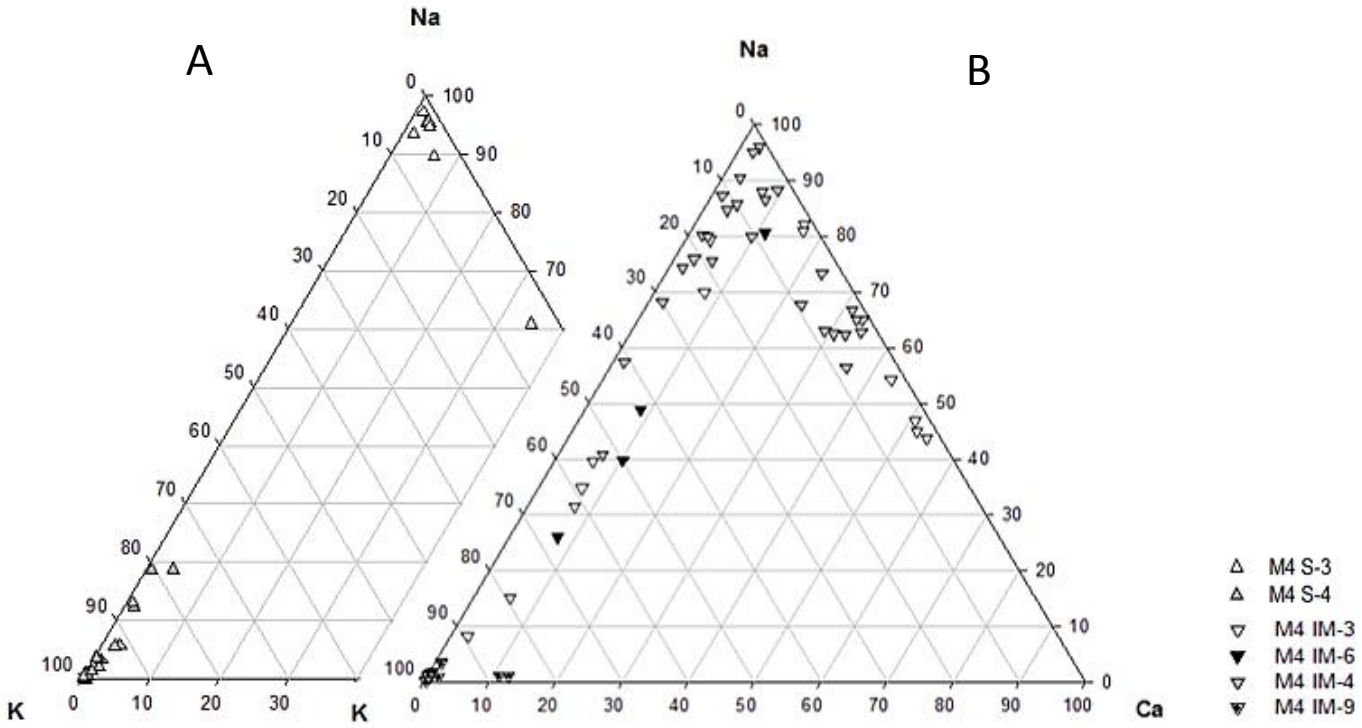

Figure 4.2: Ca-K-Na ternary plots for feldspar from impactite samples. **A)** Suevites are denoted (S) and **B)** MMBr are denoted (IM).

4.4.2 Biotite and chlorite

4.4.2.1 Granitoid gneisses

Biotite in the granitoid target rocks shows a range of alteration and deformation effects, including bent and kinked grains, and variable replacement by chlorite especially in the lower parts of the core, prehnite spindles parallel to cleavage, and oxidation to magnetite or ilmenite in the upper parts of the core. It is almost completely absent from the mafic rocks and good stoichiometric analyses were not obtained from these samples.

Representative averaged biotite analyses for the granitoid gneisses are presented in Table 4.4. In general, the dioritic and granodioritic gneisses show a similar range of X_{Mg} and Ti contents (Figure 4.3); however, individual samples show a wide range of K, Ti, Al^{vi} and X_{Mg} contents. This is interpreted as being the result of post-impact alteration, although there is also evidence of pre-impact alteration (see Section 2.5.1), and biotite clasts in impactites show prehnite spindles that suggest that the prehnite could predate the impact. The X_{Mg} of biotite in granitic gneiss samples ranges from 0.67 – 0.86; whilst that of granodiorite ranges from 0.56 – 0.82 (Appendix 4A). The X_{Mg} for dioritic gneisses shows a narrower range from 0.65 – 0.71 (Table 4.3) with one or two outliers (Figure 4.3).

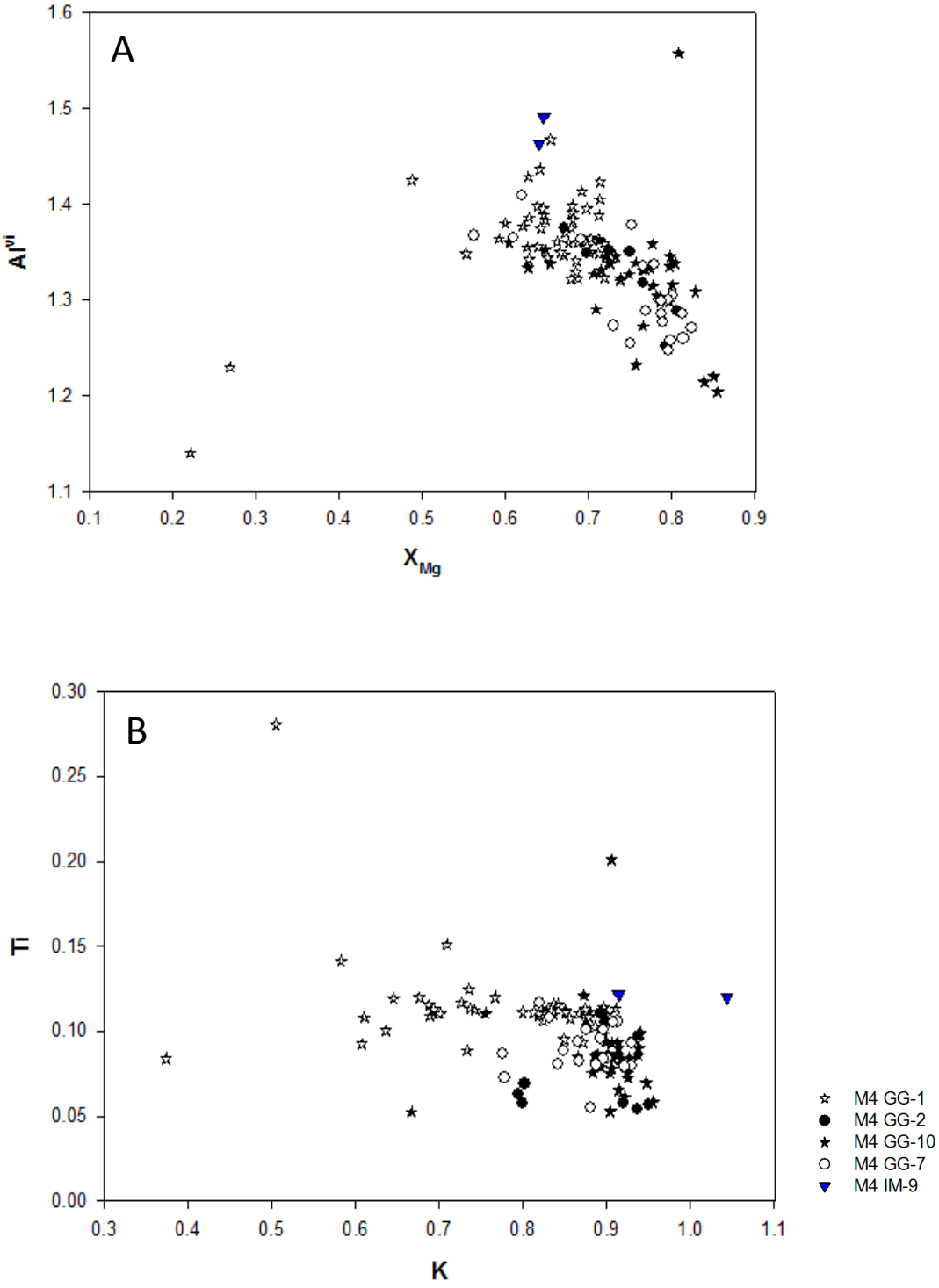

Figure 4.3: Plot of **A)** X_{Mg} versus Al^{vi} atoms per formula unit and **B)** K versus Ti a.p.f.u. abundances for biotite in granitic gneisses and dioritic gneisses and from an MMBr sample M4 IM-9.

The "chlorite" in dioritic gneiss sample M4 AM-1 (Table 4.4) is not stoichiometrically-consistent with chlorite data. All the analysis is too rich in K_2O to be true chlorite. Petrographically it appears as chloritized biotite (see Figure 2.8), but when analysed geochemically it is similar to biotite. These analyses were excluded from the plots in Figure 4.3 as these intensely shocked and chloritized biotite require further study. Biotite clasts in suevite and MMBr in the composite impactite sample M4 IM-9 show slightly anomalous compositions relative to the granitoid gneiss biotites (Table 4.4). It is not clear if this is significant, as the analyses partially overlap the main field of biotite compositions in Figure 4.3.

4.4.2.2 Metadolerite and dolerite

Relict highly chloritised and oxidised biotite grains were observed in several metadolerite samples but, despite numerous analyses being attempted in sample M4 A-1, no stoichiometrically-consistent biotite data were collected, and analyses approach a chlorite composition with some K_2O and variable SiO_2 content. The obtained average chlorite from the metadolerite sample has an X_{Mg} of 56 (Table 4.4). This is not a typical composition for chlorite.

4.4.2.3 Biotite chemistry of mineral clasts enclosed in impactites

Biotite mineral clasts are relatively abundant in most suevite dyke matrices and are generally found as part of the cataclased segments of the variegated melt occurring together with quartz and feldspar. Biotite is commonly partially replaced by prehnite (Figure 2.36E). Stoichiometric biotite analyses are quite limited and variable but Figure 4.3 shows general agreement with a derivation of clasts from the granitoid gneisses (GG-1 or GG-7).

4.4.3 Clinopyroxene and amphibole

4.4.3.1 Clinopyroxene and amphibole in target rocks

Amphibole is observed in both the metadolerite and dolerite and also occurs in a lithic clast in suevite (M4 S-6). Only dolerite clinopyroxene analyses are reported, as although relict clinopyroxene was identified in the metadolerite (see Section 2.4.4), no stoichiometric analyses could be obtained owing to extensive uralitization and oxidation. The analyses of the clinopyroxene from the dolerite yielded an average augite composition of $Wo_{33}En_{39}Fs_{28}$ (Figure 4.4). The X_{Mg} of the clinopyroxene ranges

from 0.44-0.75 (Appendix 4A), although if outlying low-X_{Mg} values are removed, the range is 0.60-0.75. As no consistent zoning trends were noted, the variable magnesium number may be indicative of variable alteration experienced by these pyroxenes. Amphiboles in the metadolerite and dolerite range from actinolite to magnesiohornblende according to the classification scheme of Leake et al. (1997; Figure 4.5).

The amphibole in the metadolerite sample M4 A-1 displays a relatively uniform X_{Mg} (average 0.71), whereas the amphibole in the dolerite shows more variability and is less magnesian (average X_{Mg} = 0.57); however, the amphiboles in the metadolerite show a wider range of Si content (Table 4.4 and Figure 4.5), which might be consistent with the zoned metamorphic reaction texture described in section 2.3.4.3. Based on Deer et al. (1997) Al^{vi} vs Na+K classification, the amphiboles in both rocks fall along a similar overlapping trend in the hornblende field, but with slightly higher overall Al^{vi} and alkali contents in the metadolerite (Figure 4.6).

4.4.3.2 Pyroxene chemistry of mineral and lithic clasts enclosed in impactites

In Figure 4.4B, none of the pyroxene compositions from the enclosed lithic clasts actually fit Figure 4.4A's spread. Analyses from the lithic clast from suevite sample M4 S-4 come close to the dolerite pyroxene compositions, but are less calcic. Data from sample M4 S-6 data show diopside compositions, which could be the result of the unusual exotic ultramafic clast component, consistent with bulk geochemistry (Section 3.3.1). Pyroxene microprobe data shows augite ($En_{16-19}Wo_{36-43}Fs_{42-46}$) is dominant in the analysed lithic clasts in grey suevite (sample M4 S-4, Appendix 4C), which is consistent with a dolerite source (compare Figure 4.4A). Augite is also found in MMBr samples M4 IM-6 and IM-3. Actinolite and hornblende compositions from metadolerite/dolerite lithic clasts enclosed in M4 impactites are shown in Appendix 4B. The amphibole in samples M4 IM-4 (average X_{Mg} = 0.65) and M4 S-4 (average X_{Mg} = 0.69) is more magnesian compared to the hornblendic amphibole in M4 IM-3 (average X_{Mg} = 0.59) and the M4 S-6 samples with an average X_{Mg} = 0.44 (Appendix 4B). When these data are plotted in classification diagrams (Figure 4.5B), it is clear that the amphibole types such as actinolite and magnesiohornblende are present in the clasts in the impactites. These closely resemble those found occurring in M4 target rocks (see Figure 4.5A). Once again, the suevite sample M4 S-6 is anomalous as its amphiboles lie in the fields of ferro-actinolite and ferro-hornblende (Figure 4.5B) and (Figure 4.6B).

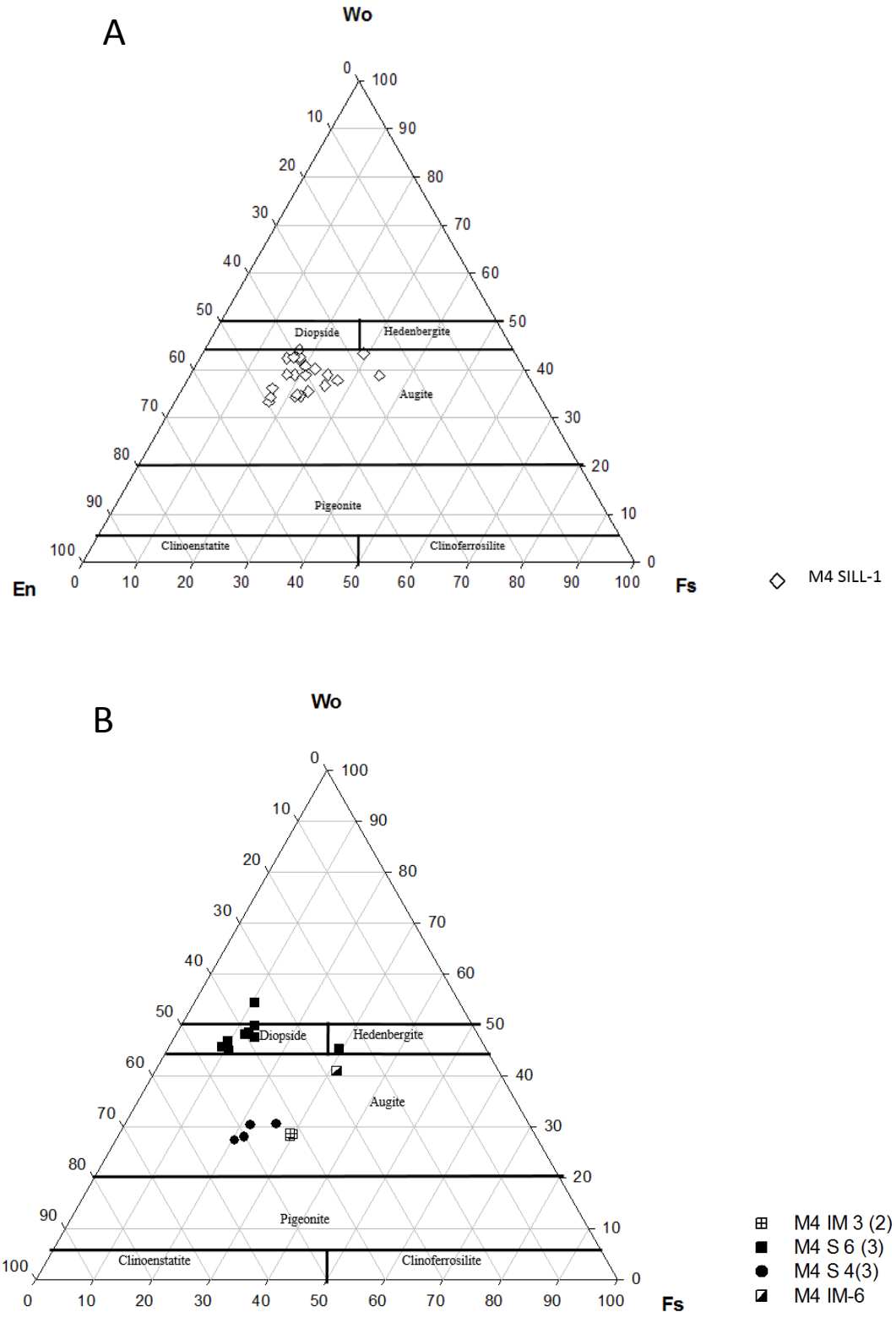

Figure 4.4: Pyroxene ternary plots (after Morimoto, 1988). **A)** Data from dolerite sample M4 SILL-1. **B)** Data from dolerite and possibly metadolerite lithic clasts in impactite samples.

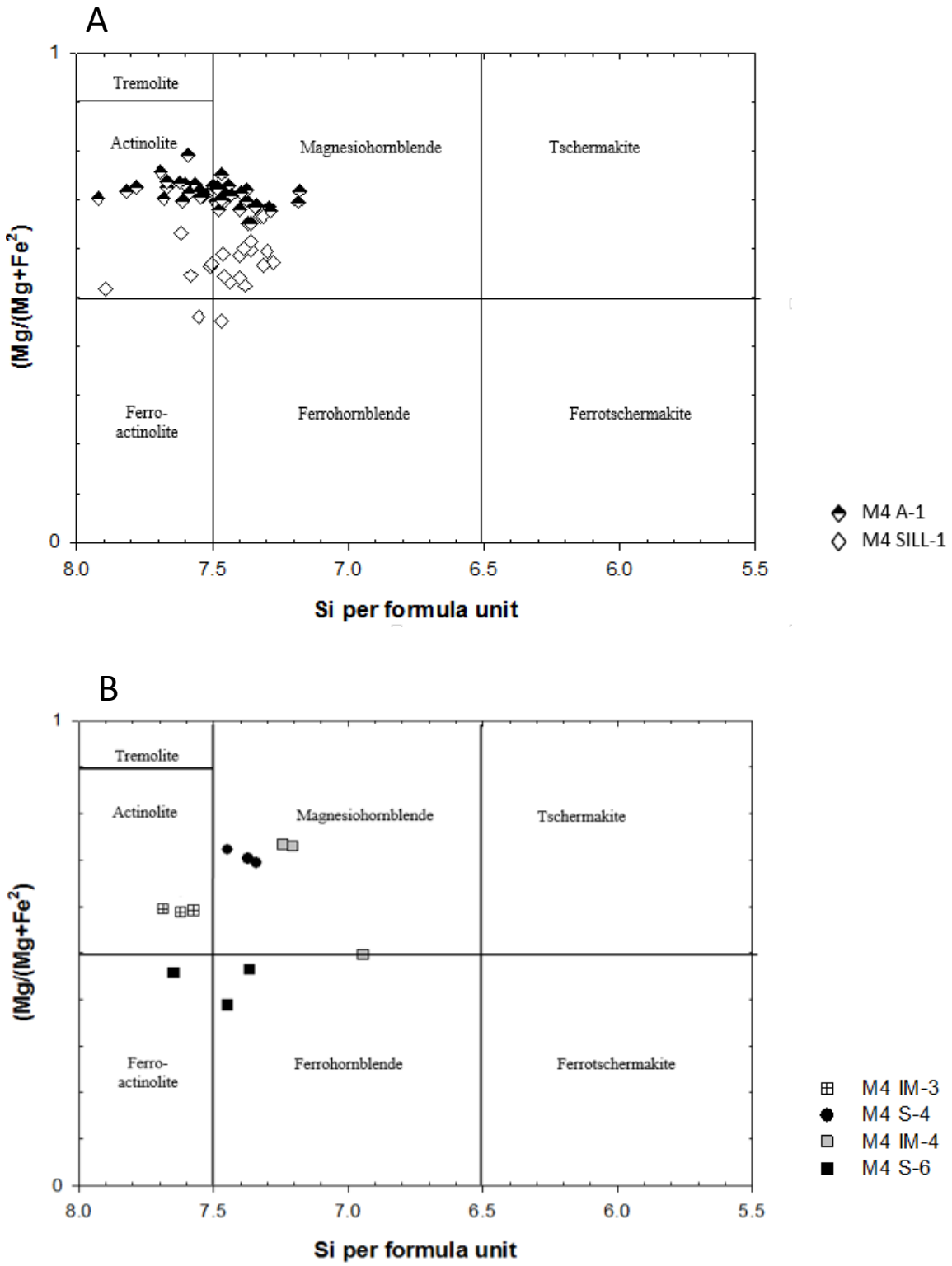

Figure 4.5: Amphibole compositions plotted on the calc-amphibole classification diagram of Leake et al. (1997). **A)** Data from dolerite and metadolerite samples. **B)** Amphibole compositions from mineral and lithic clasts in impactite samples.

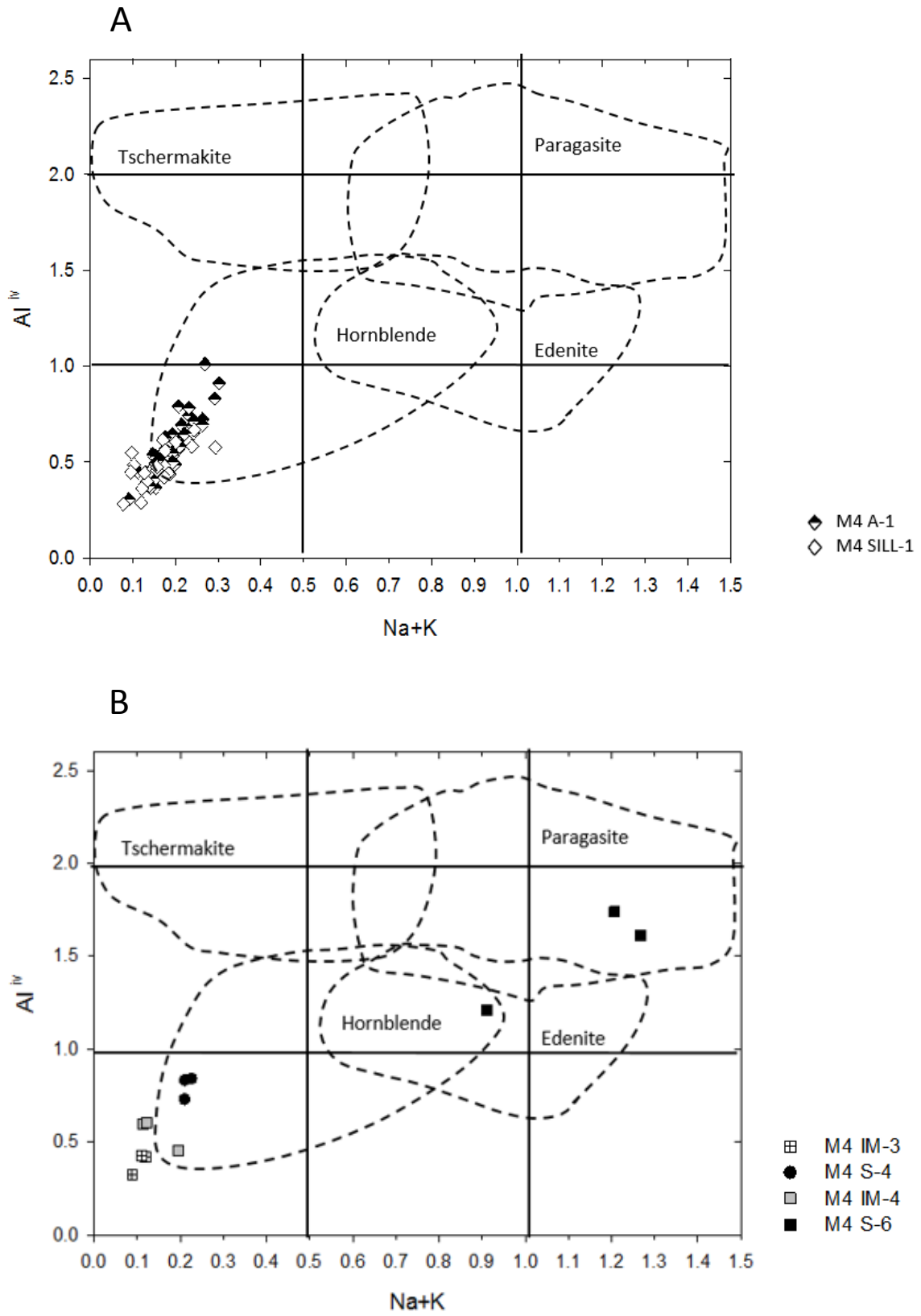

Figure 4.6: Amphibole compositional data plotted on the classification diagram of Deer et al. (1997). **A)** Data from dolerite and metadolerite in the M4 core. **B)** Data from mineral and lithic clasts from impactite samples in the M4 core.

4.4.4 Minor constituents and accessory minerals

Primary and pre-impact alteration minor constituents and accessory minerals that were noted in the M4 core target rocks include epidote, titanite, apatite, zircon and opaque minerals (titanomagnetite, ilmenite and magnetite). Compositional data for these minerals (except for zircon, which was not analysed) are presented in Appendix 4A. Data for epidote, which shows some variation, are listed in Table 4.7 and discussed below. In addition, epidote, magnetite, haematite, pyrite and a range of minor sulphides form part of the post-impact alteration assemblage with quartz, calcite, zeolites, clays and gypsum – these are discussed in section 4.7. Abundant chlorite and epidote were noted petrographically in green suevite samples (M4 S-6) (see Appendix 4B). Ilmenite is the most abundant oxide examined though petrographically, magnetite was also noted in impactites.

4.4.4.1 Epidote

Epidote is considered as part of the primary assemblage in the granitoid gneisses because of its coarse grain size and common association with biotite and titanite, but it is also found as small laths with biotite as inclusions in plagioclase cores in the granitic gneisses (see section 2.3.3.2). Epidote is also found in trondhjemitic gneiss, dioritic gneiss and metadolerite (Table 4.4). It is most common as a matrix mineral in the dioritic gneiss. In the metadolerite epidote is part of a fine-grained upper greenschist facies metamorphic assemblage associated with fractures. Additionally, it forms part of the fine-grained hydrothermal assemblage with chlorite, pyrite and garnet in fractures and vugs in the granitoid gneisses and impactites in the lower parts of the core.

The pistacite component ($Ps = 100*Fe^{3+}/(Fe^{3+} + Al)$) of epidote decreases from the dioritic gneiss (40%) to the trondhjemitic gneisses (29%) and the metadolerite (19%). Epidote compositions in the metadolerite are more variable and possibly not fully stoichiometric as a result of its fine grain size or compositional zoning, as suggested for the amphiboles (see section 4.4.3).

4.4.4.2 Titanite

Titanite is common as a primary mineral phase in dioritic and trondhjemitic gneiss and as a finer-grained metamorphic phase in metadolerite. The compositional data for titanite, presented in Appendix 4A, shows no variation between samples.

4.4.4.3 Oxides

Magnetite, ilmenite and titanomagnetite occur commonly as primary igneous/metamorphic mineral phases in most target rocks as well as clasts in the impactites and can be distinguished from the post-impact oxides by their larger grain size and their location outside of fractures (see Appendix 4A for the EMPA data). In most samples in the upper parts of the core magnetite is altered to haematite to varying degrees as a result of post-impact hydrothermal effects. In the lower parts of the core, however, magnetite may itself be replacing pyrite in fractures. Titanomagnetite shows distinctive ilmenite lamellae in SEM back-scattered images (see Figure 2.28F). Apart from this, the oxide minerals display uniform compositions.

4.4.4.3 Apatite

Apatite was noted in both the granitoid target rocks and as clasts in the impactites. It is most abundant in the dioritic gneiss. Compositional data for apatite (Appendix 4A) indicate that it is hydroxylapatite.

4.5 Mineralogical and geochemical analysis of impactites

Transmitted light and BSEM image analysis indicates that the MMBr matrix and melt particles in the MMBr consist of a micro- to cryptocrystalline mineralogy rather than glass (Chapter 2, Section 2.4.2), however such techniques can only cover small areas of a sample. Red-brown melt clasts in the suevite display a similar crystalline texture consisting of <10 μm long colourless phyllosilicate and 1-3 μm opaques that are relatively homogeneously distributed over areas > 1mm^2 (Figure 2.30B). Distributed through this matrix are rounded quartz grains as small as 10-50 μm (Figure 2.23B). Taken together with transmitted light evidence of abundant microscopic mineral clasts within the melt, it is then probably not too surprising that bulk-rock XRF and ICP-MS geochemical analysis techniques (Chapter 3) show that the MMBr composition is approximately similar to target rocks. In the suevites, petrographic and BSEM image analysis also shows that the angular mineral clast fragments are cemented by phyllosilicates and opaque minerals (Figures 2.28F, 2.37C). However, some melt clasts in the suevite and melt particles in the MMBr, such as the orange melt clasts in sample M4 S-4 and M4 IM-6, show a different microtexture, variegated, irregular extensively altered grains (Figures 2.30E, 2.37A, B). They also show signs of fracture-controlled mineral growth, with aggregates growing into the clasts from fractures (Figure 2.37), and with the fractures containing pyrite, magnetite/haematite, silica or zeolite fill, that suggest fluid infiltration and at least some open-system

chemical behaviour. In order to investigate the fine-grained post-impact mineralogy and to try to investigate the source of the melt clasts and the MMBr, it was decided to perform a bulk-rock XRD analysis together with defocussed-beam EMPA.

Post-impact alteration in the M4 core impactites is macro- and microscopically evident (Figure 2.37). The XRD, BSE-EDX compositional analysis and EMPA methods were utilised to try to characterise the melt particles and the matrices of both the suevites and MMBr (Appendix 4B). Based on transmitted light microscopy, two main types of melt clast have been identified in the M4 suevites (Chapter 2) – the most common type is black to reddish-brown or brown, which is commonly flow banded the second type is the less common, smaller orange, pink or green clasts. The first type looks identical to the melt matrix of the MMBr. Viscously deformed melt particles in the MMBr also appear to belong to the first group. The black and red-brown melt clasts and MMBr matrix appear isotropic under crossed polarizers, except for quartz and feldspar clasts and felsic bands, which are interpreted as bands of clastic breccia incorporated into flowing melt.

Because the melts are cryptocrystalline, both defocussed-beam (10 μm beam diameter) EMPA and powder XRD were used to try to investigate the chemical composition and mineralogy of the melt clasts and MMBr matrix. The XRD results, which also include suevite matrix samples, are presented in Section 4.5.1.3 and the EMPA data for MMBr matrix in Section 4.5.1.2. Each technique has its limitations: the XRD analysis cannot discriminate between clasts and melt devitrification products, and the spectra are extremely complex, which has made it difficult to identify all phases from peak analysis; and even using a much more narrowly focussed beam for EMPA of melt particles and MMBr matrix traverses produced very erratic, commonly low, totals. These are interpreted as the result of a combination of a) a low-grade replacement assemblage of mostly clays and zeolites with H_2O up to 20% (Bergaya and Lagaly, 2013; see Section 4.5.2), b) the cryptocrystalline grain size (giving a possibility of mixed analyses), and c) natural sample porosity, as shown by BSEM (Figure 2.23F). Nevertheless, the very fine grain size in the melt clasts and MMBr matrix allowed a defocussed EMPA beam to be used to evaluate general compositional variation of the melts particles (clasts in suevites).

Table 4.5: List of analysed melt-bearing samples (suevites and melt matrix breccias) of the M4 drillcore. All XRD analysis were conducted at the University of the Witwatersrand.

Sample	Depth (m)	XRD	SEM Analysis	EMPA
M4 INJ-1	140.30	✓ (MMBr matrix)		
M4 S-1	144.09	✓ (Suevite matrix)		
M4 S-7	146.68	✓ (Suevite matrix)	✓ (Rhodes) (Wits)	✓ (Rhodes)
M4 S-2	156.35	✓ (Suevite matrix)		
M4 INJ-2	158.06	✓ (MMBr matrix)		
M4 S-3	159.98	✓ (Melt particle)	✓ (UJ) (Rhodes) (Wits)	
M4 S-11	167.50	✓ (Suevite matrix)		
M4 IM-1	176.60	✓ (MMBr matrix)		
M4 A-INJ	189.00	✓ (MMBr matrix)	✓ (Rhodes)	✓ (Rhodes)
M4-S 15	208.49	✓ (Suevite matrix, melt clasts)	✓ (Rhodes)	✓ (Rhodes)
M4 IM-2	234.33	✓ (MMBr matrix, melt particles)	✓ (Rhodes)	✓ (Rhodes)
M4 IM-4	259.11	✓ (MMBr matrix, melt particle and lithic clast)	✓ (UJ) (Rhodes) ✓ (Wits)	✓ (UP)
M4 IM-5	262.60	✓ (MMBr matrix, schlieric melt)		
M4 IM-3	265.55		✓ (Rhodes) (Wits)	✓ (UP)
M4 IM-6	271.17	✓ (MMBr matrix)	✓ (Rhodes)	✓ (UP) ✓ (Rhodes)
M4 B-1	284.85	✓ (Bulk composition)		
M4 S-4	285.03	✓ (Suevite matrix)	✓ (Rhodes)	✓ (UP) ✓ (Rhodes)
M4 S 5	285.97	✓ (Suevite matrix)	✓ (Wits)	
M4 IM-9	299.76	✓ (Suevite and MMBr matrix, cataclasite)	✓ (UJ) (Rhodes)	✓ (Rhodes)
M4 S-6	316.52	✓ (Suevite matrix, melt clasts)	✓ (Rhodes) (Wits)	✓ (UP) ✓ (Rhodes)
M4 SB-3	355.37	✓ (Suevite matrix)		

* *Rhodes University (Rhodes); University of the Witwatersrand (Wits); University of Johannesburg (UJ); University of Pretoria (UP).*

4.5.1 XRD Analysis of melt particles and breccia matrices

A total of 30 XRD spectra were obtained using a Bruker D2 PHASER Powder X-ray Diffractometer in the School of Chemistry at the University of the Witwatersrand, using small amounts of powder drilled from a total of 20 samples. These analyses aimed to (a) establish if any glass was present in the MMBr and melt clasts; (b) investigate the mineralogy of both individual melt clasts and the mineralogy of suevite and MMBr matrices; and (c) investigate whether there is a variation of hydrothermal mineralogy with increasing depth.

The samples analysed include 9 suevite samples representing each suevite type (red, grey and green), 4 thin MMBr dykes with injection morphologies, 6 MMBr samples and 1 highly altered, haematised, dolerite sample. Multiple powders were taken from several samples to investigate melt clasts versus matrix compositions (Table 4.11). Powder samples were obtained either directly from drilling into the larger melt clasts or, for the matrix powders, by avoiding sampling the larger melt and lithic clasts. The individual XRD profiles for each sample are shown Appendix 4C.

The bulk-powder XRD approach does not allow discrimination between different generations of minerals; this information can only be provided through transmitted light petrography and, in such fine-grained samples, by BSEM analysis. In the present study, for instance, this means that it is impossible to tell whether the presence of quartz and feldspar in the spectra refer to clasts from the target rocks, melt crystallization products, or post-impact hydrothermal phases, or more than one type. A second problem is that many feldspar, clay and zeolite minerals form part of solid solution series, commonly involving more than one cation. In complex spectra such as shown in Appendix 4C, interpretation of peaks may suggest more than one feldspar, clay or zeolite mineral may be present. This means that without more advanced XRD analysis using mineral separation prior to analysis, the spectra should be interpreted in only a general way.

Based on petrographic evidence presented in Chapter 2, the following complications could happen in interpreting the M4 XRD spectra:

1) Albitic plagioclase is a major constituent of the granitoid gneisses in the M4 core (Section 2.3.1) but is also common in zeolite facies hydrothermal assemblages (Goldsmith, 1982).

2) Intermediate to calcic plagioclase peaks could correspond to mineral clasts from the doleritic rocks or to a high-temperature crystallization product from impact-generated melts.

3) Augite could be either a relict clast from dolerite or a high temperature crystallization phase from impact-generated melt.

4) Quartz could be a clast from the original granitoid target rocks, vein quartz, a melt crystallization product or a part of the hydrothermal assemblage.

5) Chlorite could be related to pre-impact alteration of biotite, pyroxene or amphibole or could be part of the post-impact hydrothermal assemblage.

6) Epidote could come from the target rock assemblage either as part of the original granitoid and dioritic gneiss paragenesis or inclusions in plagioclase cores (Chapter 2, Section 2.3.3), or be part of the post-impact hydrothermal assemblage.

7) Magnetite, titanomagnetite and ilmenite may either be clasts from any of the pre-impact lithologies, high-T melt crystallisation products or post-impact hydrothermal alteration minerals.

As far as can be determined from BSEM image analysis (Figure 2.23F), no high temperature igneous-looking feldspar, pyroxene, amphibole or biotite has been found in the MMBr matrix or melt particles or clasts. This does not mean that these might not have originally existed, however, textural analysis suggests that the hydrothermal alteration is comprehensive.

4.5.1.1 Alteration of target rocks

In contrast to the granitoid and dioritic gneisses, the doleritic rocks in the M4 core show extensive alteration to cryptocrystalline minerals that often make identification of minerals and textures difficult. As part of the XRD study, an altered dolerite specimen was compared with an altered dolerite clast in a MMBr. The mineralogy of the dolerite clast was also compared with the MMBr matrix next to it.

The spectrum from the dolerite sample M4 B-1 (Appendix 4C), suggests that it still contains some of its igneous mineralogy (clinopyroxene + plagioclase) but that it contains a high proportion of quartz as well, which is most likely part of the alteration assemblage. Magnetite appears to be absent, but haematite is abundant. The rest of the assemblage consists of both zeolites and clays, with montmorillonite (Na+Mg+Al) and chlorite (Fe+Al) the most abundant. The matched zeolites include heulandite (Ca+Al), epistilbite (Ca+Al) and natrolite (Na+Al), whilst halloysite (Al) is a minor clay constituent. The spectrum from the dolerite lithic clast in sample M4 IM-4 (B-dolerite lithic clast), indicates augite and a similar abundance of quartz and haematite to sample M4 B-1, but no calcic plagioclase. Sepiolite (Mg + Fe) and illite appear to be more abundant than montmorillonite, whilst

talc is also present. The presence of albite suggests it must be part of the alteration assemblage. Comparatively, the MMBr matrix in this sample (M4 IM-4C (A)) shows considerably more albite and lacks any augite, but it does contain richterite, which could be formed by hydrothermal replacement of augite if extra Na was available. Quartz is once again dominant and the main clays are palygorskite and saponite, which suggest a Mg-rich source. With abundant haematite, this supports a mafic source for the MMBr. The zeolite present is dachiardite, which is consistent with alteration of intermediate plagioclase compositions. Peaks corresponding to zeolites mordenite (Ca+Na+K) and clays montmorillonite, illite and talc are noted. Contrary to the MMBr matrix no saponite and dachiardite peaks were found.

4.5.1.2 Glass in melt clasts and MMBr matrix?

XRD analysis of crystalline mineral phases should produce sharp peaks and glass is typically identified by a broad, low intensity peak (Warren and Ransom, 1992). Whilst it is difficult to expect to see too much detail in spectra such as those shown in Appendix 4C, there appears to be no broad low intensity peaks that would indicate that glass was present. This observation is consistent with BSEM images which show no evidence of glass spherules or interstitial glass miniscii in cavities in the suevite or MMBr. However, this does not mean that glass was not originally present. The extremely fine grain size and homogeneous distribution of the alteration minerals in the melt clasts and in the MMBr matrix relative to the suevite matrix (e.g. Figure 2.37) suggests that they most likely formed from alteration of a homogeneous, glassy, phase, rather than crystalline minerals, which would be expected to have caused more variability in the distribution of the alteration products.

The XRD spectra for the matrix portions of MMBr were analysed from samples M4 IM-4, M4 IM-5, M4 IM-6, M4 IM-9 C, M4 INJ-A, M4 INJ-1 and M4 INJ-2. All the samples display similar XRD profiles which consist of quartz, albite, haematite and augite (unless otherwise specified). MMBr matrix (A) from sample M4 IM-4 showed the presence of clays palygorskite (Mg+Al) and saponite (Mg+Al), and the zeolite dachiardite (Na+Ca+Al). In sample M4 IM-5(A), the MMBr matrix analyses indicate the presence of clays saponite (Mg+Al), vermiculite (Mg + Al), and montmorillonite (Na+Ca+Al+Mg) and the zeolite mordenite (Ca+Na+K) with lesser natrolite (Na + Al) and dachiardite (Na+Ca+Al). The M4 IM-6 MMBr matrix only showed the presence of mordenite (Ca+Al) and natrolite (Na+Ca), however the overall profile is similar to other MMBr matrix profiles noted. Sample M4 IM-9C is the MMBr component of the composite dyke sample. The MMBr section notably consist of saponite + montmorillonite clays and natrolite + mordenite + chabazite (the

chabazite could relate to the thin fracture fill veins seen in the thin section). The results from this sample is discussed in detail in Section 4.5.1.4.

Sample M4 IM-2 differs from the other MMBr samples in its colour (orange, pink and white; Figure 2.34C) and in the relatively coarse hydrothermal alteration mineralogy. It lies close to an area of significant core loss that suggests a fracture or fault zone that could have focussed high fluid movement and alteration, and it is not possible to actually confirm that the original sample was MMBr. The XRD spectrum for the sample matrix (M4 IM-2 (B); Appendix 4C) indicates a lack of FeMg minerals, with illite-montmorillonite clays (K+Al) and chabazite (Ca), epistilbite (Ca) and mordenite (Ca+Ba) zeolites in addition to quartz and albite. If M4 IM-2 is a MMBr, then this would suggest a granitoid source, unless Na-K metasomatism completely changed the rock chemistry.

The thin MMBr injection dyke sample M4 INJ-A, is located within the metadolerite interval. In addition to quartz, albite and haematite, it contains Mg-rich clays (sepiolite – Mg+Fe and vermiculite – Mg+Al+Fe) that are consistent with a mafic source. It also contains Na zeolites (natrolite – Na+Al), mordenite – Rb+Al). MMBr dyke samples M4 INJ-1 and INJ-2 are quartz-albite-dominated, but haematite is secondary to palygorskite clays (Mg+Al). Sample M4 INJ-1also contains some montmorillonite-illite (Al+K). Mordenite (Ca+Ba+Al) is second only to quartz and albite, with subsidiary zeolites being natrolite (Li+Na+Al) and epistilbite (Ca+Al). The zeolites are consistent with a predominantly intermediate to calcic plagioclase source, and the presence of augite and calcic plagioclase peaks would support these being clast phases. The zeolites in sample M4 INJ-2 are dominated by stilbite (Ca + Na), with secondary dachiardite (Na+K+Ca+Al) and mordenite (Na+Al). It also contains pargasitic amphibole, which was also noted in EMPA in the suevite sample M4 S-6, which contains exotic lithic clasts. This could, however, also be a pre-impact alteration product of clinopyroxene in the metadolerite.

Melt particles were analysed in MMBr samples M4 IM-2 and M4 IM-4 (see Appendix 4C). BSEM indicates that the melt particles show a broadly homogeneous distribution of minerals despite their devitrified nature. In sample M4 IM-2, the melt particle (A) analysed represents the pink melt and the (B) portion is the cataclased schlieric portion. The melt particle is dominated by quartz and albite, with zeolites likely derived from alteration of plagioclase (stilbite – Ca+Na, natrolite – Na +Al) and alkali feldspars (dachiardite – Na+K+Ca), and an Na+Mg+Al clay (montmorillonite). Although it appears less potassic than the host matrix (M4 IM2 (B)) it is similar in lacking haematite, supporting a granitoid gneiss source.

4.5.1.3 XRD spectra for melt clasts in suevite and suevite matrices

Suevite samples investigated by XRD include: M4 S-1, S-2, S-3, S-4, S-5, S-6, S-7, S-11 and S-15 and SB-3 (Table 4.5). Of these, bulk-rock compositional data are available for M4 S-1, S-2, S-3, S-5 and S-6 (Chapter 3). BSEM analysis of suevite matrices (Section 2.4.3.2) suggest that they are mostly made up of clasts of quartz and feldspar with minor titanomagnetite/ilmenite/magnetite and biotite, cemented by phyllosilicates or zeolites (Figure 2.28F). XRD analysis of the suevite samples suggests that, in general, in addition to quartz, albite and haematite/magnetite, the suevites appear to be dominated by zeolite minerals such as stilbite (Ca+Na), natrolite (Na+Al), mordenite (Ca+Al), heulandite (Na+Ca+Al) and chabazite (Ca+Al), with phyllosilicates (montmorillonite, illite, saponite and rare chlorite) being less common. The zeolites could suggest a strong plagioclase source, which fits with the mineralogy of the target rocks (Chapter 2).

The suevite matrix from the red suevite sample M4 S-1 shows a zeolite (Ca>Na) assemblage, with heulandite (Ca+Al), stilbite (Ca+Al) and natrolite (Na+Al), and halloysite (Al) as the clay mineral. M4 S-2 peaks coincide with the zeolites heulandite (Na+Ca+Al), natrolite (Na), dachiardite (Ca) and mordenite (Ca).

Matrix from the grey suevite sample M4 S-4 also contains some haematite, but with a lower abundance than the red suevites. Quartz shows a strong peak, similar to M4 S-11 and M4 S-15. Stilbite (Ca+Na) is the dominant zeolite, with secondary mordenite (Ca+Na+K) and natrolite (Na+Al). No clays are noted, but pargasitic amphibole, possibly a clast phase, is. Haematite is abundant in the matrix from grey suevite sample M4 S-5, which is dominated by clays such as chlorite and illite (K+Na+Mg+Fe+Al), halloysite (Al) and palygorskite (Mg+Al). The only zeolite matched was mordenite (Ca+Na+K).

In sample M4 S-7, zeolites include mordenite (Ca+Al), chabazite (Ca+Al) and natrolite (Na+Al) and the clay is palygorskite (Mg+Al). Sample M4 S-11 suevite matrix contains Ca-Mg montmorillonite clay and zeolites dachiardite (Ca), mordenite (Ca+Ba) and natrolite (Na+Al) that suggest alteration of plagioclase and/or a Ca-Mg phase such as clinopyroxene or amphibole. With abundant Fe (haematite), this could be compatible with a more mafic source, such as the wallrock metadolerite. The matrix powder in suevite sample M4 S-15 (C) contains illite (K) clay and epistilbite (Ca+Al) and chabazite (Ca+Al) zeolites. Sample M4 SB-3 contains quartz, albite and Na-Ca zeolites (stilbite, dachiardite and natrolite) and illite-montmorillonite, with minor halloysite clay that could be consistent with derivation from the dioritic gneiss wallrock.

Melt clasts analysed were from suevite samples M4 S-3, M4 S-6 and M4 S-15 (see Appendix 4C). The complex spectrum for the variegated melt particle from the reddish brown suevite M4 S-3 shows

relatively low quartz and albite peaks, abundant haematite and illite-montmorrillonite (K+Al) clays, and peaks corresponding to heulandite (Ca), dachiardite (Ca+Na); natrolite (Na+Ca+Al) and mordenite (Ca+K+Al) zeolites. In the grey suevite sample M4 S-15; two melt clasts were analysed separately from the matrix. The homogeneous brown melt clast (M4 S-15A) is enriched in Mg, Fe (may be due to found montmorillonite – Ca+Mg+Al), palygorskite – Mg+Al) and sepiolite – Mg+Fe)) and Ca; likewise, the zeolites are mostly Ca-bearing (mordenite and chabazite). The zeolites found include mordenite (Ca+Ba), natrolite (Na+Al) and chabazite (Ca+Al). The variegated clast (M4 S-15B) also contains the only recorded occurrence of chlorite in the suevite XRD sample set. The spectra for the melt particles in M4 S-15 showed the presence of mordenite, montmorillonite, chabazite and natrolite. The location of this suevite next to metadolerite can explain the source of the enclosed mafic melt clasts as well as the clasts of augite and intermediate plagioclase.

Bulk-rock XRF analysis of Sample M4 S-6 (Chapter 3) established that it has a highly unusual composition relative to both the other impactites and the M4 target rocks, being silica-poor and Mg-rich. Both the matrix and melt clasts are dark green (Figure 2.25C), and EPMA has revealed predominance of amphibole (Section 4.5.2). To investigate the source of the formed melt clasts, three powders, comprising two melt clasts (A, B) and the matrix (C) were analysed. The powders vary significantly – melt clast A is Ca-Na-Mg-Al dominated, with significant carbonate in addition to albite; dachiardite and stilbite are the main zeolites, and montmorillonite is the main clay. Quartz appears to be absent, in contrast to the two other powders. Melt clast B is dominated by Mg-Al clays (halloysite, antigorite, kaolinite and vermiculite) and very little zeolite. The matrix powder C also contains limited zeolites, but contains alkali feldspar, magnetite and clays (antigorite, illite, kaolinite). The alkali feldspar and K-rich clay (illite) supports the bulk-rock XRF data which suggest K_2O enrichment (Figure 3.8H). Augite looks like it is present in all three powders, but could be relict clasts.

Sample M4 S-2 is the only suevite located in granodioritic gneiss, however, the absence of a K-bearing hydrothermal phase suggests that it may have been derived from a K-feldspar-poor source, or it is possible that leaching occurred. Diorite-hosted samples M4 S-1, M4 S-7, and samples M4 S-3 and M4 S-11 that cut diorite in close proximity to metadolerite, display similar mineralogy to M4 S-2. These are primarily Na>Ca aluminosilicates and either suggest a primarily plagioclase feldspar source or that K (from the alkali-feldspar component of the granitoid gneisses) was preferentially leached by the hydrothermal fluids. There are no significant differences between melt particles enclosed in suevite and those enclosed in MMBr, as similar zeolites and clays are present in both; with zeolites being more dominant.

4.5.1.4 XRD analysis of composite impactite dyke

Sample M4 IM-9 from 299.76 m depth represents a composite breccia dyke in which a central MMBr is flanked by suevite and a monomict clastic breccia, with all breccias showing evidence of contemporaneous development (Figure 2.29). This sample was not examined using bulk-rock XRF, owing to its internal complexity; however, micro-samples of each breccia type were extracted and analysed to investigate whether the 3 breccia types could possibly all have been derived from the granitic wallrock.

The monomict breccia (sample M4 IM-9 (A)) shows the simplest spectrum. In addition to quartz and albite, it contains stilbite (Na + Ca zeolite) and illite (K clay), which are consistent with alteration of sodic plagioclase and alkali feldspar, respectively. The extreme quartz and albite peaks relative to the other IM-9 spectra, and to other M4 samples, could be interpreted as the result of clasts of these minerals, although at least some could be hydrothermal. No haematite was detected in this section of the sample.

Powder M4 IM-9 (B) from the suevite section shows somewhat lower, but still high, quartz and albite peaks and a more complex spectrum. The principal zeolite is mordenite and the clay is kaolinite, although chlorite is also suggested. The zeolite and clay mineral compositions support derivation from plagioclase and alkali feldspar sources, which would confirm the optical microscopy and BSEM analysis that the suevite matrix shows a dominantly granitoid component. The haematite and anatase peaks indicate significant FeTi phases which fits petrographic and BSEM observations of the suevite band being darker than the monomict breccia (e.g. Figure 2.29).

Comparative qualitative analysis of peak heights in the spectra shows that the MMBr powder (M4 IM-9 C) is significantly less siliceous and more mafic than the monomict and suevite breccias. Saponite (Mg) and montmorillonite (Ca + Mg) are the dominant clays, supporting a mafic source. The MMBr also differs from the other breccia layers in having augite. As in the other MMBr powders, this is interpreted as most likely a clast phase, but would require that the MMBr was derived from a mafic source, unlike the suevite and monomict breccia layers. The MMBr does contain both haematite and anatase, like the suevite. Although Na-bearing clays/zeolites (natronite, mordenite) are relatively common, albite is a minor component, in contrast to the flanking breccias. The presence of chabazite might be related to the thin cross-cutting veins seen in Figure 2.29C

As the base of the metadolerite interval lies within a few metres of sample M4 IM-9, it seems most likely that the MMBr is derived mostly from melting of the metadolerite. In contrast, the suevite appears to be intermediate compositionally between the MMBr and monomict (cataclastic) breccia, which is consistent with the mechanical mixing model between cataclasite and melt proposed in

Chapter 2 (see also Chapter 6). Qualitatively, zeolite dominates over clay minerals in the suevite matrices, whereas clays dominate over zeolites in the MMBr and glass fragments. A possible reason for this is that the melt-derived glasses are more enriched in Fe, Mg and Ca owing to a more mafic (metadolerite and/or dolerite) source, and this favoured the formation of Fe-Mg-Ca clay minerals, whereas the suevite is dominated by a cataclastic granitoid gneiss source that contains mostly Na and K feldspars.

4.5.1.5 Variation in XRD mineralogy within impactite types and with depth

In Section 2.5.2 it was noted that the granitoid gneisses below 310 m depth in the M4 core show significant darkening that is attributed to increased chloritisation of biotite. Chlorite is developed in the shear fractures, which indicates that it grew during the post-impact hydrothermal alteration. This darkening is not seen in the upper portion of the core. In a single sample from 316.52 m depth (M4 S-6), epidote and andradite garnet (Figure 2.36E, F) were also noted intergrown with zeolite. Kirsimae and Osinski (2012) proposed that a cooling impact hydrothermal system will pass through an initial garnet-epidote-albite-K-feldspar phase at >320 ℃, and that chlorite-smectite-zeolite forms at ~320-120 ℃ phase at lower temperatures carbonate/sulphide and Fe-oxhydrate minerals grow. Based on their proposal, it might be possible that the deeper levels of the M4 core, as represented by sample M4 S-6, experienced higher post-impact temperatures. This could also be supported by the decrease in abundance of cross-cutting carbonate veins with depth; however, XRD analysis confirms that M4 S-6 and other samples from below 300 m depth also show zeolites, clays, and Fe-oxides, and also small amounts of calcite in fractures. Only a preliminary optical microscopy study of the alteration features of the M4 samples was done. This suggested that a full textural analysis, including BSEM, will be needed to unravel the relationships; however, examples were found where the final phase assemblages occur in fractures that cut across other alteration assemblages. In the case of the deep levels of the M4 core it is then possible that garnet, epidote and chlorite may have formed at higher temperatures than other parts of the hydrothermal assemblage in the same rock, like zeolites and clays. The bulk-powder approach used here shows no variation in mineralogy that matches Kirsimae and Osinski's (2012) sequence and, thus, it is not known if a significant vertical temperature zonation existed in the rocks of the M4 core. A full XRD analysis of the clay mineralogy that might reveal vertical zonation will require more advanced mineral separation techniques than were possible in this study.

4.5.2 EPMA analysis of MMBr matrix and melt clasts

Backscatter SEM (Chapter 2) and XRD (Section 4.5.1) analysis of the M4 core impactites confirms the presence of a mostly cryptocrystalline low-T alteration assemblage consisting mainly of zeolites and clay minerals cementing the matrices of the cataclasite and suevite and replacing the MMBr matrix and melt clasts in the suevite. BSEM does not provide quantitative mineral compositional data, and XRD is not able to tell the difference between different generations of minerals, and the bulk powder technique also produced extremely complex spectra that have been difficult to confidently interpret (Appendix 4C). Quantitative mineral compositional analysis was thus attempted using electron microprobe facilities at the University of Pretoria and Rhodes University (Table 4.5). A variety of techniques (single point, traverses, X-ray maps of small areas) were attempted mostly to try to understand the composition of the melt clasts and MMBr matrix and, from this, their source. In the end, once mineral clasts are removed (see Appendix 4B, for the lithic and mineral clast data), analytical oxide totals between 70 and 95% were found and it was difficult to identify stoichiometrically-consistent results. Initially it was thought that this result indicated that some of the BSEM-homogeneous, optically isotropic, melt clasts and MMBr matrix areas could contain glass and that the low totals could reflect poor sample preparation, as much difficulty was experienced in making the thin sections. Later BSEM analysis of more samples showed a cryptocrystalline mineralogy with significant natural porosity (e.g. Figures 2.23F, 2.24 and 2.28E). In the MMBr matrix and melt clasts, mineral phases appear to be intergrown on the <10 μm scale, making it impossible to obtain pure mineral compositions by EMPA. It was at this point that bulk powder XRD analysis was performed. As shown in the previous section, this was also only partly successful. In the end, a defocussed beam technique was used in an attempt to understand broad compositional patterns in the melt fragments and MMBr. In general, the oxide totals that were obtained are consistent with the range expected in hydrous low-temperature minerals such as clays and zeolites (Warren and Ransom, 1992), which seem to be present based on the XRD analysis, but very few analyses turned out to be stoichiometric.

Given the complexity of clay and zeolite minerals caused by solid solution and small-scale intergrowths, only a semi-quantitative approach is used below. Although plots of major oxides should not be used to represent mineral chemical data, it was felt that the general non-stoichiometric nature of the analyses, which do not correspond to the common minerals identified by XRD, means that using oxide plots is feasible to establish broad compositional patterns if the melt clasts and MMBr were originally glass that has now devitrified under hydrothermal conditions. The aim of the rest of this section is, thus, to investigate (a) whether the devitrified melt glasses can be explained by the

types of minerals found in the target rocks in the M4 core, and (b) what types of hydrothermal alteration minerals would be consistent with the EMP analyses.

In detail, 2 MMBr matrices (M4 IM-3, M4 IM-6), 3 melt clasts with different colours from sample M4 S-5, 4 melt particles from sample M4 IM-4, 4 melt particles from sample M4 IM-3 and 5 melt clasts from sample M4 S-6 were analysed (Table 4.5). Duplicate analyses of three impactite samples (M4 IM-4, M4 S-4, M4 S-3) were done to check the analytical precision between the data obtained from EMPA at University of Pretoria and that from EMPA at Rhodes University (Appendix 1E for details). These confirmed that the low totals are not due to analytical error but are a result of high volatile content of the zeolites and clays, and natural porosity. Compositional data for selected melt particles and representative melt traverses are shown in Appendix 4D.

4.5.2.1 Bulk data analysis

Figure 4.12, shows all EMPA data from the MMBr matrices and melt particles and melt clasts in the suevites in the M4 core that displayed analytical totals of ≥70 wt%. The ternary plot was originally used by Nesbitt and Young (1984) to evaluate sediment provenance by accounting for the loss of mobile CaO and Na_2O during weathering (Figure 4.12). According to Nesbitt and Young (1984), during weathering, bulk rock compositions will shift in the direction of the arrow in Figure 4.12. In Figure 4.7, EMPA data are used holistically instead of bulk composition data. They show the generally K_2O-poor character of the MMBr matrix and melt particles and the suevite melt clasts in the M4 core. Almost all the data plot above the tie-line between the $CaO+Na_2O$ apex and biotite data from the target rocks. Within this triangular area, two main clusters can be seen. The main cluster overlaps the plagioclase field for the target rocks and the second cluster overlaps the smectite-kaolinite-gibbsite-chlorite fields plotted from mineral end-member data (Figure 4.7D). However, some data lies closer to the $CaO+Na_2O$ apex than the line defined by the granitoid and doleritic ("basalt") bulk rock compositions in Figure 4.12), which shows that amphibole and/or clinopyroxene contributed with biotite to the melts. This would support a metadolerite and/or dolerite source, but it must also be noted that many of these analyses come from melt clasts in suevite sample M4 S-6, which has a highly unusual bulk and clast composition (Chapters 2 and 3). In the same way, the main cluster suggests a much stronger plagioclase contribution to the melts than K-feldspar (Figure 4.7D). This could also be interpreted as meaning that doleritic rocks were more important sources of the melts than the granitoid gneisses, but it was shown in Chapter 2 that the gneisses are also characterised by plagioclase > alkali feldspar contents. It is beyond the scope of this study to investigate whether the concentration of data towards the Al_2O_3 apex in Figure 4.7A indicates anything about loss of CaO and/or Na_2O during hydrothermal alteration. As will be seen in Figures

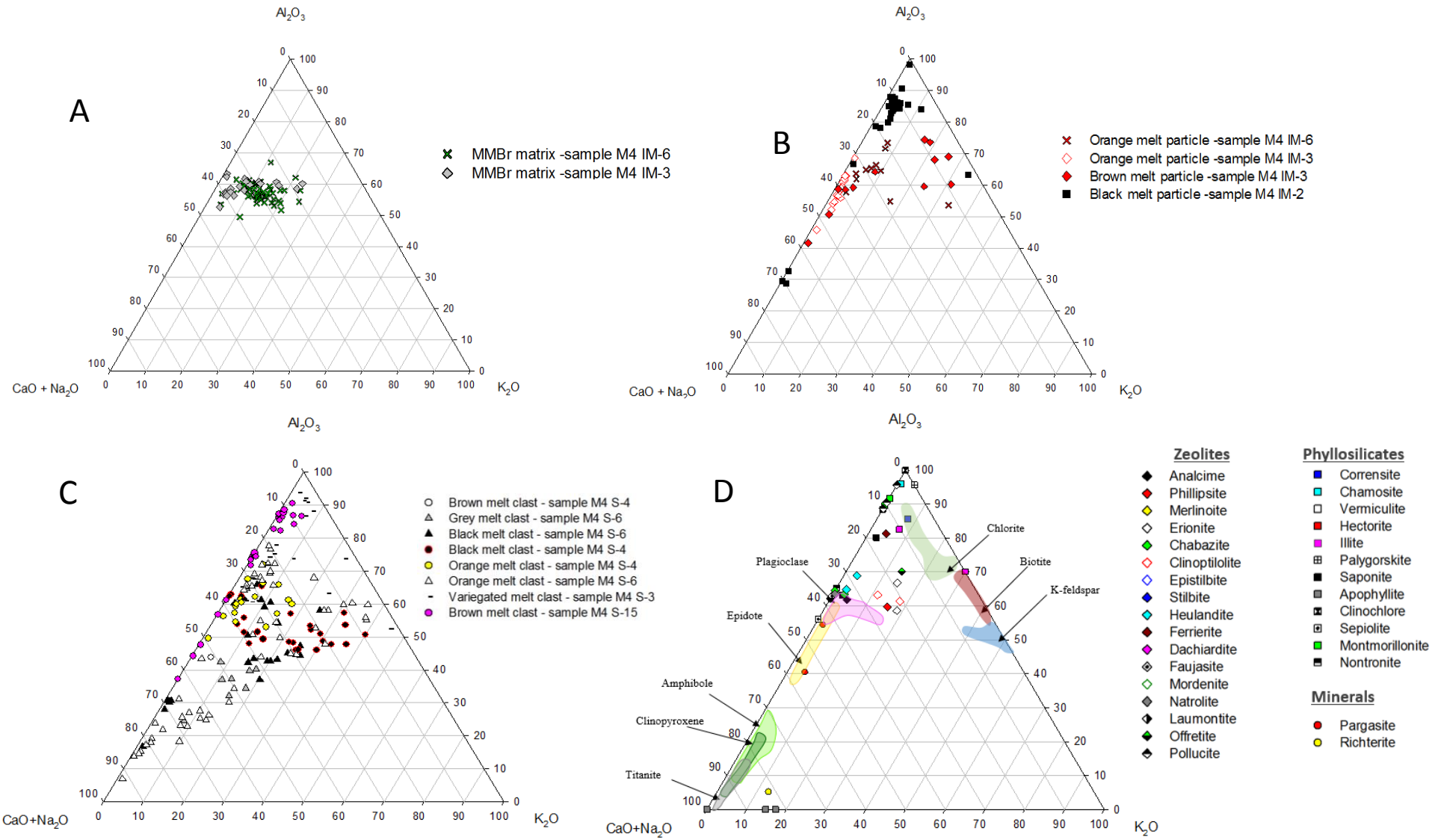

Figure 4.7: Ternary plots of Al_2O_3-(CaO + Na_2O)-K_2O for the M4 impactites. **A)** Melt matrices analysed by EMPA for MMBr. **B)** Melt particles in MMBr. **C)** Melt clasts in suevite. **D)** Mineral constituents of M4 core target rocks and secondary mineral compositions (after Anthony et al., 2011) plotted for comparison.

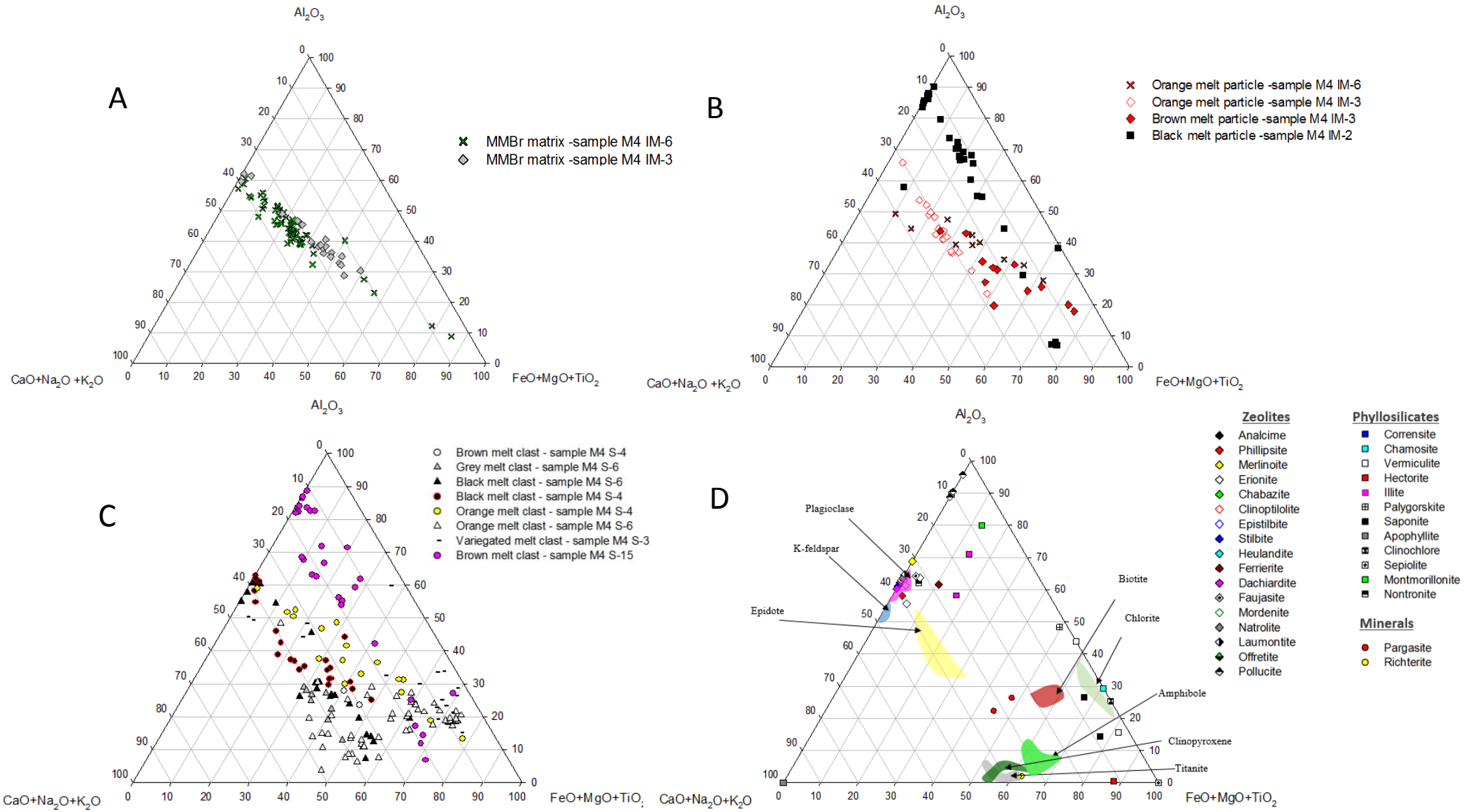

Figure 4.8: Ternary diagram of Al_2O_3 – ($CaO+Na_2O+K_2O$) – ($FeO+MgO+TiO_2$) for **A)** Melt matrices analysed by EMPA for MMBr. **B)** Melt particles in MMBr. **C)** Melt clasts in suevite. **D)** Secondary minerals (after Anthony et al., 2011) in relation to the fields of the minerals analyzed in this study.

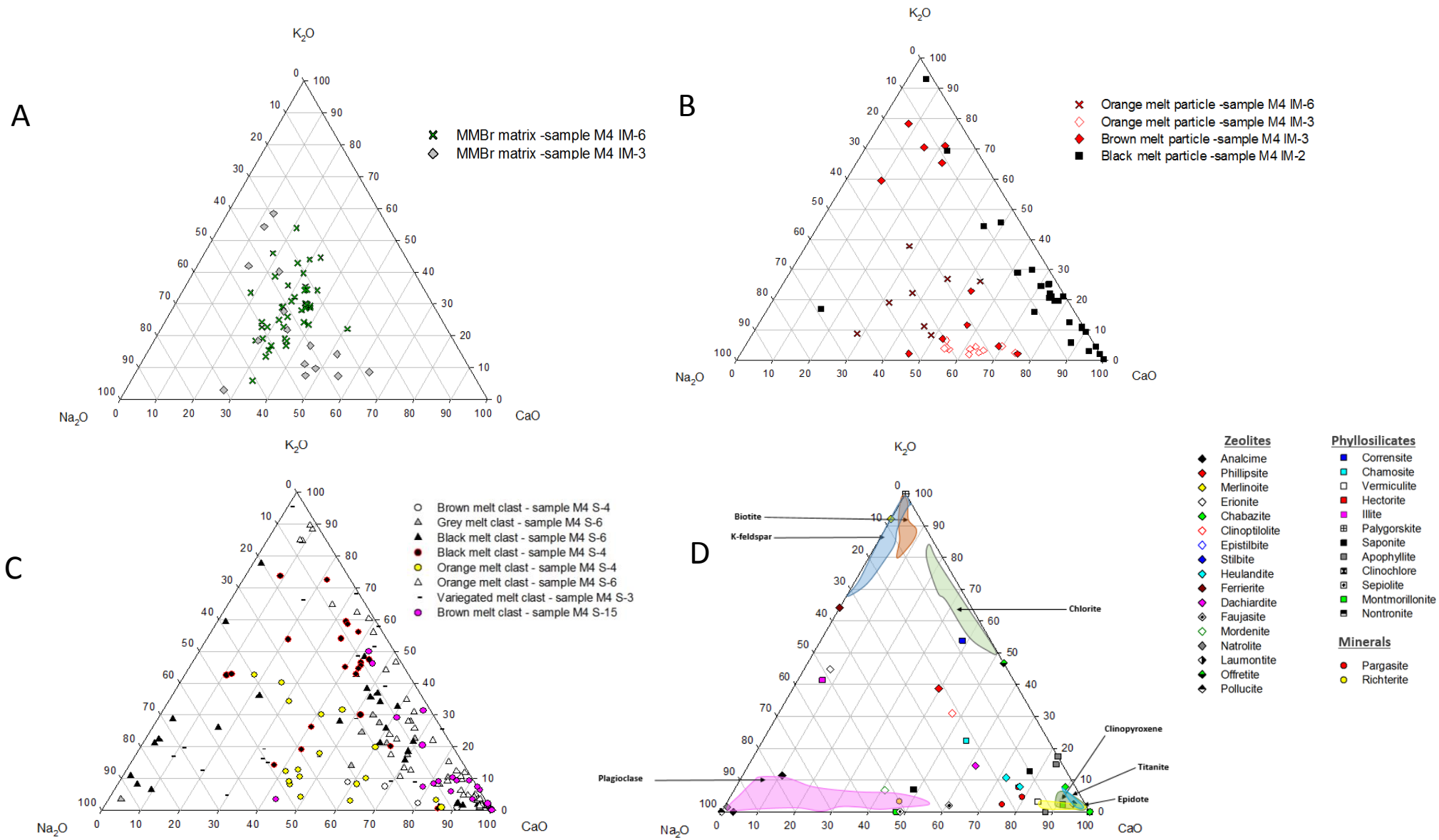

Figure 4.9: Ternary diagram of K_2O – Na_2O – CaO for: **A)** Melt matrices analysed by EMPA for MMBr. **B)** Melt particles in MMBr. **C)** Melt clasts in suevite. **D)** Secondary mineral compositions (after Anthony et al., 2011) plotted together with the fields of the minerals from this study.

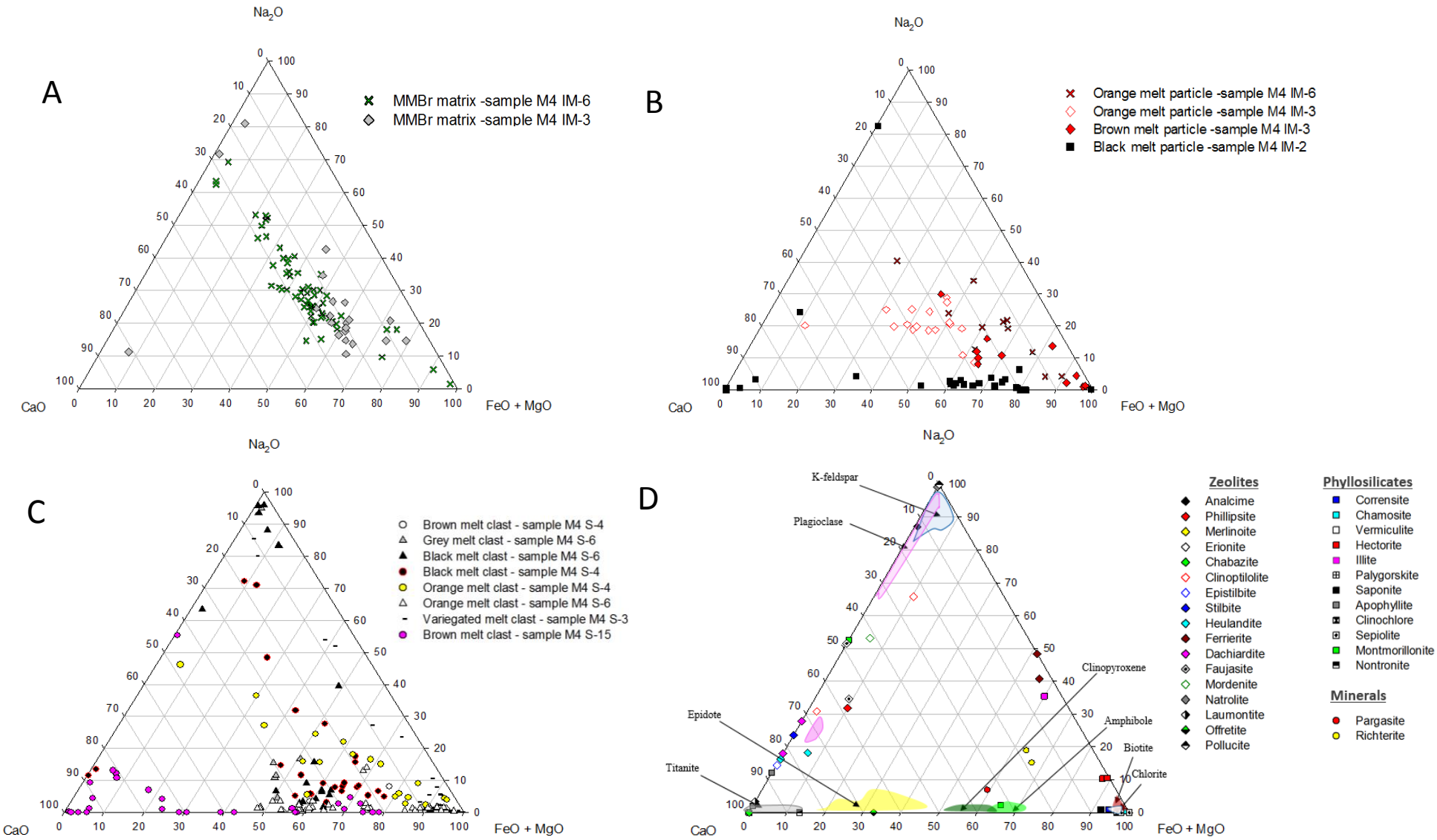

Figure 4.10: Ternary diagram of Na_2O - CaO – (FeO+MgO) for: **A)** Melt matrices analysed by EMPA for MMBr. **B)** Melt particles in MMBr. **C)** Melt clasts in suevite. **D)** Mineral constituents of M4 core target rocks and secondary mineral compositions (after Anthony et al., 2011) plotted for comparison.

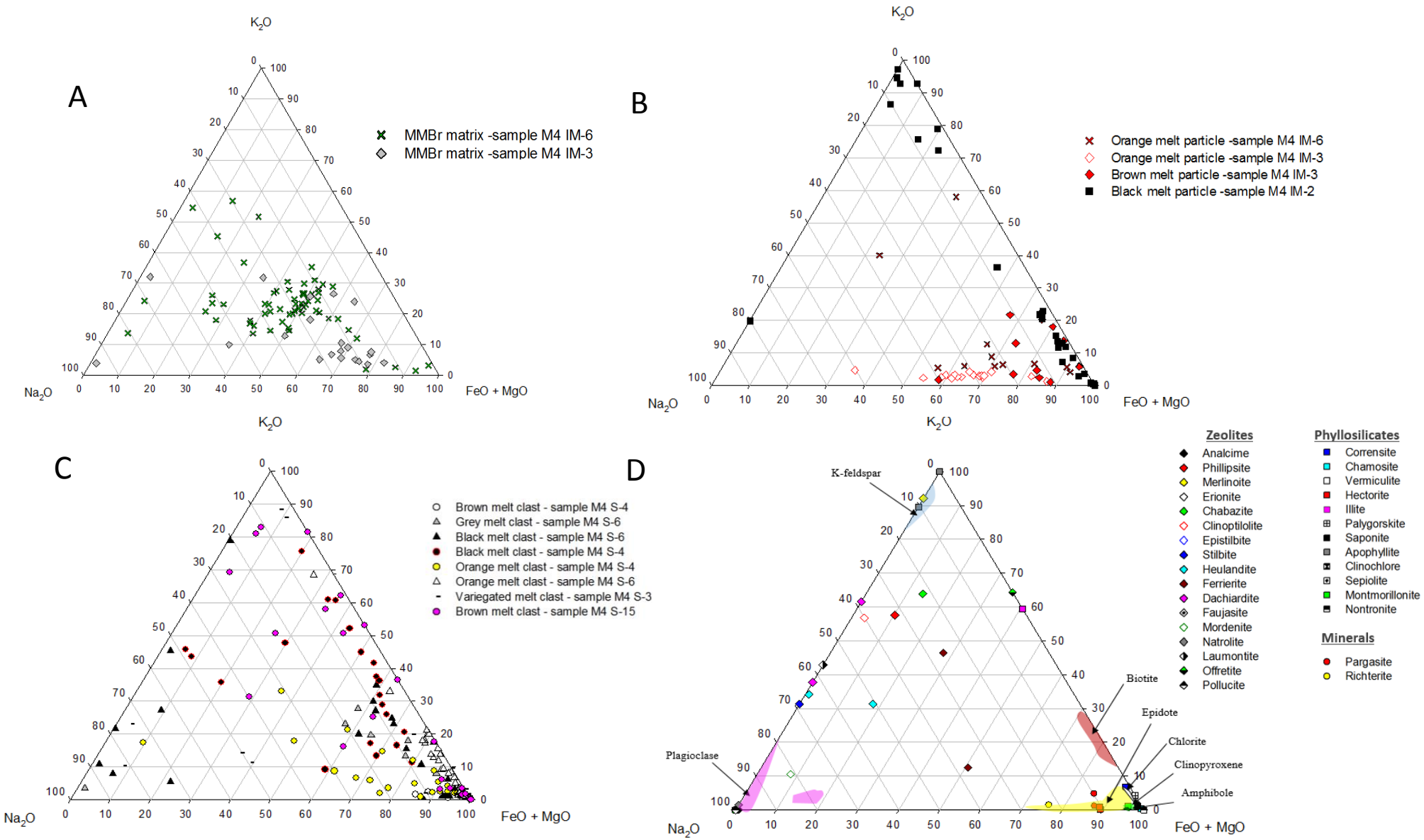

Figure 4.11: Ternary diagram of K_2O - CaO – (FeO+MgO) for: **A)** Melt matrices analysed by EMPA for MMBr. **B)** Melt particles in MMBr. **C)** Melt clasts in suevite. **D)** Mineral constituents of M4 core target rocks and secondary mineral compositions (after Anthony et al., 2011) plotted for comparison.

4.8-4.11, the EMPA data are mostly non-stoichiometric but this is most likely due to the generally smaller grain size of the hydrothermal minerals relative to the defocused beam diameter meaning that multiple grains were sampled in most analyses, so the plots in Figure 4.12A cannot be proven to exactly correlate with true original glass compositions. In Figure 4.11, all analyses (melt clasts, melt particles and MMBr matrices lie close to the FeO+MgO apex (with the exception of M4 IM-2, where some of the analyses spreads towards the K_2O apex).

4.5.2.2 MMBr melt matrix

Matrix compositions from two MMBr samples are shown in different plots in Figures 4.7A-4.11A. Analyses display SiO_2 contents between 36 and 63 wt%, with most plotting between 50 and 60 wt. %. The range of compositions indicates heterogeneity, but it is not possible at this stage to tell if this is because of varying ratios of intergrown phases or variation in the original glass composition, which would possibly signify that the melts were not able to homogenise. Heterogeneity is shown by the presence of melt particles up to several cm in size (e.g. Figure 2.24F), and on the smaller scale by banding, but a significant part of the MMBr heterogeneity may be caused by physical and chemical assimilation of cataclasite into the melt matrix (Section 2.4.2). This could mean that the melts may originally have been quite homogenous compositionally. This may be a further clue that the MMBr melt was not a superheated impact melt, so small scale heterogeneity in the M4 MMBr melts would support the bulk-rock geochemical evidence in Chapter 3 and the structural evidence in Chapter 2 that the melts are locally derived, relatively small volume and so may have been insufficiently superheated, or had insufficient time, to homogenise.

The ternary plot of Al_2O_3 versus $CaO+Na_2O+K_2O$ vs $FeO+MgO+TiO_2$ shows a strong correlation between EMPA results for the MMBr matrices in samples M4 IM-3 and M4 IM-6 (Figure 4.8A), with most lying on a line between the target rock feldspar and biotite compositions presented in Section 4.4.1 (Figure 4.8D). Sample M4 IM-6 shows some analyses that could suggest an almost pure Fe-Mg-Ti oxide end member, or these could also be microclasts. Given the general <5 μm grain size of the opaque minerals in the MMBr matrix (e.g. Figure 2.23F); it would not be surprising that the analyses are non-stoichiometric (compare with Figure 4.8D). The main set of analyses in M4 IM-6 shows a slightly steeper trend that extends between plagioclase and amphibole. A small number of analyses from samples M4 IM-3 and M4 IM-6 have overlap with the zeolites stilbite, dachiardite, natrolite, erionite, phillipsite and mordenite that could be derived from feldspars, but most analyses do not correspond to any known minerals, suggesting mixtures. Although there is no direct overlap of

specific analyses with actual mineral compositions, the opposite end of the linear trend extends towards montmorillonite, vermiculite and saponite clays. Natrolite and mordenite were identified in the XRD spectrum of sample M4 IM-6 (Appendix 4C). No clay minerals were matched.

No obvious trend exists for the MMBr melt matrix analyses on the K_2O vs Na_2O vs CaO plot (Figure 4.9A). The analyses generally show intermediate Na:Ca ratios, which would support dolerite- or metadolerite-derived melts, although Ca could also be derived from clinopyroxene or amphibole. The slight elongation towards the K_2O apex could mean that either a biotite or K-feldspar component is involved, with biotite being more likely, if the trend in Figure 4.8A is considered. Chlorite could also not be ruled out for sample M4 IM-6. Comparison with bulk-rock compositional data (Figure 3.7) shows that the M4 IM-3 data correspond relatively well to the diorites, with some trend towards metadolerite/dolerite and towards granitic-granodioritic gneisses. Sample M4 IM-6 shows a closer clustering of data, which are more calcic than the granitic-granodioritic gneisses and would favour a stronger doleritic source. The EMPA data do not correspond to any obvious zeolite or clay phases, but mixing between clinoptilolite-natrolite/erionite-analcime and stilbite-dachiardite zeolites and clays like chamosite and saponite could explain much of the variation.

Figure 4.10A (Na_2O vs CaO vs FeO+MgO) displays a relatively strong linear trend for the melt matrix analyses extending between an oligoclase-type plagioclase and amphibole and possibly a weaker biotite/chlorite end-member (Figure 4.10D). Sample M4 IM-3 shows the strongest trend towards amphibole and is more Fe-Mg-rich than sample M4 IM-6, except for a few analyses from M4 IM-6. The most likely zeolite and clay mixtures that could explain this trend would be mordenite and montmorillonite.

In Figure 4.11, almost all melt matrix analyses show no correspondence to end-member mineral compositions, but some of the analyses from sample M4 IM-6 plot close to zeolites of ferrierite and heulandite (Figure 4.11D) and to chlorite/epidote or amphibole and clinopyroxene compositions.

4.5.2.3 Melt particles in MMBr

Melt particles were analysed in samples M4 IM-3 (brown, orange), IM-6 (orange) and IM-2 (black). Most are enriched in Al_2O_3 relative to CaO, Na_2O and K_2O (Figure 4.7B, with clustering close to plagioclase compositions from the target rocks (Figure 4.7D) and some overlapping chlorite). The black melt particle in sample M4 IM-2 shows the most Al_2O_3-rich compositions that overlap with ferrierite and pollucite zeolites, and montmorillonite clay; but also, some Al_2O_3-poor analyses, which suggests compositional variation. In Figure 4.8B, the orange melt particle in M4 IM-6 shows a slightly shallower trend than the orange melt particle in M4 IM-3, which is the reverse of the

relationship for the matrices in the two MMBr samples (Figure 4.8A). This could mean that both samples contain two similar melts that have mixed in different proportions, with each being included as a clast in the other. Sample M4 IM-6 data lie on a mixing line between stilbite-dachiardite-natrolite and saponite-montmorillonite and/or vermiculite, with chamosite as an outside chance. The brown melt particle in M4 IM-3 is depleted in the feldspathic/zeolite component relative to the orange particles and the MMBr matrix (Figure 4.7A), however, it lies on the same trend as the matrix and orange particles analyses. It could be relatively enriched in clays (saponite, clinochlore, vermiculite).

Analyses from the black melt particle in sample M4 IM-2 have a distinctly different trend. They are significantly more depleted in $CaO+Na_2O+K_2O$ and show a constant:

$(CaO+Na_2O+K_2O)/(Al_2O_3+FeO+MgO+TiO_2)$ ratio. This trend does not correspond to known target rock minerals, but overlaps well with the clays montmorillonite/illite/pollucite and a weaker trend towards hectorite. In Section 2.5.2, it was discussed that sample M4 IM-2 was one of two samples that may show signs of extreme hydrothermal fluid flow. This may support the view that these fluids may have been able to preferentially remove Ca, Na and K from the impactites (see Figure 4.7), which would relate to Figure 4.12.

In Figure 4.9B, the orange melt particle in sample M4 IM-6 shows a broad scatter, similar to the sample matrix (Figure 4.9A) that does not correspond to any stoichiometric mineral plots, but it is slightly more CaO-rich than the matrix. The analyses of the orange particle in sample M4 IM-3 show very little K_2O and overlap with intermediate to calcic plagioclase and zeolites such as mordenite and faujasite, as well as montmorillonite, nontronite and saponite clays. The brown melt particle in sample M4 IM-3 displays a bimodal distribution of analyses with weak K_2O-rich and K_2O-poor clusters. The K_2O-poor cluster shows weak overlap with montmorillonite, saponite and chamosite clays and the K_2O-richer cluster overlaps with ferrierite zeolite (Figure 4.9D).

In Figure 4.10, the relative contributions of FeO+MgO vs CaO and Na_2O are evaluated to test the hypothesis that plagioclase and biotite/amphibole/clinopyroxene are the major melt sources of the melt particles. The analyses from the orange melt particle in M4 IM-6 (Figure 4.10B) display a broad linear trend between an oligoclase-type plagioclase and biotite or chlorite (Figure 4.10D). Analyses show little correspondence to known clay or zeolite compositions, except a few overlapping saponite, clinochlore and corrensite. The analyses for the orange melt particle in sample M4 IM-3 form a less obvious trend but fit a more calcic source. The brown melt particle in M4 IM-3 is more ferromagnesian. Some analyses overlap with saponite, clinochlore, corrensite.

In Figure 4.10B, analyses from the black melt particle in sample M4 IM-2 are mostly strongly Na_2O-depleted. They are also enriched in a ferromagnesian component that closely correlates with

amphibole and some clinopyroxene analyses from the target rocks, with a few Ca-rich outliers. This pattern supports the proposal made in Chapter 2 based on BSEM as it confirms the higher amounts of fine-grained opaques (e.g. Figure 2.23F) that the black melt clasts are from a more mafic source than the other melts. The main cluster overlaps with montmorillonite clay, whereas the Ca-rich analyses may correspond to chabazite and laumontite zeolites. In Figure 4.11B and D, the M4 IM-2 melt particle has components that cluster close to K_2O. Some of this data matches montmorillonite and apophyllite clays, however, most of the other points cluster next to the FeO+MgO apex and match clays such as saponite, palygorskite and corrensite. This data notably spreads towards the biotite field (Figure 4.11D).

In summary, the EMPA data from the melt particles in the MMBr display a wider compositional range than the MMBr matrices. If there is no difference in the grain size of the clays and zeolites in the particles and matrix, this would support the MMBr matrices being more homogenized compositions. The analyses generally support the proposal that the melts are derived from plagioclase and a combination of biotite and amphibole and possibly clinopyroxene, Black and brown melt particles appear to be more enriched in a ferromagnesian component. However, as for the matrices, there is only limited correspondence of EMPA analyses to known clay and zeolite mineral compositions.

4.5.2.4 Melt clasts in suevite

Data for the melt particles in suevite are shown in Figures 4.7C-4.11C. The clasts show a wider range of compositions (Figire 4.7C) compared to the MMBr matrix and melt particles (Figure 4.7A, B), but if the analyses from the black and orange melt clasts in sample M4 S-6 and the black melt clast in M4 S-4 are excluded, then the pattern is very similar. As the M4 S-4 and S-6 analyses all lie on a trend between amphibole/clinopyroxene and biotite (Figure 4.7D), they can still be explained as melts from target rocks found in the core. In Figure 4.8C, the orange melt clast in sample M4 S-4 shows the same trend and range as the orange particle in MMBr sample M4 IM-6 (Figure 4.8B), with a slight bias to higher Fe-Mg-Ti values. The analyses are non-stoichiometric but would fit mixing between zeolites such as dachiardite, stilbite and natrolite, and clays such as vermiculite, clinochlore and saponite (Figure 4.8D). From XRD analysis of the matrix of M4 S-4, stilbite, as well as mordenite and natrolite were identified, but no clays (Section 4.5.1). In contrast, the orange melt clast in sample M4 S-6 shows two groups of analyses, with one cluster being less aluminous and corresponding to the field of amphibole and clinopyroxene compositions seen in the doleritic lithologies in the core (Figure 4.8D) whilst the other overlaps the Fe-Mg-Ti end of the trend seen in the MMBr matrices as well as the

orange melt clasts in the other suevite samples. This cluster extends to more Fe-Mg-Ti rich values than the biotite found in the M4 granitoid gneisses and overlaps the compositions of clays such as saponite, vermiculite and clinochlore (Figure 4.8D). These differences fit with the petrographic and compositional evidence that sample M4 S-6 involves some exotic components not seen elsewhere in the core, and confirms the XRD profile that suggests clays dominate over zeolites, with vermiculite, antigorite, kaolinite and halloysite being present in the bulk sample (Appendix 4C). The grey melt clast in sample M4 S-6 also shows anomalously low Al content relative to the other clasts, but is less Fe-Mg-Ti rich as well. This is consistent with the alkali-richer bulk composition of the sample relative to the other suevite samples (Section 3.3.2).

The brown melt clast in sample M4 S-4 displays slightly lower Al_2O_3 values than the orange melt clast in the same sample, but overlaps one end of a steep trend in Figure 4.8C that is defined by the analyses for another brown melt clast from sample M4 S-15, which consists of 3 groups. The largest cluster for the M4 S-15 melt clast overlaps the compositions of Fe-Mg-Ti-free montmorillonite clay and pollucite zeolite, whilst the intermediate group lies close to illite clay and ferrierite zeolite (Figure 4.8D).

Suevite samples M4 S-3 and S-4 contain variegated melt clasts that are generally poorer in $CaO+Na_2O+K_2O$ than all other melt clasts except the black melt particle in M4 IM-2 (compare Figures 4.8B, C). The clast in M4 S-3 shows a bimodal distribution that defines a similar broad trend to what is seen in the MMBr matrices and orange melt clasts, one cluster lies close to average feldspar compositions, consistent with dachiardite, stilbite and/or natrolite zeolites, and a stronger cluster overlaps clinochlore, saponite and vermiculite clays.

The analyses of the orange melt clast in sample M4 S-4 are strongly scattered in Figure 4.9C, but overlap broadly with those for the MMBr matrices (Figure 4.9A) and the orange melt particle in M4 IM-6 (Figure 4.9B), whereas the orange melt clast in sample M4 S-6 shows depleted Na_2O and a strong variability in CaO/K_2O, consistent with a mixture of mordenite and faujasite zeolites and montmorillonite and saponite clays. Some of the data spreads towards merlinoite and palygorskite (Figure 4.9D). The brown melt clast in M4 S-4 is K_2O-depleted but is also Na_2O-poor. Analyses partly overlap with heulandite and dachiardite zeolites. In contrast, the brown melt clast in sample M4 S-15 contains a wider spread of analyses with low Na_2O and a strong cluster towards the CaO apex that would be consistent with laumontite and chabazite zeolites and montmorillonite and saponite clays

The grey melt clast in M4 S-6 is enriched in CaO relative to alkalis. Analyses correspond most closely to an alteration assemblage that would include dachiardite and chamosite (Figure 4.9D).

The variegated melt clast in sample M4 S-3 shows a broad scatter of analyses that is difficult to interpret. Analyses from the variegated clast are Na_2O rich which suggests a small sodic plagioclase component. The most common zeolites in this assemblage would be predicted to be erionite and analcime which contain a sodic component. In Figure 4.9D, these are the zeolites near the M4 S-3 variegated melt clasts data points.

In Figure 4.10C, the analyses for the orange melt clast in sample M4 S-4 are slightly more calcic and ferromagnesian than the orange melt particle in sample M4 IM-6 but generally agree well with the MMBr matrix analyses in Figure 4.10A, except for a few low-Na_2O and highly ferromagnesian analyses that lie close to the amphibole/clinopyroxene and biotite/chlorite fields, respectively. The array spreads between faujasite and erionite zeolites and saponite, hectorite and montmorillonite clays. The M4 S-6 orange melt clast is poor in Na_2O and analyses spread between the biotite/chlorite and amphibole/clinopyroxene fields, suggesting a very mafic source. Montmorillonite, saponite, chamosite and sepiolite clays are the most likely alteration products (Figure 4.10D). The data does spread towards zeolite offretite. The brown melt clasts in M4 S-4 and M4 S-15 show a similar Na_2O-depleted character to the orange clast in M4 S-6 but the M4 S-15 clast analyses are Ca-richer with analyses lying close to laumontite, nontronite, apophyllite and montmorillonite. (Figure 4.10D). The grey melt clast in sample M4 S-6 displays analyses that are likely to represent montmorillonite.

Analyses from the black melt clast in sample M4 S-4 in Figure 4.10C cluster towards amphibole ± clinopyroxene, with a slight trend towards sodic plagioclase. The black melt clast in sample M4 S-6 shows a similar trend that is biased towards clinopyroxene compositions, but with a second grouping towards the Na_2O apex (feldspar). In 4.9D, the M4 S-6 black melt clast analyses show some correspondence with a mixture of hydrothermal minerals such as analcime, clinoliptolite, and natrolite zeolites, and chamosite, montmorillonite clay. These melt clast analyses also scatter more than the range of analyses for the MMBr matrix (Figure 4.10A). The variegated clast in sample M4 S-3 are CaO-poor and spread from a strong cluster near the FeO+MgO apex (biotite/chlorite) towards the Na_2O apex (plagioclase; Figure 4.10C). The analyses could be a mixture of analcime and clinchlore/saponite/hectorite (Figure 4.10D). In Figure 4.11C, too much scatter is observed in the melt clasts enclosed in suevite. Most data points do however cluster around the FeO+MgO apex; but it is difficult too clearly match this data in to that in Figure 4.11D with confidence.

In summary, the melt clasts in the suevite display significant compositional variation but are also most consistent with a feldspar + ferromagnesian mineral (clinopyroxene/amphibole) source. They show broad compositional similarity to both the melt matrix of the MMBr and melt particles in the MMBr, which supports the model proposed in Chapter 3 that the melt clasts in the suevites come from fragmentation of MMBr intruding cataclasite-filled fractures.

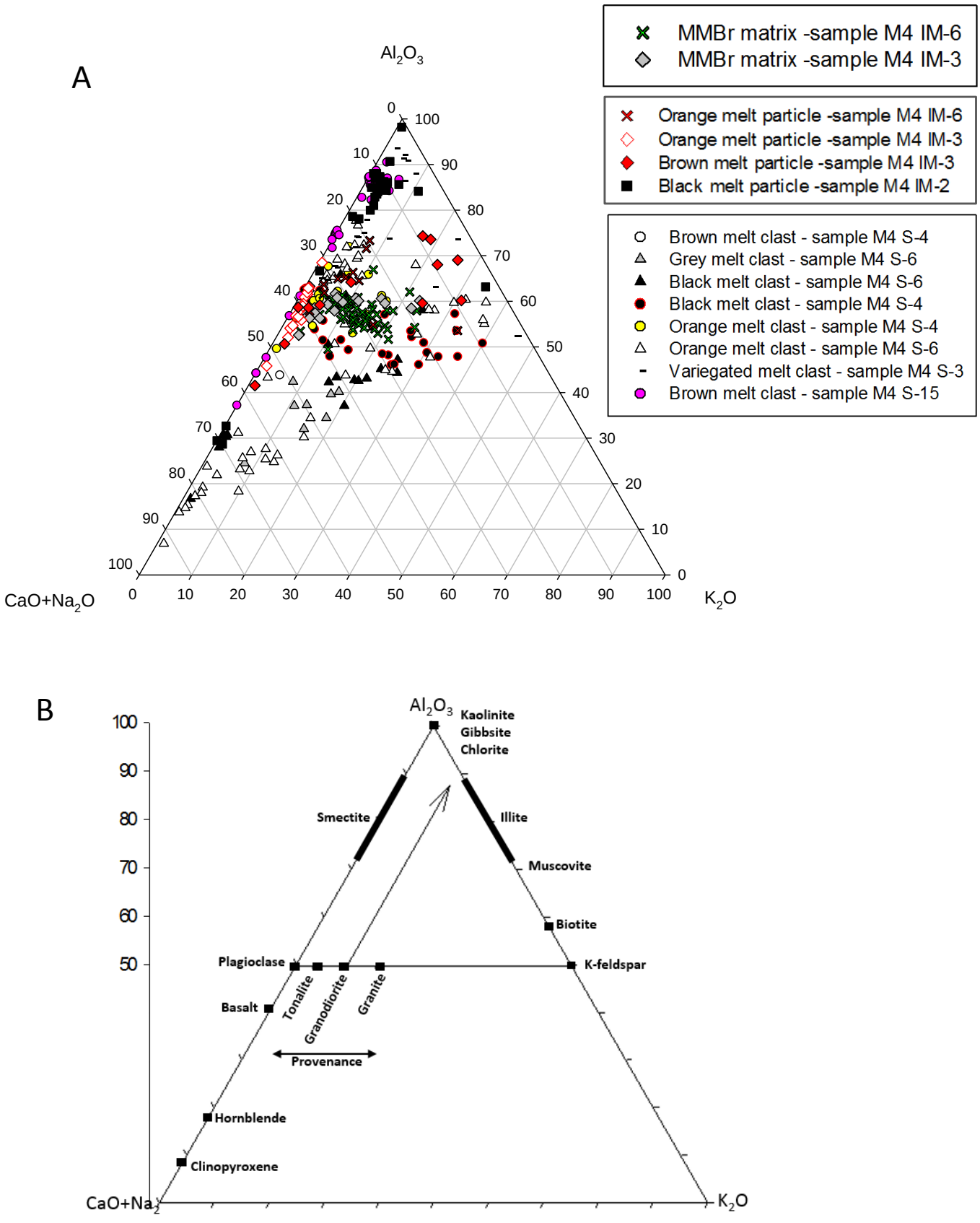

Figure 4.12: **A)** Ternary plot of Plot of Al_2O_3-(CaO + Na_2O)-K_2O showing EMPA data for melt particles, MMBr matrices and melt clasts in M4 core impactites. **B)** Al_2O_3-(CaO* + Na_2O)-K_2O plot showing the standard weathering trend is shown for comparison (Nesbitt and Young, 1984; Fedo et al., 1995). Note that vertical line on the left is the CIA scale.

4.6 Summary

Electron microprobe analysis of the M4 target rocks has confirmed most mineral compositions, although some difficulty was found with measuring stoichiometric clinopyroxene and amphibole compositions in the metadolerite and dolerite. Plagioclase in the metadolerite appears to be mostly oligoclase and overlaps slightly with the plagioclase in the granitoid gneisses, which extends between albite and oligoclase.

Attempts to analyse mineral clasts in the impactites confirmed that variable alteration has occurred but that they are mostly derived from the M4 target rocks. Problems were encountered with EMPA of the melt matrix of the MMBr and melt particles and clasts. After BSEM analysis confirmed that they are made up of a cryptocrystalline, slightly porous, hydrothermal alteration assemblage made up mostly of zeolite and clay minerals with an Fe-bearing oxide and are not glass, defocussed-beam analysis was used to try to understand possible source minerals and the alteration assemblage. More work is needed to understand both of these questions. Overall, the EMPA data support the interpretation that, with the exception of M4 S-6, the melts in the M4 core impactites were derived from the M4 target rocks. Attempted XRD analysis also produced very complex spectra that require further investigation, but confirmed the transmitted light microscopic and BSEM results that suggest that the MMBr contains microclasts of target rock minerals as well as a hydrothermal alteration assemblage.

Chapter 5

Shock Petrography

5.1. Introduction

Shock pressures produced in an impact event range from 100-400 GPa near the point of impact to ≤ 2 GPa near the final crater rim (French, 1998), depending on the size of the event/crater. As the high-pressure shock wave propagates away from the point of impact, the target rocks are shattered, deformed, melted and even vaporized (Stöffler and Langenhorst, 1994; French, 1998). Unequivocally shock-diagnostic deformation features are developed in only a small volume of target rock near the impact point; at greater distances from the impact point deformation takes place at pressures and temperatures approaching or equivalent to lithostatic conditions and, as a consequence, produces features similar to those produced by tectonic processes (Melosh, 1989). Where present, though, distinctive shock-metamorphic effects preserved in shocked rocks and minerals can be used to constrain the pressure and temperature conditions to which the rocks and their constituent mineral grains were exposed (Stöffler and Langenhorst, 1994; French, 1998; French and Koeberl, 2010). Although the shock-diagnostic features are consistent and reproducible during calibrated shock experiments, the short duration and the scale of these experiments versus natural impacts adds an element of uncertainty to absolute correlation of structures with shock pressures (Robertson and Grieve, 1977; Melosh, 1989; Stöffler and Langenhorst, 1994, French, 1998, Langenhorst, 2002).

The microscopic shock-diagnostic deformation features within individual minerals include (French, 1998; French and Koeberl, 2010): planar fractures (5-10 GPa) and planar deformation features (PDF) in quartz (10-30 GPa); diaplectic glass in a variety of minerals (30-45 GPa); and selective mineral melting (40-60 GPa) (Table 5.1). PDF can also develop in feldspar, sillimanite, cordierite, garnet, apatite and zircon as a function of shock pressure (French and Koeberl, 2010). Minerals such as quartz, feldspar (plagioclase and K-feldspar) and olivine are the most sensitive shock indicators (Stöffler and Langenhorst, 1994, Grieve et al., 1996). The low-pressure (<5 GPa), non-diagnostic, impact deformation effects that are commonly reported in impact structures but that are indistinguishable from those resulting from normal tectonic deformation include fracturing and brecciation, kink bands in micas, and mosaic extinction in quartz and other minerals. A more detailed summary of shock features and their usefulness in impact verification studies is presented in Section 1.4.

Table 5.1: Correspondence between shock features in common rock-forming minerals and shock pressure and post-shock temperature (after French, 1998).

Shock pressure (GPa)	*Post-shock temperature (°C)*	*Shock metamorphic effects*
2 - 6	< 100	Brecciation and random micro-fracturing of quartz + feldspars Shatter cones
		Kink-banding in micas
5 - 8		Planar fractures in quartz (0001) and 1011
> 8	100	Mosaicism in felsdspars (onset of mosaicism at lower pressures in K-feldspar than in plagioclase – Ostertag, 1983)
8 - 10	100	Basal Brazil twins (0001) in quartz
12 - 15	150	PDF in quartz $\{10\ \bar{1}\ 3\}$ and K-feldspar
		Microfracturing in quartz is suppressed as shock mosaicism becomes more pervasive
		Quartz phase transformation to stishovite
13	150	Graphite phase transformation to diamond
14	150	PDF in plagioclase (Ostertag, 1983)
19		Partial isotropisation of quartz (Sazonova et al., 2005)
20	170	Quartz with PDF – $\{10\ \bar{1}\ 2\}$ predominantly, with additional orientations appearing toward higher shock pressures
>23.5		Grain-boundary melting in biotite (Sazonova et al., 2005)
28 – 30	275	Total isotropisation in plagioclase – Ostertag (1983)
30	275	Quartz, plagioclase and K-feldspar exhibit lowered birefringence and reduced refractive indices
>32	275	Total isotropisation in alkali feldspars – Ostertag (1983)
33		Onset of biotite shock melting (Lambert and Mackinnon, 1984)
35	300	At pressures > 30 GPa, quartz phase transformation to stishovite
30 - 45		Quartz and feldspar diaplectic glasses
45	900	Vesiculated feldspar shock melt
52		Near-complete isotropisation of quartz (Sazonova et al., 2005)
60	> 1500	Whole-rock shock melt (quenched from liquids)
80 - 100	> 2500	Whole-rock shock melt (condensed from vapour)

Data from Stöffler (1972, 1974, 1984); Lambert and Mackinnon (1984); Melosh (1989); Huffman et al. (1993); Stöffler and Langenhorst (1994).

In this chapter, particular emphasis is placed on documenting shock textures in the respective target rocks and impactites in the M4 core. The main aims are to determine maximum shock pressures experienced by the M4 core lithologies, to examine whether any consistent shock pressure variation exists between target lithologies and impactites, and to ascertain if there is any consistent variation in shock pressure with depth. Constraining the shock pressure conditions that the M4 lithologies were subjected to during the impact allows constraints to be placed on the likely location of the M4 core within the final impact crater and, from there, on the likely location of the M4 target rock package during the initial cratering process. Since the current study is based on a drill core, information about impact-related fracture phenomena such as shatter cones, and orientations of impact-induced fractures and breccias is very limited. The main focus is thus on the examination and characterisation of microscopic shock metamorphic features observed in quartz and feldspar via transmitted light microscopy. A detailed search for high-pressure polymorphs of quartz (coesite and stishovite), graphite and zircon was beyond the scope of this study, although no evidence of these was found in the bulk-powder XRD analysis (Chapter 4). This chapter is restricted to microdeformation effects in largely intact minerals; mineral and rock melt features are discussed in Chapter 2.

5.1.1 Shock pressure determination using PDF crystallographic orientations in quartz

PDF measurements in quartz are a reliable parameter for quantitatively estimating the intensity of shock (French, 1998; Ferrière et al., 2009, and references therein). As defined in Section 1.4.2.2.2, PDF are single or multiple sets of parallel, narrow, 1-2 μm, (glass) lamellae that have a spacing of 2–10 μm (Stöffler and Langenhorst, 1994). The crystallographic orientation of quartz PDF relative to the c-axis has been used extensively to determine peak shock pressures in the range between 5 and 35 GPa, by comparison with experimental calibrations (e.g., Grieve and Robertson (1976); Feldman (1994); Feldman et al., 1996; Dressler et al., 1998; Ferrière et al., 2008).

From studies by Robertson and Grieve (1977) and Feldman (1994), shock barometry can commonly be constrained using 4 groups of PDF orientations in quartz: 1) Type A (P > 7.5 GPa): basal PDF only - **c** (0001); 2) Type B (P > 10 GPa): appearance of **ω** $\{10\bar{1}3\}$ planes, with basal planes; 3) Type C (P > 15 GPa): appearance of **a** $\{22\bar{4}1\}$, **r** $\{10\bar{1}1\}$, **z**$\{01\bar{1}1\}$, and **ξ**$\{11\bar{2}2\}$ planes; and 4) Type D (P > 16 GPa): appearance of **π** $\{10\bar{1}2\}$ planes. The minimum shock pressure required for the formation of PDF orientations parallel to the c axis (0001) is 5-10 GPa, and the **ω** $\{10\bar{1}3\}$ orientation forms from 12 – 15 GPa (Table 5.1) to above 16 GPa (Grieve et al., 1996; French, 1998). PDF become more abundant and more closely spaced in minerals with increasing shock intensity, with up to 3-10 sets being recognized within single grains (Stöffler and Langenhorst, 1994, French, 1998). At > 25 GPa shock pressures, Stöffler and Langenhorst (1994) list only $\{10\bar{1}2\}$ and $\{10\bar{1}3\}$ orientations (Table 1.2).

Table 5.2: Crystallographic orientations of planar deformation features (PDF) in shock-deformed quartz. Specific orientations of PDF are diagnostic of specific shock pressures (estimates from Stöffler and Langenhorst, 1994; Langenhorst, 2002; Ferrière et al., 2009).

Symbol	Miller-Bravais indices	Polar angle (angle between pole to plane and quartz c-axis)	Shock pressure
c	* (0001)	0°	>5 GPa
ω	*{10$\bar{1}$3};{01$\bar{1}$3}	22.95°	>10 GPa
π	*{10$\bar{1}$2};{01$\bar{1}$2}	32.42°	>20 GPa
r, z	*{10$\bar{1}$1};{01$\bar{1}$1}	51.79°	>20 GPa
m	{10$\bar{1}$0}	90.00°	
ξ	{11$\bar{2}$2};{2$\bar{1}\bar{1}$2}	47.73°	>22 GPa
s	{11$\bar{2}$1};{2$\bar{1}\bar{1}$1}	65.56°	
a	{11$\bar{2}$0};{2$\bar{1}\bar{1}$0}	90.00°	
	*{22$\bar{4}$1};{4$\bar{2}\bar{2}$1}	77.20°	
t	{40$\bar{4}$1};{04$\bar{4}$1}	78.87°	
k	{51$\bar{6}$0};{6$\bar{1}\bar{5}$0}	90.00°	
x	{51$\bar{6}$1};{6$\bar{5}\bar{1}$1}; {6$\bar{1}\bar{5}$1};{15$\bar{6}$1}	82.07°	
	{31$\bar{4}$1};{4$\bar{3}\bar{1}$1}; {4$\bar{1}\bar{3}$1};{13$\bar{4}$1}	77.91°	
ρ	{21$\bar{3}$1};{3$\bar{2}\bar{1}$1}; {3$\bar{1}\bar{2}$1};{12$\bar{3}$1}	73.71°	
e	{10$\bar{1}$4}	17.62°	

** Common planes in shocked quartz grains*

PDF sets are straight and do not cross grain boundries, although in deformed quartz, bending of PDF has been observed (Trepmann and Spray, 2006). Common crystallographic orientations of PDF and their relative shock pressure ranges from numerous researchers are shown in Tables 5.1 and 5.2. The shock pressure estimates tabled in Table 5.2 are used as a reference in this study.

The crystallographic orientation of PDF in quartz remains the most widely used shock barometer because PDF in quartz are not affected by post-impact thermal events unless quartz is recrystallized (Grieve et al., 1996). Decorated PDF form because of annealing recrystallization, whereby water exsolves from the shock glass lamellae as they recrystallize to produce tiny fluid inclusion trails along the original PDF (Grieve et al., 1996). Therefore, decorated PDF can be measured with confidence even in old, annealed or highly altered rocks as they still preserve the original PDF orientations (Grieve et al., 1990; Grieve et al., 1996; Langenhorst, 2002), although it is possible that the finer, high-pressure,

PDF orientations may be obliterated during annealing (e.g., Grieve et al., 1990). Basal PDF (Brazil twins - c (0001)) are multiple, mechanical PDF which are difficult to identify if they are not partially annealed and decorated (Grieve et al., 1996). They develop at shock pressures of 8–10 GPa and post-shock temperatures of 100 °C (Table 5.1). Grieve et al. (1996) suggested that in old impact structures it is common to observe mostly basal PDF, as the annealing process can cause their overall dominance over the high index crystallographic orientations.

5.1.2 Previous work

Shock petrographic studies in the Morokweng impact structure (MIS) are limited to Corner et al. (1997), Hart et al. (1997) and Reimold et al. (1999). Corner et al. (1997) examined 82 surface and outcrop samples collected from the vicinity of the central geophysical anomaly. In-situ Archaean granite samples (with cataclasite veining), collected 70 km southeast of the centre of the MIS show microdeformation evidence in the form of undulatory extinction in quartz. The in situ Black Reef Formation quartzite samples from 80 km south of the centre showed only fracturing and localized annealing along fractures (Corner et al., 1997). However, decorated PDF were reported in outcrop samples of fragmental breccia of banded ironstone (from 47 km west of the centre of the structure) and an allochthonous quartzite boulder (collected in the stream bed at a locality approximately 75 km south of the centre of the MIS) (Corner et al., 1997). Eighteen quartz grains were selected from 3 thin sections cut from the two breccia samples. Although up to five sets of PDF per grain were noted, only three sets per grain were reliably identified based on 22 measurements (Corner et al., 1997). The sets correspond to shock-diagnostic orientations $\{10\bar{1}3\}$ and $\{10\bar{1}2\}$, that is, polar angles of 22.95° and 32.42°, respectively. From these observations shock pressures of 10-16 GPa were deduced (Corner et al., 1997). Subsequent re-investigation of the banded ironstone outcrop failed to find any other PDF-bearing quartz samples (M. Andreoli, pers. comm., 2015).

Hart et al. (1997) found highly shocked quartz grains in pebbles from a 50 cm thick conglomerate bed (representing the base of the Kalahari beds) in the WF5 drillcore. Measurements in 21 grains (6 grains with two PDF sets, 15 grains with one PDF set, and 3 unindexed planes) revealed PDF orientations of (0001), $\{10\bar{1}3\}$, $\{10\bar{1}2\}$, $\{21\bar{3}1\}$, $\{51\bar{6}1\}$ and $\{10\bar{1}0\}$. These results provided evidence that rocks and minerals in the central parts of the MIS were subjected to shock pressures of at least 10 - 25 GPa (Hart et al., 1997).

Studies by Reimold et al. (1999) focused on the ~ 50 m wide granitoid mega-breccia zone intersected by the WF5 borehole from the central region of the MIS (Figure 1.13). The granitoids in this interval (225 – 271.30 m) below the melt rock are petrographically similar to those enclosed as lithic clasts in

the lower sections of the impact melt body in WF5 (Reimold et al., 1997). The recrystallized granite samples from the megabreccia zone contain quartz with multiply oriented sets of decorated PDF. Additionally, a number of granitoid samples were noted to contain up to two sets of PDF in plagioclase and alkali feldspar (Reimold et al., 1999). The degree of shock deformation in the samples was documented in photomicrographs and detailed descriptions; however no statistical analysis of the PDF orientations was presented. Reimold et al. (1999) noted that the granitic clasts in the melt rock samples MO32 and MO70B also contained quartz with decorated PDF, as well as diaplectic quartz glass and ballen quartz. They observed no notable change in shock intensity from top to bottom of the 50 m zone.

5.2 Methodology

Mineral shock metamorphic features are distributed heterogeneously even at the thin section scale (Melosh, 1989; Stöffler and Langenhorst, 1994; French, 1998). Several experiments indicate that this is due to differences in the orientation of grain boundaries and crystallographic axes with respect to propagation direction of the shock front (Stöffler, 1972; Kieffer and Simonds, 1980; Melosh, 1989; Stöffler and Langenhorst, 1994). As a result, a statistical approach is used in measurements of crystallographic orientations of PDF in shocked quartz to constrain the peak shock pressure that a sample has experienced (Stöffler and Langenhorst, 1994; French, 1998; Ferrière et al., 2009). To acquire a quantitative estimate of the shock pressure values, the technique involves using a 4-axis Leitz Universal Stage mounted on a petrographic microscope to measure the angles between the quartz c-axis and the poles to the PDF planes (see Appendix 1E for operational details and Stöffler and Langenhorst (1994) and Ferrière et al. (2009) for a detailed account). Measurement of the azimuth and inclination of the c-axis (optic axis) and for all PDF sets present was done in each measured quartz grain. The orientation of the c-axis and each PDF set done twice (i.e., stage was rotated by 180 degrees then a second measurement was taken for each set). This repetitive process ensures accuracy and reduces human error dramatically (Huber et al., 2011). Data was then indexed using the ANIE v1.0 program by Huber et al. (2011); which is an automated indexing program based on mathematical methods and computer algorithms. Cross checking of the indexed results was done randomly using the Wulff net and NSPT of Ferrière et al. (2009), to verify the accuracy of the ANIE program. Once the data has been indexed, two histograms are presented; one with the frequency distribution of polar angle values in intervals of 5°, and one with the absolute frequency of indexed PDF with Miller-Bravais indices (Figures 5.5, 5.7 and 5.10. and Appendix 5C). The error (5° error envelope) used for analysis is indicated on the graph for indexed PDF, and on the graph it is displayed whether data was processed based on averages or ranges of values. According to Ferrière et al. (2009), an accurate estimate involves measurements of between 100 and 600 grains in a thin section. However, according to French and

Koeberl (2010); measurements of 20-50 grains per thin section is acceptable. The assigned shock pressure is based on comparison with experimentally deduced PDF patterns (Table 5.2).

Evidence of shock metamorphism in the M4 core is observed in both the target rocks and in the impactites. Ninety-five thin sections showed shock features, with even the quartz-poor dolerite sample showing PDF in the granophyric quartz (Figure 5.1 C and D). The M4 samples typically carry considerably fewer than 100 shocked quartz grains in a thin section; hence in this study 14 samples were selected that contained a considerable number of quartz grains with PDF. In some samples a maximum of 20 grains with PDF per thin section were measured. The exception is dioritic gneisses and melt matrix breccias (MMBr), where even fewer PDF-bearing quartz grains were present. Although shock effects are observed in feldspar grains (Section 5.4), it was not possible to measure their orientations owing to the complex crystallographic character of feldspar.

The 14 samples with the highest number of shocked quartz grains that were subjected to Universal Stage analysis comprise two sets: 1) Eight target rock samples were analyzed from different depths to establish if maximum shock pressure varies as a function of depth in the M4 core. The 8 target rock samples studied were M4 GG-4 (depth: 109.20 m), M4 GG-2 (depth: 131.90 m), M4 IS 2 (depth: 211.41 m), M4 FZ-2 (depth: 219.30 m), M4 GG-17 (depth: 274.15 m), M4 AM-2 (depth: 338.15 m), M4 AM-1 (depth: 340.70 m) and M4 AM-5 (depth: 362.63 m). The PDF crystallographic measurements for target rocks are presented in Appendix 5A. 2) Six impactite samples (three suevites, two MMBr and one MMBr injection dyke) were analyzed to compare shock levels between the different breccia types and to compare with the levels of shock in the target rocks. The suevite samples are represented by 3 samples: M4 S-7 (depth: 146.68 m), M4 S-2 (depth: 156.35 m) and M4 S-5 (depth: 285.97 m). The MMBr are represented by samples M4 IM-2 (depth: 234.33 m), M4 IM 6 (depth: 271.17 m) and the MMBr injection vein sample M4 A-INJ (depth: 189.00 m). The PDF crystallographic measurements for impactites are presented in Appendix 5B. For all data sets, absolute frequencies (in %) are reported, where absolute frequency (after Engelhardt and Bertsch, 1969) is defined as:

$$\mathbf{F_{hkil} = (q_{hkil}/Q)*100}$$

where q_{hkil} is the actual number of measured symmetrically equivalent deformation planes {hkil} observed in n quartz grains; and Q is the total number of all measured sets of PDF (indexed and unindexed) observed in quartz grains of a thin section (Stöffler and Langenhorst, 1994; Ferrière et al., 2009).

5.3 Shock microdeformation features in the M4 core lithologies

The shock metamorphic features identified using transmitted light microscopy include (Figures 5.1, 5.2, 5.4, 5.6, 5.8, 5.13) a variety of planar deformation features in quartz and feldspar (including feather features, planar fractures and decorated planar deformation features), toasted quartz, mosaic extinction and reduced birefringence in feldspar, kink bands in biotite, and melt particles. Although it cannot be completely proven, planar fractures in titanite (see Figure 5.13B) may also be linked to the shock deformation. The petrographic and chemical features of the melt particles are discussed separately, in Chapters 2 and 4, respectively. Multiple sets of decorated PDF were identified in quartz grains from both target rocks and impactites.

5.3.1 Petrographic properties of shocked quartz in the M4 core lithologies

Quartz is found in all target rocks, including vein quartz in metadolerite; only the pristine dolerite samples lack quartz (except the granophyric texture) (see Chapter 2, section 2.3.4). In the impactites, quartz occurs in lithic clasts or as individual mineral clasts (Figures 5.5 and 5.6). The quartz grains encountered in this study are variably shocked. All samples analysed show grains with multiple sets of PDF (Figures 5.1 – 5.4 and Appendix 5A). The summary of PDF set abundance and indexed PDF crystallographic orientations in quartz is shown in Table 5.3.

In addition to the decorated PDF, evidence of fractured quartz is noted (Figures 5.1A, D and 5.2). Planar fractures (PF) are noted in a few samples (e.g., Figure 5.2A, C) and may be associated with feather features (FF) (Figures 5.2G and 5.6C, D). Figure 5.1E shows evidence of recrystallization of quartz to a fine- to medium-grained aggregate, with relics of quartz displaying PDF. Such recrystallization is only noted in the MMBr and is, consequently, attributed to heat from the cooling melt. In contrast, the somewhat coarser crystalline aggregate texture in Figure 5.1F is attributed to pre-impact recrystallization in the zone of faulting and vein quartz precipitation.

Feather features (FF) are common in clasts in the upper reddish brown suevites and trondhjemitic gneiss sample M4 FZ-2a (Figures 5.2E and 5.6C, D). Feather features are parallel to subparallel to PDF lamellae that branch off from planar fractures (Poelchau and Kenkmann, 2010). These structures are suggested to form by shearing of planar fractures (Poelchau and Kenkmann, 2010).

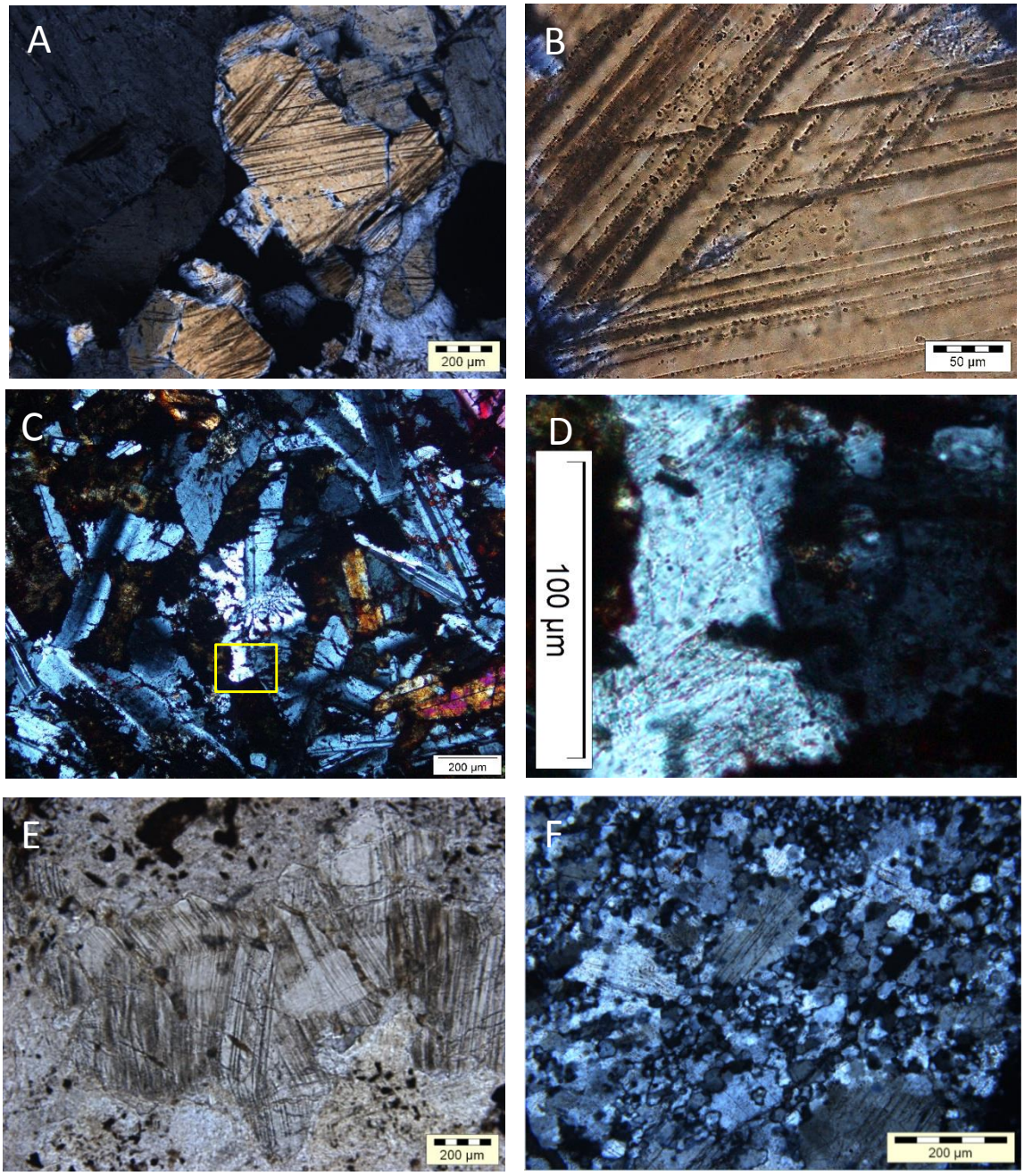

Figure 5.1: Characteristics of decorated PDF in quartz from the M4 core lithologies. **A)** Sample M4 GG-4 (depth: 109.20 m), showing intensely shocked quartz grain with two prominent PDF sets. XPL. **B)** Enlargement of A, showing the planar fluid inclusion trails marking the original glass lamellae, with a possible third PDF set at top, right. XPL. **C)** Granophyric quartz from dolerite sample M4 SILL-1 (depth: 268.30 m). XPL. **D)** Enlargement of C, showing two sets of decorated PDF. XPL. **E)** Suevite sample M4 S-7 (depth: 146.68 m) showing toasted quartz in polycrystalline clast. The toasted appearance is more visible in the grain on the right side of the clast. PPL. **F)** MMBr sample M4 IM 3, (depth: 265.55 m), shows recrystallized shocked quartz clast. These grains mostly contain one set of PDF. XPL. PPL = plane polarized light, XPL = crossed polarized light.

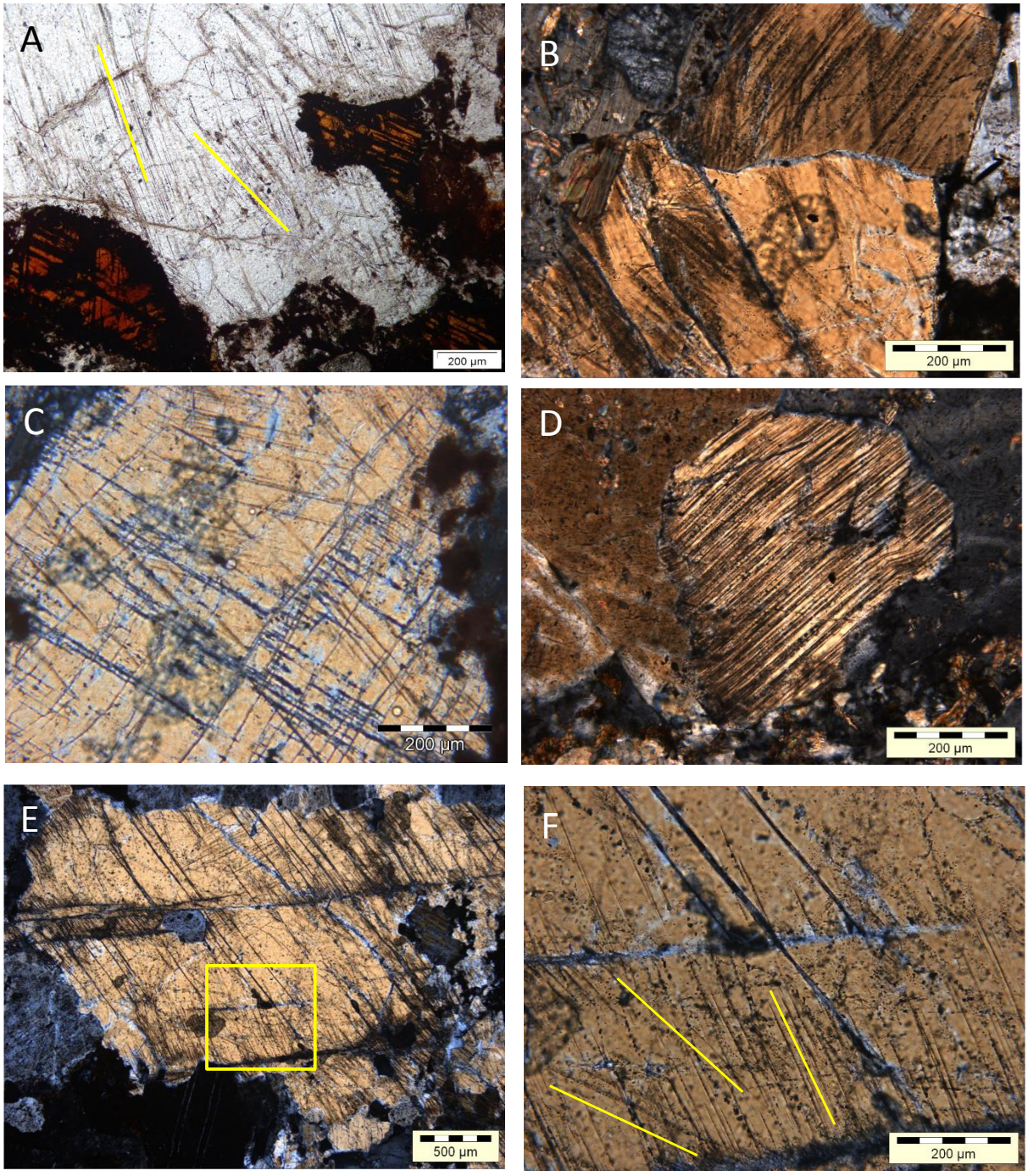

Figure 5.2: Planar shock microdeformation features in quartz from the M4 core. **A)** Granodioritic sample M4 GG-4 (depth: 109.20 m), showing shocked quartz grain displaying two PDF sets (solid lines). Note the kinked, oxidized biotite around the quartz grain. PPL. **B)** Dioritic gneiss sample M4 AM-2 (depth: 338.15 m), displaying PF and PDF. XPL. **C)** Silicified metadolerite sample M4 IS-2 (depth: 211.41 m) showing quartz grain containing 2 sets of PDF and PF. XPL. **D)** Intensely shocked granitic gneiss sample M4 MG-2 (depth: 334.52 m) showing 2 sets of PDF and PF. Note the deflection and the slight bending of PDF in the lower part of the grain. XPL. **E)** Trondhjemitic gneiss sample M4 FZ-2 (depth: 219.30 m) showing PDF. XPL. **F)** Enlargement of E showing 3 PDF sets (solid lines). XPL. PPL = plane polarized light, XPL = crossed polarized light.

5.3.2 PDF measurements for the M4 core lithologies

Locally quartz grains with 3 or 4 PDF sets are observed under the optical microscope (Figures 5.1B and 5.2 C, F). Although PDF are present in feldspars (Figure 5.14) and possible PF in titanite (Figure 5.13B), only the PDF in quartz were measured using the Universal Stage technique. Slight bending of PDF is observed in some cases (e.g., Figure 5.2D); in addition, changes in the PDF orientation in some quartz grains correspond to deformation bands and tiltwalls that are visible under crossed polars. As the PDF deflection is usually significantly larger than the lattice misorientation in the host quartz, it is concluded that the quartz was strained before the PDF formed. This is attributed to the pre-impact cataclastic deformation and quartz veining seen in the middle section of the core. The locations of samples examined for the characterization of microscopic shock metamorphic features are shown in Figure 5.3.

A total of 357 PDF sets in 199 quartz grains were measured, comprising 136 grains (263 sets) from the target rocks, 35 grains (50 sets) from the suevites, and 28 grains (44 sets) from the melt-matrix breccias. The limited data obtained from the MMBr samples are also reported. The indexed PDF are summarized in Table 5.3, the complete measurements are presented in Appendix 5A and B. Histograms of absolute frequency percent of indexed PDF in quartz for both the target rocks and impactite samples are presented in Figures 5.5 and 5.7. On average, 2 PDF sets per grain have been noted (Table 5.3).

5.3.2.1 PDF crystallographic orientations in target rocks

PDF in the M4 drillcore target rocks are measured mainly from granitoid gneiss samples. Irrespective of the sample, the original PDF glass lamellae have been replaced by planar fluid inclusion trails (Figure 5.1 B). On average 2 (rarely 3) sets of PDF have been observed in individual grains in granitoid gneiss samples (see Figures 5.1A and 5.4). The following results were obtained in order of abundance (see Table 5.3): **M4 GG-4:** 0° - (0001), 17.62° - {$10\bar{1}4$}, 22.95° - {$10\bar{1}3$}, 32.42° - {$10\bar{1}2$} and 65.56° - {$11\bar{2}1$}; **M4 GG-2:** 22.95° - {$10\bar{1}3$}, 0° - (0001), 17.62° - {$10\bar{1}4$} and 32.42° - {$10\bar{1}2$}; **M4 FZ -2: :** 0° - (0001), 32.42° - {$10\bar{1}2$}, 22.95° - {$10\bar{1}3$},17.62° - {$10\bar{1}4$} and 73.71° -{$21\bar{3}1$}; **M4 IS-2:** 0° - (0001), 22.95° - {$10\bar{1}3$}, 17.62° - {$10\bar{1}4$} and 32.42° - {$10\bar{1}2$}; **M4 GG-17:** 0°-(0001), 22.95°-{$10\bar{1}3$}, 17.62° - {$10\bar{1}4$}, 32.42° - {$10\bar{1}2$}, 65.56°, 77.20° - {$22\bar{4}1$}, 65.56° - {$11\bar{2}1$} and 73.71° -{$21\bar{3}1$}; **M4 AM-1:** 22.95° - {$10\bar{1}3$}, 0° - (0001), 17.62° - {$10\bar{1}4$}, 32.42° - {$10\bar{1}2$} and 73.71° -{$21\bar{3}1$}; **M4 AM-2:** 0° - (0001), 22.95° - {$10\bar{1}3$}, 32.42° - {$10\bar{1}2$}, 47.73° - {$11\bar{2}2$} and 17.62° - {$10\bar{1}4$} and **M4 AM-5** of 22.95° - {$10\bar{1}3$}, 0° - (0001), 17.62° - {$10\bar{1}4$}, 77.20° - {$22\bar{4}1$}, 82.07° - {$51\bar{6}1$} and 32.42°-{$10\bar{1}2$}. Figure 5.5 and Table 5.3 confirm that the PDF orientations in quartz grains in the target rocks are dominated by **c** (0001), and **ω** {$10\bar{1}3$} and a systematic dominance/abundance of the 22.95° - {$10\bar{1}3$}

set with depth is notable (Figure 5.5). In the deepest analysed samples around ~270 m depth, crystallographic orientations at high angles to the c-axis are more frequent (Figure 5.5). Sample M4 FZ-2 from 219.30 m depth has approximately equal abundances of 17.62° - $\{10\bar{1}4\}$, 22.95° - $\{10\bar{1}3\}$ and 32.42° -$\{10\bar{1}2\}$ orientations. The $\{10\bar{1}3\}$ and $\{10\bar{1}2\}$ orientations are typical of peak shock pressures of >25 GPa when occurring exclusively and ~ 20 GPa when occurring together with other sets (see Stöffler and Langenhorst, 1994). These results show that the M4 target rocks were highly shocked (Table 1.2). However based on these limited results, evidence is not enough to justify systematic variation in peak pressure estimates with depth.

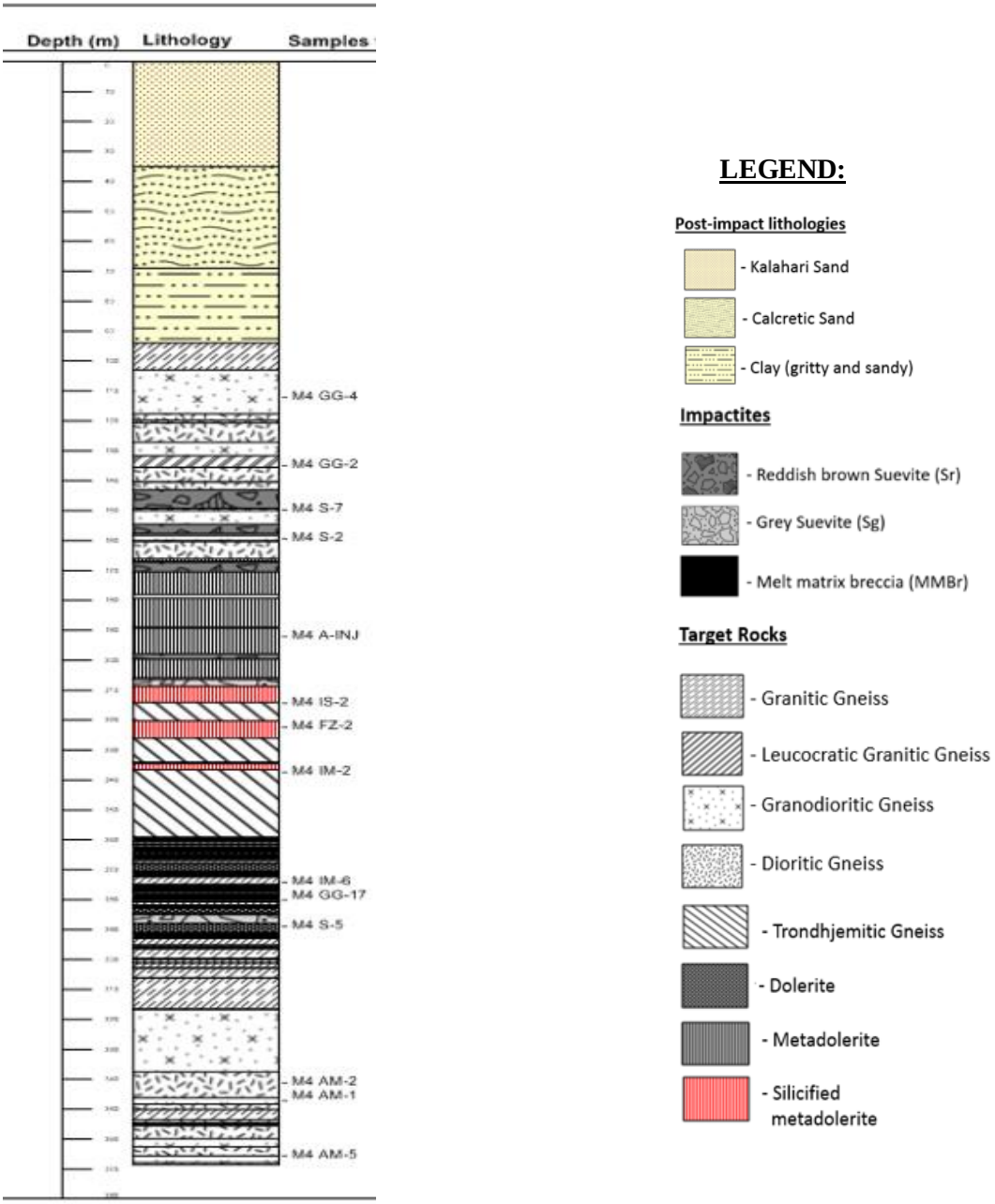

Figure 5.3: Lithostratigraphy of the M4 core showing the depth intervals where the samples were taken for PDF crystallographic analysis.

Table 5.3: PDF sets and absolute frequencies (%) of individual PDF orientations in quartz grains from target rocks, derived from PDF planes indexed using ANIE program with a 5° envelope of measurement error and the range value of measurements for indexing. Full data set is presented in Appendix 5A.

	Rock Type	Granodioritic Gneiss	Granitic Gneiss	Trondhjemitic Gneiss	Metadolerite (Silicified)	Granitic Gneiss	Dioritic Gneiss	Dioritic Gneiss	Dioritic Gneiss
	Sample no.	M4 GG-4	M4 GG-2	M4 FZ-2	M4 IS-2	M4 GG-17	M4 AM-2	M4 AM-1	M4 AM-5
	Depth (m)	109.20	131.90	219.30	211.41	274.15	338.15	340.70	362.63
		(%)	(%)						
Number of investigated grains	(n)	20	20	20	18	18	10	10	20
Number of measured sets	(Q)	40	44	40	36	37	18	17	31
Number of PDF sets/grain	(Q/n)	2	2.2	2	2	2.1	1.8	1.7	1.6
Polar angles and PDF crystallographic orientations		Absolute frequency (%)							
0.00°	**c** (0001)	35	20	33	36	38	33	35	19
	**{10 $\bar{1}$ 4} / {10 $\bar{1}$ 3}		8	5	13	6			
22.95°	**ω** {10 $\bar{1}$ 3}	13	34	18	22	22	22	35	29
32.42°	**π** {10 $\bar{1}$ 2}	10	9	20	6	5	17	6	6
51.79°	**r, z** {10 $\bar{1}$ 1}								
90.00°	**m** {10 $\bar{1}$ 0}								
47.73°	**ξ,** {11 $\bar{2}$ 2}						11		
65.56°	**s** {11 $\bar{2}$ 1}	3				3			
73.71°	**ρ** {21 $\bar{3}$ 1}			3		3		6	
82.07°	**x** {51 $\bar{6}$ 1}								3
90.00°	**a** {11 $\bar{2}$ 0}								
77.20°	{22 $\bar{4}$ 1}								3
77.91°	{31 $\bar{4}$ 1}					5			3
78.87°	**t** {40 $\bar{4}$ 1}								
90.00°	**k** {51 $\bar{6}$ 0}								
17.62°	**e** {10 $\bar{1}$ 4}	28	16	18	11	11	6	6	16
Unindexed		13	14	5	14	8	11	12	19

** n.d. - none detected; Std.Dev. - Standard deviation; unindexed orientations are those which provide measurements that do not correspond to the rational PDF crystallographic orientations*

*** PDF planes of {10 $\bar{1}$ 4} and {10 $\bar{1}$ 3} crystallographic orientations overlap*

Table 5.4: PDF sets and absolute frequencies (%) of individual PDF orientations in quartz grains suevites and MMBr samples, derived from PDF planes indexed using ANIE program with a 5° envelope of measurement error and the range value of measurements for indexing. Full data set is presented in Appendix 5B.

	Rock Type	Suevite (reddish brown)	Suevite (reddish brown)	Suevite (grey)	MMBr injection dyke	Melt matrix breccia	Melt matrix breccia
	Sample no.	M4 S-7	M4 S-2	M4 S-5	M4 A-INJ	M4 IM-2	M4 IM-6
	Depth (m)	146.68	156.35	285.97	189.00	234.33	271.17
		(%)	(%)	(%)	(%)	(%)	(%)
Number of investigated grains	(n)	5	15	15	12	10	6
Number of measured sets	(Q)	6	28	16	20	14	10
Number of PDF sets/grain	(Q/n)	1.2	1.9	1.1	1.6	1.4	1.6
Polar angles and PDF crystallographic orientations		Absolute frequency (%)					
0.00°	**c** (0001)	50	36	44	40	36	20
	**{10 $\bar{1}$ 4} / {10 $\bar{1}$ 3}		4			8	
22.95°	**ω** {10 $\bar{1}$ 3}	17	32	25	20	36	30
32.42°	**π** {10 $\bar{1}$ 2}		4	6	20		
51.79°	**r, z** {10 $\bar{1}$1}						
90.00°	**m** {10 $\bar{1}$0}						
47.73°	**ξ,** {11 $\bar{2}$ 2}						20
65.56°	**s** {11 $\bar{2}$1}	17					10
73.71°	**ρ** {21 $\bar{3}$1}						
82.07°	**x** {51 $\bar{6}$1}						
90.00°	**a** {11 $\bar{2}$0}						
77.20°	{22 $\bar{4}$1}						
77.91°	{31 $\bar{4}$1}						
78.87°	**t** {40 $\bar{4}$1}						
90.00°	**k** {51 $\bar{6}$0}						
17.62°	**e** {10 $\bar{1}$ 4}	17	7	13	5	14	
Unindexed		-	18	13	15	7	20

* *n.d. - none detected; Std.Dev. - Standard deviation; unindexed orientations are those which provide measurements that do not correspond to the rational PDF crystallographic orientations*

** *PDF planes of {10 $\bar{1}$ 4} and {10 $\bar{1}$ 3} crystallographic orientations overlap*

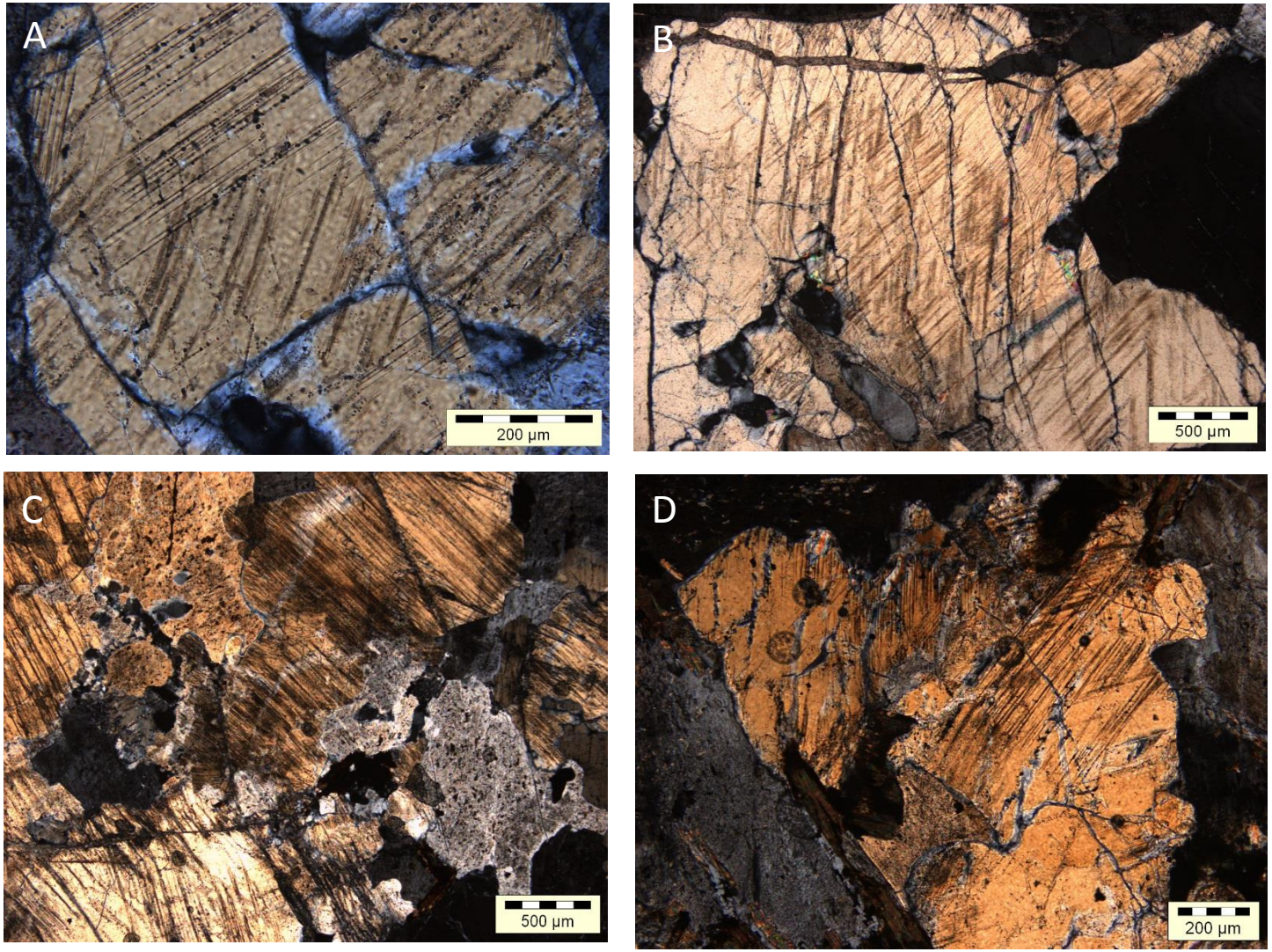

Figure 5.4: Representative photomicrographs of planar deformation features in quartz grains from M4 core target rock samples selected for Universal Stage analysis. **A)** Quartz grains in granitoid gneiss sample M4 GG-2 (depth: 131.90 m), showing 2 main and 2 subsidiary sets of decorated PDF. XPL. **B)** A second quartz grain from Sample M4 GG-2 showing PF and PDF and irregular fractures in shocked quartz (up to 4 sets of PDF). Note the quartz grain is cut by a post-impact hydrothermal calcite vein (top of image, E-W). XPL. **C)** Trondhjemitic gneiss sample M4 FZ-2 (depth: 219.30), showing closely spaced PDF forming a toasted quartz texture. XPL. **D)** Dioritic gneiss sample M4 AM-5 (depth: 362.63 m) quartz displays two sets of PDF. XPL. PPL = plane polarized light, XPL = crossed polarized light.

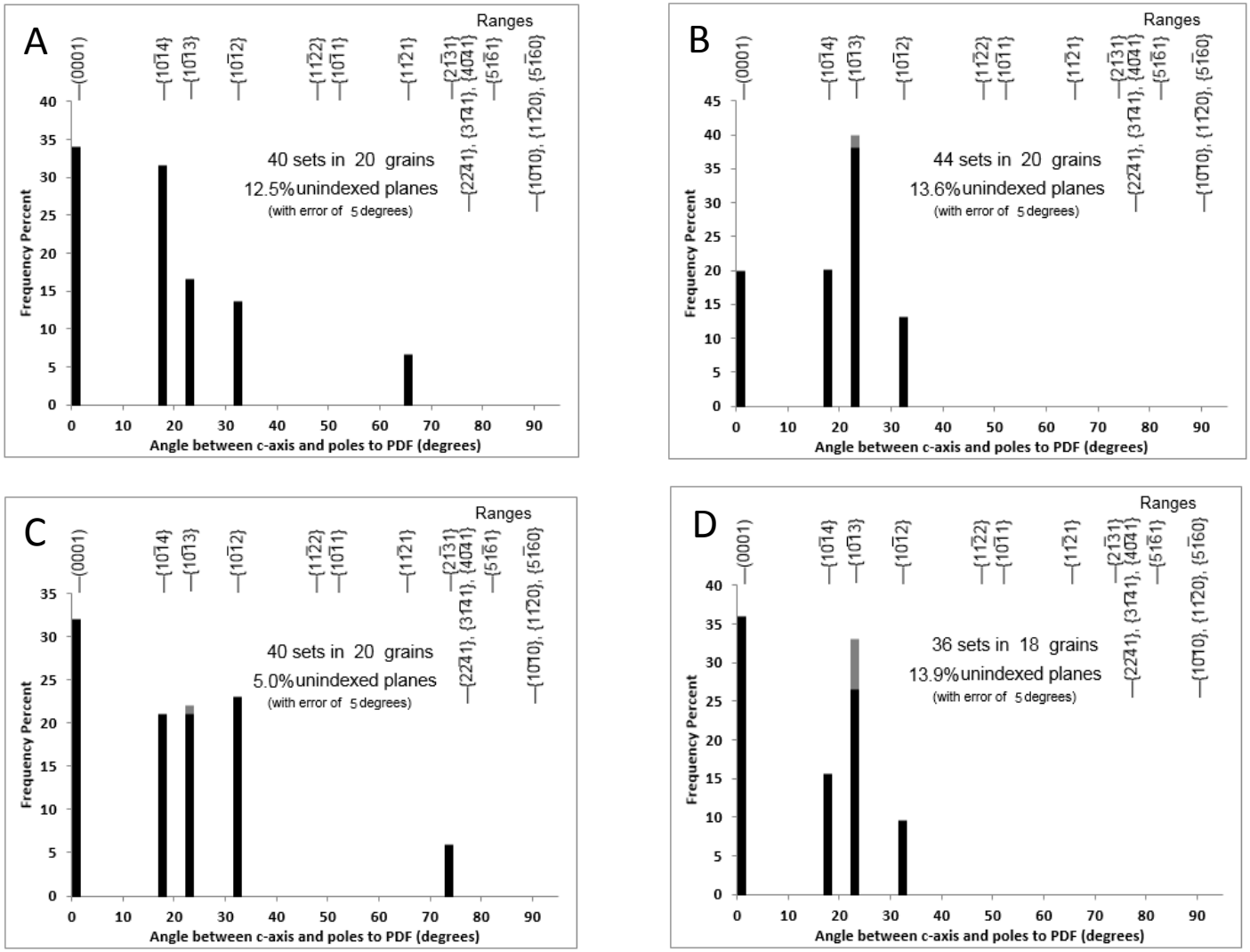

Figure 5.5: Histograms showing absolute frequency percent for indexed PDF crystallographic orientations of quartz grains from M4 core target rock samples; recalculated to 100% (excluding the unindexed PDF). **A)** Granodioritic gneiss sample M4 GG-4 (depth: 109.20 m). **B)** Granitic gneiss sample M4 GG-2 (depth: 131.90 m). **C)** Trondhjemitic gneiss sample M4 FZ-2 (depth: 219.30 m). **D)** Silicified metadolerite sample M4 IS-2 (depth: 211.41 m). The data was processed on the ANIE program based on ranges of values. The grey bars seen in B, C and D indicate PDF planes which plot in the overlapping zone between {10 $\bar{1}$ 4} and {10 $\bar{1}$ 3} orientations; here denoted under the {10 $\bar{1}$ 3} bar.

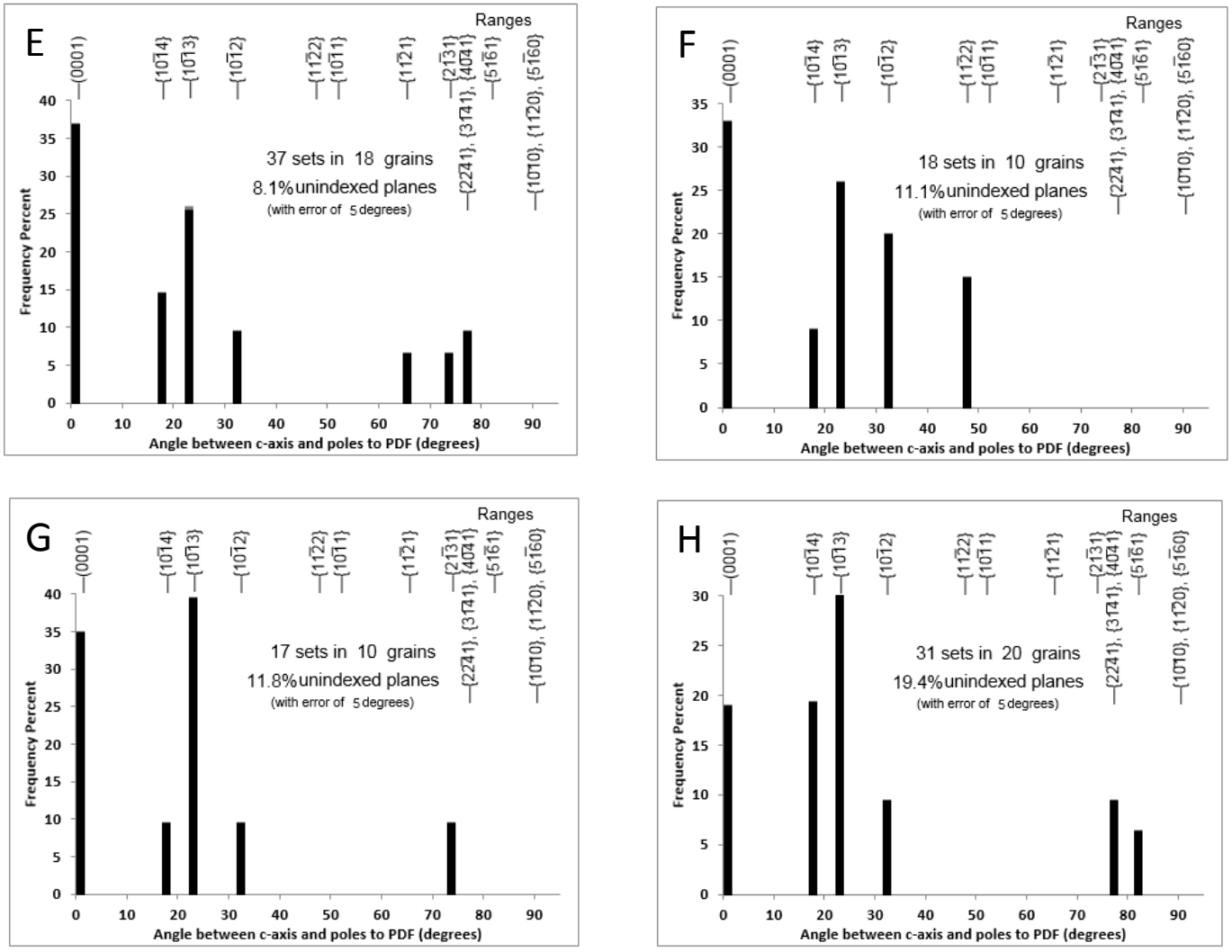

Figure 5.5: *Continued*…: **E)** Granitic gneiss sample M4 GG-17 (depth: 274.15 m). **F)** Dioritic gneiss sample M4 AM-2 (depth: 338.15 m). **G)** Dioritic gneiss sample M4 AM-1 (depth: 340.70 m). **H)** Dioritic gneiss sample M4 AM-5 (depth: 362.63 m). The data was processed on the ANIE program based on ranges of values.

5.3.2.2 PDF crystallographic orientations in impactites

Impactites involve mixtures of rock and mineral fragments that can be sourced from different parts of the impact crater and, thus, potentially from different shock pressure zones (French, 1998). Whilst this might pose problems when trying to constrain a peak shock pressure, as discussed previously, studies of autochthonous target rocks show that shock metamorphic features can be highly heterogeneous even on an inter-grain scale. In Chapter 3 it was argued that, with the exception of sample M4 S-6, the M4 drillcore impactites show little compositional evidence for an exotic derivation; consequently, the levels of shock in their clasts are likely to reflect the shock levels experienced by the local target rocks. The obvious heterogeneity of this shock is seen in the close spatial association of suevites and MMBr (and, possibly, cataclasite), and in the range of shock levels – from grains lacking any shock features to mineral and whole-rock melts – seen in their clasts. Quartz grains within the suevites of the M4 drillcore occur either as single grains (mineral clasts), as grains within polycrystalline lithic clasts, or as undigested mineral clasts enclosed in melt clasts (Figure 5.6 and 5.8). Mineral clasts as small as 20 μm show single sets of closely-spaced, parallel, planar fluid inclusion trails.

5.3.2.2.1 PDF crystallographic orientations in suevite samples

The suevite samples are represented by 2 reddish brown suevites - M4 S-7 (depth: 146.68 m) and M4 S2 (2) (depth: 165.35 m); and 1 grey suevite - M4 S-5 (depth: 285.97 m). All suevites contain a similar proportion of quartz. Quartz occurs as a constituent within lithic clasts and as single-crystal grains within the suevite matrix (Figure 5.6). The angular lithic fragments range in size from 50 mm to 5 cm. (see Chapter 2, section 2.5.4).

The dominant set in all the suevite samples is the basal type c, 0° - (0001), with the abundance of > 30% in each sample (Table 5.4). Sample M4 S-2 is notably the only one with an equivalent abundance of 0° - (0001) and 22.95° - $\{10\bar{1}3\}$ orientations (Figure 5.7B). Orientations of 32.42° - $\{10\bar{1}2\}$ are missing in sample M4 S-7, but uniquely the only suevite recording the presence of 65.56°- $\{11\bar{2}1\}$ orientation. Based on these crystallographic orientations, the implied shock pressure estimates for suevites are high (see Table 5.2). Notably the FF, which by definition are parallel to subparallel lamellae PDF that branch off from planar fractures and are of lower shock pressures (Poelchau and Kenkmann, 2010), are common in shallow reddish brown suevite samples (Figure 5.6 C, D).

5.3.2.2.2 PDF crystallographic orientations in melt-matrix breccias

The MMBr enclose fewer clasts than the suevites, and are mostly limited to quartz mineral clasts as a result of more complete melting of the feldspar component in the target rocks (Section 2.4.2). This, and evidence of more intense recrystallization of the quartz clasts, means that fewer PDF measurements were possible in these samples. Three representative MMBr samples were studied: sample M4 IM-2 (depth: 234.33 m), M4 IM-6 (depth: 271.17 m) and M4 A-INJ (depth: 189.00 m). Based on petrographic analysis (Section 2.4), the clasts are mainly derived from the granitoid gneisses and vein quartz. Figure 5.8 shows typical examples of shocked quartz mineral clasts enclosed in the MMBr. Dynamically recrystallized quartz is often noted in matrices of the MMBr (Figure 5.8F), and no traces of PDF are observed, thereby further reducing the number of quartz mineral clasts that can be measured for crystallographic orientation measurements. Owing to the limited number of clasts with PDF that could be measured (Table 5.3), multiple thin sections were cut; in the end, however, the results for three samples are presented (Figure 5.10). The PDF orientation data (Figure 5.10 and Appendix 5B) in the MMBr samples are similar to those in both the target rocks and suevites, with 0° - (0001), and 22.95° - $\{10\bar{1}3\}$ making up >60% of the combined total. The MMBr samples (M4 IM-2 and IM-6), display different distributions (Figure 5.10) – although they both show overall dominance of the 22.95°$\{10\bar{1}3\}$ orientation, and both lackPDF with the 32.42° $\{10\bar{1}2\}$ orientation; the M4 IM-6 showed additional orientations of 47.73° - $\{11\bar{2}2\}$ and 65.56° - $\{11\bar{2}1\}$. Sample M4 IM-6 is the only measured sample without the $\{10\bar{1}4\}$ orientation. Given the limited number of measurements and the differences in the data between the two MMBr samples, no further general interpretation is justified for MMBr samples.

Thin MMBr injection dykes are considered separately here to investigate whether they contain markedly different shock features to the more voluminous MMBr intersections; i.e., whether the thinner injection veins are offshoots of larger veins or whether they might be more autochthonous in character. MMBr injection dyke sample M4 A-INJ contains quartz clasts that generally display 1 set of PDF (rarely 2 sets are noted) (Figure 5.9, Appendix 5B). Measured PDF in quartz are dominated by orientations of 0° - (0001), 22.95° - $\{10\bar{1}3\}$, 32.42° - $\{10\bar{1}2\}$ and 17.62° - $\{10\bar{1}4\}$, with relative abundances of 40%, 20%, 20% and 5%, respectively (Figure 5.10). This distribution closely resembles that of other MMBr samples (Figure 5.10), although it lacks the high angle PDF crystallographic orientation seen in sample M4 IM-6. At a first approximation, there is little to suggest that the MMBr injection dykes are anything other than offshoots of the more voluminous MMBr, although a more detailed spatial analysis would be required to properly test this.

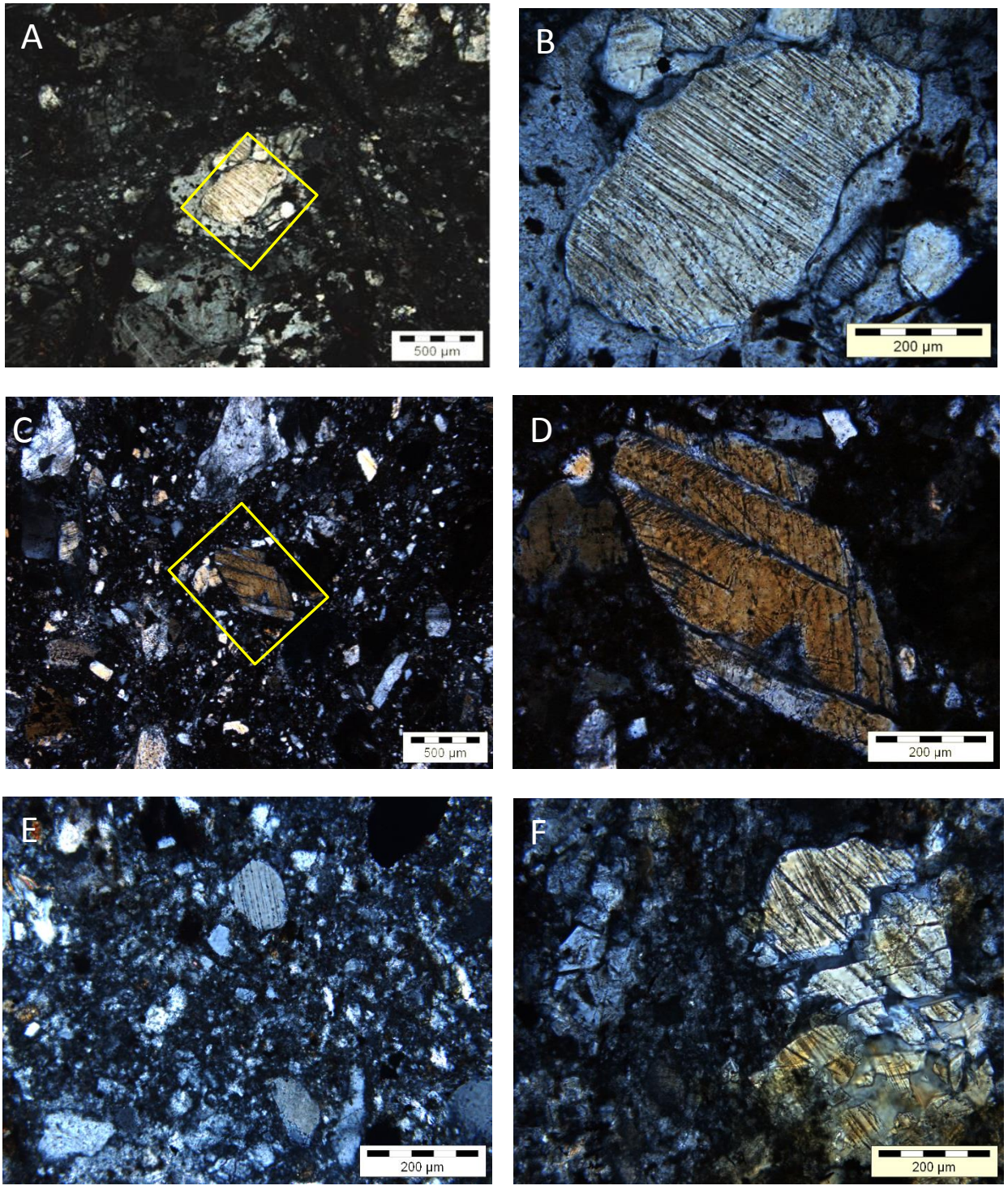

Figure 5.6: Shock deformation features in M4 suevites. **A)** Lithic granitoid gneiss clast in suevite Sample M4 S-7 (depth: 146.00 m), shows decorated PDF in quartz grains. XPL. **B)** Enlargement of A - the shocked quartz grain shows two prominent sets of PDF. XPL. **C)** Angular quartz mineral clast, from suevite sample M4 S-2 (depth: 156.35 m). XPL. **D)** Enlargement of C displaying feather features. XPL. **E)** Lithic and mineral clasts in suevite sample M4 S-5 (depth: 285.97 m), showing quartz with 1 set of decorated PDF. XPL. **F)** Fractured and shocked quartz from suevite sample M4 S-1 (depth: 144.09 m), showing quartz with 2 sets of decorated PDF. XPL. PPL = plane polarized light, XPL = crossed polarized light.

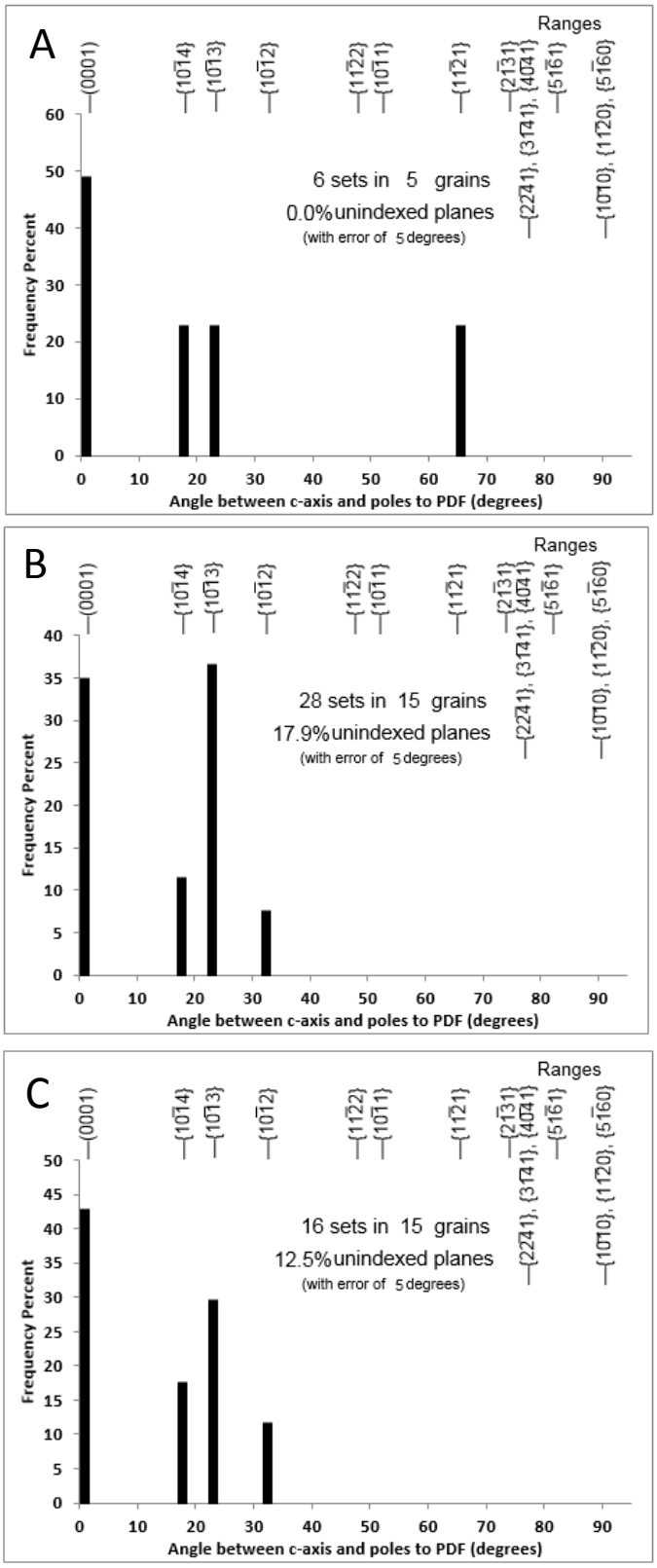

Figure 5.7: Histograms showing absolute frequency percent for indexed PDF crystallographic orientations of quartz clasts in M4 core suevite samples; recalculated to 100% (excluding the unindexed PDF). **A)** M4 S-7 (depth: 146.00 m). **B)** M4 S-2 (depth: 165.35 m). **C)** Sample M4 S-5 (depth: 285.97 m). The data was processed on the ANIE program based on ranges of values.

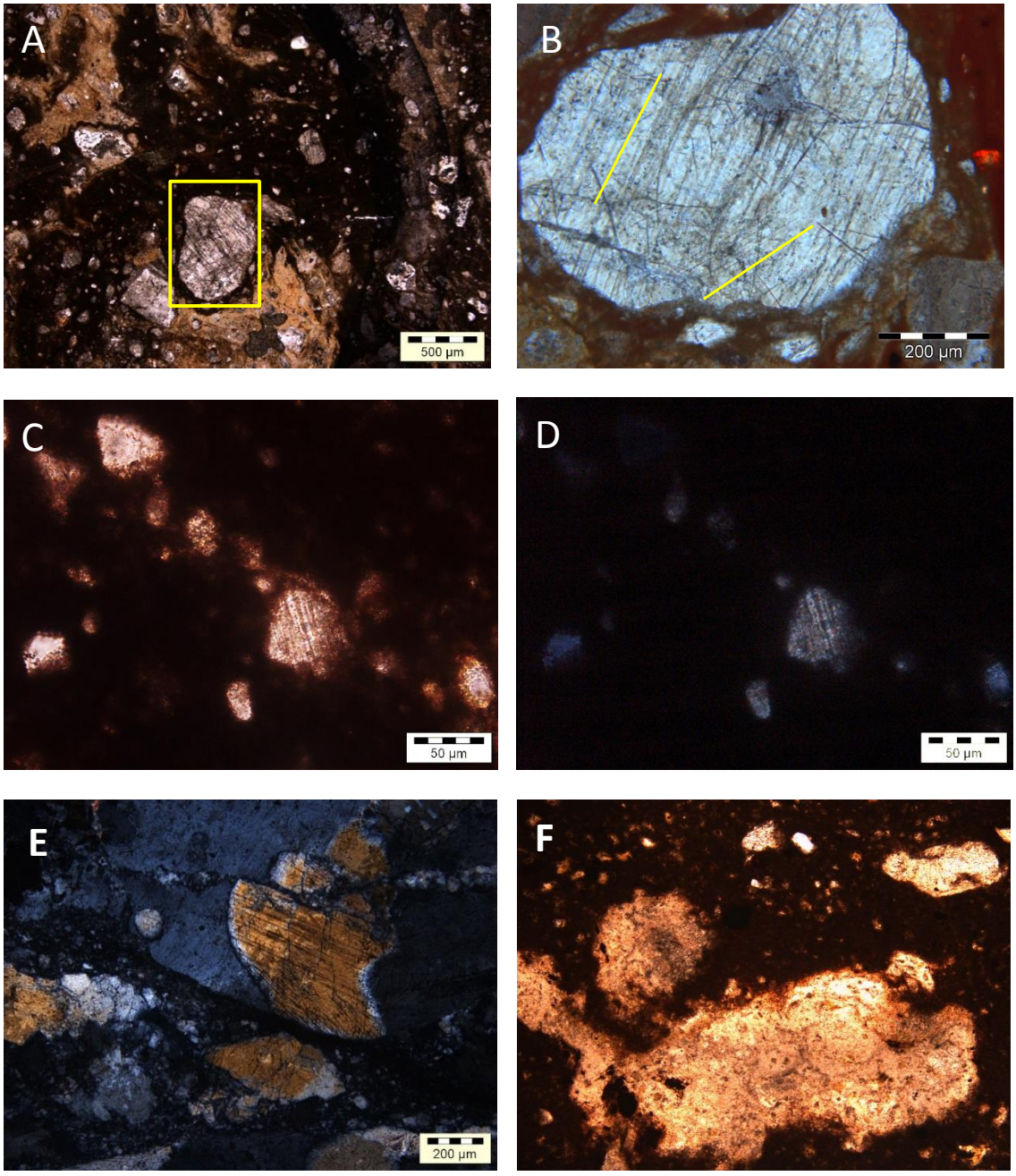

Figure 5.8: Shock deformation features in M4 core meltmatrix breccia. **A)** Variegated melt particle in MMBr showing internal flow textures and shocked quartz mineral clasts from sample M4 IM-2 (depth: 234.33 m). XPL. **B)** Rotated enlargement of A. XPL. Note the 2 sets of PDF. **C)** PPL and **D)** XPL images of sample M4 IM-6 (depth: 271.17 m) showing < 50 µm quartz mineral clasts enclosed in an altered cryptocrystalline matrix. **E)** PPL image of sample M4 IM-9 (depth: 299.76 m) showing a rare granitoid gneiss lithic clast with shocked quartz grain. XPL. **F)** Dynamically recrystallized quartz enclosed in cryptocrystalline matrix of the MMBr sample M4 IM-4 from 259.11 m depth. PPL. PPL = plane polarized light, XPL = crossed polarized light.

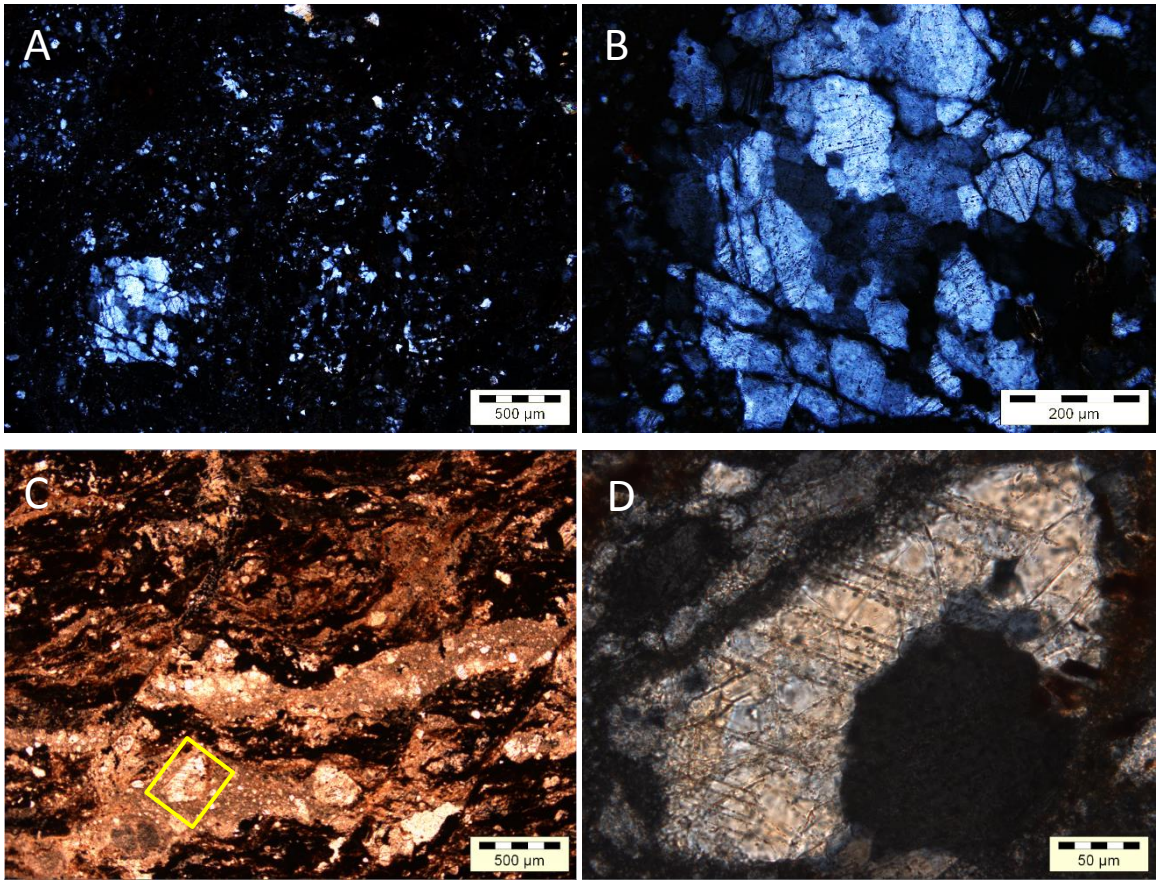

Figure 5.9: PDF features in sample M4 A-INJ (depth: 189.00 m). **A)** Slightly recrystallized, fractured, quartz clast in a partially disaggregated melt clast in MMBr matrix. XPL. **B)** Enlargement of A, showing one set of PDF. XPL. **C)** Elongate, strung out cataclasite in MMBr. Note the oblique shear fractures. PPL. **D)** Enlargement of C shows decorated PDF in a quartz grain. XPL. PPL = plane polarized light, XPL = crossed polarized light.

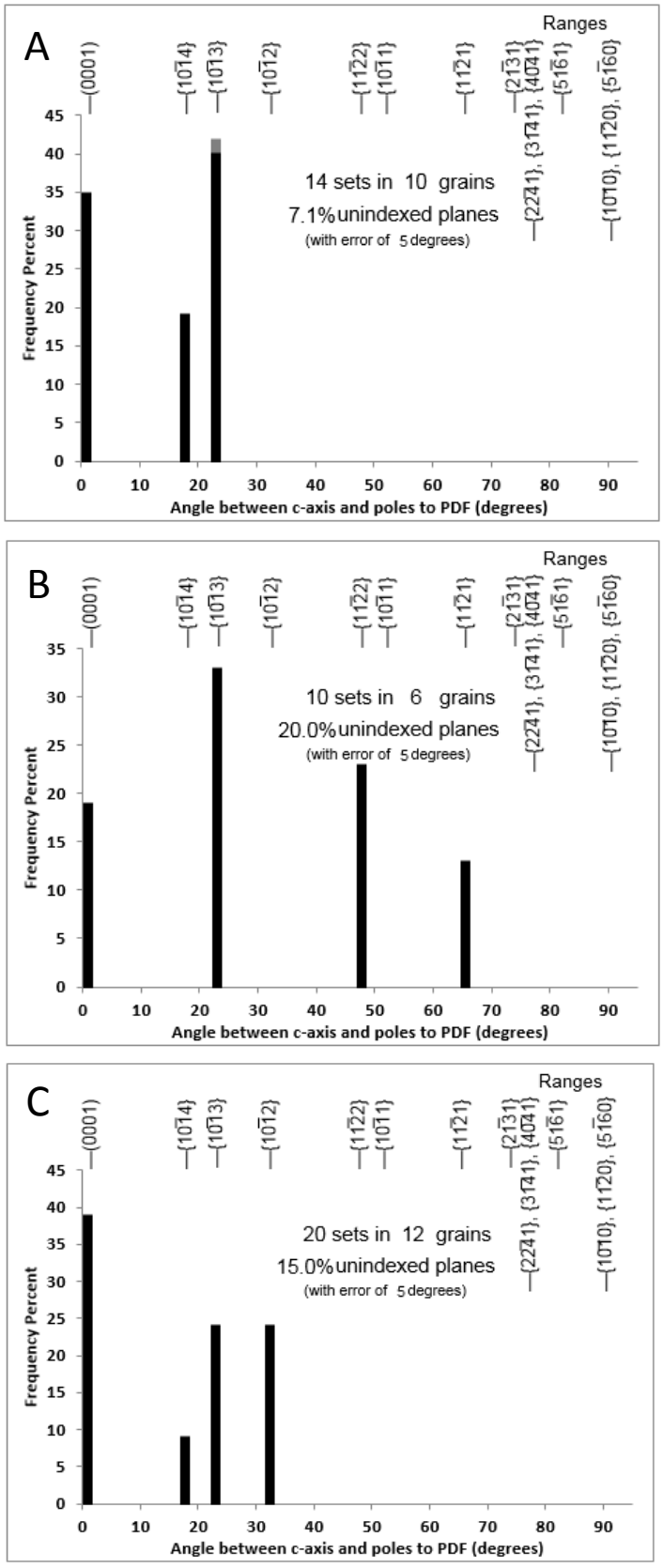

Figure 5.10: Histograms showing absolute frequency percent for indexed PDF crystallographic orientations of quartz clasts from M4 core MMBr samples; recalculated to 100% (excluding the unindexed PDF). **A)** PDF data from M4 IM-2 (depth: 234.33 m). The grey bar indicates PDF planes which plot in the overlapping zone between $\{10\bar{1}4\}$ and $\{10\bar{1}3\}$ orientations; here denoted under the $\{10\bar{1}3\}$ bar. **B)** Data for sample M4 IM-6 (depth: 271.17 m). **C)** MMBr injection dyke sample M4 A-INJ from 189.00 m depth. The data was processed on the ANIE program based on ranges of values.

5.4 Shock metamorphic evidence in other minerals

Petrographic evidence of shock metamorphism in M4 core lithologies is observed in both plagioclase and alkali feldspar (Figure 5.11 and 5.12), and possibly also in biotite and titanite (Figure 5.13) in both the target rocks and in lithic or mineral clasts in the impactites. Despite their importance in many crustal rocks and their presence in many quartz-poor terrestrial and non-terrestrial rocks of mafic composition, feldspar shock barometry has not been quantified to the extent that has happened for quartz, and has focused mainly on the solid-state transformation of feldspar to diaplectic glass (> 30-35 GPa; Stöffler, 1971; Stöffler et al., 1991; Singleton et al. 2011). Stöffler et al. (1991) proposed that PDF in plagioclase normally develop above 15-20 GPa, however, Singleton et al. (2011) suggested a range between 10 and 35 GPa (Table 5.1). Shock effects in feldspars include a range of features such as planar fractures and offset twins, checkerboard texture, alternate twin deformation (e.g., ladder texture; isotropization of alternate albite twins, preferential alteration of alternate-twin lamellae, and patchy or partial isotropization of grains) (Engelhardt et al., 1968; French et al., 1997; Schultz et al., 2006; Harris et al., 2010; Pati et al., 2010; Pickersgill et al. 2013).

In the M4 drillcore samples, plagioclase and microcline are present in almost all the target rocks, although K-feldspar is rare in the trondhjemitic gneiss and absent in the dolerite and metadolerite; they also occur as mineral clasts or in lithic clasts within the impactites. Feldspar grains in both target rocks and impactites commonly display planar fractures that offset twin lamellae, kinking or bending of twins, and undulose and patchy extinction (Figure 5.12 and 13 B, C) and spindle-shaped lamellae in feldspar are noted in sample M4 GG-16 from 360.18 m (Figure 5.13D). Many fractures are intergranular, crosscutting multiple grains, suggesting that they cannot be true shock features. As such they are related to cataclastic microbreccias that are most likely linked to the impact, even though some evidence exists for pre-impact brittle deformation (Section 2.3.2). There is also abundant evidence that post-impact hydrothermal activity led to chalcedonic quartz, calcite and/or zeolite precipitation in fractures. An attempt is made in Chapter 6 to reconcile the diverse features with broadly contemporaneous shock and cataclastic processes during crater formation.

Both plagioclase and microcline contain “PDF” that occur as 1–5 μm wide planar to spindle-shaped lamellae oriented oblique to twin planes and visible under crossed polars (Figure 5.11A, B and 5.12). The lamellae are not isotropic and, thus, cannot be true PDF. Pickersgill et al. (2015) suggested that similar features in plagioclase from the Mistastin Lake impact represent compositionally-distinct

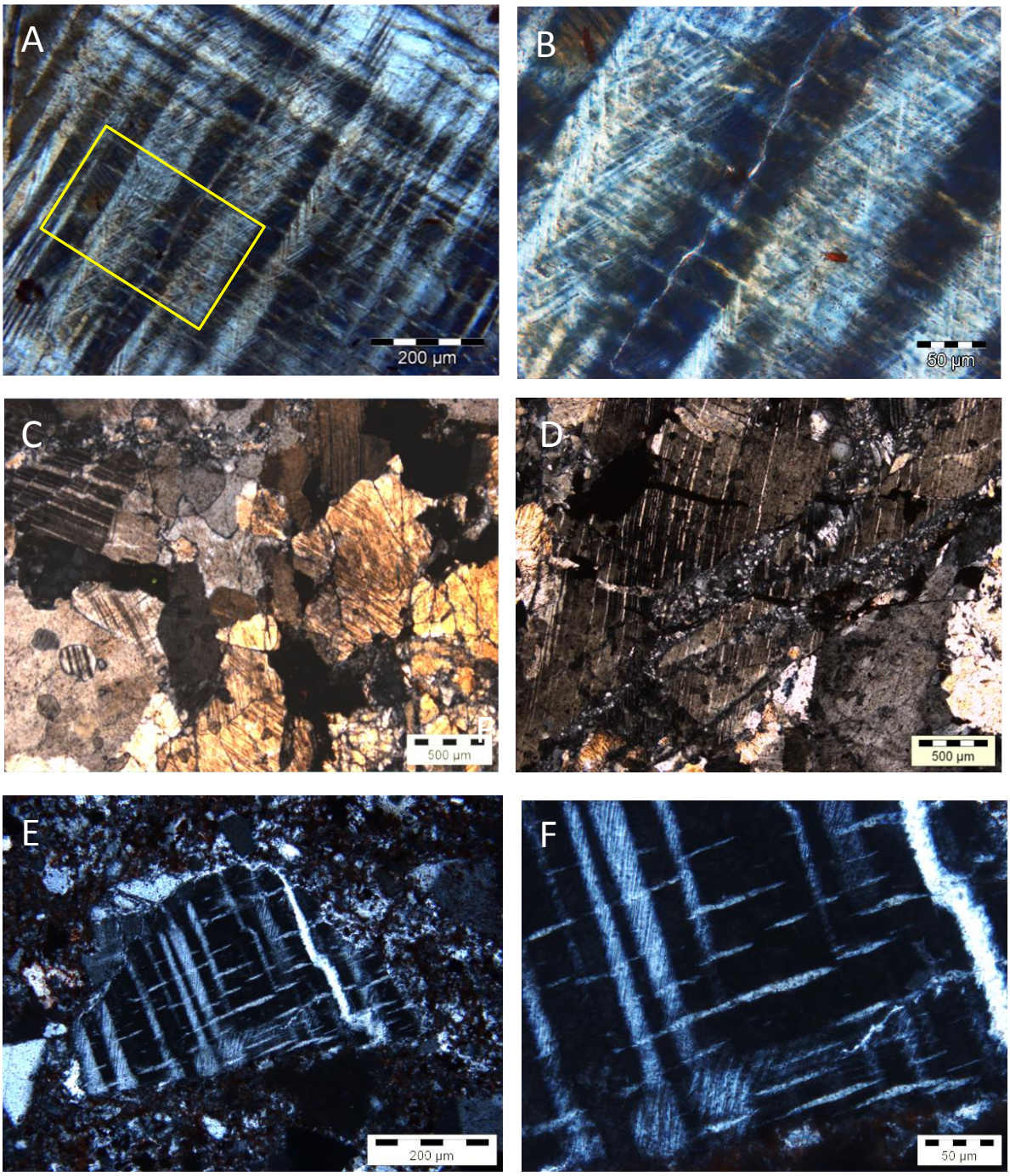

Figure 5.11: Impact-related deformation effects observed in feldspar in the M4 core lithologies. **A)** Microcline grain in granitic gneiss sample M4 GG-2 (depth: 131.90 m), with two sets of oblique, closely-spaced, spindle-shaped lamellae. XPL. **B)** Enlargement of A, showing spindle-shaped lamellae trending N-S and NE-SW across the image; locally forming a chevron pattern. XPL. **C)** Sample M4 GG-14 (depth: 316.38 m), showing fractured plagioclase (top left) and PDF-laden quartz clasts (right and bottom). Plagioclase twins are displaced by multiple parallel fractures. XPL. **D)** Sample M4 FZ-4 (depth: 233.48 m), showing plagioclase grain cut by cataclastic microfractures. XPL. **E)** Antiperthitic plagioclase clast enclosed in suevite sample M4 S-2 (depth: 156.35 m), with a single set of oblique lamellae along alternate twins. K-feldspar exsolution lamellae lie ENE in image. XPL. **F)** Enlargement of E showing oblique lamellae. XPL. PPL = plane polarized light, XPL = crossed polarized light.

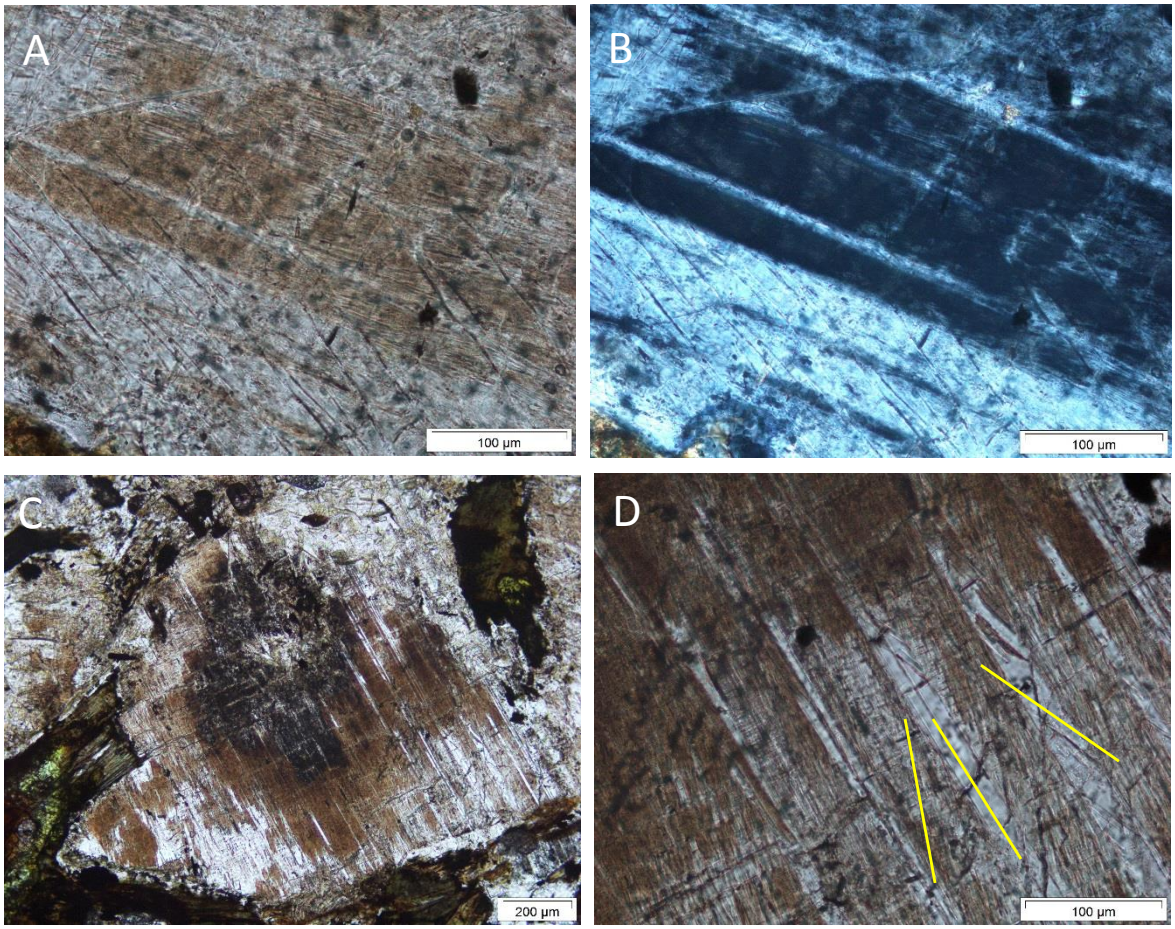

Figure 5.12: Shock deformation features in plagioclase feldspar from dioritic gneiss sample M4 AM-5 (depth: 362.63 m). **A)** Yellow discoloration of alternate twin lamellae and PDF aligned oblique to, but cross-cutting, twin lamellae. The lamellae are displaced by a micro-fracture (top, left). **B)** XPL of A. **C)** Patchy yellowing effect on alternate lamellae in the plagioclase grain interior. This is accompanied by reduced birefringence but not full isotropization. PPL. **D)** Close up of C, showing 3 sets of PDF in plagioclase (one set is parallel to the twin lamellae and the other 2 are oblique). XPL. PPL = plane polarized light, XPL = crossed polarized light.

lamellae. Multiple sets of these closely-spaced lamellae locally form a chevron pattern in microcline and show evidence of overlap between the different sets (Figure 5.11A, B). The lamellae may also extend across multiple microcline twins and alternate twin lamellae in plagioclase (Figure 5.12). In addition to the PDF in plagioclase, plagioclase in the granitoid gneisses throughout the core shows irregular patchy to twin-related pale yellow discoloration under PPL (Figure 5.12 C, D). These patches or alternate twins display reduced birefringence relative to the rest of the grain. Under high magnification the discoloration appears to be linked to very fine inclusions, and it is suggested that this might be similar to the toasted quartz phenomenon described by Ferrière et al. (2009). It is unclear whether any of these patches may have originally been glass (the absence of feldspar glass would restrict

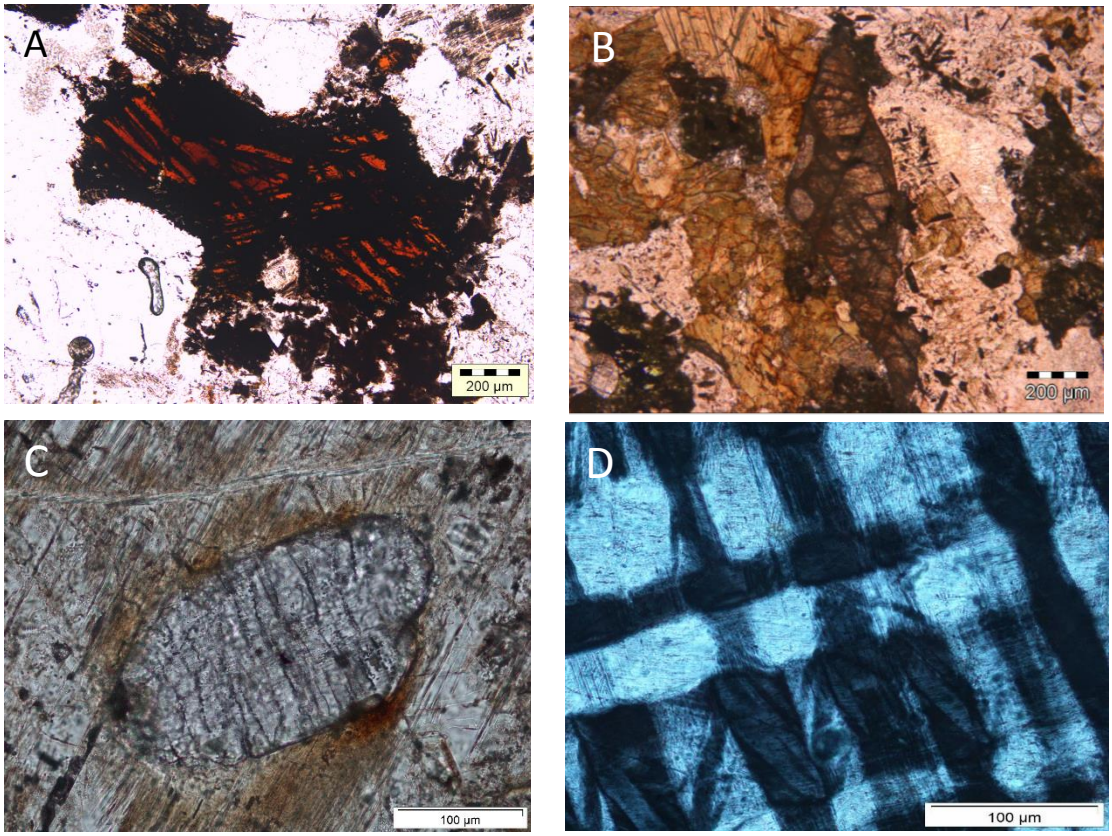

Figure 5.13: Possible shock metamorphic features in M4 core target lithologies. **A)** Highly oxidised biotite displaying intense kink bands from sample M4 GG-4 (depth: 109.20 m). PPL. **B)** Titanite grain with planar fractures, possibly of shock origin, from sample M4 AM-1 (depth: 340.10 m). PPL. **C)** Subplanar fractures defined by fluid inclusion trails in zircon from dioritic gneiss sample M4 AM-5 (depth: 362.63 m). **D)** Wide, irregularly-distributed, spindle-shaped lamellae in microcline defining a chevron pattern from sample M4 GG-16 (depth: 360.18 m). The irregular distribution suggests a strong crystallographic control similar to other shock microdeformation phenomena. XPL. PPL = plane polarized light, XPL = crossed polarized light.

peak background shock pressures in the target rocks to < 30 GPa (Stöffler, 1971; Stöffler et al., 1991; Singleton et al., 2011). No PDF features were observed in the more calcic plagioclase in the dolerite and metadolerite. Pickersgill et al. (2015) speculate that the triclinic form of the plagioclase series may play a role in restricting PDF development. Certainly, PDF are much rarer in the sodic plagioclase relative to the microcline but, in the case of the the metadolerite plagioclase an additional constraint might be their high degree of alteration.

Given the evidence for at least some pre-impact deformation, the kinks in biotite grains (Figure 5.13A) cannot be unequivocally linked to the impact, as this feature is common in tectonic strain environments. The biotite grains are typically strongly oxidized at their margins in both the upper target rocks and impactites. Oxidation of biotite is likey the result of hydrothermal alteration (Chapter 4). Ogilvie et al. (2011) reported biotite shock melts at P > 30 GPa. The absence of evidence of such melts in the M4

drillcore target rocks may place an upper limit on peak background shock pressures; however, it is impossible to tell if such melts were originally present or not, giving the high levels of alteration. The 120° titanite fracture cleavage (Figure 5.13B) resembles shock-activated mineral cleavage seen in amphiboles in the Vredefort Dome (Gibson and Reimold, 2005) but also cannot be unequivocally linked to shock. Intense, slightly irregular, fractures in zircon (Figure 5.13C) are similarly ambiguous.

5.5 Timing of micro-scale deformation

It is clear from the inclusion of metadolerite with quartz veining as lithic clasts in the M4 impactites that the target rocks experienced at least some brittle deformation and fluid-related alteration prior to the impact event. In Chapter 3 this fracturing-veining event was also suggested as the source of silicification and albitization of adjacent granitoid gneisses that produced trondhjemitic compositions.

Apart from the hand specimen evidence that the cataclasites were sufficiently open for intrusion of suevite and MMBr to occur along fractures, and that they display evidence of flow along with host suevite and MMBr, micro-scale evidence shows that cataclastic microfractures may cut fractured quartz grains with PDF (Figure 5.14D), or that PDF-bearing quartz and shocked feldspar fragments are very common in the cataclasites. The petrographic evidence is most compatible with shock deformation of the quartz and feldspar occurring before grain-scale fracturing and cataclasis/disaggregation. This model, in which the cataclasites, suevites and MMBr have formed broadly simultaneously (within seconds to minutes of each other) is explored further in Chapter 6.

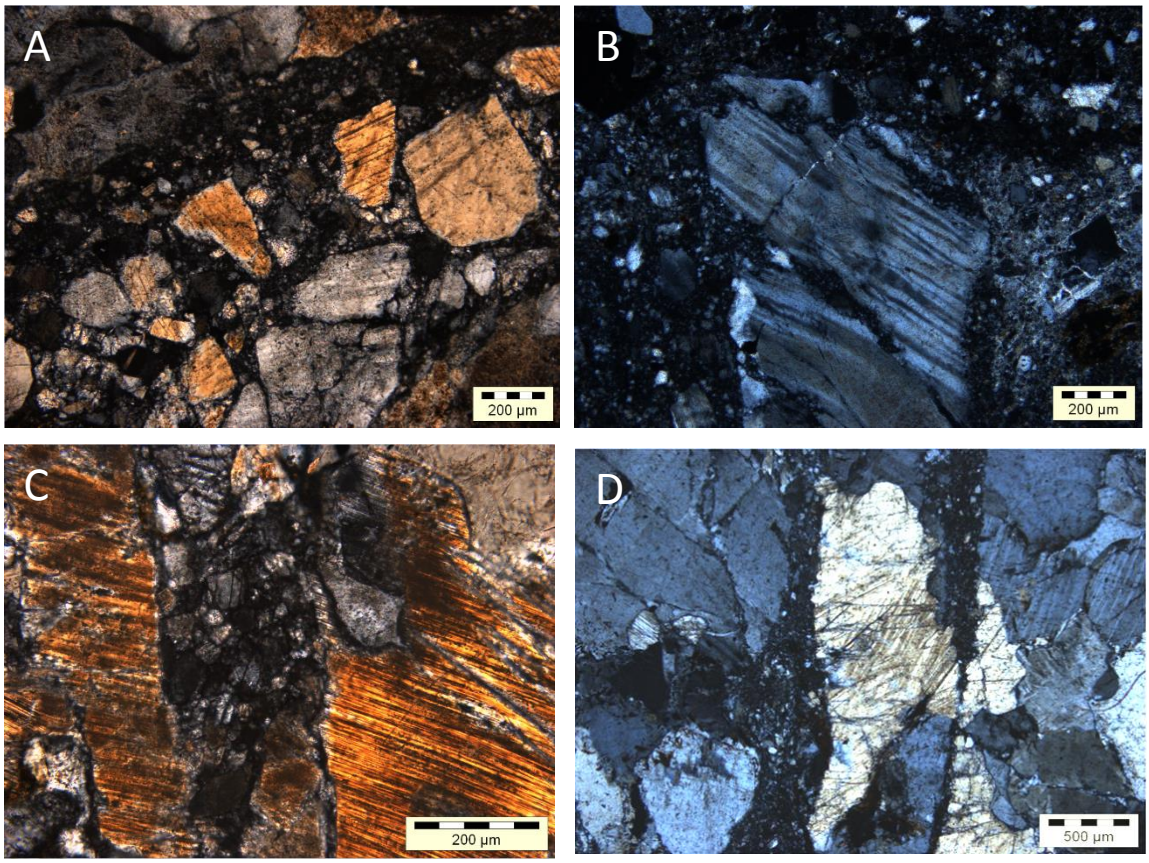

Figure 5.14: A) Cataclasite hosting quartz fragments with PDF within target rock sample M4 GG-11 (from 178.05 m depth). XPL. **B)** Microcline grain with spindle-shaped lamellae of inferred shock origin from sample M4 IM-9 (depth: 299.76 m) is cut by small fractures that are continuous with cataclastic matrix. XPL. **C)** Sample M4 AM-4 (depth: 359.60 m) shows two quartz fragments that are slightly rotated pieces of a single original PDF-laden grain, separated by cataclasite. XPL. **D)** Sample IM-9 (depth: 299.76 m), shows shocked quartz grains cut by cataclasite. The quartz grains contain up to three sets of PDF. XPL. PPL = plane polarized light, XPL = crossed polarized light.

5.6 Comparison of shock intensity in M4 core target and impactite samples with previous studies

In general, petrographic analysis suggests that the impactites in the M4 core display fewer PDF-laden quartz grains and PDF sets compared to the target rocks. No significant difference in shock intensity was noted in quartz clasts in the suevite versus those in MMBr. Most significantly, however, measured PDF orientations of quartz clasts within the suevite appear consistent with those obtained from quartz grains in the various target rocks. Most stricking is the similarity in PDF orientations present in dioritic gneiss sample M4 GG-4 and M4 S-7 (with the exception of polar angle frequency). These common orientations are - 0° - (0001) and 22.95°- $\{10\,\bar{1}\,3\}$. Corner et al. (1997), who only observed 22.95° and

32.42° orientations in the samples they studied (the latter concluded these are consistent with 10-16 GPa peak shock pressures). This is not surprising, given that M4 is located 18 km from the MIS centre, whereas Corner et al.'s (1997) samples were taken at 47 km (in situ breccia), and 75 km (river boulder) from the centre respectively. The M4 core results thus suggest that the lithologies of the M4 core originally lay closer to the centre of the impact than Corner et al.'s (1997) site.

Hart et al. (1997) showed 0°, 22.95°, 32.42°, 73.71°, 82.07°, 90.00° sets in an erosional product of the Morokweng impact structure lithologies now enclosed as pebbles in a conglomerate bed unconformably overlying the centre of the MIS. These researchers estimated 10-25 GPa shock pressures for the WF5 core lithologies, but no detailed statistical analysis was conducted/reported. The results by Hart et al. (1997) are notably similar to those obtained for the M4 core samples in terms of the PDF crystallographic orientations obtained. Finally, the evidence presented by Reimold et al. (1999) refers to diaplectic glass (now altered) in WF5 which would imply shock pressures > 30 GPa; this would be consistent with WF5 having been drilled at or near the centre of the impact structure.

5.7 Summary

Based on petrographic analysis of 95 thin sections from the M4 core samples and Universal Stage measurements of PDF orientations of quartz in 14 samples, the following conclusions can be made:

1) This study represents the largest integrated petrographic and Universal Stage PDF analysis of in-situ rocks in the MIS to date.

2) Microscopic shock effects observed in the M4 lithologies include: planar fractures, decorated planar deformation features (PDF), feather features, mosaic extinction and toasting in quartz; reduced birefringence and patchy (mosaic) extinction, and oblique and chevron-style spindle-shaped lamellae in plagioclase and microcline; and possibly planar fractures in titanite, kink bands in biotite and closely spaced fractures hosting fluid inclusion trails in zircon.

3) Plagioclase and microcline feldspars commonly display evidence of shock (multiple twin-oblique lamellae, crystallographically-controlled reduction in birefringence/toasting) below the onset of diaplectic feldspar glass formation, suggesting that peak background shock pressure was < 30 GPa.

4) There are notable differences in the absolute frequency percentages of the observed PDF sets but overall the same PDF are indexed in quartz from both the target rocks and impactite samples. As a result there is no significant difference in maximum estimated shock pressure between the quartz-rich granitoid target rocks, MMBr and suevite, as defined by quartz PDF and feldspar shock textures, although the impactites do contain rock and/or mineral melts.

5) PDF crystallographic orientations of quartz were measured in 14 samples (8 target rocks and 6 impactites). Common orientations are:0°-(0001), 22.95°{$10\bar{1}3$}, 17.62°{$10\bar{1}4$}, 32.42°{$10\bar{1}2$}; which suggests peak shock pressures in the target rocks of 10-25 GPa; based on calibrations presented in Table 5.2 and those by Stöffler and Langenhorst (1994). The data in Figures 5.5 and 5.10 suggest an overall dominance of 0° - (0001) and 22.95°-{$10\bar{1}3$} orientations. The dominant orientations in the target rock samples are similar to those in the impactites. These findings are inline with the observation by French (1998) that the (0001), {$10\bar{1}3$} and {$10\bar{1}1$} PDF orientations are common in impact sites. In this study these sets constitute ~80% of the data.

6) The PDF sets observed in the M4 core lithologies match those on shock stage 3 and 4 in Table 1.2. This indicates that the M4 core lithologies are moderately to strongly shocked.

7) The exclusive occurrence of 0° - (0001), 22.95° {$10\bar{1}3$}, 17.62° {$10\bar{1}4$}, 32.42° {$10\bar{1}2$}; especially in suevite sample M4 S-5 (depth: 285.97 m) and the fact that no high-index measurements were obtained could be an indication of shock progression / change at depth. However due to the limited number of measured samples; not much can be concluded at this point.

8) The shock pressure estimates postulated in this study are in line with those of 10 - 25 GPa by Hart et al. (1997).

9) Though PDF orientations at high angles to the c-axis become abundant from ~270 m depth. No clear evidence of systematic variation in peak shock pressure with depth in the core is postulated in the target rocks. A recommendation for more measurements in order to validate this is necessary.

10) Whilst mineral or whole-rock melting to form the melt clasts in the suevites and MMBr matrix might argue for higher local shock pressures, this would only apply if an alternative, friction melting, origin for the melts can be ruled out (see Chapter 6).

11) The high shock pressures generally recorded in the M4 core samples indicate that these rocks must have been located close to the floor of the transient cavity of the MIS (see Figures 1.3 and 1.4).

12) The presence of decorated PDF in quartz indicates that the originally amorphous PDF were altered by post-impact hydrothermal-metamorphic processes that also altered all glass or melt rock. This recrystallization of the PDF glass lamellae could possibly have caused annealing of the high index PDF (e.g., Grieve et al., 1990), leaving the more robust c (0001); hence its dominance throughout the measured sets.

13) The relatively high abundances of decorated PDF, toasted quartz grains and the presence of altered melt clasts in suevite (discussed further in Chapter 4) is indicative of post-impact hydrothermal alteration conditions experienced by the Morokweng target rocks.

Chapter 6

Discussion and Conclusions

6.1 Introduction

In Chapters 2-5 it has been shown that the lower ~268 m of the M4 core beneath the Kalahari Group unconformity consists of a highly heterogeneous sequence of shocked, brecciated and cataclased granitoid gneisses, metadolerite and dolerite that were intruded by mm- to m-scale dykes of MMBr and suevite. The overall aim of studying the petrography and whole-rock and mineral geochemistry was to understand and establish the origin for the M4 core impactites. This required a detailed examination of the intersected target lithologies and their contribution into the formed impactites. Most of the M4 core comprises target rocks that include granitic-granodioritic gneisses, trondhjemitic gneiss, dioritic gneiss, dolerite and metadolerite. Apart from regional metamorphism that formed the foliation in the granitoid gneisses, the metadolerite also experienced low-T metamorphism before the impact. These rocks were also locally sheared and brecciated, with associated fluids silicifying and possibly also metasomatically altering the granitoid gneisses and metadolerite. In this chapter, the nature of the target rocks is discussed in the context of the regional geotectonic setting and then the origin of the MMBr and suevite is explored. The source of the post-impact alteration of the impactites is also discussed and, finally, the significance of all these impact-related features is discussed to propose a setting for the rocks intersected in the M4 core within the MIS.

6.2. Nature of the M4 target rocks

The pre-impact lithologies (granitoid gneisses, dolerite and metadolerite) present in the M4 borehole core have been described lithologically, structurally, petrographically, and geochemically in detail in the preceding chapters. In this section the results obtained are discussed in the context of the regional MIS setting and the greater western Kaapvaal Craton setting.

6.2.1. Granitoid gneisses

A detailed petrographic study of the granitoid rocks shows the same fundamental mineralogy throughout the main package (quartz, plagioclase, K-feldspar, biotite ± titanite, epidote, Fe-Ti oxides), although variations in the modal proportions of these minerals and rock textures exists, particularly in the extent of biotite and epidote mineral inclusions in plagioclase. All of the granitoid rocks are

gneissic, but the more leucocratic varieties have a weaker foliation. Geochemically, the granitic, granodioritic and trondhjemitic gneisses in the M4 core are classified as a TTG assemblage as they are Archaean rocks (R. Gibson, pers. comm., 2015) and show SiO_2 compositions > 70 wt. % (Condie, 2005). These granitoid gneisses range from 72.83-75.30 wt. % SiO_2 (average of SiO_2 = 74.19 ± 0.85 wt. %), proving to have more felsic compositions than the intermediate, SiO_2-poor diorite, which has 55-60 wt% SiO_2. A steep REE pattern without a Eu anomaly is seen, which is typical of Archaean crustal rocks (Taylor and Mc Lennan, 1985). The REE profiles for the granitoid rocks are relatively parallel and overlap (Figure 3.13A); this could indicate that these rocks are co-magmatic (Philipp et al., 2008); however, the dioritic gneiss samples are enriched in the HFSE (Figure 3.13C, 3.14A). All the geochemical analysis suggests the dioritic gneiss may be somewhat distinctive. The trondhjemitic gneiss composition may be a metasomatic feature as it occurs in a pre-impact fault breccia zone with quartz veining.

6.2.1.1 M4 granitoids in comparison to Morokweng impact structure granitoids

Granitoid rocks are exposed in the vicinity of Ganyesa southeast of the centre of the MIS where the Kalahari Group cover has been removed (Figure 1.1). Other samples come from pebbles in the basal Kalahari Group conglomerate or as clasts in (Koeberl and Reimold et al., 2003) or below (Hart et al., 1997) the impact melt intersected in the central cores. The M4 drillcore lithologies data is compared to these granitoids (Figure 6.1). The granitoids intersected near the bottom of the WF5 drillcore were found to be petrographically similar to those enclosed as clasts in the lower parts of the impact body (Reimold et al., 1999). They consist of granitic to granodioritic lithologies, cross-cut by fine grained aplitic and quartz-feldspar pegmatitic veins that are shocked and strongly thermally altered (Reimold et al., 1999). These rocks are significantly more mafic that the M4 rocks.

6.2.1.2 M4 granitoids in comparison to regional granitoids

Figure 1.10 shows that outcrop in the western Kimberley block is very limited. The largest granitoid outcrop occurrences occur surrounding the Amalia and Kraaipan greenstone belts, which have been studied by Anhaeusser and Walraven (1999). U-Pb single-zircon geochronology (R. Gibson, pers. comm. 2015) shows that the granitoid gneisses in the M4 core formed at 2.91-2.92 Ga. These ages differ from the ones reported by Poujol et al. (2003) for the Kraaipan – Amalia components of the Kaapvaal Craton. Intrusive ages of 2749 Ma - 2880 Ma were obtained for granitoid samples from the Kraaipan region (Anhaeusser and Walraven, 1999); and 2791 ± 8 Ma, to as old as 3008 Ma, for the

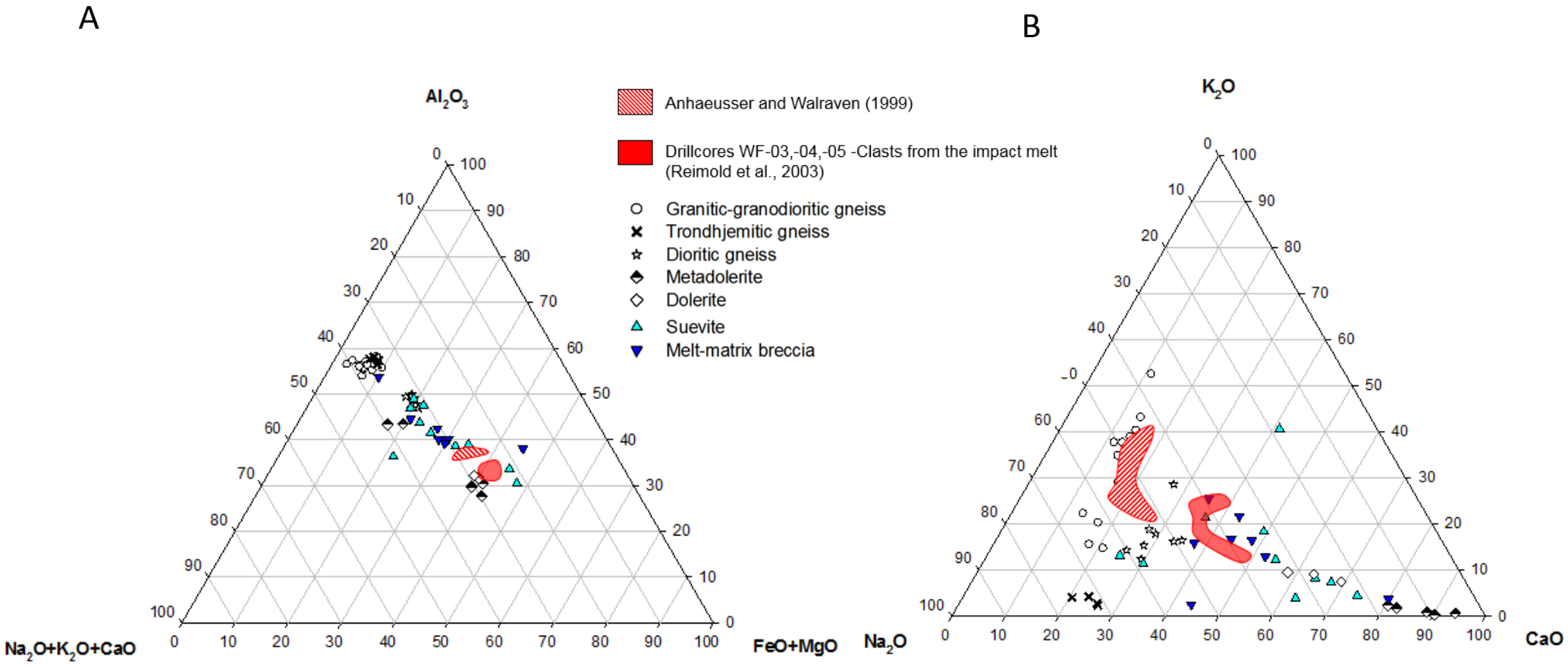

Figure 6.1: Geochemical compositions of M4 core target rocks compared with data from the Amalia-Kraaipan region (Anhaeusser and Walraven, 1999) and other MIS cores (Reimold et al., 2003). **A)** Al_2O_3-(FeO+MgO)-(Na_2+K_2O+CaO) ternary diagram. **B)** K_2O - Na_2O - CaO ternary discrimination diagram.

The M4 core granitoid and dioritic gneisses show a far more diverse set of bulk compositions than the samples from the Amalia and Kraaipan areas (Figure 6.1), but it must be remembered that the M4 samples are restricted in size, which is a problem in coarse-grained rocks. They are significantly less mafic than Amalia-Kraaipan rocks (Figure 6.1A). The K_2O-Na_2O-CaO plot suggests the Amalia-Kraaipan rocks are slightly more calcic than the M4 granitoid gneisses, but less than the M4 dioritic gneiss. Unfortunately, no REE or Trace Element data were presented by Anhaeusser and Walraven (1999) for further comparison.

6.2.2 Metadolerite and dolerite

Two generations of doleritic rock also form part of the pre-impact lithologies in the M4 core. Although their contacts with the granitoid gneisses all appear to be structural and mostly related to the impact, at least one of the structural contacts could be a pre-impact shear zone or fault. Given its state of preservation, it is possible that the dolerite could be linked to the ENE dyke trend that is cut by the impact structure (Figure 1.11), but direct geochemical comparison is not possible as the ENE dyke swarm is not exposed. The occurrence of metadolerite in the MIS is mentioned in Hart et al. (1997), as part of recrystallized inclusions in the impact melt, but no detailed account of the metadolerite composition is mentioned, and this metamorphism could be related to heat from the impact melt. Misra and Andreoli (2012) describe the Machavie and ~100 km long Paddakoor dykes that show radial trends to the MIS (Figures 1.1 and 1.11), but these are post-impact intrusions that cut across the MIS and so are not compared further.

Apart from the fact that the M4 metadolerite and dolerite are petrographically different, they are also geochemically distinct in most Harker plots (Figure 3.9) and in the REE plots (Figure 3.13F). The metadolerite composition does show much wider scatter, particularly in the highly-silicified contact zone with the trondhjemitic gneiss (Figure 2.1) where it also shows an intense shear foliation and strong oxidation. Whilst it is difficult to estimate the grade of metamorphism when the granitoid rocks developed their gneissosity, it is assumed that it was higher than the mid- to upper greenschist facies grade that affected the metadolerite, and so the metadolerite is interpreted as younger than the granitoid gneisses.

6.2.2.1 Comparison of M4 metadolerite and dolerite with regional dykes

After the intrusion of the granitoids at 2.91 Ga (R. Gibson, pers. comm., 2015), several possible regional mafic dyke intrusive events have occurred on the Kaapvaal Craton (Ventersdorp, Bushveld, Umkhondo, Karoo). It is not possible to tell the age of the metamorphism, but the most likely

possibility would be that the metadolerite is a 2.7 Ga Ventersdorp-age intrusion that was metamorphosed to greenschist grade during shearing or faulting at about the same time due to the high heat flow caused by the large volumes of mafic magmas that intruded the craton to feed the overlying Ventersdorp lavas that are extensively exposed in the region. In Table 6.1, the geochemical features of the metadolerite are compared with data for mafic intrusions from the Dominion Group, Klipriviersberg Group (Ventersdorp Supergroup), Bushveld Complex, Umkhondo Event and Karoo Supergroup from Pybus (1995) and De Kock et al. (2014). The Klipriviersberg Group basalts have been described geochemically by Myers et al. (1990). The geochemistry of the Dominion Group has been described by Jackson (1994) see Table 6.1. In Figure 3.10, the M4 core metadolerite and dolerite plotted across the Dominion Group and Klipriviersberg Group fields when assessed based on the classification diagram of Bowen et al. (1986). Given that the Kimberley Block only joined the Witwatersrand Block of the Kaapvaal Craton at 2.9 Ga, which is 200 million years after the extrusion of the Dominion Group lavas (Armstrong et al., 1991), it seems unlikely that the M4 metadolerite has a Dominion age. However, when comparing certain element concentrations of the metadolerites, they compare significantly with the Klipriviersberg Group (Type II) in Table 6.1.

The lack of metamorphism of the M4 core dolerite supports a younger age than the metadolerite. According to De Kock et al. (2014), the ENE dyke trend seen on aeromagnetic images (Figure 1.12) could be related to the 1.11 Ga Umkhondo dykes. At this stage, however, Karoo-age dykes cannot be completely ruled out, although the generally accepted age of rifting to form the South Atlantic (135 Ma) is slightly younger than the impact event, so the Karoo magmatism is more likely the source of the post-impact dykes such as the Paddakoor and Machavie dyke.

Table 6.1: Comparison of compositional data for M4 core dolerite and metadolerite with common dyke intrusions in the central Kaapvaal Craton (modified after Pybus, 1995) and data from the Umkhondo dykes (De Kock et al., 2014).

	Type I	**Type II**	**Type III**	**Type IV**	**Type IV**	**Umkhondo dykes (De Kock et al., 2014)**	**M4 Metadolerite**	**M4 Dolerite**
Classification	Mafic-ultramafic meta-intrusions	Basaltic komatiite to high Fe-tholeiitic basalt	Tholeiitic basalt	Tholeiitic basalt	Tholeiitic basalt			
Chronological Data	3.074 ± 0.009 (Armstrong et al., 1991)	2714 ± 8 Ma (Armstrong et al., 1991)	~ 2054 ± 2 Ma (Walraven and Hattingh, 1993)	1052+/-11 Ma (Reimold et al., 2000)	184 – 179 Ma (Duncan et al.,1997)	1.11 Ga (De Kock et al., 2014)		
Correlation	Dominion Group	Klipriviersberg Group (Ventersdorp Supergroup)	Bushveld Complex	Anna's Rust Sheet	Karoo Supergroup			
Major Oxides (wt. %)	SiO_2: 53.01 TiO_2: 0.71 *Fe_2O_3:10.85 P_2O_5:0.16	SiO_2: 50-56 TiO_2: < 1 *Fe_2O_3: 8-13 P_2O_5:0-0.15	SiO_2: 48-53 TiO_2: > 1.15 *Fe_2O_3: 11-17 P_2O_5:0.12-0.21	SiO_2: 48-53 TiO_2: > 1.15 *Fe_2O_3: 11-17 P_2O_5:0.12-0.21	SiO_2: 50-52 TiO_2: ± 1 *Fe_2O_3: 11 P_2O_5:0.18	SiO_2: 43-49 TiO_2: 1-2.5 *Fe_2O_3: 11-17 P_2O_5:0.1-0.4	SiO_2: 55 TiO_2: 0.9 **FeO: 9.1 P_2O_5:0.13-0.14	SiO_2: 53-54 TiO_2:1.3 **FeO:11.56 P_2O_5: 0.13-0.14
Trace Elements (ppm)	Y: 19 Nb: 82 V: 206 Cu: 64 Zn: 92 Zr: 82 Th: 0.33 Eu: 1.19	Y: 0-22 Nb: 0-5 V: 100-250 Cu: 0-100 Zn: 50-110 Zr: 10-120 Th: 1-4 Eu: 2-10	Y: 20-38 Nb: 5-10 V: 220-320 Cu: 70-200 Zn: 80-130 Zr: 100-150 Th: 2-4 Eu: 11-18	Y: 20-38 Nb: 5-10 V: 220-320 Cu: 70-200 Zn: 80-130 Zr: 100-150 Th: 2-4 Eu: 11-18	Y: 23 Nb: 5 V: 220 Cu: 70 Zn: 85 Zr: 100 Th: 1-1.5 Eu: 12-17	Y: 21-35 Nb: 3.3-9.2 V: 191-371 Cu:*n.d* Zn: *n.d* Zr: 81-193 Th: 0.9-3 Eu: 1.2-2.17	Y: 15-22 Nb: 2.3-4.45 V: 212-221 Cu: 29-46 Zn: 36-63 Zr: 56-80 Th: 0.9-1.4 Eu:0.9	Y: 20 Nb: 3.7-5.86 V:264-314 Cu: 63-143 Zn: 69-214 Zr: 55-107 Th:1.9-2.2 Eu:0.9-1.19

**Fe*$_2O_3$ - All Fe as Fe_2O_3, **All Fe as FeO, n.d.: not determined*

6.2.3 Geotectonic setting of the MIS target granitoids

Figure 1.10 shows that the MIS lies centrally within the western part of the Kaapvaal Craton, called the Kimberley Block by Schmitz et al. (2004). Schmitz et al. (2004) proposed that the Kimberley block formed a long lived volcanic arc above a west-dipping subduction zone from >2.97 Ga ago. This explains the older TTG ages obtained by Poujol et al. (2003) from the Amalia-Kraaipan region near the eastern edge of the Kimberley Block, at the same time as the West Rand Group was being deposited in the Witwatersrand Basin. The two continental blocks finally collided between 2.93 and 2.88 Ga to form the Kaapvaal craton (Figure 6.2). The 2.91-2.92 Ga age of the granitoid and dioritic gneisses in the M4 core correlate with this collision event. The absence of any amphibole or pyroxene in the granitoid gneisses suggests that they were emplaced and metamorphosed in the mid- to upper crust, rather than the lower crust. Post-collision erosion must have exposed them before 2.71 Ga when the Ventersdorp lavas were deposited over the central and western parts of the craton.

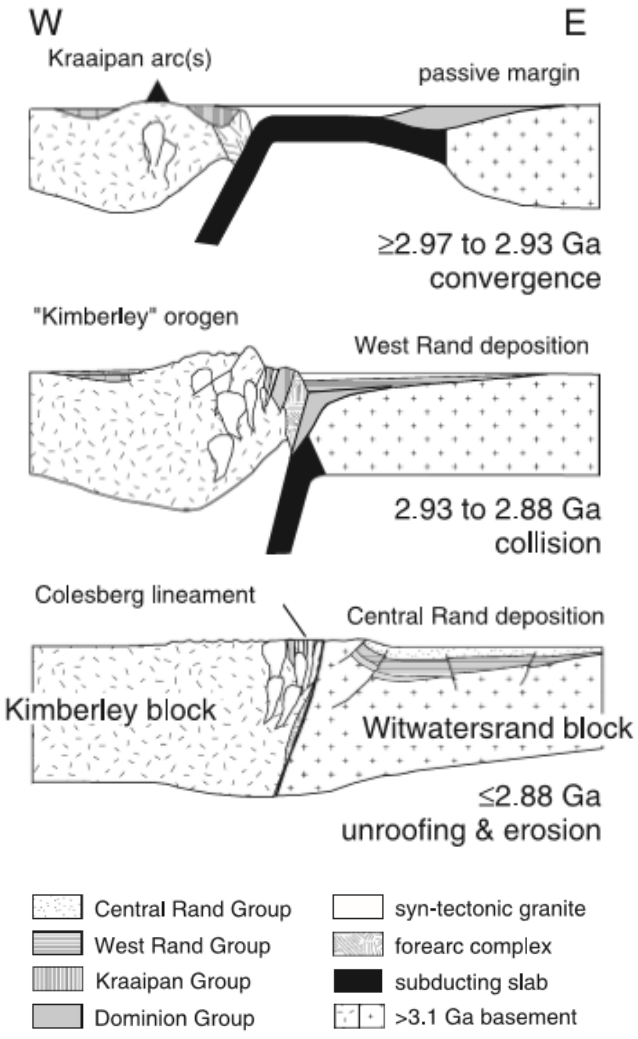

Figure 6.2: Cartoon cross-section showing the 2.88 Ga – 2.93 Ga collision of the Kimberley and Witwatersrand blocks to form the Kaapvaal Craton (from Schmitz et al., 2004).

6.2.4 M4 granitoid gneiss compositions in comparison to average crust

The M4 core is dominated by granitoid rocks ranging from granitic-granodioritic and trondhjemitic gneisses to dioritic gneisses. In this section the geochemistry of the target rocks is assessed in relation to crustal averages (upper continental crust, lower continental crust and bulk continental crust). The chrondrite normalization factors used for the REE plots are from Taylor and McLennan (1985). The lower crust value is taken from Rudnick and Fountain (1995) and the upper crust value and bulk continental crust value are from Rudnick and Gao (2004). According to Taylor and McLennan (1985), the lower crust (LC) is represented by crust between ~10 km depth and the Moho, but Rudnick and Fountain (1995) consider the LC to only be crust below 25 km, hence the values from Rudnick and Fountain (1995) are used here.

Chondrite-normalized rare earth element (REE) patterns for M4 core granitoid target rocks (Figure 6.3) distinctly show the difference between the granitic-granodioritic-trondhjemitic gneisses and the dioritic gneiss. The M4 rocks all show steeper profiles than the crustal averages. The LREE and HREE for the granitic-granodioritic-trondhjemitic gneisses are depleted in almost all REE compared to those of upper, lower and bulk crustal REE abundances, although there is some overlap in LREE with the lower crustal average. Dioritic gneisses are more enriched in most REE, but especially LREE, relative to upper crust and lower crust but overlap with these averages in terms of HREE (Figure 6.3). As shown in Figure 6.3, the distinct Eu anomaly seen in the target rocks is lacking for the average crustal values profiles.

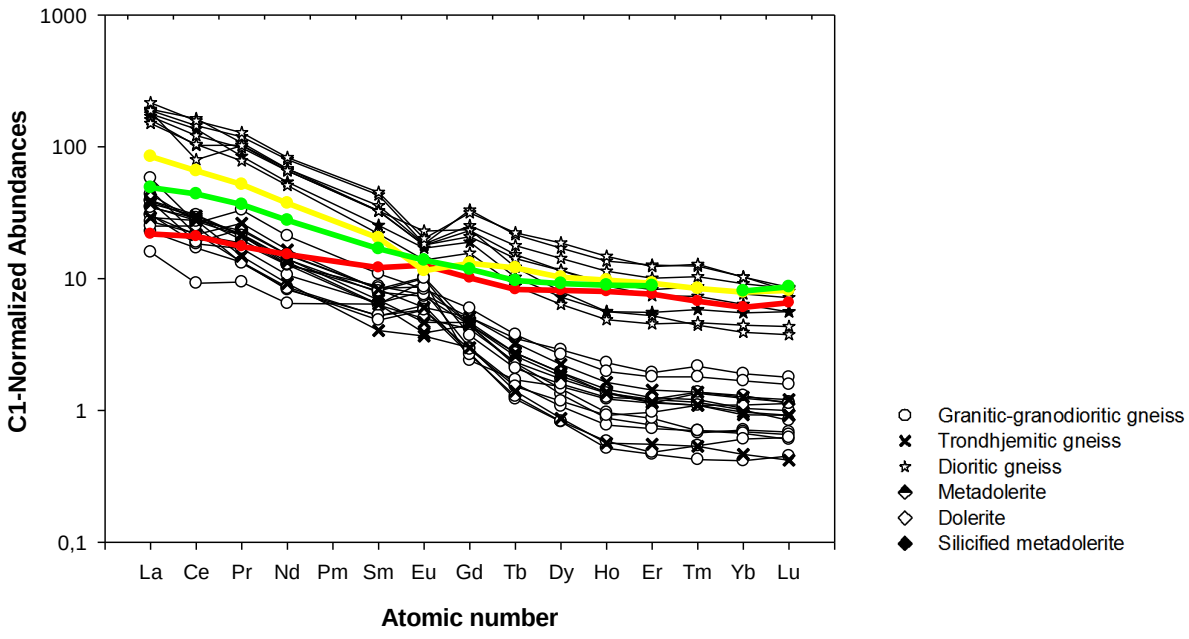

Figure 6.3 Comparison of chrondrite-normalized rare earth element (REE) patterns for M4 core granitoid rocks against average crustal values. Normalization values from Taylor and Mc Lennan (1985). (KEY: Yellow line-upper crust; green line- average continental crust, red line: lower crust).

6.3 Nature of the M4 impactites

Whole-rock major, trace and REE XRF and ICP-MS data of melt-matrix breccia and suevite dykes presented in Chapter 3 showed that the compositions of the impactites broadly fit with them being derived from the target rocks intersected in the M4 core. This is perhaps not surprising as the MMBr and suevite both contain lithic and mineral clasts down to the <50 μm scale but, importantly, the dykes still show spatial variation in their compositions linked to their immediate wallrock (except for sample M4-S6; see Figure 3.8. The local source of the impactites is supported by macroscopic and microscopic analysis in Chapters 2 and 5 that show that (a) the target rock lithic clasts in the breccias appear in approximately the same proportions as these rocks occur in the core overall; and (b) mineral clasts are also consistent with being derived from the target rocks, both in terms of mineral type and composition (Chapter 4) and in terms of shock levels (Chapter 5). Sample M4 S-6 has been shown petrographically to be anomalous as it encloses unusual ultramafic-derived clasts together with granitoid clasts. Ultramafic clasts have also been found in the impact-melt rock (Reimold et al., 1999), showing that such a rock is also part of the target even though it was not cored/intersected in M4.

6.3.1 Comparison of the M4 impactites to Morokweng impact melt

Despite the evidence for local derivation of the M4 impactites, it is important to consider whether the MMBr could represent part of the impact melt sheet that intruded into highly brecciated crater floor. This is the model that is mostly preferred to explain the "suevite and dike breccias" related to impact melt rock dykes in the floors of other impact structures (Stöffler, 1977). The central drillcores in the MIS have primarily intersected a differentiated impact melt, with geochemical studies reported by Koeberl et al. (1997), Andreoli et al. (1999), Reimold et al. (1999) and Koeberl and Reimold (2003). The average impact melt rock composition obtained from these studies is: 65.75 SiO_2 (wt.%), 0.49 TiO_2 (wt.%), 13.48 Al_2O_3 (wt.%), 5.87 FeO (wt.%), 0.08 MnO (wt.%), 3.70 MgO (wt.%), 3.41 CaO (wt.%), 3.89 Na_2O (wt.%), 2.15 K_2O (wt.%), and 0.12 P_2O_5 (wt.%) (Koeberl et al., 1997; Reimold et al., 1999). Significantly high siderophile contents of Cr (440 ppm), Co (50 ppm), Ni (780 ppm) and Ir (32 ppm) were noted (Koeberl et al., 1997), which indicates a significant meteoritic component. From these siderophile contents, Koeberl et al. (1997) concluded that the Morokweng impact melt contains one of the highest meteoritic contamination factors of any known impact melt, at 5-8%. By comparison, on average, the M4 MMBr contain Cr (123 ppm), Co (22 ppm) and Ni (82 ppm). However, no Ir and PGE fire-assay analyses were done on the M4 core impactites.

In Figures 6.4 and 6.5 the geochemical compositions for the M4 impactite dykes are compared to the known Morokweng impact melt compositions in order to further test the "contaminated impact melt" idea for the MMBr and to examine the precursor rock composition(s). The average impact melt data

taken from WF3, WF4 and WF5 data is from Koeberl and Reimold (2003) and the M3core data are from studies conducted by McDonald et al. (2001). The REE data of M4 lithologies are presented in Appendix 3.

The MIS impact melt samples form a much tighter cluster than the M4 impactites (Figure 6.4A) and a mostly narrower range in Figure 6.4B. The impact melt samples lie centrally within a triangular field defined by granitoid gneisses, dioritic gneiss and dolerite + metadolerite. The suevite and MMBr samples also mostly plot inside this triangle, but with more scatter (Chapter 3). In contrast to the other major oxides, in Figure 6.4A the impact melt shows a distinctly different trend to the M4 impactites that can only be explained by a low-SiO_2, low TiO_2 source that is different from the metadolerite and dolerite in the M4 core. Figure 6.4B shows that this source was also more ferromagnesian than any of the M4 target rocks. In Figure 6.4B, the impact melt from the M3 core forms a distinct cluster that is different from the data from the MWF cores.

The LREE data for the impact-melt rock from the M3 core overlap the M4 impactites but, on average, show a more pronounced negative Eu anomaly and are more enriched in HREE (Figure 6.5). Together with the HREE enrichment, it is clear that the Morokweng impact melt requires a significant additional more mafic/ultramafic component than is present in the M4 target rocks. Interestingly, sample M4 S-6 might provide clues to this source, as it plots near some of the impact-melt rock samples in the major oxide plots (Figure 6.5); however, it is anomalously enriched in LREE (Figure 6.5A), so does not look like the source. The MIS impact melt rock contains small ultramafic rock inclusions (Reimold et al., 1999) and a hidden greenstone belt (see Figure 1.10) in the sub-Kalahari Group basement has been proposed from water borehole studies by E. van Wyk (pers. comm., 2016).

From the evidence, the MMBr dykes noted in the M4 drillcore do not appear to be contaminated Morokweng impact melt.

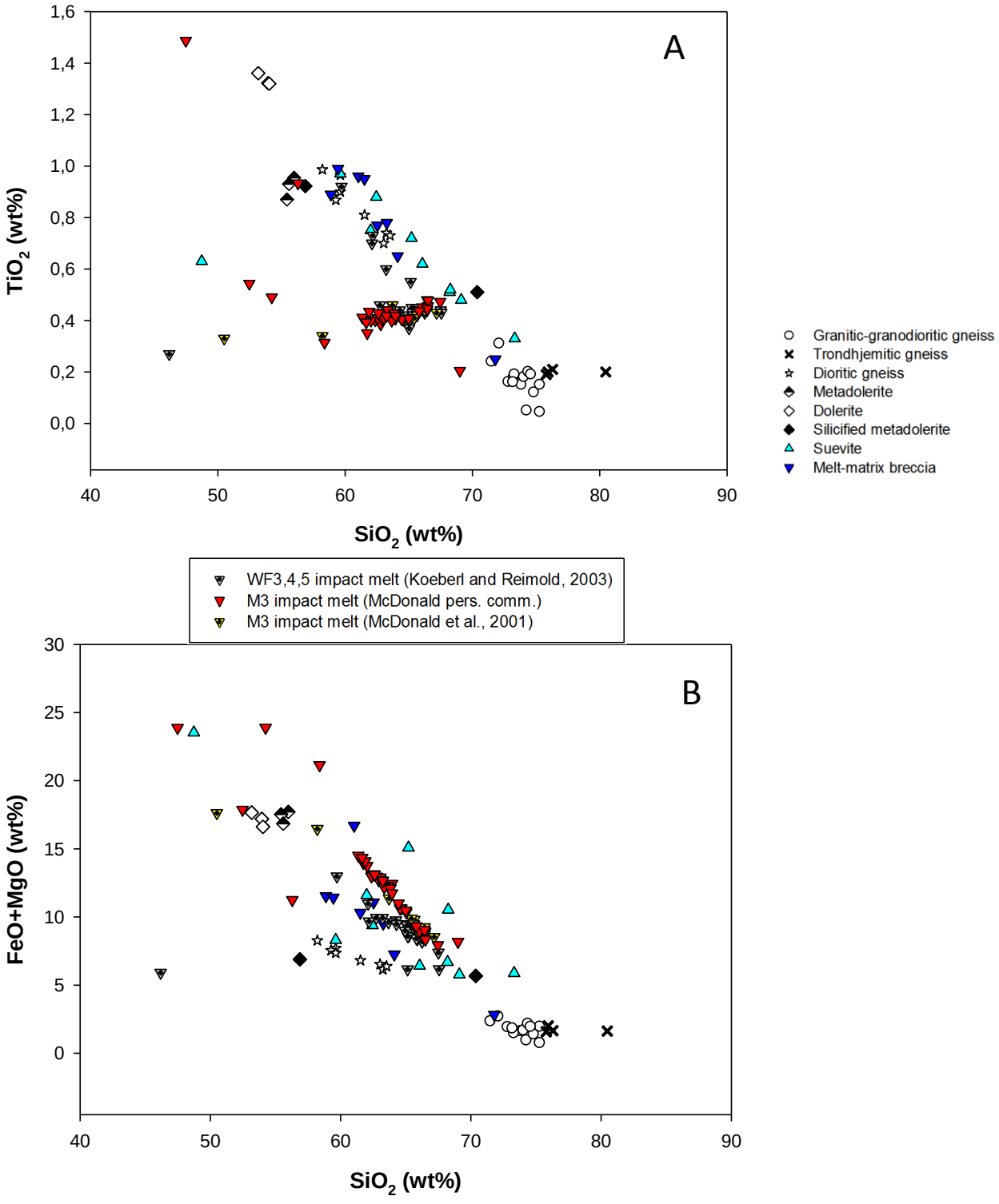

Figure 6.4: Harker plots for M4 core lithologies plotted with impact melt from WF3, -4, -5 and M3 drillcores. **A)** Major oxide TiO_2 plotted versus SiO_2. **B)** Bivariate plot of FeO+MgO versus SiO_2. Data for WF3, WF4 and WF5 are from Koeberl and Reimold (2003) and M3 borehole data are from studies conducted by McDonald et al. (2001 and pers. comm., 2012).

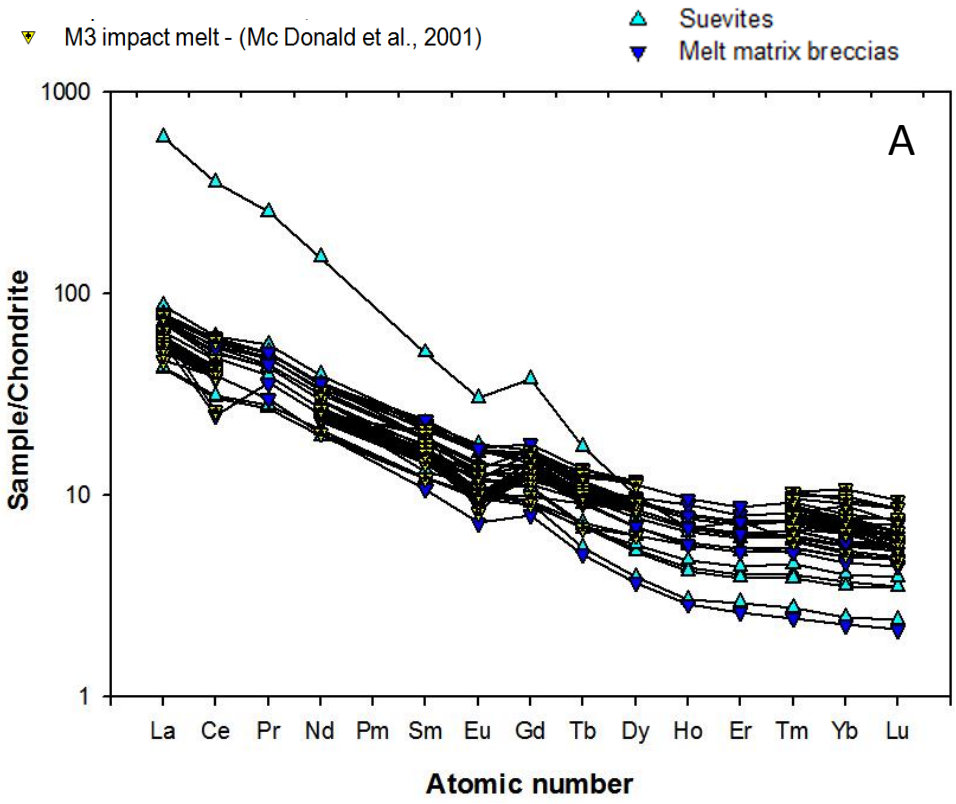

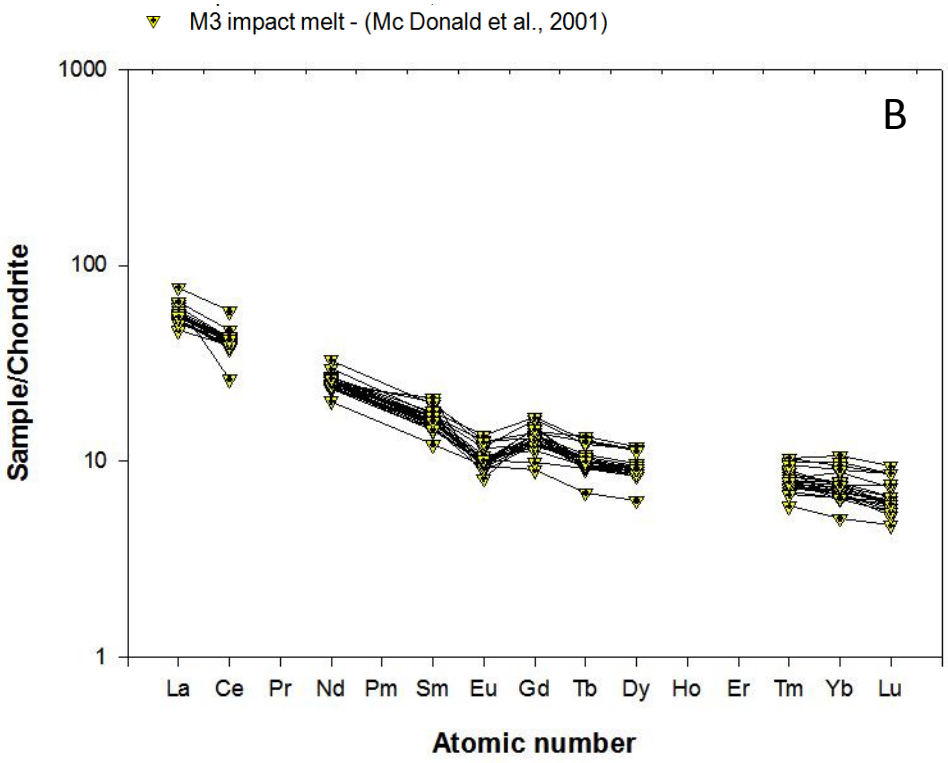

Figure 6.5: Chondrite-normalized rare earth element (REE) patterns for **A)** M4 impactites (this study) and impact melt rock samples from M3 (McDonald et al., 2001). **B)** M3 data only. Normalization factors from Taylor and McLennan (1985).

6.3.2 Origin of melt-matrix breccia in the M4 core

In section 6.3.1, it was argued that the MMBr are locally-derived and are not injections of impact melt from the main melt sheet seen in the M3 core. Part of the evidence used was geochemical, even though using geochemistry in clast-rich melt rocks to try to understand their origin must be treated with caution as it is never possible to completely remove all the clasts from the rock powders for analysis, and assimilation of clasts by the hot melt also means that the present melt composition is contaminated and not the original composition. Even the fact that the individual MMBr dyke compositions seem to be closely similar to their immediate wallrocks could be disputed if the melts assimilated high proportions of clasts, but this argument needs to consider how much assimilation would be possible for such a melt before it quenched. The structural evidence in Chapter 2 may be a stronger argument to suggest that the MMBr are locally derived and that their intrusion is closely related to the cataclasite network in time as well as spatially, although a 5 cm wide core gives only limited structural information. In this section, this relationship is explored more closely by referring to evidence of melt rocks in the floor rocks of other impact structures.

Several workers have suggested that localised melting can occur in the crater floor by two main processes, namely shock melting and friction melting.

Martini (1978) and Lambert (1981) have describes the A-type shock melts which are equivalent to what Spray (1998) refers to as the S-type (shock dominant pseudotachylite). The A-type (i.e. S-type shock melts; are generally random, thin (<1-2 mm) and could be caused by localised shock pressure increase which in turn is amplified by strong impedance contrasts or collapse of narrow cavities, such as joints, in the rock (e.g., Fiske et al., 1995; Kenkmann et al., 2000). The syn-contact and compression stage can cause conditions where high-pressure polymorphs develop confirming melt crystallization under shock conditions. High pressure polymorph-bearing veins have been noted in meteorites (e.g., Stoffler et al. 1991)

Some researchers have also described in detail friction melts which are referred to as B-type by Martini (1978) and Lambert (1981). The B-type friction melts are equivalent to melts described by Spray (1998) as the E-type (endogenic type pseudotachylite). The B-type (i.e. E-type) is friction melt that is extensive as it may be up to metres wide. Kenkmann et al. (2014) suggests that this type forms during modification stage, but may also be possible that form during excavation stage. Some workers have suggested friction melt may aid temporary weakening of crater basement, allowing flow-like large-scale behaviour, although Melosh (2005) calculated that such melts would only form less than a few % of the rock volume.

The M4 MMBr range from a few mm wide to a few dm wide. No high-P polymorphs were detected in XRD spectra (Appendix 4C) or microscopically, but the spectra did not come from the thinnest MMBr; also, it seems to be very unlikely that such minerals could survive the post-impact hydrothermal alteration. MMBr are closely associated with the cataclastic shear fractures (Section 2.4.1). Spray (1992) showed experimentally that the brecciation and cataclasis are first necessary steps in a fault zone to increase frictional sliding and fragment surface area to volume ratio to assist melting. The M4 MMBr contain polycrystalline mineral + lithic clasts that show micro- to crypto-crystalline cataclastic edges (e.g. Figure 2.21 and 2.23D), that might support this model, but there is also evidence that cataclasite was physically enclosed in a viscously flowing melt which could suggest cataclasite formed separately from melt; i.e. the melt was emplaced into cataclasite and not necessarily formed in it.

Finding thin (< 1 mm) melt dykes in the M4 core is complicated by the high levels of alteration that make it impossible to tell if thin, haematite-rich fracture fillings were once melt or the result of hydrothermal fluids infilling fractures after the impact. Many lithic clasts contain cm- to mm-scale irregular melt-like masses associated with closely spaced shear fractures that differ in colour from the enclosing MMBr (e.g., Figure 2.21). These might be in situ melts related to the shear fractures but they are all highly altered. In one sample, from 259.11 m depth, however, a fortuitous preservation of melt has occurred. Figure 6.6 shows an elongate "tongue" of orange "melt" (now completely altered to zeolite) with a slightly bulging front edge that still preserves a flow pattern parallel to its edge. This melt appears to be intruding towards the left side into a breccia of granitic gneiss lithic and mineral fragments that also contains several red and orange melt clasts. One of the "lithic" clasts in the breccia near the front edge of the melt tongue appears to have passively bent around the melt tongue. Microscopic analysis shows that this "clast" is actually mostly cataclasite and so it is suggested that the clast, despite its angular outline, was only weakly cohesive when the melt tongue intruded. This allowed it to deform when the melt intruded nearby. The melt tongue extends backwards into a zone of highly cataclased granitic gneiss with a sigmoidal shear structure, but it is also partially broken up by wedge-shaped microfractures. This is the strongest evidence found in the M4 core that melt formed along shear fractures, but it also shows the complexity of the impact deformation processes that formed the impactite dykes. The following sequence of events is proposed for Figure 6.6.

1. Shear fracturing causes microbrecciation and cataclasis along closely-spaced fractures that continue to slip during a single event, leading to friction melting.

2. Volume increase of melt relative to rock, and/or compressional stresses along melt generation planes force the melt to extrude away from the generation plane.

3. Almost at the same time as (2), the fractured rock experiences explosive fragmentation that pulls it apart in 3D. This may also have "sucked" the melt into the breccia.

4. Melt quenches after limited flow and immediately is fractured and starts to break up because movement continues in the breccia related to movement between larger, breccia-bounded, blocks.

5. Further movement between blocks disrupts and moves melt fragments, mixing them into the breccia-cataclasite.

One of the reasons why textures like the one seen in Figure 6.6 may not be more common in the M4 core is that the orange and pink melts, which are interpreted as having a granitoid composition, are much less common than the red-brown to black melts, which are more mafic (Chapter 2). Granitic melts are more viscous than mafic melts and so could be less likely to escape from the place where they form, but another factor could also be melt volume, as the granitoid gneisses contain very limited amounts of biotite (<5-10%), whereas mafic minerals (clinopyroxene ± amphibole, biotite) in metadolerite and dolerite make up about 50%. Spray (1992) noted that the strong cleavage in mafic minerals allows them to be more easily broken up into small fragments, which would increase the amount of friction melting. Biotite and amphibole also have much lower melting temperatures than feldspar and quartz, and the H_2O in biotite and amphibole could also increase melting. With the granitoid gneisses producing only small individual melt volumes, it is also likely that they cooled more quickly, which is another reason why they could be preserved close to their generation place.

Overall, the MMBr dykes in the M4 core show no clear evidence that they could be contaminated impact melt injections. Whilst a shock origin might be possible for some of the thinner melts, it also cannot be proved, and many of the MMBr dykes have volumes that are much larger than the accepted size of shock melt veins in impact structures and meteorites (Kenkmann et al., 2014). The MMBr matrices have compositions that show a local compositional control, including their own mm- to cm-scale melt particles that indicate that there was not enough time for homogenisation such as happened in the impact melt (Maier et al., 2006). The local origin of the MMBr is also shown by their lithic and mineral clasts that can be linked to the host rocks. They are also closely associated with a shear fracture network that appears to have locally stayed active even after melt quenching (Figure 6.6B, C). All of these features are consistent with friction melts and, thus, despite the strong hydrothermal alteration, the M4 MMBr can be called pseudotachylite. In conclusion, then, the MMBr fits the pseudotachlylite characteristics in that they are fracture associated, show compositional evidence of being locally derived and contain clasts derived from the immediate wallrock. The contemporaneous nature of cataclasite, MMBr and suevite development can be seen macroscopically and microscopically (Figure 2.32).

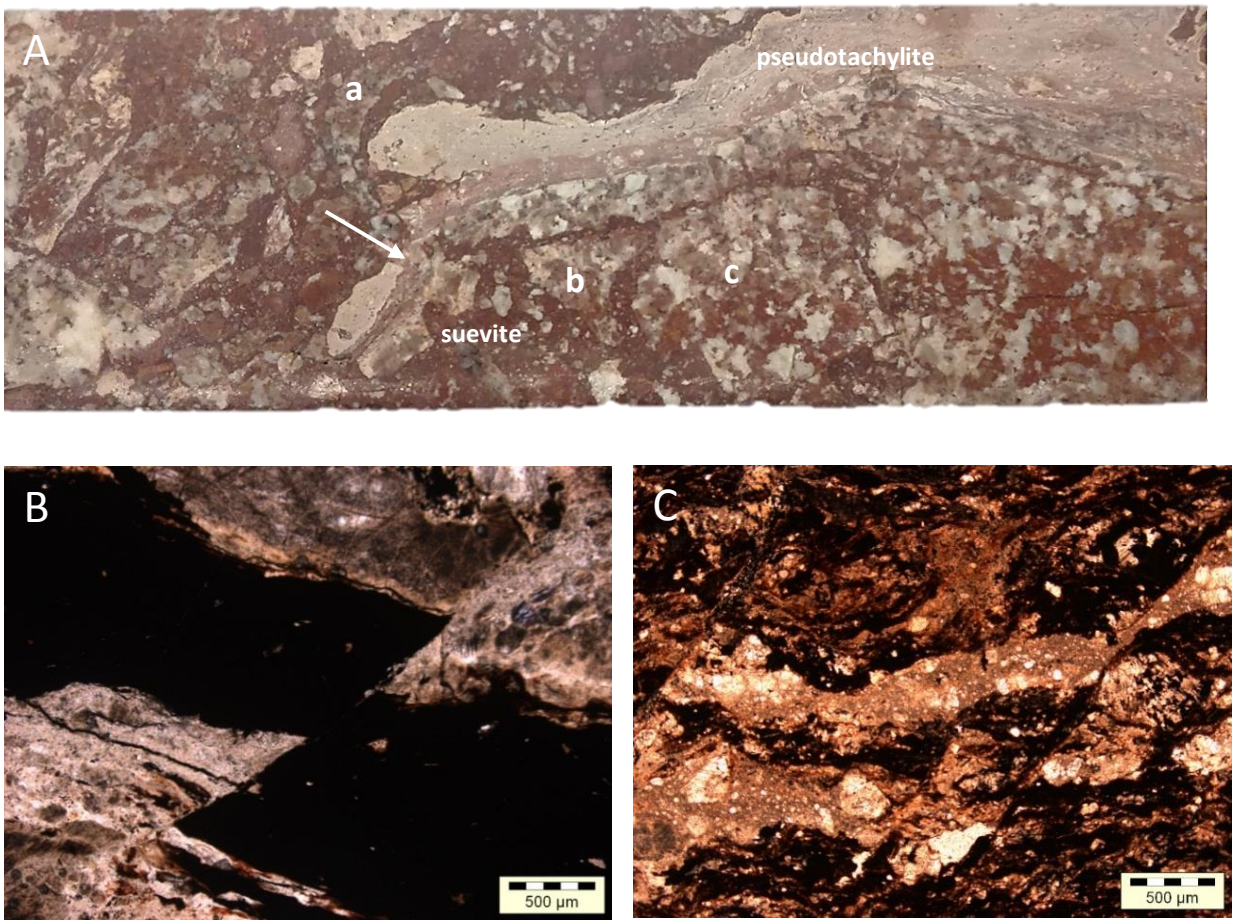

Figure 6.6: A) Sample from 148.00 m depth showing an elongate melt tongue still attached to wallrock with shear fractures. Note the infolding of the upper edge of the melt with the lithic breccia, the curvature of a "lithic clast" at the left edge of the melt tongue (a), and the melt clast that shows a bulbous shape with a sharply fractured upper edge. Note clasts b and c forming angular lithic clasts. **B)** Shear fracture displacing a haematised melt particle. **C)** MMBr injection dyke sample (M4 INJ-A) from 189.00 m depth showing shear fractures displacing cataclased zones. Note the cataclased zones are being sheared along the fractures. PPL. PPL = plane polarised light.

6.3.3 Origin of suevite in the M4 core

Like the MMBr, the suevite dykes in the M4 core show chemical compositional and lithic and mineral clast clues that they are locally derived. Not only can the lithic and mineral clast compositions be linked to the major target rock types in the core (with the exception of sample M4 S-6), they also show the same levels of shock and same cataclastic features seen in the M4 target rocks. This differs from the only other suevite dyke previously described in the MIS from the KHK-1 core, which

contains metasedimentary rocks, glass fragments and shocked quartz from granitoids in unshocked wallrocks (Reimold et al., 2002). Although Reimold et al. (2002) do not give the composition of the altered glass particle in this 10 cm suevite dyke, the difference in shock suggests that the KHK-1 dyke formed by injection of crater fill suevite into the unshocked cater wall or floor, which is the most common interpretation for suevite dykes in crater floor rocks (Stöffler, 1977). The fact that at 889.1 m depth this polymict breccia is surrounded by narrow cataclasite zones is suggestive of frictional movement that could have aided to the formed suevite during the impact event (Reimold et al., 2002).

An alternative origin for crater floor suevite dykes was proposed Stöffler et al. (2013) in the Ries crater. Stöffler et al. (2013) proposed that m-scale dykes in the crater floor and in a megablock formed during the modification stage of cratering by mechanical fragmentation and cataclasis of impact melt dykes. The model requires early downward intrusion of the melt dykes by up to tens of metres and then later crater modification stage fault-related movement, which must happen within tens of seconds to, at most, 1-2 minutes of the intrusion. The M4 suevite dykes clearly show evidence of brittle (Figure 6.6B, C) and even flow-type deformation after their formation (e.g. Figures 2.27 A, B), and many melt clasts show evidence of brittle fracturing (e.g. Figures 2.30A, 6.6B); however, the melt clasts in the suevite have variable compositions and are consistent with local sources. This evidence does not support brecciation and cataclasis of a homogeneous impact melt intruding downwards into the crater floor. Instead, macro- and microscopic evidence of cataclasite lenses and bands in the MMBr (pseudotachylite) (Figure 6.6C), and composite dykes showing intimate infolding of cataclasite and suevite into the MMBr (Figure 2.29), as well as rare, lobate, tongue-like intrusions of pseudotachylite into lithic breccia/suevite (Figure 6.6A) and small schlieric melt clasts (Figure 2.34D) suggest that the MMBr/pseudotachylite melt must have intruded into a loosely coherent or incoherent lithic breccia formed by the cataclasite-bearing shear fractures. It is possible that the shear fractures are smaller-scale versions of larger faults that may have been able to develop cataclasite zones up to decimetres to metres wide and that these larger slip zones were where most of the friction melt formed. These larger faults may have been focussed along older fault structures, such as the quartz-rich fracture zone between the trondhjemitic gneiss and metadolerite, or they could have exploited lithological boundaries between the doleritic and granitoid rocks (Figure 6.7A). Another possibility is that, whilst shear fractures formed in certain orientations, purely tensile fractures opened up explosively perpendicular to the extensional stress direction at the same time (Figure 6.7A). A third possibility is that initially deformation occurred along shear fractures with mm- to cm-scale slip displacements and that a change in the stress pattern reactivated some of these fractures as extensional features, which broke the M4 target rocks up into a block-like pattern. All of these scenarios are possible in the shocked crater basement of a large impact structure like the MIS, which would have experienced strong shearing and large differential stresses in different orientations during vertical and

radial movements during the excavation and modification stages (Ivanov, 2005; Senft and Stewart, 2009).

From the relationships described in Chapter 2 and summarised above, the proposed model for the formation of the M4 suevite dykes (Figure 6.7) is that they are a hybrid rock produced by injection of friction melt into monomict to locally polymict lithic breccias formed by shear fracturing with or without simultaneous or immediately later opening up of extensional fractures. The melt may have been forcefully injected into the lithic breccia/cataclasite or sucked in as space opened up along the extensional fractures. The weak coherence of the lithic breccia/cataclasite allowed flow-type interaction with the melt until the melt quenched and hardened. Continued deformation in the mixed breccia-pseudotachylite fracture fill, possibly accommodated by complex, 3-dimensional, block movements and rotations, fractured the quenched melt and mechanically entrained melt fragments as clasts in the still-flowing cataclasite (Figure 6.7E). It is impossible to tell from a 5 cm wide core how far the friction melts moved before quenching, or how much further movement occurred after they quenched to allow the amount of disruption seen, but the presence of exotic clasts in the sample M4 S-6 could support metres to possibly even tens of metres of flow, and the presence of pure suevite dykes suggests that the movement and flow after quenching of the friction melt intrusions was large enough to completely disrupt and separate the quenched melt fragments. This characteristic of the M4 impactites – that friction melt flowed into a loosely packed breccia that allowed interfolding and assimilation of a large proportion of clasts that were not actually located at the site of melting (Figure 6.7C-E) – makes the M4 core pseudotachylite (MMBr) different from most other pseudotachylite occurrences reported in the literature. The addition of the melt fragments to the clast-matrix lithic breccia means that the resultant hybrid can be described as suevite according to the definition of Stoffler and Grieve (2007).

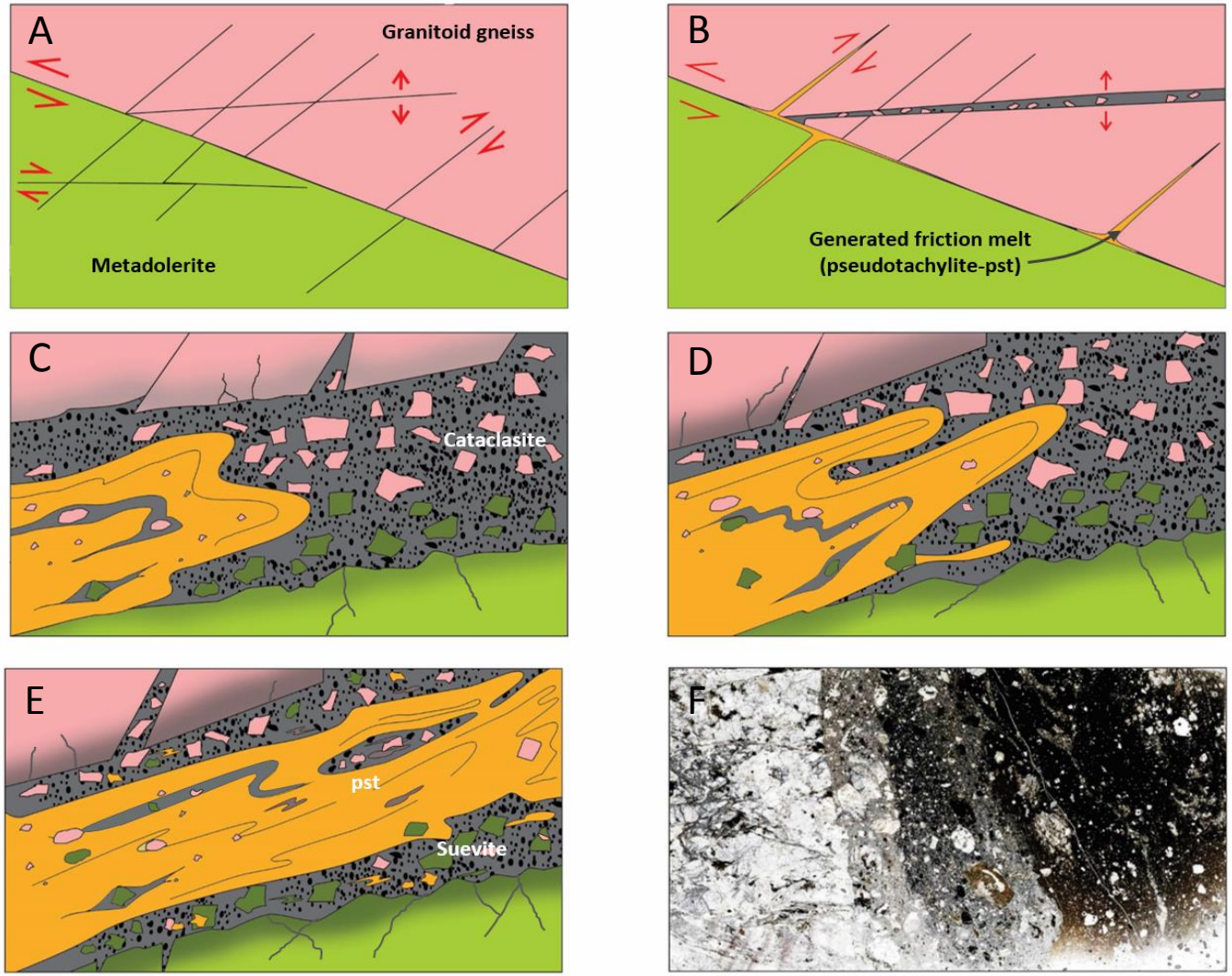

Figure 6.7: Cartoon showing the proposed model for genesis of the M4 impactites. In D-E, the generated friction melt (pseudotachylite) quenches and gets cut off and is incorporated into the cataclasite consisting of shocked target rock fragments. In this way, the hybrid suevite is thus formed. Enlargement of the box in F; showing a thin section scan of sample M4 IM-9 (299.76 m depth)

6.4 Hydrothermal alteration of the M4 drillcore lithologies

Approximately one third of Earth's impact structures show impact-induced hydrothermal alteration of their impactites and floor rocks (Naumov, 2005; Osinski, 2005). For a hydrothermal system to form, a heat source, a fluid source and rock permeability/porosity are needed. In impact structures, the main sources of heat could be the overlying impact melt sheet and other crater fill breccias, shock heat in the underlying central crater basement, and uplift of deeper crustal levels in the central peak that would have been pre-heated by the geothermal gradient. Fluid may come from the shock decomposition of hydrous minerals in the target rocks and crystallisation of the impact melts to anhydrous minerals but the main source of fluid would be likely to be marine or meteoric water that could flood into the crater or flow inwards with groundwater along major fractures in the crater basement as part of a circulation cell caused by the heat anomaly in and below the crater. Finally, impact causes extensive fracturing that may even extend beyond the crater rim, but which becomes more intense in the crater basement towards the crater centre, and particulate-matrix breccias like suevite could also have high initial porosity. It is therefore not surprising that impact structures are good sites for hydrothermal alteration (Kirsimäe and Osinski, 2013).

Macroscopic evidence of post-impact alteration in the M4 core includes calcite, quartz, zeolite and gypsum veining, oxidation of magnetite and sulphides to haematite and possibly other iron hydroxides, vugs in the impactites and poor core preservation marked by core loss. The overall colour zonation of the suevites may be caused by the different alteration effects with red (haematite), grey (magnetite) and green (chlorite-pyrite) zones with increasing depth. The hygroscopic nature of the MMBr and melt clasts in the suevite, which suggests that the melt glasses are altered to clay and zeolite minerals, was confirmed by BSEM, XRD and EMPA (Chapters 2 and 4), although the exact compositions of the mostly cryptocrystalline alteration assemblages could not be confirmed (Section 4.5.2). Glass is also not found any more in the PDF in quartz, which are all decorated with fluid inclusions (Chapter 5). Clay and zeolite alteration occurs throughout the core, but below ~300 m depth, chlorite alteration is stronger in the target rocks and locally within the fractures, and in vugs chlorite is found with epidote and andradite garnet (see Figure 2.36C. D). Pyrite and other sulphide minerals are found in the deeper parts of the core as well, whereas magnetite and haematite occur in the upper levels. This pattern is consistent with decreasing oxidation with the expected increase in the temperature of the hydrothermal fluids downwards. Zeolites and clays are, however, still found in the deepest parts of the core, which would also be consistent with cooling of the hydrothermal system with time so that lower-T clay and zeolite minerals overprint higher-T assemblages like chlorite-epidote-garnet. The last phase of the system is the carbonate veins that locally contain sulphides and iron oxides or hydroxides that cross-cut all mineral assemblages in the altered dykes. This sequence

matches the one proposed by Kirsimäe and Osinski (2013), who suggested that the cooling hydrothermal system would pass through 3 main stages: at T > 320 ℃, garnet-epidote and albite ± K-feldspar would form; between 320 and 120 ℃, chlorite would form together with smectite clays and zeolites; and at T < 100 ℃, carbonate would form with sulphide or iron oxyhydrates. Andradite garnet forms at temperatures of > 300 ℃ and their presence is indicative of high temperature hydrothermal fluids (Zürcher and Kring, 2004). The presence of pyrite in-between quartz laden with PDF is further proof of the post impact hydrothermal system that ensued in the Morokweng impact structure (Figure 2.35 F).

Evidence from the Puchezh-Katunki structure (Naumov, 2005) and numerical modelling (e.g. Abramov and Kring, 2007) suggest that initial post-impact geothermal gradients may be >100 ℃ vertically, and possibly even laterally, in large impact structures that have central uplifts. A more detailed study of the alteration patterns in the M4 core might provide information about vertical differences in post-impact temperatures, but this is beyond the scope of the present study. The target rocks in the M4 core experienced peak shock pressures of 10 - ≥25 GPa. According to Stoffler (1984), shock heating would have been ~200 ℃. If the M4 rocks were initially buried between 5 and 10 km below the surface, their pre-impact temperature would have been at least 100 ℃. This would suggest that their post-shock temperature would have been a minimum of 350 ± 50 ℃. Other sources of heat could have been frictional heating along shear fractures and faults, and from the pseudotachylite melts, as well as overlying hot crater fill deposits that could have included impact melt. It is important to remember that the M3 core is located only 6 km from the M4 core and that it intersected 800 m of impact melt that would probably have started having a temperature of >1800 ℃ (French, 1998). The top of the impact melt sheet was eroded away before the deposition of the Kalahari Group, so the melt sheet was originally even thicker. Such a thick melt sheet may have caused additional heating or hydrothermal effects in the M4 core. Numerical modelling of the Chicxulub crater (Abramov and Kring, 2007) suggests that rocks within 2 km of the surface in the peak ring of the crater would have experienced T > 300 ℃ but that this would only occur for ~20,000 yrs, although lower temperature alteration would continue for at least several hundred thousand years. Although Morokweng is smaller (see Section 6.6.1), the post-impact hydrothermal activity would also have continued for tens to hundreds of thousands of years.

Palaeogeographic reconstructions suggest that the Morokweng impact occurred into an area that was being eroded by a large, palaeo-Orange River drainage system (Stanley et al., 2015). This would suggest that hydrothermal fluids would have been well supplied by rivers and meteoric sources after the impact.

6.5 Shock distribution within the M4 drillcore and MIS

Analysis of the extent of deformation, distribution and characteristics of shock-related metamorphic features in both the country rocks (target rocks) and the impactites is important in providing information on the location of the rocks at the time of impact and through the following stages of cratering (French, 1998). Shock metamorphic features in the country rocks as well as the impactites include (Chapter 5) 2 to 3 (rarely 4) sets of decorated PDF in quartz as well as planar microstructures in plagioclase and microcline, reduced birefringence and toasting appearance most likely caused by dense aggregates of very fine-grained fluid inclusions in feldspars and quartz grains, and feather features in quartz. Fracturing in quartz, feldspar, titanite and zircon, as well as kink banding in biotite, are also found, but are not conclusive impact features. Shock pressure estimates based on PDF measurements in quartz show no evidence of variation in shock intensity with core depth, or between the target rocks and the impactites. Peak shock pressure estimates are 10-25 GPa. The absence of diaplectic quartz or feldspar shock glasses supports peak shock pressure remaining below 30-35 GPa (Stöffler, 1984).

Peak shock pressure declines exponentially away from the point of impact (Figure 1.4; Melosh, 1989) although the exact rate depends on the size and velocity of the projectile (Ahrens and O'Keefe, 1977). Assuming a maximum shock pressure of 100-200 GPa in the centre of the crater, this would mean that the M4 target rocks most probably lay within 5 km radially of the point of impact. According to Kenkmann et al. (2014), target rocks that experience shock pressures of >25 GPa seldom remain as part of the autochthonous crater basement during the excavation and modification stages, either becoming allochthonous or parautochthonous. This would mean that the M4 rocks also probably lay close to the transient cavity floor during the excavation and crater modification stages. Numerical modelling shows that rocks in this part of the crater floor would experience strong extensional forces after the passing of the shock wave (excavation stage) and complex and strong shear movements during the formation of the central uplift (modification stage).

Only limited shock P data is available for the MIS to compare with the M4 data. Corner et al. (1997) estimated a peak shock pressure of 10-16 GPa from a fragmental breccia boulder consisting of banded ironstone and a quartzite 40 km west of the centre of the MIS. If this sample is not a boulder or an allochthonous block, it would suggest that the Morokweng crater may originally have been considerably larger than suggested (see Section 6.6.1) or that the level of erosion of the MIS was limited, but a reinvestigation of the sampling site (M. Andreoli, pers. comm., 2016) did not reveal any other shocked samples. Hart et al. (1997) observed PDF in quartz in a granitoid pebble at the base of the Kalahari Group in the WF5 core, that are similar to the ones described in Chapter 5, consistent with shock pressure ranges of 10-25 GPa. Reimold et al. (1999) observed PDF, diaplectic glasses and mineral melting in the granitoid rocks towards the bottom of the WF5 core. They concluded that this

evidence meant shock pressures from 10 GPa to 45 GPa. Multiple sets of PDF (mostly one set, but up to three sets were recognised) were noted also in lithic and mineral clasts in the impact melt body (Reimold et al., 1999). The higher shock pressure estimates in the WF5 core fit with its closer position (~9 km; Figure 1.12B) to the centre of the MIS, although Reimold et al. (1999) proposed that the granitoid gneiss was part of a large block in the impact melt, so it could also be allochthonous.

In autochthonous crater basement, shock metamorphic effects should be spatially confined to the central uplift (Grieve and Therriault, 2004), although allochthonous ejected blocks, and blocks in the crater fill that may have moved radially outwards during the excavation and crater modification stages could also contain evidence of equally high, or even higher, shock pressures (Kenkmann et al., 2014). So, if the M4 core intersects autochthonous crater basement then its rocks should be part of the central uplift of the MIS. This has implications for the minimum size of the MIS, and is discussed further in the next section.

6.6 A peak ring setting for M4 core?

The M4 core is highly unusual relative to the other four central MIS cores because it contains no impact melt rock (whereas all the other cores contain at least several hundred metres of impact melt rock; Figure 1.13). Instead, it consists mostly of crystalline target rocks, with ~12% suevite and melt-matrix breccia that both look like they are locally derived (from bulk rock geochemistry, lithic and mineral clast composition, shock levels and geometry). Although Reimold et al. (1999) proposed that the 47 m intersection of granitoid gneisses in the WF5 core must be a lithic block inside the impact melt sheet, this is not certain, as the bottom of the core ended in the gneisses. No blocks of tens of metres in size have been found in any other parts of the central cores (Figure 1.13) so, unless a significant post-impact fault displacement lies between the M3 and M4 sites, the M4 core is either an autochthonous part of the original crater floor strongly uplifted relative to the M3 site during the crater modification stage, or a parautochthonous block lying at or close to the crater floor.

The age of the MIS (145 ± 2 Ma) does not exclude the possibility that the rifting to form the South Atlantic, which started at about 132 Ma (Renne et al., 1996) could have caused post-impact faults, but the MIS lies ~850 km from the west coast of southern Africa, so it is unlikely that any large faults would be found so far inland. Also, M4 lies slightly further west than M3 (Figure 1.1), so it would be more likely that it would be on the down-faulted side of any such fault, which would have produced the opposite effect. Finally, although several radial faults have been inferred from geophysical studies (Figure 1.1), Figure 1.12B shows no sign of a significant structural feature between the M3 and M4 sites.

If post-impact faulting can be ruled out, then the only remaining question is whether the M4 rocks are autochthonous or whether they are part of a large, parautochthonous to allochthonous, block of the crater basement lying in the crater fill. Many studies of impact structures show that the crater basement is divided up into blocks that can be up to hundreds of metres in size, depending on rock type and distance from the centre, with larger blocks further from the centre (Kenkmann et al., 2014), and large blocks can slide both outwards from the rising central uplift and inwards from the collapsing crater walls. Slumping from the crater wall can be ruled out because of the high shock pressure effects seen in the M4 rocks, which mean that the rocks must come from the central parts of the crater. Whether the M4 rocks represent a parautochthonous slumped block from the central uplift, rather than autochthonous crater basement is more difficult to test and would require deeper drilling to look for underlying impact-melt rock or crater fill breccias

The most logical explanation for why crater basement is intersected directly in M4 but >800 m of impact melt is found only 6 km away in the M3 core is that the M4 core intersects part of the uplifted peak ring of a complex crater and that this peak ring acted as a moat to trap the impact melt in the central parts of the crater. The transition diameter from central peak to peak-ring craters on Earth is between 13 and 23 km (Pike, 1985) so the MIS fits the main criterion.

6.6.1 MIS in comparison to other peak-ring impact structures

Although several workers have proposed diameters as large as 240-340 km for the MIS, Henkel and Reimold (2002) proposed a 70-80 km diameter, which would place it in the same range as the 100 km Popigai and 90 km Manicouagan impact structures (Earth Impact Database: *http://www.passc.net/EarthImpactDatabase/index.html*). Popigai has a clear peak ring with a 35-37 km diameter (Figure 6.8; Masaitis et al., 1999), but recent drilling results in the eroded Manicoaugan structure found a complicated horst-and-graben structure below the central impact melt sheet but no peak ring (Spray and Thompson, 2008). Peak rings are interpreted as the result of outward collapse of the central uplift that overrides the inward-collapsing crater walls. The annular trough caused by the inward slumping should extend at least a similar distance to the radius of the peak ring. In other words, if the MIS peak ring had a radius of 18 km, then the minimum diameter of the Morokweng crater should have been ~72 km. But it should also be remembered that there is no proof that M4 was drilled into the highest point of the peak ring, as it is eroded, and the ~ 180-200 km diameter Chicxulub crater has a peak ring that is more than 10 km wide (Grieve et al., 2008; Morgan et al., 2016), so final diameter estimates are not well defined this way if the crater has been eroded. The fact that Reimold et al. (2002) found a 10 cm wide suevite dyke in the KHK-1 core that was drilled 40 km from the centre of the MIS would support this as a minimum estimate. To obtain a closer estimate of

the true diameter of the MIS would require (a) a much more comprehensive drilling programme and (b) a good constraint on the depth of erosion prior to the deposition of the Kalahari Group.

The landscape in the region of the MIS lies at an elevation of ~1150 m, which places it within the interior plateau of southern Africa. This plateau is a region of anomalously high elevation (>1000 m) relative to the global average for continents of 500 m. Stanley et al. (2015) applied apatite (U-Th)/He thermochronometry and kimberlite xenolith studies along a 600 km traverse approximately 200 km south of the MIS to investigate when exhumation of the interior plateau happened. The (U-Th)/He thermochronometer is sensitive to erosional effects in the 0.5-3.5 km range. Stanley et al.'s (2015) reconstructions suggest that the region in which the MIS is located was covered by up to 1600 m of Karoo Supergroup sediments and basalts at 120 Ma during the final phases of Group 2 kimberlite eruptions that included the Makganyene pipe that is located ~200 km south of the MIS. Their results suggest that, between 110 Ma and 90 Ma, over 800 m of erosion must have taken place by the palaeo-Orange River drainage system. Using apatite fission-track results from a combination of Group 2 and the 90 Ma Group 1 kimberlites in the Kimberley area 300 km SSE of the MIS, Hanson et al. (2009) showed that, out of a total of 1350 m of erosion since 120 Ma, ~850 m of erosion occurred since 90 Ma. If these estimates apply to the MIS, they would suggest that a minimum estimate of the amount of erosion of the MIS would be about 1.5 km since 110-120 Ma; however, these studies cannot investigate the amount of additional erosion that could have happened between 145 Ma and 110-120 Ma. However, Tinker et al. (2008a, b) and Guillocheau et al. (2012) found increased sediment volumes between ~150 and 112 Ma in the offshore Orange River Basin along the west coast of South Africa. This may mean that a more reasonable minimum estimate of the pre-Kalahari Group exhumation of the MIS is 1.5-2 km. With such deep levels of erosion, the current apparent diameter of the MIS would be smaller than the original diameter. This would make it possible that the MIS may have been originally equivalent in size, or even larger, than the Popigai impact structure. A Morokweng crater diameter of this size might explain the KHK-1 core suevite, which is found 40 km southwest from the centre of the MIS.

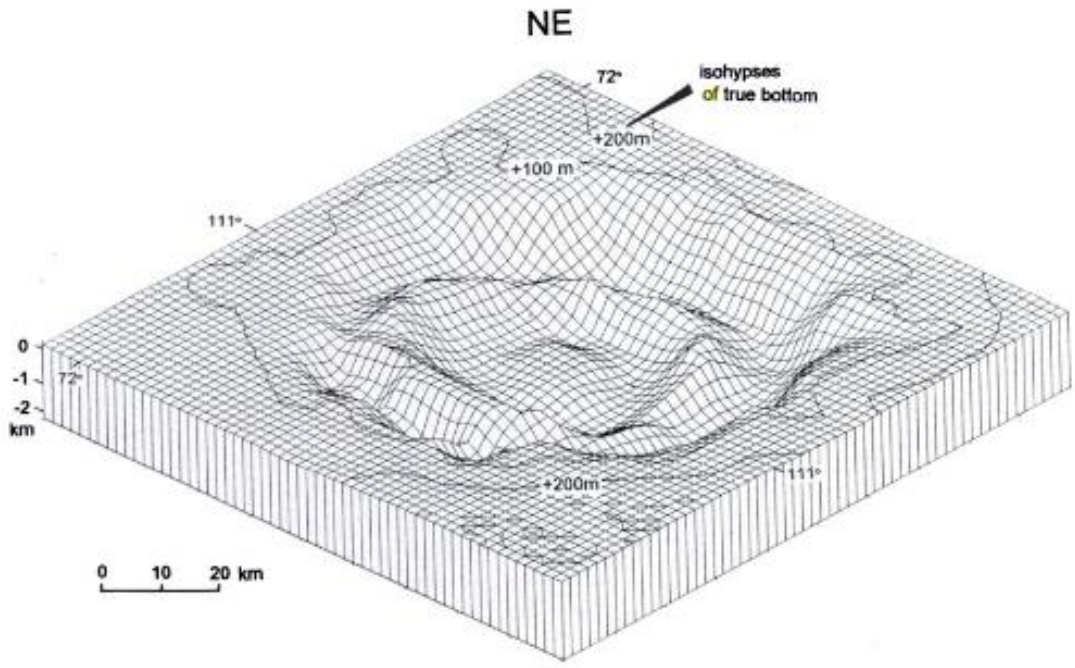

Figure 6.8: Reconstruction of the floor morphology of the Popigai Crater floor showing the peak ring, annular trough, and a small, flat central uplift (Masaitis et al., 1999).

Initial estimates of an ~400 m thick impact melt sheet in the Manicouagan impact structure were revised after further drilling into the structure revealed melt sheet thickness of up to ~1500m (Spray and Thompson, 2008). Spray and Thompson (2008) showed that the variations were caused by a horst and graben crater floor morphology. They related this faulting to collapse of the central peak, and a similar pattern could explain why >800 m of impact melt could occur only 6 km from the M4 core (Figure 6.9). Brittan et al. (1999) showed that the peak ring of the Chicxulub crater has a relief of several hundred metres, and detailed borehole and geophysical studies of the Popigai structure (Masaitis et al., 1999) also show that the actual crater floor is more complexly irregular than the crater floor model shown in Figure 6.8, and that there is hundreds of metres of relief of the crater floor over the km scale.

The M4 core intersects ~270 m of crystalline rocks with at least two significant concentrations of melt-matrix or suevite breccia that could represent the edges of large basement blocks. However, if this is a megablock, there is no way to tell what the actual dimensions or shape would be in crystalline rocks that have no orientation markers. Only deeper drilling will be able to prove if the rocks are part of a block detached from the crater floor. Until this can happen, it is proposed that the most reasonable interpretation is that the M4 lithologies are a part of the peak ring of the MIS and that, although peak rings are likely to display complex internal faulting, fragmentation and internal block rotations as the outward-collapsing central peak meets the inward-collapsing crater wall material, the

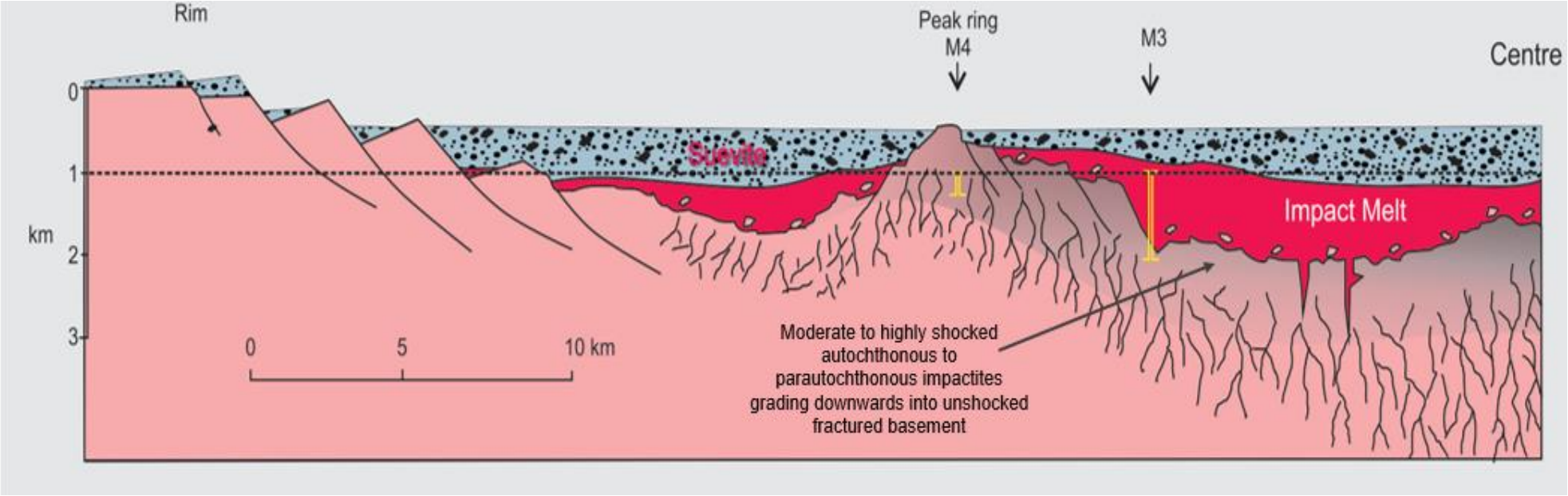

Figure 6.9: Proposed model for the location of the M4 drillcore in the Morokweng impact structure, and its relation to the M3 drillcore. Intense fracturing, faulting and brecciation has not been shown in the shocked (par)autochthonous impactites (grey). The erosion level of 1 km is a conservative estimate. The vertical scale is exaggerated.

post-impact erosional history of the MIS suggests that the M4 rocks were located more than 1.5 km below the surface right after the impact and that they should thus be autochthonous.

In summary, the impact breccias in the M4 core are interpreted as a dynamically-deforming network of autochthonous to parautochthonous cataclasite dykes intruded by melt that became contaminated by mechanical mixing with the poorly consolidated cataclasite to form the suevite, which underwent further injection into the vein/dyke network as large blocks in the peak ring continued to move.

6.7 Conclusions and Recommendations

This work based on the 368 m deep M4 drillcore provides additional important information about the impact processes that affected the target rocks of the Morokweng impact structure. Though in this study ample evidence exists that the structure has been modified by erosion and that the impactites are extensively hydrothermally altered, significant data was obtained to petrographically and geochemically characterise the M4 drillcore sequence and the various impact-formed breccias that occur in them. From this study the main conclusions that can be made about the Morokweng impact structure are as follows:

1) Kalahari Group beds lie directly on shocked target rocks; this is proof of erosion of crater fill.

2) Based on the combined macroscopic, petrographic and geochemical evidence the target rock geology is dominated by Archaean granitoids. The granitic gneisses, granodioritic gneisses, and dioritic gneisses are part of the same genetic sequence. The trondhjemitic gneisses may represent metasomatised granites or diorites. This metasomatism was likely linked to pre-impact faulting.

3) Two generations of doleritic rocks intruded the gneisses before the impact. The older one is metamorphosed to mid- to upper greenschist facies and the younger one is un-metamorphosed. Their contacts with the granitoid gneisses appear to be faulted.

4) Although it was not possible to conclusively determine whether the granitoids that were intersected at the base of the M4 core are autochthonous crater floor or a series of megablocks, the evidence of general similarities in the rocks in the upper and lower parts of the core, and estimates of the pre-Kalahari Group erosion level would support the sequence being autochthonous.

5) The target rocks show a variety of mineral-scale shock effects that show that they experienced moderately high to high peak shock pressures of 10 - 25 GPa. No significant change in peak shock pressure is noted with depth.

6) Petrographic, macroscopic and geochemical results support the hypothesis that the M4 impactites were derived locally from similar rock types to the ones seen in the core, and that they are not contaminated impact melt.

7) The target rocks are intensely fractured and cataclased on a cm- to dm-scale as a result of the impact event. Shear and extensional fractures acted as emplacement sites for the melt-matrix breccia and suevite dykes, which make up ~12% of the core.

8) The MMBr are interpreted as friction melts (pseudotachylite) formed along shear fractures or faults during the excavation and/or crater modification stages.

9) The M4 suevite is interpreted as a hybrid mixture of monomict/polymict lithic breccia and cataclasite, and friction melt in which the quenched pseudotachylite was fractured and mechanically mixed into the clastic breccia by continued movement along or across the cataclasite fractures.

10) The fact that the shock levels in clasts in the suevite and MMBr are not different from the shock levels in the target rocks supports only limited movement (metres to tens of metres) of the impactite breccias from their source.

11) The core is strongly hydrothermally altered and any glass or melt crystallisation products in the impactites are replaced by cryptocrystalline clays and zeolites. Iron oxidation is particularly strong in the upper parts of the core. Slightly higher temperature alteration assemblages involving chlorite occur below ~300 m depth, but samples from here also contain clays and zeolites. More work is needed to establish if the core shows different mineral zones related to the hydrothermal system.

12) Based on the elevated location of crater basement in the M4 core relative to the other central cores in the MIS that all contain impact melt rock, it is proposed that the M4 core intersects a rock sequence that represents the partially eroded peak ring of the MIS and that the Morokweng impact crater must have had an original diameter of at least 70 km, but could have been substantially larger.

In summary, data from this research is of value as it contributes to the understanding of the pre-impact history of the MIS as well as the syn-impact deformational, shock and melting processes and the post-impact hydrothermal alteration processes. Limitations arising in the current study create a window of opportunity for further work to be done. There is a case to be made in support of deeper drilling to confirm that the rocks are autochthonous, and to search for signs of shock pressure decline with increasing depth and increasing post-impact hydrothermal temperatures with increasing depth.

References

Abramov, O., and Kring, D. A. (2007). Numerical modeling of impact-induced hydrothermal activity at the Chicxulub crater. Meteoritics and Planetary Science, 42(1), pp.93-112.

Aghazadeh, M., Prelević, D., Badrzadeh, Z., Braschi, E., van den Bogaard, P. and Conticelli, S. (2015). Geochemistry, Sr–Nd–Pb isotopes and geochronology of amphibole-and mica-bearing lamprophyres in northwestern Iran: Implications for mantle wedge heterogeneity in a palaeo-subduction zone. Lithos, 216, pp.352-369.

Ahrens, T.J. and Okeefe, J.D. (1977). Equations of state and impact-induced shock-wave attenuation on the Moon. In Impact and explosion cratering: Planetary and terrestrial implications, pp. 639-656.

Andreoli, M.A.G., Ashwal, L.D., Hart, R.J., Smith, C.B., Webb, S.J., Tredoux, M., Gabrielli, F., Cox, R. and Hambleton, B.B. (1995). The impact origin of the Morokweng ring structure, southern Kalahari, South Africa. Geological Society of South Africa, Centennial Geocongress, Johannesburg, Extended Abstract. Vol. I, pp.541-544.

Andreoli, M.A.G., Ashwal, L.D., Hart, R.J. and Tredoux, M. (1996). The charnockitic rocks of the sand-covered Morokweng impact structure, Southern Kalahari, South Africa: Evidence for a possible impact melt origin (abstract). Lunar and Planetary Science XXVII, pp.29-30.

Andreoli, M.A.G., Ashwal, L.D., Hart, R.J. and Huizenga, J.M. (1999). A Ni and PGE-enriched quartz norite impact melt complex in the Late Jurassic Morokweng impact structure, South Africa, in: Dressler, B.O., and Sharpton, V.L. (1999). Large Meteorite Impacts and Planetary Evolution II, Geological Society of America, Special Papers, 339, pp.91-108.

Andreoli, M.A.G., Hart, R.J., Cooper, G.R.J., Stengel, I., Webb, S., Haddon, I., Skala, R., and Viola, G. (2007). The 144 Ma Morokweng impact crater, South Africa: geophysical and borehole evidence for a ~240 km structure. 10th SAGA Biennial Conference, ISBN: 978-0-620-38241, 4 pp.

Andreoli, M.A.G., Hart, R.J., Cooper and Webb, S. (2008a). The Morokweng impact crater, South Africa: A large complex, multiring structure with a ~ 130 km radius external ring and asymmetric radial sectors. Large Meteorite Impacts and Planetary Evolution IV, Abstract 3048.

Andreoli, M.A.G., Maier, W.D., McDonald, I., Barnes, S.J., Roelofse, F.,Cloete, M.C., Okujeni, C. and Hart, R.J. (2008b). Siderophile minerals in the melt sheet of the Morokweng impact crater, South Africa: similarities and differences with the Sudbury deposits. Large Meteorite Impacts and Planetary Evolution IV, Abstract 3049.

Anhaeusser, C.R. and Walraven, F. (1999). Episodic granitoid emplacement in the western Kaapvaal Craton: evidence from the Archaean Kraaipan granite-greenstone terrane, South Africa. Journal of African Earth Sciences, 28(2), pp.289-309.

Anthony, J.W., Bideaux, R.A., Bladh, K.W. and Nichols, M.C. (2011). Eds., Handbook of Mineralogy, Mineralogical Society of America, Chantilly, VA 20151-1110, USA. (http://www.handbookofmineralogy.org/.)

Armstrong, R.A., Compston, W., Retief, E.A., Williams, I.S., Welke, H.J. (1991). Zircon ion microprobe studies bearing on the age and evolution of the Witwatersrand triad. Precambrian Research, 53, pp.243-266.

Baker, D.M., Head, J.W., Neumann, G.A., Smith, D.E. and Zuber, M.T. (2012). The transition from complex craters to multi-ring basins on the Moon: Quantitative geometric properties from Lunar Reconnaissance Orbiter Lunar Orbiter Laser Altimeter (LOLA) data. Journal of Geophysical Research: Planets, 117(issue E12). E00H16, doi: 10.1029/2011JE004021.

Baratoux, D. and Reimold, W.U. (2016). The current state of knowledge about shatter cones: Introduction to the special issue. Meteoritics and Planetary Science, 51(8), pp.1389-1434.

Barker, F. (1979). Trondhjemite: definition, environment and hypotheses of origin. Trondhjemites, dacites and related rocks. Elsevier, Amsterdam, pp.1-12.

Bergaya, F., Lagaly, G. (2013). Handbook of Clay Science, 2nd ed. Elsevier, 1752pp.

Bischoff, A., and Stöffler, D. (1984). Chemical and structural changes induced by thermal annealing of shocked feldspar inclusions in impact melt rocks from Lappajärvi crater, Finland: Journal of Geophysical Research, v. 89, pp.645–656

Bland, P.A. (2005). The impact rate on Earth. Philosophical Transactions: Mathematical, Physical and Engineering Sciences, Vol. 363, No. 1837, Astronomy and Earth Science, pp.2793-2810.

Bootsman, C.S., Reimold, W.U., and Brandt, D. (1999). Evolution of the Molopo drainange and its possible disruption by the Morokweng impact event at the Jurassic-Cretaceous boundary. Journal of African Earth Science, 29, pp.669-678.

Bowen, T.B., Marsh, J.S., Bowen, M.P. and Eales, H.V. (1986). Volcanic rocks of the Witwatersrand triad, South Africa. I: Description, classification and geochemical stratigraphy. Precambrian Research, 31(4), pp.297-324.

Brandt D. (1999). The Tswaing Crater: One of the World's Best Preserved and Museums Plans for the Site, Meteoritics, 34, A17.

Brittan, J., Morgan, J., Warner, M. and Marin, L. (1999). Near-surface seismic expression of the Chicxulub impact crater. Special Papers-Geological Society of America, pp.269-280.

Chen, M. and El Goresy, A. (2000). The nature of maskelynite in shocked meteorites: not diaplectic glass but a glass quenched from shock-induced dense melt at high pressures. Earth and Planetary Science Letters, 179(3), pp.489-502.

Clemens, J.D., Yearron, L.M. and Stevens G. (2006). Barberton (South Africa) TTG magmas: geochemical and experimental constraints on source-rock petrology, pressure of formation and tectonic setting. Precambrian Research, 151(1), pp.53-78.

Collins, G. S., Melosh, H. J., and Osinski, G. R. (2012). The impact-cratering process. Elements, 8(1), pp.25-30.

Condie, K.C. (2005). TTGs and adakites: are they both slab melts?. Lithos, 80(1), pp.33-44.

Corner, B., Durrheim, R.J. and Nicolaysen, L.O. (1986). The structural framework of the Witwatersrand basin as revealed by gravity and magnetic data. In Abstracts 21st Congress Geological Society South Africa, Johannesburg, pp. 27-30.

Corner, B., Reimold, W.U., Brandt, D., and Koeberl, C. (1997). Morokweng impact structure, Northwest Province, South Africa: Geophysical imaging and some preliminary shock petrographic studies. Earth and Planetary Science Letters, 146, pp.351-364.

De Kock, M. O, Ernst, R., Soderlund, U., Jourdan, F., Hofmann, A., Le Gall, B., Bertrand, H., Chisonga, B. C., Beukes, N., Rajesh, H. M., Moseki, L. M. and Fuchs, R. (2014). Dykes of the 1.11 Ga Umkondo LIP, Southern Africa: clues to a complex plumbing system. Precambrian Research, 249, pp.129-143.

Deer, W.A., Howie, R.A. and Zussman, J. (1992). An introduction to the rock-forming minerals (Vol. 2). Hong Kong: Longman Scientific and Technical, 558 pp.

Deer, W.A., Howie, R.A. and Zussman, J. (1997). Rock-forming minerals: single-chain silicates, Volume 2A (eds). Geological Society of London, 932 pp.

Dence, M. R. (1972). The nature and significance of terrestrial impact structures. 24th International Geological Congress, Montreal, Canada. Proceedings Section 15, pp77-89.

Dressler B. O. (1984). The effects of the Sudbury event and the intrusion of the Sudbury igneous complex on the footwall rocks of the Sudbury structure. In The geology and ore deposits of the Sudbury structure, edited by Pye E. G., Naldrett A. J., and Giblin P. E. Special Volume 1. Toronto: Ontario Geological Survey. pp. 97–136.

Dressler, B.O and Reimold, W.U. (2001). Terrestrial impact melt rocks and glasses. Earth Science Reviews, 56, pp.205-284.

Dressler, B.O. and Reimold, W.U. (2004). Order or chaos? Origin and mode of emplacement of breccias in floors of large impact structures. Earth-Science Reviews, 67(1), pp.1-54.

Dressler, B.O., Sharpton, V.L., Schnieders, B. and Scott, J. (1996). Formation of impact breccias at the Slate Islands structure, Northern Lake Superior, Ontario, Canada. In Lunar and Planetary Science Conference (Vol. 27), pp.325–326.

Dressler, B. O., Sharpton V. L., and Schuraytz B. C. (1998). Shock metamorphism and shock barometry at a complex impact structure: Sltate Islands, Canada. Contributions to Mineralogy and Petrology 130, pp.275–287.

Earth Impact database: http://www.passc.net/EarthImpactDatabase/index.html (accessed on 18 January 2017).

Engelhardt, W.V. and Bertsch, W. (1969). Shock induced planar deformation structures in quartz from the Ries crater, Germany. Contributions to Mineralogy and Petrology, 20(3), pp.203-234.

Engelhardt, W. V., Horz, F., Stöffler, D., and Bertsch, W. (1968). Observations on quartz deformation in the breccias of West Clearwater Lake, Canada and the Ries Basin, Germany, in French, B. M., and Short, N. M., Eds., Shock metamorphism of natural materials: Baltimore, Maryland, Mono Book Corporation, pp. 475-482.

Feldman V. I. (1994). The conditions of shock metamorphism. In Large meteorite impacts and planetary evolution, edited by Dressler B. O., Grieve R. A. F., and Sharpton V. L. Boulder, Colorado: Geological Society of America Special Paper, 293, pp.121–132.

Fel'dman, V. I., Sazonova L. V., and Kotel'nikov S. I. (1996). Distribution of the shock pressure in the rocks of the Vorotilov hole, Puchezh-Katunki astrobleme. Doklady Akademii Nauk SSSR 349(5), pp.658–660.

Ferrière, L., and Osinski, G. R. (2013), Shock metamorphism, in Impact Cratering: Processes and Products, edited by G. R. Osinski, and E. Pierazzo, Wiley-Blackwell, Chichester, West Sussex, U. K., pp. 106–124.

Ferrière, L., Koeberl, C., Ivanov, B.A. and Reimold, W.U. (2008). Shock metamorphism of Bosumtwi impact crater rocks, shock attenuation, and uplift formation. Science, 322(5908), pp.1678-1681.

Ferrière L., Morrow J. R., Amgaa T., and Koeberl C. (2009). Systematic study of universal-stage measurements of planar deformation features in shocked quartz: Implications for statistical significance and representation of results. Meteoritics and Planetary Science, 44, pp.925–940.

Ferrière, L., Koeberl, C., Libowitzky, E., Reimold, W. U., Greshake, A., and Brandstätter, F. (2010). Ballen quartz and cristobalite in impactites: New investigations. Geological Society of America Special Papers, 465, pp.609-618.

Fiske, P.S., Nellis, W.J., Lipp, M., Lorenzana, H., Kikuchi, M. and Syono, Y. (1995). Pseudotachylites generated in shock experiments: Implications for impact cratering products and processes. Science, 270, pp.281-283.

French, B. M. (1998). Traces of Catastrophe: A Handbook of Shock-Metamorphic Effects in Terrestrial Meteorite Impact Structures. Lunar and Planetary Institute Contribution No. 954, Lunar and Planetary Institute, Houston, Texas, 120 pp.

French B.M. and Short N.M. (1968). Shock Metamorphism of Natural Materials. Mono Book Corporation, eds. Baltimore, 644 pp.

French, B. M., and Koeberl, C. (2010). The convincing identification of terrestrial meteorite impact structures: What works, what doesn't, and why. Earth-Science Reviews, 98(1), 123-170.

French B. M., Cordua W. S., and Plescia J. B. (2004). The Rock Elm meteorite impact structure, Wisconsin: Geology and shock-metamorphic effects in quartz. Geological Society of America Bulletin 116, pp.200–218.

Fritz, J. and Greshake, A. (2009) High-pressure phases in an ultramafic rock from Mars. Earth and Planetary Science Letters, 288, pp.619–623.

Gibson, R.L. and Reimold, W.U. (2001). The Vredefort impact structure, South Africa: the scientific evidence and a two-day excursion guide. Memoir-geological survey (Pretoria).

Gibson, R. L., and Reimold, W. U. (2005). Shock pressure distribution in the Vredefort impact structure, South Africa. Geological Society of America Special Papers, 384, pp.329-349.

Gibson, R.L. and Reimold, W.U. (2008). Geology of the Vredefort Impact Structure: A Guide to Sites of Interest. Council for Geoscience Memoir 97, 181 pp.

Gillet, P., El Goresy, A., Beck, P. and Chen, M. (2007). High- pressure mineral assemblages in shocked meteorites and shocked terrestrial rocks: mechanisms of phase transformations and constraints to pressure and temperature histories , in Advances in High-Pressure Mineralogy (ed. E. Ohtani), Geological Society of America Special Paper 421, Geological Society of America, Boulder, CO, pp. 57–82.

Grieve, R.A.F. (1978). The melt rocks at Brent crater, Ontario, Canada. In Lunar and Planetary Science Conference Proceedings, vol. 9, pp. 2579-2608.

Grieve, R.A.F. (1987). Terrestrial impact structures. Annual Review of Earth and Planetary Sciences, 15(1), pp.245-270.

Grieve R. A. F. and Robertson P. B. (1976). Variations in shock deformation at the Slate Islands impact structure, Lake Superior, Canada. Contributions to Mineralogy and Petrology 58, pp.37–49.

Grieve, R.A.F. and Dence, M.R. (1979). The terrestrial cratering record: II. The crater production rate. Icarus, 38(2), pp.230-242.

Grieve, R. A. F., and Pilkington, M. (1996). The signature of terrestrial impacts. AGSO Journal of Australian Geology and Geophysics, 16(4), pp.399-420.

Grieve R.A.F. and Therriault A. (2000). Vredefort, Sudbury, Chicxulub: Three of a kind? Annual Reviews of Earth and Planetary Science, 28, pp.305-338.

Grieve, A.M.T.R.A. and Pilkington, M. (2002). The recognition of terrestrial impact structures. Bulletin of the Czech Geological Survey, 77(4), pp.253-263.

Grieve, R. A.F., and Therriault, A. M. (2004). Observations at terrestrial impact structures: Their utility in constraining crater formation. Meteoritics and Planetary Science, 39(2), pp.199-216.

Grieve, R.A.F. and Therriault, A.M. (2013). Impactites: Their characteristics and spatial distribution. Impact cratering: Processes and products, pp.90-105.

Grieve, R. A. F., Robertson, P. B., and Dence, M. R. (1981). Constraints on the formation of ring impact structures, based on terrestrial data. In Multi-ring basins: Formation and evolution (Vol. 1), pp. 37-57.

Grieve, R. A. F., Coderre, J. M., Robertson, P. B., and Alexopoulos, J. (1990). Microscopic planar deformation features in quartz of the Vredefort structure: Anomalous but still suggestive of an impact origin. Tectonophysics, 171(1), 185-200.

Grieve, R.A., Langenhorst, F. and Stöffler, D. (1996). Shock metamorphism of quartz in nature and experiment: II. Significance in geoscience. Meteoritics and Planetary Science, 31(1), pp.6-35.

Grieve, R.A.F., Cintala, M.J., and Tagle, R. (2007). Planetary Impacts. Encyclopedia of the Solar System (Second edition), pp. 813-828.

Grieve, R.A., Reimold, W.U., Morgan, J., Riller, U. and Pilkington, M. (2008). Observations and interpretations at Vredefort, Sudbury, and Chicxulub: Towards an empirical model of terrestrial impact basin formation. Meteoritics & Planetary Science, 43(5), pp.855-882.

Grobler, D.F. and Walraven, F. (1993). Geochronology of Gaborone Granite Complex extensions in the area north of Mafikeng, South Africa. Chemical Geology, 105(4), pp.319-337.

Gucsik, A. (2009). Shock metamorphism of terrestrial impact structures and its application in the earth and planetary sciences. In Cathodoluminescence and its Application in the Planetary Sciences. Springer Berlin Heidelberg, pp.23-43.

Guillocheau, F., Rouby, D., Robin, C., Helm, C., Rolland, N., Le Carlier de Veslud, C. and Braun, J. (2012). Quantification and causes of the terrigeneous sediment budget at the scale of a continental margin: a new method applied to the Namibia–South Africa margin. Basin Research, 24(1), pp.3-30.

Gutzmer, J., Banks, D.A., Lüders, V., Hoefs, J., Beukes, N.J. and Von Bezing, K.L. (2003). Ancient sub-seafloor alteration of basaltic andesites of the Ongeluk Formation, South Africa: implications for the chemistry of Paleoproterozoic seawater. Chemical Geology, 201(1), pp.37-53.

Hanson, E.K., Moore, J.M., Bordy, E.M., Marsh, J.S., Howarth, G. and Robey, J.V.A. (2009). Cretaceous erosion in central South Africa: Evidence from upper-crustal xenoliths in kimberlite diatremes. South African Journal of Geology, 112(2), pp.125-140.

Harris R. S., Jaret S. J., Rodesney S. N., King D. T., and Schultz P. H. (2010). Alternate twin deformation of plagioclase at low shock pressures: Implications for recognizing and interpreting impacts in basalt (abstract). AGU Meeting of the Americas, P41A-03.

Hart, R.J., Andreoli, M.A.G., Tredoux, M., Moser, D., Ashwal, L.D., Eide, E., Webb, S.J., and Brandt, D. (1997). Late Jurassic age for the Morokweng impact structure, southern Africa. Earth and Planetary Science Letters, 147, pp.25-35.

Hart, R. J., Cloete, M., McDonald, I., Carlson, R. W. and Andreoli, M. A. G. (2002). Siderophile-rich inclusions from the Morokweng impact melt sheet, South Africa: possible fragments of a chondritic meteorite. Earth and Planetary Science Letters, 198, pp.49 - 62.

Henkel H. and Pesonen L.J. (1992) Impact craters and craterform structures in Fennoscandia. Tectonophysics, 216, pp.31-40.

Henkel, H. and Reimold, W. U. (2002). Magnetic model of the central uplift of the Vredefort impact structure, South Africa. Journal of Applied Geophysics, 51, pp.43– 62.

Henkel, H., Reimold, W. U., and Koeberl, C. (2002). Magnetic and gravity model of the Morokweng impact structure. Journal of Applied Geophysics, 49 (3), pp. 129-147.

Hildebrand, A.R., Penfield, G.T., Kring, D.A., Pilkington, M., Camargo, A., Jacobsen, S.B. and Boynton, W.V. (1991). Chicxulub crater: a possible Cretaceous/Tertiary boundary impact crater on the Yucatan Peninsula, Mexico. Geology, 19(9), pp.867-871.

Huber, M.S., Ferriere, L., Losiak, A. and Koeberl, C. (2011). ANIE: A mathematical algorithm for automated indexing of planar deformation features in quartz grains. Meteoritics and Planetary Science, 46(9), pp.1418-1424.

Huffman, A.R., Brown, J.M., Carter, N.L. and Reimold, W.U. (1993). The microstructural response of quartz and feldspar under shock loading at variable temperatures. Journal of Geophysical Research: Solid Earth, 98(B12), pp.22171-22197.

Ivanov, B.A. (2005). Numerical modeling of the largest terrestrial meteorite craters. Solar System Research, 39(5), pp.381-409.

Ivanov, B.A. and Stöffler, D. (2005). The Steinheim impact crater, Germany: Modeling of a complex crater with central uplift. In 36th Annual Lunar and Planetary Science Conference, XXXVI, 1443.

Ivanov BA, Basilevsky AT, Sazonoya LV. (1982). Formation of the central uplift in meteoritic craters. Meteoritika 40, pp.60–81. In Russian. (Engl. tech. transl. 1986. NASA TM-88427).

Jackson, M.C. (1994). Geochemistry and metamorphic petrology of Dominion Group metavolcanics in the Vredefort area, South Africa. South African Journal of Geology, 97(1), pp.62-77.

Keil, K., Stoeffler, D., Love, S.G. and Scott, E.R.D. (1997). Constraints on the role of impact heating and melting in asteroids. Meteoritics and Planetary Science, 32(3), pp.349-363.

Kenkmann, T. and Ivanov, B.A. (2006). Target delamination by spallation and ejecta dragging: An example from the Ries crater's periphery. Earth and Planetary Science Letters, 252(1), pp.15-29.

Kenkmann, T., Hornemann, U. and Stöffler, D. (2000). Experimental generation of shock-induced pseudotachylites along lithological interfaces. Meteoritics and Planetary Science, 35(6), pp.1275-1290.

Kenkmann, T., Poelchau, M.H. and Wulf, G. (2014). Structural geology of impact craters. Journal of Structural Geology, 62, pp.156-182.

Kieffer, S. W., and Simonds, C. H. (1980). The role of volatiles and lithology in the impact cratering process. Reviews of Geophysics and Space Physics, 18(1), pp.143-181.

Kieffer S.W., Phakey P.P. and Christie J.M. (1976). Shock processes in porous quartzite: Transmission electron microscope observations and theory. Contributions to Mineralogy and Petrology, 59, pp. 41–93.

Kirsimäe, K., and Osinski, G. R. (2013), Impact-induced hydrothermal activity, in Impact Cratering: Processes and Products, edited by G. R. Osinski, and E. Pierazzo, Wiley-Blackwell, Chichester, West Sussex, U. K., pp.76-89.

Koeberl, C. (1992). Water content of glasses from the K/T boundary, Haiti: An indication of impact origin. Geochimica et cosmochimica acta, 56(12), pp.4329-4332.

Koeberl, C. (1994). African meteorite impact craters: characteristics and geological importance. Journal of African Sciences, 18, pp.263-295.

Koeberl, C., and Martinez-Ruiz, F. (2003). The stratigraphic record of impact events: A short overview. In Impact markers in the stratigraphic record. Springer Berlin Heidelberg, pp.1-40.

Koeberl, C. and Reimold, W.U. (2003). Geochemistry and petrography of impact breccias and target rocks from the 145 Ma Morokweng impact structure, South Africa. Geochemica et Cosmochimica Acta, 67, pp.1837-1862.

Koeberl, C., Armstrong, R.A., and Reimold, W.U. (1997). Morokweng, South Africa: A large impact structure of Jurassic-Cretaceous boundary age. Geology, 25, pp.731-734.

Koeberl, C., Claeys, P., Hecht, L. and McDonald, I. (2012). Geochemistry of impactites. Elements, 8(1), pp.37-42.

Lafond, E.C. and Dietz, R.S. (1964). Lonar Crater, India, a meteorite crater?. Meteoritics and Planetary Science, 2(2), pp.111-116.

Lamb, W.M., Guillmette, R., Popp, R. K., Fritz, S. J., and Chmiel, G. J. (2012). Determination of $Fe^{3+/}Fe$ using the electron microprobe: A calibration for amphiboles. American Mineralogist, 97 (5-6), pp.951-961.

Lambert, P. (1981). Breccia dikes-Geological constraints on the formation of complex craters. In Multi-ring basins: Formation and evolution, pp.59-78.

Lambert, P. and Mackinnon, I.D.R. (1984). Micas in experimentally shocked gneiss. In Lunar and Planetary Science Conference Proceedings, vol. 14, pp.685-699.

Lana, C., Gibson, R. L., Kisters, A. F., and Reimold, W. U. (2003). Archean crustal structure of the Kaapvaal craton, South Africa–evidence from the Vredefort dome. Earth and Planetary Science Letters, 206(1), pp.133-144.

Lana, C., Reimold, W. U., Gibson, R. L., Koeberl, C., and Siegesmund, S. (2004). Nature of the Archean midcrust in the core of the Vredefort Dome, central Kaapvaal Craton, South Africa. Geochimica et Cosmochimica Acta, 68(3), pp.623-642.

Langenhorst F. (1994). Shock experiments on α- and β- quartz: II. X-ray investigations. Earth and Planetary Science Letters, 128, pp.638–698.

Langenhorst F. (2002). Shock metamorphism of some minerals: Basic introduction and micro-structural observations. Bulletin of the Czech Geological Survey, 77, pp.265-282.

Leake, B.; Woolley, A.; Arps, C; Birch, W; Gilbert, M.C.; Grice, J.; Hawthorne, F.; Kato, A.; Kisch, R; Krivovichev, V.; Linthout, K.; Laird, J.; Mandarino, J.; Maresch, W; Nickel, E.; Rock, N; Schumacher, J.; Smith, D.; Stephenson, N; Ungaretti, L.; Whittaker, E.; Youzhi, G. (1997). Nomenclature of amphiboles: Report of the Subcomittee on amphiboles of the International Mineralogical Association, Comission on new minerals and mineral names. Canadian Mineralogist 35 (1), pp.219-246.

Maier, W.D., Andreoli, M.A.G., McDonald, I., Higgins, M.D., Boyce, A.J., Shukolyukov, A., Lugmair, G.W., Ashwal, L.D., Graser, P., Ripley, E.M. and Hart, R.J. (2006). Discovery of a 25 cm asteroid clast in the giant Morokweng impact crater, South Africa. Nature, 441, pp. 203-206.

Martini, J.E.J. (1978). Coesite and stishovite in the Vredefort dome, South Africa. Nature, 272, pp.715-717.

Masaitis, V.L., Naumov, M.V. and Mashchak, M.S. (1999). Anatomy of the Popigai impact crater, Russia. Special Papers-Geological Society of America, pp.1-18.

McCall, G.J.H. (2009). Half a century of progress in research on terrestrial impact structures: A review. Earth Science Reviews, 92, pp. 99-116.

McDonald, I., Andreoli, M.A.G, Hart, R.J. and Tredoux, M. (2001). Platinum-group elements in the Morokweng impact structure South Africa: Evidence for the impact of a large ordinary chondrite projectile at the Jurassic-Cretaceous boundary, Geochimica et Cosmochimica Acta, vol. 65 (2), pp.299-309.

Melosh H.J. (1989). Impact Cratering: A Geologic Process. Oxford University Press, New York, 245 pp.

Melosh, H.J. (2005). The mechanics of pseudotachylite formation in impact events. In Impact tectonics. Springer Berlin Heidelberg, pp.55-80.

Melosh H.J. and Ivanov B.A. (1999). Impact crater collapse, Annual Review of Earth and Planetary Science, 27, pp.385-415.

Middlemost, E.A. (1994). Naming materials in the magma/igneous rock system. Earth-Science Reviews, 37(3-4), pp.215-224.

Milton, D. J. (1977). Shatter cones-An outstanding problem in shock mechanics. In Impact and Explosion Cratering: Planetary and Terrestrial Implications (Vol. 1), pp.703-714.

Misra, S., and Andreoli, M. A. G. (2012). Post-Impact Dolerite Dykes in the~ 145 Ma Morokweng Crater, South Africa: Impact Related?. In Lunar and Planetary Institute Science Conference Abstracts (Vol. 43), p.1078.

Montanari, A. and Koeberl, C. (2000). Impact Stratigraphy: The Italian Record. Lecture Notes in Earth Sciences, volume 93, Springer Verlag, Heidelberg, 364pp.

Morgan J., Warner M. and Grieve R.A.F. (1997). Size and morphology of the Chicxulub impact crater. Nature, 390, pp.472-476.

Morgan, J.V., Warner, M.R., Collins, G.S., Melosh, H.J. and Christeson, G.L., (2000). Peak-ring formation in large impact craters: Geophysical constraints from Chicxulub. Earth and Planetary Science Letters, 183(3), pp.347-354.

Morgan J. V., Gulick S. P. S., Bralower T., Chenot E., Christeson G., Claeys Ph., Cockell C., Collins G. S., Coolen M. J. L., Ferrière L., Gebhardt C., Goto K., Jones H., Kring D. A., Le Ber E., Lofi J., Long X., Lowery C., Mellett C., Ocampo-Torres R., Osinski G. R., Perez-Cruz L., Pickersgill A., Pölchau M., Rae A., Rasmussen C., Rebolledo-Vieyra M., Riller U., Sato H., Schmitt D. R., Smit J., Tikoo S., Tomioka N., Urrutia-Fucugauchi J., Whalen M., Wittmann A., Yamaguchi K. E., and Zylberman W. (2016). The formation of peak rings in large impact craters. Science, 354 (6314), pp.878–882.

Morimoto, N. (1988). Nomenclature of pyroxenes. Mineralogy and Petrology, 39(1), pp.55-76.

Mthembi, P. (2014). A multi-proxy study of the Kalkkop impact Crater Lake deposits in south-central South Africa: implications for late neogene climate evolution (Doctoral dissertation, University of Cape Town).

Myers, R.E., McCarthy, T.S., Bunyard, M., Cawthorn, R.G., Falatsa, T.M., Hewitt, T., Linton, P., Myers, J.M., Palmer, K.J. and Spencer, R. (1990). Geochemical stratigraphy of the Klipriviersberg Group volcanic rocks. South African Journal of Geology, 93(1), pp.224-238.

Naumov, M. V. (2005). Principal features of impact-generated hydrothermal circulation systems: mineralogical and geochemical evidence. Geofluids, 5(3), pp.165-184.

Nesbitt, H.W. and Young, G.M. (1984). Prediction of some weathering trends of plutonic and volcanic rocks based on thermodynamic and kinetic considerations. Geochimica et Cosmochimica Acta, 48(7), pp.1523-1534.

Ogilvie, P., Gibson, R.L., Reimold, W.U., Deutsch, A. and Hornemann, U. (2011). Experimental investigation of shock metamorphic effects in a metapelitic granulite: The importance of shock impedance contrast between components. Meteoritics and Planetary Science, 46(10), pp.1565-1586.

Ohtani, E., Kimura, Y., Kimura, M., Takata, T., Kondo, T. and Kubo, T. (2004). Formation of high-pressure minerals in shocked L6 chondrite Yamato 791384: constraints on shock conditions and parent body size. Earth and Planetary Science Letters, 227(3), pp.505-515.

O'Neill, C. and Heine, C. (2005). Reconstructing the Wolfe Creek meteorite impact: deep structure of the crater and effects on target rock. Australian Journal of Earth Sciences, 52(4-5), pp.699-709.

Osinski, G. R. (2005). Hydrothermal activity associated with the Ries impact event, Germany. Geofluids, 5(3), pp. 202-220.

Osinski G. R., and Pierazzo E. (2013). Processes and products of impact cratering: An overview. In: Impact Cratering: Processes and Products (Eds. Osinski G. R. and Pierazzo E.). Wiley Blackwell: Oxford. pp. 1–20.

Osinski, G.R. and Ferrière, L. (2016). Shatter cones :(Mis) understood?. Science advances, 2(8), p.e1600616.

Osinski, G.R., Tornabene, L.L. and Grieve, R.A. (2011). Impact ejecta emplacement on terrestrial planets. Earth and Planetary Science Letters, 310(3), pp.167-181.

Ostertag, R. (1983). Shock experiments on feldspar crystals. Journal of Geophysical Research: Solid Earth, 88(S01).

Passchier, C.W. and Trouw, R.A.J. (2005). Microtectonics (2nd edition). Berlin, Sopringer–Verlag.

Pati J. K., Jourdan F., Armstrong R. A., Reimold W. U., and Prakash K. (2010). First SHRIMP U-Pb and 40Ar/39Ar chronological results from melt breccia from the Paleoproterozoic Dhala impact structure, India. In Large meteorite impacts and planetary evolution IV, vol. 465, edited by Gibson R. L. and Reimold W. U. Boulder, Colorado: Geological Society of America Special Paper, pp.571–591.

Philipp, R.P., Lusa, M. and Nardi, L.V. (2008). Petrology of dioritic, tonalitic and trondhjemitic gneisses from Encantadas Complex, Santana da Boa Vista, southernmost Brazil: paleoproterozoic continental-arc magmatism. Anais da Academia Brasileira de Ciências, 80(4), pp.735-748.

Pickersgill A. E., Osinski G. R., and Flemming R. L. (2013). Shock metamorphism in plagioclase from the Mistastin Lake impact structure, Canada. Proceedings, 44th Lunar and Planetary Science Conference. p. 2471.

Pickersgill, A.E., Osinski, G.R. and Flemming, R.L. (2015). Shock effects in plagioclase feldspar from the Mistastin Lake impact structure, Canada. Meteoritics and Planetary Science, 50(9), pp.1546-1561.

Pike R. J. (1985). Some morphologic systematics of complex impact structures. Meteoritics 20, pp.49–68.

Pilkington, M. and Grieve, R.A.F. (1992). The geophysical signature of terrestrial impact craters. Reviews of Geophysics, 30(2), pp.161-181.

Poag C.W., Hutchinson D.R., Colman S.M. and Lee M.W. (1999). Seismic expression of the Chesapeake Bay impact crater: Structural and morphologic refinements based on new seismic data. In Large Meteorite Impacts and Planetary Evolution II (B.O. Dressler and V.L. Sharpton, eds.), Geological Society of America Special Paper, 339, pp.149-164.

Poag C.W., Koeberl C. and Reimold W.U. (2004). The Chesapeake Bay Crater: Geology and Geophysics of a Late Eocene Submarine Impact Structure. Impact Studies Series, Springer, Berlin-Heidelberg, 522 pp.

Poelchau, M. H., and Kenkmann, T. (2010). Feather Features: Microstructural Deformation in the Low-Shock Pressure Regime. In Lunar and Planetary Science Conference (Vol. 41), p. 1987.

Poelchau, M. H., and Kenkmann, T. (2011). Feather features: A low-shock-pressure indicator in quartz. Journal of Geophysical Research: Solid Earth (1978–2012), 116(B2).

Poujol, M. and Anhaeusser, C.R. (2001). The Johannesburg Dome, South Africa: new single zircon U–Pb isotopic evidence for early Archaean granite–greenstone development within the central Kaapvaal Craton. Precambrian Research, 108(1), pp.139-157.

Poujol, M., Robb, L.J., Respaut, J.P. and Anhaeusser, C.R. (1996). 3.07-2.97 Ga greenstone belt formation in the northeastern Kaapvaal Craton; implications for the origin of the Witwatersrand Basin. Economic Geology, 91(8), pp.1455-1461.

Prevec, S.A., Anhaeusser, C.R. and Poujol, M. (2004). Evidence for Archaean lamprophyre from the Kaapvaal Craton, South Africa. South African journal of science, 100(11-12), pp.549-555.

Pybus, G.Q.J. (1995). Geochemical and mineralogical analysis of some mafic intrusions in the Vredefort Dome, Central Witwatersrand Basin. MSc dissertation, University of the Witwatersrand, Johannesburg, South Africa, 282 pp.

Reimold, W.U. (1995). Pseudotachylite in impact structures—generation by friction melting and shock brecciation?: A review and discussion. Earth-Science Reviews, 39(3), pp.247-265.

Reimold, W.U. (1998). Exogenic and endogenic breccias: a discussion of major problematics. Earth-Science Reviews, 43(1), pp.25-47.

Reimold, W.U. and Gibson R.L. (2006). The melt rocks of the Vredefort impact structure- Vredefort Granophyre and pseudotachylitic breccias: Implications for impact cratering and the evolution of the Witwatersrand Basin. Chemie der Erde, 66, pp.1-35.

Reimold, W.U. and Koeberl, C. (2014). Impact structures in Africa: A review. Journal of African Earth Sciences, 93, pp.57-175.

Reimold, W.U., Koeberl, C., Reddering, J.S.V. (1998). The Kalkkop impact crater, Eastern Cape Province, South Africa: stratigraphy, petrography, and geochemistry of the 1992 drillcore, and age. Journal of African Earth Sciences, 26, pp.573–592.

Reimold, W.U., Koeberl, C., Brandstatter, F., Armstrong, R.A., and Bootsman, C. (1999). The Morokweng impact structure, South Africa: Geologic, petrographic and isotopic results, and implications for the size of the structure. In Large Meteorite Impacts and Planetary Evolution II. (B.O. Dressler and V.L. Sharpton, eds.), Geological Society of America Special Paper, 339, pp.61-90.

Reimold, W.U., Armstrong, R.A., and Koeberl, C. (2002). A deep drillcore from the Morokweng impact structure, South Africa: petrography, geochemistry and constrains on the crater size. Earth and Planetary Science Letters, 201, pp. 221-232.

Reimold, W.U., Horton, J.W. and Schmitt, R.T. (2008). Debate about impactite nomenclature-recent problems (abstract #3033). 4th Large Meteorite Impacts and Planetary Evolution Conference, 17–21 August, Vredefort Dome, South Africa.

Renne, P.R., Glen, J.M., Milner, S.C. and Duncan, A.R. (1996). Age of Etendeka flood volcanism and associated intrusions in southwestern Africa. Geology, 24(7), pp.659-662.

Robertson P.B. and Grieve R.A.F. (1977). Shock attenuation at terrestrial impact structures. In Impact and Explosion Cratering (D.J. Roddy, R.O. Pepin and R.B. Merrill, eds.), Pergamon Press, New York, pp. 687-702.

Robertson P.B., Dence M.R. and Vos M.A. (1968). Deformation in rock-forming minerals from Canadian craters. In Shock metamorphism of natural materials (B.M. French and N.M. Short, eds.). Mono Book Corp., Baltimore, pp.433-452.

Rock, N.M.S. (1984). Nature and origin of calc-alkaline lamprophyres: minettes, vogesites, kersantites, and spessartites. Transactions of the Royal Society of Edinburgh: Earth Sciences, 74 (4), pp. 193-227.

Rollinson, H.R. (1993). Using geochemical data, 352 pp.

Rollinson, H.R. (2014). Using geochemical data: evaluation, presentation, interpretation. Routledge.

Rudnick, R.L. and Fountain, D.M. (1995). Nature and composition of the continental crust: a lower crustal perspective. Reviews of geophysics, 33(3), pp.267-309.

Rudnick, R.L. and Gao, S. (2003). Composition of the continental crust. Treatise on geochemistry, 3, p.659.

Rudnick, R.L. and Gao, S. (2004). Composition of the Continental Crust. In: Treatise on Geochemistry. Holland, H.D. and Turekian, K.K. (Editors), Elsevier, Amsterdam. 3, pp.1-64.

Sazonova, L.V., Fel'Dman, V.I., Miljavskij, V.V., Borodina, T.I. and Sokolov, S.N. (2005). Some Peculiarities of Quartz, Biotite and Garnet Transformation in Conditions of Step-like Shock Compression of Crystal Slate. Meteoritics, 45, pp.122-130.

Schmieder, M., and Buchner, E. (2007). Is ‘‘ballen quartz’’diagnostic for shock metamorphism. Geochim. Cosmochim. Acta, 71, A897.

Schmitz, M.D., Bowring, S.A., de Wit, M.J. and Gartz, V. (2004). Subduction and terrane collision stabilize the western Kaapvaal craton tectosphere 2.9 billion years ago. Earth and Planetary Science Letters, 222(2), pp.363-376.

Schultz P. H., Orphal D. L., Miller B., Borden W. F., and Larson S. A. (1981). Multi-ring basin formation: Possible clues from impact cratering calculations. In Proceedings of the Conference on Multi-ring Basins: Formation and Evolution, edited by Schultz P. H. and Merrill R. B. New York: Pergamon Press, pp.181–196.

Schultz, P.H., Zárate, M., Hames, W.E., Harris, R.S., Bunch, T.E., Koeberl, C., Renne, P. and Wittke, J. (2006). The record of Miocene impacts in the Argentine Pampas. Meteoritics and Planetary Science, 41(5), pp.749-771.

Senft, L.E. and Stewart, S.T. (2009). Dynamic fault weakening and the formation of large impact craters. Earth and Planetary Science Letters, 287(3), pp.471-482.

Sharpton, V.L. and Grieve, R.A.F. (1990). Meteorite impact, cryptoexplosion, and shock metamorphism; A perspective on the evidence at the K/T boundary. Geological Society of America Special Papers, 247, pp.301-318.

Sharpton V.L., Dalrymple G.B., Marin L.E., Ryder G., Schuraytz B.C. and Urrutia-Fucugauchi J. (1992). New links between the Chicxulub impact structure and the Cretaceous/Tertiary boundary. Nature, 359, pp.819-821.

Shoemaker, E.M. (1987). Meteor Crater, Arizona. Centennial Field Guide, 2, pp.399-404.

Short, N.M. (1970). Anatomy of a meteorite impact crater: West Hawk Lake, Manitoba, Canada. Geological Society of America Bulletin, 81(3), pp.609-648.Sharpton, V.L. and Grieve, R.A.F., 1990. Meteorite impact, cryptoexplosion, and shock metamorphism; A perspective on the evidence at the K/T boundary. Geological Society of America Special Papers, 247, pp.301-318.

Singleton, A.C., Osinski, G.R., Mc Causland, P.J. and Moser, D.E. (2011). Shock-induced changes in density and porosity in shock-metamorphosed crystalline rocks, Haughton impact structure, Canada. Meteoritics and Planetary Science, 46(11), pp.1774-1786.

Smit, P. J. (1977). Die Geohidrologie in die Opvanggebied van die Moloporivier in die Noordelijke Kalahari, Bloemfontein: University of the Orange Free State. Unpublished Ph. D. Thesis

Spray, J.G. (1992). A physical basis for the frictional melting of some rock-forming minerals. Tectonophysics, 204(3-4), pp.205-221.

Spray, J.G. (1998). Localized shock-and friction-induced melting in response to hypervelocity impact. Geological Society, London, Special Publications, 140(1), pp.195-204.

Spray, J.G. and Thompson, L.M. (2008). Constraints on central uplift structure from the Manicouagan impact crater. Meteoritics and Planetary Science, 43(12), pp.2049-2057.

Spudis, P.D., (2005). The geology of multi-ring impact basins: The moon and other planets (Vol. 8). Cambridge University Press, 263 pp.

Stanley, J.R., Flowers, R.M. and Bell, D.R. (2015). Erosion patterns and mantle sources of topographic change across the southern African Plateau derived from the shallow and deep records of kimberlites. Geochemistry, Geophysics, Geosystems, 16(9), pp.3235-3256.

Stöffler, D. (1972). Deformation and transformation of rock forming minerals by natural and experimental shock processes: I. Behavior of minerals under shock compression. Fortschritte der Mineralogie 49, pp.50–113.

Stöffler, D. (1977). Research drilling Nördlingen 1973: Polymict breccias, crater basement, and cratering model of the Ries impact structure. Geologica Bavarica, 75, pp.443-458.

Stöffler, D. (1982). Terrestrial impact breccias. In Lunar Breccias and Soils and their Meteoritic Analogs, 139pp.

Stöffler, D. (1984). Glasses formed by hypervelocity impact. Journal of Non-Crystalline Solids, 67(1), pp.465-502.

Stöffler, D. and Grieve, R.A.F. (1994). Classification and nomenclature of impact metamorphic rocks: A proposal to the IUGS subcommission on the systematics of metamorphic rocks. In Lunar and Planetary Science Conference, 25, p. 1347.

Stöffler D. and Langenhorst F. (1994). Shock metamorphism of quartz in nature and experiment: I. Basic observation and theory. Meteoritics, 29, pp.155-181.

Stöffler, D., and Reimold, W. U. (2006). "Geologic setting, properties, and classification of terrestrial impact formations." In Papers to First International Conference on Impact Cratering in the Solar System, pp.8-12.

Stöffler, D. and Grieve, R. A. F. (2007) Impactites, Chapter 2.11 in Fettes, D. and Desmons, J. (eds.) Metamorphic Rocks: A Classification and Glossary of Terms, Recommendations of the

International Union of Geological Sciences. Cambridge University Press, Cambridge, United Kingdom, pp.82-92.

Stöffler, D., Keil, K., and Scott E. R. D. (1991). Shock metamorphism of ordinary chondrites. Geochimica et Cosmochimica Acta, 55(12), pp.3845-3867.

Stöffler, D., Reimold, W. U., Jacob, J., Hansen, B. K., Summerson, I. A. T., Artemieva, N. A., and Wünnemann, K. (2013). Ries crater and suevite revisited – Observations and modeling, Part I: Observations. Meteoritics and Planetary Science 48, pp.515-589.

Streckeisen, A. (1974). Classification and nomenclature of plutonic rocks recommendations of the IUGS subcommission on the systematics of igneous rocks. Geologische Rundschau, 63(2), pp.773-786.

Stettler, E.H. (1987). Preliminary interpretation of aeromagnetic and gravity data covering a section of the Thlaping-Thlaro-Ganyesa districts in Bophuthatswana. In Colloquium on African geology, 14, pp. 339-342.

Taylor, S.R. and McLennan, S.M. (1985). The continental crust: its composition and evolution. Blackwells Scientific, Oxford, 312 pp.

Therriault, A. M., Grieve, R. A. F., and Pilkington, M. (2002). The recognition of terrestrial impact structures. Bulletin of the Czech Geological Survey, 77(4), pp.253-263.

Tinker, J., de Wit, M. and Brown, R. (2008a). Mesozoic exhumation of the southern Cape, South Africa, quantified using apatite fission track thermochronology. Tectonophysics, 455(1), pp.77-93.

Tinker, J., de Wit, M. and Brown, R. (2008b). Linking source and sink: evaluating the balance between onshore erosion and offshore sediment accumulation since Gondwana break-up, South Africa. Tectonophysics, 455(1), pp.94-103.

Walraven, F., Martini, J. (1995). Zircon Pb-evaporation age determinations of the Oak Tree Formation, Chuniespoort Group, Transvaal Sequence: implications for Transvaal-Grqualand West basin correlations. South African Journal of Geology, 98, pp.58-67.

Warren, E.A. and Ransom, B. (1992). The influence of analytical error upon the interpretation of chemical variations in clay minerals. Clay Minerals, 27(2), pp.193-209.

White, W.M. (1998). Geochemistry. Wiley-Blackwell:
(http://www.imwa.info/Geochemie/Chapters.html).

Whitehead, J., Spray, J. G., and Grieve, R. A. (2002). Origin of "toasted" quartz in terrestrial impact structures. Geology, 30(5), pp. 431-434.

Wieland, F., Reimold, W.U. and Gibson, R.L. (2006). New observations on shatter cones in the Vredefort impact structure, South Africa, and evaluation of current hypotheses for shatter cone formation. Meteoritics and Planetary Science, 41(11), pp.1737-1759.

Winter, J.D. (2010). Principles of Igneous and Metamorphic Petrology, second edition. Prentice Hall, New Jersey, 702 pp.

Wittmann A., Kenkmann T., Schmitt R. T., and Stoffler D. (2006). Shock-metamorphosed zircon in terrestrial impact craters. Meteoritics and Planetary Science 41, pp.433–454.

Wood, C.A. and Head, J.W. (1976). Comparison of impact basins on Mercury, Mars and the Moon. In Lunar and Planetary Science Conference Proceedings, vol. 7, pp. 3629-3651.

Yanagi, T. (2011). Chemical composition of continental crust and the primitive mantle. In Arc volcano of Japan, Springer, Tokyo, pp.9-17.

Zürcher, L., and Kring, D. A. (2004). Hydrothermal alteration in the core of the Yaxcopoil-1 borehole, Chicxulub impact structure, Mexico. Meteoritics and Planetary Science, 39(7), pp.1199-1221.